

# ACTA DE QUALIFICACIÓ DE LA TESI DOCTORAL

Reunit el tribunal integrat pels sota signants per jutjar la tesi doctoral:

Títol de la tesi: .....

Autor de la tesi: .....

Acorda atorgar la qualificació de:

- No apte
- Aprovat
- Notable
- Excel·lent
- Excel·lent Cum Laude

Barcelona, ..... de/d'..... de .....

El President

El Secretari

.....  
(nom i cognoms)

.....  
(nom i cognoms)

El vocal

El vocal

El vocal

.....  
(nom i cognoms)

.....  
(nom i cognoms)

.....  
(nom i cognoms)





Departament de Teoria  
del Senyal i Comunicacions



UNIVERSITAT POLITÈCNICA DE CATALUNYA

Ph. D. Dissertation

## Marine applications of SAR polarimetry

Gerard Margarit Martín

Thesis Advisor: Jordi J. Mallorquí

Barcelona, April 2007



*A Sara*



“A person who never made a mistake never tried anything new.”

*“La persona que nunca a cometido ningún error es que nunca a probado  
de hacer nada nuevo.”*, Albert Einstein (1879-1955)





# Pròleg

Sembla impossible però la feina que va començar al Setembre del 2002 arriba a la seva fi. Han estat gairebé quatre anys i mig d'intensa activitat que es compilaran en aquest llibre. Tot el que s'ha après en aquest temps no hi està present, només allò que es refereix a la part tècnica de SAR, la més aburrida. La part més divertida i interessant me la reservo per a poder fruit dels records i amics que me'n duc.

Vull començar agraint al meu director de tesis Jordi J. Mallorquí per la seva ajuda en el desenvolupament de la mateixa i per haver-me recolzat en els moments més fluixos. Els seus consells han estat fonamentals per a poder escriure aquestes línies i poder formar-me en un camp totalment desconegut per a mi. El seu esperit crític i la idea de fer la feina ben feta m'han empès a saber reconèixer els meus errors i a aprendre'n d'ells. D'un mode més general, vull agrair al grup de teledetecció de la UPC l'oportunitat que m'ha donat de poder fer la tesi amb ells, en especial al Xavi, Albert, Toni, Carlos i Paco per als bons moments que em passat junts tant a dins com a fora del departament.

Durant el temps que he estat al departament, he tingut molts companys però sobretot he fet un bon grapat d'amics. Entre tots ells, destaco als companys de despatx amb els quals he tingut moments memorables que només recordar-los se't dibuixa un somriure. M'arriscaré a posar els seus noms, tot i assumint que algun d'ells pot caure en l'oblit: Sandra, Marivi, Maria, Luca, Roberto, Juanfer, Pablo, Jordi, Hugo, Txema, Omar, Jesús, Pau i Sergi. També destacar als membres del despatx del pis d'adalt amb els quals mantenim una sana rivalitat. Entre ells, l'Oscar mereix un petit homenatge per als duríssims moments que ha hagut de viure. A més a més, tots aquells projectistes que he tingut el gust de poder dirigir els seus projectes han estat importantíssims per la tasca desenvolupada i també mereixen un bon reconeixement.

Altres amics fora de l'àmbit de la universitat han estat importants. Entre tots i sense cap mena de dubte, hi ha el David amic de la infància i que s'ha convertit en el rival a vèncer en els clàssics partits de Pàdel dels dimarts i dijous. També, hi ha l'Olga, Àngel, Sandra, Alicia i Paco; el grup d'amics de la universitat: el Jose, Dani i Pedro; el Juanma i David d'Alacant i els amics que es varen fer a Italia.

Però sense cap mena de dubte, la meva família es mereix les últimes línies d'aquest pròleg. Per una banda, als meus pares i germà que són un puntal indestructible que sempre estan quan els necessites. Per l'altra banda, els meus tiets, tietes i cosins que sempre els tinc present en el meu cor encara que només ens poguem veure uns pocs dies a l'any.

I per últim i no per això menys important, està la meva estimada Sara que en el més de Setembre de l'any d'enguany es convertirà, si ella vol, en la meva dona. Amb el temps que portem junts m'ha donat el millor de la meva vida. Ella és el telescopi amb el que puc veure les estrelles.

A tots ells, gràcies.

Gerard Margarit Martin

Barcelona, Abril 2007



# Preface

It seems impossible, but the work started in September 2002 is finished. Four years and a half of intense activity followed that now are gathered in this book. Not all I have learned in this time is included, but only those aspects referred to the technical side of SAR, the most boring one. In fact, I reserve the funniest and most interesting part for delighting myself with the memories and friends that I take with me.

I want to start by thanking my thesis advisor, Jordi J. Mallorquí, for helping me on developing this thesis and for supporting me in the hard moments. His advices have been fundamental to write these lines and to educate myself in a totally unknown research area. His critical comments and the idea of pursuing a complete job have led me to know how to recognize my errors and learn from them. In a more general way, I want also to thank the Remote Sensing Laboratory of UPC for giving me the chance to develop my PhD, in special Xavi, Albert, Toni, Carlos and Paco for the good moments that we have shared in and out the department.

Along this time, I have had several colleagues, but specially I have made some good friends. Among them, I emphasize my office's colleagues with who I have shared memorable moments that draw me a smile when they come to my mind. I risk to name these guys, even in the case that someone may be forgotten: Sandra, Marivi, Maria, Luca, Roberto, Juanfer, Pablo, Jordi, Hugo, Txema, Omar, Jesús, Pau i Sergi. I want also to mention the colleagues of the office upstairs with who there is a friendly rivalry. Among them, Oscar deserves a little homage due to the hardest moments that he has had to live. Those people whom I have the pleasure to supervise their final degree projects have been also important for the work carried out and they also deserves appreciation for their efforts.

Other friends out the university have been important. Without any doubt, David, a childhood's friend, is the most important one and he becomes the adversary to win in the Padel games of Tuesdays and Thursdays. There are also Olga, Angel, Sandra, Alicia and Paco; the friends from the university: Jose, Dani and Pedro; Juanma and David from Alacant and the friends that I have made in Italy.

But with any doubt my family deserves the final lines of this preface. On the one hand, my parents and brother who are always an indestructible support that are near me when I really need them. On the other hand, my uncles, aunts and cousins that there are always on my heart, although we can meet together only few days per year.

And last but not least, there is my lovely Sara who in September of the current year will become, if she wishes, my wife. She gave me the best of my live in the time we are together. She is the telescope through whom I can see the stars.

To all them, thank you

Gerard Margarit Martin

Barcelona, Abril 2007



# Acknowledgements

The author want to acknowledge the following institutions:

- MEC (Ministerio de Educación y Ciencia) of Spanish Government for providing financial support in terms of the PhD grant AP2002-2313.
- CICYT (Comisión Interministerial de Ciencia y Tecnología) for providing financial support for part of the research undertaken in this thesis, under the projects TIC2002-04451-C01-01 and TEC2005-06863- C02-01.
- The European Comission (EC) in the scope of the IMPAST (Improving vessel Monitoring through Passive and Active Satellite Technologies) project Q5RS-2001-02266.
- The Institute for the Protection and Security of the Citizen (IPSC) at the EC's Joint Research Center (JRC) in Ispra for accepting the author as a guest scientist for a period of four months (from September 2004 to December 2004) and for providing the author with the EMISAR's dataset used in this work.
- The Microwaves and Radar Institute from the Deustches Zentrum für Luft- und Raumfahrt e.V. (DLR) for providing the author with the ESAR's dataset used in this work.



# Contents

<b>1</b>	<b>Introduction</b>	<b>1</b>
1.1	Marine Environment Monitoring . . . . .	2
1.2	Objectives and Structure of the Thesis . . . . .	3
<b>2</b>	<b>State of the Art in Vessel Monitoring</b>	<b>7</b>
2.1	Transponder-based Systems . . . . .	7
2.2	Passive Remote Sensing . . . . .	10
2.2.1	Optical Sensors . . . . .	10
2.2.2	Acoustic Sensors . . . . .	10
2.3	Synthetic Aperture Radar . . . . .	11
2.3.1	Clustering . . . . .	12
2.3.2	Multidimensional Data . . . . .	14
<b>3</b>	<b>Synthetic Aperture Radar</b>	<b>19</b>
3.1	SAR Operating Principle and Geometry . . . . .	19
3.1.1	Imaging Geometry . . . . .	20
3.1.2	System Resolutions . . . . .	23
3.1.3	Azimuth and Range Ambiguities . . . . .	26
3.1.4	Orbital Imaging . . . . .	28
3.2	SAR Impulse Response . . . . .	29
3.2.1	Bi-dimensional Impulse Response . . . . .	29
3.2.2	A Simple Processing Chain . . . . .	34
3.2.3	SAR Image Distortions . . . . .	36

3.3	SAR Interferometry . . . . .	40
3.3.1	Across-Track Configuration . . . . .	41
3.3.2	Along-Track Configuration . . . . .	44
3.3.3	A Basic Processing Chain . . . . .	47
3.4	Inverse SAR . . . . .	49
3.4.1	Imaging Geometry . . . . .	50
3.4.2	Data Acquisition . . . . .	52
3.4.3	Processing Chain . . . . .	53
3.5	SAR Imaging in Sea Scenarios . . . . .	57
3.5.1	Vessel Motions . . . . .	57
3.5.2	Vessel-Sea Interaction . . . . .	63
<b>4</b>	<b>SAR Polarimetry</b>	<b>65</b>
4.1	Wave Polarization . . . . .	65
4.1.1	Ellipse of Polarization . . . . .	69
4.1.2	Jones Vector Representation . . . . .	72
4.1.3	Stokes Vector Representation . . . . .	73
4.1.4	Polarization Basis Transformation . . . . .	75
4.2	Target Polarimetric Descriptors . . . . .	76
4.2.1	The Sinclair Matrix . . . . .	77
4.2.2	Power Matrices . . . . .	84
4.3	Target Decomposition Theory . . . . .	86
4.3.1	Coherent Target Decompositions . . . . .	87
<b>5</b>	<b>SAR Simulation Environment for Complex Targets</b>	<b>101</b>
5.1	Simulator Overview . . . . .	101
5.2	Electromagnetic Simulation . . . . .	102
5.2.1	High-Frequency Methods . . . . .	105
5.2.2	Discretization Errors . . . . .	110
5.2.3	Bitmap Processing . . . . .	111



5.2.4	Reflection on the Sea . . . . .	112
5.2.5	Control Parameters . . . . .	114
5.3	Target Modeling . . . . .	115
5.4	SAR Signal Simulation . . . . .	120
5.4.1	Simulation of the Imaging Geometry . . . . .	121
5.4.2	Synthesization of the SAR Signal . . . . .	130
5.4.3	Advanced SAR modes . . . . .	134
5.5	Validation . . . . .	137
5.5.1	Influence of the Rendering Error . . . . .	142
<b>6</b>	<b>Vessel Scattering Study</b>	<b>145</b>
6.1	Analysis of Inverse SAR data . . . . .	145
6.1.1	L band . . . . .	147
6.1.2	S band . . . . .	152
6.1.3	C band . . . . .	157
6.1.4	X band . . . . .	160
6.1.5	Additional Tests . . . . .	160
6.2	Analysis of POLSAR data . . . . .	168
6.2.1	C band . . . . .	168
6.2.2	X band . . . . .	173
6.2.3	Influence of the Sea Surface . . . . .	177
6.3	Real Data Analysis . . . . .	184
6.4	Summary . . . . .	193
<b>7</b>	<b>The Unsupervised PaulInSAR Ship Identification Method</b>	<b>195</b>
7.1	Method Description . . . . .	195
7.1.1	The Algorithm . . . . .	196
7.1.2	Classification Patterns . . . . .	198
7.1.3	The Similarity Value . . . . .	200
7.2	Advantages and Limitations of the PaulInSAR Method . . . . .	204

7.3	Analysis with Simulated Data . . . . .	207
7.3.1	First Example . . . . .	208
7.3.2	Performance Evaluation as a Function of System Resolution . . . . .	208
7.3.3	Performance Evaluation as a Function of System Baseline . . . . .	215
7.3.4	Performance Evaluation as a Function of the Geometry of Ships . . . . .	217
7.3.5	Performance Evaluation as a Function of Bearing . . . . .	218
7.3.6	Performance Evaluation with Single Channel Interferometry . . . . .	218
7.4	Summary . . . . .	221
<b>8</b>	<b>SAR Sensor Configurations in Vessel Monitoring</b>	<b>223</b>
8.1	Main Design Parameters . . . . .	223
8.1.1	Basic Formulae . . . . .	224
8.1.2	Comparative Graphs . . . . .	230
8.2	SAR Design . . . . .	236
8.2.1	Standard Mode . . . . .	236
8.2.2	Ping-Pong Mode . . . . .	238
8.3	Summary . . . . .	240
<b>9</b>	<b>Conclusions</b>	<b>241</b>
<b>A</b>	<b>Coordinate Systems</b>	<b>247</b>
A.1	Definition . . . . .	247
A.1.1	POCS . . . . .	247
A.1.2	ECI . . . . .	248
A.1.3	ECEF . . . . .	249
A.1.4	GRECO <sup>®</sup> system . . . . .	249
A.2	Transformation Matrices . . . . .	251
A.2.1	POCS → ECI . . . . .	251
A.2.2	ECI → ECEF . . . . .	252
A.2.3	ECEF → GRECO . . . . .	252

<b>B</b>	<b>Yaw steering in <i>GRECOSAR</i></b>	<b>255</b>
B.1	Compute position . . . . .	255
B.2	Compute fd . . . . .	258
<b>C</b>	<b>Wave model of <i>GRECOSAR</i></b>	<b>261</b>
<b>D</b>	<b>Vessel Scattering Study with Polarimetric ISAR images</b>	<b>265</b>
D.1	L Band . . . . .	265
D.2	S Band . . . . .	275
D.3	C Band . . . . .	291
D.4	X Band . . . . .	304
<b>E</b>	<b>Vessel Scattering Study with Polarimetric SAR images</b>	<b>309</b>
E.1	C Band . . . . .	309
E.2	X Band . . . . .	316
E.2.1	X Band with Motions . . . . .	323
E.2.2	X Band with Sea Surface . . . . .	330
	<b>References</b>	<b>337</b>



# Chapter 1

## Introduction

The sea is a huge source of natural resources. It is estimated that around 30% of food worldwide is obtained from the sea, which implies more than 130 million tonnes. In addition, the sea is the habitat of around 230,000 catalogued marine life-forms (more than 15,000 are marine fish species) that represent the 5% of the global known population. With these numbers, the sea provides a complex ecosystem chain that links the smallest plankton with the largest creature of the Earth, the blue whale. But besides a source of resources, the sea is one of the most important means of transport. Along the history, human beings have used the sea to create important economic ties and to transport passengers and goods. In these days, the globalization of the economy has increased in a huge amount the number of transportation corridors that now connect almost all the countries of the world. Only in Europe, 1500 billion tonne-kilometer (tkm) of goods were transported by sea in 2001, which represented 40% of the total [1]. This implies a great economic activity that employs more than 3 million people and generates as much as 5% of the Europe's Gross Domestic Product (GDP) [1]. The weight of the sea in the economy of a country has an evident social impact as it forces important migration fluxes that increase the pressure over the coastal environment. In this sense, it is estimated that 44% of world's population is within 150 Km of the coast.

Therefore, oceans and coastal areas support a complex and fragile chain that links a high number of biological, sociological and economical factors. In these days, human activity is endangering it and one of the main hot spots is overfishing. Certainly, it is estimated that 80% of world's fisheries are overfished or at least very close to their maximum sustainable production. In 2003, world captures were close to the production of 1996 (90 million tones) showing a marked descendent tendency [2]. Although there are some factors that can explain this production decreasing, for instance "el Niño" meteorological phenomenon, these numbers are the first symptom of overexploitation. If no treated with the proper care, overfishing will become in a near future an important demographical factor. A study carried out by the Food and Agriculture Organization (FAO) in 2003 shows that 16% of world animal protein

consumption by humans comes from the fish [3]. In developing countries, this ratio is more important making the fish to be the primary source of animal protein for 1 billion people.

In this framework, authorities worldwide have become aware about the necessity to protect the marine environment and, in special, fisheries in order to assure the safety and sustenance of human beings. They have promoted a set of laws oriented to preserve the quality and productivity of the environment, and to avoid the depletion of fishing-grounds. But the regulation of the sea needs from fisheries policy that *monitor* the activities of ships.

## 1.1 Marine Environment Monitoring

The necessity of vessel monitoring has engaged the development of different methodologies. First operational solutions appeared in the Nineties when transponders were used to provide tracking capabilities at real-time and independently of the environmental conditions. Example is the Vessel Monitoring System (VMS) from the Directorate of Fisheries and Maritime Affairs of the European Commission (EC), which is mandatory since January 1<sup>st</sup> of 2006 for all the Community vessels [4] [5], or the Automatic Identification System (AIS) from the International Maritime Organization (IMO), which were fully operative by December 31<sup>st</sup> of 2004 [6]. In both cases, the experience have shown that the possibility of such systems to be disconnected becomes an important limitation for vessel monitoring.

As a support, *Remote Sensing* (RS) has been considered due to it provides the autonomy that transponders does not have. In a broad sense, RS is understood as the acquisition of information about an object without being in physical contact with it. In practical terms, it concerns the science that collects, processes and interprets the interaction between electromagnetic (EM) energy and matter. RS technologies can be *passive* (PRS), if the sensors measure the radiation, spontaneous or due to an external source, of the scene; or *active* (ARS), if the sensors measure the scattering/reflection of the energy that they emit.

Regarding passive sensors, the optical ones working at visible wavelengths have been widely used because they take photographs of the scene and, thus, vessels can be identified with high certainty. Example is the SPOT series [7] supporting VMS polls [8]. However, these sensors need favorable sunlight reflection conditions and, thus, they are only useful at day time in cloudless areas. Other passive solutions are infrared instruments or acoustic sensors. The former are able to go through clouds, but they deal with resolutions useless for accurate vessel identification. The latter detect the underwater noise generated by the ship engine [9]. They need a large network of sea sensors that, as transponders, can be disabled.

With active sensors, vessel identification is based on the analysis of the EM reflectivity/scattering properties of vessels. They mainly use microwave radar technology as it is

not affected by any atmospheric phenomena and is independent of day/night cycle. In this field, an advanced coherent 2D technology referred as Synthetic Aperture Radar (SAR) is the most suitable option [10] [11] [12]. It uses the linear motion of the platform to synthesize an antenna aperture larger than the real one. This allows to provide reflectivity images of the scene with an extension of some tens of kilometers and a resolution of few meters. Since the Eighties, SAR has been widely used in applications related to Earth monitoring, for instance landslide, terrain classification or ground targets tracking.

In vessel monitoring, SAR imagery has proven its performances for vessel detection and nowadays there are different algorithms providing notable confidence [13] [14] [15]. They take profit of the fact that vessels normally backscatter more power than the sea and, hence, they appear in SAR images as bright spots. But identifying vessels via their reflectivity properties is not easy as the isolation of geometrical features from signal scattering is not evident. There are two main limitations, namely: 1) the resolution of current SAR systems that appears to be not enough and 2) the distortions of SAR signatures experimented when vessels are imaged at sea. In this field, the so-called *speckle noise* and azimuth spreading are the most important ones. The former is inherent in radar and generates a granular aspect in SAR images that distorts linear features [16] [17]. The latter causes spreading and shifts of the impulse response of scatterers along the azimuth dimension [18] [19].

In this framework, SAR imagery has been under consideration for complementing transponder systems. The results have shown that, despite SAR can help on locating vessels which transponder is out of order, it does not provide sufficient information for trying to identify them in a reliable form [8]. Ancillary information is required for this step and *multidimensional* SAR data can provide it. The concept of multidimensional data refers to the possibility to acquire different SAR images by modifying one or more imaging parameters. In the scope of vessel classification, there are two main options, namely: 1) *SAR polarimetry* (PolSAR) that refers to the usage of the two *polarization components* of the EM wave and 2) *SAR interferometry* (InSAR) derived by combining two SAR images acquired from slightly different positions. On the one hand, the polarization of an EM wave is an intrinsic feature of the wave that helps on identifying specific geometrical features via Target Decomposition (TD) theory [20] [21] [22] [23]. On the other hand, Interferometry takes profit of the phase difference between the two SAR images to retrieve the third dimension of the scene [12] [24].

## 1.2 Objectives and Structure of the Thesis

PolSAR and InSAR have great potentialities for supporting vessel monitoring as they can overcome some of the limitations of classical methods (transponders, PRS and single polarization SAR). Unfortunately, they have not been exploited yet for vessel monitoring due to the difficulties on having at one's disposal data imagery with such characteristics and

reliable ground-truth. Only some preliminary works are currently available for PolSAR imagery [25] [26] pointing out its usefulness in vessel identification. In this framework, the current thesis is focused to evaluate up to which extent PolSAR and InSAR imagery are reliable for vessel monitoring. For such purpose, four main goals are proposed, namely:

1. The development of an efficient SAR simulation environment that provides realistic vessel SAR images and overcomes the current data deficiency related to marine scenarios.
2. The identification of the main polarimetric scattering mechanisms observed in vessel SAR images and how they are related with the geometries of vessels.
3. A performance study of current analysis tools of PolSAR data in vessel classification.
4. The development of a novel and efficient methodology for vessel identification.

The organization of the thesis is as follows.

Chapter 2 reviews the different vessel identification methods currently available. The focus is placed on transponders systems as they provide an operational solution and on SAR imagery as it appears to be an efficient technology for supporting transponder polls. The current techniques for SAR, PolSAR and InSAR are a matter of concern.

Chapter 3 is devoted to review the theory of SAR imagery. In the first part, the operating principle is briefly described highlighting some ideas about image resolutions, signal ambiguities and orbital imaging. Then, a detailed formulation of the SAR impulse response is provided. It allows to emphasize the main characteristics of SAR images as well as the main distortions that can be observed in real scenarios. In the second part, InSAR theory is introduced. A geometrical analysis helps to derive the expressions for the interferometric phase, which are essential for height retrieval. The discussion is supported with some remarks on the different interferometric configurations, the concept of coherence and a basic processing chain. In the third part, the extended Inverse SAR (ISAR) imagery mode is introduced. After a brief review of the operating principle and imaging geometry, the signal impulse response and the related processing chain are highlighted. In the last section of the Chapter, the SAR image distortions observed in sea scenarios are related. The azimuth shifts due to vessel motions will deserve special attention.

Chapter 4 provides a comprehensive overview of the basic principles of radar polarimetry. First of all, those parameters and tools that allow to process and interpret the polarization state of an electromagnetic wave are briefly reviewed. Then, this general theory is adapted to the scattering problem of SAR sensors and the concept of polarimetric descriptors is introduced. The coherent ones will be the main concern as they are specific for vessel SAR images.



Target Decomposition takes the last section of the Chapter. It refers to all those methodologies used for interpreting PolSAR data to infer useful physical/geometrical information. After a brief outline, an in-depth analysis of the coherent theorems is performed.

Chapter 5 describes the simulation environment used in this work. It corresponds to a SAR simulator of complex targets, *GRECOSAR*, developed at UPC that can provide large amounts of data in realistic, perfectly controlled and flexible scenarios. It works with the GRaphical Electromagnetic COmputing (*GRECO*<sup>®</sup>) solver that estimates the Radar Cross Section (RCS) of three-dimensional targets via high-frequency methods. The main steps of the simulator as well as details of its validation are exhaustively related. The influence of different numerical and/or discretization errors in the final results is also evaluated.

Chapter 6 is devoted to analyze the polarimetric scattering properties of vessels in order to shed light on the relation between the reflectivity information and the observed geometry. This work is performed with *GRECOSAR* using both Polarimetric ISAR and PolSAR imagery modes. The former provides centimetric scattering maps that allow to accurately relate the main scattering centers with specific parts of vessels. The latter helps to know how this information is combined in SAR images and if it is possible to isolate particular polarimetric features useful for vessel identification. The simulated data have been generated for different operating frequencies, vessel models and environmental conditions. Real images from airborne sensors have been also used to support the discussion. In all the cases, data interpretation is carried out by means of CTD. The obtained results confirm that the definition of an efficient classification approach based on the scattering properties of ships is possible.

Chapter 7 presents a novel vessel classification method. It works on single-pass polarimetric SAR interferometry and uses the particular scattering properties of vessels to provide an accurate 3D representation of their geometries. The algorithm is exhaustively described in the first part of the Chapter deserving further remarks the generation of the pattern database and the correlation process demanded to obtain a classification decision. The advantages and limitations of the method are analyzed next. In this field, it is shown that the capability to deal with a quantitative measurement of the geometry of vessels becomes an important improvement. The performances of the proposed method are evaluated in last section of the Chapter with *GRECOSAR*. Different vessel models are evaluated within diverse scenarios for a sensor configuration similar to the incoming Tandem TerraSAR-X. The results show that a high rate of positive matches can be retrieved even under adverse environmental conditions.

Chapter 8 evaluates which reliable system design may fulfill the requirements demanded for the proposed vessel identification method. Different combinations are tested and that design providing the best balance between sensor coverage and system resolution is selected.

Chapter 9 summarizes the obtained results and draws the main conclusions which come out from this study.



## Chapter 2

# State of the Art in Vessel Monitoring

The aim of this chapter is to present a bibliographical review of the techniques employed in vessel monitoring. The most relevant concepts related to transponder-based systems are firstly outlined as such systems provide an operational approach to the problem. The usage of RS as a supporting technology to solve the limitations of transponders is then considered. Although different options such optical imagery or acoustic sensors are commented, the focus is placed on SAR sensors because they are well suited for vessel monitoring. The last part of the Chapter is devoted to review the different methods currently available for single-polarimetric SAR, Polarimetric SAR and Interferometric SAR. This analysis will show that vessel monitoring based on SAR is still an open issue that needs from further research.

### 2.1 Transponder-based Systems

The necessity of vessel monitoring has engaged the development of different methodologies oriented to provide the best trade-off among the following items [4]:

1. **Goal:** Vessel monitoring must provide a set of control tools that ensure law compliance, citizen protection and surveillance support. In addition, they should provide evidence that, when required, allow to take legal actions against vessels. These facts must assure with total certainty the presence of the reported vessel at the location and time where the illegal action takes place.
2. **Users:** End users of vessel monitoring systems are official agencies, institutions, governments and authorities that need real time operability.

3. **Outputs:** The system must be able to provide a set of outputs that allow easy data interpretation for quick vessel identification.
4. **Autonomy:** The system should operate in 24/7 format providing the maximum temporal and spatial coverage possible. In this sense, it should be independent of any atmospheric factor and external device that can not be controlled by system managers.
5. **Costs:** The system should be affordable. The different authorities can share the required investments even with the participation of private partnerships.

First attempts in vessel monitoring were at the Eighties when photographic cameras and one-dimensional Ground-Based (GB) radars started to “observe” local areas near the coast [4]. The necessity of larger coverage forced to explore other alternatives and it has not been until the early Nineties when the first reliable operational system was defined. It was based on transponders and it was benefited from the advent of commercial communication satellites and the maturity of Global Positioning System (GPS) devices.

Transponder-based monitoring systems take profit of transponders located on board the vessels to known via satellite communications (mainly INMARSAT [27]) a set of key parameters that allow their location and identification. The main advantage of such systems is the possibility to work at real time, independently of the environmental conditions and with global coverage. The main disadvantage is the possible disconnection, accidentally or intentionally, of such devices that can avoid tracking stations to locate the vessels.

Nowadays, some systems are available, for instance the Vessel Monitoring System (VMS) from the Directorate of Fisheries and Maritime Affairs of the European Commission (EC) and the Automatic Identification System (AIS) from the International Maritime Organization (IMO) [6]. The former is mandatory since January 1<sup>st</sup> of 2006 for all the Community vessels [4] [5] <sup>1</sup> whereas the latter applies for all vessels built after July 1<sup>st</sup> of 2002 and for the ships engaged on international voyages constructed before July 1<sup>st</sup> of 2002 <sup>2</sup>. The operating scheme for VMS is presented in Fig. 2.1 <sup>3</sup>. There, it is shown that each vessel under monitoring has to be equipped with a transponder that sends to the Fisheries Monitoring Centers (FMC) the GPS position, course, speed and identification number via a communication satellite.

The origin of VMS is at 1994 when thirteen European Union (EU) Member States have engaged a set of pilot projects oriented to assess the capabilities of satellite monitoring for

---

<sup>1</sup>VMS has been applied in three phases having different restrictions and exceptions for all them. The provided date corresponds to the most recent one. Third country vessels subjected to VMS are obliged to have an operational satellite tracking device installed on board when they are in Community waters.

<sup>2</sup>As in the case of VMS, there is a timetable for applying the regulations [6]

<sup>3</sup>A similar scheme is valid for AIS. However, in this case the network is improved with GB polling systems (some kind of “Radio Lighthouse”) that are located in strategic locations near the cost with a high density of transportation corridors, for instance the Strait of Gibraltar.



Figure 2.1: VMS scheme.

improving the effectiveness of classical methods [4]. These projects have been carried out due to the recommendations stressed by the Council regulation 2847/93 that proposes the introduction of a continuous monitoring system based on communication satellites. The results were completely satisfactory as they shown that around 20% of maritime surveillance costs (estimated in € 100 million) can be saved [4]. This effectiveness was crucial for the final approval at 1996 of VMS as a reliable control system applicable to Common Fisheries Policy (CFP). Since then, VMS has allowed to develop more effective policies.

But the lessons learnt in real scenarios have shown that the lack of autonomy, totally dependent on the active devices, is an important drawback for detecting those vessels that *want* to be “hidden” from the tracking stations. For such situations, transponders need additional technologies that help on the identification process. In this field, *Remote Sensing* (RS) is a good alternative as it provides the demanded tracking independence that transponders are not able to provide. Current research is showing that the synergy of transponder-based systems and RS technology appears to be the most advisable solution for vessel monitoring.

## 2.2 Passive Remote Sensing

Regarding PRS, optical and acoustic devices have been mostly used in vessel identification.

### 2.2.1 Optical Sensors

Optical sensors work with optical wavelengths, specially at visible bands. Normally, they use the sun light reflection over the bodies to take photographs of the scene. The methodology is quite simple. Remote devices boarded on planes or satellites monitor an area of interest by means of successive photographs. Then, human operators supported by image analysis algorithms analyze the images and determine with total certainty which vessel was at the specified time and location. As with any photograph, image resolutions are high and, for orbital sensors, they can be close to a meter or even lower.

Optical sensors are an important aid for transponder systems. Example is the SPOT series providing supporting imagery for VMS [8]. The SPOT programme started at 1986 when France, Belgium and Sweden collaborated together for developing a high-resolution imagery sensor operating at visible bands [7]. The result was the SPOT-1 satellite, which carried up a visible instrument with a spatial resolution of 10 meters for a swath width of 60 km. Since then, the programme provided five satellites being the SPOT-5 the only one currently operative <sup>4</sup>. This sensor has improved resolutions with 10 meters in multispectral mode and up to 2.5 meters in the panchromatic one. Some snapshots for this last case are presented in Fig. 2.2.

But optical sensors have an important limitation related to weather conditions. Certainly, visible wavelengths are not able to go through clouds and, hence, they provide no information in cloudy areas or in areas with adverse humidity conditions. In addition, the necessity of sunlight reflection makes these systems to be not operative at night. An alternative to these limitations may lie on infrared instruments as they measure the heat radiation. However, their resolutions are limited for vessel monitoring (20 m for the SPOT sensor).

### 2.2.2 Acoustic Sensors

The other PRS option is acoustic sensors that placed within the sea detect the signals that are emitted by the ship due to its interaction with the environment. These methods base the identification in signal patterns and they are widely used in military applications. Most of the research is concentrated to study the underwater noise generated by the engine of

---

<sup>4</sup>The prime contractors are CNES, SPOT Image and Astrium under a partnership that is responsible of system, satellite and commercial designs.



Figure 2.2: Panchromatic SPOT-5 image with a resolution of 2.5 meters for the city of Arzew in Algeria (a). FORMOSAT image with a resolution of 2 meters for the city of Mokpo in the Rep. of South Korea (b). Courtesy of Spot Image.

the ship. Different signal analysis techniques are used, such audio processing applied in the frequency domain [28], nonlinear regularities such as fractal or chaotic features [29] or wavelet transform embedded in neural networks [30]. Other methods focus on studying the magnetic field variation due to vessel motions [31]. For civil monitoring, acoustic sensors are not reliable because they need a large network of sea sensors that, as transponders, can be disabled or damaged<sup>5</sup>. In addition, the measured signal has a high sensitivity with respect to the Signal-to-Noise Ratio (SNR) and suffers from acoustic interferences due to internal waves and/or unexpected changes in water pressure.

## 2.3 Synthetic Aperture Radar

An efficient alternative to optical sensors (the most efficient ones within PRS sensors) are active microwave systems as they are not affected by the atmospheric effects and are independent of the day/night cycle. Active sensors provide radar images of the scene where each pixel gives a complex reflectivity value that can be related with the geometrical structure of the imaged scatterers<sup>6</sup> (see Fig. 2.3). In this way, the pixel distribution can be used to estimate the overall geometry of the imaged targets. Two dimensions define the image, namely: 1) the *azimuth* dimension fixed by the path of the sensor and 2) the *range* dimension fixed by antenna pointing. For vessel monitoring, Synthetic Aperture Radars (SAR) are specially suitable as they can cover areas of some tens of kilometers with resolutions of few

<sup>5</sup>In militar applications, patrol ships boarding the sensors are used. This implies excessive logistic costs for civil applications.

<sup>6</sup>Reflectivity images can be understood as a kind of photographs, but obtained with microwave technology.

meters [10] [11] [12]. SAR sensors are coherent radars able to synthesize an antenna aperture larger than the real one by processing the doppler information induced by the linear motion of the platform. This allows an azimuth resolution independent of the nominal range.

The actual performance of SAR imagery in vessel monitoring has not been completely assessed. Research in this field has shown that reliable vessel detection is possible and, nowadays, there are different algorithms providing notable confidence [13] [14] [15]. They take profit of the fact that vessels normally backscatter more power than the sea and, hence, they appear in SAR images as bright spots. Unfortunately, the same performance is not achieved yet in vessel identification. Different works have pointed out the difficulties on identifying vessels by means of their reflectivity properties [9] [32] [33]. On the one hand, the resolution of current SAR systems appears to be not enough for discriminating vessels from their pixel distribution. On the other hand, the distortions that SAR images can experiment within sea scenarios make this process more difficult. In this field, two main phenomena are normally observed, namely: 1) the *speckle noise* and 2) the azimuth shifts. The former is typical of radar systems and generates a grainy appearance in SAR images that limits the capability to identify linear features as edges [16] [17]. The latter is caused by vessel motions that modify the doppler history of the scene used to focus the image. The result is an important azimuth defocusing and spreading of the vessel signature [18] [34].

### 2.3.1 Clustering

In single SAR (and ISAR) images, the basic methodology for vessel identification is *clustering*. The idea is to segment images into *clusters* according to the reflectivity properties and stochastic behavior of pixels. These clusters are evaluated with a set of pre-defined rules that identify the scattering properties of the monitored ships. According to the rule that better describes the measured distribution of clusters in terms of their position and reflectivity, a classification decision is provided. In some cases, this classification process can be supported by macro-scale features such as ship length and/or bearing as they help to discard noisy clusters. Examples of vessel signatures are provided in Fig. 2.3 where a marine scene between the city of Algeciras (Spain) and the city of Gibraltar (British Overseas Territory) is attached. The image has an azimuth x range extension of 20 x 23 km and has been acquired by RADARSAT with Fine Beam mode (F4) at September 26<sup>th</sup>, 2003 [35]. The colored rectangles locate the vessel signatures zoomed in Fig. 2.4. As observed, these signatures can be clearly isolated from the surrounding clutter presenting different shapes according to their dimensions. In the three cases, it seems that the targets are cargo vessels as the cabin is over the stern.



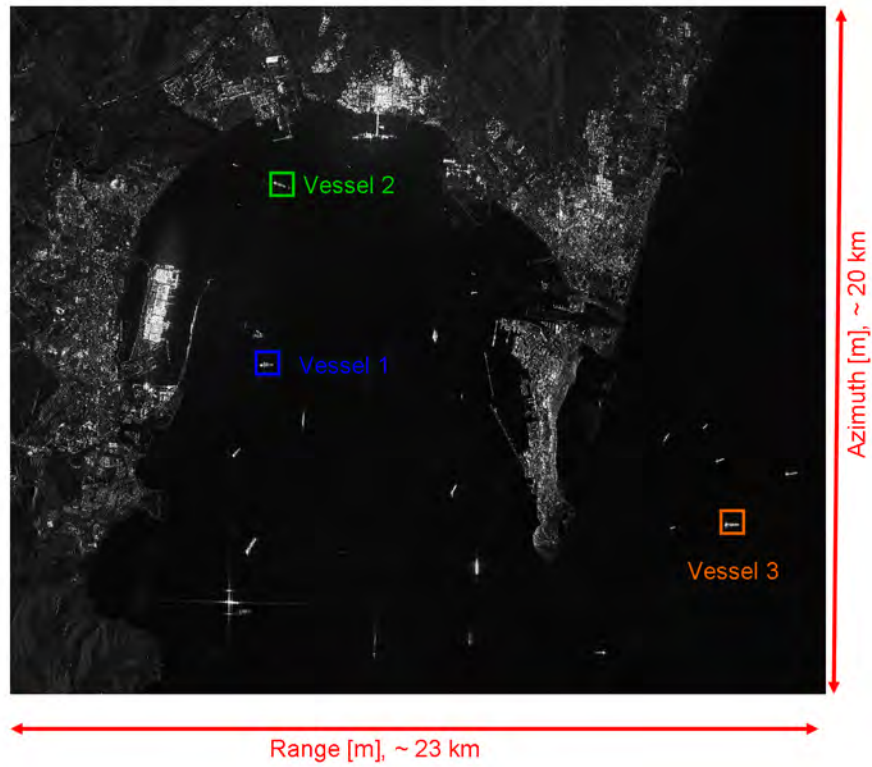


Figure 2.3: Scene of the marine area between Algeciras (Spain) and Gibraltar (UK) acquired by RADARSAT Fine Beam mode (F4) at September 26<sup>th</sup>, 2003. Azimuth x range resolution is 5 x 5 m whereas the incidence angle 35°. The colored rectangles locate the vessel signatures presented in Fig. 2.4.

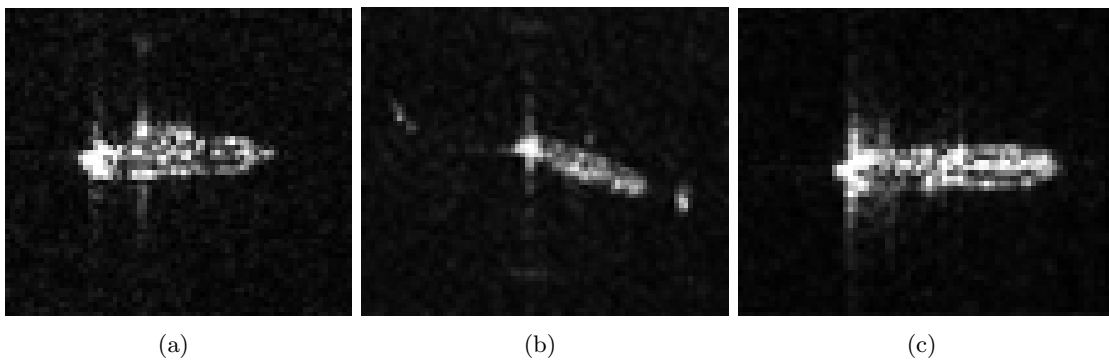


Figure 2.4: Three vessel signatures obtained from the image presented in Fig. 2.3. As before, range dimension is horizontally oriented whereas azimuth dimension vertically oriented. The azimuth x range dimensions for these images are 330 x 380 m (vessel 1) (a), 450 x 525 m (vessel 2) (b) and 320 x 390 m (vessel 3) (c).

The most common and efficient algorithms used to segment the image deal with Neural-Networks (NN). In some works [33], the pixels of clusters are the network inputs, which are arranged in vectorial form after a windowing process. These vectors are correlated with the coefficients of the different intermediate units of NN that have been previously *trained* with a set of reference vectors. The process ends in a set of output values that reflect the confidence or the degree of similarity of the measured signature with respect to the different kind of vessels considered by the algorithm. The highest value provides the classification decision.

In other classifiers, the input network information is based on vessel length and orientation [32] [9]. They assume that vessels are much longer than wider. So, their SAR response is concentrated around a line (*center line*) which orientation is fixed by vessel bearing. The ships accomplishing this premise are termed *line ships*. The operating principle consists on segmenting the image by means of speckle filtering and pixel thresholding. Then, the center line is estimated with the Hough Transform or the least-square-fit method applied through the principal axes. With the cluster distribution, center line and vessel length, the method provides a classification decision based on a set of *production rules*. They establish a set of statements (normally based on “if” decisions) that determine which vessel has been observed provided that some conditions are met or not.

One of the main limitations of clustering is the necessity of a good image segmentation. In some situations, this is not possible because speckle noise can be neither properly filtered nor characterized (see Chapter 3). As a result, two main undesired effects can be observed, namely: 1) the generation of clutter-based clusters that can add uncertainty to NN and 2) the reduction of the available vessel-related pixels that can increase the false alarm rate.

### 2.3.2 Multidimensional Data

In this framework, the interest of embedding SAR imagery in transponder-based vessel monitoring systems has increased in the last years. Example is the IMPAST (*Improving fisheries Monitoring by integrating Passive and Active Satellite based Technologies*) project promoted by EC and oriented to evaluate how SAR imagery can help VMS [8]. The project defined an operational prototype service that integrates VMS polls with SAR-based vessel detection working at near real-time. The results have shown that, despite SAR can reliably locate those vessels which transponder is out of order, it does not support a reliable identification. Ancillary information is required for this step and *multidimensional* SAR data can provide it.

The concept of multidimensional data is based on the idea of diversity and it refers to the possibility to acquire SAR images from different “points of view”, that is, by modifying one or more imaging parameters among acquisitions. This can allow to measure additional physical

and/or geometrical characteristics that can provide more reliability or improve the available information in the identification process. In SAR imagery, there are three main options, namely: 1) *multi-frequency SAR* or the acquisition of SAR images at diverse frequencies, 2) Polarimetric SAR (PolSAR) that exploits the polarimetric information of the EM wave and 3) Interferometric SAR (InSAR) that combines a master and slave acquisition separated by a fixed baseline. In the scope of vessel classification, PolSAR and InSAR modes are the most suitable ones. In fact, they will be the main concern of the current thesis.

The polarization of an EM wave is an intrinsic feature that describes the vector field of the wave. It is defined by means of two orthogonal components, namely: 1) *horizontal* (H) and 2) *vertical* (V). Each one of these components isolates particular scattering properties and, thus, allows to infer different details of the observed geometry. PolSAR has been widely used in classification applications related to complex targets as well as to extended surfaces, such as land, oceans, forest, . . . [20] [21] [22] [23]. Regarding interferometry, the phase difference between the two SAR images is used to retrieve the third dimension of the scene [12] [24]. In this case, Earth's surface monitoring applications, for instance subsidence or Digital Elevation Maps (DEM) generation, have become benefited. In vessel identification, the possibility to deal with the three-dimensional shape of the structure of ships can be an important advantage.

### Simulation Environments

Despite their potentialities for supporting transponder-based identification systems, neither PolSAR nor InSAR modes have been exploited yet for vessel monitoring due to the lack of useful data. On the one hand, there are in these days few air- or space-borne sensors providing PolSAR and InSAR data under an operational basis<sup>7</sup>. Most of them belong to official agencies (due to the costs and the scientific purposes) and this restricts data availability. On the other hand, large measurement campaigns must be carried out for developing/testing new methods. This is not easy in real scenarios as besides the excessive logistic costs, it is necessary to control the environment for retrieving accurate ground-truth.

In this framework, an option for this research area lies on simulated environments as they allow to deal with high amounts of images in flexible and controlled scenarios. The idea is to reproduce in a computer vessel SAR signatures similar to those acquired in real scenarios. Nowadays, there are different codes available in the literature. Most of them are focused to work with distributed targets [39] [40] [41] or to use different Radar Cross Section (RCS) prediction tools to derive Inverse SAR (ISAR) data [42] [43]. The former are oriented to ocean simulation and they make some simplifications that would not properly work for complex targets, for instance the no consideration of diffraction and multiple scattering. The

---

<sup>7</sup>Most of the currently operative sensors are boarded in airborne platforms. Examples are the Danish EMISAR sensor [36], the German E-SAR sensor [37] or the French RAMSES sensor [38].

latter are mainly designed to isolate scattering centers for military applications.

To author's knowledge, none of the currently available numerical tools is suitable for evaluating vessels within the sea or, if available, they are not accessible. With the aim to solve this deficit and to provide a new framework for making progress in PolSAR and InSAR applied to vessel monitoring, Chapter 5 presents a new proposal that may fulfill this requirement. It corresponds to a SAR simulator developed at UPC (*GRECOSAR*) [19] [44] and based on the UPC's GRaphical Electromagnetic COmputing (*GRECO*<sup>®</sup>) solver [45] [46] [47]. It works in the frequency domain and estimates via high-frequency methods the RCS of three-dimensional complex targets. Tests carried out in complex scenarios have validated its proper performance [34] [48] [49]. In this thesis, *GRECOSAR* has been exploited to analyze the potentialities of PolSAR and InSAR imagery in vessel classification.

## PolSAR

Regarding polarimetry, current research is focused to the analysis of PolSAR data via Coherent Target Decompositions (CTD). These theorems decompose the complex polarimetric behavior of each pixel in terms of canonic scattering mechanisms. These mechanisms are normally related to some structures common in most vessels and, hence, their distribution in the image can be useful for achieving a reasonable vessel discrimination. The potentialities of CTD in vessel classification have been studied in some works [25] [26]. They mainly use the so-called Symmetric Scattering Characterization Method (SSCM) to interpret the main scattering centers with mapping points in the surface of the Poincaré sphere. The relative distance of the resulting points with respect to the location of reference scatterers (trihedral, dihedral, ...) is used to characterize the observed mechanisms. The analysis of real data obtained from the Canadian airborne C/X band sensor [50] has shown that it is possible to find within the structure of vessels *permanent quasi-symmetric scatterers* (PSS). Such scatterers correspond to well-defined parts of vessels that have associated a high RCS and an angular response similar to the trihedral one. So, they can be easily recognized in SAR images for a range of bearing and incidence values around  $30^\circ$  and, according to their distribution along vessel structure, they may provide a feasible identification of the observed vessel.

The validation and extension of the previous results will be a matter of concern in Chapter 6. There, a scattering study that describes the polarimetric behavior of vessels and evaluates the performance of CTD for the widest observation conditions possible will be presented. Two main items will be studied, namely: 1) if and how a classification algorithm can be developed with CTD and 2), if possible, how this new algorithm would help to improve the ratio of positive matches. Both issues are very important because CTD can only support the classification decision with a qualitative estimate, rather than by inferring quantitative physical and/or geometrical parameters.

## InSAR

The application of SAR interferometry in complex target classification is at the primary stages of development. Only one work (to author's knowledge) has been recently proposed [51] [52]. It is oriented to generate well-focused 3D images of moving targets with an almost null sensitivity with respect to the motions that they can experiment. If available, this product will be extremely useful for vessel classification. For such purpose, this approach considers a single-pass interferometric system built by one master and two slave antennas. One slave antenna is located along path dimension (along-track) whereas the other two in the perpendicular direction to it (across-track). The method deals with an acquisition system similar to the circular spotlight mode adopted for ISAR imagery. The idea is to retrieve the angular motion of scatterers in the cross-range plane (the plane perpendicular to the range dimension) and isolate their position. With this information and the range location, three SAR images can be generated providing the scatter distribution in each of the three reference planes.

Simulated images have shown promising results for this approach as a reasonable 3D reconstruction of the imaged targets can be obtained. However, there are some limitations. First, the proposed acquisition system needs the target to be in linear motion within a disk of known radius (in order to simulate the ISAR-like circular spotlight imagery mode). This implies that all the scatterers of the target move together in the same way with neither rotational nor translational motions. For ground targets, this simplification is reasonable as it is adapted to the expected motions. But for vessels it does not seem quite suitable as the presence of complex motions will break the signal model. Another problem lies on the necessity to know *a priori* the number of echoes expected to receive, i.e. the number of significant scattering centers of the target. This is, in practice, unreliable, except for the case that an specific target have to be monitored. Besides the problems related with the used methodology, the simulations appear to be excessively simple. Certainly, the scatterers are assumed to be isolated elements with the same scattering properties. This implies that the echoes received by the antennas correspond *exclusively* to the scatterers with no influence of multi-reflection, diffraction or masking phenomena. As observed in Chapter 6, this is not accurate according to the scattering properties of vessels.

In this thesis, InSAR for vessel classification is tackled in a simpler way. One slave antenna in single-pass operating mode is used. The idea is to measure directly the height of the main scattering centers in vessels and retrieve a three-dimensional representation of the observed geometry. As observed in Chapter 7, this simple configuration can lead to a new vessel classification proposal based on the results obtained in the scattering study outlined in Chapter 6. The exhaustive tests performed in Chapter 7 show that the combination of polarimetric data analysis performed via CTD with typical height retrieval techniques may provide promising results.



## Chapter 3

# Synthetic Aperture Radar

This chapter reviews the basic theory of SAR systems. In the first part, the operating principle and imaging geometry is explained placing the focus on image resolutions, signal ambiguities and orbital imaging. Then, the impulse response of SAR systems is mathematically formulated. This allows to introduce a simple processing chain that relates how SAR images are obtained from signal measurements and which are the most typical distortions expected for real scenarios. In the third part of the Chapter, the extended SAR imagery modes, SAR interferometry and Inverse SAR, are explained. In both cases, the operating principle, imaging geometry and processing chain are described. The Chapter ends by pointing out the typical distortions that SAR images can experiment in marine scenarios. The azimuth shifts caused by vessel motions will be the main concern.

### 3.1 SAR Operating Principle and Geometry

Synthetic Aperture Radar (SAR) is a coherent active microwave remote sensing technique able to provide bi-dimensional reflectivity images of large areas <sup>1</sup> with fine resolutions, normally on the order of few meters [53], [11], [10] [12]. This short definition compiles a large and complex theoretical framework that is the result of an intensive research work started around the fifties of the last century and still under development. The large datasets of SAR images collected along the last thirty years have contributed to achieve a significant progress in a wide range of applications related to Earth monitoring.

The key concept of SAR imagery is the synthesization of an antenna aperture larger than

---

<sup>1</sup>According to the system configuration, the imaged area can have an extension of 500 Km. This is the case of the Canadian RADARSAT or the ESA's ENVISAT sensors operating in ScanSAR mode. Other sensors, such as the ESA's ERS series, have a nominal value of 100 km. Incoming systems with advanced features and higher resolutions drops notably the effective area around 20 or at maximum 30 km.

the real one that allows to achieve an azimuth resolution equal to half the antenna length. Such value is an important improvement in relation to any conventional pulsed bi-dimensional *Real Aperture Radar* (RAR) where the nominal resolution is directly proportional to the system range. This makes in practice that usual values become limited at best to some tens of meters<sup>2</sup>. In order to achieve the aperture synthesization effect, SAR platforms are in motion along a convenient path. This forces each scatter of the scene to have a different and particular doppler history according to their location. In this way, scatter discrimination is achieved by processing the received signal in terms of the doppler information.

The SAR methodology is the next in line from the former works in doppler beam sharpening developed by Carl Wiley in 1954 [54] where the targets were distinguished according to their different iso-doppler positions. After that experiment most of the work were developed by the U.S. Department of Defense and it is still classified. It has not been until the late Sixties and early Seventies when NASA started to sponsor the usage of SAR systems for civil applications. First operational systems were boarded on a plane at 1966 and on a satellite at 1978 within the SEASAT-A mission. Since then, the proliferation of SAR systems were really high with the development of several airborne, orbital and, even, interplanetary missions (for instance, the Venus Radar Mapper in the Magellan mission to Venus or the Titan Radar Mapper embedded in the Huygens-Cassini mission to Saturn). Examples of airborne sensors are the Danish EMISAR [36], the Canadian CCRS C/X [50] or the German ESAR [37]. Regarding orbital missions, the ESA'S ENVISAT [55], the ESA'S ERS series [56] and the Canadian RADARSAT [35] are maybe the most popular sensors currently operative. The near future for SAR technology is quite promising with the launching of new missions with improved performances that will allow to make notably progress in a wide range of research areas. Examples are the Japanese ALOS-PALSAR [57], German TerraSAR-X mission [58] or the second version of RADARSAT.

### 3.1.1 Imaging Geometry

The basic imaging acquisition scheme is the scenario presented in Fig. 3.1. It corresponds to a standard *stripmode* configuration where the sensor is moving along the azimuth direction with an ideal linear path<sup>3</sup> and almost constant velocity  $\overrightarrow{V}_{plat}$ . In this configuration, the antenna beam has an angular resolution of  $\Delta\Omega$  degrees and points to a particular area of the Earth's surface with a fixed *squint* angle  $\beta$ . This angle measures the orientation of the pointing direction with respect to the perpendicular of the azimuth line. For  $\beta = 0^\circ$ , we have the so-called *boresight* geometry whereas for the other values the *squinted* one. The positive

<sup>2</sup>For orbital sensors, the resolution value is at least two orders of magnitudes higher

<sup>3</sup>The linear path is widely used when introducing the SAR concepts as makes SAR processing simpler. In practice, such situation is not normally true due to irregularities in platform motion. However, such drawbacks can be almost compensated with advanced techniques and, then, the linear approximation can be considered good enough.



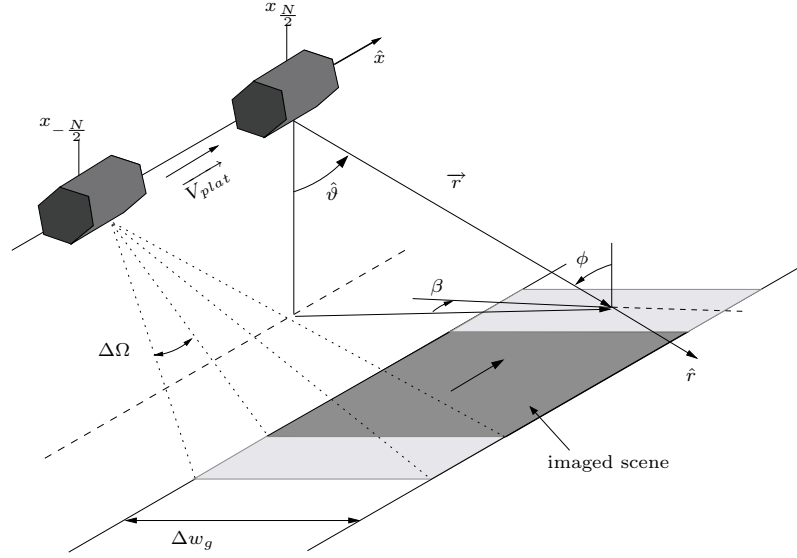


Figure 3.1: Scheme of the acquisition geometry for the standard strip mode

and negative sign of  $\beta$  allows to distinguish between forward and backward configurations.

The sensor-to-target pointing direction is termed *range* direction and its projection over the ground, *ground-range* direction. The angle  $\phi$  measuring its inclination with respect to the vertical is the *incidence* angle. Such angle should not be equal to zero, i.e. the antenna should never point to the *nadir* direction, as otherwise it would not be possible to discriminate the different scatters that could be located in the same iso-doppler line at both sides of the nadir. The location of the scatters is fixed by the cylindrical coordinate system  $(\hat{x}, \hat{r}, \hat{\vartheta})$  depicted at Fig. 3.1 as it is the reference system that better fits the imaging geometry.

The width of the imaged scene in range  $\Delta w_g$  is termed *swath width* and it mainly depends on the direction and elevation width of the mainlobe of the antenna. In azimuth, the scene has not a fixed length and it is normally limited by the storage and processing capabilities of the sensor. The interval time where a particular scatterer is within the radar footprint is the *observation time* and it is defined as

$$t_{obs} = \frac{\Delta\Omega \cdot |\vec{r}|}{|\vec{V}_{plat}|} \approx \frac{\lambda \cdot r_o}{L \cdot V_{plat}} \quad (3.1)$$

where  $\lambda$  is the operating wavelength and  $L$  the effective antenna length in the azimuth direction.

In addition to the stripmode geometry, SAR sensors can adopt other geometries that

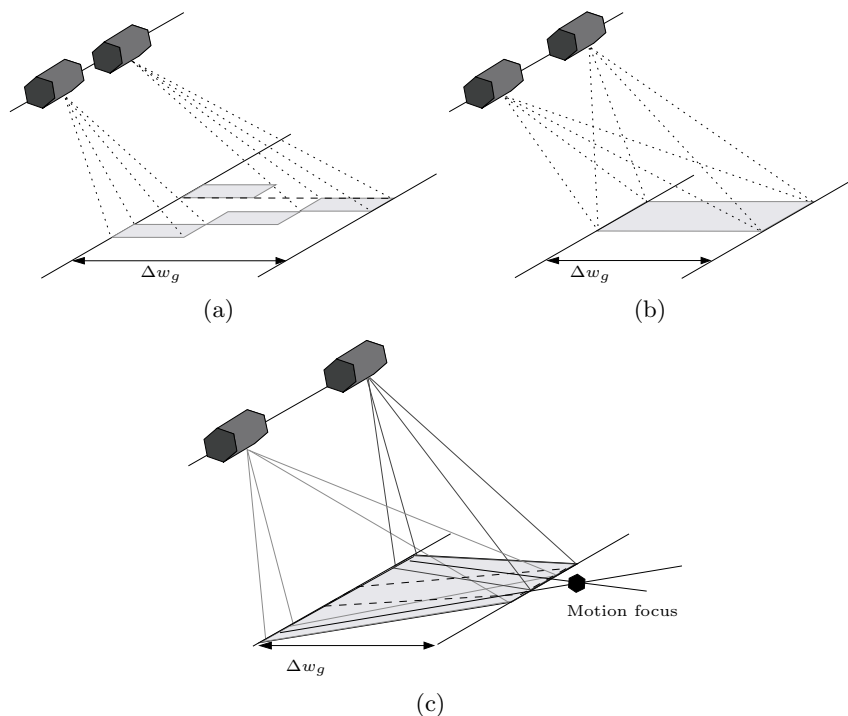


Figure 3.2: Scheme of the ScanSAR (a) Spotlight (b) and Sliding Spotlight (c) acquisition modes

preserve the SAR operating principle and add some interesting features. The most important ones are the so-called *ScanSAR* and *Spotlight* (see Fig. 3.2). On the one hand, the ScanSAR imagery mode takes different subswaths along range direction in order to increase the swath width (see Fig. 3.2(a)) [59] [60] [61]. This avoids the fully synthetic aperture length to be available to each scatterer of the scene dropping, thus, azimuth resolution. On the other hand, the Spotlight imagery mode steers the antenna beam around the central point of the imaged area in order to increase the azimuth resolution (see Fig. 3.2(b)) [62]. However, this operation limits the azimuth coverage as it is fixed by the azimuth width of the mainlobe of the antenna. A balance between both items can be achieved by moving the focus of the steering motion away in range (at the infinite, the stripmap mode is synthesized). This operating mode is termed *sliding spotlight* (see Fig. 3.2(c)) and it is embedded as experimental mode in the incoming German TerraSAR-X sensor [63].

Independently on the acquisition geometry, SAR sensors are digital systems and, then, the signal related to both imaging directions must be sampled before processing. For such purpose, SAR sensors operate with signal pulses sampled according to the sampling frequency  $f_{SF}$  of the on-board receiving channel. The separation among pulses is normally constant and fixed by the inverse of the *Pulse Repetition Frequency* (PRF)  $f_{PRF}$ . Beyond this simple scheme, it is possible to use complex configurations that allow, for example, to receive the echo of a pulse after  $n$  subsequent pulses or modify the PRF along the aperture.

### 3.1.2 System Resolutions

The resolution stands for the sensor's capability to discriminate different nearby targets. It indicates the minimum distance that such targets have to be separated in any imaging direction in order to be properly differentiated in the final image. As commented previously, the main advantage of SAR systems lies on the improvement of the azimuth resolution whereas in the range direction they behave as any common radar system.

#### Range resolution

The *range* resolution is normally referred as

$$\delta_r = \frac{c\tau}{2} = \frac{c}{2\Delta f} \quad (3.2)$$

where  $c$  is the speed of light in the vacuum,  $\tau$  the time length of the emitted pulse and  $\Delta f$  the signal bandwidth. In normal pulses, the time extension is inversely proportional to the signal bandwidth and, hence, range resolution can only be improved by shortening the pulse. But shortening the pulse implies to increase the peak power as the mean power prescribed to the sensor has to be balanced according to signal-to-noise considerations. In practice, high peak powers are quite rare and, then, range resolution becomes greatly limited.

To solve this drawback, *pulse compression* techniques [64] [65] have been widely used. The idea is to modulate the pulses in such a way that high bandwidths and, thus, high resolution can be achieved with large pulse lengths. In radar and, more specifically, SAR systems, the commonest modulation is the *chirp* one that emits pulses with a linear time dependence in the instantaneous frequency. In a mathematical form, the unitary chirp pulse in baseband is

$$S_{chirp} = e^{j2\pi\alpha\frac{t^2}{2}} \text{rect}\left[\frac{t}{\tau}\right] \quad (3.3)$$

where  $\alpha$  is the *chirp rate*,  $\text{rect}[\dots]$  is a rectangular pulse of length  $\tau$  and  $0 < t < \tau$ . According to the sign of  $\alpha$ , *up-* ( $\alpha > 0$ ) or *down-chirp* ( $\alpha < 0$ ) pulses can be generated. In Fig. 3.3, a snapshot for the first case is presented.

In the previous equation, the derivative of the complex phase along time

$$f_{inst}(t) = \frac{d\Theta}{2\pi dt} = \alpha t \quad (3.4)$$

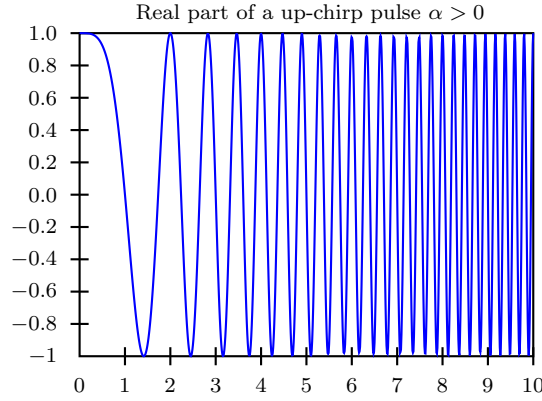


Figure 3.3: Snapshot of a the real part of a up-chirp pulse for  $\alpha > 0$ . Arbitrary units.

points out the linear dependence of the instantaneous frequency with respect to the emission time. From this equation, the signal bandwidth results  $\Delta f = \alpha\tau$ , which now is directly proportional to the pulse time length. This represents the main advantage of the chirp modulation as

$$\delta_r = \frac{c}{2\Delta f} = \frac{c}{2\alpha\tau} \quad (3.5)$$

and, then, the available bandwidth becomes the only constraint for the range resolution.

### Azimuth resolution

The azimuth resolution is defined by

$$\delta_{azi}^{system} = \Delta\Omega^{system} \cdot r_o = \frac{\lambda \cdot r_o}{L^{system}} \quad (3.6)$$

where  $\Delta\Omega^{system}$  is the angular resolution of the system and  $L^{system}$  the effective antenna length in the along-track direction. In RAR systems,  $L^{system} = L$  and, then, the range dependence of this formula greatly restricts the possible resolution values reachable by the sensor. In the case that high resolutions are demanded (in the range of 1-10 m), antenna lengths as long as some tens of meters will be at best required. But with the synthesization of an aperture larger than the real one, SAR systems overcome this limitation. Certainly,  $L^{system}$  is now equal to (see Fig. 3.4)

$$L^{system} = \frac{\lambda r_o}{L_{real}} \quad (3.7)$$

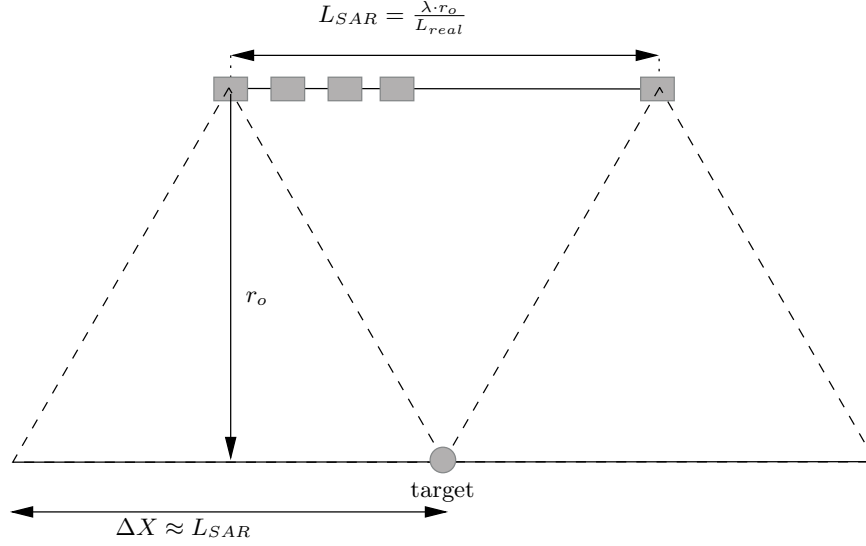


Figure 3.4: Azimuth geometry of a SAR system performing an antenna array configuration

and, then, Equation 3.6 becomes range independent

$$\delta_{azi} = \delta_{azi}^{SAR} = \Delta\Omega^{SAR} \cdot r_o = \frac{\lambda \cdot r_o}{2L^{SAR}} = \frac{L}{2} \quad (3.8)$$

In this formula, the factor 2 is caused by the doubling of phase shifts associated with the two-way path of the received signals. Despite this formula indicates that the azimuth resolution only depends on the effective azimuth antenna length, there are other parameters that can indirectly influence on the design value. Typical values range from 25 to 1 m.

Another classical way to introduce the azimuth resolution lies on the usage of the doppler frequency expression with respect to the time. Such formula takes the general form of [11]

$$f_D(t) = \frac{1}{2\pi} \frac{\partial \Theta(t)}{\partial t} = f_d + f_r \cdot t = -\frac{2V_{plat}}{\lambda} \sin \beta - \frac{2V_{plat}^2}{\lambda r_o} \cos \beta^3 \cdot t \quad (3.9)$$

where  $\Theta(t)$  stands for the phase term of the azimuth propagation factor,  $f_d$  is the constant doppler term so-called *doppler centroid* and  $f_r$  is the doppler rate term so-called *doppler rate*. Under the assumption of low squint angles, the doppler frequency associated with a particular target that at  $t = t_o$  is at the center of the antenna beam is

$$f_D(t_o) = -\frac{2V_{plat}}{\lambda r_o} \cdot x_o \quad (3.10)$$

with  $x_o = V_{plat} \cdot t_o$ . If this expression is derived along the x-coordinate (azimuth direction), it follows

$$\delta f_D = -\frac{2V_{plat}}{\lambda r_o} \cdot \delta x \quad (3.11)$$

From basic signal processing theory, the doppler resolution  $\delta f_D$  is the inverse of the observation time  $t_{obs}$  as this parameter fixes the length of the rectangular pulse modulating the signal acquired along the azimuth direction. This allows to solve Equation 3.11 with Equation 3.1 and, thus, the final value  $\delta x = \frac{L}{2}$  is also obtained. It is worth noting that for very large squints the azimuth resolution is degraded by a factor of  $\cos \beta$ . In practice, it can be considered that Equation 3.8 applies.

### 3.1.3 Azimuth and Range Ambiguities

In SAR imagery, the emitted signal can be *ambiguously* recorded generating distortions in the final image. Two kind of ambiguities can be distinguished: *Range ambiguities* and *Azimuth ambiguities*.

On the one hand, range ambiguities appear when the echo of a pulse overlap the subsequent emitted pulses. This is caused by the time interval between two consecutive pulses, which is smaller than the time extension of each echo. To avoid this interference, it is necessary that PRF be smaller than <sup>4</sup>

$$f_{PRF} = \frac{1}{T} \leq \frac{1}{2 \cdot (\tau + \frac{\Delta w}{c})} \quad (3.12)$$

where  $\tau$  is the time pulse length and  $\Delta w = \Delta w_g \sin \phi$ .  $\Delta w_g$  is the swath width and it is expressed in terms of the effective antenna length in range  $L_r$  as

$$\Delta w_g = \frac{r_o \lambda}{L_r \cos \phi} \quad (3.13)$$

On the other hand, azimuth ambiguities are related to the overlapping of the azimuth SAR spectrum when the received signal does not accomplish the Nyquist criteria. The particular acquisition scheme of SAR sensors make the azimuth spectrum (also referred as doppler spectrum) to be a periodic collection of single spectra separated  $f_{PRF}$ . Due to the

---

<sup>4</sup>This value represents the upper bound of PRF for a given imaging geometry. In advanced timing configurations, the reception of a pulse echo can be synchronized some pulse after its emission. This helps to increase this maximum value.

doppler frequencies generated by the platform motion, these spectra expand increasing their bandwidths up to the so-called *doppler bandwidth*  $\Delta f_D = f_r \cdot t_{obs}$ . In the case that this bandwidth is higher than PRF, then the single spectra overlap causing azimuth ambiguities. This interference is avoided if

$$\frac{2V_{plat}}{L_a} \leq f_{PRF} \quad (3.14)$$

where  $L_a = L$  is the effective antenna length in azimuth <sup>5</sup>. In some cases, azimuth ambiguities are solved by limiting the doppler bandwidth at the processing chain degrading, thus, the azimuth resolution.

The combination of Equations 3.12 and 3.14 defines the range of useful PRF values

$$\frac{2V_{plat}}{L_a} \leq f_{PRF} \leq \frac{1}{2 \cdot \left(\tau + \frac{\Delta w}{c}\right)} \quad (3.15)$$

Normally, both PRF bounds are used to fix a minimum value for the effective area of the antenna. Certainly, as the minimum PRF threshold must be always lower than the maximum one and assuming that  $\tau \ll \frac{\Delta w}{c}$ , the following inequality results

$$L_r L \geq \frac{4V_{plat} r_o \lambda}{c} \tan \phi \quad (3.16)$$

Note that this formula indirectly fixes a minimum bound for the azimuth antenna length and, in turn, for the azimuth resolution. When dealing with polarimetric systems, the previous equation become more restrictive. In this case, timing schemes are more complex because at best two measures have to be done for the slot time of one pulse. This modifies the upper PRF bound and, consequently, the value of the swath coverage. In Chapter 8, a further analysis of this issue within marine environments is provided.

In some cases, the azimuth and range ambiguity terms are used to refer to the displacement of *ghost targets* in unexpected areas, for instance the presence of high reflectivity targets in low reflectivity areas. This phenomenon is caused by the interferant signals collected by the secondary lobes of the radiation pattern [66]. A proper antenna pattern design mostly solves this problem. Two important parameters are defined for such purpose, namely: the *Range Ambiguity to Signal Ratio* (RASR) and the *Azimuth Ambiguity to Signal Ratio* (AASR). They relate for each imaging dimension the mean power of the signals detected by secondary lobes with respect to the mean power of the main lobe [11], [67].

<sup>5</sup>Low squint angles have been assumed. For large squints, a factor of  $\cos \beta$  is required.

### 3.1.4 Orbital Imaging

Up to now, the imaging geometry has been assumed to be associated with an airborne sensor. The migration to the orbital case is not excessively complex as the same concepts apply and only some minor considerations have to be taken into account. The most important ones are, namely: 1) the Earth rotational effects that modify the radial velocity of targets and, thus, the associated doppler history, 2) the fact that the scene is not planar and 3) the non-linear platform path irregularities that break with the linear path assumption.

Taking attention on the first phenomenon, it can be shown that Earth rotation replaces the previous expressions for the doppler centroid and doppler rate terms by [11]

$$f_d = \frac{2}{\lambda r_o} (\sin \varphi_o \cos \vartheta_o R_T v_{eff} - \cos \varphi_o \sin \vartheta_o (R_T + h) v_\vartheta) \quad (3.17)$$

$$f_r = \frac{2K_v v_{eff}^2}{\lambda r_o} \left[ \cos \varphi_o - \left( \frac{\lambda f_d}{2\sqrt{K_v} v_{eff}} \right)^2 \right] \quad (3.18)$$

where

$$v_{eff} = V_{plat} - \frac{v_\varphi}{K_v} \quad (3.19)$$

$$K_v = \frac{R_T}{R_T + h} \cos \vartheta_o \quad (3.20)$$

with  $v_\varphi = R_T \Omega \cos l \sin i$  and  $v_\theta = R_T \Omega \cos l \cos i$  being the azimuth and range velocity component of the imaged target due to the Earth rotation,  $\varphi_o$  the antenna squint angle,  $\vartheta_o$  the range antenna pointing angle also referred as *look-angle*,  $R_T$  the equatorial Earth range,  $h$  the nominal platform height,  $l$  the target latitude,  $i$  the orbit inclination and  $\Omega$  the Earth's angular velocity. As observed, the value of  $f_D$  can vary during acquisition time according to the local elevation and squint angle. This complex behavior is very difficult to be estimated in the SAR processing step and, consequently, it can lead to severe focusing inaccuracies [68]. An efficient compensation technique lies on externally balancing the effects of Earth rotation velocity by using a proper squint angle. The value of such angle can be derived from Equation 3.17 by equalling the two main terms. The result is

$$\varphi_o^{f_d0} = \arctan \frac{\sin \theta_o v_\theta}{K_v V_{plat} - v_\varphi} \quad (3.21)$$

that now depends on the latitude of the scene. Such process is termed *yaw-steering* as the balancing squint angle is reached by applying an steering operation on the orbital platform



in the so-called yaw angular direction [68]. In practice, it is not possible to totally cancel the doppler centroid due to some instabilities on the antenna pointing mechanics. It is normally enclosed within a range of values where most of the undesired effects can be neglected. The sensor coverage also influences in a possible remaining doppler. If swath width is very large, the doppler centroid take different values along the latitude of the scene. This makes that an unique doppler term is not enough for compensating the Earth-induced doppler.

Independently of the yaw-steering process, it can be shown that the azimuth resolution in orbital SAR imaging is factorized by  $K_v$ . This parameter is always lower than one and, then, the azimuth resolution in orbital imaging is, for the same system configuration, lower than in the airborne case. However, the reduction factor is not so important as  $K_v$  takes normally values around 0.95 for current platform altitudes.

## 3.2 SAR Impulse Response

The two-dimensional signal collected by SAR sensors is normally referred as *raw data* and, despite it provides the reflectivity information of the scene, it needs a processing step to properly focus each observed scatter. In order to achieve this goal, an accurate knowledge of the SAR system *Impulse Response*, i.e. the return due to a *unitary point target*, is mandatory. Such expression will characterize in a compact mathematical form a SAR system summarizing all the modifications that a particular emitted signal can experiment due to the SAR imaging process. The knowledge of the impulse response is essential to understand all the physical processes involved in the generation of a SAR image. This allows to describe the inherent characteristics of SAR images as well as the possible distortions that an image can experiment.

### 3.2.1 Bi-dimensional Impulse Response

#### Time domain

The first step is to know the waveform related to an elementary scatterer. For sake of simplicity, the chirp signal defined in Equation 3.3 is assumed. Let to consider the cylindrical coordinate system of Fig. 3.5 where a platform images within an ideal linear path a static target located at  $P_t = (x, r, \vartheta)$ <sup>6</sup>. The signal received on-board can be expressed, but for the fast-varying  $e^{j\omega t}$  term, by

<sup>6</sup>The term  $\vartheta$  is added for sake of completeness but it is not relevant for the following analysis.

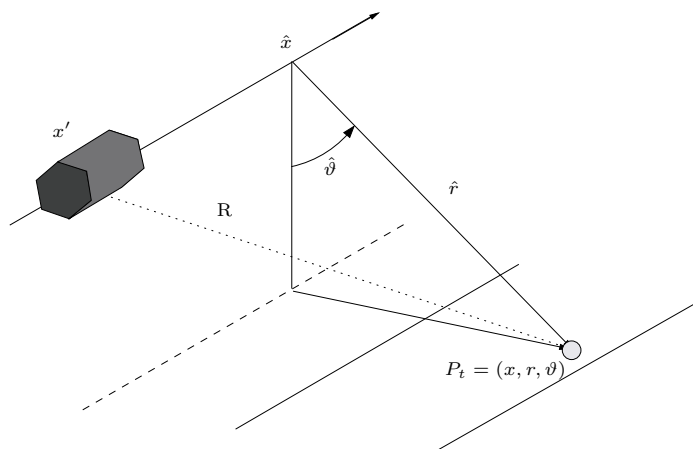


Figure 3.5: Cylindrical coordinate system geometry.

$$s(x' - x, t - t', r) = \rho \cdot e^{-j\frac{4\pi R}{\lambda}} e^{j\pi\alpha(t-t'-\frac{2R}{c})^2} \text{rect}\left[\frac{t - t' - \frac{2R}{c}}{\tau}\right] \omega^2[x' - x, r] \quad (3.22)$$

where  $x' = V_{plat}t'$  is the x-coordinate of the center of phase of the antenna, normally referred as the time-dependent platform position. In this formula,  $\text{rect}[\cdot]$  is a rectangular pulse of length  $\tau$  seconds,  $\omega[\cdot]$  the function describing the antenna radiation pattern <sup>7</sup> and  $\rho$  a complex constant that includes the complex reflectivity term of the scatter.  $R$  is the time-dependent sensor-to-target distance

$$R = \sqrt{r^2 + (x' - x)^2} \quad (3.23)$$

which quadratic shape form summarizes the doppler effect induced by the platform motion. Certainly, the doppler frequency is defined as  $-\frac{2}{\lambda}$  times the derivative of  $R$  along time and, in this way, it takes the expected linear dependence with respect to the observation time. Such behavior can be observed in Fig. 3.6 where the range (Fig. 3.6(a)) and doppler (Fig. 3.6(b)) plots for a static scatter in the absence of squint are presented with respect to the observation time. As observed, the minimum range <sup>8</sup> is reached at the sensor position (or azimuth time value) where the doppler is null. That position is normally referred as *zero doppler position* and, for this particular situation, corresponds to the middle of the synthetic aperture ( $t' = 0$ ). Displacements on the zero doppler position are observed in squinted geometries or in situations where a scatter has a radial velocity component.

<sup>7</sup>This function is squared as it is considered the same antenna in emitting and receiving mode.

<sup>8</sup>In this case, the minimum value is equal to 0, but in real scenarios it corresponds to the sensor-to-target radial distance,  $r$ .

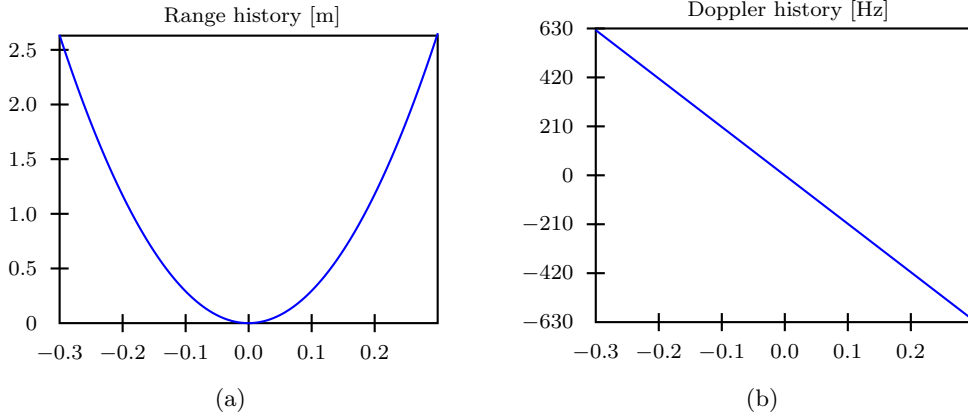


Figure 3.6: Range (a) and doppler (b) history for a static target. Arbitrary units.

At this point, Equation 3.22 can be rearranged in order to compact the mathematical expression. First of all, the time variable ( $t'$ ) can be substituted by the range variable ( $r'$ ) via the coordinate transformation  $r' = \frac{c(t-t')}{2}$ <sup>9</sup>. Thus,

$$s(x' - x, r', r) = \rho \cdot e^{-j\frac{4\pi R}{\lambda}} e^{j\pi\alpha\left(\frac{r'-R}{c/2}\right)^2} \text{rect}\left[\frac{r' - R}{c\tau/2}\right] \omega^2 [x' - x, r] \quad (3.24)$$

In addition,  $R$  can be decomposed in  $R = \Delta R + r$  in order to isolate the propagation phase factor related to the range location of the target  $r$ . The term  $\Delta R$  provides the normalized quadratic range history and it stands for all the variations that the SAR acquisition geometry *causes* in the range parameter. This is a key parameter in SAR processing as it has implicitly associated the system-induced doppler information of the scene. With these transformations, a new expression for  $s(x' - x, r', r)$  is

$$\begin{aligned} s(x' - x, r', r) &= \rho \cdot e^{-j\frac{4\pi r}{\lambda}} e^{-j\frac{4\pi\Delta X\Delta R}{\lambda}} e^{j\pi\alpha\tau^2\left(r'-r-\frac{2\Delta X}{c\tau}\Delta R\right)^2} \text{rect}\left[r' - r - \frac{2\Delta X}{c\tau}\Delta R\right] \\ &\cdot \omega^2 [x' - x, r] = \rho \cdot e^{-j\frac{4\pi r}{\lambda}} \cdot g(x' - x, r' - r, r) \end{aligned} \quad (3.25)$$

where the variables  $r'$  and  $r$  have been normalized to the pulse spatial extension,  $c\tau/2$ , and the  $x', x$  and  $\Delta R$  ones to the antenna footprint  $\Delta X \approx \lambda r_o/L$  with  $r_o$  being the closest approach of the sensor to the center of the swath<sup>10</sup>. Such normalization modifies the expression of

<sup>9</sup>In practice  $x'$  and  $r'$  are discrete variables, but for sake of simplicity they are assumed continuous.

<sup>10</sup>Despite of the normalization, the same notation of the non-normalized variables (Equation 3.24) has been used for the normalized ones (Equation 3.25).

$\Delta R$  by

$$\Delta R = \sqrt{\left(\frac{c\tau r}{2\Delta X}\right)^2 + (x' - x)^2} - \frac{c\tau r}{2\Delta X} \quad (3.26)$$

Equation 3.25 provides an expression for the *impulse response of the SAR system*. Such expression, which is compiled in  $g(x' - x, r' - r, r)$ , compacts all the signal information induced by the SAR imaging process and its knowledge is essential for retrieving the reflectivity information of the scatter,  $\rho \cdot e^{-j\frac{4\pi r}{\lambda}}$ . This process is the main casuistic of SAR processing that from a signal processing point of view is normally understood as an adapted filter problem. It is worth noting that the final result obtained in SAR images is an *estimate* of the reflectivity information as normally the impulse response of the system can not be perfectly described or reproduced. Some simplifications that introduce small errors are normally applied to achieve a better computer efficiency.

In a general form, the raw signal received on-board the sensor is the addition of all echoes backscatter by all the scatters present in the scene. Thus, we have, but for an amplitude constant resulting from the previous normalization,

$$h(x', r') = \int \int \gamma(x, r) e^{-j\frac{4\pi r}{\lambda}} \cdot g(x' - x, r' - r, r) dx dr \quad (3.27)$$

where the integral bounds are fixed by image dimensions.  $\gamma(x, r)$  is the reflectivity of the scene expressed in terms of the azimuth ( $x$ ) and range ( $r$ ) position. Note that if the  $r$ -dependence of  $g[\cdot]$  can be neglected Equation 3.27 simplifies to a convolution operation, which is an usual way to introduce the impulse response of SAR systems in basic works.

### Wavenumber domain

Before tackling SAR processing, it is interesting to evaluate the impulse response in the wavenumber domain as most codes use this domain to simplify all the required operations. The 2D *Fourier Transform* of  $h(x', r')$  in the wavenumber domain (spatial frequencies) is

$$H(f_{x'}, f_{r'}) = \int \int \gamma(x, r) e^{-j\frac{4\pi r}{\lambda}} e^{-jf_{x'}x} e^{-jf_{r'}r} G(f_{x'}, f_{r'}, r) dx dr \quad (3.28)$$

being

$$G(f_{x'}, f_{r'}, r) = \int \int g(x' - x, r' - r, r) e^{-jf_{x'}(x' - x)} e^{-jf_{r'}(r' - r)} dx' dr' \quad (3.29)$$

the Fourier Transform of the impulse response also referred as *Transfer Function*. According to Equation 3.25 and considering the new variables  $X' = x' - x$  and  $R' = r' - r - \frac{2\Delta X}{c\tau}\Delta R$ , the general form of the Transfer Function is

$$G(f_{x'}, f_{r'}, r) = \int e^{-j(f_{x'}X' + \frac{4\pi\Delta X}{\lambda}\Delta R + f_{r'}\frac{2\Delta X}{c\tau}\Delta R)} \omega^2 [X', r] dX' \int e^{-j(f_{r'}R' - \pi\Delta f\tau R'^2)} \text{rect}[R'] dR' \quad (3.30)$$

where  $f_{x'}$  and  $f_{r'}$  are respectively the azimuth and range spatial frequencies. This general expression do not allow to reach a closed form for the Transfer Function and, then, some approximations are required. The most usual one is the *stationary phase method* that takes profit of the fast-varying phase terms in both integrals. This approximation can be applied if  $\frac{2\pi\Delta X}{\lambda r_o}$  is large, a constraint that is normally fulfilled in real scenarios [69]. After some manipulations and assuming  $\omega^2[\cdot] \approx \text{rect}[\cdot]$ , it can be shown that the asymptotic result is [10]

$$G(f_{x'}, f_{r'}, r) \approx \frac{\pi}{\sqrt{\Delta f_{x'}\Delta f_{r'}}} \text{rect}\left[\frac{f_{r'}}{2\Delta f_{r'}}\right] \text{rect}\left[-\frac{f_{x'}}{2\Delta f_{x'}}\right] e^{-j\left(\frac{f_{r'}^2}{4\Delta f_{r'}} - 2\Delta f_{x'}\left(\frac{L}{\lambda}\right)^2 \left(1 + \frac{f_{r'}\Delta f}{f} \frac{1}{2\Delta f_{r'}}\right) \frac{r}{r_o} + \frac{Lr}{\lambda r_o} \sqrt{(2\Delta f_{x'}\frac{L}{\lambda})^2 \left(1 + \frac{f_{r'}\Delta f}{f} \frac{1}{2\Delta f_{r'}}\right)^2 - f_{x'}^2}\right)} \quad (3.31)$$

with  $f$  being the operative frequency and

$$2\Delta f_{x'} = 2\pi \frac{\Delta X}{L/2} \quad (3.32)$$

$$2\Delta f_{r'} = 2\pi \Delta f \tau \quad (3.33)$$

the bandwidth in the azimuth and range spatial frequency dimensions. It is worth noting that the denormalization of the azimuth spatial bandwidth to the frequency domain (the factor  $V_{\text{plat}}/\Delta X 2\pi$  has to be applied) leads to the well-known doppler bandwidth expression  $2V_{\text{plat}}/L$ <sup>11</sup>.

A closer form for Equation 3.31 can be achieved if the square root term of the global phase is simplified by means of a series expansion around  $f_{x'} = f_{DC}$ . This operation is possible as  $f_{x'}$  is lower than the remaining terms of the expression. Finally, it follows that

<sup>11</sup>Such expression can also be achieved by evaluating Equation 3.9 with  $t_{\text{obs}}$  for a null squint.

$$G(f_{x'}, f_{r'}, r) \approx \frac{\pi}{\sqrt{\Delta f_{x'} \Delta f_{r'}}} \text{rect} \left[ \frac{f_{r'}}{2\Delta f_{r'}} \right] \text{rect} \left[ \frac{f_{x'}}{2\Delta f_{x'}} \right] e^{-j \left( \frac{f_{r'}^2}{4\Delta f_{r'}} - \frac{f_{x'}^2}{4\Delta f_{x'} \frac{r_0}{r} \left( 1 + \frac{f_{r'} \Delta f}{2\Delta f_{r'} f} \right)} \right)} \quad (3.34)$$

Note that the first and second phase terms of the previous expression are respectively related with the asymptotic solution of the second and first integral of Equation 3.30. This means that the second phase term gathers the contribution of the normalized quadratic range response,  $\Delta R$ , whereas the first one only depends on the spectral characteristics of the emitted chirp signal. In the case that the ideal SAR geometry becomes modified by a squint angle, by an orbital platform or by unexpected motions in the platform or observed target, the normalized quadratic response  $\Delta R$  and, consequently, the second phase term of the Transfer Function varies accordingly. This forces to change the reference signal in SAR processing as otherwise the final image will experiment *defocusing* effects, i.e. remaining signal terms add to the scatter reflectivity estimate. In most cases, it is possible to mathematically describe the phenomena modifying the inherent SAR geometry<sup>12</sup>, but in other ones not. This is the case of target motions as depend on something external to the sensor that is very difficult to measure at real time.

### 3.2.2 A Simple Processing Chain

Equation 3.34 is the reference signal used in SAR processing. This means that the reflectivity information can be basically retrieved by applying a matched filter in both dimensions. In a mathematical form, this means to multiply in the wavenumber domain  $H(f_{x'}, f_{r'})$  by  $G^*(f_{x'}, f_{r'}, r)$  where  $[\cdot]^*$  indicates complex conjugate. The way this operation is performed in terms of the domain, techniques and approximations used distinguishes the different codes currently available in the literature (an excellent analysis is done in [70]). A basic approach to the problem is commented following. It normally starts by isolating the two main terms of Equation 3.34

$$G_1(f_{r'}) = \frac{\pi}{\sqrt{\Delta f_{r'}}} \text{rect} \left[ \frac{f_{r'}}{2\Delta f_{r'}} \right] e^{-j \frac{f_{r'}^2}{4\Delta f_{r'}}} \quad (3.35)$$

$$G_2(f_{x'}, f_{r'}, r) = \frac{\pi}{\sqrt{\Delta f_{x'}}} \text{rect} \left[ \frac{f_{x'}}{2\Delta f_{x'}} \right] e^{j \left( \frac{f_{x'}^2}{4\Delta f_{x'} \frac{r_0}{r} \left( 1 + \frac{f_{r'} \Delta f}{2\Delta f_{r'} f} \right)} \right)} \quad (3.36)$$

<sup>12</sup>This is the case of squinted and orbital geometries where the new Transfer Function can be accurately described and, then, inverted [10]

Both terms are formally equal, except for the coupling term  $\frac{f_{r'}\Delta f}{2f\Delta f_{r'}}$ . If this term can be neglected, the previous expressions reduce to the Fourier Transform of two chirps with particular chirp rates. In some works, both expressions are termed *range and azimuth chirps* and they are respectively associated to fast- and low-varying time variables. In this way, a simple processing procedure may consider three steps, namely:

1. *Range compression* that is devoted to compensate the range chirp by multiplying  $H(f_{x'}, f_{r'})$  with  $G_1^*(f_{r'})$ .
2. *Range Cell Migration (RCM) Compensation* that try to estimate and erase the coupling term  $\frac{f_{r'}\Delta f}{2f\Delta f_{r'}}$ .
3. *Azimuth compression* that apply the adapted filter to the remaining azimuth chirp in a similar way than in step 1.

Once the Transfer Function is compensated, it is necessary to return to the space domain in order to obtain an estimation of the 2-D reflectivity information, which actually is the final image. In this process, an Inverse FT (IFT) operation is required. For a punctual target, the result of this focusing process is

$$\hat{\gamma}(x', r') = C(x, r)e^{-j\frac{4\pi r}{\lambda}} \text{sinc}(\Delta f_{r'} \cdot (r' - r)) \text{sinc}(\Delta f_{x'} \cdot (x' - x)) \quad (3.37)$$

where  $C(x, r)$  is a complex constant that gathers among others the reflectivity coefficient at the position  $(x, r)$ . The variables  $x'$  and  $r'$  are discrete and they provide the azimuth and range position of the center point of each cell in the final image. The two *sinc* functions are normally known as the *spread function* and they outline the basic function used to present the reflectivity information. Their bandwidths at 3dB correspond to the image resolutions. In azimuth, it follows that  $\Delta f_{x'} = \delta_x = L/2$  m whereas in range  $\Delta f_{r'} = \delta_r = c/(2\Delta f)$  m. The values of pixel dimensions are fixed in azimuth by  $V_{plat}/PRF$  m whereas in range by  $c/(2f_{SF})$  m. In most real sensors, these parameters are designed in order to have a safety margin of 1.1% with respect to image resolutions.

When considering complex scenarios with several scatters located at different positions, the final result is the coherent addition of all the contributions defined by Equation 3.37. In this case, one can find

$$\hat{\gamma}(x', r') = \sum_{p_i=1}^{N_{x', r'}} C(x_i, r_i)e^{-j\frac{4\pi r_i}{\lambda}} \text{sinc}(\Delta f_{r'} \cdot (r' - r_i)) \text{sinc}(\Delta f_{x'} \cdot (x' - x_i)) \quad (3.38)$$

where  $N_{x',r'}$  stands for the number of scatters present in the imaged area and  $C(x_i, r_i)$  is the reflectivity coefficient of scatter  $i$  at the position  $p_i = (x_i, r_i)$ . This formula is general for the overall image and it considers *all* the contributions within the image. This means that the variables  $x'$  and  $r'$  can refer to any pixel.

The previous expression is also valid to describe the signal retrieved in a particular pixel. In such a case,  $N_{x',r'}$  expresses the number of scatters within that resolution cell. Normally, the result is interpreted as the contribution of an imaginary scatter located at the *center of phase*, i.e. that position resulting of adding the different complex phase contributions. The center of phase is a parameter very difficult to predict as it depends on the number, orientation and distribution of scatters within a cell as well as on the SAR geometry.

### Image quality enhancement

SAR images as expressed in Equation 3.38 can suffer from a set of known aberrations that can drop the final quality of the data. To overcome them, it is very usual to use a set of post-processing operations [70]. The most important ones are oriented to reduce: 1) the interferences caused by signals incoming from the secondary lobes of the antenna pattern 2) the mismatches due to platform motions and 3) the presence of the so-called *speckle noise*. Also important is the calibration step that compensates all the known constants of Equation 3.38 to isolate the Radar Cross Section (RCS),  $\sigma$ , from  $C(x_i, r_i)$ . RCS is an important parameter in radar remote sensing because it provides a measurement of the scattering strength of targets according to their size, shape and orientation. It depends on the wavelength and on the polarization of the signal. In SAR images, the presence of natural surfaces makes more convenient to work with the *normalized RCS*  $\sigma_o$ , which can be understood as the RCS estimate within each resolution cell  $\sigma_o = \sigma/\delta_x\delta_r$ .

The result of all this SAR processing procedure may be the *Single-Look Complex* (SLC) SAR image shown in Fig. 3.7. It corresponds to an area of the city of Munich and it has been obtained with the German airborne sensor ESAR [37] for a range x azimuth resolution of 1 x 2 meters.

### 3.2.3 SAR Image Distortions

#### Geometrical distortions

According to Equation 3.38, the dimensions of a SAR image are performed by the azimuth and slant-range directions. This means that the response of the observed scatters are projected into the *image plane* defined by such directions. According to the incidence angle and the



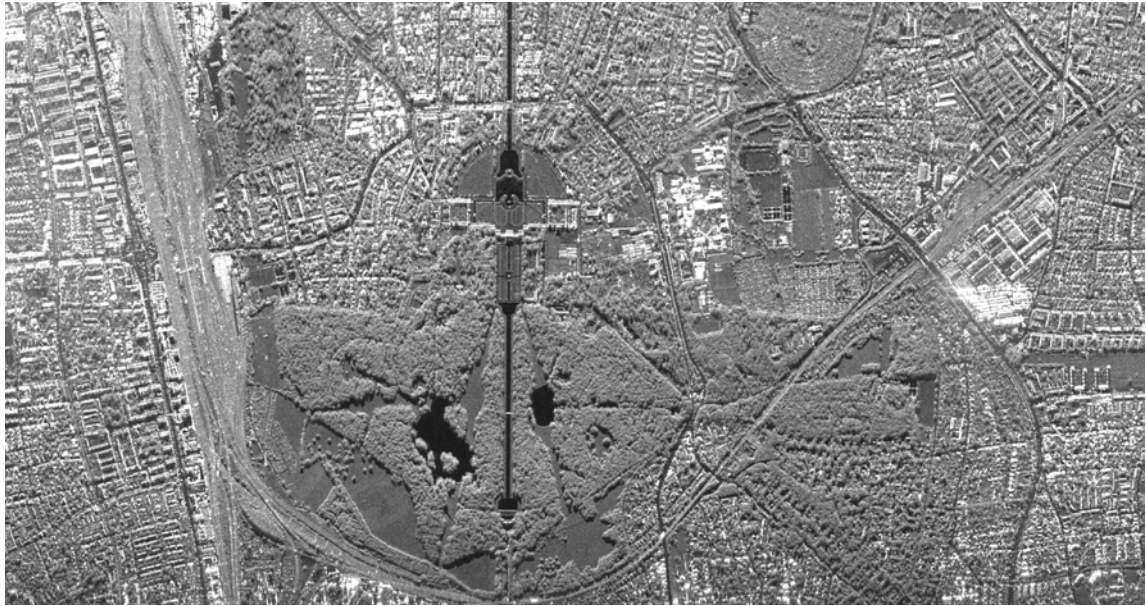


Figure 3.7: Example of a SLC SAR image of the city of Munich acquired by the German airborne SAR sensor ESAR for a range-azimuth resolution of 1 x 2 meters. Courtesy of DLR.

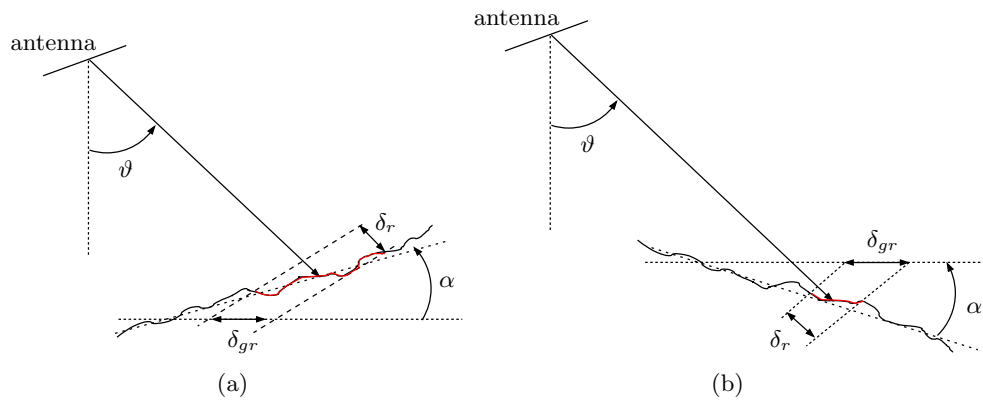


Figure 3.8: Relevant to foreshortening. Dilation of the resolution cell on the ground is observed for  $0 < \alpha < \vartheta$  (a) and compression for  $-\vartheta < \alpha < 0$  (b)

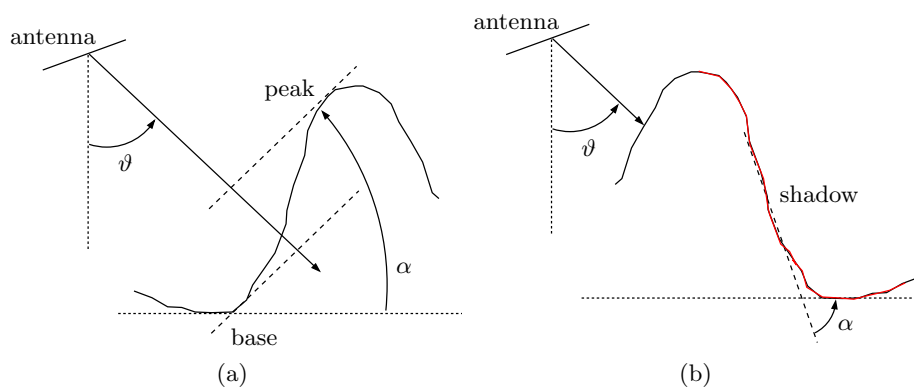


Figure 3.9: Relevant to layover (a) and shadowing (b)

ography of the scenario, a set of geometrical distortions can be observed, namely:

1. The ground extension covered by each pixel depends on the range position. At *near-range*, this area is larger than at *far-range*.
2. *Foreshortening* that relates the dilation ( $0 < \alpha < \phi$ ) (see Fig. 3.8(a)) and compression ( $-\phi < \alpha < 0$ ) (see Fig. 3.8(b)) of the resolution cell on the ground with respect to the planar case.
3. *Layover* that causes an inversion of the image geometry ( $\alpha > \phi$ ). This implies for example that the peaks of the mountains are imaged at the location expected for the base and viceversa (see Fig. 3.9(a)).
4. *Shadowing* that avoids the terrain to backscatter any signal ( $\alpha < \phi - \pi/2$ ) (see Fig. 3.9(b)).

To avoid that these distortions affect the interpretation of SAR data, it is usual to apply a *geocoding* post-processing step that allows to project the SAR images within a earth-fixed grid [11] [10].

### Speckle Noise

Each single scatter that coherently contributes to the response of a particular cell has a reflectivity phase term that depends among others on the sensor-to-target range and scatter orientation. In SAR imagery, these parameters fluctuate along time due to the motion of SAR platforms generating a random process commonly known as *fading*. The effect that fading has in SAR images is fixed by the number and characteristics of the scatters within each cell.

For a large number of scatters with similar scattering properties, a grainy appearance referred as *speckle noise* is generated [16]. This phenomenon is commonly observed in *distributed* targets, such as land or sea surfaces. It causes an statistical behavior in the real and imaginary parts of the signal that is normally modeled by a zero mean Gaussian probability density function [16]. When analyzing the statistics of the module and phase expressions, it follows that they have respectively a Rayleigh and an uniform distribution. This means that the reflectivity phase term of a single scatter is scatter-independent, that is, it takes with an uniform probability a value within the range  $[0 - 2\pi]$  that does not depend on the physical properties of the target.

Speckle noise is an important problem for SAR image interpretation as it greatly drops the capability for detecting linear features. This increases the problems for developing classification and parameter retrieval techniques based on the shape of the target signature. For

vessel classification, this issue is specially important due to the relative low vessel dimensions in relation to the pixel size [13]. The most simple speckle reduction technique is the one referred as *multi-look* that consists on incoherently average two or more statistically uncorrelated speckle patterns. The operating principle is based on dividing the full aperture in a set of sub-apertures or *looks*, mainly in the frequency domain, and sum under an intensity basis the corresponding sub-images. But this methodology suffers from some important problems, namely: 1) image resolutions are degraded a factor of  $1/N$  according to the number of looks ( $N$ ) and 2) the image becomes significantly smeared losing most of those image features that with speckle noise would be reasonably detected. In spite of overcoming such limitations, some advanced methods are currently available providing a notable performance on speckle noise filtering [17] [71] [72]. However, this matter is up to now an open issue as it seems that the statistics of the SAR signal have not been properly defined yet [73].

The previous statistical development is subjected to the application of the Central Limit Theorem, which is only valid for those resolution cells having a large number of scatters<sup>13</sup>. When this constraint is not fulfilled, the signal can not be considered distributed anymore and the effect of the speckle noise almost disappears. This can be observed in the response of *non-distributed* scenarios, for instance complex targets or urban areas that have a few number of main mechanisms dominating the behavior of each cell. Actually, speckle noise disappears completely in the ideal case in which all the single scatters are isolated in different resolution cells. This happens when the imaged area has a low density of scatters or, alternatively, the sensor resolution is lower than the separation among the scatters. With current system designs and operating wavelengths, it is quite unlikely to meet any of these two conditions and, then, a little speckle noise remaining is always expected. There is only one situation where speckle can be considered null. It refers to such pixels exclusively dominated by the response of *deterministic* canonical scatters, i.e. targets with a perfectly known scattering behavior. Such scatters describes elemental geometrical shapes that are very useful for calibration issues.

### Azimuth shifts

As commented previously, the spread function of a particular scatter is located in azimuth according to the doppler information induced by the sensor. This is true if the scatter is static. In the case that the scatter has radial velocity components, its inherent doppler history becomes modified by new doppler frequencies. This causes a displacement of the zero doppler position, which, in turn, shifts the azimuth position of the spread function. In SAR images, this phenomenon can generate important distortions. The simplest case is for ground targets as they have an unique linear motion that makes SAR signatures to appear *uniformly* shifted in azimuth. This property has been exploited for developing *Moving Target Indicator*

---

<sup>13</sup>Note that the definition of an statistic requires a minimum number of samples. So, it can only be associated with large areas of the scene.

(MTI) applications where the displacement observed between the target and a reference scatter, for instance a road, is used to estimate the velocity vector [74] [75]. In contrast, the most adverse situations are for vessels imaged at sea due to the different kind of motions that they can experiment. In this case, the shape of the signature is not only displaced, but also distorted. This issue is further analyzed in Section 3.5.

### 3.3 SAR Interferometry

InSAR is an advanced SAR technique that allows to retrieve the third dimension of the observed scene and, hence, reconstruct its proper geometrical configuration [24]. This is an important advantage in relation to single SAR imagery as, in that case, the reflectivity information experiments an altitude-dependent projection into the image plane. This causes severe distortions that in many cases worsen data interpretation.

In the past, interferometry techniques have been successfully applied in radio astronomy [76]. Their first usage in SAR imagery was at the early seventies and it was oriented to Earth observation [77]. Since then, the applications of InSAR have been proliferated in a wide range of areas. Some examples are topography and Digital Elevation Map (DEM) generation [78] [79] [24] [80] [81] [82] [83], motion mapping and subsidence [84] [85] [86] [87], glaciers monitoring [88] [24] [89] or tree height retrieval [90]. The theoretical framework of InSAR has been described in detail by many sources, such as [24] or [91]. Following, a brief review is provided.

InSAR consists basically on acquiring two SAR images from two slightly different positions. The main goal is to retrieve a direct measure of the sensor-to-target path difference, from which the height of scatters can be directly inferred. To achieve this, it is necessary to multiply one image (*master*) with the complex conjugate of the other (*slave*) building the so-called *interferogram*. As commented later, this operation cancels the phase term related to the reflectivity of scatters.

The way the two images are acquired generates different interferometric configurations. According to the alignment of the antennas, *across-* and *along-track* geometries can be distinguished. If both images are obtained at nearby times, i.e. at the same orbital pass or airborne flight, the sensor operates at *single-pass*. Otherwise, it works at *repeat-pass* mode with a time interval that ranges from a fraction of seconds to years. The combination of these interferometric operating modes diversify and specialize the different applications of InSAR.

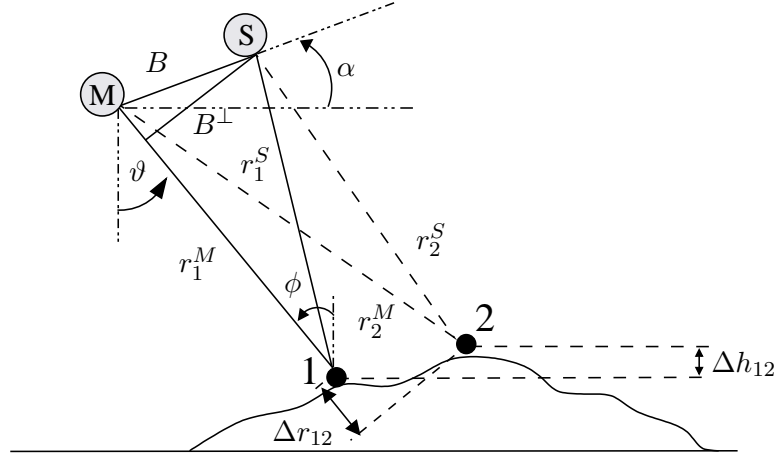


Figure 3.10: Imaging geometry for across-track interferometry

### 3.3.1 Across-Track Configuration

Let us consider the across-track configuration presented in Fig. 3.10. In that scheme, the sensor is traveling through the paper with a pair of antennas master (M) and slave (S) placed in the across-track plane, i.e. the plane defined by the slant-range and nadir directions. The separation between both antennas is fixed by the *baseline* vector,  $\vec{B}$ , which projection into the perpendicular direction of slant-range is termed *perpendicular baseline*,  $B^\perp$ . The baseline orientation with respect to the horizontal is measured by the *tilt* angle  $\alpha$ .

At a specific time, the master antenna emits a signal that returns back to the sensor. The phase of the signal backscattered by scatterer 1 at the master antenna is

$$\psi_1^M = -\frac{4\pi r_1^M}{\lambda} + \psi_r^M \quad (3.39)$$

where  $\psi_r^M$  stands for the backscattering-related phase of the scatterer,  $\lambda$  is the operating wavelength and  $\psi_1^M \in [-\pi : \pi]$  due to the acquisition system. Similarly, at the slave antenna

$$\psi_1^S = -\frac{4\pi r_1^S}{\lambda} + \psi_r^S \quad (3.40)$$

In InSAR, the positions of both acquisitions can be considered nearby enough as to assume  $\psi_r^M \sim \psi_r^S \sim \psi_r$ . Then, the difference between master and slave phases leads to

$$\Delta\psi = -\frac{4\pi}{\lambda} (r_1^M - r_1^S) = -\frac{4\pi}{\lambda} \Delta r \quad (3.41)$$

Such expression gives the *absolute interferometric phase* of a single point. But in InSAR it is usual to work with differential interferometric phases  $\Delta\psi_{12}$ <sup>14</sup> in order to avoid the ambiguities besides of any unknown propagation delays. As stated in [92], such parameter takes the form

$$\Delta\psi_{12} = \Delta\psi_{flat} + \Delta\psi_{topo} = \frac{4\pi B^\perp}{\lambda r_o} \left( \frac{\Delta r_{12}}{\tan \phi} + \frac{\Delta h_{12}}{\sin \phi} \right) \quad (3.42)$$

where the terms  $\Delta\psi_{flat}$  and  $\Delta\psi_{topo}$  expresses respectively the contributions of a *flat* Earth surface and topography. The first factor highlights the interferometric phase due to the different ground-range location of the scatters, i.e. the phase that a hypothetical terrain with a null slope would provide. In the second one, the interferometric phase is exclusively induced by the different height of the scatters.

As observed,  $\Delta\psi_{flat}$  and  $\Delta\psi_{topo}$  have a linear dependence with respect to the related geometrical parameters. If  $\Delta r_{12}$  and  $\Delta h_{12}$  are large in terms of the operating wavelength, the phase will take *out-of-bounds* values. In such a case, the acquisition system will *wrap* the phase within the range of available values  $[-\pi, \pi]$  generating a set of *fringes* in the phase of the interferogram. This wrapping process is very usual in real scenarios as the used wavelength is so short. The fringe distribution in the final interferogram is fixed among others by the perpendicular baseline, the wavelength and the local slope of the terrain [24]. For slopes facing towards the sensor, the fringe frequency increases whereas it decreases for slopes facing away the radar (see Fig. 3.11(b)).

It is worth noting that the previous phase formulas have been derived by considering the so-called *ping-pong* measurement mode in which each antenna transmits and receives their own echoes sequentially. For the so-called *standard mode* where the master antenna transmits and both antennas receive the echoes, the phase expressions are scaled a factor of 1/2 and, consequently, the effective baseline is half the real one [24].

Fig. 3.11 presents an example of an interferometric acquisition. It corresponds to the area surrounding the city of Bachu in China (around of 100 x 80 km of extension) imaged by the ESA's SAR satellites ERS-1/2 [56]. The sensor travels horizontally pointing the scene from the upper edge of the image. Fig. 3.11(a) and Fig. 3.11(b) show respectively the magnitude and phase of the interferogram whereas Fig. 3.11(c) the derived DEM map. First of all, note the relationship between the fringe frequency and the slope of the terrain. In planar areas the fringe edges can be easily identified by simple eye inspection whereas in the mountains this operation becomes more complicated. In addition, observe the dependence of the fringe frequency in relation to the slope alignment with respect to the pointing direction.

<sup>14</sup>For the following, this parameter will be termed *interferometric phase* despite it stands for the difference between two absolute interferometric values.

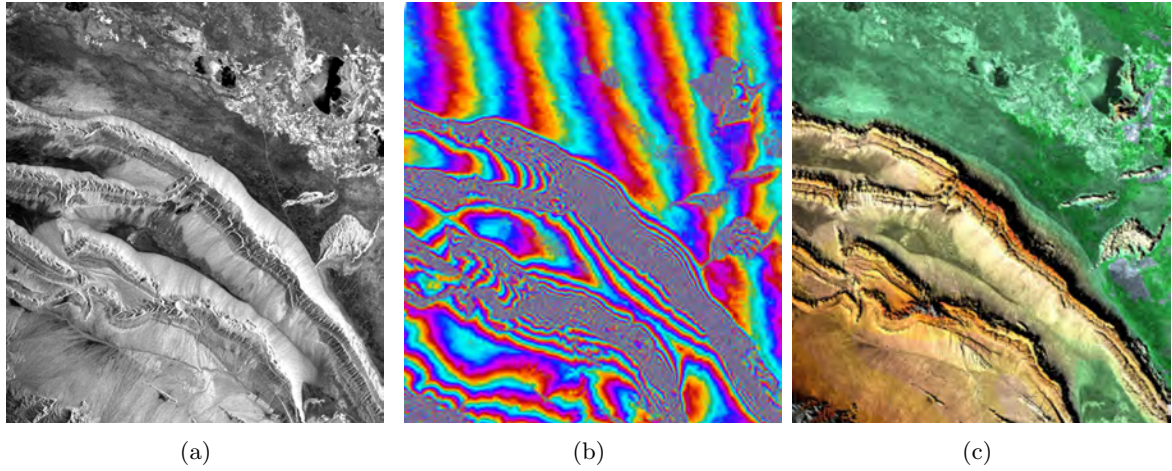


Figure 3.11: Example of the interferogram magnitude (a), phase (b) and DEM (c) for a SAR dataset acquired by the ESA's SAR satellites ERS-1/2 at the area surrounding the city of Bachu in China (around of 100 x 80 km of extension). The sensor travels horizontally pointing the scene from the upper edge of the image.

### Repeat-Pass Interferometry (RPI)

Across-track geometries can be synthesized in repeat-pass mode with one or two sensors performing the acquisitions at different times. As result, the interferometric phase become modified by [92]

$$\Delta\psi_{12} = \Delta\psi_{flat} + \Delta\psi_{topo} + \Delta\psi_{deform} = \frac{4\pi B^\perp}{\lambda r_o} \left( \frac{\Delta r_{12}}{\tan \phi} + \frac{\Delta h_{12}}{\sin \phi} \right) + \frac{4\pi}{\lambda} \Delta\rho_{12} \quad (3.43)$$

where  $\Delta\rho_{12}$  expresses the deformation increment in slant-range between the points 1 and 2. Now, the interferometric phase has information of terrain motions, which can be isolated by subtracting the topographical information via an external DEM. This methodology is referred as *Differential SAR Interferometry* (DInSAR) and it has been firstly applied in the nineties with good results. Nowadays, this technique has achieved a high level of development that makes possible, for example, to retrieve both the along- and across-track components of the deformation velocity vector as well as its acceleration [93]. The main areas of application are those dealing with low motions (up to mm/year), such as landslide [94] or ground subsidence and uplift [95]. Note that RPI configurations makes possible to *recycle* single SAR systems for interferometric applications. This has made possible, for example, that sensors like ERS and ENVISAT allowed and, allow in these days, the development of applications related with landslide or subsidence at a global scale.

### 3.3.2 Along-Track Configuration

The other main interferometric geometry is along-track in which the antennas are aligned along flight direction <sup>15</sup>. This configuration is specially designed for detecting terrain motions as the interferometric phase would be in the ideal case insensitive to topography [24] [87]. Certainly if  $r_1^M = r_2^M, r_1^S = r_2^S$ , the factors  $\Delta\psi_{flat}$  and  $\Delta\psi_{topo}$  are null and, hence,  $\Delta\psi_{12}$  exclusively depends on the radial displacements of the scatters. Often, along-track interferometry (ATI) is understood as a particular case of RPI schemes.

As before, ATI can be reached with single-pass or repeat-pass operating modes. For the former case, lapse times are short and, then, interferometric measurements are only sensitive to fast-varying motions, such as in seismic [96], volcanic [97] and oceanographical tidal processes [98]. The latter scheme is quite rare in practice because it requires a near-perfect retracing of the sensor. However, some studies have been successfully developed in glacier monitoring [99]. In general, it is assumed that both RPI and ATI are not able to repeat exactly the track of the sensor. Thus, the baseline vector has cross-track components sensitive to the topographic information.

### The Coherence Parameter

The usage of RPI geometries with a specific time interval between both acquisitions gives sense to the definition of the concept of *coherence*. As commented in Section 3.2.1 and Section 3.2.3, the number of scatters expected for a resolution cell is normally higher than one because the resolution of SAR systems is large in terms of the operating wavelength. This means that the interferometric phase becomes modified by the coherent addition of all the scatter contributions acquiring a statistical behavior similar to that described for the speckle noise.

In this framework, it appears the idea that master and slave images may not match the conditions of the ideal case or, as referred in interferometric theory, they may not be *resemblant*. The degree of resemblance between master and slave images is measured by the complex *coherence* parameter. It provides a quantitative measurement of the quality of the interferometric phase and, hence, an estimation of the reliability of the retrieved height values. Mathematically, it is defined as

$$\gamma = \frac{\langle M \cdot S^* \rangle}{\sqrt{\langle |M|^2 \rangle \cdot \langle |S|^2 \rangle}} \quad (3.44)$$

<sup>15</sup>In the scheme of Fig. 3.3.1, both antennas are overlapped at the same point.



where  $M$  and  $S$  indicates respectively the return of the master and slave images and  $\langle \cdot \rangle$  is the expectation operator normally implemented as a spatial averaging. The magnitude of  $\gamma$ <sup>16</sup> range from 0 to 1 and it measures the resemblance between both images. A coherence of 0 means totally uncorrelated images and, then, the interferometric phase has no relation with topography. In the contrary, a unit coherence highlights resemblant images that provide interferograms of high quality, i.e. quite close to the ideal case.

The number of independent samples spatially averaged in the complex interferogram or *number of looks* depends on the statistical behavior and characteristics of the observed target. The higher the number of looks, the higher the quality of the retrieved height but the lower the resolution. This behavior is compiled in the standard-phase deviation parameter, which is described by the following Cramer-Rao bound [100]

$$\sigma_\phi = \frac{1}{\sqrt{2N_L}} \frac{\sqrt{1-\gamma^2}}{\gamma} \quad (3.45)$$

where  $N_L$  is the number of looks. From this expression, the standard height deviation can be derived [100]. This parameter compiles the height errors due to *decorrelation effects*, i.e. all those phenomena that can cause a loss of coherence. Normally, it is referred as *height sensitivity* and it is equal to

$$\sigma_h = \frac{\lambda r_o \tan \vartheta}{4\pi |\vec{B}|} \sigma_\phi \quad (3.46)$$

In this expression, it becomes evident that short baselines increases the noise of height results. This is consistent with the expression 3.43 where short baselines reduce the sensitivity of the interferometric phase with respect to the height. In other words, the accuracy of the retrieved height reduces.

In real scenarios, there are some decorrelation effects that drop the overall coherence of the system increasing the error on the final results. The most important ones are:

- **Thermal noise decorrelation.** This source of decorrelation is related with the thermal noise of the receivers of both antennas, which may modify the phase components of both signals. The result is a coherence degradation expressed by the factor  $0 \geq \gamma_{SNR} \geq 1$

$$\gamma_{SNR} = \frac{1}{1 + SNR^{-1}} \quad (3.47)$$

where  $SNR$  is the signal-to-noise ratio of both receivers.

---

<sup>16</sup>For the following,  $|\gamma|$  will be understood as *coherence*

- **Baseline decorrelation.** The fact to observe the scene from two different positions makes each receiver to measure a particular portion of the range reflectivity spectrum. This behavior can be appreciated in the ground-range wavenumber expressions  $k_y$

$$k_y^M = \frac{4\pi f}{c} \sin \vartheta_M \quad (3.48)$$

$$k_y^S = \frac{4\pi f}{c} \sin \vartheta_S \quad (3.49)$$

where  $f$  points out any frequency value within the system bandwidth  $\Delta f$ , and  $M$  means master and  $S$  slave. In such expressions, the local look angle difference between both acquisitions causes that the slave spectrum becomes a shifted and stretched version of the master one. As a consequence, both spectra do not fully overlap having specific disjoint sections that contribute as noise in the interferometric phase. This effect is so-called *baseline decorrelation* [101] [102]. The degree of overlapping can be predicted from the expression of the frequency shift between both spectra [102]

$$\Delta f = \frac{f_o |B^\perp|}{r_o \tan(\vartheta - \alpha)} \quad (3.50)$$

where  $f_o$  is the carrier frequency. This formula shows that the frequency shift increases proportionally with the perpendicular baseline. The higher the baseline, the higher the disjoint areas of the spectra and, then, the lower the *coherent* areas from which a reliable height can be retrieved. The limit is fixed by that baseline that induce a frequency shift equal to the system bandwidth, in such a case the interferogram will become completely noisy and useless. The threshold is referred as *critical baseline* and it is defined by

$$B_c^\perp = \frac{Bw \cdot r_o \cdot \tan \vartheta - \alpha}{f_o} \quad (3.51)$$

This expression details the maximum value for the baseline and it represents one of the most important parameters to be considered when designing an interferometric system. It affects the height sensitivity expression of Equation 3.46 limiting the capability of the baseline to reduce the height errors due to decorrelation effects.

- **Volume decorrelation.** Volume decorrelation appears when targets with volume scattering are imaged. This scattering property is inherent in those targets that are electromagnetically described by a cloud of scattering centers that have random orientations and are located within a volume. Typical examples are natural surfaces, such as land or vegetated areas. There are two main techniques for reducing volume decorrelation, namely: 1) filtering applied in the wavenumber domain and 2) data polarimetric processing. Last works show that the latter provides better results [103].

- **Temporal decorrelation.** In RPI systems, the large time interval between both acquisitions makes quite probable to find variations on the reflectivity properties of the target. These variations affect the received signal and, consequently, the ideal expression of the interferometric phase. The result is a loss of coherence termed temporal decorrelation. As before, the significance of this decorrelation effect can be dropped if polarimetric techniques are used.

The different sources of decorrelation allow to factorize the expression of coherence (Equation 3.44) as

$$\gamma = \gamma_{SNR} \cdot \gamma_{B^\perp} \cdot \gamma_{vol} \cdot \gamma_{temp} \quad (3.52)$$

where in all the cases the coherence factors of the different decorrelation effects range from 0 to 1.

### 3.3.3 A Basic Processing Chain

In real scenarios, there are some factors that move the imaging geometry far from the ideal case. In order to minimize their effects and assure high quality interferograms, a processing chain is required. The main goal is to compensate the geometrical distortions inherent in the imaging scheme as well as the noise that may appear in the interferometric phase. The basic steps are, namely

- **Co-registration.** The first step is called co-registration and it is devoted to compensate *spatial decorrelation* effects. They are caused by the different positions and time instants from which both images are acquired. This makes the origins of both azimuth and range slave dimensions to be shifted with respect to the master image. As a consequence, the same pixel in the master and slave images does not image the same area of the scene. Currently, there are lot of advanced techniques that try to reduce as far as possible the influence of such effects [104] [105] [106]. The main casuistic is to test different offsets for the reference position of the range and azimuth slave dimensions still find a peak of correlation with the master image. Nowadays, the accuracy of such processes is high enough as to assure that in almost all the cases the slave image is properly *co-registered* in relation to the master one.
- **Spectral filtering.** The second step consists on balancing the frequency shifts due to baseline decorrelation. A common technique used for such purpose is the wavenumber shift filtering. The main problem that arises with spectral filtering is that the frequency

shift depends on the local slope of the scene (see Equation 3.50). So, the frequency shift can not be estimated globally for the overall image, but in blocks of specific dimensions that improve the description of the local spectral properties. The procedure is quite simple and it consists on cross-correlating the FFT of the different blocks in the master image with the FFT of the corresponding blocks in the slave one. In this process, different frequency shift values are tested and that providing the peak of correlation is selected to be the compensating offset.

- **Interferogram generation.** Once the slave image has been properly co-registered and spectrally filtered, the interferogram can be built. In this process, it is very typical to obtain a coherence map from the normalized magnitude of the interferogram. This map is useful for assessing the quality of the height values as well as develop classification applications.
- **Flat Earth Removal.** The next step removes the flat Earth term  $\Delta\psi_{flat}$  of the interferometric phase in order to isolate the height contribution. This makes possible to use a conventional horizontal ground plane for showing the results.
- **Interferogram filtering.** In this step, the interferometric phase is *cleaned* from any phase noise. There are many factors that can degrade the phase information, such as white noise, mis-registration, temporal decorrelation, etc. Their presence generates additional linear phase terms that shift the related spectral components. Normally, this noisy information has a spectral band different to the useful data and, hence, a proper filtering process helps on reducing its weight. As in spectral filtering, adaptive filtering is required because noisy bands are modified by the inhomogeneity of the scene [70].
- **Phase Unwrapping.** The final processing step applied to the interferometric phase corresponds to unwrap the phase from the bounds  $[-\pi, \pi]$ , i.e. provide the absolute phase value. The basic operating principle consists on evaluating the first differences of the phase at each image point in either image dimension and, then, integrate the result. However, such methodology allows local errors that can lead to errors across the full SAR scene. In this field, there are more complex methodologies that provide better results [107], [108], [109]. An example of an unwrapping process is illustrated in Fig. 3.12.
- **Geocoding.** The final product in InSAR is normally projected in a standard coordinate system, such as UTM, in order to geocode the height values. This issue has been widely studied in [110] [111] [11]. In some cases, specially for the airborne case, it is necessary to apply a *calibration* step prior geocoding in order to compensate mismatches on estimating some parameters related with the imaging geometry, for instance platform position, attitude angles or baseline [70]. In addition, platform motions can be an important limiting factor.

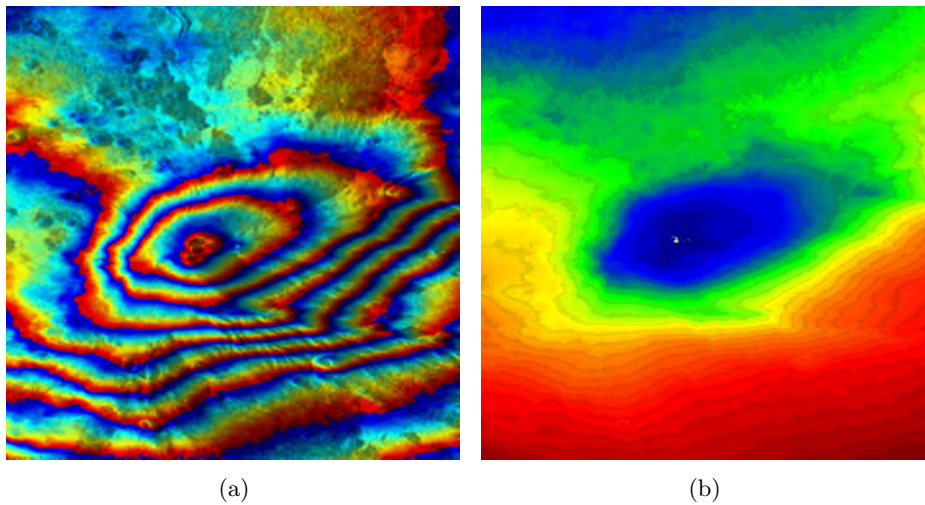


Figure 3.12: A detail of the phase unwrapping process. The *wrapped* interferometric samples measured from the real scene (a) are transformed into *absolute* values with no phase transitions (b).

### 3.4 Inverse SAR

Inverse SAR (ISAR) imagery is a variant of SAR imagery in which the doppler effect is generated by means of target motions. This represents the *inverse* way in relation to common SAR geometries wherein the platform is in motion and the target static. ISAR assumes that all the scatters of the scene experiment a rotation of an specific angular velocity within the incidence plane. This motion makes the scatters to have different radial velocities and, in turn, different doppler frequencies according to their cross-range locations. A similar effect can also be achieved with translational motions. In this case, the track of the sensor have to be locally approximated to an arc belonging to a circle which radius is much higher than the nominal radar range [112].

With this operating principle, ISAR breaks with the traditional geometry of SAR systems. The fact that the doppler is not induced by platform motions but by the target ones forces to change the processing techniques. The result is a kind of image that differ a lot from the SAR ones. Now, reflectivity maps of particular and isolated complex targets are retrieved instead of the reflectivity images of large scenes. These images make possible to locate the reflectivity spots of targets and to develop classification approaches based on the shape and/or distribution of the scattering centers within the signature. With this feature, ISAR imagery has been widely used for aircrafts and vessel monitoring.

But ISAR imagery has an important restriction. The necessity to cover a minimum of angular section in order to observe the rotational motions limits in excess the nominal range. In practice, this means to work in local areas. This explains why ISAR imaging is more developed in military applications than in the civil ones [113].

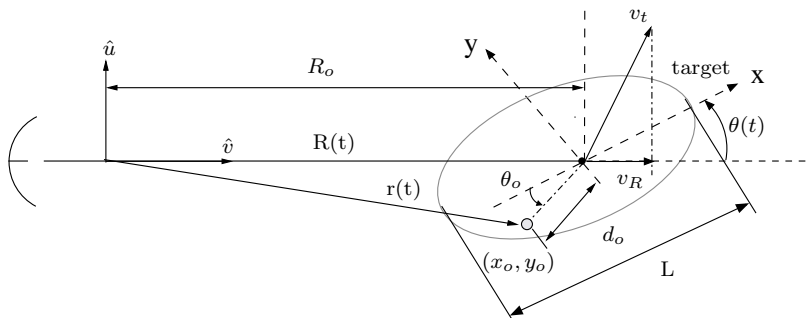


Figure 3.13: Imaging geometry of a generic ISAR sensor.

### 3.4.1 Imaging Geometry

Let us consider the imaging geometry of Fig. 3.13. In this scheme, the sensor observes a target that experiments a rotation with respect to a fixed axis perpendicular to the incidence plane. This plane is the plane of the paper performed by the slant- ( $\hat{u}$ ) and cross-range ( $\hat{v}$ ) directions. The instantaneous angular velocity is  $\theta(t)$  [rad/s] that, according to the observation time,  $T$ , provides the angular section observed by the sensor  $\Delta\theta = \theta(T) - \theta(0)$ . In addition, the target has a translational motion defined by the radial velocity  $v_R$  and acceleration  $a_R$ . This forces the sensor to have a moving antenna beam that always track the area surrounding the target of interest. Under such conditions and assuming that  $R_o \gg d_o$ , the time-varying range ( $r(t)$ ) between the sensor and the scatter  $S_o$  located at  $P = (x_o, y_o)$  is [114]

$$r(t) = R(t) + x_o \cos \theta(t) - y_o \sin \theta(t) \quad (3.53)$$

where  $R(t)$  is the time-varying range between the sensor and the center of rotation, and  $\theta(t)$  the time-varying rotational angle. These parameters can be expressed in terms of a Fourier series expansion truncated at the second order element. The result is

$$R(t) = R_o + v_R t + \frac{1}{2} a_R t^2 \quad (3.54)$$

$$\theta(t) = \theta_o + \Omega t + \frac{1}{2} a_\theta t^2 \quad (3.55)$$

where  $R_o$  is the range to the center of rotation of the target,  $\theta_o = \tan^{-1} \left( \frac{-y_o}{x_o} \right)$  the initial rotational angle,  $\Omega$  the angular velocity of the target and  $a_\theta$  the angular acceleration of the

target. According to Equation 3.53, the doppler frequency related to the scatter  $S_o$  is

$$f_D(t) = -\frac{1}{2\pi} \frac{d}{dt} \left( \frac{4\pi f}{c} r(t) \right) \quad (3.56)$$

where the evaluation of the derivative along time leads to

$$f_D(t) = -\frac{2f}{c} (f_D^{trans} + f_D^{rot}) \quad (3.57)$$

In this formula,  $f_D^{trans}$  and  $f_D^{rot}$  are the doppler frequencies due to translational and rotational motions. They are defined by

$$f_D^{trans} = v_R + a_R^2 t \quad (3.58)$$

$$f_D^{rot} = -x_o \sin \left( \theta_o + \Omega t + \frac{1}{2} a_\theta t^2 \right) (\Omega + a_\theta^2 t) - y_o \cos \left( \theta_o + \Omega t + \frac{1}{2} a_\theta t^2 \right) (\Omega + a_\theta^2 t) \quad (3.59)$$

In the case that  $\Omega t$  was very small and no target and angular acceleration was observed, Equation 3.57 reduces to [114]

$$f_D(t)|_{\Omega t \ll 1} \simeq \frac{2f}{c} (-v_R + x_o (\Omega \sin \theta_o + \Omega^2 t \cos \theta_o) + y_o (\Omega \cos \theta_o - \Omega^2 t \sin \theta_o)) \quad (3.60)$$

These formulas point out that the doppler history expressed with respect to the observation time varies according to the location of the different scatters and, then, it can be used to resolve the scatters in the cross-range dimension. But they also show that even in the case that  $\Omega$  was constant,  $f_D(t)$  would still be time-varying. As commented later, this issue complicates ISAR processing as it causes a set of important distortions that needs from advanced techniques to correct them. In some cases, it is not possible to completely compensate them, specially when the target experiments high angular velocities or the sensor covers large aspect angles for increasing the resolution. The result is an spatially dependent smearing effect in the cross-range dimension known as *blurring* [115], [114] [112].

### Circular spotlight imagery mode

The previous imaging geometry can be simplified in the particular case that the target has no translational motions ( $R(t) = R_o$ ). In such situation, the rotational motion can be understood

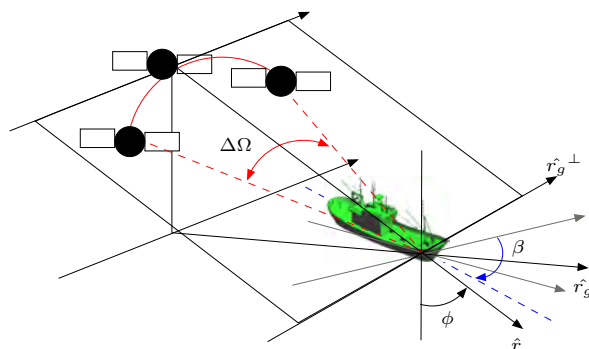


Figure 3.14: Detail of the circular spotlight imagery mode.

in terms of a SAR spotlight imagery mode where the linear path is changed by a circular one (*circular spotlight*) (see Fig. 3.14) [113]. In this sense, it is equivalent to achieve the rotational effect by moving the target and keep the sensor static or viceversa. The main advantage of the circular spotlight imagery mode is it makes easier to reproduce ISAR imaging geometries under laboratory conditions. In most cases, testing and measuring facilities, such anechoic chambers, are better adapted to put sensors in motions rather than complex targets. In fact, this option has been selected for the current thesis.

### 3.4.2 Data Acquisition

The basic scheme of data acquisition in ISAR sensors is based on taking, at fixed times, signal bursts or *range profiles* of  $n$  pulses. These pulses are sampled at the receiving chain and they can deal with any modulating waveform. Two typical examples are the chirp-pulse compression used in SAR or the stepped-frequency approach. Some works have found that the latter is more suitable for ISAR imagery, specially when the application requires high resolutions [113]. Stepped-frequency schemes emit a set of narrowband pulses centered at different frequencies with a separation among successive values of  $\delta f$ . In this way, the instantaneous bandwidth required for transmitting a single pulse is much lower than the total covered bandwidth. In most cases, the frequency step is selected constant for all the frequencies, despite it is possible to use non-uniform schemes or pseudo-random series. With the stepped-frequency waveform, the reflectivity information is acquired in the frequency domain and, hence, discrete Fourier operations are required for building the range profiles of the image.

As in SAR imagery, both range and doppler spectra must meet the Nyquist criteria in order to *unambiguously* sample the scene. For the range dimension, the spectrum is characterized by a periodic collection of single spectra with a bandwidth of  $c/2L$  and separated



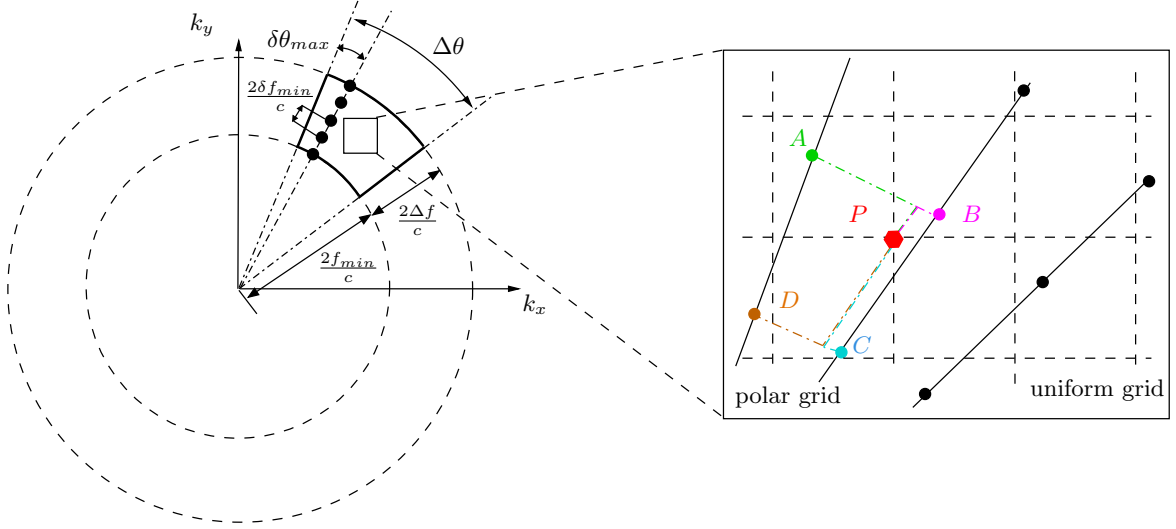


Figure 3.15: Scheme of the ISAR spectrum. The framed area provides a detail of the bidimensional interpolation

$\delta f$ . So, overlapping is avoided if

$$\delta f > \delta f_{min} = \frac{c}{2L} \quad (3.61)$$

For the cross-range dimension, the criteria assures that the arc drawn by the target between two bursts is not higher than the minimum wavelength. This fixes a maximum angular step of

$$\delta\theta_{max} = \frac{\lambda_{min}}{2L} \quad (3.62)$$

The particular acquisition scheme of ISAR sensors based on angular sections makes the reflectivity spectrum to be sampled in polar format. As shown in Fig. 3.15, this means that samples are organized within a specific *spectral corona* of angular extension  $\Delta\theta$  and width  $2\Delta f/c$ . In this spectral corona, the  $N$  bursts are disposed over a set of  $N$  radial lines with an angular separation of  $\delta\theta_{max}$ . For each line, the  $n$  samples are placed each  $2\delta f_{min}/c$ .

### 3.4.3 Processing Chain

To obtain the final ISAR image, it is necessary to express the reflectivity information measured in the frequency-time domain into the range-doppler one. According to the ISAR

geometry of Fig. 3.13, the signal backscattered by the scatter  $S_o$  is [114]

$$S(f, t) = \rho(x_o, y_o) e^{-j \frac{4\pi}{\lambda} r(t)} \quad (3.63)$$

where  $\rho(x_o, y_o)$  is the reflectivity function of the point scatter and  $r(t)$  is the time-varying sensor-to-target range. For all the contributions present in the scene, it can be shown that [114]

$$S(f, t) = e^{-j \frac{4\pi}{\lambda} R(t)} \int_{-\infty}^{\infty} \int_{-\infty}^{\infty} \rho(x, y) e^{-j 2\pi (x f_x(t) - y f_y(t))} dx dy \quad (3.64)$$

where  $f_x(t)$  and  $f_y(t)$  are the spatial frequencies in both dimensions

$$f_x(t) = \frac{2f}{c} \cos \theta(t) \quad (3.65)$$

$$f_y(t) = \frac{2f}{c} \sin \theta(t) \quad (3.66)$$

Equation 3.64 shows that the reflectivity density function  $\rho(x, y)$ , which actually is the final ISAR image, can be inverted by means of two simply FFT operations<sup>17</sup>. For such goal, a processing step adapted to the observations conditions is required.

### Circular spotlight mode

In the case that no translational motions are present in the scene,  $R(t) = R_o$  and, hence, the term  $e^{-j \frac{4\pi}{\lambda} R(t)}$  is constant. As commented previously, this allows to adopt the circular spotlight imagery mode used in this thesis. The related processing procedure is summarized as follows.

- **Interpolation.** The spectrum of ISAR images is not adapted to Fourier operations as they are not disposed over an uniform rectangular grid. For such reason, the first step is devoted to apply a bi-dimensional interpolation to the input data (see Fig. 3.15).
- **Data compression.** Once the data is sampled in rectangular format, image reconstruction is performed with a n-point IFT applied over frequency dimension, i.e. to each burst, followed by a N-point FFT applied over time dimension, i.e. to each range cell.

<sup>17</sup>The term  $e^{-j \frac{4\pi}{\lambda} R(t)}$  has to be properly compensated.

- **Image conditioning.** The final ISAR image is obtained by taking the magnitude of the resulting compressed data. At this point, it is optional to express the result in the local coordinate system of the target  $(x, y)$  or to apply a radial-dependent windowing operation oriented to reduce the weight of the secondary lobes. Note that it is possible to process specific angular sectors to isolate the reflectivity information related to particular views.

The previous procedure is known as *Range-Doppler* (RD) and it results on the following Point Spread Function (PSF) [115]

$$I(x, y) = \Delta f T_{obs} \left| \text{sinc} \left( \frac{u - u_o}{\delta_{r_s}} \right) \text{sinc} \left( \frac{v - v_o}{\delta_{r_c}} \right) \right| \quad (3.67)$$

where  $u_o$  and  $v_o$  are the projections of the scatter position  $P = (x_o, y_o)$  into the coordinate system of the incidence plane and,  $\delta_{r_c}$  and  $\delta_{r_s}$  are the cross- and slant-range resolutions

$$\delta_{r_c} = \frac{\lambda_{max}}{2\Delta\theta} \quad (3.68)$$

$$\delta_{r_s} = \frac{c}{2\Delta f} \quad (3.69)$$

Note that the spread function of ISAR systems is very similar to the SAR one detailed in Equation 3.37. In both cases, the bi-dimensional impulse response is made by the product of two *sinc* functions. It is worth noting that the expression of Equation 3.67 is only valid for those situations in which the doppler frequency has a low time dependence. This is the case of the current thesis where small aspects angles are processed. In addition, the value of  $\delta_{r_c}$  becomes modified if the operating frequency changes as well as the target extend. Certainly, to modify the target physical length ( $L$ ) implies to modify the electrical one ( $L^e = L/\lambda$ ) that, in practical terms, means to modify the operating frequency.

### General case

In the most general case, in which both rotational and translational motions are present in the scene even with second-order terms, ISAR processing is not so easy. First of all, the term related to target motion,  $e^{-j\frac{4\pi}{\lambda}R(t)}$  is not constant and, thus, it must be compensated before Fourier operations. For such purpose, an accurate estimation of the range, radial velocity and radial acceleration of the target is demanded for the whole observation time. This process is commonly known as *range tracking* [114] and, for constant values, it is relatively easy. For

time-dependent parameters, gyrocompass and differential GPS information becomes very useful [112]. Inaccurate range tracking makes the received echoes to move or *walk* out from the burst cell where they should be. If this happens, the integration time for that scatter will reduce degrading the quality of the image. This phenomenon is known as *range walks* and it can cause two main effects, namely: 1) a cross-range smearing effect in the distorted spread function that can affect other neighboring scatters and 2) an interference in the slant-range cells where the echoes walk in.

Due to the presence of second-order terms in target motions, the doppler frequency has an appreciable time dependence. As a result, the second term of the PSF expression becomes spatially variant inducing the previously commented phenomenon of *blurring* [115] [114]. To overcome this distortion, an efficient option lies on *time-frequency analysis*. It consists normally on expressing the signal in terms of the Cohen's time-frequency distribution (CTFD) [116]

$$CTFD(t, \omega) = \int \int \int e^{-j\vartheta t} e^{-j\xi\omega} e^{-j\vartheta\tau} K(\vartheta, \xi) S^* \left( \tau - \frac{\xi}{2} \right) S \left( \tau + \frac{\xi}{2} \right) d\tau d\xi d\vartheta \quad (3.70)$$

where  $K(\vartheta, \xi)$  is the kernel function and  $S(\cdot)$  the measured signal to transform. According to the kernel parameter, different transformations are obtained. Whatever the transformation results, the practical implementation of CTFD distribution is achieved by low-pass filtering the bi-dimensional IFT between the kernel function  $K(\vartheta, \xi)$  and the so-called *Wigner-Ville* (*WV*) transform [117]

$$WV(t, \omega) = \int S^* \left( t - \frac{\xi}{2} \right) S \left( t + \frac{\xi}{2} \right) e^{-j\xi\omega} d\xi \quad (3.71)$$

The most usual selection for the kernel function is the so-called Smoothed-Pseudo Wigner-Ville (SPWV) function defined as

$$K(\vartheta, \xi) = F(\vartheta)G(\xi) \quad (3.72)$$

where  $F(\vartheta)$  and  $G(\xi)$  are the FT of two smoothing window functions, such as the Hamming one. It can be shown that with this Time-Frequency Transformation (TFT) the impulse response becomes spatially invariant removing the effect of blurring. Different variants have been developed, such as the Time-Frequency Distribution Series (TFDS) [114] [118] or the Range Instantaneous Doppler (RID) [115]. In summary, a generic ISAR processing chain may be the one performed by the following steps, namely: 1) range tracking, 2) Interpol-

tion, 3) Range compression (the n-point IFT applied over the frequency dimension), 4) TFT transformation 5) Image conditioning.

Once the image is focused, an additional distortion so-called *cell migration* may be observed. It appears when the radial excursion of a particular scatter during the observation time is higher than the resolution cell dimensions. This means that the signature of that scatter would be focused in an erroneous cell of the ISAR image breaking with the correct scatter distribution of the complex target. The number of cells shifted by a scatter depends on the radial excursion, i.e. the observed scene, as well as on the resolution cell dimension, i.e. the used sensor. An option to drop the significance of such distortion is to select an aspect angle that assures that the radial excursion of a target with a length of  $L$  is limited to less than one resolution cell. This threshold is called *blur angle* and it is defined as

$$\Delta\theta_{blur} = \frac{\delta_r}{L} \quad (3.73)$$

where  $\delta_r$  represents the minimum value of the two pixel dimensions. Beyond the classical ISAR configuration, nowadays ISAR imaging is used in combination with other technologies to improve the quality of ISAR data and/or extend the areas where this imaging technique can be applied. The most promising solution is that one trying to infer tri-dimensional ISAR plots by means of interferometry. Some examples can be found on [51] [52] [112] [119]. Other approaches try to use ISAR theory for developing moving target algorithms within a distributed clutter [120].

## 3.5 SAR Imaging in Sea Scenarios

In this section, the particular characteristics that SAR images may have when imaging sea scenarios are further analyzed. Among them, the azimuth shifts due to the radial motions of vessels is the main concern.

### 3.5.1 Vessel Motions

It is well-known that a scatter with a radial velocity component  $v_r$  induces an azimuth displacement of [121]

$$\Delta x = -\frac{r_o v_r}{V_{plat}} \quad (3.74)$$

In some situations, this displacement may have the contributions of slant-range accelerations  $a_r$  [121] [18]. This happens if the following inequality is satisfied

$$\frac{a_r \cdot r_o}{V_{plat}^2} \gg 1 \quad (3.75)$$

In real scenarios, the ratio  $r_o/V_{plat}^2$  is normally low and, hence, very large acceleration ( $a_r \sim 10m/s^2$ ) are required for observing appreciable azimuth shifts [18]. In practice, it is assumed that radial accelerations have no influence on azimuth shifts. However, they have a notable significance on azimuth defocusing, specially for single-look images with longer integration times [18] [121]. In this field, the azimuth component of target velocity can also become an important defocusing factor [122].

The estimation of the overall distortion in vessel SAR images needs from the superposition of all the single displacements related to each scatter. The result is not straightforward as it depends on the structure and motions of the target as well as on the imaging geometry. Regarding motions, the influence of the sea makes ships to have up to six degrees of freedom, namely: swaying, surging, heaving, pitching, rolling and yawing. The former three are termed *translational* whereas the remaining ones *rotational*. Translational motions provide, jointly with the cruising speed, the most simple situation in which all the scatters have the same radial velocity. As commented previously, this causes *uniform shifts* leading to geolocation errors. In most situations, the impact of translational motions in such kind of errors can be considered negligible [18].

In contrast, rotational motions induce more notable distortions. In this case, the different scatters of a vessel acquire diverse slant-range velocities which magnitude and sense depend on the location of the scatters with respect to the rotation axes. This makes the spread functions to be affected by different displacements generating *non-uniform azimuth shifts*. In SAR images, this phenomenon generates distortions in the shape of the vessel signature causing length overestimation. Examples of such distortions in real data are presented in Fig. 3.16 and Fig. 3.17. On the one hand, Fig. 3.16 shows the image of a 57 m long vessel acquired by RADARSAT [35] in Scansar Narrow mode (pixel size of 25 x 25 m). The presence of vessel motions distorts the signature increasing the estimated length up to 200 m, more than 3 times the actual value. On the other hand, Fig. 3.17 show a collection of vessel SAR images acquired also by RADARSAT in Fine Beam mode (F4) (pixel size of 5 x 5 m) at the surroundings of the bay of Gibraltar. These snapshots have been isolated from the marine scene presented in Fig. 3.18. In this case, no ground-truth is available and, hence, an in-depth analysis can not be performed. However, the presence of important motions induces a notable azimuth spreading of the signatures. Specially adverse are the situations of vessel 1 (Fig. 3.17(a)) and vessel 2 (Fig. 3.17(b)) where the effects of rotational motions are evident.

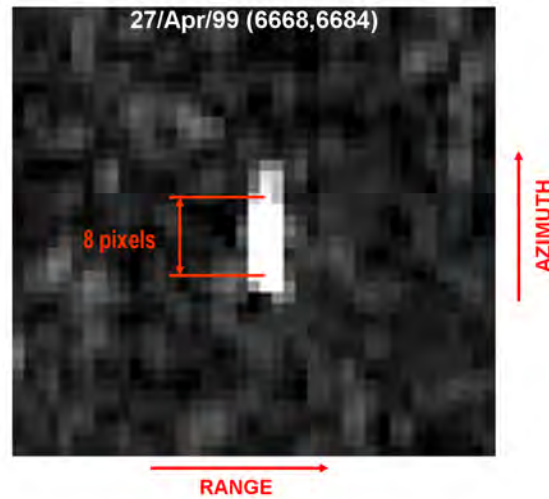


Figure 3.16: Vessel SAR image with azimuth distortions acquired by the RADARSAT sensor in Scansar Narrow mode (pixel size 25 x 25). It corresponds to a vessel with a length of 57 m.

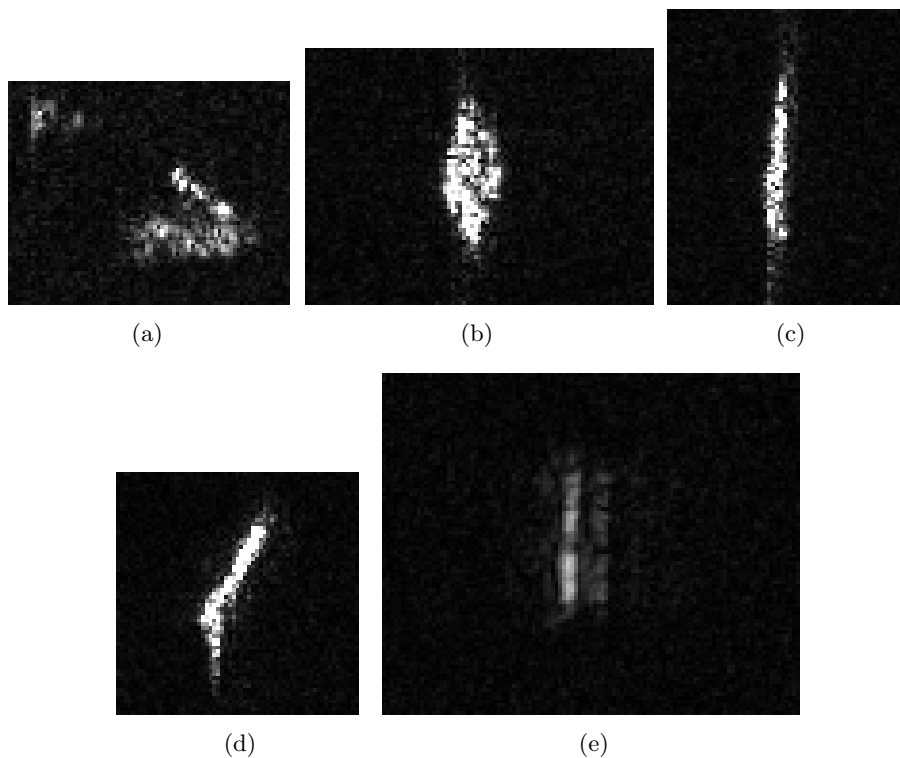


Figure 3.17: Five vessel signatures obtained from the image presented in Fig. 3.18. As before, range dimension is horizontally oriented whereas azimuth dimension vertically oriented. The azimuth x range dimensions for these images are 300 x 370 m (vessel 1) (a), 360 x 460 m (vessel 2) (b), 385 x 315 m (vessel 3) (c), 315 x 315 m (vessel 4) (d) and 445 x 545 m (vessel 5) (e).

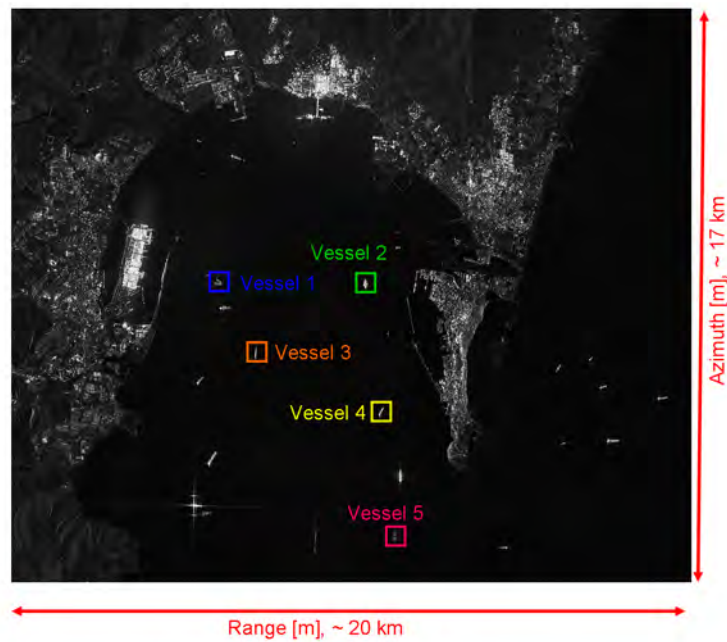


Figure 3.18: Scene of the marine area between Algeciras (Spain) and Gibraltar (British Overseas Territory) (azimuth x range extension of 17 x 20 km) acquired by RADARSAT Fine Beam mode (F4) at September 26<sup>th</sup>, 2003. Azimuth x range resolution is 5 x 5 m whereas the incidence angle 35°. The colored rectangles locate the vessel signatures presented in Fig. 3.17.



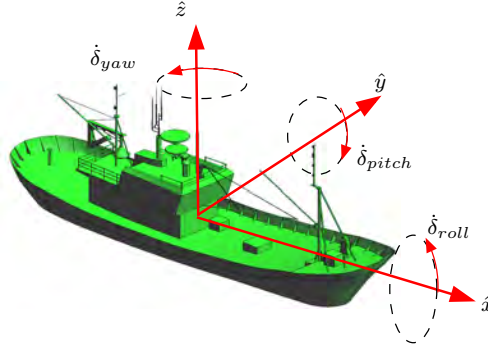


Figure 3.19: Local coordinate system for vessel motions

According to the imaging geometry and scatter distribution, different kind of distortions can be observed. They can be analyzed by evaluating the radial velocity as a function of the scatter location, vessel motion and incidence angle  $\phi$ . In this field, the radial contribution of the cruising speed for the  $i$ -th scatter is [48]

$$v_{r,speed}^i = |v_t| \cos \eta \sin \phi \quad (3.76)$$

where  $\eta$  is the vessel bearing measured counterclockwise with respect to ground-range direction. The contributions of rolling, pitching and yawing can be approximated to [48],

$$v_{r,roll}^i = L_i^{\hat{x}} \dot{\delta}_{roll} \left[ \sin \theta_i^{\hat{y}} \sin \eta \sin \phi - \cos \theta_i^{\hat{y}} \cos \phi \right] \quad (3.77)$$

$$v_{r,pitch}^i = L_i^{\hat{y}} \dot{\delta}_{pitch} \left[ \cos \theta_i^{\hat{z}} \cos \eta \sin \phi + \sin \theta_i^{\hat{z}} \cos \phi \right] \quad (3.78)$$

$$v_{r,yaw}^i = L_i^{\hat{z}} \dot{\delta}_{yaw} \sin \phi \left[ \sin \theta_i^{\hat{x}} \cos \eta + \cos \theta_i^{\hat{x}} \cos \eta \right] \quad (3.79)$$

where in all the cases  $\dot{\delta}_k, k \in \{k = roll, pitch, yaw\}$  is the angular velocity of the corresponding motion expressed in radians per second,  $L_i^k, k \in \{k = \hat{x}, \hat{y}, \hat{z}\}$  is the shortest distance in meters from the  $i$ -th scatter to the specific rotation axis and  $\theta_i^k, k \in \{k = \hat{x}, \hat{y}, \hat{z}\}$  is the orientation angle in degrees of the  $i$ -th scatter with respect to the labeled axis. All these parameters are defined according to the local coordinate system presented in 3.19. They are illustrated in Fig. 3.20 for an schematized ship with pitching.

According to these formulas, the commonest distortions for rolling and pitching are illustrated in Fig. 3.21. They are classified according to the incidence angle (high  $\rightarrow \phi \ll$ , low  $\rightarrow \phi \gg$ ) and target orientation (parallel to ground-range  $\rightarrow \eta \approx 0$ , parallel to azimuth  $\rightarrow \eta \approx 90$ ). Black lines presents the shape of the expected signature whereas red lines the

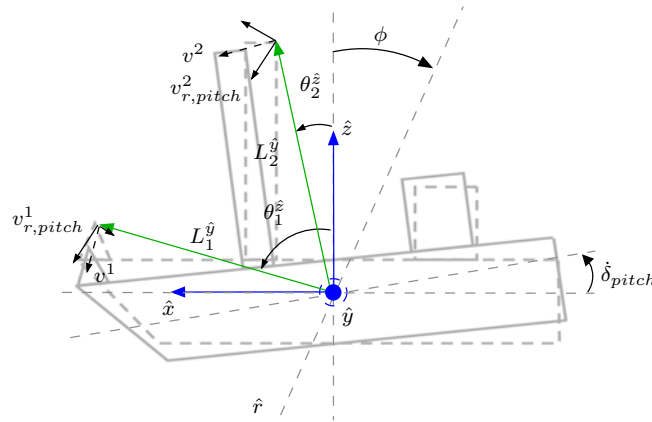


Figure 3.20: Illustration of the radial velocities for two scatters in a simple vessel with pitching.

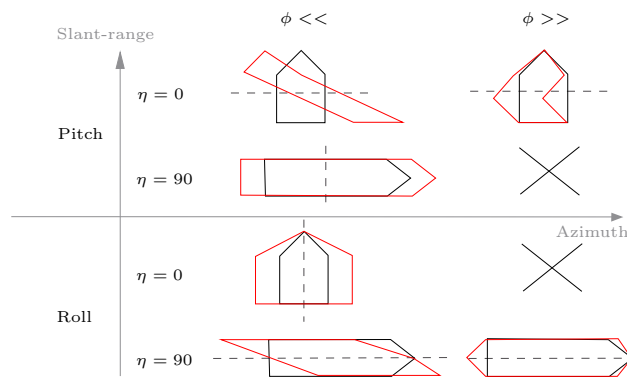


Figure 3.21: Schematization of common SAR image distortions due to pitching and rolling. Dash lines indicates the rotation axis for each case.

resulting distorted shape. In those situations where no important distortions are expected a cross is drawn.

The analysis of this graphic shows that the distortions with pitching may be more significant. This is due to the fact that the scatters located at the bow and stern of a vessel have the largest distance with respect to the rotation axis acquiring, thus, the largest radial velocity values. The result is a notable spreading of the vessel signature, as observed in the real data of Fig. 3.18. The particular way in which vessels cruise in real scenarios, normally perpendicular to the wave front, makes pitching to be the dominant motion in most situations and, then, the related distortions may be observed the highest number of times.

In order to assess the reliability of these conclusions, a set of simulations have been performed for the array of canonical scatters presented in Fig. 3.22. There, seven trihedrals with a 1 m long edge and facing the satellite schematize in a simple way a possible deck.

Table 3.1: Environmental conditions for the simulations presented in Fig. 3.21

Simulation label	$v_r$ [m/s]	$\dot{\delta}_{roll}$ [rad/s]	$\dot{\delta}_{pitch}$ [rad/s]	$\dot{\delta}_{yaw}$ [rad/s]
CALM	0	0	0	0
ROLL	3	0.015	0	0
PITCH	3	0	0.015	0
YAW	3	0	0	0.015

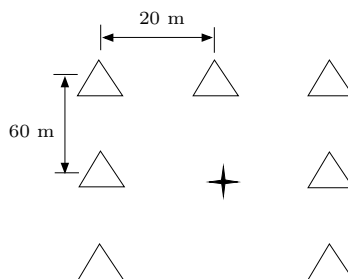


Figure 3.22: Array of seven trihedrals emulating the structure of a deck. Each scatterer has an edge length of 1 m.

Their relative distances are selected quite unrealistic in order to make the distortion analysis clearer. This target has been processed by *GRECOSAR* (see Chapter 5) for an ERS like sensor. Four different scenarios have been considered according to the environmental conditions summarized in Table 3.1. The results are presented in Fig. 3.23 in terms of the zero-padded (scale of 32) and normalized log-magnitude of the SAR images acquired for the HH channel. As observed, both uniform and non-uniform distortions are quite evident following the patterns described in Fig. 3.21. Note that they break the original geometry of the target making more difficult to relate the pixel distribution with the details of the structure [48].

### 3.5.2 Vessel-Sea Interaction

Another important issue in SAR imaging within sea scenarios is the interaction of vessel and the sea. This can generate new scattering mechanisms that can add to the inherent ones due to the geometry of the vessel. According to the incidence angle and vessel bearing, the weight of these mechanisms may be notable, even masking those related with the vessel. In such conditions, the interpretation of the reflectivity information will fail. The commonest sea-induced mechanism is performed at the lateral side of hull. It behaves as a dihedral and, thus, its reflectivity diagram is characterized by a narrow mainlobe with a high peak power. It becomes more evident when the vessel is oriented parallel to the sensor track. An example of such phenomenon is presented in Fig. 3.17(e).

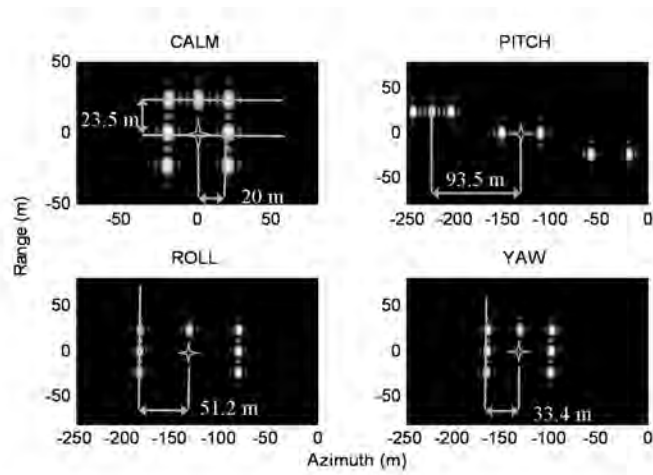


Figure 3.23: Illustration of the distortions experimented by the array of seven trihedral for rolling, pitching and yawing. The images are zero-padded by a factor of 32.

## Chapter 4

# SAR Polarimetry

This Chapter reviews the main concepts of radar polarimetry. It provides a comprehensive overview of the basic principles, parameters and tools that allow to isolate, process and interpret the polarization state of an electromagnetic wave. The Chapter starts by summarizing the most important issues related to the characterization of wave polarization. Then, this general theory is adapted to the scattering problem of SAR sensors where the concept of polarimetric descriptors is introduced. These parameters compile the most important polarimetric properties of targets providing an useful framework for inferring physical and/or geometrical information. Target Decomposition theory is used for such purpose. It relates the different methodologies used to characterize the observed scene according to a set of pre-defined physical models and how they can be inverted from polarimetric measurements. After a brief outline of the different options currently available, the focus is placed in coherent decompositions because they are suitable for analyzing complex targets data.

### 4.1 Wave Polarization

The concept of polarization in an electromagnetic wave can be clearly introduced from Maxwell's equations. For any point in the space defined by the vector  $\vec{r}$  and time  $t$  in the arbitrary coordinate system  $(x', y', z')$ , it is widely known that the electric ( $\vec{E}(\vec{r}, t)$ ) and magnetic ( $\vec{H}(\vec{r}, t)$ ) field vectors are related by the following equations

$$\nabla \times \vec{E}(\vec{r}, t) = -j\omega\mu\vec{H}(\vec{r}, t) \quad (4.1)$$

$$\nabla \cdot \vec{E}(\vec{r}, t) = \frac{1}{\epsilon'} \cdot \rho(\vec{r}, t) \quad (4.2)$$

$$\nabla \times \vec{H}(\vec{r}, t) = j\omega\epsilon_r\epsilon_o\vec{E}(\vec{r}, t) \quad (4.3)$$

$$\nabla \cdot \vec{H}(\vec{r}, t) = 0 \quad (4.4)$$

where  $\omega = 2\pi f$  is the angular frequency,  $f$  the wave frequency,  $\mu$  the medium permeability,  $\epsilon'$  the medium permittivity,  $\rho(\vec{r}, t)$  the charge density and

$$\epsilon_r = \frac{\epsilon'}{\epsilon_o} + i\frac{\sigma}{\omega\epsilon_o} = \epsilon'_r + i\epsilon''_r \quad (4.5)$$

the relative complex dielectric constant. In this formula,  $\epsilon_o$  is the free space permittivity and  $\sigma$  the medium conductivity. From these equations, it can be derived the *wave equation* that details the complex value of the electric field for any point within a specified medium. For the simple situation of free-source isotropic lossless homogeneous mediums, Maxwell's equations reduce to

$$\nabla^2 \vec{E}(\vec{r}, t) + k^2 \vec{E}(\vec{r}, t) = 0 \quad (4.6)$$

where

$$k = \omega\sqrt{\mu\epsilon'} \quad (4.7)$$

is the *wave number* parameter. The solution of the previous wave equation leads to the expression of the electric monochromatic planar wave <sup>1</sup>

$$\vec{E}(\vec{r}, t) = \Re \left\{ \vec{E}(\vec{r})e^{j\omega t} \right\} \quad (4.8)$$

where  $\Re$  is the real operator of complex numbers and the term  $\vec{E}(\vec{r})$  is defined by

$$\vec{E}(\vec{r}) = \vec{E}_o e^{-j\vec{k}\cdot\vec{r}} \quad (4.9)$$

---

<sup>1</sup>The *plane* concept stands for the fact that the *isophase* surfaces are planar.

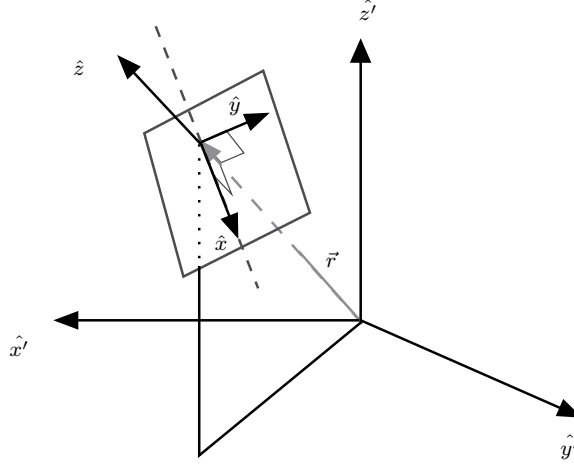


Figure 4.1: The Cartesian coordinate system.

with  $\vec{k} = \hat{k}k$  expressing the propagation direction of the wave and  $\vec{E}_o \perp \hat{k}$  the vector describing the starting position from which the electric field is evaluated.

In order to make mathematical operations easier, the Cartesian coordinate system  $(x, y, z)$  depicted at Fig. 4.1 is normally adopted. It accomplishes that  $\hat{z} \parallel \vec{r}$  and, then, forces the electric field vector to be embedded within the plane perpendicular to the propagation direction (the *wave plane*). This allows to write the expression of Equation 4.8 as

$$\vec{E}(\vec{r}, t) = E_x \hat{x} + E_y \hat{y} \quad (4.10)$$

with

$$E_x = E_{ox} \cos(\omega t - kz + \delta_x) \quad (4.11)$$

$$E_y = E_{oy} \cos(\omega t - kz + \delta_x + \delta) \quad (4.12)$$

In this formula,  $E_{oi}$  is the amplitude of the x- ( $i = x$ ) and y-component ( $i = y$ ),  $\delta_x$  the phase of the x-component and  $\delta = \delta_y - \delta_x$  the relative phase between both components. The evaluation of Equation 4.10 makes possible to describe the geometrical evolution of the tip of the electric field vector within the wave plane as a function of time. The result is

$$\frac{E_x^2}{E_{ox}^2} + \frac{E_y^2}{E_{oy}^2} + \frac{2E_x E_y}{E_{ox} E_{oy}} \cos \delta = \sin^2 \delta \quad (4.13)$$

that corresponds to the geometrical form of an ellipse. The previous formula is very important in the electromagnetic theory as outlines the concept of *wave polarization*. Actually, this concept concerns the shape and locus that the electric field describe within the wave plane along time. In a general form, wave polarization corresponds to an ellipse, as shown by Equation 4.13<sup>2</sup>, despite particular cases appear for linear or circular shapes. The most important characteristic of wave polarization is its dependence in relation to the *index of refraction*, which is fixed by the medium permittivity, medium permeability and medium conductivity. This means that when a narrow-band wave (ideally a single-frequency wave) passes through a medium of changing index of refraction and/or it becomes reflected by complex targets or scattering surfaces, the polarization state becomes modified and the wave re-polarized. This feature allows to study and characterize some physical properties of reflecting targets according to the polarization states of the incoming and received waves are analyzed. The result is a new framework for the identification and classification of targets by means of remote sensing measurements.

All the theory developed around the study, characterization, manipulation and interpretation of wave polarization is termed *polarimetry*. In a wide sense, it can be considered that this discipline started two centuries ago with the introduction of simple concepts in light or material theory. But this is not exactly true. Polarimetry concerns the control of *coherent* polarization properties of radio waves and it has not been until the Forties of the last century when the first phase control devices were available<sup>3</sup>. With the advent of such devices, the mathematical development of polarimetry advanced rapidly. First works were mainly oriented to formalize the 2 x 2 radar backscattering matrix once the dual polarized antenna technology was ready to use [123]. Then, the interest was focused on introducing and detailing the concept of optimal polarization, which had been essential in later developments around the Fifties and Sixties. [124]. At that time, the studies diversified a lot covering different concepts such as the geometrical representation of the polarization state within the so-called *Poincaré sphere* [125] [126], the polarization efficiency [127] or the diagonalization of the scattering matrix [128] that allowed a new eigenvalue approach for the treatment of the polarimetric information [129].

Beyond this initial work, polarimetry experimented an important explosion of ideas when at the early Seventies appeared the concept of adapting the general theory to the phenomenology of targets, i.e. the physical processes related with scattering [130]. This founded the basis of Target Decomposition (TD) theory that has been essential for developing target identification applications by means of polarimetric scattering. Despite first attempts on polarimetric information inversion were made along the Sixties [131] [132], it has not been until the Eighties when the importance of polarimetry in inverse scattering has been rigorously pointed out [133] [20]. These works can be considered an inflexion point in polarimetry

---

<sup>2</sup>In most works, the polarization of a wave is introduced as the ellipse of the electric field.

<sup>3</sup>This development has been partly due to the World War II.



because they demonstrate the improvements that polarimetry could cause in remote sensing applications. Since then, the major contributions to the literature were oriented to advance in TD theory. Important items were the introduction of wave synthesis and polarimetric signature concepts [134], and the definition of a rigorous formalism for tackling TD theory [22]<sup>4</sup>.

Nowadays, the theory of monostatic polarimetry is mature. It is compiled in some excellent works that unify concepts and notation within a complete and accurate mathematical framework [20] [135] [21] [136] [137] [138]. Following an overview of the most important concepts is provided stressing those ideas and parameters that will be more useful for the scope of this thesis.

#### 4.1.1 Ellipse of Polarization

According to Equation 4.13, the general form of wave polarization is described by an ellipse inscribed within a rectangle of sides  $2E_{ox}$  and  $2E_{oy}$  (see Fig. 4.2). Two main angles characterize the ellipse, namely: 1) the *orientation* angle  $0 \leq \psi \leq \pi$  and 2) the *ellipticity angle*  $-\frac{\pi}{4} \leq \chi \leq \frac{\pi}{4}$ . The orientation angle is defined by

$$\tan 2\psi = \tan (2\alpha) \cos \delta \quad (4.14)$$

where  $0 \leq \alpha \leq \frac{\pi}{2}$  is equal to

$$\tan \alpha = \frac{E_{oy}}{E_{ox}} \quad (4.15)$$

The inversion of Equation 4.14 leads to

$$\psi = \frac{1}{2} \arctan \left( \frac{2\Re \{\rho\}}{1 - \rho\rho^*} \right) \quad (4.16)$$

with  $\rho$  standing for the *complex polarization ratio*

$$\rho = \left| \frac{E_y}{E_x} \right| e^{j\delta} \quad (4.17)$$

---

<sup>4</sup>In the last part of this chapter a complete review of TD theory is provided focusing the attention in all those concepts related with coherent decompositions.

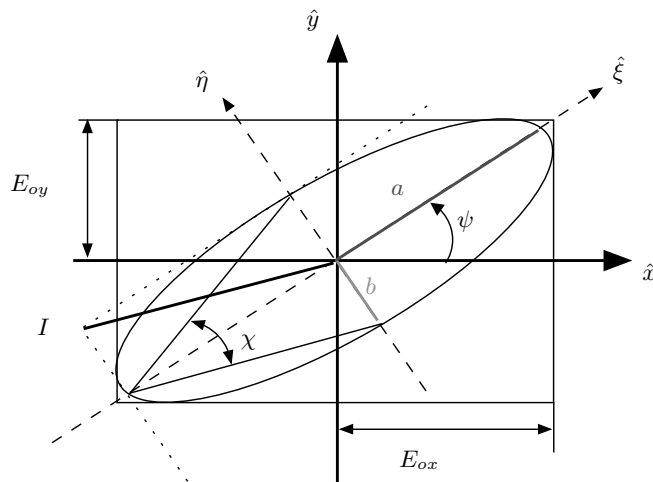


Figure 4.2: The ellipse of polarization. The wave plane is presented frontwards.

The *ellipticity angle* is fixed by

$$\chi = \pm \frac{b}{a} \quad (4.18)$$

where  $a$  and  $b$  are respectively the major and minor semi-axes of the ellipse. The sign of the ellipticity angle, which is fixed by the sign of the relative phase  $\delta$ , is essential for knowing the sense of rotation of  $\vec{E}(\vec{r}, t)$ . For *positive* values, the electric field rotates *counterclockwise* and, then, it is considered that the wave will have a *left-handed* polarization. In the contrary, *negative* values point out an electric field that rotates *clockwise* acquiring a *right-handed* polarization. These definitions are constrained to the IEEE standard that has the reference point at the rear of the wave. After some trigonometrical manipulations, it can be shown that  $\chi$  can be alternatively expressed as

$$\sin 2\chi = \sin(2\alpha) \sin \delta \quad (4.19)$$

and, in its inverse form, as

$$\chi = \frac{1}{2} \arcsin \left( \frac{2\Im\{\rho\}}{1 - \rho\rho^*} \right) \quad (4.20)$$

$$(4.21)$$

with  $\Im$  being the imaginary operator of complex numbers.

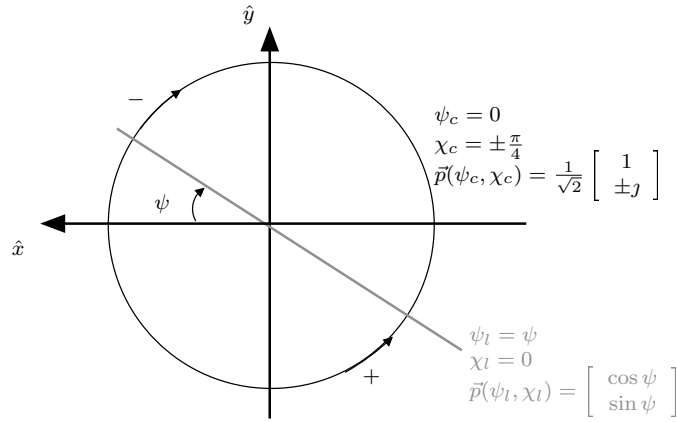


Figure 4.3: Linear and Circular polarization states. The wave plane is presented backwards.

In general, it is assumed that the polarization state of a wave is completely characterized by four parameters. The selection of such parameters depends mainly on the pursued application and the kind of information that has to be dealt with. The simplest and most intuitive set is the one related to the *geometrical* description of the ellipse of polarization. It is built by the ellipticity angle  $\chi$ , the orientation angle  $\psi$ , the differential phase  $\delta$  and wave intensity  $I = \{a^2 + b^2\}^{\frac{1}{2}}$ <sup>5</sup>. Other sets refer to the *mathematical* characterization of the electric field (*Jones Vector* representation) or to an alternative presentation of the polarization state by means of the so-called *Poincaré sphere* (*Stokes Vector* representation). All these sets provide complementary information and they are related by complex formulae (for further details see [137] and the references herein).

According to the values of these *descriptive* parameters, particular polarization states can be recognized (see Fig. 4.3). In the absence of ellipticity, i.e.  $\delta = m\pi$  for  $m = 0, \pm 1, \pm 2, \dots$ , the *linear* polarization results having different versions according to the orientation of the ellipse. In the contrary, when the ellipticity is equal to  $\chi = \pm \frac{\pi}{4}$ , i.e.  $E_{ox} = E_{oy}$  and  $\delta = m\frac{\pi}{2}$  for  $m = \pm 1, \pm 3, \pm 5 \dots$ , the wave acquires a *circular* polarization with two possible senses. They are solved by the sign of the ellipticity that, as before, provides *left-handed circular* polarization for *positive* values and *right-handed circular* polarization for *negative* ones.

The analysis of descriptive parameters allow to know the changes that the polarization of a wave experiments when the physical properties of a medium vary. This information is useful for building patrons of change that relate the variations of the polarimetric information with the targets that induce them. This is the base of inversion scattering problems.

<sup>5</sup>This parameter is related to the extent of the ellipse of polarization in terms of the coordinate system defined in Fig. 4.2.

### 4.1.2 Jones Vector Representation

The previous explanation has pointed out that the polarization state of a wave does not depend on the propagation term of  $\vec{E}(\vec{r}, t)$  ( $e^{j(\omega t - kz)}$ ). This means that in polarimetry the full expression of the electric field is not required, but a simplified version that only accounts for the useful polarimetric parameters. This new representation of the electric field is termed *Jones vector*, despite some authors refer it as the *polarization vector*. In a general form, the Jones vector is defined as

$$\vec{E}(\vec{r}, t) = E_{ox} e^{j\delta_x} (\hat{x} + \rho \hat{y}) \quad (4.22)$$

where the parameters  $\alpha$ ,  $E_{ox}$ ,  $\delta_x$  and  $\delta$  can be considered the *Jones* set of descriptive parameters, also referred as *Deschamps* parameters [135]. In some cases it is useful to work with the parametric formulation of the Jones vector [130]

$$\vec{E}(\vec{r}, t) = I e^{j\delta} \begin{bmatrix} \cos \psi & -\sin \psi \\ \sin \psi & \cos \psi \end{bmatrix} \begin{bmatrix} \cos \chi \\ j \sin \chi \end{bmatrix} \quad (4.23)$$

that can be understood as a coordinate system transformation between the set  $\{\hat{\xi}, \hat{\eta}\}$ , which is derived from the principal axes of the ellipse, and the nominal  $\{\hat{x}, \hat{y}\}$  one. In the case that the constant terms was removed, the polarization vector would simplify to <sup>6</sup>

$$\vec{p}(\psi, \chi) = \begin{bmatrix} \cos \psi \cos \chi - j \sin \psi \sin \chi \\ \sin \psi \cos \chi + j \cos \psi \sin \chi \end{bmatrix} \quad (4.24)$$

This equation provides the simplest expression for qualitatively describing the polarization state of a wave and it is normally used to introduce the concept of *polarization basis*. The polarization basis is a system reference that characterize an arbitrary polarization vector by means of two simple and orthogonal polarization states. In principle, there are infinite polarization basis. Certainly, it can be shown that, for any polarization state defined by a given polarization vector  $\vec{p}_o(\psi, \chi)$ , an orthogonal counterpart [130]

$$\vec{p}_\perp = \vec{p}\left(\psi + \frac{\pi}{2}, -\chi\right) \quad (4.25)$$

---

<sup>6</sup>This vector is theoretically termed normalized polarization vector. For sake of simplicity, this notation has not been adopted.

that satisfies

$$\vec{p}_o^\dagger \cdot \vec{p}_\perp = 0 \quad (4.26)$$

can always be found. Some simple examples are the linear horizontal-vertical basis  $\{\vec{p}_h, \vec{p}_v\} \propto \{H, V\}$ ,

$$\vec{p}_h = \vec{p}_o(0, 0) = \begin{bmatrix} 1 \\ 0 \end{bmatrix} \quad (4.27)$$

$$\vec{p}_v = \vec{p}_o\left(\frac{\pi}{2}, 0\right) = \begin{bmatrix} 0 \\ 1 \end{bmatrix} \quad (4.28)$$

the left-right handed circular basis  $\{\vec{p}_l, \vec{p}_r\} \propto \{L, R\}$

$$\vec{p}_l = \vec{p}_o\left(0, \frac{\pi}{4}\right) = \frac{1}{\sqrt{2}} \begin{bmatrix} 1 \\ j \end{bmatrix} \quad (4.29)$$

$$\vec{p}_r = \vec{p}_o\left(0, -\frac{\pi}{4}\right) = \frac{1}{\sqrt{2}} \begin{bmatrix} 1 \\ -j \end{bmatrix} \quad (4.30)$$

or the linear 45°-135° basis  $\{\vec{p}_{45^\circ}, \vec{p}_{135^\circ}\} \propto \{45^\circ, 135^\circ\}$

$$\vec{p}_{45^\circ} = \vec{p}_o\left(\frac{\pi}{4}, 0\right) = \frac{1}{\sqrt{2}} \begin{bmatrix} 1 \\ 1 \end{bmatrix} \quad (4.31)$$

$$\vec{p}_{135^\circ} = \vec{p}_o\left(\frac{3\pi}{4}, 0\right) = \frac{1}{\sqrt{2}} \begin{bmatrix} -1 \\ 1 \end{bmatrix} \quad (4.32)$$

### 4.1.3 Stokes Vector Representation

The third set of parameters that can be used for characterizing the polarization state of a wave were introduced with the main aim to achieve the same physical dimension for all them. They are termed *Stokes parameters* and they are defined in the linear basis  $\{H, V\}$  by

$$q = \begin{bmatrix} q_0 \\ q_1 \\ q_2 \\ q_3 \end{bmatrix} = \begin{bmatrix} |E_x|^2 + |E_y|^2 \\ |E_x|^2 - |E_y|^2 \\ 2|E_x||E_y|\cos\delta \\ 2|E_x||E_y|\sin\delta \end{bmatrix} = \begin{bmatrix} I^2 \\ I^2 \cos(2\psi) \cos(2\chi) \\ I^2 \cos(2\psi) \sin(2\chi) \\ I^2 \sin(2\chi) \end{bmatrix} \quad (4.33)$$

where  $q$  is the so-called *Stokes vector*.  $q_o^2$  is equal to

$$q_o^2 = q_1^2 + q_2^2 + q_3^2 \quad (4.34)$$

and  $q_1$ ,  $q_2$  and  $q_3$  are respectively related to the power density of the simple polarized components of the  $\{H, V\}$ ,  $\{45^\circ, 135^\circ\}$  and  $\{L, R\}$  basis.

The most important characteristic of the Stokes parameters lies on their capability to provide observable power terms, instead of the usual amplitude and phase information. This feature is very useful for characterizing *partially polarized waves* or waves which polarization state changes randomly around an average or *mean* configuration<sup>7</sup>. This implies a redefinition of the Stokes vector in order to take the distributed nature of the problem into account. The result is

$$q = \begin{bmatrix} q_o \\ q_1 \\ q_2 \\ q_3 \end{bmatrix} = \begin{bmatrix} \langle E_x E_x^* \rangle + \langle E_y E_y^* \rangle \\ \langle E_x E_x^* \rangle - \langle E_y E_y^* \rangle \\ \langle E_x E_y^* \rangle + \langle E_y E_x^* \rangle \\ j \langle E_x E_y^* \rangle - j \langle E_y E_x^* \rangle \end{bmatrix} \quad (4.35)$$

where  $\langle \dots \rangle = \lim_{T \rightarrow \infty} \left[ \frac{1}{2T} \int_{-T}^T \dots dt \right]$  is the temporal or ensemble averaging operator. The advantage of this new representation is the possibility to arrange the Stokes parameters in terms of a 2x2 complex hermitian positive semi-definite wave coherency matrix  $[J]$ . As observed later, this formulation simplifies the physical interpretation as separates the different intensities from the cross-correlation terms. In addition, it shows that a polarization state of a wave can be geometrically represented by an unique and exclusive point P within the Cartesian coordinate system defined by  $(q_1, q_2, q_3)$ . From Equation 4.33, it follows that this point is mapped on the surface of a sphere of radius  $I$ . This sphere is the *Poincare sphere* and it is pictorially described in Fig. 4.4. The angles  $2\psi$  and  $2\chi$  define the longitude and latitude of the point P, and according to their values some important characteristics can be derived, namely:

1. Left-handed polarizations are at the upper hemisphere ( $\chi > 0$ ) whereas the right-handed ones at the lower hemisphere ( $\chi < 0$ ).
2. Circular polarizations are mapped on the poles whereas the linear ones on the equatorial plane. Within this plane, horizontal and vertical polarizations are over the  $\hat{q}_1$  axis whereas the  $45^\circ$  and  $135^\circ$  linear ones over the  $\hat{q}_2$  axis.

---

<sup>7</sup>The extreme situations appears for *completely polarized waves*, i.e. waves with a fixed and static polarization state, and for *completely unpolarized waves*, i.e. waves with a totally random polarimetric behavior.

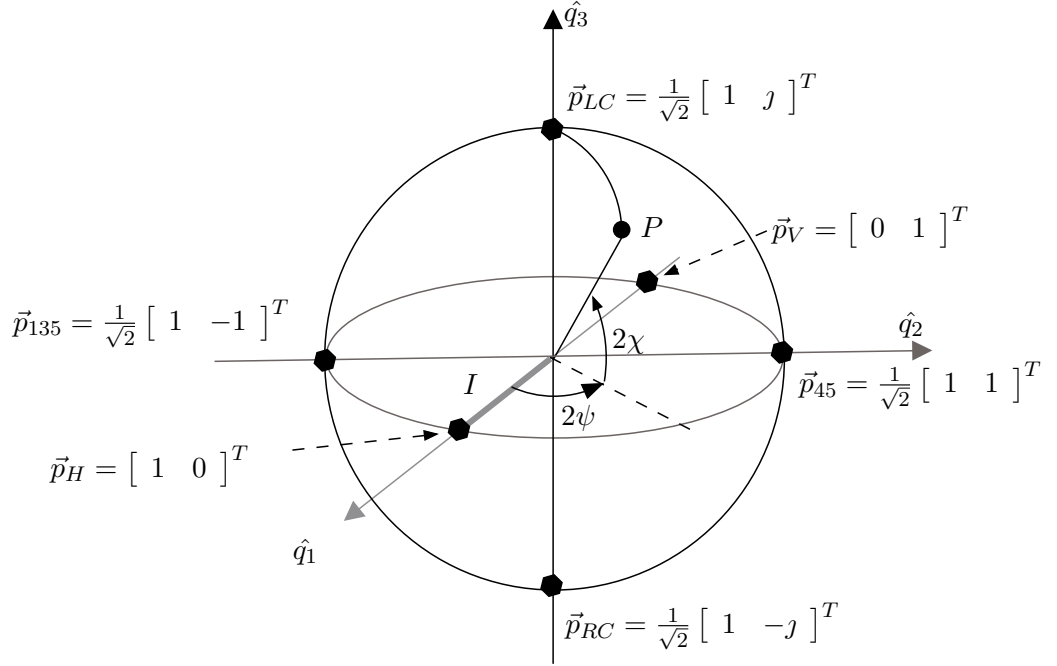


Figure 4.4: The Poincaré sphere with the location of some basic polarization states.

- Other parameters can be used to describe the same mapping point, for instance the  $\alpha$  and  $\delta$  parameters of the Jones descriptive set or the complex polarization ratio  $\rho$  [137].

#### 4.1.4 Polarization Basis Transformation

In previous points, the linear  $\{H, V\}$  basis (see Equation 4.27) has been used to define the basic concepts of polarimetry. However, there are other basis where the same polarimetric information can be presented in a more convenient way according to the polarization state of the wave. Some examples are the circular  $\{L, R\}$  and linear  $45^\circ$ - $135^\circ$  basis  $\{45^\circ, 135^\circ\}$ , both defined in Equation 4.29 and 4.31 respectively. The transformation operation among these bases is performed by an unitary and unique matrix  $[U_2]$

$$[U_2] = \frac{1}{\sqrt{1 + \rho\rho^*}} \begin{bmatrix} 1 & -\rho^* \\ \rho & 1 \end{bmatrix} \begin{bmatrix} e^{j\delta_i} & 0 \\ 0 & e^{j\delta_i} \end{bmatrix} \quad (4.36)$$

where  $\rho$  and  $\delta_i$  are respectively the polarization ratio and phase reference of the new basis. With this matrix, it becomes possible to express the polarization state of a wave in terms of

any arbitrary elliptical basis. The operation consists on a simple matrix multiplication

$$\vec{p}_{m'n'} = [U_2] \cdot \vec{p}_{mn} \quad (4.37)$$

where  $\vec{p}_{mn}$  and  $\vec{p}_{m'n'}$  provides the polarization state of a wave expressed respectively in the former  $\{\hat{m}, \hat{n}\}$  and transformed  $\{\hat{m}', \hat{n}'\}$ , elliptical basis. In some cases, the reference phase is equal to  $\delta_i = 0$ .

It is worth noting that the unitary matrix satisfies the wave energy conservation criteria ( $[U_2][U_2]^\dagger = [I_2]$  with  $[I_2]$  being the identity matrix) and, hence, the transformation operation does not affect the amplitude of the wave. In addition, the matrix  $[U_2]$  points out a new expression for the polarization vector in terms of the complex polarization ratio

$$\vec{p}(\rho) = \frac{1}{\sqrt{1 + \rho\rho^*}} \begin{bmatrix} 1 \\ \rho \end{bmatrix} \quad (4.38)$$

## 4.2 Target Polarimetric Descriptors

Once the basic theory related with the study and characterization of the polarization state of a wave (*wave polarimetry*) has been reviewed, the focus is placed on application issues. This concerns to *radar polarimetry* which main goal lies on solving invert scattering problems. For such purpose, *Target Polarimetric Descriptors* (TPD) are used because they gather all the useful and non-redundant polarimetric information related to target scattering. With TPD, TD theory provides the required analysis methodology for inferring valuable physical parameters of the scene.

Before going further in the explanation, it is essential to fix the coordinate system in which all the parameters will be defined. Up to now, there are two main conventions, namely: 1) the *Forward (anti-monostatic) Scattering Alignment* (FSA) and 2) the *Backward Scattering Alignment* (BSA). The first one, also referred as *wave coordinates*, defines the horizontal and vertical unitary vectors with respect to the direction of propagation. This means that for the backscattering case the horizontal unitary vector of the outgoing wave has an opposite sense in relation to the vector used for the incoming one. This does not happen with BSA, also referred as *antenna coordinates*, because the unitary vectors are defined with respect to the antenna polarization reference<sup>8</sup>. This makes BSA to be more suitable for radar remote sensing because it allows to reach a symmetric formulation in backscattering situations<sup>9</sup>.

<sup>8</sup>Actually, the original formulation of BSA was for bistatic situations. Here, it has been simplified to the monostatic case.

<sup>9</sup>The FSA convention is specially suited for optical remote sensing.



Such property helps on simplifying all the involved formulae and, for such reason, the BSA convention will be used in the following explanations.

### 4.2.1 The Sinclair Matrix

The most simple TPD is the *Sinclair matrix* (or *scattering matrix*)  $[S]$  that relates the two components of the electric field incident on a scatter ( $\vec{E}^i = E_h^i \hat{h}^i + E_v^i \hat{v}^i$ ) with respect to the components of the scattered one ( $\vec{E}^s = E_h^s \hat{h}^s + E_v^s \hat{v}^s$ ). According to the BSA convention,  $[S]$  is defined as <sup>10</sup>

$$\begin{bmatrix} E_h^s \\ E_v^s \end{bmatrix} = [S] \begin{bmatrix} E_h^i \\ E_v^i \end{bmatrix} = \frac{e^{-jkr}}{\sqrt{4\pi r}} \begin{bmatrix} S_{h^s h^i} & S_{h^s v^i} \\ S_{v^s h^i} & S_{v^s v^i} \end{bmatrix} \begin{bmatrix} E_h^i \\ E_v^i \end{bmatrix} \quad (4.39)$$

where  $r$  is the distance from the target to the receiver,  $\frac{1}{\sqrt{4\pi r}}$  the attenuation factor between the scatter and the antenna due to the spherical nature of the wave,  $(S_{h^s h^i}, S_{v^s v^i})$  the so-called *co-polar* terms and  $(S_{h^s v^i}, S_{v^s h^i})$  the so-called *cross-polar* ones. The four elements of the scattering matrix summarizes the scattering behavior of the target according to the polarization basis, i.e. how a particular incident polarization is modified due to the presence of the target. They depend on the physical and geometrical properties of targets as well as on their relative orientation with respect to the sensor. For measuring them, it is necessary to configure the polarizations of the transmitting and receiving antennas according to the convention pointed out by Equation 4.39. For example, the second element  $S_{h^s v^i}$  is retrieved when the transmitter is vertically polarized and the receiver horizontally polarized. Equation 4.39 simplifies in the case that both antennas were co-located and the medium between the target and the sensor was reciprocal. In such situation, referred as *mono-static*,  $S_{h^s v^i} = S_{v^s h^i}$  and, hence, the scattering matrix would have only three degrees of freedom. For the following and due to the scope of this thesis, this assumption is adopted.

### Unitary transformation of the scattering matrix

The scattering matrix can be expressed in terms of any elliptical basis as happens for the polarization vector. It only requires the following transformation operation

$$[S]_{m'n'} = [U_2][S]_{mn}[U_2]^T \quad (4.40)$$

where  $[U_2]$  is defined in Equation 4.36,  $[\dots]^T$  is the transpose operator, and  $\{\hat{m}\hat{n}\}$  and

---

<sup>10</sup>Pure polarization states are assumed.

$\{\hat{m}'\hat{n}'\}$  expresses the former and latter arbitrary elliptical basis. For any change of basis, there are three parameters of the scattering matrix that keep *invariant*, namely:

1. The so-called *matrix span*  $\kappa_3$ , which is defined in the linear  $\{HV\}$  basis as

$$\kappa_3 = \text{Span}[S] = |S_{HH}|^2 + 2|S_{HV}|^2 + |S_{VV}|^2 \quad (4.41)$$

2. The difference between the cross-polar terms  $S_{mn} - S_{nm} = S_{m'n'} - S_{n'm'}$ , which warrants the symmetry of the scattering matrix in any basis.
3. The determinant of the matrix ( $\text{Det}\{[S]_{mn}\} = \text{Det}\{[S]_{m'n'}\}$ ) due to the fact that the matrix  $[U_2]$  is unitary.

It is worth noting that the relation  $[G] = [S]^\dagger[S]$  (where  $[\dots]^\dagger$  is the transpose conjugate operation) denotes the so-called Graves matrix, which play an important role for optimal polarization procedures [124] [139] [140].

### Vectorization of the scattering matrix

When dealing with partially polarized waves, the vectorial formulation of the scattering matrix becomes very useful because it allows to introduce a set of polarimetric descriptors more suitable for distributed applications. Such formulation is derived from the vector signal estimation theory and it allows to express the matrix  $S$  in terms of an equivalent four-dimensional scattering feature vector  $\underline{f}_4$ <sup>11</sup>. This vector is defined by

$$\underline{f}_4 = V\{[S]\} = \frac{1}{2}\text{Trace}\{[S][\Psi]\} = [f_0 \ f_1 \ f_2 \ f_3]^T \quad (4.42)$$

where  $V\{\dots\}$  is the vectorization operator,  $\text{Trace}\{\dots\}$  the sum of the diagonal elements of the matrix and  $[\Psi]$  a complete set of 2x2 complex basis matrices under a hermitian inner product. Nowadays, there are two main bases used in the literature, namely: 1) the *lexicographic* basis  $[\Psi_L]$  and 2) the *Pauli* basis  $[\Psi_P]$ <sup>12</sup>. Both keep the Euclidean norm of the feature vector invariant and they are defined as

$$[\Psi_L] = \{\Psi_L^i, i = 0 \dots 3\} = 2 \left\{ \begin{bmatrix} 1 & 0 \\ 0 & 0 \end{bmatrix} \quad \begin{bmatrix} 0 & 1 \\ 0 & 0 \end{bmatrix} \quad \begin{bmatrix} 0 & 0 \\ 1 & 0 \end{bmatrix} \quad \begin{bmatrix} 0 & 1 \\ 0 & 1 \end{bmatrix} \right\} \quad (4.43)$$

<sup>11</sup>For the mono-static case, the vector is reduced to three dimensions.

<sup>12</sup>The Pauli basis is a renowned version of the complex Pauli spin matrix used in Quantum Physics.

$$[\Psi_P] = \{\Psi_P^i, i = 0 \dots 3\} = \sqrt{2} \left\{ \begin{bmatrix} 1 & 0 \\ 0 & 1 \end{bmatrix} \quad \begin{bmatrix} 1 & 0 \\ 0 & -1 \end{bmatrix} \quad \begin{bmatrix} 0 & 1 \\ 1 & 0 \end{bmatrix} \quad \begin{bmatrix} 0 & -j \\ j & 0 \end{bmatrix} \right\} \quad (4.44)$$

The evaluation of Equation 4.42 with Equation 4.43 and 4.44 leads, for the monostatic case, to the following feature vectors

$$\underline{f_{3L}} = [ f'_0 \quad f'_1 \quad f'_2 ] = [ S_{HH} \quad \sqrt{2}S_{HV} \quad S_{VV} ]^T \quad (4.45)$$

$$\underline{f_{3P}} = [ f_0 \quad f_1 \quad f_2 ] = \frac{1}{\sqrt{2}} [ S_{HH} + S_{VV} \quad S_{HH} - S_{VV} \quad 2S_{HV} ]^T \quad (4.46)$$

where  $S_{HH}$ ,  $S_{VV}$  and  $S_{HV}$  are the elements of the scattering matrix expressed in the linear basis  $\{HV\}$ . The expression of the Pauli feature vector allows to factorize the input matrix  $[S]$  as

$$[S] = \begin{bmatrix} f_0 + f_1 & f_2 \\ f_2 & f_0 - f_1 \end{bmatrix} \quad (4.47)$$

which, as commented following, is the base of a coherent target decomposition.

- Unitary Transformation of feature vectors

As with previous parameters, the basis transformation operation can also be applied to feature vectors. For the lexicographic approach, the change of basis is achieved by

$$\underline{f_{3L}}(m'n') = [U_{3L}]\underline{f_{3L}}(mn) \quad (4.48)$$

where

$$[U_{3L}] = \frac{1}{1 + \rho\rho^*} \begin{bmatrix} 1 & \sqrt{2}\rho & \rho^2 \\ -\sqrt{2}\rho^* & 1 - \rho\rho^* & \sqrt{2}\rho \\ \rho^{*2} & -\sqrt{2}\rho^* & 1 \end{bmatrix} \quad (4.49)$$

Similarly, for the Pauli basis

$$\underline{f_{3P}}(m'n') = [U_{3P}]\underline{f_{3P}}(mn) \quad (4.50)$$

where

$$[U_{3P}] = [D_3][U_{3L}][D_3]^\dagger = \frac{1}{2(1 + \rho\rho^*)} \begin{bmatrix} 2 + \rho^2 + \rho^{*2} & \rho^{*2} - \rho^2 & 2(\rho - \rho^*) \\ \rho^2 - \rho^{*2} & 2 - \rho^2 - \rho^{*2} & 2(\rho + \rho^*) \\ 2(\rho - \rho^*) & -2(\rho + \rho^*) & 2(1 - \rho\rho^*) \end{bmatrix} \quad (4.51)$$

In this formula,  $[D_3]$  and  $[D_3]^\dagger$  are defined by

$$[D_3] = \frac{1}{\sqrt{2}} \begin{bmatrix} 1 & 0 & 1 \\ 1 & 0 & -1 \\ 0 & \sqrt{2} & 0 \end{bmatrix} \quad (4.52)$$

$$[D_3]^{-1} = [D_3]^\dagger = \frac{1}{2} \begin{bmatrix} 1 & 1 & 0 \\ 0 & 0 & \sqrt{2} \\ 1 & -1 & 0 \end{bmatrix} \quad (4.53)$$

and they accomplish

$$\underline{f_{3P}} = [D_3]\underline{f_{3L}} \quad (4.54)$$

$$\underline{f_{3L}} = [D_3]^{-1}\underline{f_{3P}} \quad (4.55)$$

As before, this transformation keeps the norm of the feature vector thanks to the constants applied to the bases and the fact that  $[U_3]$  satisfies the wave energy conservation criteria ( $[U_3][U_3]^\dagger = [I_3]$  with  $[I_3]$  being the identity matrix).

### Polarimetric signatures

The scattering matrix can be used to provide an interesting representation of the polarimetric properties of targets by means of the so-called *Power Density Plots* (PDP) or *Polarimetric Signatures*. The idea consists on evaluating the relative power that a particular target would backscatter for any polarization state that the incident wave would have. To understand the meaning of such words, let to consider a target which scattering matrix is measured by a wave with a specific polarization state. Then, according to the transformation operations defined in Equation 4.40, it is possible to find the power response of the target for any desired polarization state, i.e. the relative power that the target would backscatter if the

wave had such polarization. In the case that this operating principle is repeated for a large set of polarization states, the results can be compiled in a graph that may be used to outline useful information about the scattering properties of targets. This graph is what is called polarimetric signature.

Mathematically, three different PDP can be defined, namely: 1) the co-polarized PDP  $P_c$ , 2) the orthogonal co-polarized PDP  $P_{c\perp}$  and 3) the cross-polarized PDP  $P_x$ . They take the following expressions

$$P_c = |V_{AA}(\psi, \chi)| = |p^T(\psi, \chi)[S(HV)]p(\psi, \chi)|^2 \quad (4.56)$$

$$P_{c\perp} = |V_{BB}(\psi, \chi)| = |p_{\perp}^T(\psi, \chi)[S(HV)]p_{\perp}(\psi, \chi)|^2 \quad (4.57)$$

$$P_x = |V_{AB}(\psi, \chi)| = |p_{\perp}^T(\psi, \chi)[S(HV)]p(\psi, \chi)|^2 \quad (4.58)$$

where  $p(\psi, \chi)$  is the normalized polarization vector defined in Equation 4.24,  $p_{\perp}(\psi, \chi)$  the orthogonal normalized polarization vector as defined in Equation 4.25,  $[S(HV)]$  the measured or reference scattering matrix expressed in the linear  $\{H, V\}$  basis,  $[\dots]^T$  the transpose operation and  $[\dots]^{\dagger}$  the transpose conjugate operation. According to the previous expression, PDP is a tri-dimensional plot where the x- and y-axis refers respectively to the orientation  $\psi$  and ellipticity  $\chi$  angle<sup>13</sup>. However, a two-dimensional version can be achieved if the polarization vector is only expressed in terms of the complex polarization ratio  $\rho$  as outlined in Equation 4.38. From Equation 4.56, three additional parameters can be defined, namely: 1) the co-polarized Phase Correlation Plots (PCP)  $R_c$ , 2) the cross-polarized PCP  $R_x$  and 3) the orthogonal cross-polarized PCP  $P_{x\perp}$

$$R_c = |\arg\{V_{AA}(\psi, \chi)\} - \arg\{V_{BB}(\psi, \chi)\}| \quad (4.59)$$

$$R_x = |\arg\{V_{AA}(\psi, \chi)\} - \arg\{V_{AB}(\psi, \chi)\}| \quad (4.60)$$

$$R_{x\perp} = |\arg\{V_{BB}(\psi, \chi)\} - \arg\{V_{AB}(\psi, \chi)\}| \quad (4.61)$$

where  $\arg[\dots]$  is the argument operator.

The main utility of polarimetric signatures lies on the possibility to map into the Poincaré sphere the polarimetric behavior of the observed targets. According to the orientation and ellipticity angles related to the local maxima of the derived plots, this allows to characterize the measured mechanisms according to a set of reference ones (dihedral, trihedral, ...). As a result, the observed geometry can be studied and a target classification approach developed.

<sup>13</sup>The angle step is selected by optimizing the trade-off between graph accuracy and number of iterations.

But in order to perform such process, it is necessary that each resolution cell has one important scattering mechanism. In the case that this condition is not fulfilled, the phase terms due to the relative distances can lead to unpredictable results. To appreciate this, Fig. 4.5 shows the value of  $P_c$  and  $P_x$  when in a resolution cell there are a trihedral and a dihedral separated an specific amount in slant-range. Fig. 4.5(a) and 4.5(b) corresponds to a relative slant-range distance of 2 m whereas Fig. 4.5(c) and 4.5(d) to 3 meters. These figures are presented with twice the range of actual  $\psi$  angles ( $0^\circ < \psi < 90^\circ$ ) in order to emphasize the symmetry of the responses. Two important issues are observed, namely: 1) the graphics have only one maximum (the other is a projection of the former one) which location differs from one situation to the other. This avoids to distinguish the number and type of scatters within the pixel; 2) the related angles do not match the reference positions for a trihedral ( $\psi = 0^\circ, \chi = 0^\circ$ ), a dihedral ( $\psi = 90^\circ, \chi = 0^\circ$ ) and, even, a dipole ( $\psi = 45^\circ, \chi = 0^\circ$ ). Therefore, it does not seems that the polarimetric signature may apport useful information for vessel classification. Even the alternative interpretation of polarimetric signatures in terms of changes of the polarization basis does not add any useful information.

### Canonical targets

At this point, it becomes very interesting to put some numerical values to the previous polarimetric descriptors in order to know which kind of physical information can be retrieved from polarimetric measurements. For such purpose, the so-called *canonical targets* are very suited. These scatters are simple geometrical shapes which scattering properties are well known and depend only on two of the three dimensions of the space. A summary of the basic characteristics for the most common targets is presented in Fig. 4.6. Due to their high RCS and relatively wide angular response, specially for the case of trihedrals, these targets are often used in calibration issues inasmuch as they demand a less restrictive pointing alignment.

In Polarimetry, the main advantage of this kind of targets is that they allow to characterize simple scattering behaviors that can help to describe more complex ones. In fact, this is the casuistic of TD theorems that use the presence, weight and distribution of these simple behaviors along the signature to identify complex scattering mechanisms. The values of their scattering matrices  $[S]$  and feature vectors  $\underline{f}_{3L}, \underline{f}_{3P}$  are included along Section 4.3 (see Equations 4.74, 4.88 and 4.108-4.113). They point out that these targets have the simplest behaviors that in polarimetry one can have. For example, trihedrals are related to mechanisms with an odd number of reflections whereas dihedrals to mechanisms with an even number of reflections.

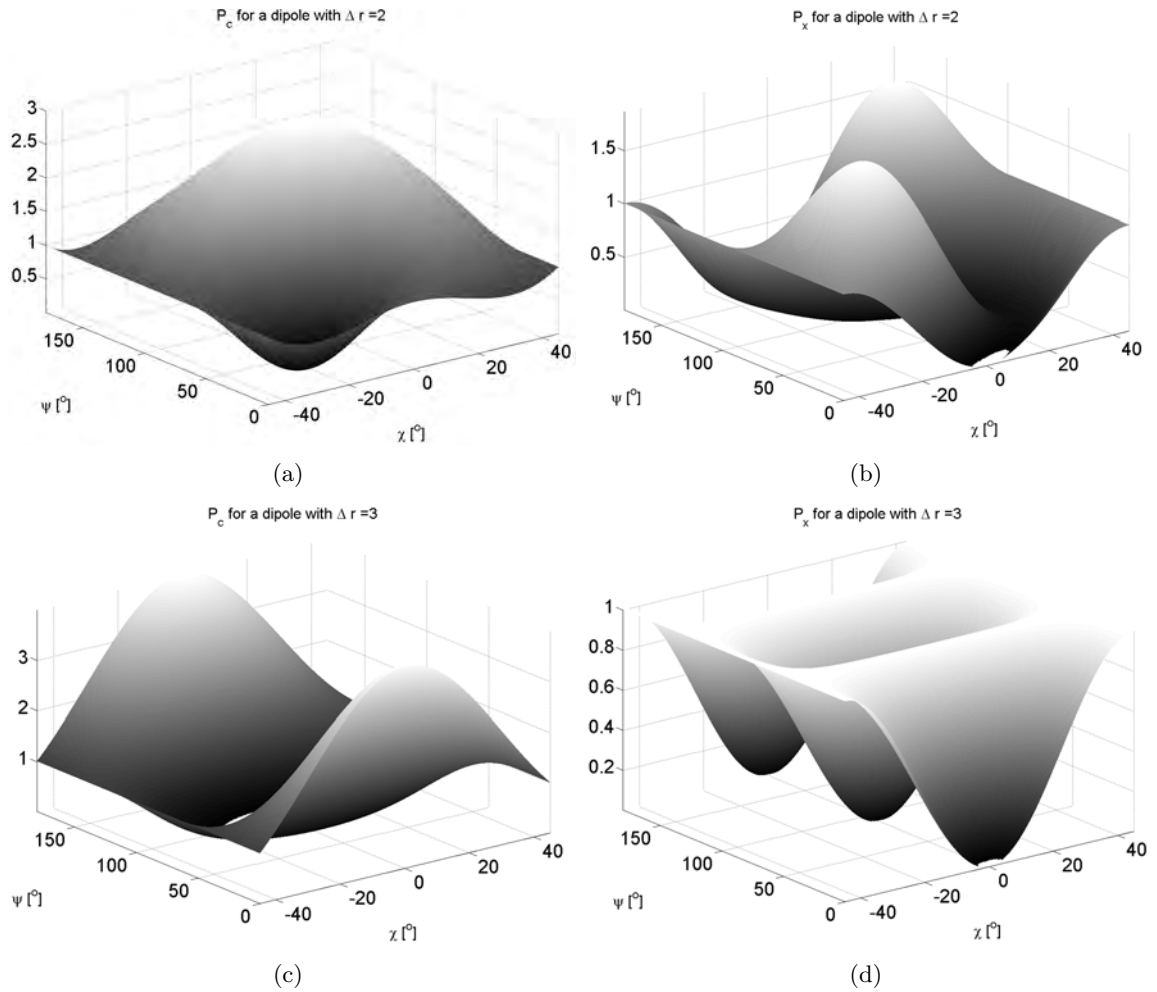


Figure 4.5: Co- ( $P_c$ ) and Cross-polar ( $P_x$ ) polarimetric signatures obtained for the combination of a trihedral and dihedral within the same resolution cell and separated an specific amount in slant-range ( $\Delta_r$ ).  $P_c$  has been evaluated for  $\Delta_r = 2m$  (a) and  $\Delta_r = 3m$  (c) whereas  $P_x$  for  $\Delta_r = 2m$  (b) and  $\Delta_r = 3m$  (d).

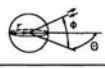


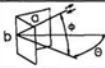

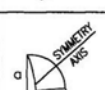
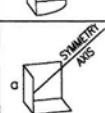
Type	Dimensions	Maximum RCS, $\sigma$	Angular Response for $\sigma$	
			$\theta$	$\phi$
Sphere		$\pi r^2 = 3.14r^2$	360°	360°
Cylinder		$\frac{2\pi ab^2}{\lambda} = 6.28 \frac{ab^2}{\lambda}$	360°	$\pm 13 \frac{\lambda}{b}$ degree to $\frac{1}{2}$ max
Rectangular Flat Plate		$\frac{4\pi a^2 b^2}{\lambda^2} = 12.6 \frac{a^2 b^2}{\lambda^2}$	$\pm 13 \frac{\lambda}{b}$ degree to $\frac{1}{2}$ max	$\pm 13 \frac{\lambda}{b}$ degree to $\frac{1}{2}$ max
Rectangular Dihedral Corner		$\frac{8\pi a^2 b^2}{\lambda^2} = 25.1 \frac{a^2 b^2}{\lambda^2}$	$\pm 15^\circ$ to $\frac{1}{2}$ max $\pm 32^\circ$ to $\frac{1}{10}$ max	$\pm 13 \frac{\lambda}{a}$ degree to $\frac{1}{2}$ max
Triangular Trihedral		$\frac{4\pi a^4}{3\lambda^2} = 4.19 \frac{a^4}{\lambda^2}$	Approx. 40° total cone angle about axis to $\frac{1}{2}$ max	
Circular Trihedral		$15.6 \frac{a^4}{\lambda^2}$	Approx. 32° total cone angle about axis to $\frac{1}{2}$ max	
Square Trihedral		$\frac{12\pi a^4}{\lambda^2} = 37.8 \frac{a^4}{\lambda^2}$	Approx. 23° total cone angle about axis to $\frac{1}{2}$ max	

Figure 4.6: Basic characteristics of common canonical targets.

## 4.2.2 Power Matrices

In Section 4.1.3, it has been pointed out that the polarimetric characteristics of partially polarized waves are better described with second order parameters. The same happens for distributed targets, in such a case the so-called *power matrices* becomes very suited.

### The Mueller matrix

The first power matrix is the *Mueller* matrix  $[M]$  that relates the averaged Stokes vector (see Equation 4.35) of the incident  $q^{inc}$  and scattered  $q^{sca}$  wave as

$$q^{sca} = [M]q^{inc} \quad (4.62)$$

where

$$[M] = \begin{bmatrix} A_o + B_o & C & H & F \\ C & A_o + B_o & E & G \\ H & E & A_o - B_o & D \\ -F & -G & -D & A_o - B_o \end{bmatrix} \quad (4.63)$$



is the parametric version of the Mueller matrix<sup>14</sup>. Equation 4.62 shows that the Mueller matrix plays the same role than the scattering matrix, but for the case of partially polarized waves. Note that normally a particular Mueller matrix has not a unique corresponding scattering matrix, but many of them. Only for the particular case in which a set of constraints are fulfilled, it is achieved the uniqueness property between both matrices [22]. In Polarimetry, the Mueller matrix has been often used in optimization processes oriented to maximize the backscattered power by matching the incoming polarization with the antenna one.

### The Coherency and Covariance matrices

The power polarimetric descriptors that are specially suitable for developing applications are the so-called *Coherency*  $[C_{3P}]$  and *Covariance*  $[C_{3L}]$  matrices. They are respectively defined as the outer product of the Pauli and lexicographic feature vectors with the corresponding transpose conjugate. In a mathematical form,

$$[C_{3P}] = \langle \underline{f}_{3P} \cdot \underline{f}_{3P}^\dagger \rangle \quad (4.64)$$

$$[C_{3L}] = \langle \underline{f}_{3L} \cdot \underline{f}_{3L}^\dagger \rangle \quad (4.65)$$

where  $\underline{f}_{3P}$  and  $\underline{f}_{3L}$  are respectively defined in Equation 4.46 and 4.45. Both matrices result on

$$[C_{3P}] = \frac{1}{2} \begin{bmatrix} \langle |S_{HH}+S_{VV}|^2 \rangle & \langle (S_{HH}+S_{VV})(S_{HH}-S_{VV})^* \rangle & \langle (S_{HH}+S_{VV})2S_{HV}^* \rangle \\ \langle (S_{HH}-S_{VV})(S_{HH}+S_{VV})^* \rangle & \langle |S_{HH}-S_{VV}|^2 \rangle & \langle (S_{HH}-S_{VV})2S_{HV}^* \rangle \\ \langle 2S_{HV}(S_{HH}+S_{VV})^* \rangle & \langle 2S_{HV}(S_{HH}-S_{VV})^* \rangle & \langle 4|S_{HV}|^2 \rangle \end{bmatrix} \quad (4.66)$$

$$[C_{3L}] = \begin{bmatrix} \langle S_{HH}S_{HH}^* \rangle & \sqrt{2}\langle S_{HH}S_{HV}^* \rangle & \langle S_{HH}S_{VV}^* \rangle \\ \sqrt{2}\langle S_{HV}S_{HH}^* \rangle & 2\langle S_{HV}S_{HV}^* \rangle & \sqrt{2}\langle S_{HV}S_{VV}^* \rangle \\ \langle S_{VV}S_{HH}^* \rangle & \sqrt{2}\langle S_{VV}S_{HV}^* \rangle & \langle S_{VV}S_{VV}^* \rangle \end{bmatrix} \quad (4.67)$$

where  $\langle \dots \rangle$  stands for the ensemble average operator. It can be shown that both matrices are hermitian positive semi-definite sharing the same eigenvalues. This is due to the fact that these matrices are related by the unitary transformation

$$[C_{3P}] = [D_3][C_{3L}][D_3]^\dagger \quad (4.68)$$

<sup>14</sup>The meaning of the different parameters will be clarified in the next point.

where  $[D_3]$  and  $[D_3]^\dagger$  are defined in Equations 4.52 and 4.53. The expression of the coherency matrix can be formulated in a parametric version in terms of the Mueller parameters. The result is

$$[C_{3P}] = \begin{bmatrix} A_o + A & C - jD & H + jG \\ C + jD & B_o + B & E + jF \\ H - jG & E - jF & B_o - B \end{bmatrix} \quad (4.69)$$

from which the Mueller parameters can be inverted. It is worth noting that the covariance and coherency matrix can be expressed in terms of the power density and phase correlation parameters defined in Section 4.2.1. For the covariance matrix the result is [137]

$$[C_{3L}(\rho)] = \begin{bmatrix} P_c(\rho) & \sqrt{2}R_x(\rho) & R_c(\rho) \\ \sqrt{2}R_x(\rho)^* & 2P_x(\rho) & \sqrt{2}R_{x\perp}(\rho)^* \\ R_c(\rho)^*\sqrt{2} & R_{x\perp}(\rho) & P_{c\perp}(\rho) \end{bmatrix} \quad (4.70)$$

where  $P_c(\rho), P_{c\perp}(\rho), P_x(\rho), R_c(\rho), R_x(\rho), R_{x\perp}(\rho)$  are defined in Equations 4.56- 4.61 by substituting the normalized polarization vector  $p(\psi, \chi)$  with the equivalent expression  $p(\rho)$  of Equation 4.38. Such relations allow to fix a set of useful polarimetric variables, such as the degree of coherence  $\mu(\rho)$  and polarization  $D(\rho)$  [137]

$$\mu(\rho) = \frac{|R_x(\rho)|}{\sqrt{P_x(\rho)P_c(\rho)}} \quad (4.71)$$

$$D(\rho) = \frac{\sqrt{[P_c(\rho) - P_x(\rho)]^2 + 4|R_x(\rho)|^2}}{P_c(\rho) + P_x(\rho)} \quad (4.72)$$

### 4.3 Target Decomposition Theory

As outlined before, the main goal of radar polarimetry is to infer physical and geometrical characteristics of targets from the polarimetric analysis of the received wave. For such purpose, a set of polarimetric descriptors were defined in order to compile the most relevant issues about target scattering. The methodology related with the interpretation of such information is what is called Target Decomposition (TD) Theory. Its basic principle consists on expressing the measured complex polarimetric behavior in terms of simple mechanisms related to well-known physical processes. From a mathematical point of view, this means to *decompose* the used polarimetric descriptors into a sum of independent and simple elements

identifying the basic mechanisms. This procedure makes data interpretation and inversion easier.

Nowadays, TD has achieved a high degree of development. A prove of this is the high diversification that the different applications dealing with radar polarimetry have reached. Such success is partly due to the intensive theoretical work developed from the Seventies [130] to the Nineties [22] oriented to provide a unified analysis framework and mathematical characterization of the problem. TD can be classified in two main groups, namely: 1) *coherent* and 2) *incoherent*. The former works with the first order polarimetric descriptors, such as the Sinclair matrix  $[S]$  whereas the latter with power matrices, specially the coherency and covariance ones.

In this thesis, it is assumed that vessels, as any man-made target, behave as non-distributed targets and, hence, coherent decomposition methods are more suitable for the analysis of their signatures<sup>15</sup>. This is due to the fact that vessel SAR images have in each resolution cell some significant scatters that present diverse polarimetric mechanisms and RCS. This differs from the scattering behavior of distributed targets that forces each resolution cell of the image to have a lot of scatters with similar scattering properties acquiring thus a stochastic nature. For such reason, Coherent Target Decompositions (CTD) are the main concern of this thesis.

### 4.3.1 Coherent Target Decompositions

CTD assumes that the matrix  $[S]$  of the  $j$ -th pixel can be decomposed in a *coherent* sum of basic matrices  $[S_i]$

$$S^j = \sum_{i=0}^N \alpha_i^j [S_i] \quad (4.73)$$

where  $\alpha_i$  are complex constants expressing the weight of each simple mechanism identified by  $[S_i]$ . The number  $N$  is in practice finite (despite from a mathematical point of view can be infinite) and normally it is not higher than three. The key point of the previous formula is the fact that  $\{[S_i], i = 0 \dots N\}$  express the scattering behavior of simple and common geometrical shapes, normally canonical targets. This means that the values of  $\{\alpha_i, j = 1 \dots N_{pixels}\}$  allow to build a set of additional "weight maps", one per each simple mechanism, that highlights which geometrical shape dominates the response of each pixel. Such maps can be considered the *polarimetric trace* of vessels and they allow to infer geometrical features of targets. The idea is reflected in Fig. 4.7.

<sup>15</sup>In the literature, it is widely assumed that any man-made target behave as a non-distributed targets.

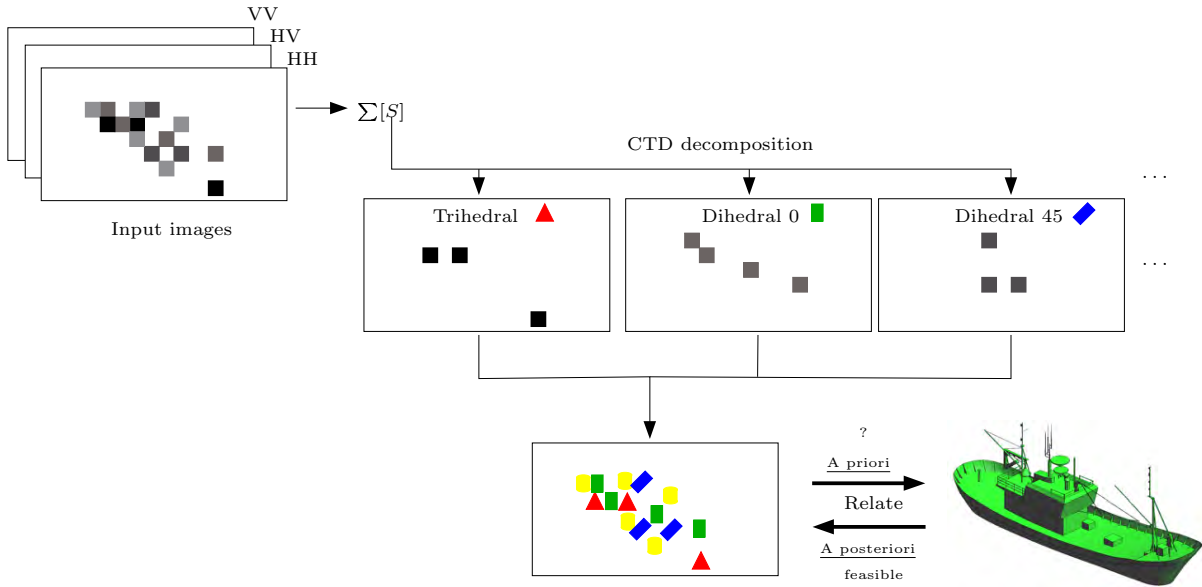


Figure 4.7: Scheme of the operating principle of CTD. The complex polarimetric behavior is expressed in terms of maps providing the weight of each simple mechanism for the selected theorem.

According to the basic matrices, different methods are currently available. Following, those CTD with a proven practical utility are going to be reviewed. Other ones such as the *similarity approach* [141] or the *Huynen target decomposition* [142] are not included because they almost provide the same information than others CTD. Certainly, the former work is formally equal to Pauli or SDH whereas the later one to the symmetric analysis of Cameron.

## Pauli

The most simple CTD is the one derived from the factorization of the scattering matrix via the elements of the Pauli vector. According to Equation 4.47, it follows that

$$[S] = \begin{bmatrix} f_0 + f_1 & f_2 \\ f_2 & f_0 - f_1 \end{bmatrix} = f_0[\Psi_P^0] + f_1[\Psi_P^1] + f_2[\Psi_P^2] \quad (4.74)$$

where  $\{f_i, i = 0 \dots 2\}$  are the elements of the Pauli vector (Equation 4.46) and  $\{\Psi_P^i, i = 0 \dots 2\}$  the matrices of the Pauli basis (Equation 4.44). This decomposition is called *Pauli CTD* and it has been widely used in radar polarimetry due to its simplicity and the orthogonality of its basis. This property can be easily shown by checking the vectorial form of

Equation 4.74

$$\underline{f}_{3P} = f_0 \hat{f}_0 + f_1 \hat{f}_1 + f_2 \hat{f}_2 \quad (4.75)$$

where  $\hat{f}_0 = [1, 0, 0]^T$ ,  $\hat{f}_1 = [0, 1, 0]^T$  and  $\hat{f}_2 = [0, 0, 1]^T$  perform an orthogonal basis. As explained previously, each basic matrix can be associated with a specific physical process. In this case,  $\Psi_P^0$  is related to mechanisms with an odd number of reflections, such as those induced by a flat plane, sphere or trihedral, whereas  $\Psi_P^1$  and  $\Psi_P^2$  to double-bounce mechanisms generated by dihedrals with an orientation of 0 and 45 degrees respectively. As observed later, such mechanisms are very common within vessels and their distribution is very useful for developing reliable classification methods.

It is worth noting that in general the Pauli decomposition is *unique*. This means that the above expression applies for any polarization basis and, hence, it has a unique polarization interpretation. The only variations are on the factors  $f_i$ ,  $i = 0 \dots 2$ , which are modified according to the expressions of the simple behaviors in the new basis. For example, in the circular basis  $\{LR\}$  the Pauli vector is

$$\underline{f}_{3P}^{LR} = [U_3]_{HV \rightarrow LR} \underline{f}_{3P}^{HV} = \frac{1}{\sqrt{2}} \begin{bmatrix} 2jS_{HV} \\ S_{HH} - S_{VV} \\ 2j(S_{HH} + S_{VV}) \end{bmatrix} \quad (4.76)$$

where  $[U_3]_{HV \rightarrow LR}$  is the unitary transformation matrix from the  $\{HV\}$  to the  $\{LR\}$  basis derived by evaluating Equation 4.51 with  $\rho = j$ <sup>16</sup>. This expression is formally equal to the former one and the only differences are on the elements of the vector. In this way,  $\underline{f}_{3P}^{LR}$  points out that trihedral or spheres maximize the response of the LR channel whereas dihedrals of the LL and RR ones. This result is consistent with the polarimetric characterization of these simple targets in the circular basis. Then, it is possible to find with  $\underline{f}_{3P}^{LR}$  the weight of the same mechanisms than those isolated with the linear basis.

### Sphere-Diplane-Helix

The Sphere-Diplane-Helix (SDH) decomposition [143] is a variant of the Pauli one, but taking into account the orientation of the dihedral with respect to the Line-Of-Sight (LOS). The mathematical form is

<sup>16</sup> $j$  is the complex polarization ratio of the left-handed circular polarization

$$[S]' = \begin{bmatrix} |a'|e^{j\phi_{a'}} + |b'|e^{j\phi_{b'}} & |c'|e^{j\phi_{c'}} \\ |c'|e^{j\phi_{c'}} & |a'|e^{j\phi_{a'}} - |b'|e^{j\phi_{b'}} \end{bmatrix} = [R]^T [S] [R] = k_s [S]_s + e^{j(\phi_{b'} - \phi_{a'})} (k_d [S]_d + k_h [S]_h) \quad (4.77)$$

where

$$[R] = \begin{bmatrix} \cos \Psi & -\sin \Psi \\ \sin \Psi & \cos \Psi \end{bmatrix} \quad (4.78)$$

is a rotation matrix,  $k_s$ ,  $k_d$  and  $k_h$  are real quantities

$$k_s = |a'| \quad (4.79)$$

$$k_d = \left\{ (|b'| - |c'| \operatorname{sign}(\tau_m) \sin(\phi_{c'} - \phi_{b'})) + (|c'| \cos(\phi_{c'} - \phi_{b'}))^2 \right\}^{\frac{1}{2}} \quad (4.80)$$

$$k_h = 2|c'| \sin(\phi_{c'} - \phi_{b'}) \quad (4.81)$$

and

$$[S]_s = \begin{bmatrix} 1 & 0 \\ 0 & 1 \end{bmatrix} \quad (4.82)$$

$$[S]_d = \begin{bmatrix} \cos 2\theta_d & \sin 2\theta_d \\ \sin 2\theta_d & -\cos 2\theta_d \end{bmatrix} \quad (4.83)$$

$$[S]_h = \frac{1}{2} \begin{bmatrix} 1 & \pm j \\ \pm j & 1 \end{bmatrix} \quad (4.84)$$

In these formulae, the sign ambiguity of  $[S]_h$  is fixed by the sign of the *degree of similarity*  $\operatorname{sign}(\tau_m) = \operatorname{sign}(\phi_{c'} - \phi_{b'})$ <sup>17</sup> and  $\theta_d$  is the orientation angle of the dihedral measured in the plane perpendicular to LOS

$$\theta_d = \frac{1}{2} \arctan \left\{ \frac{|c'| \cos(\phi_{c'} - \phi_{b'})}{|b'| - |c'| \operatorname{sign}(\tau_m) \sin(\phi_{c'} - \phi_{b'})} \right\} \quad (4.85)$$

<sup>17</sup> $\tau_m$  and  $\Psi$  are two of the so-called *Huynen* parameters [130].

The rotation operator is mandatory in order to assure the *uniqueness* property of the decomposition. This implies to equal  $\Psi$  to  $\theta_d$  as in that way the maximum of backscattered power is reached [143] [144].

The three different behaviors performing the basis of the decomposition, which is not orthogonal, are, namely: 1) *single-bounce mechanisms* with an odd number of reflection  $[S]_s$ , 2) *double-bounce mechanisms* induced by dihedrals with any orientation  $[S]_d$  and 3) *helix mechanisms* that generate a change in the polarization of a wave from linear to circular  $[S]_h$ . This last behavior is rare in practice. It is related to antisymmetric components and it can be induced by two or more dihedrals with specific relative orientations and displacements.

At this point, it is useful to evaluate the vectorial form of SDH as allows to find easier and more intuitive expressions, specially for  $\Psi$ . It can be shown that [144]

$$\underline{f_{3P'}} = \begin{bmatrix} 1 & 0 & 0 \\ 0 & \cos 2\Psi & \sin 2\Psi \\ 0 & -\sin 2\Psi & \cos 2\Psi \end{bmatrix} \underline{f_{3P}} = e^{j\phi_s} \left\{ f_s \hat{f}_s + e^{j\phi_r} \left[ f_d \hat{f}_d + f_h \hat{f}_h \right] \right\} \quad (4.86)$$

where

$$f_s = |f'_0| \quad (4.87)$$

$$f_d = |f'_1| \sqrt{(1 + |\Im\{f_n\}|)^2 + (\Re\{f_n\})^2} \quad (4.88)$$

$$f_h = 2|f'_1| |\Im\{f_n\}| \quad (4.89)$$

and

$$\hat{f}_s = \hat{f}'_0 \quad (4.90)$$

$$\hat{f}_d = \frac{|f'_1|}{f_d} \left[ 0 \quad 1 + |\Im\{f_n\}| \quad \Re\{f_n\} \right]^T \quad (4.91)$$

$$\hat{f}_h = \frac{|f'_1| |\Im\{f_n\}|}{f_h} \left[ 0 \quad 1 \quad j \operatorname{sign}(|\Im\{f_n\}|) \right]^T \quad (4.92)$$

In these expressions,  $\underline{f}_{3P'} = \{ f'_0 \ f'_1 \ f'_2 \}$ ,  $e^{j\phi_s}$  is the absolute phase that can be neglected,  $e^{j\phi_r} = \arg\{f_n\}$ ,  $f_n = f'_2/f'_1$ ,

$$\theta_d = \frac{1}{2} \arctan \left\{ \frac{\Re\{f_n\}}{1 + |\Im\{f_n\}|} \right\} \quad (4.93)$$

and

$$\Psi = \frac{1}{2} \arctan \left\{ \frac{\Re\{f_2 f_0^*\}}{\Re\{f_1 f_0^*\}} \right\} \quad (4.94)$$

Note that the expression for the target orientation could lead to a set of indeterminacies in the value of  $\Psi$  that must be solved before applying Equation 4.86. For such purpose, the algorithm presented in Fig. 4.8 has to be used. With the resulting value, the 3x3 rotation matrix can be applied and the SDH decomposition inferred.

## Cameron

The Pauli and SDH CTD are based on the mathematical manipulation of the Pauli feature vector and, thus, they have in principle no physical motivation because their physical meaning has been derived *a posteriori* once the mathematical expressions were available. This peculiarity has been used for some authors to argue that these CTD are not suitable for real scenarios. Among them, Cameron was the most prolific one as he proposes a new method to exploit the inverse approach to the problem [145] [23]. The main idea was to select a set of physical radar properties that may be useful for target classification and, then, derive all the mathematical formulation required to isolate their presence in the overall polarimetric behavior.

Cameron selected two main properties, namely: 1) the reciprocity and 2) the symmetry. The first one stands for all those targets that obey the reciprocity law ( $S_{HV} = S_{VH}$ ). In general, this property allows to decompose the lexicographic feature vector in two orthogonal components: *reciprocal*  $\underline{f}_{3L_{rec}}$  and *non-reciprocal*  $\underline{f}_{3L_{norec}}$ . In this thesis, it is assumed that  $\underline{f}_{3L_{norec}}$  is always null and, hence,  $\underline{f}_{3L} = \underline{f}_{3L_{rec}}$ . The other property is related to those targets having an axis of symmetry in the plane of LOS. They are characterized by a scattering matrix that is diagonalizable by the rigid rotation transformation  $[R]$  defined in Equation 4.86. Such property allows to decompose  $\underline{f}_{3L}$  in [145] [23]

$$\underline{f}_{3L} = C_a \left[ \cos \varrho \hat{f}_{rmax} + \sin \varrho \hat{f}_{rmin} \right] \quad (4.95)$$



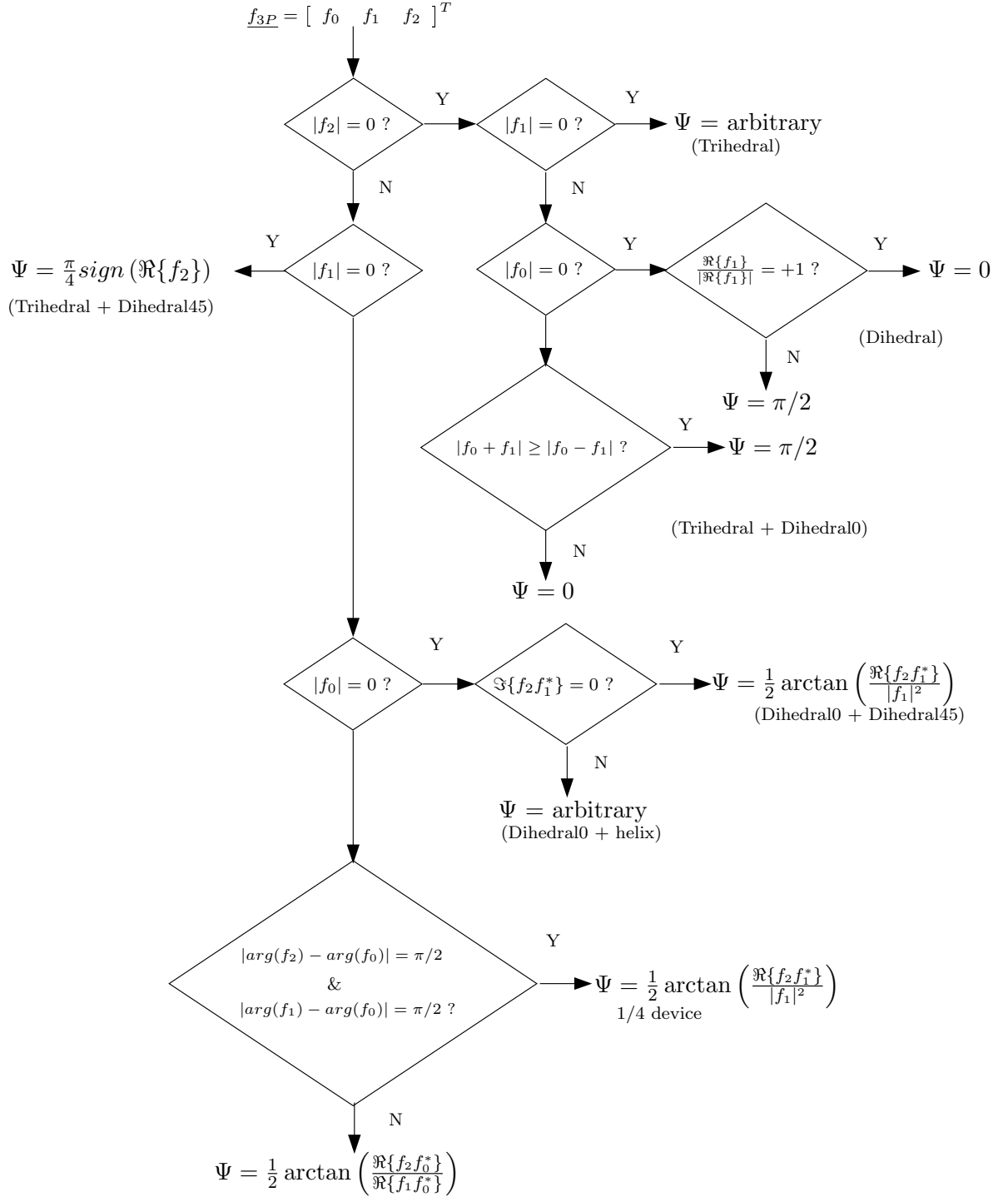


Figure 4.8: Algorithm for solving the indeterminacies of  $\Psi$  in Equation 4.94.

where  $C_a = \|\underline{f}_{3L}\|$  is a constant,  $0 \leq \varrho \leq \frac{\pi}{4}$  the degree of symmetry defined as

$$\varrho = \arccos \left| \frac{(f_{3L}, Df_{3L})}{\|\underline{f}_{3L}\| \cdot \|Df_{3L}\|} \right| \quad (4.96)$$

and

$$\hat{f}_{rmax} = \frac{Df_{3L}}{\|Df_{3L}\|} \quad (4.97)$$

$$\hat{f}_{rmin} = \frac{(I - D)f_{3L}}{\|(I - D)f_{3L}\|} \quad (4.98)$$

the basic feature vectors identifying respectively the maximum and minimum of symmetry. In these expressions, the operator  $D$  is defined as

$$Df_{3L} = (f_{3L}, \hat{f}'_0) \hat{f}'_0 + (f_{3L}, \hat{f}') \hat{f}' \quad (4.99)$$

where  $(u, v) = u \cdot v^*$  stands for the inner product. In this formula, the vector  $\hat{f}'$  is defined by

$$\hat{f}' = \cos(\varsigma/2) \hat{f}'_1 + \sin(\varsigma/2) \hat{f}'_2 \quad (4.100)$$

being  $\varsigma$  equal to

$$\tan \varsigma = \frac{f_1 f_2^* + f_1^* f_2}{|f_1|^2 - |f_2|^2} \quad (4.101)$$

The components  $\hat{f}'_0$ ,  $\hat{f}'_1$  and  $\hat{f}'_2$  are fixed by

$$\hat{f}'_0 = \frac{1}{\sqrt{2}} [ 1 \ 0 \ 1 ] \quad (4.102)$$

$$\hat{f}'_1 = \frac{1}{\sqrt{2}} [ 1 \ 0 \ -1 ] \quad (4.103)$$

$$\hat{f}'_2 = \frac{1}{\sqrt{2}} [ 0 \ 1 \ 0 ] \quad (4.104)$$

whereas  $f_i, i = 0 \dots 2$  are the Pauli elements of Equation 4.46. For the case that  $f_1 f_2^* + f_1^* f_2 = |f_1|^2 - |f_2|^2 = 0$ , then an indeterminacy appears that is solved by updating directly  $\varsigma$  to 0.

At this point, the main difference of the Cameron approach with respect to the Pauli or SDH ones is the fact that the decomposition is not performed directly over Equation 4.95 as happens previously. In contrast, it is defined a metric that compares the feature vector of the measured target with a set of reference vectors identifying particular types of targets. The result is an *unique* reference mechanism providing the best characterization for the measured scattering properties. Note that this differs from the output of the Pauli and SDH CTD oriented to provide for each pixel the weight of *all* the basic mechanisms considered by these theorems. The Cameron metric is applied to symmetric scatters ( $\varrho \leq \pi/8$ )<sup>18</sup> by using the *diagonalized* feature vector of the maximum symmetric component  $\hat{\Lambda}_{rmax}(z)$ . This parameters is defined by

$$\hat{\Lambda}_{rmax}(z) = \frac{1}{\sqrt{1 + |z|^2}} [ 1 \quad 0 \quad z ]^T, z \in C, |z| \leq 1 \quad (4.105)$$

and, in practice, it is obtained by

$$\hat{\Lambda}_{rmax}(z) = R(\Psi_d) \hat{f}_{rmax} \quad (4.106)$$

where  $R(\Psi_d)$  is the rotation matrix defined in Equation 4.86 for  $\Psi_d = -\varsigma/4$  defined in the range  $\varsigma \in (-\pi, \pi]$ . The definition of the rotation angle generates a set of indeterminacies in the extreme cases that can be solved by using the algorithm provided in [23].

The  $z$  parameter is the key parameter of the Cameron decomposition as identifies the scattering properties of the measured scatters. It allows to map these scatters by means of unique and exclusive points within the unit disc of the complex plane. According to the position of the reference scatters, the measured mechanisms are identified/characterized by *that* simple scatter providing the minimum relative  $z$  distance. The used metric is defined as follows [23]

$$d(z_{mea}, z_{ref}) = \arccos \left\{ \frac{\max \left[ |1 + z_{mea} z_{ref}^*|, |z_{mea} + z_{ref}^*| \right]}{\sqrt{(1 + |z_{mea}|^2)(1 + |z_{ref}|^2)}} \right\} \quad (4.107)$$

where  $z_{mea}$  and  $z_{ref}$  are the measured and reference  $z$  locations. The Cameron CTD deals with six reference scatters

<sup>18</sup>Targets with  $\varrho \geq \pi/8$  are termed as *non-symmetric* and they are not classified by the method

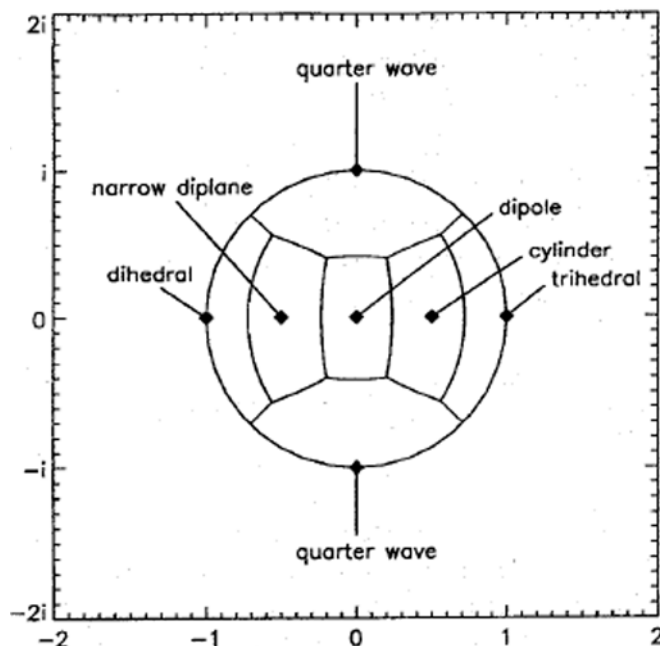


Figure 4.9: Complex unity disc for mapping the results of the symmetric analysis of Cameron. Full diamonds highlight the reference location of the simple mechanisms with the corresponding area of influence.

$$\text{Trihedral} \rightarrow f_{tri} = \hat{\Lambda}_{rmax}(1) \quad (4.108)$$

$$\text{Dihedral} \rightarrow f_{dih} = \hat{\Lambda}_{rmax}(-1) \quad (4.109)$$

$$\text{dipole} \rightarrow f_{dip} = \hat{\Lambda}_{rmax}(0) \quad (4.110)$$

$$\text{Cylinder} \rightarrow f_{cyl} = \hat{\Lambda}_{rmax}(1/2) \quad (4.111)$$

$$\text{Narrow Diplane} \rightarrow f_{ndi} = \hat{\Lambda}_{rmax}(-1/2) \quad (4.112)$$

$$1/4 \text{ Device} \rightarrow f_{dev} = \hat{\Lambda}_{rmax}(\sqrt{1}) \quad (4.113)$$

According to Equation 4.107 and 4.108, the complex plane is mapped as shown in Fig. 4.9. In this scheme, the full diamonds determines the locations of the reference scatters and the dotted lines their *area of influence*, i.e. the areas where any point within is identified by the corresponding reference scatter. These areas are delimited by finding those locations where the distances with respect to the neighboring reference scatters are the same. Therefore, the Cameron approach identifies the scatters measured in the different pixels according to the area of the complex plane where their  $z$  values falls. Once classification is finished, the distance between the measured and corresponding reference scatters is termed *class dispersion*. It is related with the channel imbalance of the SAR system that describes the mismatch between HH and VV channels [146].

### Symmetric Scattering Characterization Method

The Symmetric Scattering Characterization Method (SSCM) is a variant of the symmetric analysis of Cameron, but with new intermediate steps oriented to assess the coherence nature of the processed pixels [25]. This new CTD has been motivated by two main issues, namely:

1. The class segmentation of Cameron's CTD provide a coarse characterization with a class dispersion up to  $\pm 8$  dB. This value is extremely large in relation to the maximum channel imbalance demanded for current SAR sensors ( $\leq \pm 1$  dB) and, then, the performances of Cameron's CTD are notably reduced. Certainly, if a radiometric decision of  $\pm 1$  dB is introduced in the flowchart of the Cameron decomposition, the results become meaningless and dominated by pixels classified as non-symmetric.
2. The lack of tools in classical CTD assessing the coherence of the processed pixels, which is an essential property for a proper data polarimetric interpretation.

To overcome this last limitation, SSCM adopts the so-called *Radiometric Rician threshold* to evaluate the phase stability, which is related to the pixel coherence. This threshold is based on the Rician statistics for fully developed speckle noise [147] and fixes which Signal-to-Clutter (SNC) ratio<sup>19</sup> is demanded for assuring a reasonably stable phasor. Typical conventions state that for a phase variations (or uncertainties) lower than  $\pm \pi/4$  the phase can be considered stable and, hence, the target coherent. This implies a SNC higher than 15 dB. More restrictive conventions fix a phase variations of  $\pm 5^\circ$  that implies a SNC threshold of 20 dB. In addition, SSCM also deals with another coherence test procedure suitable for distributed targets, which are related to partially polarized waves. It consists on applying a sliding window of fixed dimensions (normally 5x5) and evaluate the degree of coherence [25]

$$p_{coh} = \frac{\sqrt{(\langle |f'_0|^2 - |\epsilon|^2 \rangle)^2 + 4|\langle f'_0 \epsilon^* \rangle|^2}}{\langle |f'_0|^2 + |\epsilon|^2 \rangle} \quad (4.114)$$

with  $\epsilon = f'_1 \cos(\varsigma/2) + f'_2 \sin(\varsigma/2)$ . This parameter is useful for distinguishing complex targets in distributed environments, such as ships within the sea. SSCM normally applies this last coherence test to the input image and, then, the Rician one to the pixels classified as non-coherent.

Instead of the unit complex disc, SSCM uses the Poincaré sphere to map the polarimetric properties of the measured pixels. For such purpose, it expresses the diagonalized feature

---

<sup>19</sup>The signal clutter is retrieved from a specific set of pixels considered as "clutter" and it is assumed to follow the fully developed speckle noise statistics.

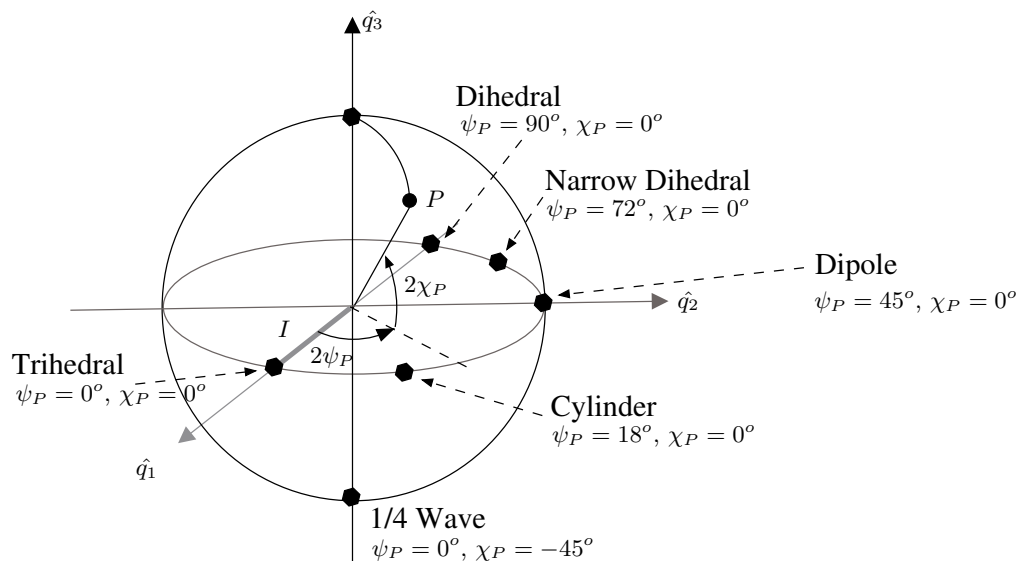


Figure 4.10: Graphical location of the reference scatters of the SSCM decomposition in the Poincaré sphere.

vector of the maximum symmetric component  $\hat{\Lambda}_{rmax}(z)$  of Equation 4.106 in terms of the longitude  $\psi_P$  and latitude  $\chi_P$  angles<sup>20</sup>

$$\hat{\Lambda}_{rmax} = [ 1 \quad \cos(2\chi_P) \cos(2\psi_P) \quad \cos(2\chi_P) \sin(2\psi_P) \quad \sin(2\chi_P) ] \quad (4.115)$$

This expression provides the coordinates of a unique point in the surface of the Poincaré sphere. For the six elemental Cameron coherent targets, the reference points are mapped as in Fig. 4.10. In order to remove the rotation phase ambiguity, only half of the sphere is used, particularly that defined by the interval  $\psi \in [0, \frac{\pi}{2}]$ . In the case that  $\psi \in (\frac{\pi}{2}, \pi]$ , the sphere coordinates  $(\psi, \chi)$  are replaced by  $(\pi - \psi, -\chi)$  and the rotation angle  $\Psi_d$  by  $\Psi_d \pm \frac{\pi}{2}$ .

The Poincaré representation points out an alternative methodology for assessing the coherence properties of pixels. Certainly, it can be considered that a completely coherent pixel is that pixel which response is dominated by a unique elemental coherent scatter. So, if the scattering mechanism of a pixel is quite close to one of these six simple scatters, then it can be concluded that the pixel is coherent. This scattering *purity* can be evaluated by inspecting the longitude and latitude angle difference of the measured mechanism with respect to the reference values. If the difference is lower than a fixed threshold, then the measured scattering mechanism can be described by one elemental scatter and, in turn, the pixel becomes coherent. For such purpose, a reasonable threshold may be  $\pm 5^\circ$ .

<sup>20</sup>Do not confuse these angles with the orientation and ellipticity ones related with the description of the ellipse of wave polarization.

The main steps of SSCM are:

1. Find the maximum symmetric component  $\hat{f}_{rmax}$  as in Equation 4.97.
2. State the degree of similarity defined in Equation 4.96 and select those pixels with  $\varrho \leq \pi/8$ .
3. Apply the distributed coherence test by using the degree of coherence  $p_{coh}$  defined in Equation 4.114
4. Apply the Rician threshold to the non-coherent class.
5. For the coherent pixels, find the diagonalized feature vector of the maximum symmetric component  $\hat{\Lambda}_{rmax}$  as defined in Equation 4.115. Map the resulting point in the Poincaré sphere and evaluate the relative distance with respect to the reference points of the six elemental scatters. That reference scatter having the smallest relative distance is the scatter selected to describe the scattering characteristics of the measured pixel.

One important problem of SSCM is its sensitivity with respect to the focus setting errors and Doppler centroid mistracking. In [148], it has been shown that these phenomena can cause a spreading of the impulse response that can lead to an important attenuation of signal intensity and may contribute to significant errors in phase estimate. If no compensated, these phenomena can worsen SSCM results as they can drop the overall coherence of pixels and, then, few of them will pass the coherence tests. Between the longitude  $\psi_P$  and latitude  $\chi_P$  angles the former is more robust against focusing and mistracking errors. The reason is  $\psi_P$  depends on the channel relative intensity whereas  $\chi_P$  on the relative phase difference between the trihedral  $\hat{f}'_0$  and dihedral  $\hat{f}'_1$  components of  $\hat{f}_{rmax}$  (see Equation 4.97). In this framework, the phase parameter is more unstable.





## Chapter 5

# SAR Simulation Environment for Complex Targets

This Chapter describes the orbital SAR simulator of complex targets, *GRECOSAR*, developed in this thesis. In the first part, the adopted EM solver is briefly described placing the focus on the graphical-based analysis procedure and the high-frequency methods used by the code. Items related with the so-called bitmap processing, the influence of the sea and the most important discretization errors are also a matter of concern. Then, the theoretical basis of SAR signal synthesization is accurately related. In this explanation, two main sections are differentiated, namely: 1) the simulation of the imaging geometry (pre-processing) and 2) the generation of the final raw data according to the EM fields (post-processing). Remarks about SAR image processing and calibration are also presented. The Chapter ends with some examples for both canonical and complex targets that validate the basic features of the simulator, for instance image focusing and the polarimetric information.

### 5.1 Simulator Overview

*GRECOSAR* is a numerical tool capable of realistically and efficiently reproduce in a computer vessel SAR signatures similar to those obtained in real scenarios [19] [44] [149] [150] [151]. It has been developed at the UPC's Remote Sensing Laboratory (RSLab) within the framework of the IMPAST project [8]. Five modules define the simulator, namely: 1) scenario characterization, 2) EM simulation with the EM solver *GRECO*<sup>®</sup> [45] [46] [47], 3) Raw data generation, 4) SAR processing with a SAR processor working with the Extended Chirp Scaling Algorithm (ECSA) [152] and 5) image conditioning and post-processing. The second and fourth modules correspond to external software codes developed at UPC whereas the remaining ones constitute one of the main contribution of this thesis.

Among the different features of *GRECOSAR*, the scenario flexibility is the most important one. On the one hand, any orbital sensor working at any band, operating mode and system resolution can be adopted with polarimetric and/or interferometric capabilities. This makes possible to support up to three imagery modes, namely: 1) PolSAR, 2) PolInSAR and 3) polarimetric ISAR (PolISAR). On the other hand, any vessel model cruising at any bearing and speed can be simulated with rotational and translational motions in scenarios where the sea surface is also included via a simple model. With these capabilities, the computational load of *GRECOSAR*, which is mostly fixed by *GRECO*<sup>®</sup>, is not excessive allowing the usage of simple Personal Computer (PC) to process large vessel models.

The block scheme of the simulator is presented in Fig. 5.1. Dark-grey inked boxes highlight the two external modules whereas the light-grey ones the main steps of a simulation. In blue, there are the input parameters, which are grouped as:

- **satellite parameters**, providing orbital position, antenna pointing and the synthetic aperture length.
- **radar parameters**, defining the chirp signal.
- **Environmental parameters**, describing the sea state, vessel speed, vessel bearing  $\beta$  and the range position of the target according to the so-called near-far angle  $\delta$ .
- **Target model file**, providing the geometrical structure of the target.

All these parameters are defined according to the imaging geometry shown in Fig. 5.2.

## 5.2 Electromagnetic Simulation

*GRECO*<sup>®</sup> is a software that computes in real time the RCS of complex targets by means of high-frequency methods. It achieves an efficient management of hardware resources as all the required graphical operations are performed via the PC's 3D graphic card. This represents an important improvement with respect to other available codes as, first, processing time is notably reduced and, second, EM computation becomes simpler and independent of the input geometry. The main steps of the procedure adopted by *GRECO*<sup>®</sup> are, namely:

1. The meshed or facet-based input model is processed with the PC's 3D graphic card in order to find which surfaces and edges are illuminated by the monostatic radar. The result is a 3D image that is stored in the card memory. In order to make that the graphic accelerator removes the useless (or hidden) surfaces, the viewpoint of the observer is

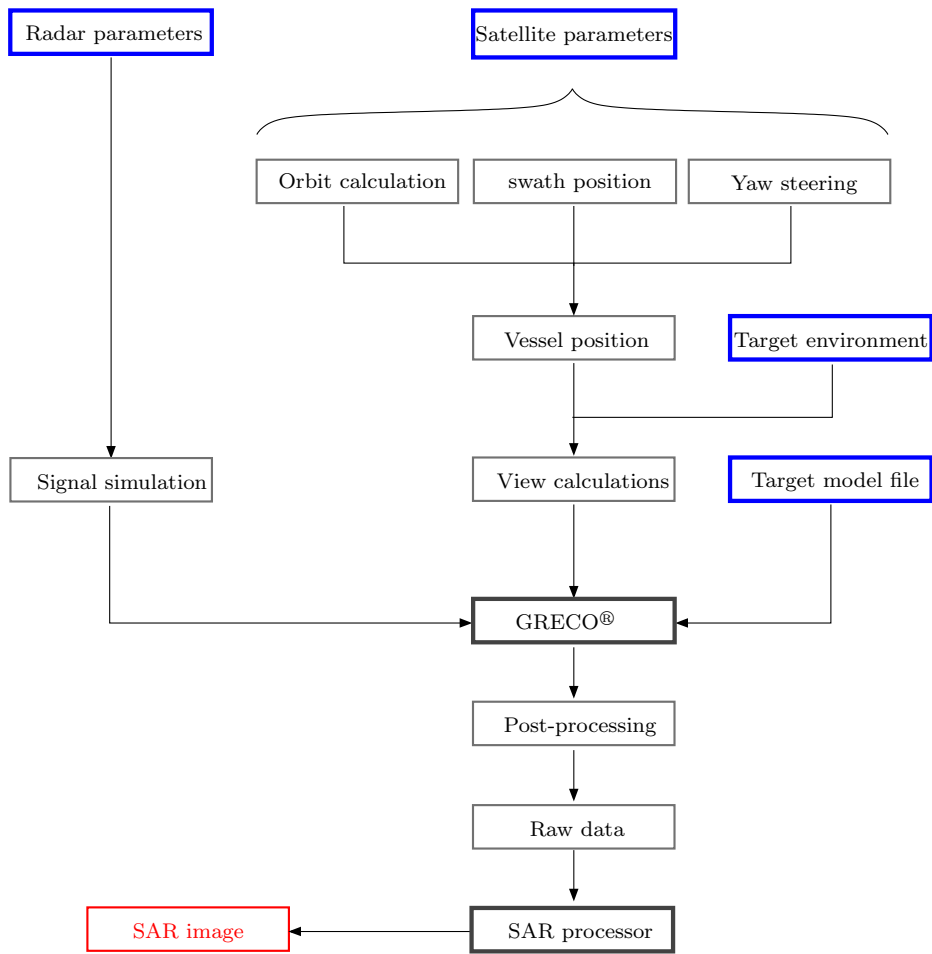


Figure 5.1: Block scheme of *GRECOSAR*.

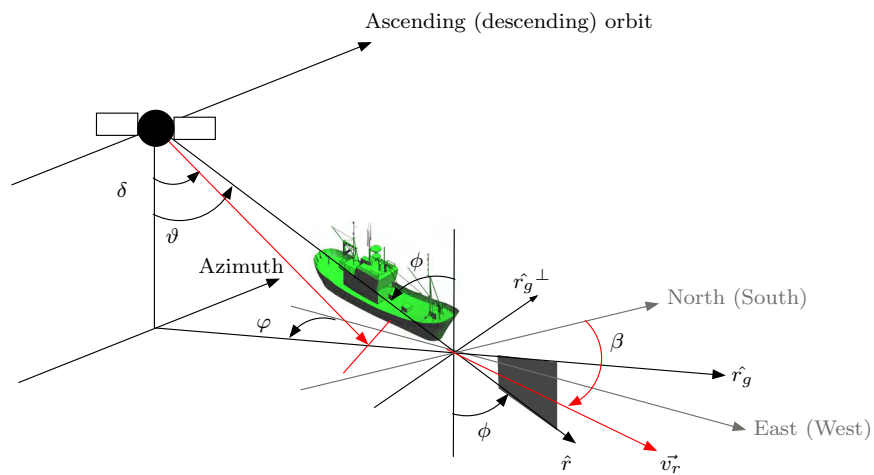


Figure 5.2: SAR imaging geometry of *GRECOSAR*.

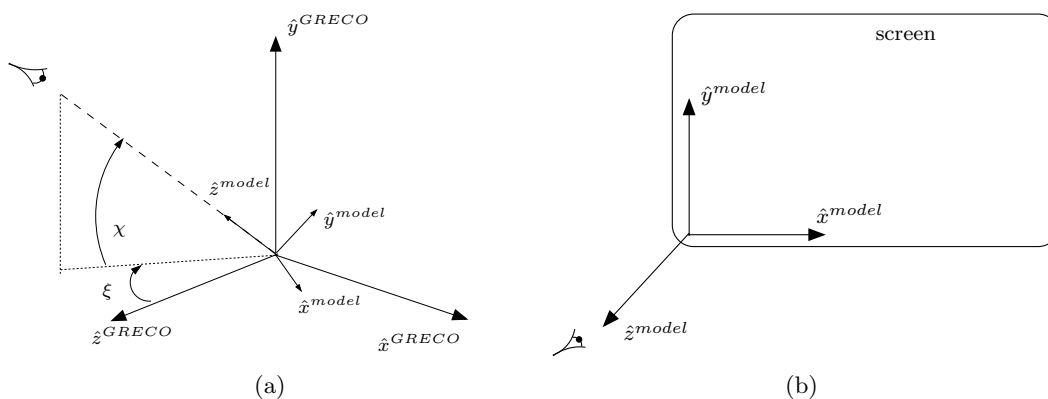


Figure 5.3: View angles defined according to the GRECO coordinate system (a). They fix the radar pointing direction and the way the target is visualized in the screen (b).

updated with the position of the radar. This position is defined in the so-called GRECO  $\{ \hat{x}^{greco} \ \hat{y}^{greco} \ \hat{z}^{greco} \}$  coordinate system by the pair of azimuth ( $\xi$ ) and elevation ( $\chi$ ) view angles shown in Fig. 5.3(a). They control the way the target is visualized on the computer screen according to the MODEL  $\{ \hat{x}^{model} \ \hat{y}^{model} \ \hat{z}^{model} \}$  coordinate system illustrated in Fig. 5.3(b). For the particular case in which both angles are equal to zero, the GRECO and MODEL reference systems match.

2. The previous image is rendered with a specific illumination source in such a way that the red, green, and blue (R, G, B) color components of each pixel become connected with the three components of the unit normal vector (see Fig. 5.4).
3. With the three coordinates of each pixel and the related normal vector, *GRECO*<sup>®</sup> applies the high-frequency methods to estimate RCS. This operation is performed for each polarimetric channel ( $\{HH, HV, VH, VV\}$ ) and single frequency. In a first approach, *GRECO*<sup>®</sup> works with *one* frequency and *one* position, despite it allows sweep operations for dealing with a range of desired values.
4. *GRECO*<sup>®</sup> has the option to provide, instead of RCS, the normalized EM field in a linear scale. Specifically, it gives, for a 1 V/m incident field, the real and imaginary part of  $r^2 E^s$  where  $r$  indicates the sensor-to-target range and  $E^s$  the scattered field. EM fields are computed by assuming the phase center at the origin of the geometrical model coordinates under the far or near field regime defined by the target length. For near-field situations, two approximations are assumed, namely: 1) the antenna points to the center of the target and 2) the angles that the surfaces and edges make with the direction of illumination in the near field are equal to those of the far field. The final EM fields are stored in four binary files (one per each polarimetric channel) using a 4 bytes single precision real number format. For  $N$  positions and  $n$  frequencies to simulate, the data is ordered in  $N$  sequences of  $n$  pairs of values (real+imaginary).

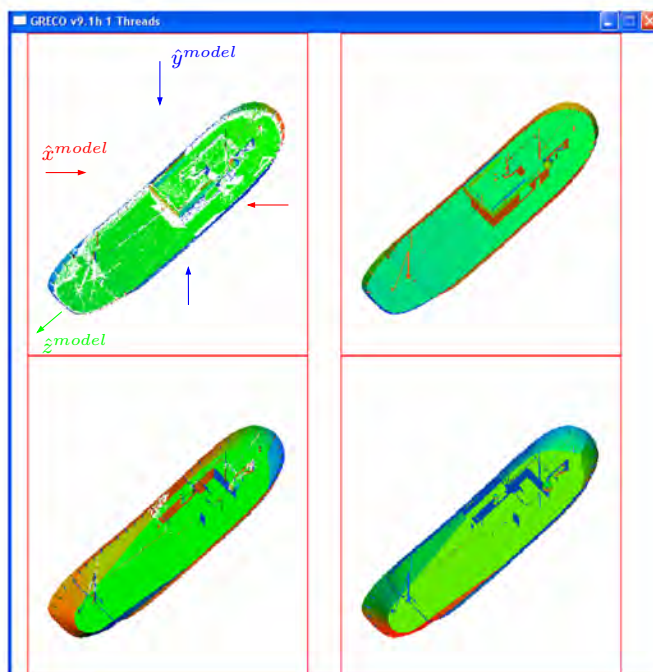


Figure 5.4: *GRECO*<sup>®</sup> screen snapshot showing the relation between the coordinates of the normal vector and the three basic color channels. The left images illustrate the visible (up) and hidden (down) surfaces whereas the right ones the visible (up) and hidden (down) edges. In the visible surfaces, the white pixels highlight those points with multi-reflection (more than 2 reflections).

Besides RCS estimation, *GRECO*<sup>®</sup> has some useful additional utilities. Among them, the so-called *GRECOPOST* is the most remarkable one because it allows to inspect the specular reflection points and the multiply reflected rays.

### 5.2.1 High-Frequency Methods

*GRECO*<sup>®</sup> deals with high-frequency methods to avoid the unrealistic computational requirements imposed by the discretization of Maxwell's equations when applied to electrically large models [153] [154]. The methods adopted by *GRECO*<sup>®</sup> are, namely:

1. Physical Optics (PO) for perfectly conducting surface.
2. Method of Equivalent Currents (MEC) with Ufimtsev's Physical Theory of Diffraction (PTD) coefficients or Mitzner's Incremental Length Diffraction Coefficients (ILDC) for perfectly conducting edges.
3. Geometrical Optics (GO) + PO Ray Tracing (RT) for multiple reflection analysis. Bi-static GO is used for all reflections except the last one, for which PO is used. GO

divergence factors for curved surfaces are computed approximately. *GRECO*<sup>®</sup> has the option to deal with a maximum of three (fast mode) or nine reflections (full mode). In this thesis, the first option has been selected as it is enough for evaluating the scattering of vessels and it provides a reduced processing time.

With these methods, *GRECO*<sup>®</sup> is able to analyze targets of electrical size as large as  $\frac{2^n \lambda}{16}$ , with a maximum phase error of  $\lambda/8$ , where  $n$  is the number of bits in which the distance to the observer is discretized. This means that with a 24-bits discretization targets as large as  $10^6 \lambda$  can be managed. Despite the previous techniques are widely explained in the literature [153] [154], some details about their particularities in *GRECO*<sup>®</sup> are commented.

## PO

The high-frequency RCS of a perfectly conducting surface computed via the PO technique can be approximated by [154]

$$\sigma^{PO} = \frac{4\pi}{\lambda^2} \left| \int_s \cos \theta e^{j2Kz} ds \right|^2 \quad (5.1)$$

where  $\theta$  is the angle between the surface normal and the direction of incidence,  $z$  is the distance from the differential of surface  $ds$  to the observer projected on the incidence direction,  $K = \frac{2\pi}{\lambda}$  the wavenumber and the surface integral  $s$  extends only over the region illuminated by the incident wave. According to the graphical-based procedure of *GRECO*<sup>®</sup>, the differential of surface on the screen  $ds'$ , which is equivalent to one pixel, is equal to  $ds' = \cos \theta ds$ . So, Equation 5.1 can be rewritten by [46]

$$\sigma_{greco}^{PO} = \frac{4\pi}{\lambda^2} \left| \int_{screen} e^{j2Kz} ds' \right|^2 \quad (5.2)$$

where the discretization of the input model into the 3D image leads to [46]

$$\sigma_{greco}^{PO} = \frac{4\pi}{\lambda^2} \left| \sum_{pixels} e^{j2Kz} \right|^2 \quad (5.3)$$

Note that the previous formula is correct if and only if a pixel radiates as an infinitesimal aperture, i.e. it corresponds to the projection on the screen of a differential of surface  $ds$  much smaller than a wavelength. With current PC, it is easy to accomplish this condition as

the number of pixels in the screen are normally large enough <sup>1</sup>. But for grazing incidences ( $\theta \rightarrow 90^\circ$ ), some problems may appear as now a pixel ( $ds'$ ) can correspond to the projection of a large differential surface ( $ds$ ) breaking with the infinitesimal aperture approximation. In such a case, a more accurate expression for the PO surface integral in the discrete domain may be [46]

$$\sigma_{greco}^{PO} = \frac{4\pi}{\lambda^2} \left| \sum_{pixels} \text{sinc} \left( K \frac{l}{\cos \theta} \text{sinc}(\theta) \right) e^{j2Kz} \right|^2 \quad (5.4)$$

where  $l$  is the size of a square pixel  $ds'$  in the screen and  $\frac{l}{\cos \theta}$  is the size of  $ds$  projected on this pixel. In this formula, it is implicitly assumed that a pixel is a rectangular aperture with uniform illumination and, hence, its contribution to the far fields can be approximated by a  $\text{sinc}(\theta)$  function.

Another important problem that arises in  $GRECO^{\text{®}}$  is the spurious oscillations that may appear in the RCS vs. frequency plot. They are caused by the abrupt transition in the equivalent currents at the boundary between the illuminated and the shadowed regions ( $\theta \rightarrow 90^\circ$ ). This phenomenon is normally solved by using a taper  $\cos^n \theta$  function. So, the final expression of PO-RCS in  $GRECO^{\text{®}}$  is [46]

$$\sigma_{greco}^{PO} = \frac{4\pi}{\lambda^2} \left| \sum_{pixels} \cos^n \theta \text{sinc} (Kl \tan \theta) e^{j2Kz} \right|^2 \quad (5.5)$$

where for  $n = 0$  the PO surface integral is rigorously computed and for  $n > 1$  errors in the sidelobes of the flat plates may be introduced.

### Impedance Boundary Condition (IBC)

The previous PO formulation may be improved with the Fresnel reflection coefficients in order to consider radar-absorbent coatings through IBC. In the generic case [155],

$$\sigma_{greco}^{PO} = \frac{4\pi}{\lambda^2} \left| \sum_{pixels} \left( \Gamma_{\parallel} E_{\parallel}^i \hat{e}_{\parallel}^i + \Gamma_{\perp} E_{\perp}^i \hat{e}_{\perp}^i \right) \cos^n \theta \text{sinc} (Kl \tan \theta) e^{j2Kz} \right|^2 \quad (5.6)$$

<sup>1</sup>With the bitmap processing related in Section 5.2.3, the number of available pixels is even higher.

with  $\Gamma_{\parallel}$ ,  $\Gamma_{\perp}$  indicating the Fresnel coefficients for the polarization parallel and perpendicular to the incidence plane and  $E_{\parallel}^i$ ,  $E_{\perp}^i$  the components of the incidence EM fields in the direction parallel ( $\hat{e}_{\parallel}^i$ ) and perpendicular ( $\hat{e}_{\perp}^i$ ) to the plane of incidence. In terms of  $ds'$ , the previous expression can be decomposed in the HH co-polar ( $\sigma_{HH}^{PO,IBC}$ ), VV co-polar ( $\sigma_{VV}^{PO,IBC}$ ) and HV cross-polar ( $\sigma_{HV}^{PO,IBC}$ ) RCS as [155]

$$\sigma_{HH}^{PO,IBC} = \frac{4\pi}{\lambda^2} \left| \int_s \left( \frac{\Gamma_{\parallel} \hat{n}_x + \Gamma_{\perp} \hat{n}_y}{\hat{n}_x^2 + \hat{n}_y^2} \right) \cos^n \theta \text{sinc}(Kl \tan \theta) e^{j2Kz} ds' \right|^2 \quad (5.7)$$

$$\sigma_{VV}^{PO,IBC} = \frac{4\pi}{\lambda^2} \left| \int_s \left( \frac{\Gamma_{\parallel} \hat{n}_y + \Gamma_{\perp} \hat{n}_x}{\hat{n}_x^2 + \hat{n}_y^2} \right) \cos^n \theta \text{sinc}(Kl \tan \theta) e^{j2Kz} ds' \right|^2 \quad (5.8)$$

$$\sigma_{HV}^{PO,IBC} = \frac{4\pi}{\lambda^2} \left| \int_s \left( \frac{(\Gamma_{\parallel} - \Gamma_{\perp}) \hat{n}_x \hat{n}_y}{\hat{n}_x^2 + \hat{n}_y^2} \right) \cos^n \theta \text{sinc}(Kl \tan \theta) e^{j2Kz} ds' \right|^2 \quad (5.9)$$

where in all the cases  $\hat{n}_x$ ,  $\hat{n}_y$  and  $\hat{n}_z$  are the components of the unit normal surface along the horizontal, vertical and incidence directions.

## MEC

MEC techniques are used to compute the EM field scattered by a wedge  $E^r$  via equivalent currents located on its edge. For the far-field monostatic case [153],

$$E^r = E^o \frac{e^{jKr}}{2\pi r} \int_{EDGE} \left( -(D_{\parallel} + D_x) \sin \gamma \hat{e}_{\parallel}^i - D_{\perp} \cos \gamma \hat{e}_{\perp}^i \right) e^{j2Kz} dl' \quad (5.10)$$

where the line integral extends along the illuminated edges, the incidence plane is built by the incidence ( $\hat{z}$ ) and edge ( $\hat{t} = \{ t_x \ t_y \ t_z \}$ ) directions and  $\gamma$  is the angle between the incident field and  $\hat{e}_{\perp}^i$ .  $D_{\parallel}$ ,  $D_x$  and  $D_{\perp}$  are the monostatic ILDC coefficients that express the dependence of the scattered field with respect to the angles  $\alpha_{MEC}$ ,  $\phi_{MEC}$  and  $\beta_{MEC}$ . These angles are defined from the unit normal vectors of the two surfaces of the wedge ( $\hat{n}_1 = \{ n_{1x} \ n_{1y} \ n_{1z} \}$ ,  $\hat{n}_2 = \{ n_{2x} \ n_{2y} \ n_{2z} \}$ ) as

$$\alpha_{MEC} = \arccos(-\hat{n}_1 \cdot \hat{n}_2) \quad (5.11)$$



$$\phi_{MEC} = \arccos \left( \frac{n_{1x}t_y - n_{1y}t_x}{\sqrt{t_x^2 + t_y^2}} \right) \quad (5.12)$$

$$\beta_{MEC} = \arcsin \left( \sqrt{t_x^2 + t_y^2} \right) \quad (5.13)$$

where

$$\hat{t} = \frac{\hat{n}_1 \times \hat{n}_2}{|\hat{n}_1 \times \hat{n}_2|} \quad (5.14)$$

Separation of the incident field into parallel and perpendicular components leads to the following expressions for the HH co-polar ( $E_{HH}^s$ ), VV co-polar ( $E_{VV}^s$ ), HV cross-polar ( $E_{HV}^s$ ) and VH cross-polar ( $E_{VH}^s$ ) scattered fields [155]

$$E_{HH}^s = E^o \frac{e^{-jKr}}{2\pi r} \int_{EDGE} \left( -D_{\parallel} \frac{t_x^2}{t_x^2 + t_y^2} + D_x \frac{t_x t_y}{t_x^2 + t_y^2} - D_{\perp} \frac{t_y^2}{t_x^2 + t_y^2} \right) e^{j2Kz} dl' \quad (5.15)$$

$$E_{VV}^s = E^o \frac{e^{-jKr}}{2\pi r} \int_{EDGE} \left( -D_{\parallel} \frac{t_y^2}{t_x^2 + t_y^2} - D_x \frac{t_x t_y}{t_x^2 + t_y^2} - D_{\perp} \frac{t_x^2}{t_x^2 + t_y^2} \right) e^{j2Kz} dl' \quad (5.16)$$

$$E_{HV}^s = E^o \frac{e^{-jKr}}{2\pi r} \int_{EDGE} \left( +D_{\parallel} \frac{t_x t_y}{t_x^2 + t_y^2} - D_x \frac{t_y^2}{t_x^2 + t_y^2} - D_{\perp} \frac{t_x t_y}{t_x^2 + t_y^2} \right) e^{j2Kz} dl' \quad (5.17)$$

$$E_{VH}^s = E^o \frac{e^{-jKr}}{2\pi r} \int_{EDGE} \left( -D_{\parallel} \frac{t_x t_y}{t_x^2 + t_y^2} - D_x \frac{t_x^2}{t_x^2 + t_y^2} + D_{\perp} \frac{t_x t_y}{t_x^2 + t_y^2} \right) e^{j2Kz} dl' \quad (5.18)$$

In these formulas, the scattered fields correspond to the contribution of the edge to the overall scattering and not to the contribution of the related surfaces of the wedge, which are computed via PO. In the most generic case, the ILDC coefficients can be exactly computed by the Mitzner approach. However, *GRECO*<sup>®</sup> deals with PTD, computationally more efficient, as for backscattering monostatic RCS problems the Mitzner's and PTD's  $D_{\parallel}$ ,  $D_{\perp}$  coefficients are equal [155]. In addition, it assumes the PTD's  $D_x$  coefficient to be equal to zero as this coefficient is almost negligible for such situation in which the edge contribution takes the

highest values<sup>2</sup>. In practical terms, it can be shown that the expressions for  $D_{||}$  and  $D_{\perp}$  can be approximated to a linear function [46]

$$D_{||} \approx \begin{cases} -\frac{\phi}{\pi} & 0 \leq \phi \leq \pi - \alpha & (1 \text{ facet visible}) \\ -(n-l) & \pi - \alpha \leq \phi \leq \pi - \alpha/2 & (2 \text{ facet visible}) \end{cases} \quad (5.19)$$

$$D_{\perp} \approx \begin{cases} -\left(\frac{m}{2} - \frac{\phi}{\pi}\right) & 0 \leq \phi \leq \pi - \alpha & (1 \text{ facet visible}) \\ \tan\left(\frac{\alpha}{2}\right) - \frac{2}{m} \cot\left(\frac{\pi}{m}\right) & \pi - \alpha \leq \phi \leq \pi - \alpha/2 & (2 \text{ facet visible}) \end{cases} \quad (5.20)$$

where  $m = (2\pi - \alpha)/\pi$ . In summary, the computation of edge contribution in *GRECO*<sup>®</sup> needs from the following procedure

1. From the unit normal to the target surface computed via graphical processing, edges are isolated by finding discontinuities in the normal vector when the z coordinate remain continuous.
2. Find the angles  $\alpha_{MEC}$ ,  $\beta_{MEC}$  and  $\phi_{MEC}$  defined in Equations 5.11, 5.13 and 5.12.
3. Find the PTD diffraction coefficients according to Equation 5.19 and 5.20.
4. Evaluate Equations 5.15 - 5.18.

### 5.2.2 Discretization Errors

The input models of *GRECO*<sup>®</sup> can be modeled with facets or with parametric surfaces meshed with a triangular tessellation. According to how this modeling procedure is performed, some errors can appear in the final results. The most important ones are:

1. *Geometrical error*: It accounts for the error made in the transition from the original surface to the CAD model. Sometimes it is referred as *chordal* error and it is negligible for parametric surfaces.
2. *Rendering error*: It is related to the error made in the transition from the CAD model to the 3D bitmap image obtained after rendering the object with a particular and fixed illumination source (rendering model). This error does not exist for facet-based models, but it can be appreciable for objects modeled with parametric surfaces having large electrical dimensions. To control the influence of the rendering error in the final

---

<sup>2</sup>This happens for incidence directions near the plane perpendicular to the edge.

results, *GRECO*<sup>®</sup> has an input parameter termed *pixel size* that controls the resolution of the bitmap image. The lower the pixel size, the better the results, but the higher the memory requirements. First versions of *GRECO*<sup>®</sup> were not able to deal with large targets because they used the limited memory resources of the graphic card. For such reason, newer versions exploit the Random Access Memory (RAM) with more storage capacity.

3. *Pixel error*: It accounts for the error made in the transition from the rendering model to the *pixel model*. The pixel model is defined as the six-dimensional information (three pixel coordinates, three normal vector components) retrieved for each pixel of the illuminated surfaces. For PO and meshed surfaces, this error does not exist as *GRECO*<sup>®</sup> adopts a triangular mesh model that derives the unit normal vector from the vertices of the triangles and not from the rendering process [156].

The influence of these errors in SAR simulation is evaluated in Section 5.4. The validation of *GRECO*<sup>®</sup> has shown that with the proper bitmap resolution the accuracy reached in RCS prediction is notably high [45] [46] [47].

### 5.2.3 Bitmap Processing

The analysis of the rendering error has shown that *GRECO*<sup>®</sup> has two different methodologies to process the graphical information of the target, namely:

- *Screen processing*. This is the original approach in which the 3D bitmap image of the target is generated at the computer screen via the 3D graphic card. This option is the fastest one as it uses the memory resources of the graphic card to store all the graphical-related information. For small targets with low complexity, such as airplanes, this technique is sufficient, but it introduces serious discretization errors for large targets as ships. The main limitation is the number of bits available to encode the color information and z coordinate, and the number of pixels of the screen.
- *Bitmap processing*. This is the alternative approach that generates the images again with the graphic card, but in a bitmap resident in the computer RAM memory. This allows to liberate the graphic card from the simulation information once the graphical processing is done. Its main advantages are:
  - The maximum size of the bitmap is only limited by the size of the computer memory (RAM + disk cache). The memory necessities for bitmap processing is 18 bytes/pixel when PO method is used and 33 bytes/pixel for PTD/RT methods.

- The z coordinate can be encoded in 26 bits, independently of the type of graphics card used.
- Color resolutions of 24 bits can be managed, even when the monitor or the graphics card do not allow this type of resolution.
- *GRECO*<sup>®</sup> can run in 'background' mode avoiding that any other application can affect the computations. This is not possible with screen processing, as other applications can change the contents of the screen.
- *GRECO*<sup>®</sup> can deal with a rectangular bitmap adapted to the dimensions of the screen projection of the object. This helps to save memory.
- Parallel to the development of this type of processing, *GRECO*<sup>®</sup> has been improved with multi-processor capability. It allows to reduce processing time according to the number of available processors.

Bitmap processing has been adopted in this thesis due to the high resolutions that it provides in simple PC configurations. It will almost free vessel SAR images from discretization errors (see Section 5.5.1).

#### 5.2.4 Reflection on the Sea

In addition to the previous features, *GRECO*<sup>®</sup> has the possibility to take into account the following mechanisms due to the sea-target interaction (see Fig. 5.5).

1. **A: Radar → Reflection on the object → Radar.** This is the usual contribution of isolated targets calculated with PO, PTD and RT (see Fig. 5.5(a)).
2. **B: Radar → Reflection on the object → Reflection in the sea → Radar** (see Fig. 5.5(b)).
3. **C: Radar → Reflection in the sea → Reflection on the object → Radar.** This contribution is equal to contribution B if the theorem of reciprocity applies to the object reflection (see Fig. 5.5(c)).
4. **D: Radar → Reflection in the sea → Reflection on the object → Reflection in the sea → Radar** (see Fig. 5.5(d)).

In all the cases, the reflections on the object can be either specular or diffuse and they are calculated with PO approximations. In contrast, the reflections on the sea are considered to be specular and they are computed with GO approximations. To determine sea reflections, some aspects of image theory are used as the original ship is mirrored so that an *image ship*

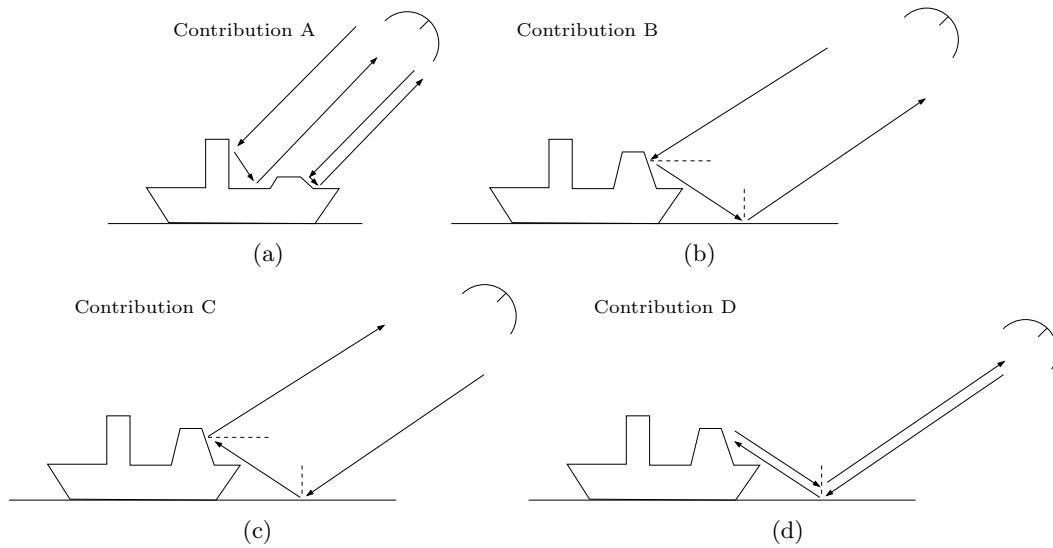


Figure 5.5: A (a), B (b), C (c) and D (d) sea-induced mechanisms considered by *GRECO*<sup>®</sup>.

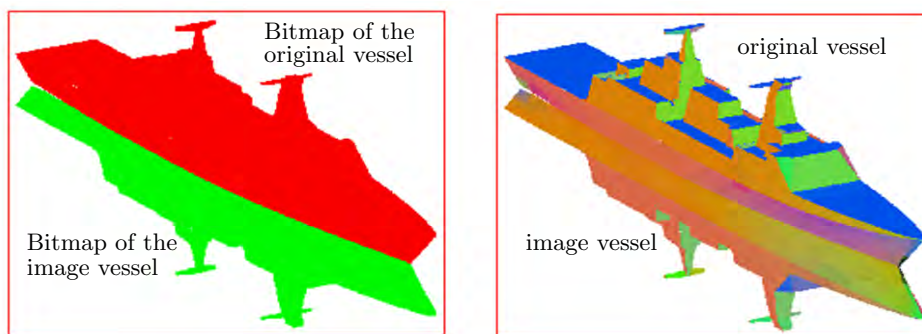


Figure 5.6: *GRECO*<sup>®</sup> screen snapshot showing the image ship used in the computations of the sea-induced mechanisms.

Table 5.1: Effective height of the wave ( $H_{1/3}$ ) as a function of the sea state

Sea State	0	1	2	3	4	5	6	7	8	> 8
$H_{1/3}$ [m]	0	0.05	0.3	0.88	1.88	3.25	5	7.5	11.4	14

that emulates the ship as reflected on the sea is obtained (see Fig. 5.6). This allows to clearly isolated those structures interacting with the sea.

To simulate the effects of ocean waves in the reflectivity properties of the sea, sea reflections are attenuated by a reflection coefficient. This parameter is computed according to the effective height of the waves, the operating frequency, the elevation of the radar above sea-level and the dielectric permittivity and conductivity of the sea. On the one hand, the effective height of the waves is derived from a user-defined sea state according to the STANAG 4194 [157] table shown in Table 5.1. On the other hand, the permittivity and conductivity of the sea, which depend on the working frequency, are calculated by interpolating a table that provides some values at fixed frequencies (taking a water temperature of 10°C and a salt content of 3.5 %).

For vessel classification, this sea model is enough because it can generate accurate vessel SAR signatures that reproduce most of the scattering mechanisms observed in real data. Obviously, it has some limitations, for instance the absence of sea dynamics due to wind conditions and hydrodynamic forces along the observation time. These features are not essential for the current study as the influence of the sea in vessel classification is the main topic of study<sup>3</sup>. However, their evaluation will be interesting in future works. Note that an accurate simulation of the sea surface in combination with vessels is not an easy task because it increases in excess the computational complexity of the simulation as well as processing time. Such work may be the origin of another Ph.D. thesis and it is out of the scope of the current one.

### 5.2.5 Control Parameters

*GRECO*<sup>®</sup> has a set of parameters that control the execution of the program and the accuracy of the high-frequency methods according to the geometrical complexity of the target. All of them are compiled in the user's manual available at the web page of RSLab [158]. For the parameters related with the high-frequency methods, the default values provided by the owner of *GRECO*<sup>®</sup> have been adopted in this thesis<sup>4</sup>.

<sup>3</sup> Note that the main effect of sea dynamics in vessel SAR imagery appears in terms of vessel motions and this issue is actually considered in *GRECOSAR* (see following sections).

<sup>4</sup>For further details, contact with [J. M. Rius](#)

### 5.3 Target Modeling

The most important input of *GRECOSAR* that affects the quality of SAR images is the target to process. In this sense, the simulator admits targets modeled with facets or parametric surfaces adopting any of the following Computer-Aided Design (CAD) formats, namely: 1) **Initial Graphics Exchange Specification (IGES)** up to version 5.2, 2) **I-DEAS** from UGS corporation, 3) **FAM**, 4) **GiD<sup>®</sup>** from the International Center for Numerical Methods in Engineering (CIMNE) at UPC [159] and 5) **MicroStation packages**. In the data presented in this thesis, the targets have been modeled via GiD<sup>®</sup> with Non Uniform Rational Basis Spline (NURBS) surfaces because they make the geometrical and pixel errors negligible (see Section 5.2.2).

According to the procedure adopted by *GRECO<sup>®</sup>*, the usage of parametric surfaces needs from a meshing *tessellation* process that discretizes the input geometry in planar elements as the processor of the graphic card can only deal with triangular or quadrangular planar surfaces. Despite *GRECO<sup>®</sup>* can perform such procedure by itself, a plug-in developed by the owner of *GRECO<sup>®</sup>* and embedded in GiD<sup>®</sup> has been used to save processing time. In this way, the tessellation procedure have to be performed only once and not each time the model is processed.

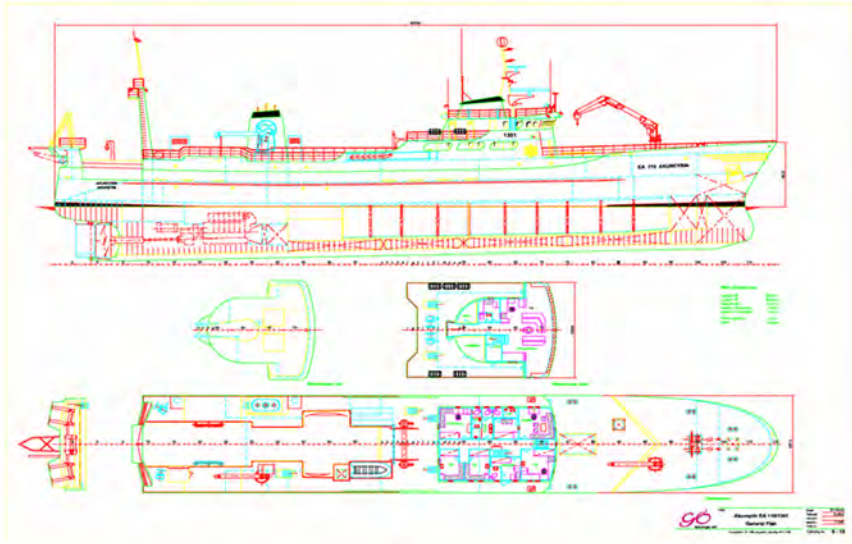
In the targets used in this thesis, the meshing procedure does not exceed the 500,000 triangular facets and it assures a discretization error (in practice, chordal error) lower than 3 mm. The following vessels have been considered, namely:

- **SPA**: Spanish fishing vessel 27 meters long and 10 meters wide. A snapshot of its blueprint and photograph is depicted in Fig. 5.7.
- **SPAv2**: An improved version of the previous model with more details in the structure.
- **ICE**: An Icelandic fishing vessel 67 meters long and 14 meters wide. A snapshot of its blueprint and photograph is depicted in Fig. 5.8.
- **FER**: A common passenger ferry 200 meters long and 25 meters wide. It has been obtained from a private Internet database.

The resulting models are presented in Fig. 5.9(a)-5.10(b). In some of them, zoomed areas provide details of the triangular tessellation procedure.





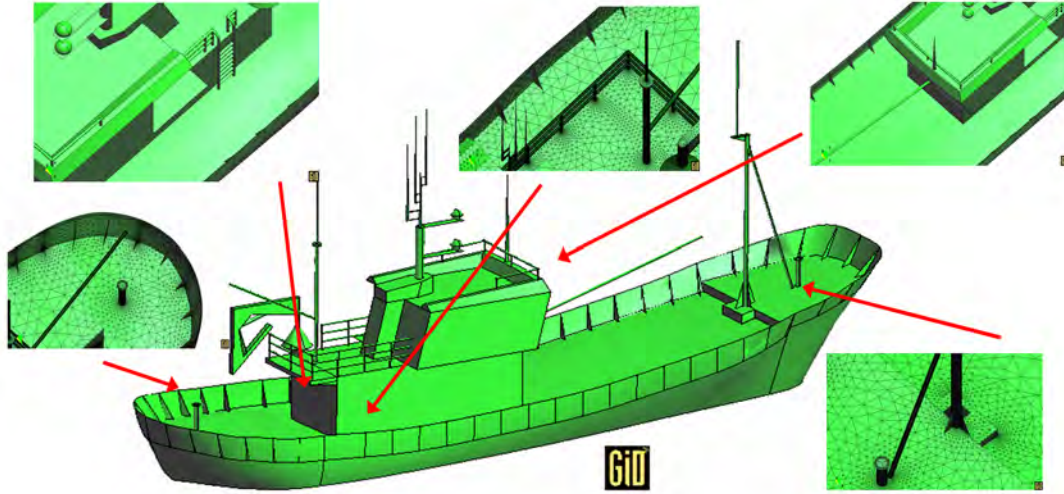


(a)

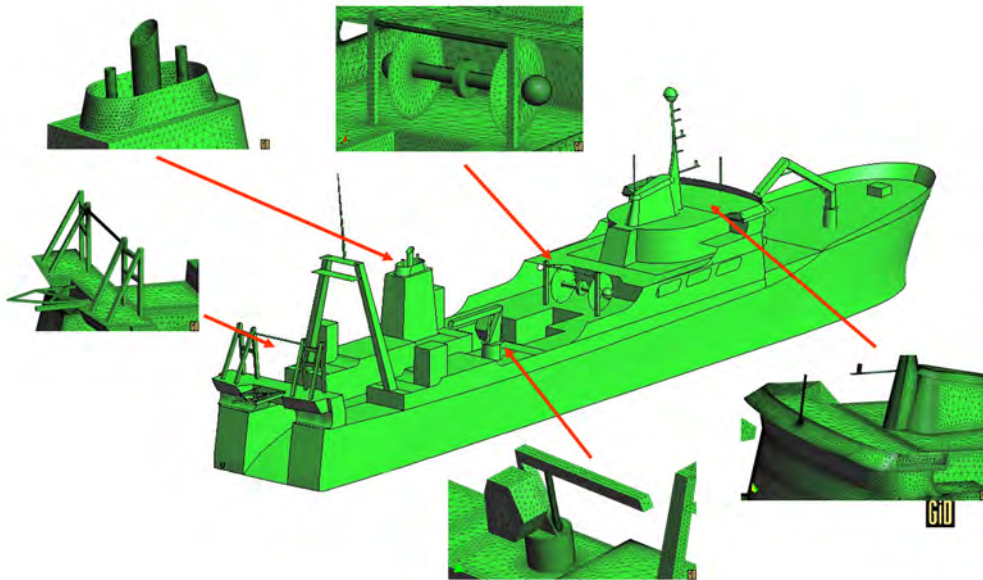


(b)

Figure 5.8: Blueprints (a) and photo (b) of the ICE vessel model.

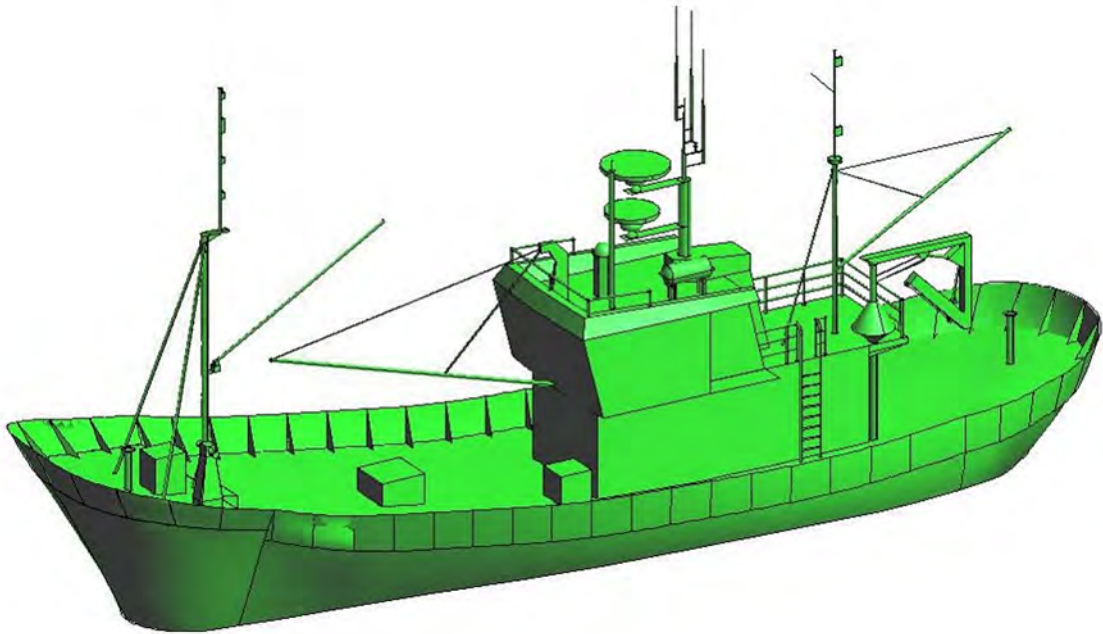


(a)

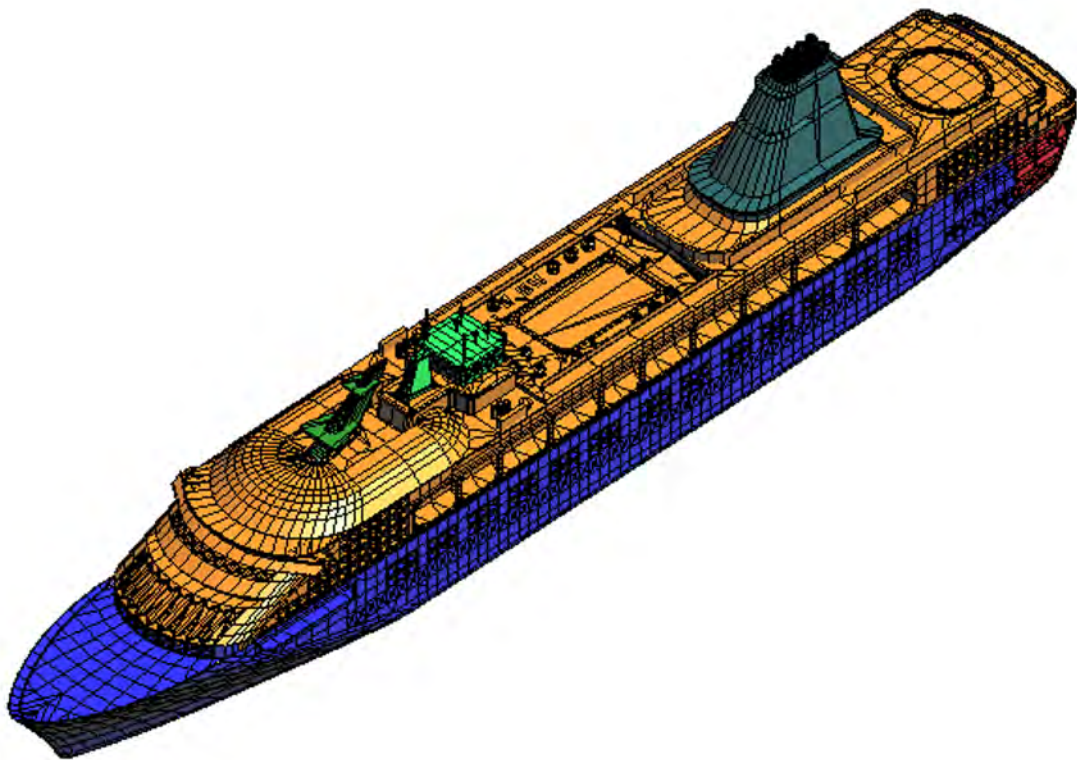


(b)

Figure 5.9: Snapshot of the SPA (a) and ICE (b) models. Zoomed areas highlight the details of the meshing procedure that discretizes real structures into facets.



(a)



(b)

Figure 5.10: Snapshot of the SPAv2 (a) and FER (b) models.

## 5.4 SAR Signal Simulation

In Chapter 3, the raw signal has been mathematically formulated by

$$h(x', r') = \int \int \gamma(x, r) s(x' - x, r', r) dx dr \quad (5.21)$$

where  $r' = \frac{c(t-t')}{2}$ ,  $x' = V_{plat}t'$  and <sup>5</sup>

$$s(x' - x, r', r) = e^{-j\frac{4\pi R}{\lambda}} e^{j\pi\alpha\left(\frac{r'-R}{c/2}\right)^2} \text{rect}\left[\frac{r'-R}{c\tau/2}\right] \omega^2[x' - x, r] \quad (5.22)$$

In these expressions,  $R = \sqrt{R_0^2 + (x' - x_0)^2}$  is the range history,  $x$  and  $r$  the azimuth and range location of the scatter,  $\omega[x' - x, r]$  the function describing the antenna footprint over the ground,  $e^{-j\frac{4\pi R}{\lambda}}$  the *azimuth chirp* related to the slow-time variable ( $t'$ ) and  $e^{j\pi\alpha\left(\frac{r'-R}{c/2}\right)^2} \cdot \left[\frac{r'-R}{c\tau/2}\right]$  the *range chirp* related to the fast-time variable ( $t$ ). The time shift term ( $2R/c$ ) is the so-called *Range Cell Migration* (RCM) and it is the responsible of the quadratic shape form of the range history and, in turn, of the linear evolution of frequency along time.

In this framework, the main casuistic of SAR simulation is to reproduce Equation 5.21 according to a set of input parameters. For such purpose, *GRECOSAR* follows two main steps, namely: 1) the estimation of  $\gamma(x, r)$  carried out by *GRECO*<sup>®</sup> (a constant related to signal power must be added) and 2) the generation of the term  $s(x' - x, r', r)$ .

The simulation of  $s(x' - x, r', r)$  can be split in two main parts, namely: 1) the simulation of the imaging geometry performed before *GRECO*<sup>®</sup> computations (*GRECO*<sup>®</sup> pre-processing) and 2) the synthesization of the SAR signal performed after *GRECO*<sup>®</sup> computations (*GRECO*<sup>®</sup> post-processing). In the first part, the view angles and the spectrum information of the chirp signal are derived to allow EM processing. For such purpose, the sensor locations along the aperture and the target position within the swath are found. This information is manipulated in order to adopt the coordinate system of *GRECO*<sup>®</sup> and to include the effects of vessel bearing, vessel speed and vessel motions. In the second part, the azimuth and range chirps are generated from range history and chirp samples. They are added to the complex EM fields computed by *GRECO*<sup>®</sup>, jointly with the RCM time shift and  $\omega[x' - x, r]$ . This process have to be done in the frequency domain because *GRECO*<sup>®</sup> works with frequency samples. This implies that an IFT operation is required in order to build the final raw data.

<sup>5</sup>In the original formulation, the term  $s(x' - x, r', r)$  was the signal including both the impulse response of the system and the complex reflectivity of the scene. Here, the latter is presented as an independent term in order to differentiate the contribution of *GRECO*<sup>®</sup> from SAR signal simulation.

### 5.4.1 Simulation of the Imaging Geometry

The simulation of the imaging geometry needs from the following coordinate systems, namely:

1. **Perifocal Orbital Coordinate System (POCS)**: It is used to express the position of a satellite within the orbital plane. The x-axis is parallel to the semi-major axis pointing to the perigee, the y-axis is parallel to the semi-minor axis and the z-axis is vertical to both. This coordinate system is strongly related to the Keplerian parameters defining the orbit of a satellite.
2. **Earth Centered Inertial (ECI)**: This coordinate system is static with the origin at the center of the Earth. The x-axis points to a reference point of the sky called *vernal point*  $\Upsilon$ , the z-axis points to the heavenly North Pole and the y-axis is perpendicular to both. With this reference system, the rotational motion of the Earth makes the orbit of the satellites to fall into planes.
3. **Earth Centered Earth Fixed (ECEF)**: The origin of this reference system is at the center of the Earth. The x-axis points within the equatorial plane to the intersection point between the equator and the Greenwich meridian, the z-axis points to the heavenly North Pole and the y-axis is perpendicular to both. In contrast with ECI, ECEF is in motion with the Earth and, thus, any geographical point over the Earth surface has the same coordinates all the time.
4. **GRECO<sup>®</sup> system**: This is the coordinate system adopted by GRECO<sup>®</sup> to calculate the view angles. For ascending (descending) orbits, it is defined with the x-axis pointing to the South (North), the z-axis pointing to the East (West) and the y-axis being perpendicular to both.

The relations and transformation matrices among these coordinates systems are gathered in Appendix [A](#).

### Observation time and platform speed

The first step of a simulation is devoted to fix the observation time. This parameter is defined by

$$t_{obs} = \frac{\lambda \cdot r_o}{L \cdot V_{plat}} \quad (5.23)$$

where  $r_o$  is the mid-slant range and  $V_{plat} = |\vec{P}^{ECEF}|$  the magnitude of the velocity vector of the satellite at the middle of the aperture expressed in ECEF. In *GRECOSAR*,  $r_o$  is calculated as the projection of the nominal height of the satellite into the slant-range plane. Thus,

$$r_o = \frac{a - R_T}{\cos \vartheta} \quad (5.24)$$

where  $R_T = 6378137$  m is the equatorial Earth radius,  $a$  the semi-major axis and

$$\vartheta = \arcsin \left\{ \frac{\sin \phi R_T}{a} \right\} \quad (5.25)$$

the so-called *look angle* (see Fig. 5.2). For the computation of the platform speed, some concepts of orbital mechanics are required. The procedure starts by finding the value of the *eccentric anomaly*  $E$  within the Kepler equation [160]

$$E - e \sin E = m_o \quad (5.26)$$

where  $m_o$  is the medium anomaly parameter provided by the user,  $e$  the Kepler eccentricity parameter and  $E$  is found via an iterative procedure that minimizes the following cost function

$$F(E_{test}) = E_{test} - e \sin E_{test} - m_o = 0 \quad \text{for } m_o < E_{test} < m_o + e \quad (5.27)$$

The final value of  $E$  is obtained with

$$E_{i+1} = E_i - \frac{E_i - e \sin E_i - m_o}{1 - e \cos E_i} \quad (5.28)$$

where  $0 < i < n$  and  $E_0 = m_o + e$ .  $n = 8$  is the number of iterations. Once the eccentric anomaly is found, the position ( $\vec{P}^{POCS} = [x, y, z]^{POCS}$ ) and velocity ( $\vec{P}^{POCS} = [\dot{x}, \dot{y}, \dot{z}]^{POCS}$ ) vectors of the satellite expressed in POCS are [160]

$$x^{POCS} = a (\cos E - e) \quad (5.29)$$

$$y^{POCS} = a \sqrt{1 - e^2} \sin E \quad (5.30)$$

$$z^{POCS} = 0 \quad (5.31)$$

$$\dot{x}^{POCS} = \sqrt{\frac{\mu}{a}} \frac{1}{1 - e \cos E} \sin E \quad (5.32)$$

$$\dot{y}^{POCS} = \sqrt{\frac{\mu}{a}} \frac{\sqrt{1 - e^2}}{1 - e \cos E} \cos E \quad (5.33)$$

$$\dot{z}^{POCS} = 0 \quad (5.34)$$

with  $\mu = 3.986005 \cdot 10^{14}$ . In ECI, these vectors become

$$\vec{P}^{ECI} = [T^{POCS \rightarrow ECI}] \vec{P}^{POCS} \quad (5.35)$$

$$\vec{\dot{P}}^{ECI} = [T^{POCS \rightarrow ECI}] \vec{\dot{P}}^{POCS} \quad (5.36)$$

where  $[T^{POCS \rightarrow ECI}]$  is the POCS to ECI transformation matrix defined in Equation A.2 of Appendix A. Finally, the position and velocity vectors in ECEF are

$$\vec{P}^{ECEF} = [T^{ECI \rightarrow ECEF}] \vec{P}^{ECI} \quad (5.37)$$

$$\vec{\dot{P}}^{ECEF} = \frac{d}{dt} [T^{ECI \rightarrow ECEF}] \vec{P}^{ECI} + [T^{ECI \rightarrow ECEF}] \vec{\dot{P}}^{ECI} \quad (5.38)$$

where  $[T^{ECI \rightarrow ECEF}]$  and  $\frac{d}{dt} [T^{ECI \rightarrow ECEF}]$  are the ECI to ECEF transformation matrices defined in Equation A.7 and A.9 of Appendix A.  $\vec{P}^{ECEF}$  is the vector used in Equation 5.23.

### Position and velocity vectors of the satellite

Once the vision time has been fixed, the position ( $\vec{P}_j^{ECEF}$ ) and velocity ( $\vec{\dot{P}}_j^{ECEF}$ ) vectors of the satellite can be computed for all the orbital positions of the simulation ( $j \in [1..N_a]$  where  $N_a = \lfloor t_{obs} \cdot PRF \rfloor$ ). This is achieved by repeating the previous procedure (from Equation 5.26 to 5.37-5.38) for the range of mean anomaly values defined by

$$\underline{m}_o' = \sqrt{\frac{\mu}{a^3}} (t_a - t_{perigee}) \quad (5.39)$$

where  $\underline{t}_a$  is a time vector of length  $N_a$  that provides the *ephemerid* time for each orbital position as

$$\underline{t}_a = \left[ -\frac{t_{obs}}{2} \dots \frac{1}{PRF} \dots \frac{t_{obs}}{2} \right] + t_{ref} \quad (5.40)$$

with  $t_{ref} = m_o / \sqrt{\frac{\mu}{a^3}}$ . The operator  $[i..s..l]$  indicates a vector of length  $N = \lfloor (l - i) / s \rfloor$  where  $i$  fixes the first sample,  $l$  the last sample and  $s$  the step between two successive samples. In Equation 5.39,  $t_{perigee}$  is the *reference* time of Kepler equation, which is always 0.

Remember that *GRECO*<sup>®</sup> does not consider the phase propagation term when computing EM information (see Section 5.2). This means that the EM fields do not experiment important phase oscillations between two successive orbital steps and, hence, EM simulations can be performed with a number of azimuth positions lower than  $N_a$ . This allows to define a new time variable

$$\underline{t}_a^{min} = \left[ -\frac{t_{obs}}{2} \dots C_s \dots \frac{t_{obs}}{2} \right] + t_{ref} \quad (5.41)$$

where  $C_s$  is a fixed sampling factor higher than  $1/PRF$ . Some tests performed with canonical and complex targets have shown that a suitable value for this constant may be  $C_s = 16/PRF$  as higher values can modify the signatures of vessels. As a result, azimuth positions become sampled reducing notably the EM processing time. But this azimuth sampling demands an azimuth interpolation before synthesizing the SAR signal in order to properly reconstruct  $t_a$  from  $\underline{t}_a^{min}$ . Such operation is performed in such a way that the first, center and last sample of  $\underline{t}_a^{min}$  are the same than those of  $t_a$ .

### Determination of antenna pointing

The next step in a simulation is the determination of antenna pointing, which is defined by the incidence  $\phi$  and squint angles  $\varphi$ . The former is obtained from the user-provided look angle  $\vartheta$  parameter via Equation 5.25 whereas the latter by applying the yaw steering procedure (see Section 3.1.4 of Chapter 3). *GRECOSAR* can perform yaw steering in two ways, namely: 1) by finding the squint angle that meets the Doppler Centroid requirement fixed by the user or, inversely, 2) by calculating the Doppler Centroid caused by the user-provided squint angle in the scene. The computation of yaw steering needs from the minimization process illustrated in Fig. 5.11. There, two main blocks are used, namely:



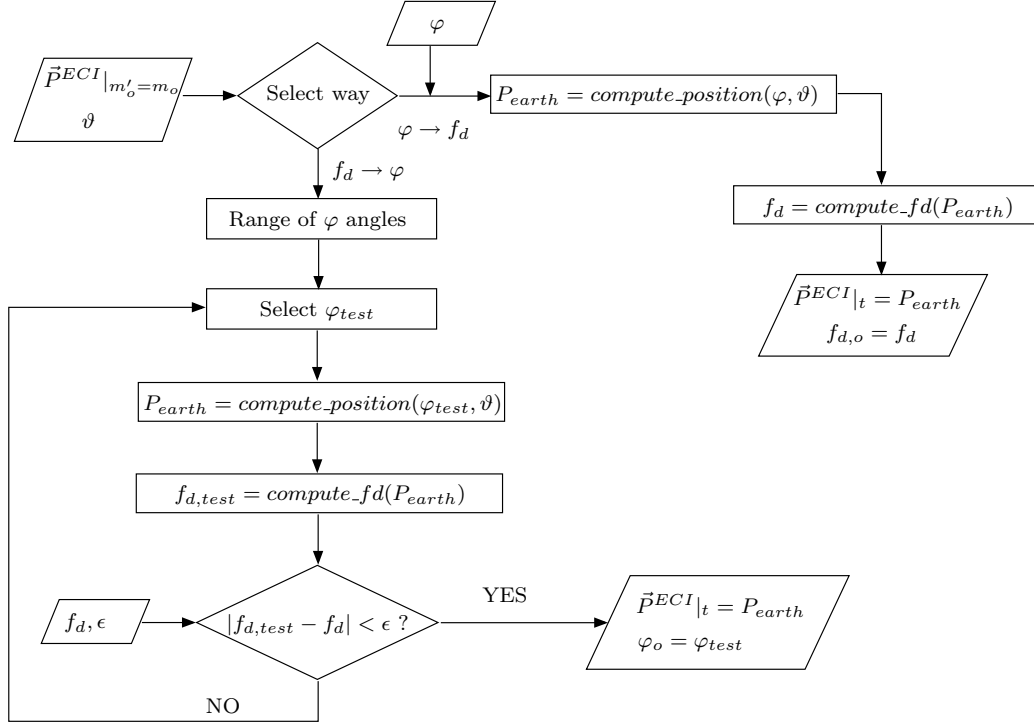


Figure 5.11: Minimization process required for performing yaw steering in *GRECOSAR*.

1. **Compute position:** Computes a generic location over the Earth surface ( $P_{earth}$ ) according to the satellite position at the middle of the aperture and the antenna pointing defined by a generic pair of squint and look angle values  $(\varphi, \vartheta)$ .
2. **Compute Doppler Centroid  $f_d$ :** Computes the Doppler Centroid value related to a generic position over the Earth surface ( $P_{earth}$ ) according the position of the satellite at the middle of the aperture.

Details of these blocks can be found in Appendix B. Note that the value of Doppler Centroid  $f_d$  (either computed or provided) is required for later data processing whereas the value of squint angle (either provided or computed) for finding the location of the target within the swath.

### Computation of target position

With antenna pointing, the target position is simply found by running the block **Compute position** for the squint angle resulting from yaw steering ( $\varphi_o$ ) and the near-far-angle fixing the range position of the target within the swath ( $\delta$ ). The result is  $P_t^{ECEF}$ , the position vector of the target expressed in ECEF.

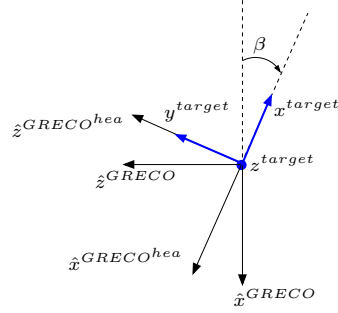


Figure 5.12: Version of the GRECO coordinate system accounting for vessel bearing information.

### Simulation of target environment

From the position vectors of the target ( $\vec{P}_t^{ECEF}$ ) and the satellite ( $\vec{P}_j^{ECEF}$ ) expressed in ECEF, the target ( $\vec{P}_t^{GRECO}$ ) and satellite ( $\vec{P}_j^{GRECO}$ ) locations in the GRECO coordinate system become

$$\vec{P}_t^{GRECO} = [T^{ECEF \rightarrow GRECO}] \vec{P}_t^{ECEF} \quad (5.42)$$

$$\vec{P}_j^{GRECO} = [T^{ECEF \rightarrow GRECO}] \vec{P}_j^{ECEF} \quad (5.43)$$

where  $j = [1..N_a]$  indicates the number of orbital position and  $[T^{ECEF \rightarrow GRECO}]$  is the ECEF to GRECO transformation matrix defined in Equation A.15 of Appendix A. With these vectors, target environment is simulated. The items considered in *GRECOSAR* are:

1. **Vessel bearing** that is added to target location by applying a simply pitch rotation to the GRECO coordinate system. As shown in Fig. 5.12, the rotation angle ( $\beta$ ) is measured clockwise from the North<sup>6</sup> and, hence, the rotation matrix becomes

$$[T^{GRECO \rightarrow GRECO^{hea}}] = \begin{bmatrix} \cos \beta & 0 & \sin \beta \\ 0 & 1 & 0 \\ -\sin \beta & 0 & \cos \beta \end{bmatrix} \quad (5.44)$$

2. **Vessel cruising speed and translational motions** that are simulated by means of first- and second-order terms under the local TARGET coordinate system  $\{x^{target}, y^{target}, z^{target}\}$  defined in Fig. 5.13. According to the geometry of Fig 5.12,

<sup>6</sup>This applies for ascending orbits. For descending orbits, it is measured clockwise from the South.

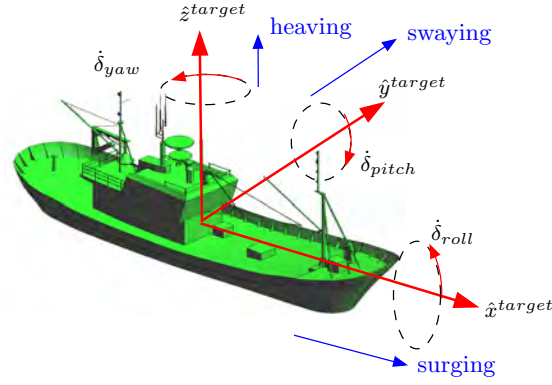


Figure 5.13: Local coordinate system for simulating vessel motions in *GRECOSAR*.

$$\vec{V}_x(j) = -((v_t + v_{surging}) \cdot t_j^m + a_{surging} \cdot (t_j^m)^2) \cdot \hat{x}^{GRECO^{hea}} \quad (5.45)$$

$$\vec{V}_y(j) = v_{heaving} \cdot t_j^m + a_{heaving} \cdot (t_j^m)^2 \cdot \hat{y}^{GRECO^{hea}} \quad (5.46)$$

$$\vec{V}_z(j) = v_{swaying} \cdot t_j^m + a_{swaying} \cdot (t_j^m)^2 \cdot \hat{z}^{GRECO^{hea}} \quad (5.47)$$

where  $\{ \hat{x}^{GRECO^{hea}} \hat{y}^{GRECO^{hea}} \hat{z}^{GRECO^{hea}} \}$  defines the GRECO coordinate system with bearing ( $GRECO^{hea}$ ).  $t_j^m$  is the time reference for target motions

$$t_j^m \in t^m = \left[ -\frac{t_{obs}}{2} \dots \frac{1}{PRF} \dots \frac{t_{obs}}{2} \right] + t_{ref}^m \quad (5.48)$$

with  $j = [1..N_a]$  and  $t_{ref}^m$  being a reference time fixed by the user that allows to modify the target position at the middle of the aperture according to motion parameters. The cruising velocity ( $v_t$ ), linear motion ( $v_x$  for  $x \in \{surging, heaving, swaying\}$ ) and acceleration motion terms ( $a_x$  for  $x \in \{surging, heaving, swaying\}$ ) of Equation 5.45 are also fixed by the user.

3. **Vessel rotational motions** that are simulated by applying the proper rotations to the  $GRECO^{hea}$  coordinate system. According to Fig. 5.12 and 5.13, the required rotation matrices are

$$\left[ T^{roll \rightarrow rolling} \right]_j = \begin{bmatrix} 1 & 0 & 0 \\ 0 & \cos \alpha_{roll,j}^{sim} & \sin \alpha_{roll,j}^{sim} \\ 0 & -\sin \alpha_{roll,j}^{sim} & \cos \alpha_{roll,j}^{sim} \end{bmatrix} \quad (5.49)$$

$$\left[ T^{yaw \rightarrow pitching} \right]_j = \begin{bmatrix} \cos \alpha_{pitch,j}^{sim} & \sin \alpha_{pitch,j}^{sim} & 0 \\ -\sin \alpha_{pitch,j}^{sim} & \cos \alpha_{pitch,j}^{sim} & 0 \\ 0 & 0 & 1 \end{bmatrix} \quad (5.50)$$

$$\left[ T^{pitch \rightarrow yawing} \right]_j = \begin{bmatrix} \cos \alpha_{yaw,j}^{sim} & 0 & -\sin \alpha_{yaw,j}^{sim} \\ 0 & 1 & 0 \\ \sin \alpha_{yaw,j}^{sim} & 0 & \cos \alpha_{yaw,j}^{sim} \end{bmatrix} \quad (5.51)$$

where the relation  $[l \rightarrow h]$  indicates the Euler rotations required for simulating rolling ( $q = roll$ ), pitching ( $q = pitch$ ) and yawing ( $q = yaw$ ).  $\alpha_{q,j}^{sim}$  are time-dependent angular velocities that describe the rotational motions via

$$\alpha_{q,j}^{sim} = -\alpha_q(t_j^m) = -(\dot{\alpha}_q \cdot t_j^m + \ddot{\alpha}_q \cdot (t_j^m)^2) \quad (5.52)$$

where the first- ( $\dot{\alpha}_q$ ) and second-order terms ( $\ddot{\alpha}_q$ ) are fixed by the user. Note that rotational motions are simulated by rotating the  $GRECO^{hea}$  coordinate system in the opposite sense of the actual motion. This explains the sign - in the previous formula. In addition,  $GRECOSAR$  has the capability to define  $\alpha_{roll}(t_j^m)$  and  $\alpha_{pitch}(t_j^m)$  from wave parameters and target dimensions via the simple wave model summarized in Appendix C.

After simulating the different environmental parameters, the original target position  $\vec{P}_t^{GRECO}$  becomes a time-dependent vector  $\vec{P}_{t,j}$

$$\vec{P}_{t,j} = \left[ T^{yaw \rightarrow pitching} \right]_j \cdot \left[ T^{pitch \rightarrow yawing} \right]_j \cdot \left[ T^{roll \rightarrow rolling} \right]_j \cdot \vec{P}_{t,j}^{GRECO}|_{hea,speed,trans} \quad (5.53)$$

where

$$\vec{P}_{t,j}^{GRECO}|_{hea,speed,transl} = \left[ T^{GRECO \rightarrow GRECO^{hea}} \right] \vec{P}_t^{GRECO} + \vec{V}_x(j) + \vec{V}_y(j) + \vec{V}_z(j) \quad (5.54)$$

### Determination of view angles

With Equations 5.42, 5.53 and the geometry of Fig. 5.3, the azimuth ( $\xi_j$ ) and elevation ( $\chi_j$ ) view angles for the orbital position  $j$  with  $j = [1..N_a]$  are

$$\xi_j = -\arctan \left\{ \frac{\Delta P_j^z}{\Delta P_j^x} \right\} \quad (5.55)$$

$$\chi_j = \arcsin \left\{ \frac{\Delta P_j^y}{|\Delta \vec{P}_j|} \right\} \quad (5.56)$$

where  $\Delta\vec{P}_j = [ \Delta P_j^x \quad \Delta P_j^y \quad \Delta P_j^z ]$  is a difference vector defined as

$$\Delta\vec{P}_j = \vec{P}_j - \vec{P}_{t,j} \quad (5.57)$$

with

$$\vec{P}_j = \begin{bmatrix} T^{yaw \rightarrow pitching} \end{bmatrix}_j \cdot \begin{bmatrix} T^{pitch \rightarrow yawing} \end{bmatrix}_j \cdot \begin{bmatrix} T^{roll \rightarrow rolling} \end{bmatrix}_j \cdot \begin{bmatrix} T^{GRECO \rightarrow GRECO^{hea}} \end{bmatrix} \cdot \vec{P}_j^{GRECO} \quad (5.58)$$

The vectors  $\vec{P}_j^{GRECO}$  and  $\vec{P}_{t,j}$  are respectively defined in Equations 5.42 and 5.53. The information of Equations 5.55-5.56 is stored in a file for the later use of *GRECO*<sup>®</sup>. In this file, the first line provides the value of  $N_a$  whereas the remaining ones the values of the triplet  $\{ \xi_j \quad \chi_j \quad |\Delta\vec{P}_j| \}$  at each orbital position.

### Chirp signal

The chirp signal is simulated at base band by discretizing the following formula

$$s(t_r) = e^{j\pi k(t_r)^2} \quad (5.59)$$

where

$$t_r = \left[ -\frac{\tau_p}{2} \dots \frac{1}{f_{FS}} \dots \frac{\tau_p}{2} \right] \quad (5.60)$$

is a vector of length  $N_r = \lceil \tau_p \cdot f_{FS} \rceil$  that gives the time reference in range. The parameters  $\tau_p$ ,  $f_{FS}$  and  $k = \Delta f / \tau_p$  are fixed by the user and they provide respectively the temporal extension of the pulse, the sampling frequency of the sensor and the chirp rate. The chirp signal is simulated with unitary amplitude because *GRECO*<sup>®</sup> provides the EM fields normalized<sup>7</sup>.

<sup>7</sup>Note that the power information is summarized in a constant that is compensated when the radiometric calibration of the SAR image is carried out.

The range of frequency values passed to *GRECO*<sup>®</sup> for EM computing are calculated according to  $N_r$

$$f_{chirp} = \left[ -\frac{\Delta f}{2} \cdot \frac{\Delta f}{N_r} \cdot \frac{\Delta f}{2} \right] + f_o \quad (5.61)$$

where  $f_o$  is the central frequency and  $\Delta f$  the signal bandwidth, both fixed by the user. Note that *GRECO*<sup>®</sup> computes the temporal window in which the signal interacts with the target. As its length is much lower than the spatial extension of the chirp signal ( $\Delta r_{chirp} = \tau \cdot c$ ), the reflectivity information can be then calculated with a number of frequencies ( $f_{chirp}^{min}$ ) lower than  $f_{chirp}$ . In this case, the new range of frequencies can be defined by

$$f_{chirp}^{min} = \left[ -\frac{\Delta f}{2} \cdot \frac{c}{2l} \cdot \frac{\Delta f}{2} \right] + f_o \quad (5.62)$$

where the sampling factor  $\frac{c}{2l}$  is much higher than  $\frac{\Delta f}{N_r}$ . The usage of  $f_{chirp}^{min}$  in *GRECOSAR* allows to notably reduce processing time<sup>8</sup>, but, as in the case of azimuth positions, it is necessary to interpolate the EM fields before synthesizing the raw data. The values of the first ( $f_{chirp}^{first} = -\frac{\Delta f}{2} + f_o$ ), last ( $f_{chirp}^{last} = \frac{\Delta f}{2} + f_o$ ) and step ( $f_{chirp}^{step} = \{\frac{c}{2l}\}$ ) frequency are inputs of *GRECO*<sup>®</sup>. The discrete values of Equation 5.59 and 5.62 are stored in a frequency file for the later synthesization of SAR signal.

#### 5.4.2 Synthesization of the SAR Signal

Once all the information required for EM computing is calculated and, the view and parameters files generated, *GRECO*<sup>®</sup> is executed. The result is a set of four binary files that store the information related to each polarimetric channel. Each file provides in consecutive range lines the complex value of the normalized EM field  $S_{m,n}^{EM}$ . Let to consider that these data is arranged in matrix form as follows

$$[S]_{N_r^s \times N_a^s}^{EM} = \begin{bmatrix} S_{1,1}^{EM} & \cdots & S_{1,N_a^s}^{EM} \\ \cdots & \cdots & \cdots \\ S_{N_r^s,1}^{EM} & \cdots & S_{N_r^s,N_a^s}^{EM} \end{bmatrix} \quad (5.63)$$

where  $N_r^s$  is the length of vector  $f_{chirp}^{min}$  in Equation 5.62 (the number of frequency samples evaluated by *GRECO*<sup>®</sup>) and  $N_a^s$  the length of vector  $t_a^{min}$  in Equation 5.41 (the number of

<sup>8</sup>The reduction factor of processing time is  $Rf_{time} = Rf_{time}^a \cdot Rf_{time}^r$  where  $Rf_{time}^a$  stands for the reduction factor due to azimuth sampling (see Section 5.4.1) and  $Rf_{time}^r$  for the reduction factor due to range sampling.

azimuth positions considered in the EM simulation). The interpolation of this matrix along the frequency dimension followed by an interpolation along the azimuth dimension results on

$$[S]_{N_r \times N_a}^{EM} = \begin{bmatrix} S_{1,1}^{EM} & \dots & S_{1,N_a}^{EM} \\ \dots & \dots & \dots \\ S_{N_r,1}^{EM} & \dots & S_{N_r,N_a}^{EM} \end{bmatrix} \quad (5.64)$$

where the interpolation pattern in range dimension depends on  $f_{chirp}^{min}$  and  $f_{chirp}$ , and in azimuth on  $t_a^{min}$  and  $t_a$ . Linear interpolation is used. With this matrix, the synthesization of the SAR signal is performed as follows:

1. Add the samples of the **chirp signal** stored in the frequency file

$$[S]_{N_r \times N_a}^{EM,chirp} = \begin{bmatrix} S(f_{chirp}^1) \cdot S_{1,1}^{EM} & \dots & S(f_{chirp}^1) \cdot S_{1,N_a}^{EM} \\ \dots & \dots & \dots \\ S(f_{chirp}^{N_r}) \cdot S_{N_r,1}^{EM} & \dots & S(f_{chirp}^{N_r}) \cdot S_{N_r,N_a}^{EM} \end{bmatrix} \quad (5.65)$$

where  $f_{chirp} = \left[ f_{chirp}^1 \cdot \frac{1}{f_{FS}} \cdot f_{chirp}^{N_r} \right]$  and  $S(f_{chirp}) = FT\{s(t_r)\}$  is the FT of the chirp signal defined in Equation 5.59.

2. Add the **propagation phase term** in the frequency domain

$$[S]_{N_r \times N_a}^{EM,chirp,R} = \begin{bmatrix} S_{1 \times 1}^{EM,chirp,R} & \dots & S_{1 \times N_a}^{EM,chirp,R} \\ \dots & \dots & \dots \\ S_{N_r \times 1}^{EM,chirp,R} & \dots & S_{N_r \times N_a}^{EM,chirp,R} \end{bmatrix} = \begin{bmatrix} e^{-j \frac{4\pi f_o |\Delta \vec{P}_1|}{c}} \cdot S(f_{chirp}^1) \cdot S_{1,1}^{EM} & \dots & e^{-j \frac{4\pi f_o |\Delta \vec{P}_{N_a}|}{c}} \cdot S(f_{chirp}^1) \cdot S_{1,N_a}^{EM} \\ \dots & \dots & \dots \\ e^{-j \frac{4\pi f_o |\Delta \vec{P}_1|}{c}} \cdot S(f_{chirp}^{N_r}) \cdot S_{N_r,1}^{EM} & \dots & e^{-j \frac{4\pi f_o |\Delta \vec{P}_{N_a}|}{c}} \cdot S(f_{chirp}^{N_r}) \cdot S_{N_r,N_a}^{EM} \end{bmatrix} \quad (5.66)$$

where  $|\Delta \vec{P}_j|$  provides the range history information defined in Equation 5.57 and stored in the view file.

3. Perform the simulation of the **RCM time shift** by applying the following property of FT

$$s(t_r - \Delta t_j^{RCM}) \Rightarrow^{FT} S(f_{chirp}) e^{-j 2\pi \Delta t_j^{RCM} f_{chirp}} \quad (5.67)$$

with  $\Delta t_j^{RCM} = 2(|\Delta \vec{P}_j| - |\Delta \vec{P}_{N_a/2}|)/c$ .  $r_o = |\Delta \vec{P}_{N_a/2}|$  is the *mid-slant* range or the sensor-to-target range at the middle of the aperture. Hence,

$$\begin{aligned}
& [S]_{N_r \times N_a}^{EM, chirp, R, RCM} = \\
& \begin{bmatrix} e^{-j \frac{4\pi f_{chirp}^1 (|\Delta \bar{P}_1| - r_o)}{c}} \cdot S_{1 \times 1}^{EM, chirp, R} & \dots & e^{-j \frac{4\pi f_{chirp}^1 (|\Delta \bar{P}_{N_a}| - r_o)}{c}} \cdot S_{1 \times N_a}^{EM, chirp, R} \\ \dots & \dots & \dots \\ e^{-j \frac{4\pi f_{chirp}^{N_r} (|\Delta \bar{P}_1| - r_o)}{c}} \cdot S_{N_r \times 1}^{EM, chirp, R} & \dots & e^{-j \frac{4\pi f_{chirp}^{N_r} (|\Delta \bar{P}_{N_a}| - r_o)}{c}} \cdot S_{N_r \times N_a}^{EM, chirp, R} \end{bmatrix} \quad (5.68)
\end{aligned}$$

4. Return to **time domain** by applying an IFT operation along range dimension

$$[s]_{raw} = IFT^{column} \left\{ [S]_{N_r \times N_a}^{EM, chirp, R, RCM} \right\} \quad (5.69)$$

where  $IFT^{column}$  indicates an IFT applied to each column.

5. Simulate the **antenna footprint** by multiplying the previous signal with  $\omega[x' - x, r]$ . In *GRECOSAR*, the footprint function is approximated to

$$\omega[x' - x, r] \cong \text{sinc} \left\{ \frac{\vartheta^r(r) \cdot w_a}{\lambda} \right\} \cdot \text{sinc} \left\{ \frac{\vartheta^a(x' - x) \cdot L_a}{\lambda} \right\} \quad (5.70)$$

where  $w_a$  provides the antenna width,  $L_a$  the antenna length and,  $\vartheta^r(r)$  and  $\vartheta^a(x' - x)$  the range and azimuth angular distance of the point located at  $(x, r)$  with respect to the center of the swath. These last parameters are defined according to the time variables  $t_a$  and  $t_r$  as (see Fig. 5.14)

$$\vartheta^r(r) = \vartheta - \arctan \left\{ \frac{t_r \cdot c + r_o \cos \vartheta \tan \delta}{r_o \cos \vartheta} \right\} \quad (5.71)$$

$$\vartheta^a(x' - x) = \arctan \left\{ \frac{V_{plat} \cdot t_a}{r_o} \right\} \quad (5.72)$$

where  $\vartheta$  is the look angle defined in Equation 5.25. Note that *GRECOSAR* only simulates the temporal window in which the chirp impinges the target. This means that the term  $t_r \cdot c$  is much lower than the other terms of Equation 5.71 and, hence,  $\vartheta^r(r)$  can be considered constant for all the simulation. In practice, it is approximated to  $\vartheta^r(r) = \vartheta^r = \vartheta - \delta$ . In the simulations presented in this thesis,  $x$  is always zero because yaw steering is computed for a null doppler centroid. Modifications of this parameter can lead to azimuth shifts of the target location from the center of the swath.

Therefore, the SAR signal synthesized from EM fields is

$$[s]_{raw, w} = [s]_{raw} \cdot \omega[x' - x, r] \quad (5.73)$$



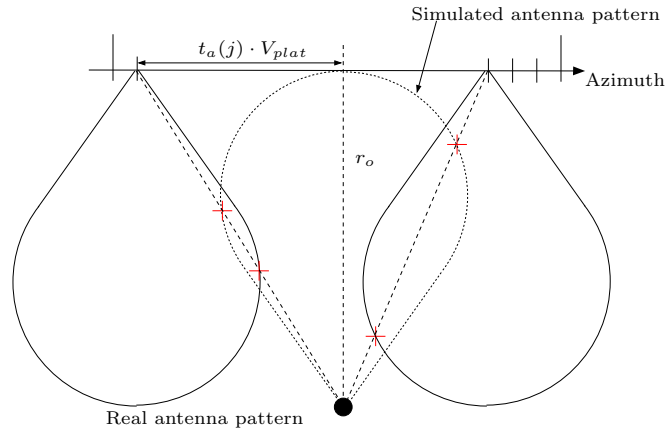


Figure 5.14: Relevant to antenna footprint in *GRECOSAR*. The signal related to each azimuth position is scaled according to its angular distance with respect to the target. The scaling factors are determined from the simulated antenna footprint, which is an equivalent footprint that reproduce the effects of the real one.

This signal is stored in a set of four binary files (one per each polarimetric channel) that are the inputs of the SAR processor embedded in *GRECOSAR*. The adopted code is a processor developed at UPC [152] and based on the Extended Chirp Scaling Algorithm (ECSA) [70]. As the algorithm is widely popular, no further comments are made here because they will not be relevant for the overall understanding of the SAR simulator. For more details, please refer to the provided references. Hereinafter, it is assumed that the SAR processor is a black box that accurately focus the synthesized raw data <sup>9</sup>.

### SAR Image Calibration

Once the SAR processor finishes the processing of the synthesized raw data, the final SAR images become available ( $[s]_{image}$ ). These images are calibrated in order to retrieve the normalized RCS  $\sigma_o$

$$\sigma_o = \frac{\sigma}{\delta_a \cdot \delta_r} \quad (5.74)$$

where  $\delta_a$  and  $\delta_r$  indicates the azimuth and range resolution of the image, and

$$\sigma = 4\pi r \frac{|E_s|}{|E_i|} \quad (5.75)$$

<sup>9</sup>Exhaustive tests have shown the proper performance of the processor.

In Section 5.2, it has been explained that *GRECO*<sup>®</sup> provides the normalized scattered EM field ( $r|E_s|$ ) for an incident EM field  $|E_i| = 1$  V/m. So, the magnitude of  $S_{m,n}^{EM}$  in Equation 5.64 is equal to

$$|S_{m,n}^{EM}| = \sqrt{\frac{\sigma}{4\pi}} \quad (5.76)$$

As the chirp signal is simulated with an unit amplitude, the power of the SAR image is

$$P_{image} = |[s]_{image}|^2 = N_r \cdot N_a \frac{\sigma}{4\pi} = \frac{\sigma_o}{F_c} \quad (5.77)$$

where  $F_c = \frac{4\pi}{N_r \cdot N_a \cdot \delta_r \cdot \delta_a}$  is the calibration factor. *GRECOSAR* has the option to provide the backscattered received power according to the transmitting peak power  $P_{peak}$

$$P_{antenna} = \frac{P_{peak} L_a w_a \sigma}{4\pi \lambda^2 r^4} \quad (5.78)$$

### 5.4.3 Advanced SAR modes

#### SAR Interferometry

*GRECOSAR* generates interferometric data by performing two independent SAR simulations: master and slave. The master simulation is run first following the procedure related from Section 5.4.1 (*Observation time and platform speed*) to Section 5.4.2 (*SAR image calibration*) whereas the slave one adopts the same procedure, but for the set of slave antenna locations ( $\vec{P}_j^{ECI,s}$ ). These locations are defined by

$$\vec{P}_j^{ECI,s} = \vec{B} + \vec{P}_j^{ECI} \quad (5.79)$$

where  $\vec{B}$  is the baseline vector linking both master and slave position, and  $\vec{P}_j^{ECI}$  the ECI position vector of the master antenna for the orbital position  $j = [1..N_a]$ . The vector  $\vec{B}$  is derived from the vector  $\hat{P}_{s \rightarrow t}^{ECI}$  defined in Equation B.6 of Appendix B by (see Fig. 5.15)

$$\vec{B} = \frac{B_n}{\cos \zeta^B} \begin{bmatrix} \cos \zeta^B & 0 & -\sin \zeta^B \\ 0 & 1 & 0 \\ \sin \zeta^B & 0 & \cos \zeta^B \end{bmatrix} \hat{P}_{s \rightarrow t}^{ECI} \quad (5.80)$$

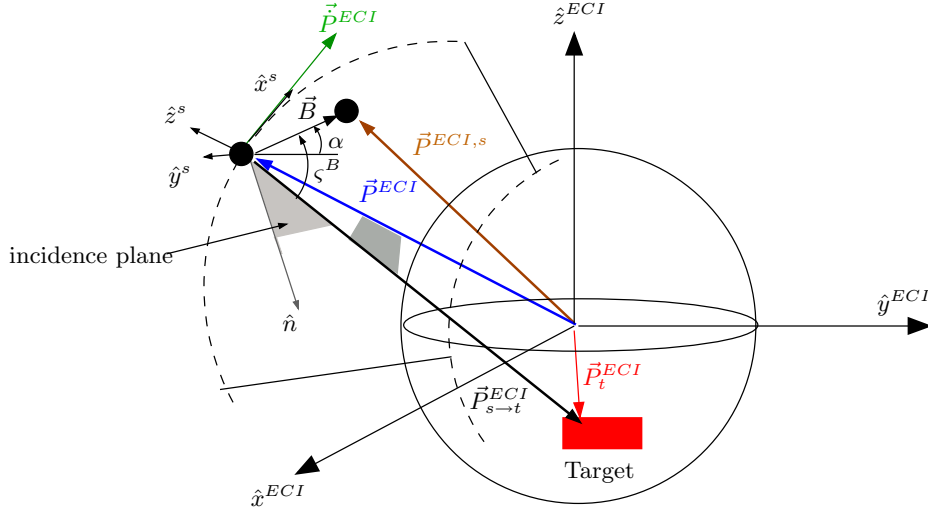


Figure 5.15: Identification of slave antenna positions from the master ones and baseline information.

with  $\zeta^B = 90 - \vartheta + \alpha$ . The parameters  $B_n$  and  $\alpha$  are fixed by the user and they provide the perpendicular baseline and tilt angle. Note that with this formulation an across-track geometry is implicitly assumed because the baseline vector falls into the incidence plane fixed by the antenna pointing ( $\hat{P}_{s \rightarrow t}^{ECI}$ ) and nadir directions ( $\hat{n}$ , Equation B.5 in Appendix B). For other geometries, the rotation matrix has to be properly modified. With the duplet  $\{\hat{P}_j^{ECI,s}, \hat{P}_t^{ECI} = \hat{P}_t^{ECEf}\}$ , the slave simulation ends as explained from Section 5.4.1 (*Simulation of target environment*) to Section 5.4.2 (*SAR image calibration*).

## Inverse SAR

*GRECOSAR* simulates Inverse SAR data by adopting the circular spotlight geometry illustrated in Fig. 5.16<sup>10</sup>. In this geometry, the radar is rotating around the target for a constant distance  $r_o$ , incidence angle  $\phi$  and angular aperture  $\Delta\theta$ . These parameters are fixed by the user and they allow to determine the sensor positions demanded for EM simulation ( $\vec{P}_{isar,j}^{GRECO}$ ). These positions are defined by

$$\vec{P}_{isar,j}^{GRECO} = \begin{bmatrix} P_{isar,j}^{GRECO,x} & P_{isar,j}^{GRECO,y} & P_{isar,j}^{GRECO,z} \end{bmatrix} = [T^{INCI \rightarrow GRECO}] \vec{P}_{isar,j}^i \quad (5.81)$$

<sup>10</sup>As commented in Section 3.4.1, this geometry makes possible to emulate the same effects observed in real scenarios that allow the acquisition of ISAR images

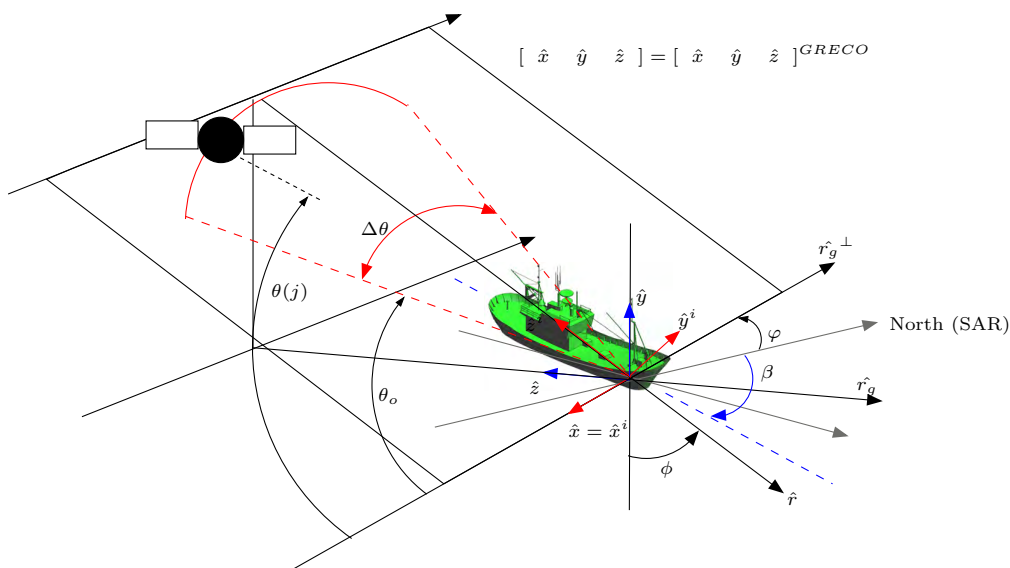


Figure 5.16: Imaging geometry of *GRECOSAR* for the ISAR imagery mode.

where

$$\vec{P}_{isar,j}^i = [ r_o \cos \theta(j) \quad 0 \quad r_o \sin \theta(j) ] \quad (5.82)$$

is an array of vectors indicating the location of the sensor in the INCI coordinate system  $\{ \hat{x}^i \ \hat{y}^i \ \hat{z}^i \}$  and  $[T^{INCI \rightarrow GRECO}]$

$$[T^{INCI \rightarrow GRECO}] = \begin{bmatrix} 1 & 0 & 0 \\ 0 & \cos(90 - \phi) & \sin(90 - \phi) \\ 0 & -\sin(90 - \phi) & \cos(90 - \phi) \end{bmatrix} \quad (5.83)$$

the transformation matrix between the INCI and GRECO coordinate systems. In Equation 5.82,  $\theta(j) \in [-\Delta\theta/2.. \delta\theta_{max}.. \Delta\theta/2] + \theta_o$  is a vector of length  $N_i = \lfloor \Delta\theta / \delta\theta_{max} \rfloor$  and sampling factor  $\delta\theta_{max}$  that provides, for each simulation position  $j$ , the angular distance of the sensor with respect to the horizontal. In this expression,  $\delta\theta_{max} = \frac{\lambda_{min}}{2L_t}$  is the maximum angular step allowed for a correct spectrum sampling and  $\theta_o$  the starting angle fixed by the user.  $L_t$  indicates the length of the target. In *GRECOSAR*, the values of  $\theta(j)$  are restricted to the upper half-space defined by the sea-level that is normally associated to the horizontal.

With  $\vec{P}_{isar,j}^{GRECO}$ , the azimuth ( $\xi_j$ ) and elevation ( $\chi_j$ ) view angles result

$$\xi_j = -\arctan \left\{ \frac{P_{isar,j}^{GRECO,z}}{P_{isar,j}^{GRECO,x}} \right\} + (360 - \beta + \varphi) \quad (5.84)$$

$$\chi_j = \arcsin \left\{ \frac{P_{isar,j}^{GRECO,y}}{|\vec{P}_{isar,j}^{GRECO}|} \right\} \quad (5.85)$$

where  $\beta$  is the bearing of the target as expressed in the SAR geometry of Fig. 5.2. As in the SAR case, the information contained in Equation 5.84 is stored in the view file, which, jointly with the parameter one, perform the input of *GRECO*<sup>®</sup>. With this information, *GRECO*<sup>®</sup> generates the four binary files storing the EM fields retrieved for each polarimetric channel. These data is processed as related in Section 3.4.3 of Chapter 3 and, then, the final scattering map derived. In this process, the user can select to process a specific angular sector within the range of angular positions simulated by *GRECO*<sup>®</sup>.

In the current configuration, the ISAR imagery mode of *GRECOSAR* has two main advantages, namely: 1) it allows to obtain scattering maps with centimetric resolutions in simple computers and 2) the imaging geometry can be connected with that of SAR simulations according to the value of  $\beta$ . This last item is very important because it makes possible to study which scattering mechanisms are expected in a SAR image according to the imaged vessels, how they can be polarimetrically described and, even more important, how they can be connected with the observed geometries.

## 5.5 Validation

*GRECOSAR* has been validated with both canonic and complex models. A first experiment has been performed for the array of canonical scatterers illustrated in Fig. 5.17 where two pairs of a trihedral and a dihedral with 1 m long edge are grouped in two different resolution cells. This target has been processed in the scenario depicted in Fig. 5.18 for the PolInSAR sensor (Sensor\_X sensor) defined in Table 5.2. The simulation has been run in a dual processor architecture PC built with two Athlon<sup>®</sup> Opteron 248, 3Gb of Random Access Memory (RAM) memory and an NVIDIA GeForce<sup>®</sup> FX 5950 Ultra graphics card. Hereinafter, this PC will be used for all the data presented in this thesis

The resulting images are gathered in Fig 5.19 and they show the magnitude of the zero-padded SAR images (scale factor of 32) retrieved for the first ( $f_0 \rightarrow$  Fig. 5.19(a)) and second Pauli channel ( $f_1 \rightarrow$  Fig. 5.19(b)). As observed, both polarimetric behaviors are perfectly isolated. The inspection of the range and azimuth cross-sections attached in Fig. 5.20 shows that the impulse responses are well-focused reaching image resolutions ( $A \times R = 2.34 \times 1.27$

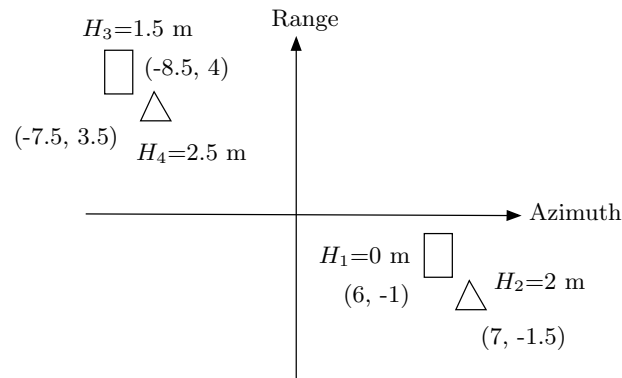


Figure 5.17: Array of two trihedrals and two dihedrals grouped in two different resolution cells. Azimuth and range positions are provided between parenthesis whereas the height by means of the label "H".

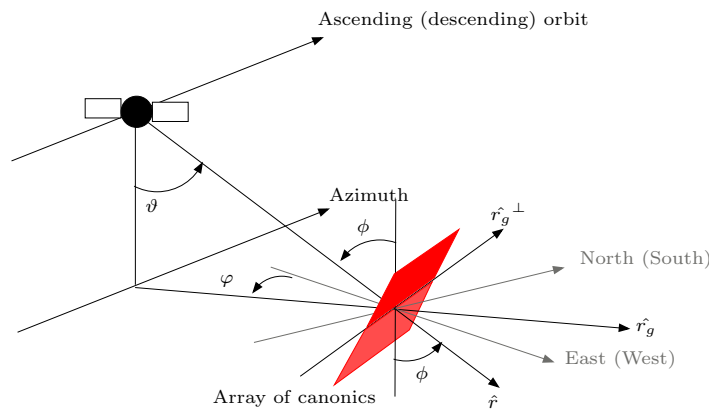


Figure 5.18: SAR imaging geometry for the simulation presented in Section 5.5. The canonical scatterers face the sensor as shows the plane of the target highlighted in red.

m) quite close to the expected values ( $A \times R = 2.3 \times 1.2$  m). The similarity between the measured ( $\sigma^{mea}$ ) and expected ( $\sigma^{the}$ ) RCS values, and between the measured ( $h^{mea}$ ) and expected ( $h^{the}$ ) heights is also high (see Table 5.3). For the RCS case, the differences are within the  $\pm 1$  dB margin, which is a common calibration criterion adopted in some orbital missions, for instance ESA's ERS series [161].

Besides this simple test, a second experiment has been performed for the SPA vessel. In this case, the hypothetical Polarimetric ISAR sensor summarized in Table 5.4 has been adopted for a bearing of  $\beta - \varphi = 315^\circ$ . This simulation provides a centimetric scattering map that allow, first, to validate the ISAR processing chain and, second, to evaluate the reliability of the scattering information according to the imaged geometry. The output image has been analyzed with the Pauli theorem and the result is presented in Fig. 5.21. There, two main hot spots are highlighted, namely: 1) the diplane interaction of the masts and banisters with

Table 5.2: Main parameters of the Sensor\_X sensor.  $D_r$  and  $D_a$  expresses the pixel extend in both range and azimuth dimensions.

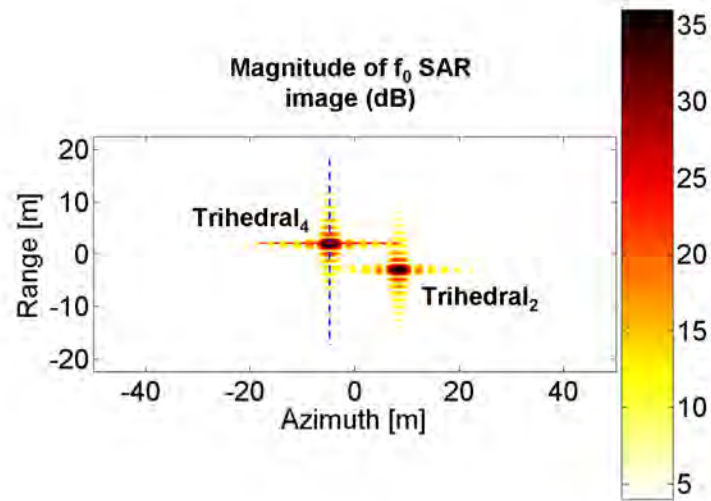
$h$ [Km]	514	$r_o$ [km]	544	$V_{plat}$ [m/s]	7686
$\phi$ [°]	20	$\varphi$ [°]	11.8	$\vartheta$ [°]	18.447
$f_o$ [GHz]	9.65	PRF [Hz]	3736	$L_a, L_r$ [m]	4.6, 0.9
$\delta f$ [MHz]	125	FS [MHz]	137.5	$\tau$ [ $\mu$ s]	28
$\delta_r$ [m]	1.2	$\delta_a$ [m]	2.3	$D_r, D_a$ [m]	1.2, 2
$B_n$ [m]	30 m	$\alpha$ [°]	0	-	-

Table 5.3: Measured ( $\sigma^{mea}$ ) and theoretical ( $\sigma^{the}$ ) RCS values for the canonical scatterers of the target depicted in Fig. 5.17. Height comparison is also attached.

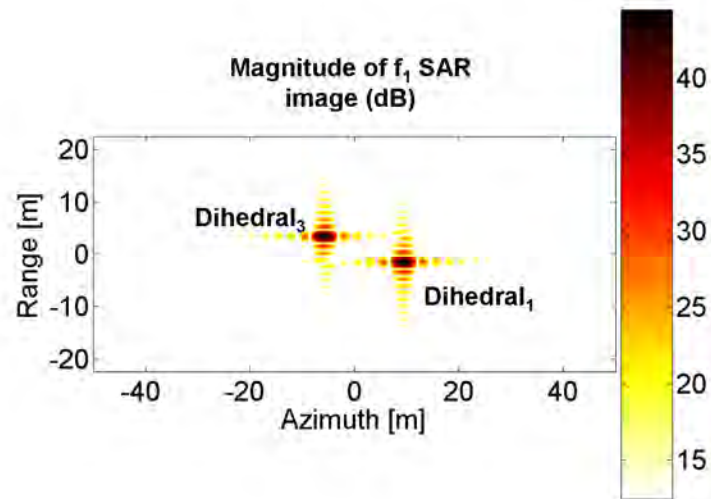
Target	$\sigma^{the}$ [dB]	$\sigma^{mea}$ [dB]	$h^{the}$ [m]	$h^{mea}$ [m]
1	$25.1 \frac{a^2 b^2}{\lambda^2}  _{a=1, b=1} = 44.45$	44.45	0	0
2	$4.19 \frac{a^4}{\lambda^2}  _{a=1} = 36.68$	35.82	2	1.97
3	$25.1 \frac{a^2 b^2}{\lambda^2}  _{a=1, b=1} = 44.45$	44.1	1.5	1.5
4	$4.19 \frac{a^4}{\lambda^2}  _{a=1} = 36.68$	36.01	2.5	2.47

Table 5.4: Main parameters of Sensor\_IC.  $\delta_{r_s}$  and  $\delta_{r_c}$  expresses the resolution in slant- and cross-range dimensions.

$r_o$ [km]	544	$\phi$ [°]	20	$\varphi$ [°]	11.8
$f_o$ [GHz]	5.3	$\Delta f$ [GHz]	1	$\Delta \theta$ [°]	5
$\delta_{r_s}$ [cm]	15	$\delta_{r_c}$ [cm]	29	-	-



(a)



(b)

Figure 5.19: Magnitude of the zero-padded SAR images related to the first  $f_0$  (a) and second  $f_1$  (b) Pauli channel (scale factor of 32) for the target illustrated in Fig. 5.17. The colored lines shows the range and azimuth cross-sections illustrated in Fig. 5.20.



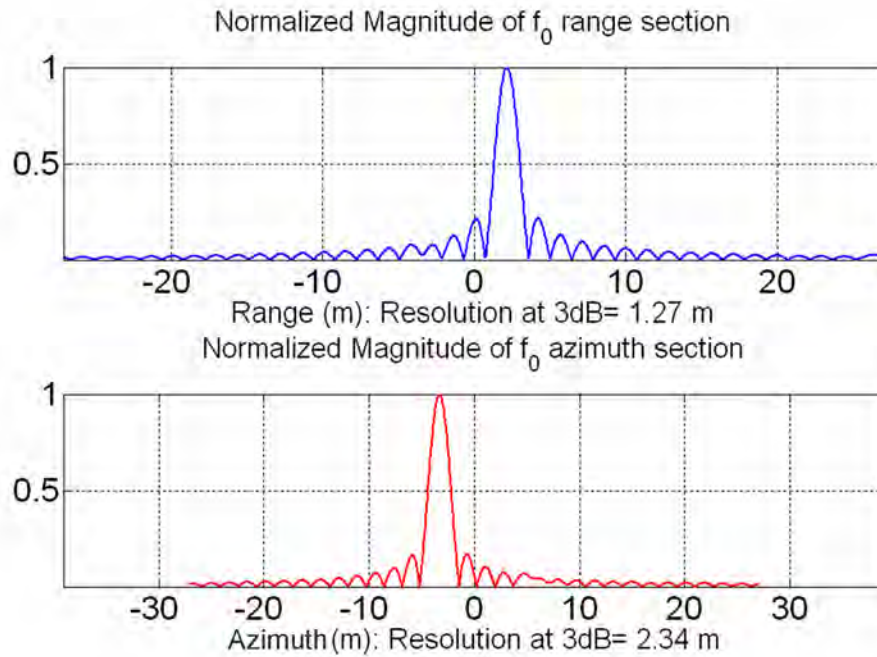


Figure 5.20: Range and azimuth cross section for the spread function of target "Trihedral 4" shown in Fig. 5.19(a).

the cabin surface and 2) the trihedral-like mechanism formed by the buttresses of the lateral flat banister. In both cases, the geometry of the target fits with the polarimetric behavior showing the consistency of *GRECOSAR*'s data. At this point, the usage of real imagery for the validation of *GRECOSAR* would be, if available, indeed interesting. However, this step has not been possible in this thesis due to the difficulties on acquiring images with detailed ground-truth. The option to carry on measurements in anechoic chambers with scaled versions of the processed models has been considered. But, the limited dimensions of the available facility at UPC have made impossible to perform such an experiment.

In order to supply this data deficiency, the validation carried out for the EM solver has been recovered. In this case, exhaustive tests performed with measurements in anechoic chambers and/or comparisons with other codes have shown the high accuracy reached in the estimation of RCS [45] [46] [47]. As *GRECO*<sup>®</sup> is the kernel of *GRECOSAR*, these results make reliable to consider that the SAR simulation environment adopted in this thesis has the enough realism for developing vessel classification studies and, even more important, to translate the obtained conclusions to real cases.

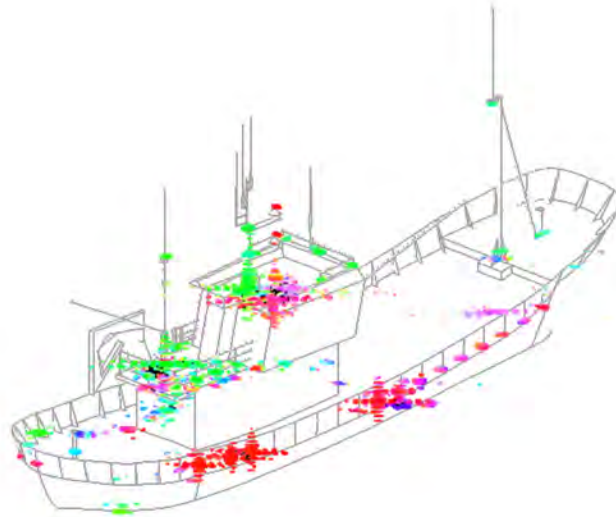


Figure 5.21: ISAR image for the SPA vessel,  $\beta + \varphi = 315^\circ$  and Sensor\_IC sensor. The scattering map has been processed with the Pauli theorem. The adopted color code is  $f_0 \rightarrow$  Red,  $f_1 \rightarrow$  Green and  $f_2 \rightarrow$  Blue.

### 5.5.1 Influence of the Rendering Error

Section 5.2.2 has pointed out that the estimation of the reflectivity of targets suffers from some errors. The most important one is the rendering error that states for the discretization inaccuracies performed when the CAD model is rendered into the bitmap one<sup>11</sup>. The distortions that this error can cause in SAR images depends on the value of the pixel size. The lower this parameter, the better the results, but the higher the demanded computer resources. In this section, the minimum value required to make the rendering error negligible without increasing in excess processing time is provided. For such purpose, a set of simulations have been carried out for an isolated trihedral. The same scenario (see Fig. 5.18) and sensor than before (see Table 5.2) have been adopted. In these simulations, four different pixel sizes (0.5 m, 0.1 m, 0.05 m, 0.01 m) have been evaluated and, for each one, the resulting impulse responses inspected. The azimuth and range cross sections related to these functions are gathered in Fig. 5.22 - 5.25. As observed, a good focusing accuracy is achieved for a pixel size of 0.01 m or lower. With that value, it can be assumed that the targets analyzed in *GRECOSAR* are, from an electromagnetically point of view, almost identical to the real ones. In Chapter 6, it will be observed that this value for the pixel size will have to be reduced up to 0.008 m when generating the centimetric scattering maps.

<sup>11</sup>Note that the geometrical error is negligible for parametric surfaces. Actually, chordal errors as lower as 1 mm that assures a high discretization accuracy can be managed by *GRECOSAR*.

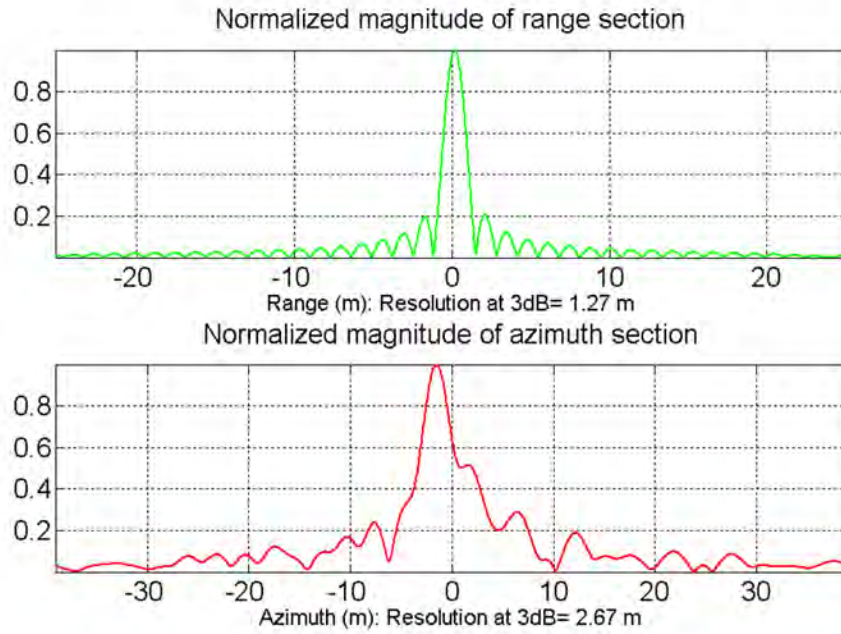


Figure 5.22: Azimuth and range cross-sections derived from the impulse response of a trihedral when the target is rendered with a pixel size of 0.5 m.

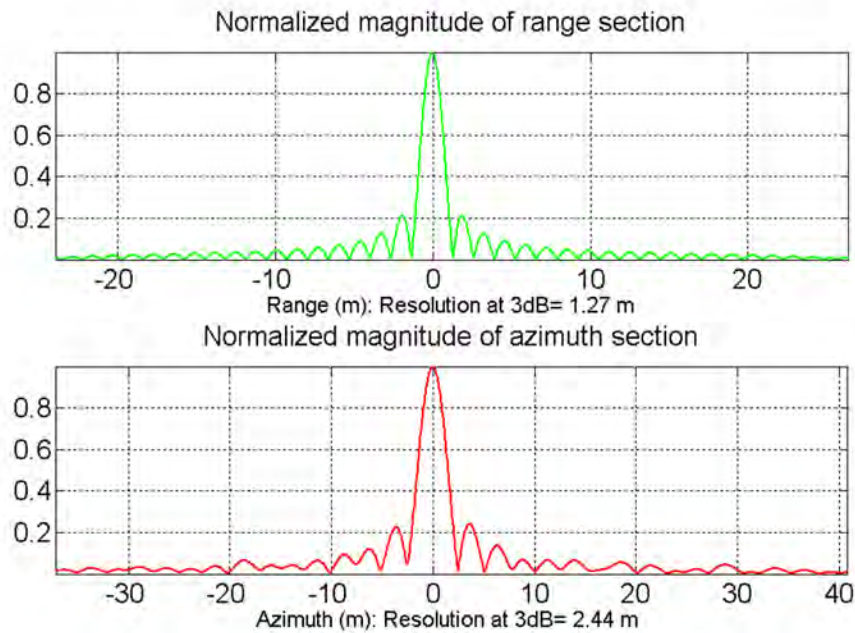


Figure 5.23: Azimuth and range cross-sections derived from the impulse response of a trihedral when the target is rendered with a pixel size of 0.1 m.

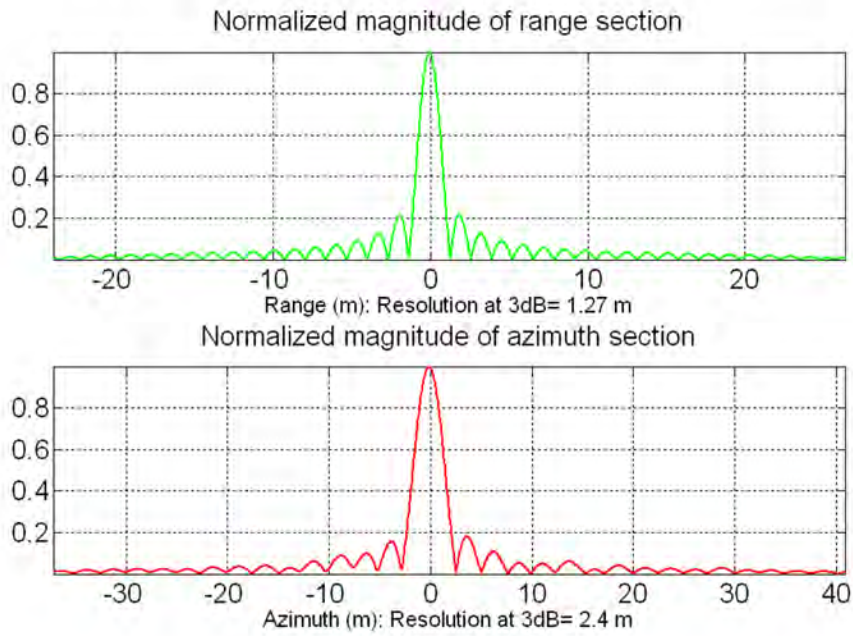


Figure 5.24: Azimuth and range cross-sections derived from the impulse response of a trihedral when the target is rendered with a pixel size of 0.05 m.

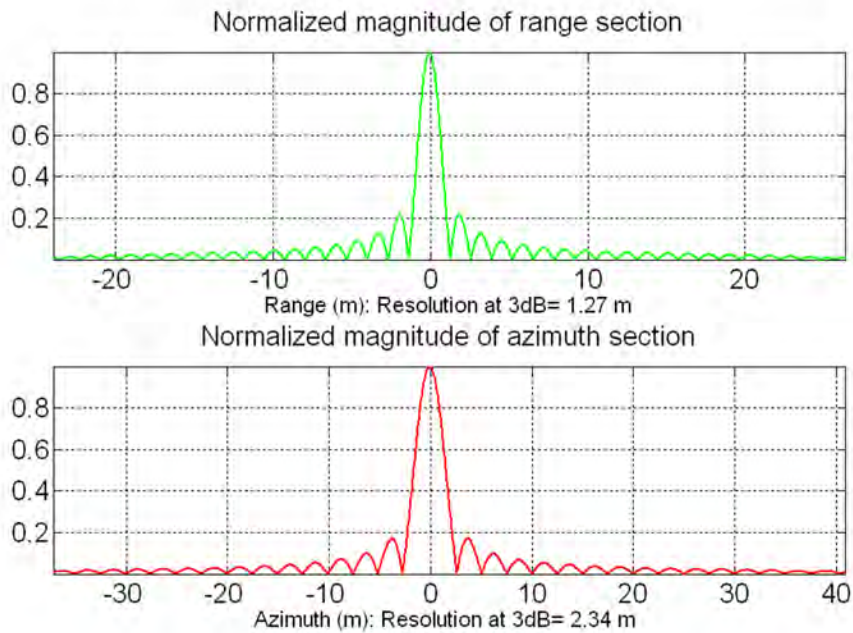


Figure 5.25: Azimuth and range cross-sections derived from the impulse response of a trihedral when the target is rendered with a pixel size of 0.01 m.

## Chapter 6

# Vessel Scattering Study

This Chapter analyzes the scattering properties of vessels with *GRECOSAR*. The main goal is to describe the polarimetric characteristics of vessel SAR images and to know which information can be retrieved for developing a proper classification method. For such purpose, large databases obtained for different imagery modes and related to diverse vessels, operating bands, resolutions and environmental conditions have been generated. Two main groups of images can be differentiated, namely: 1) polarimetric scattering maps derived via ISAR imagery with centimetric resolutions and 2) fully-polarimetric SAR images adopting resolutions around the meter. In both cases, data analysis has been carried out with CTD. Supporting the conclusions outlined from the simulated images, real images obtained from airborne sensors are also inspected at the end of the Chapter.

### 6.1 Analysis of Inverse SAR data

This section provides the results obtained from the analysis of simulated ISAR data [34]. They will allow to know the main geometries within the structure of vessels that are responsible of the scattering mechanisms observed in SAR data. Four different sensors have been considered operating at L (Table 6.1), S (Table 6.2), C (Table 6.3) and X (Table 6.4) band. The imaging geometry is depicted in Fig. 6.1 where the sea surface is not taken into account. There, the incidence angle is equal to  $\phi = 20^\circ$  as it is the incidence adopted by some orbital sensors, for instance the ESA'S ERS series [56] or the IS1/IS2 operating modes of ESA's ENVISAT [55]. The angular aperture is equal to  $\Delta\theta = 5^\circ$  so that the polarimetric information observed in a specific ISAR simulation can be reasonably linked with that retrieved in the corresponding SAR simulation performed for the same vessel bearing. Hereinafter, vessel bearing is provided in terms of  $\beta + \varphi$  because in ISAR images it is more suitable to express the orientation of vessels with respect to the direction perpendicular ( $\hat{r}_g^\perp$ ) to ground range ( $\hat{r}_g$ ).

Table 6.1: Main parameters of Sen\_IL.  $\delta_{r_s}$  and  $\delta_{r_c}$  expresses the resolution in slant- and cross-range dimensions.

$r_o$ [km]	544	$\phi$ [°]	20	$\varphi$ [°]	11.8
$f_o$ [GHz]	1.27	$\Delta f$ [GHz]	1	$\Delta\theta$ [°]	5
$\delta_{r_s}$ [cm]	15	$\delta_{r_c}$ [cm]	66	-	-

Table 6.2: Main parameters of Sen\_IS.  $\delta_{r_s}$  and  $\delta_{r_c}$  expresses the resolution in slant- and cross-range dimensions.

$r_o$ [km]	544	$\phi$ [°]	20	$\varphi$ [°]	11.8
$f_o$ [GHz]	2.6	$\Delta f$ [GHz]	1	$\Delta\theta$ [°]	5
$\delta_{r_s}$ [cm]	15	$\delta_{r_c}$ [cm]	66	-	-

Table 6.3: Main parameters of Sen\_IC.  $\delta_{r_s}$  and  $\delta_{r_c}$  expresses the resolution in slant- and cross-range dimensions.

$r_o$ [km]	544	$\phi$ [°]	20	$\varphi$ [°]	11.8
$f_o$ [GHz]	5.3	$\Delta f$ [GHz]	1	$\Delta\theta$ [°]	5
$\delta_{r_s}$ [cm]	15	$\delta_{r_c}$ [cm]	29	-	-

Table 6.4: Main parameters of Sen\_IX.  $\delta_{r_s}$  and  $\delta_{r_c}$  expresses the resolution in slant- and cross-range dimensions.

$r_o$ [km]	544	$\phi$ [°]	20	$\varphi$ [°]	11.8
$f_o$ [GHz]	9.65	$\Delta f$ [GHz]	1	$\Delta\theta$ [°]	5
$\delta_{r_s}$ [cm]	15	$\delta_{r_c}$ [cm]	18	-	-

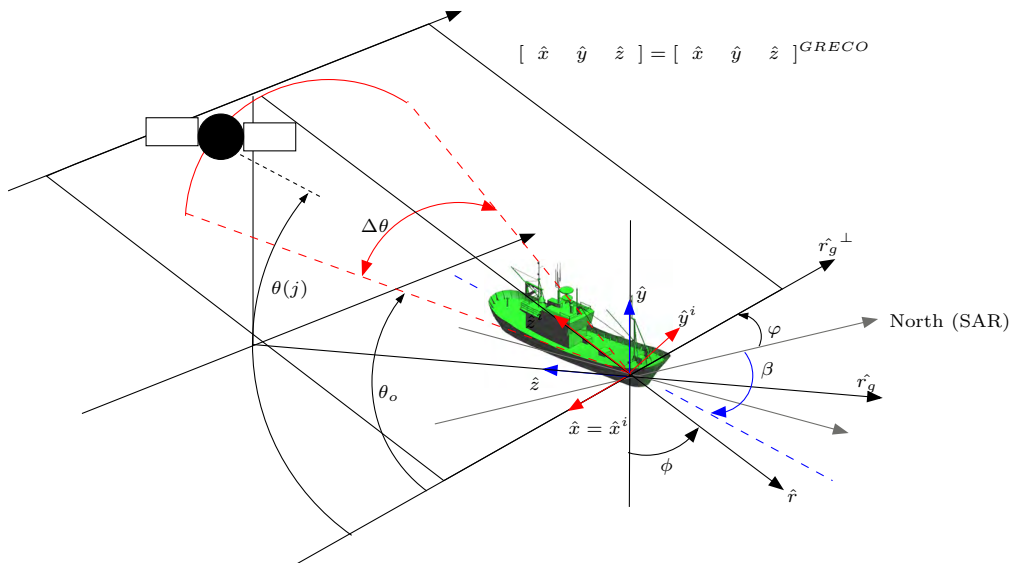


Figure 6.1: Imaging geometry of *GRECOSAR* for the ISAR imagery mode.

### 6.1.1 L band

The three vessel models, SPA <sup>1</sup>, ICE and FER (see Fig. 5.9 and Fig. 5.10), have been firstly processed at L band for seven bearings ranging from  $\beta + \varphi = 295^\circ$  to  $\beta + \varphi = 355^\circ$  in steps of  $10^\circ$ . The derived data have been analyzed with the Pauli, SDH and Cameron CTD, and the results are compiled in terms of colored images. These images are gathered in Appendix D (Section D.1, Fig. D.1 - D.9) and two samples are presented in Fig. 6.2 - 6.4. They are related to the SPA, ICE and FER models for the bearing angles  $\beta + \varphi = 295, 325^\circ$ . In these images, the Pauli and SDH decomposition theorems adopt an RGB-based color codification defined by red  $\rightarrow \{ f_0 \ f_s \}$ , green  $\rightarrow \{ f_1 \ f_d \}$  and blue  $\rightarrow \{ f_2 \ f_h \}$ , where  $\{ f_0 \ f_1 \ f_2 \ f_s \ f_d \ f_h \}$  express the weight of each simple mechanism according to the formulae of Chapter 4. In the contrary, the Cameron CTD uses the following color-mechanism relations, red  $\rightarrow \hat{f}_{tri}$ , green  $\rightarrow \hat{f}_{dih}$ , yellow  $\rightarrow \hat{f}_{dip}$ , blue  $\rightarrow \hat{f}_{cyl}$ , cyan  $\rightarrow \hat{f}_{ndi}$ , magenta  $\rightarrow \hat{f}_{dev}$  and grey  $\rightarrow$  anti-symmetric, where in this case  $\{ f_{tri} \ f_{dih} \ f_{dip} \ f_{cyl} \ f_{ndi} \ f_{dev} \}$  are binary variables indicating if the simple mechanism dominates the behavior of the pixel (1) or not (0). In all the figures, the images are overlapped to a transparent snapshot of the corresponding vessel. Their cross-range resolution depends inversely on the dimensions of the processed target.

### Comments

According to the obtained results, the following conclusions derive, namely:

1. Similar polarimetric interpretation is retrieved for each target decomposition. This is due to the fact that the scattering response of vessels is dominated by strongly polarized trihedral- and dihedral-like mechanisms.
2. Each vessel has a particular distribution of scattering mechanisms that identifies its geometrical structure. It is characterized by a set of main scattering centers that present a high RCS and keep their polarimetric properties for at least a range of bearing angles larger than  $30^\circ$ . This value is close to the angular response of some canonical scatterers, for instance the trihedral. In general, the most common structures are: 1) corner geometries behaving as trihedral and 2) the base of the masts inducing a dihedral-like mechanisms with the planar surfaces located at the bottom.
3. For this incidence, the weight of anti-symmetric mechanisms is not so important. For some bearings, their significance is notably increased, specially for the ICE vessel.
4. Adverse situations are observed for those bearings that put the vessel oriented almost parallel to the satellite track. In such a case, the polarimetric trace is notably modified

---

<sup>1</sup>This model demanded a pixel size of 8 mm in order to retrieve reliable results.

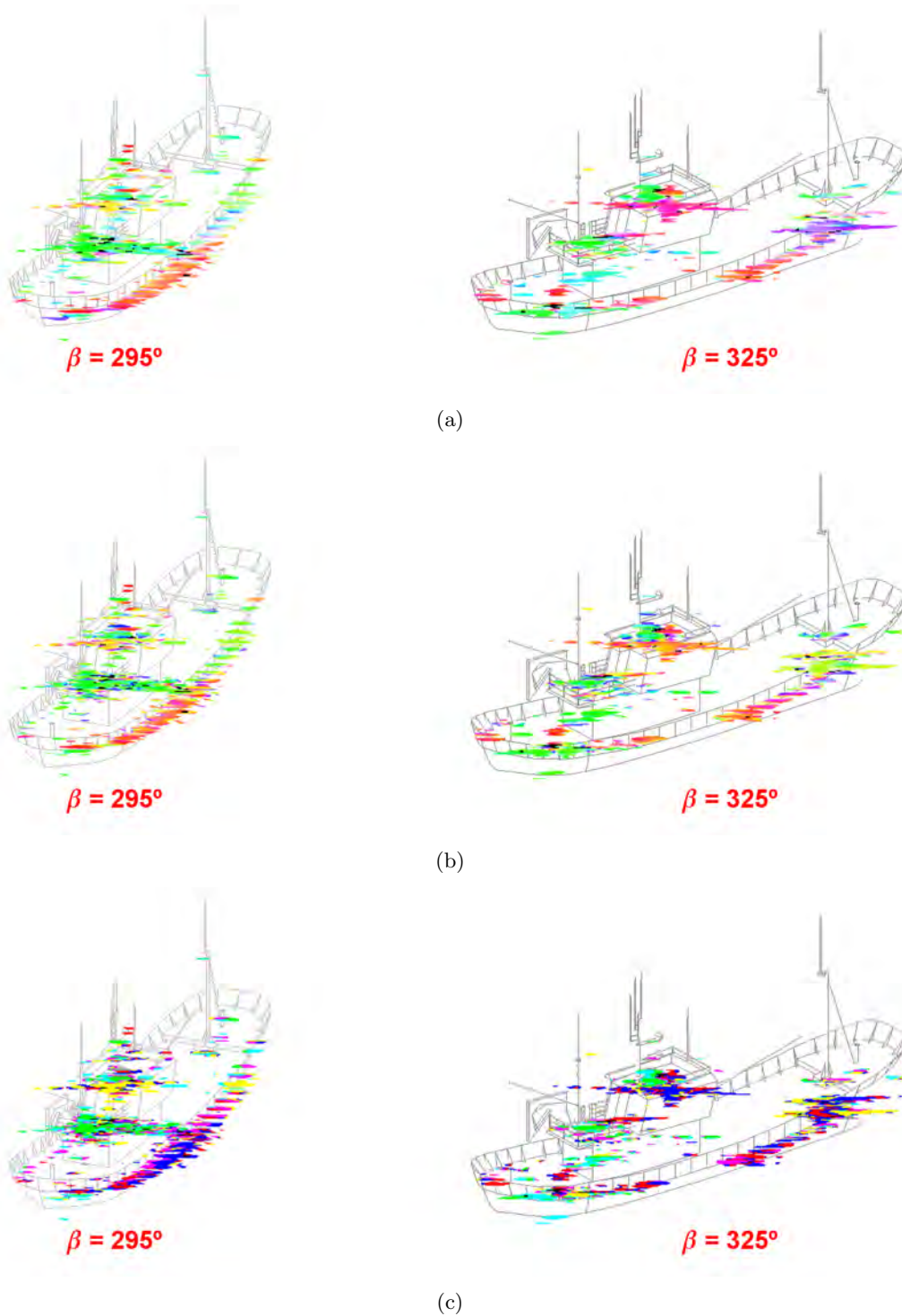


Figure 6.2: PolSAR images obtained for the SPA model at L band and  $\phi = 20^\circ$ . The bearing angles are  $\beta + \phi = 295, 325^\circ$ . The images have been analyzed with the Pauli (a), SDH (b) and Cameron (c) CTD for a dynamic range of 25 dB.



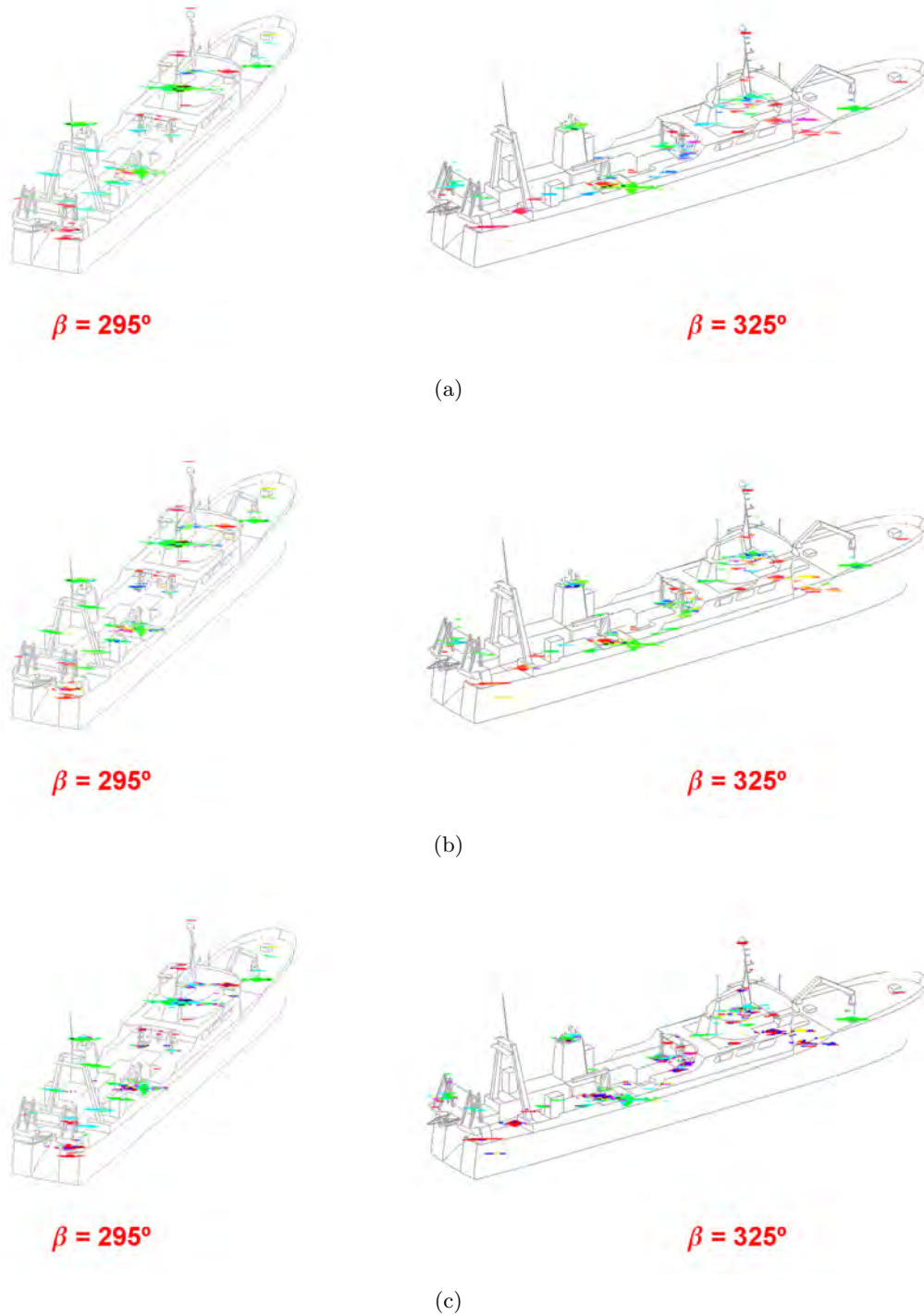


Figure 6.3: PolISAR images obtained for the ICE model at L band and  $\phi = 20^\circ$ . The bearing angles are  $\beta + \varphi = 295, 325^\circ$ . The images have been analyzed with the Pauli (a), SDH (b) and Cameron (c) CTD for a dynamic range of 25 dB.

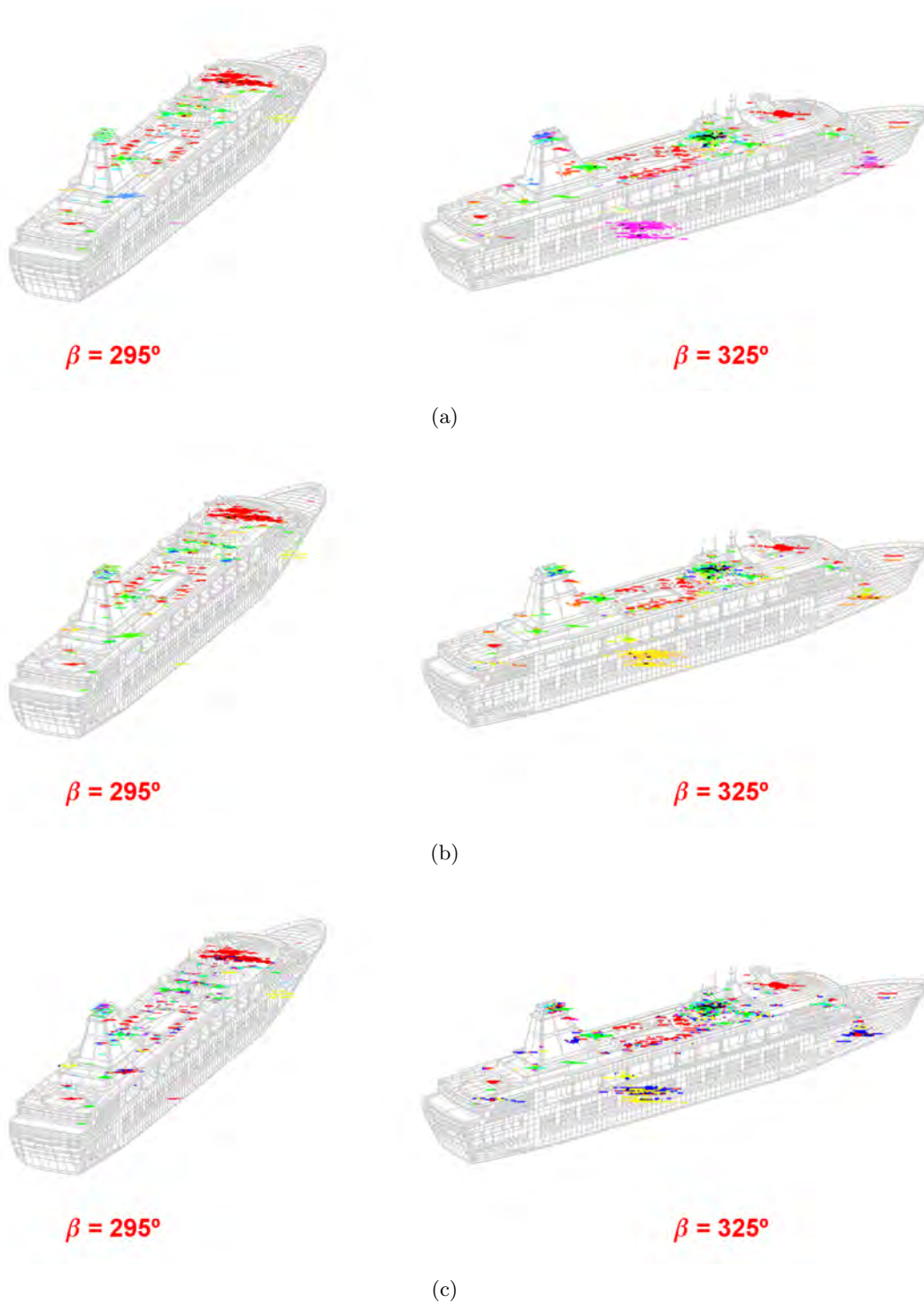


Figure 6.4: PolSAR images obtained for the FER model at L band and  $\phi = 20^\circ$ . The bearing angles are  $\beta + \phi = 295, 325^\circ$ . The images have been analyzed with the Pauli (a), SDH (b) and Cameron (c) CTD for a dynamic range of 25 dB.

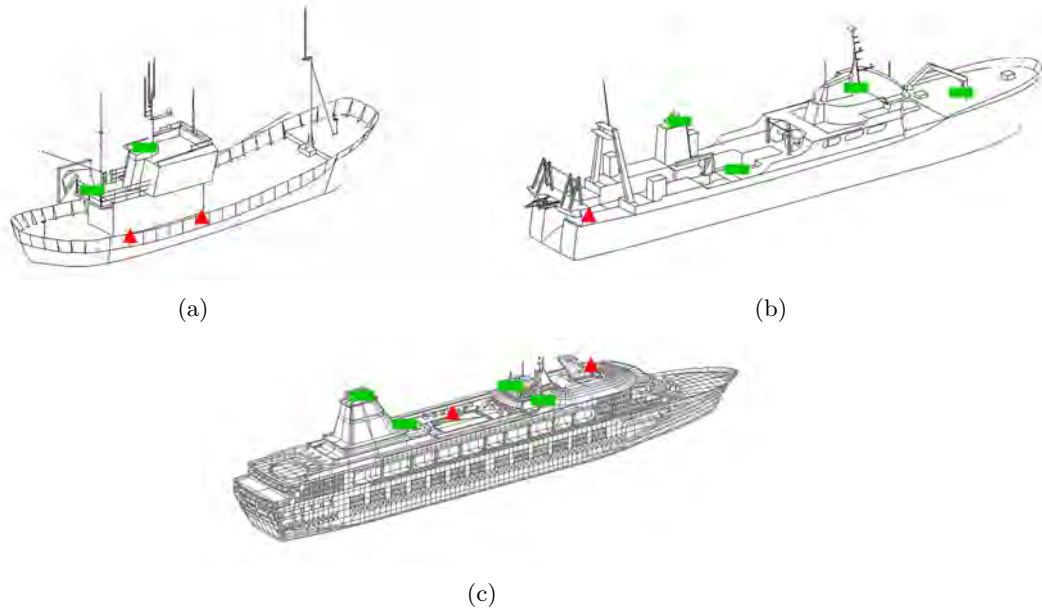


Figure 6.5: Scattering maps providing the location of the reference spots in the polarimetric traces of the SPA (a), ICE (b) and FER (c) models. They are valid at L band for the range of bearing angles defined by  $\beta = 325^\circ \pm 30^\circ$ . Full red triangles highlight trihedral-like behaviors whereas the green rectangles highlight the dihedral ones.

due to the dihedral-like mechanisms performed at the lateral sides of the cabin and hull. These mechanisms have normally associated a restrictive angular behavior with high RCS that can mask, in some punctual views, those key scattering mechanisms demanded for a proper vessel identification.

5. In general, it appears that the polarimetric behavior of vessels at L band is not excessively complex because it can be characterized by the simple Pauli mechanisms. In most cases, the overall response is dominated by few significant spots presenting a high RCS. The number, type and distribution of such spots is almost constant in all the views and this allows to provide a set of reference scattering maps that summarize the polarimetric traces observed within the analyzed bearings. These maps are illustrated in Fig. 6.5. There, the guide scatterers are selected according to two main requirements, namely: 1) they have a constant polarimetric behavior for a range of bearing angles higher than  $30^\circ$  and 2) they have the highest RCS values with a difference larger than 10 dB with respect to the surrounding scatterers<sup>2</sup>. With these scatterers, the reference maps schematize the particular geometry of each vessel providing enough information for a proper discrimination.

<sup>2</sup>Note that these requirements are not fulfilled by any anti-symmetric mechanism and, hence, none of them is included in the reference scattering maps.

### 6.1.2 S band

The previous simulations have been generated at S band. Fig. 6.6 - 6.8 shows the scattering maps related to the SPA, ICE and FER vessels for the bearing angles  $\beta + \varphi = 295^\circ, 325^\circ$ <sup>3</sup>. The remaining results can be inspected in Appendix D (Section D.2, Fig. D.10 - D.18). As observed, the conclusions derived from the L band simulations apply for the current ones. Almost the same polarimetric behavior is retrieved for all vessels and, thus, the reference scattering maps inferred in L band are valid for this frequency range. This can be appreciated in Fig. 6.9 where the comparative between L and S band is attached for the bearing  $\beta + \varphi = 295^\circ$  and Pauli theorem.

### Evaluation of scaled models

The processing of the previous ISAR simulations has demanded a high amount of RAM memory because image resolutions are extremely high. For C and X band, this memory requirement will be more restrictive because the sampling step in both image dimensions is directly proportional to the operating wavelength and inversely proportional to the target length. This means that for large vessels and short wavelengths the evaluation of the scattering maps in the available PC will become more difficult.

In the current work, problems with the available RAM memory may appear for the ICE and FER models. Two main solutions can be adopted<sup>4</sup>, namely: 1) to drop image resolutions or 2) to scale the models a specific factor. The first option is not quite feasible because the minimum values demanded for properly running the simulations in the available PC are so high than drop the quality of the images. The second one appears to be more efficient as the results at L and S band point out an apparent stability in the polarimetric scattering behavior of vessels in relation to the operating frequency (see Fig. 6.9). This implies that the reflectivity properties of vessels are not excessively sensitive to the electrical length of targets (defined as the ratio between the unit of distance and the operating wavelength) and, thus, the scattering maps of vessels may not be appreciably modified against model down scaling. In order to confirm if model scaling is feasible for future simulations, this section evaluates the polarimetric response of the ICE and FER models scaled a factor of 2. The idea is to repeat the previous simulations and to observe how the polarimetric information is modified and if it is still related with the original signature. This point is quite important because down scaled geometries can induce new scattering mechanisms different to the actual ones that can lead to a misinterpretation of the results.

<sup>3</sup>The same codification than before has been adopted.

<sup>4</sup>The option to modify the PC and to improve its performance has been considered. But the new configuration was not ready at the time this thesis was finished.

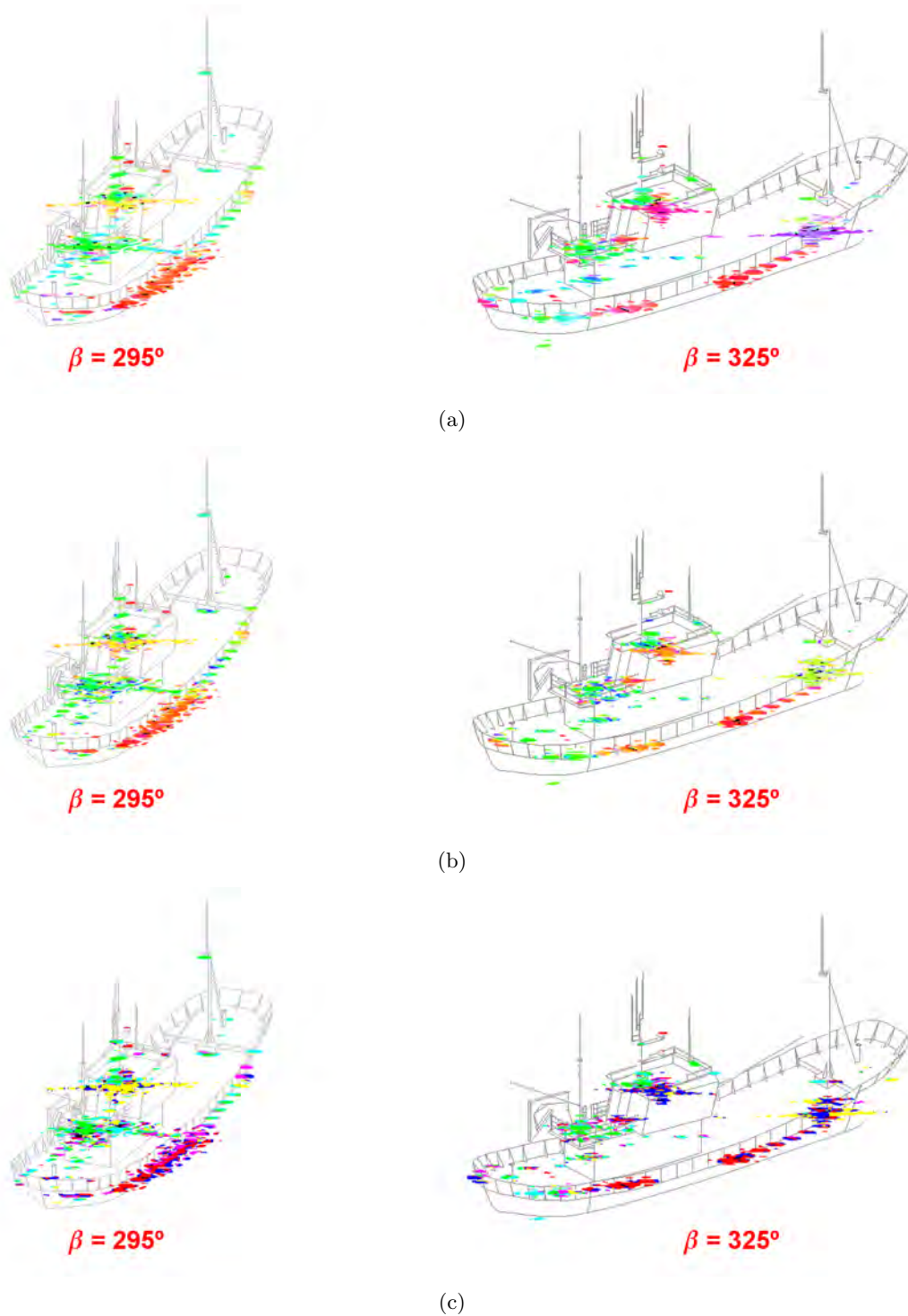


Figure 6.6: PolISAR images obtained for the SPA model at S band and  $\phi = 20^\circ$ . The bearing angles are  $\beta + \varphi = 295, 325^\circ$ . The images have been analyzed with the Pauli (a), SDH (b) and Cameron (c) CTD for a dynamic range of 25 dB.

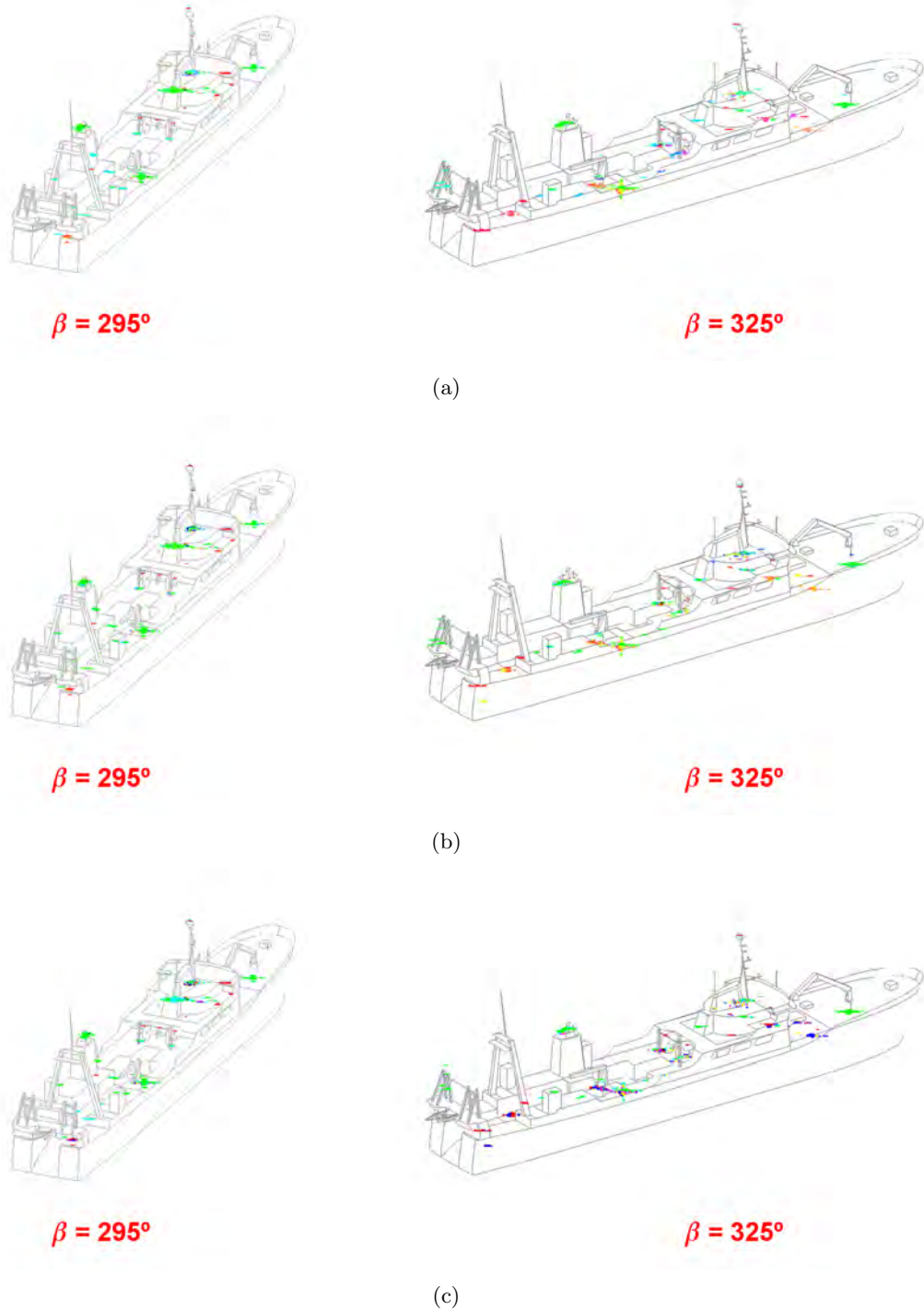


Figure 6.7: PolSAR images obtained for the ICE model at S band and  $\phi = 20^\circ$ . The bearing angles are  $\beta + \phi = 295, 325^\circ$ . The images have been analyzed with the Pauli (a), SDH (b) and Cameron (c) CTD for a dynamic range of 25 dB.

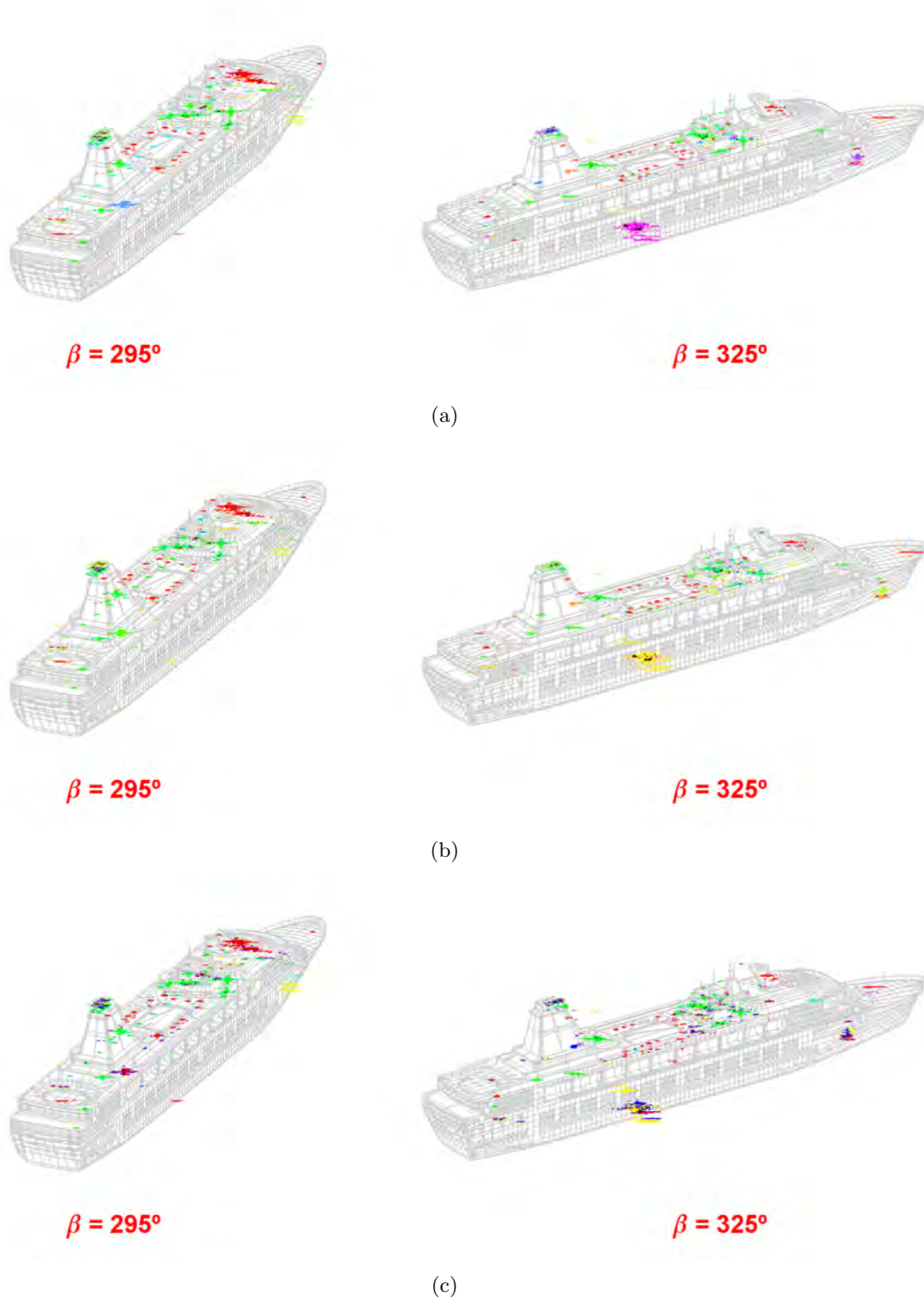


Figure 6.8: PolISAR images obtained for the FER model at S band and  $\phi = 20^\circ$ . The bearing angles are  $\beta + \varphi = 295, 325^\circ$ . The images have been analyzed with the Pauli (a), SDH (b) and Cameron (c) CTD for a dynamic range of 25 dB.

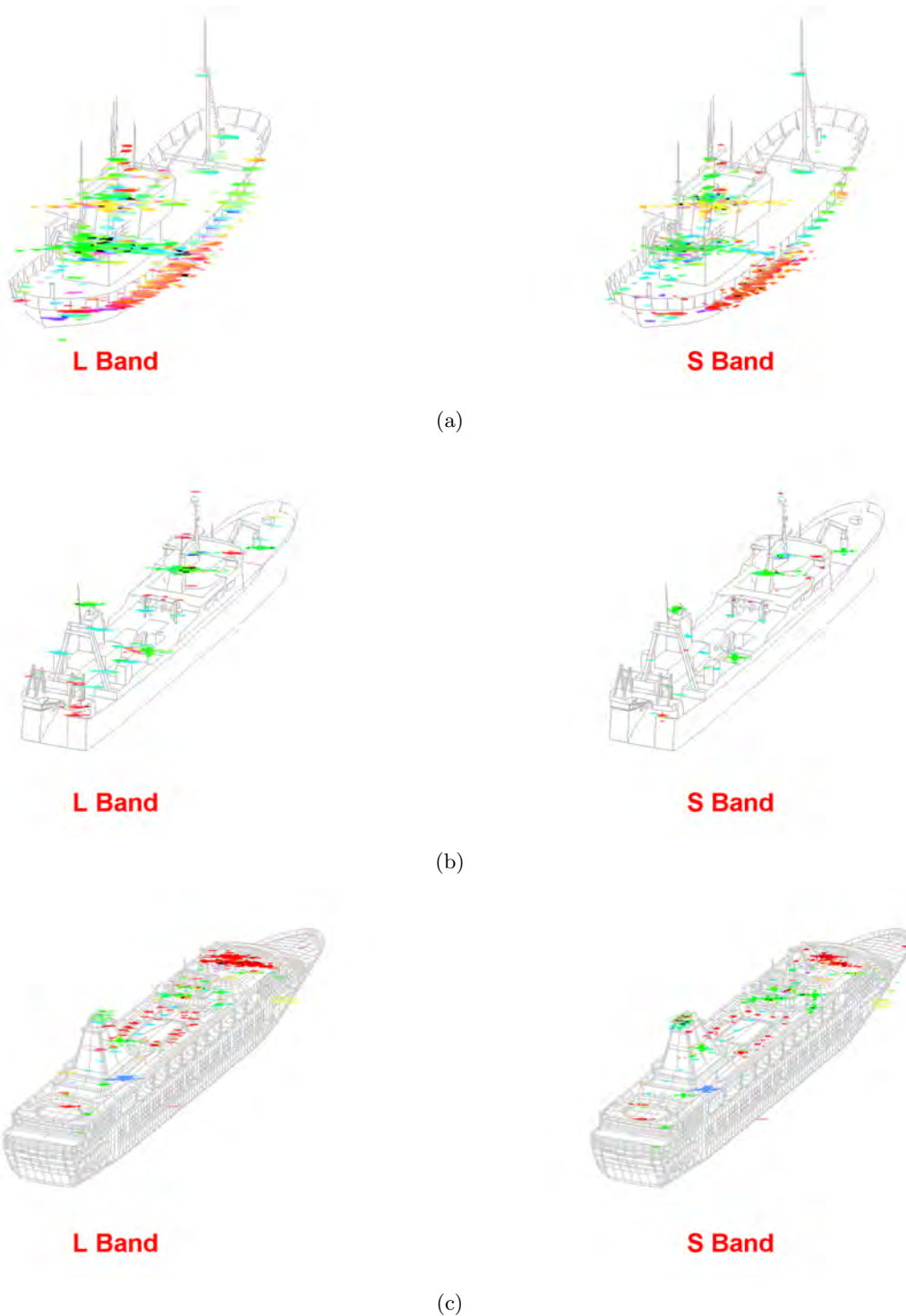


Figure 6.9: Comparative between the PolSAR images obtained at L and S band for the SPA (a), ICE (b) and FER (c) model ( $\phi = 20^\circ$ ). The bearing angle is  $\beta + \varphi = 295^\circ$ . The images correspond to the Pauli theorem for a dynamic range of 25 dB. Note the different cross-range resolution in both datasets due to the different operating wavelengths.



The new set of images providing the same information than the one included in Fig. D.13 - D.18 of Appendix D (Section D.2) is attached in Fig. D.19 - D.24 (Section D.2)<sup>5</sup>. Two samples for  $\beta + \varphi = 295, 325^\circ$  and the Pauli theorem are included in Fig. 6.10 with the corresponding images of the original model. As observed, similar results are obtained. In all the cases, the main scattering centers match with those retrieved for the original models and, hence, the reference scattering maps depicted in Fig. 6.5 apply. One reason that can explain this low dependence of the scattering behavior with respect to the ratio between the unit of distance and the wavelength is the large electrical dimensions of the main scatterers. Certainly, in all the cases the corner geometries and the masts-surface interaction can take dimensions similar to a meter, which is a value large enough for the wavelengths managed in this work. Note the different cross-range resolutions retrieved when down scaling the models (see Fig. 6.10). As commented in Chapter 3, this is due to the different electrical target length used in these simulations with respect to the simulations performed with the original models. In practical terms, this implies to modify the operating wavelength that, as observed in the previous bands, has a direct influence on the cross-range resolution value (see Fig. 6.9).

In summary, model scaling appears to be a feasible option to solve memory problems when processing very large models. However, the derived results should be treated as tentative and they should be confirmed once available with simulations performed with models preserving the dimensions of the original target. In this sense, target modeling done with the maximum degree of detail helps to increase the reliability of the results.

### 6.1.3 C band

This section analyzes the scattering behavior of vessels at C band for  $\beta + \varphi = [295..10..325]^\circ$ . The obtained results are gathered in Fig. D.25 - D.33 of Appendix D (Section D.3). Two samples for  $\beta + \varphi = 295, 325^\circ$  are presented in Fig. 6.11. In this dataset, the FER model has been scaled a factor of 2 due to restrictions in the available RAM memory. This means that the images of Fig. 6.11(c) (see also Fig. D.31 - D.33 in Appendix D) provide almost the same polarimetric information than the one retrieved in those simulations generated at S band for the original FER model (Fig. 6.8(a) and Fig. D.16 - D.18 of Appendix D)<sup>6</sup>. Certainly, in both cases the electrical length of the target is the same (see Fig. 6.12(a)).

The obtained data show that the conclusions derived at L/S band also applies at C band. However, note that the FER data have been obtained for the scaled model of the original target (factor of 2) and, hence, the related images have to be carefully interpreted. In order

<sup>5</sup>They are related to the Pauli, SDH and Cameron CTD.

<sup>6</sup>Theoretically, the polarimetric response should be identical. But due to the current images are related to a simulation environment where the EM fields are estimates of the actual ones, some differences are observed.

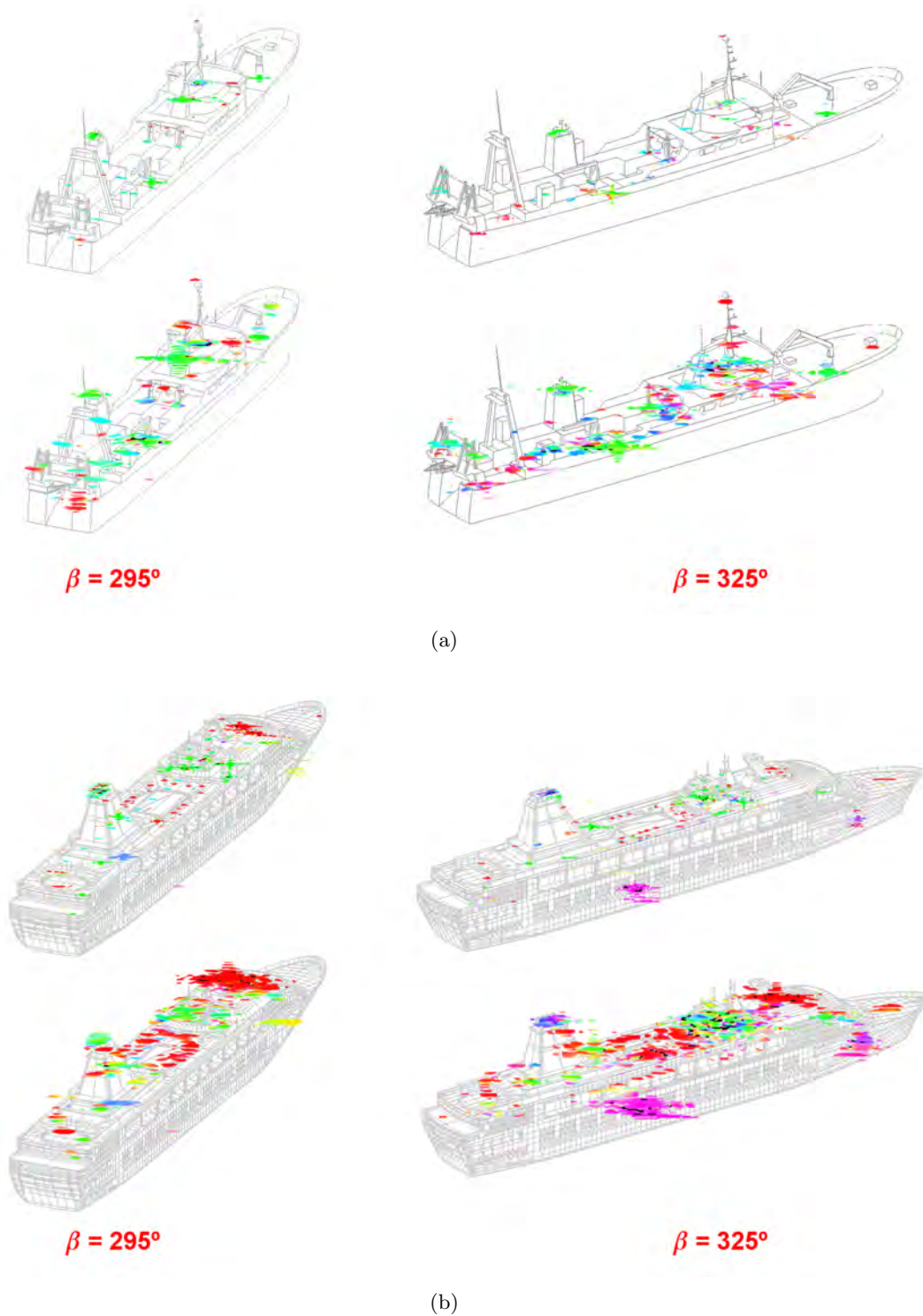


Figure 6.10: Comparative between the PolSAR images obtained at S band for the original (up) and scaled (down) versions of the ICE (a) and FER (b) vessel models ( $\phi = 20^\circ$ ). The bearing angles are  $\beta + \phi = 295, 325^\circ$ . The images correspond to the Pauli theorem for a dynamic range of 25 dB. Note the different cross-range resolution in both datasets due to the different maximum target extent.

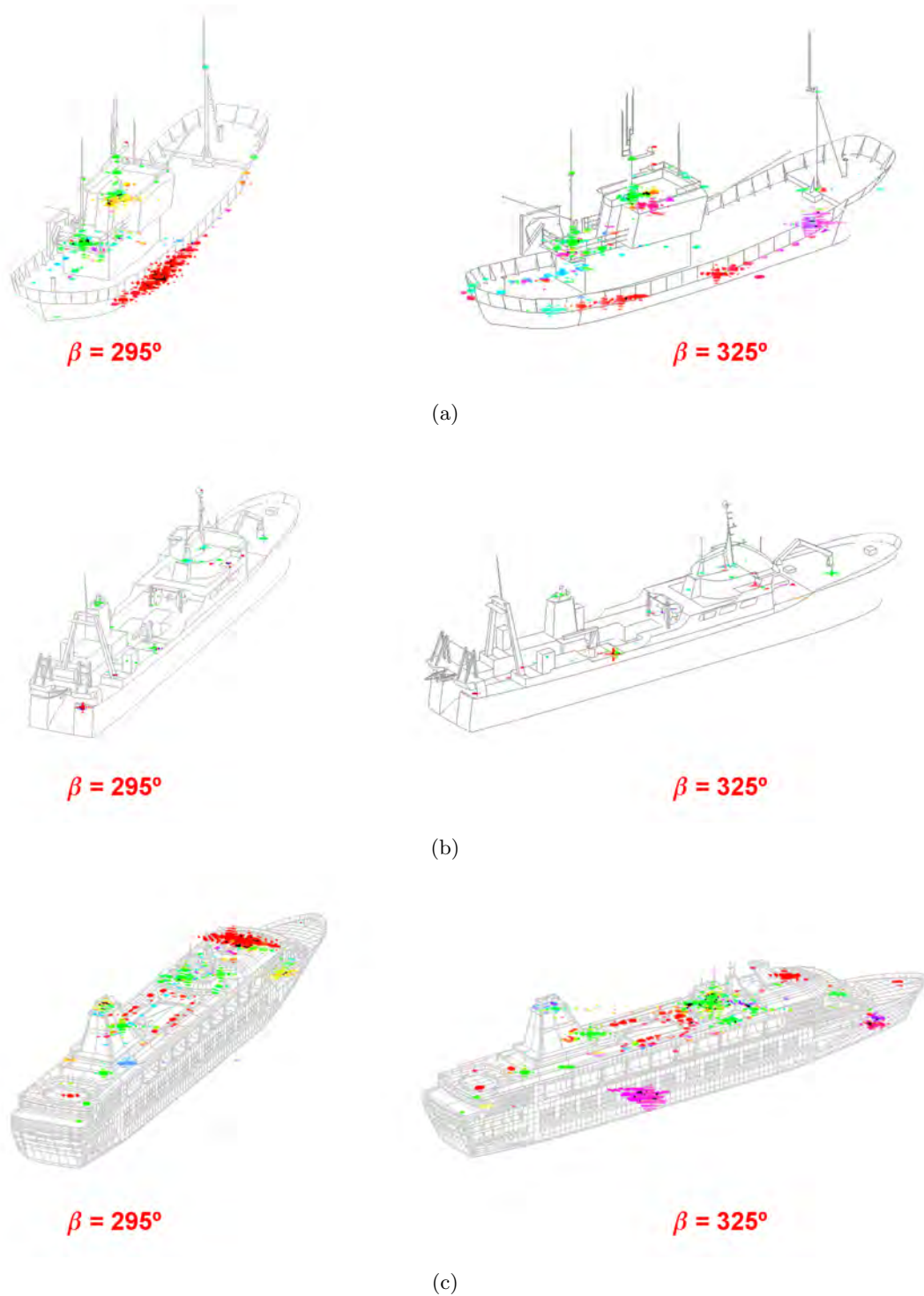


Figure 6.11: PolISAR images obtained for the SPA (a), ICE (b) and FER (c) model at C band and  $\phi = 20^\circ$ . The bearing angles are  $\beta + \varphi = 295, 325^\circ$  and the images correspond to the Pauli theorem for a dynamic range of 25 dB.

to give more reliability to such images, the scaled version of the ICE model (factor of 2) has been also processed at C band. The results are summarized in Fig. 6.12(b)<sup>7</sup> for the Pauli theorem. They show that model scaling does not affect in excess the polarimetric information and, hence, it seems feasible to think that the images obtained for the scaled version of the FER model may be valid for the model preserving the original target dimensions.

#### 6.1.4 X band

This section analyzes the scattering properties of vessels at X band. The same simulations than before have been run for the new frequency range and the obtained images are gathered in Appendix D (Section D.3, Fig. D.37 - D.39)<sup>8</sup>. Two samples are presented for the bearing angles  $\beta + \varphi = 295, 325^\circ$  and Pauli theorem in Fig. 6.13. There, the simulations related to the ICE and FER vessels correspond to the models scaled a factor of 2 because insufficient RAM memory in the available PC has made impossible to deal with the original models.

Regarding the results related to the SPA vessel, they confirm the stability of the polarimetric scattering response in relation to the operating wavelength. In all the scenarios, the retrieved scattering maps are quite similar presenting two main characteristics, namely: 1) they can be described by the simple Pauli mechanisms and 2) they are dominated by a particular set of main scattering centers which geometrical distribution and polarimetric configuration is specific of its structure. As a result, the overall size of vessels (understood as the 3D distribution of the main scattering centers) seems to be independent of the electrical length and, hence, it could be retrieved with SAR imagery. Although similar conclusions apply for the ICE and FER models, the related data should be carefully interpreted as they are partially supported in images derived for scaled models of the original targets. In this context, the different tests carried out at S and C band show that model scaling does not modify in excess the actual scattering giving reliability to the final results<sup>9</sup>.

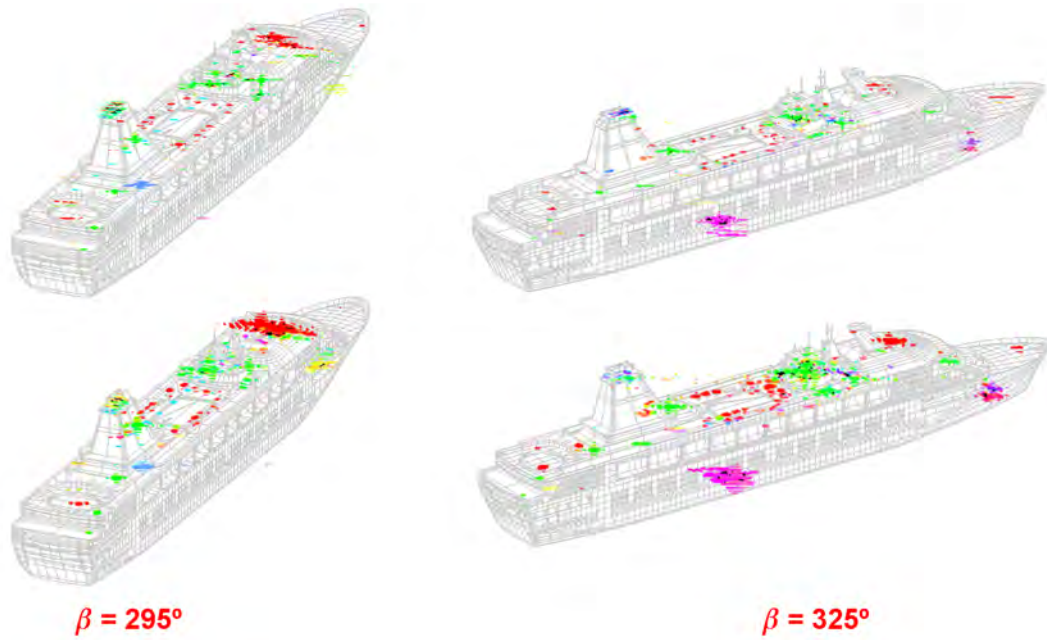
#### 6.1.5 Additional Tests

Once first conclusions about the scattering properties of vessels have been drawn, it is interesting to evaluate them as a function of certain parameters. In this section, the focus is placed on vessel bearing, the geometrical similarity of vessels, the incidence angle and the presence of the sea surface. The simulations have been generated at X band with the ICE and FER models scaled a factor of 2.

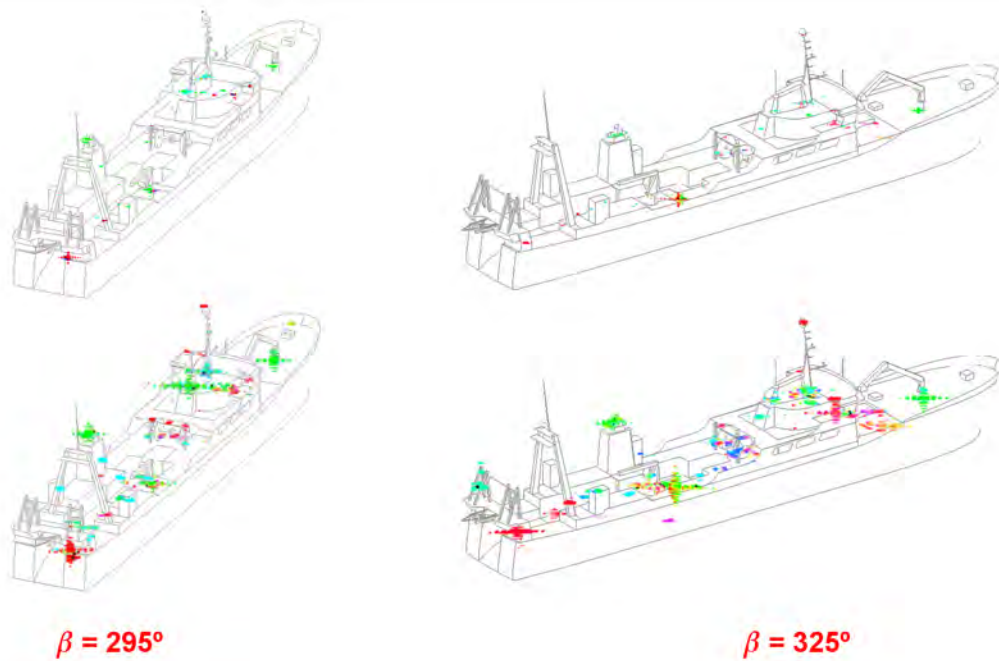
<sup>7</sup>The full images related to all the bearings and CTD are gathered in Fig. D.34 - D.36 of Appendix D.

<sup>8</sup>In this case, only the results for the Pauli theorem are attached as the interpretation provided by the SDH and Cameron CTD is almost identical.

<sup>9</sup>In fact, the scattering stability along frequency applies for the electrical length of target that implies in simulation environments stability along scale ratios.



(a)



(b)

Figure 6.12: Comparative between the PolSAR images obtained at S band for the original FER model (up) and at C band for the scaled FER model (factor of 2) (down) (a), and comparative between the PolSAR images obtained at C band for the original (up) and scaled (down) versions of the ICE model (b). In both cases, the bearing angles are  $\beta + \varphi = 295, 325^\circ$  and the images are processed with the Pauli theorem for a dynamic range of 25 dB.

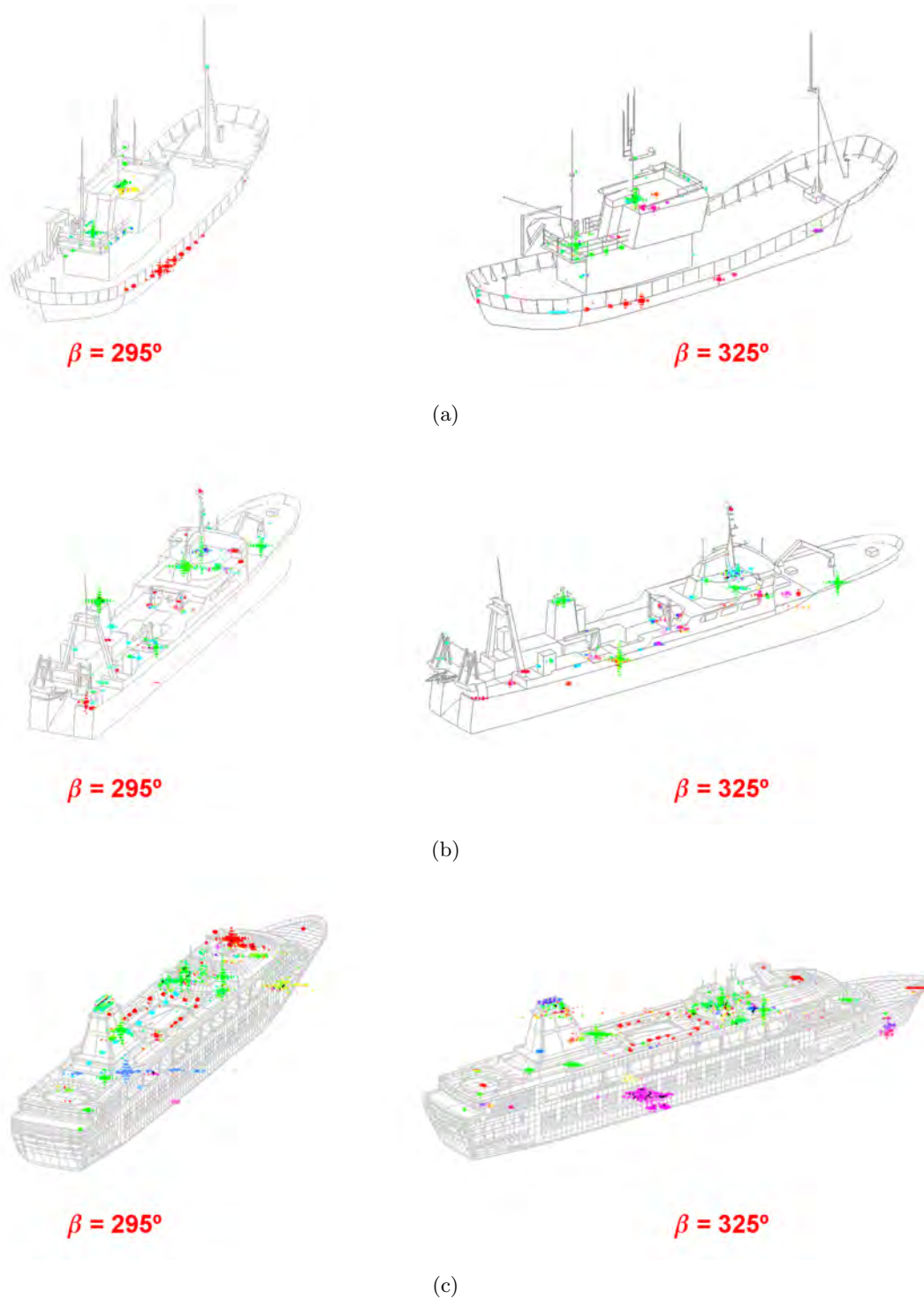


Figure 6.13: PolSAR images obtained for the SPA (a), ICE (b) and FER (c) model at X band and  $\phi = 20^\circ$ . The bearing angles are  $\beta + \varphi = 295, 325^\circ$  and the images correspond to the Pauli theorem for a dynamic range of 25 dB.

### Vessel bearing

This section evaluates the response of the SPA, ICE and FER vessels for the bearing angles  $\beta + \varphi = \{235, 145, 55\}$ . The scattering maps derived for the Pauli theorem are presented in Fig. 6.14. As observed, the marked symmetry in the structure of vessels [25] [26] makes the scattering response to be quite stable as a function of vessel bearing as each vessel is characterized by almost the same scattering centers than before. This means that a possible classification algorithm running in real scenarios may only need a reduced number of reference scattering maps for achieving a proper identification in almost all the views.

### Geometrical similarity

This section analyzes the differences that can be observed in the scattering response of two vessels with a similar macro-scale structure. For such purpose, the SPAv2 model has been processed for  $\beta + \varphi = 295 + i \cdot 10$  with  $i \in [0..6]$ . The obtained data have been analyzed with the Pauli theorem and the resulting colored images are gathered in Fig. D.40 of Appendix D (two samples are summarized in Fig. 6.15). These images show that both SPA and SPAv2 models have almost the same polarimetric response. This means that fine details does not contribute appreciably to the overall response and, hence, polarimetry permits only the discrimination of vessels with a marked macro-scale difference. Note that this result does not imply that fine details can be avoided when modeling a vessel. Actually, the recommendation is just the contrary, the higher the accuracy in the vessel models, the more reliable the results.

### Incidence angle

Some tests have been performed for the following incidence angles, namely: 1)  $\phi = 45^\circ$  as it is the upper bound for some operating modes of RADARSAT [35] and ENVISAT [55], and 2)  $\phi = 60^\circ$  because it allows to evaluate the behavior at grazing incidences. Fig. 6.16 ( $\phi = 45^\circ$ ) and Fig. 6.17 ( $\phi = 60^\circ$ ) present the Pauli RGB images obtained for the three vessels with  $\beta + \varphi = 295, 315, 335^\circ$ . As observed, the polarimetric trace of the SPA model in both situations is quite similar to the one retrieved with  $\phi = 20^\circ$  whereas for the ICE and FER models important differences can be noted. On the one hand, the scattering behavior of the ICE model is dominated in almost all the cases and specially for  $\phi = 60^\circ$  by an unique trihedral mechanism with extremely high RCS (despite in some particular cases, a similar response to the one related to  $\phi = 20^\circ$  is retrieved). This avoids to achieve a proper identification as there is not a distribution of scattering centers that schematizes the vessel geometry. On the other hand, the FER model presents a scattering behavior with a sensitivity with respect to vessel bearing higher than with  $\phi = 20^\circ$ . With these results, it appears that medium and low incidences are not suitable for vessel identification.

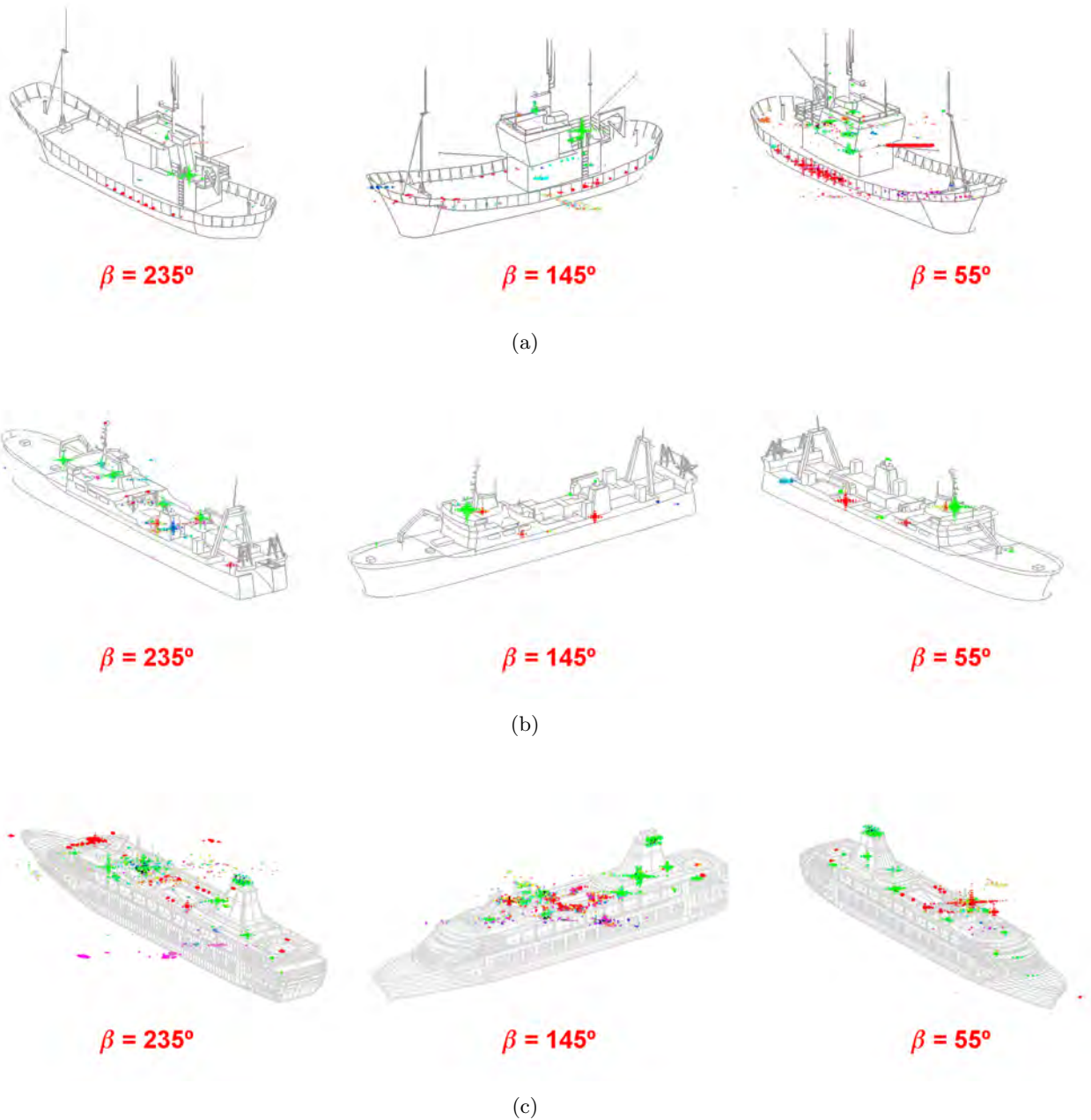


Figure 6.14: PolSAR images obtained for the SPA (a), ICE (b) and FER (c) model at X band and  $\phi = 20^\circ$ . The bearing angles are  $\beta + \varphi = 235, 145, 55^\circ$  and the images correspond to the Pauli theorem for a dynamic range of 25 dB.



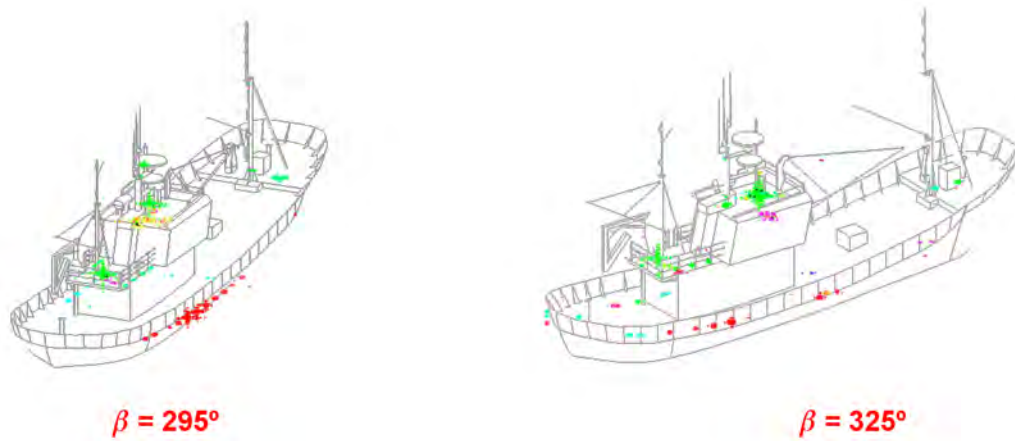


Figure 6.15: Polarimetric ISAR dataset obtained for the SPAv2 model at X band and  $\phi = 20^\circ$ . The bearing angles are  $\beta = 295, 325^\circ$  and the images correspond to the Pauli theorem for a dynamic range of 25 dB.

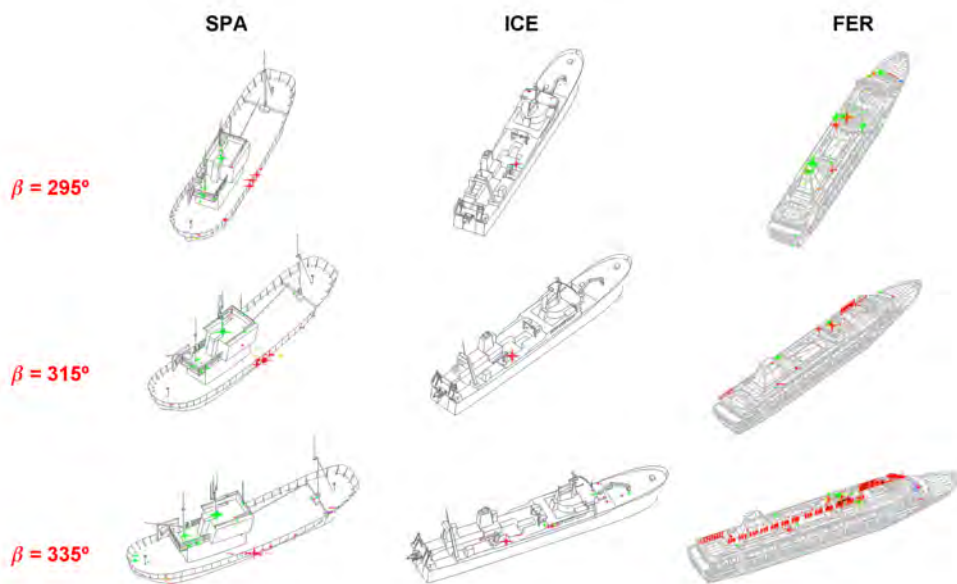


Figure 6.16: Polarimetric ISAR dataset obtained for the SPA, ICE and FER models at X band and  $\phi = 45^\circ$ . The bearing angles are  $\beta = 295, 315, 335^\circ$  and the images correspond to the Pauli theorem for a dynamic range of 25 dB.

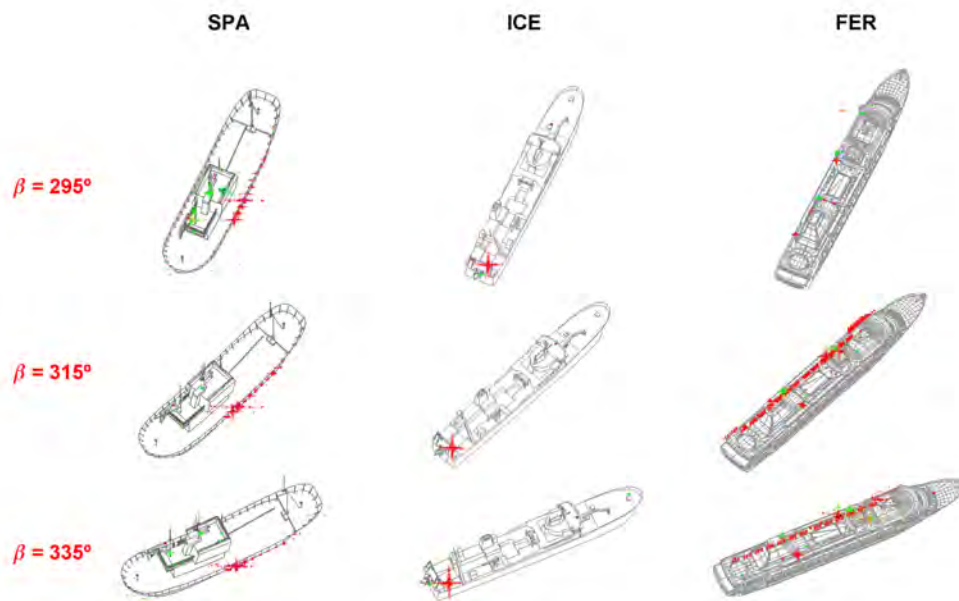


Figure 6.17: Polarimetric ISAR dataset obtained for the SPA, ICE and FER models at X band and  $\phi = 60^\circ$ . The bearing angles are  $\beta = 295, 315, 335^\circ$  and the images correspond to the Pauli theorem for a dynamic range of 25 dB.

### Sea surface

Another important item to consider when analyzing the scattering properties of vessels is the influence of the sea as it can induce new mechanisms that can modify the polarimetric traces inherent to the structure of vessels. In order to make a preliminary study about the impact of sea surface in the polarimetric behavior of vessels, four simulations have been run for the SPA model with a constant bearing of  $\beta = 295^\circ$ . Two have been performed for  $\phi = 20^\circ$  whereas the other two for  $\phi = 60^\circ$ . In both situations, one simulation deals with the simple sea surface model of *GRECOSAR* whereas in the other one not. The results are presented in Fig. 6.18 in terms of Pauli RGB images. As observed, the presence of the sea is not noticeable at high incidence as almost the same polarimetric trace is retrieved in both situations. This does not happen at low incidence because new mechanisms can be observed at the hull near the bow (see Fig. 6.19). However, their weight is not so important and they do not strongly affect the key mechanisms useful for identification.

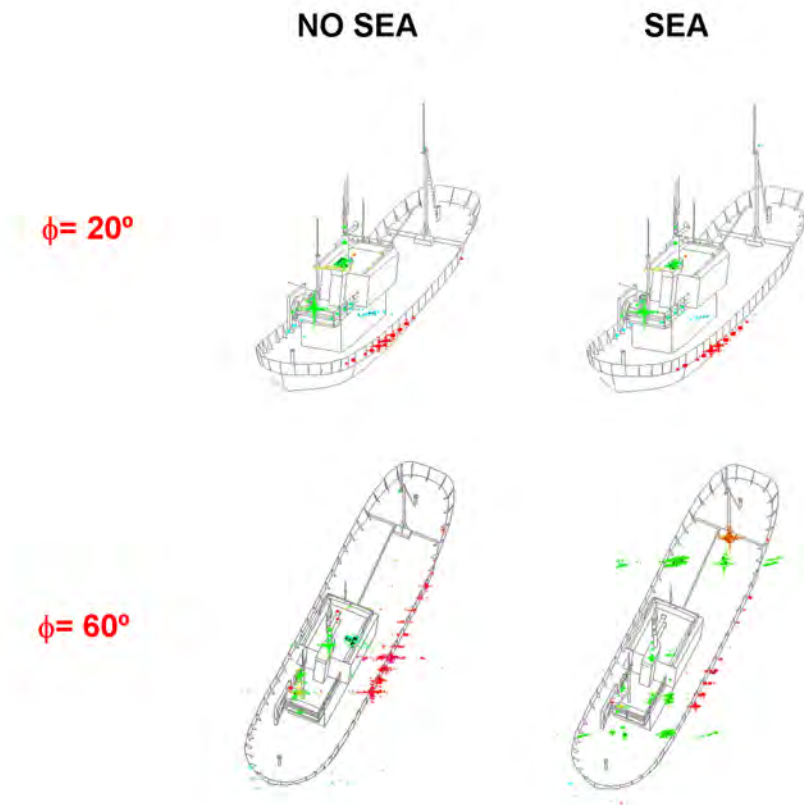


Figure 6.18: Pauli polarimetric analysis of simulated PolISAR images obtained for the SPA model at X band and, high and low incidence ( $\beta = 295^\circ$ ). Two different situations have been taken into account, with and without a sea surface model. Details of color codification can be found in the text.

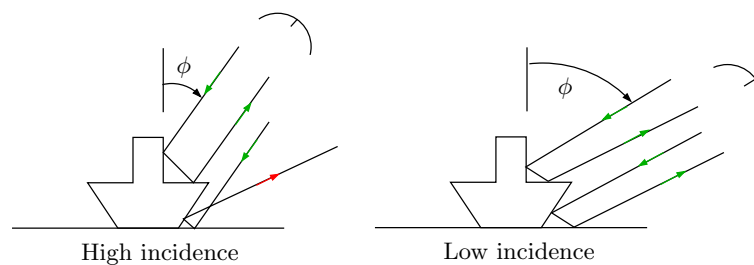


Figure 6.19: Dihedral-like mechanisms induced by the sea at the lateral side of the hull for grazing incidences.

## 6.2 Analysis of POLSAR data

This section analyzes the data obtained with the SAR imagery mode. The main goal is to observe how the simple mechanisms that describe the polarimetric response of vessels are combined in SAR images and which connection can be established with the observed geometries [162]. For such purpose, similar observation conditions than the ones adopted in the previous ISAR simulations has been selected (see Fig. 6.20). In this case, two sensors have been used, namely: 1) a C band sensor with an azimuth x range resolution of 4 x 10 m (see Table 6.5), and 2) a X band sensor with an azimuth x range resolution of 2.5 x 1.5 m (see in Table 6.6). In order to support data interpretation, all the images have a snapshot of the point of view of the satellite with the azimuth x range location of two guide scatterers. They have been selected from the scattering maps defined in Section 6.1.1 (see Fig. 6.5).

### 6.2.1 C band

First simulations have been performed at C band for the same bearing range than before  $\beta + \varphi = 295 + 10 \cdot i [^\circ]$  with  $i \in [0..6]$ . The data related to the three vessel models have been analyzed with the Pauli, SDH and Cameron CTD, and the results are gathered in Fig. E.1 - E.6 of Appendix E (Section E.1). Two sets of images can be distinguished, namely: 1) colored images providing the combined weight of the different basic mechanisms of all CTD, as in ISAR simulations (Fig. E.1 (SPA), E.3 (ICE), E.5 (FER)) and 2) gray images providing the weight of each Pauli mechanism (Fig. Fig. E.2 (SPA), E.4 (ICE), E.6 (FER)). In this section, two samples of such data are presented in Fig. 6.21 - 6.23 for  $\beta + \varphi = 295, 325^\circ$ .

According to the obtained images, the following conclusions apply, namely:

1. The scattering behavior of vessels can be described in some cases by the trihedral and dihedral simple scattering mechanisms. In contrast with the ISAR case, different polarimetric interpretation is retrieved for each CTD. This may be caused by the low image resolution that makes the main scattering mechanisms to be mixed in a complex way. Note that the isolated mechanisms are quite similar among them, for instance  $trihedral_{pauli} \rightarrow trihedral_{sdh} \rightarrow cylinder_{cameron}$  and  $dihedral_{pauli} \rightarrow dihedral_{sdh} \rightarrow narrow - diplane_{cameron}$ .
2. The polarimetric trace change a lot from one bearing to another and, hence, it is very difficult to identify the imaged ship. Certainly, it is not possible to isolate in all the images a particular distribution of scatterers that can be related with the reference scattering maps depicted in Section 6.1.1 (see Fig. 6.5) and, thus, with the geometry of the vessel. Even with the isolated Pauli polarimetric channels such information can not be retrieved (see Fig. 6.21(b) - 6.23(b)).

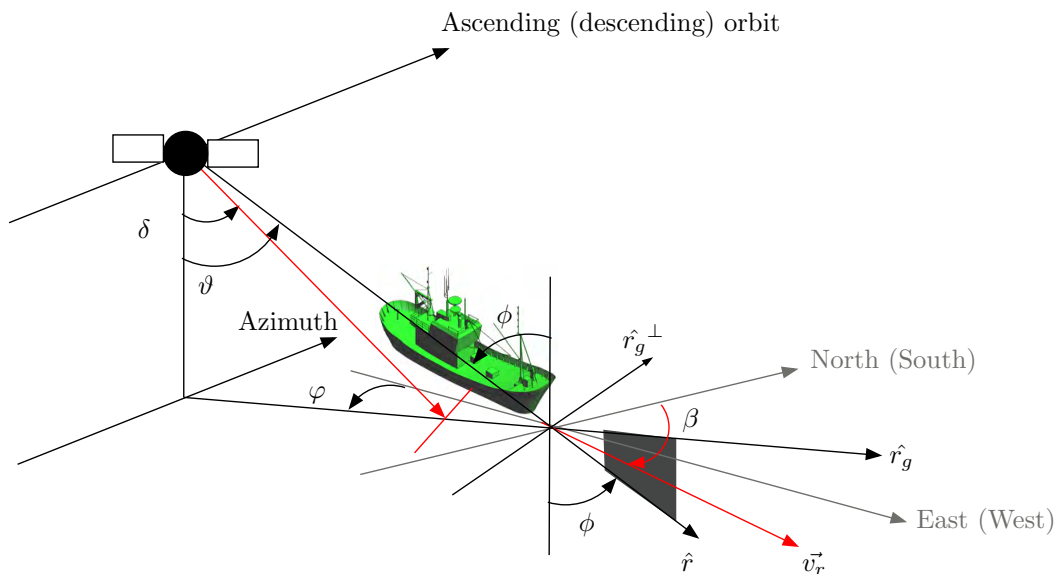


Figure 6.20: SAR imaging geometry.

Table 6.5: Main parameters of the Sensor\_C sensor.  $D_r$  and  $D_a$  expresses the pixel extend in both range and azimuth dimensions.

$h$ [Km]	785	$r_o$ [km]	856	$V_{plat}$ [m/s]	7545
$\phi$ [°]	23	$\varphi$ [°]	12.5	$\vartheta$ [°]	20.355
$f$ [GHz]	5.3	PRF [Hz]	1700	$L_a, L_r$ [m]	8.4, 1
BW [MHz]	15.5	FS [MHz]	18.96	$\tau$ [ $\mu$ s]	37.12
$\delta_r$ [m]	9.6	$\delta_a$ [m]	4.2	$D_r, D_a$ [m]	8, 4

Table 6.6: Main parameters of the Sensor\_X sensor.  $D_r$  and  $D_a$  expresses the pixel extend in both range and azimuth dimensions.

$h$ [Km]	514	$r_o$ [km]	544	$V_{plat}$ [m/s]	7686
$\phi$ [°]	20	$\varphi$ [°]	11.8	$\vartheta$ [°]	18.447
$f_o$ [GHz]	9.65	PRF [Hz]	3736	$L_a, L_r$ [m]	4.6, 0.9
$\delta f$ [MHz]	125	FS [MHz]	137.5	$\tau$ [ $\mu$ s]	28
$\delta_r$ [m]	1.2	$\delta_a$ [m]	2.3	$D_r, D_a$ [m]	1.2, 2

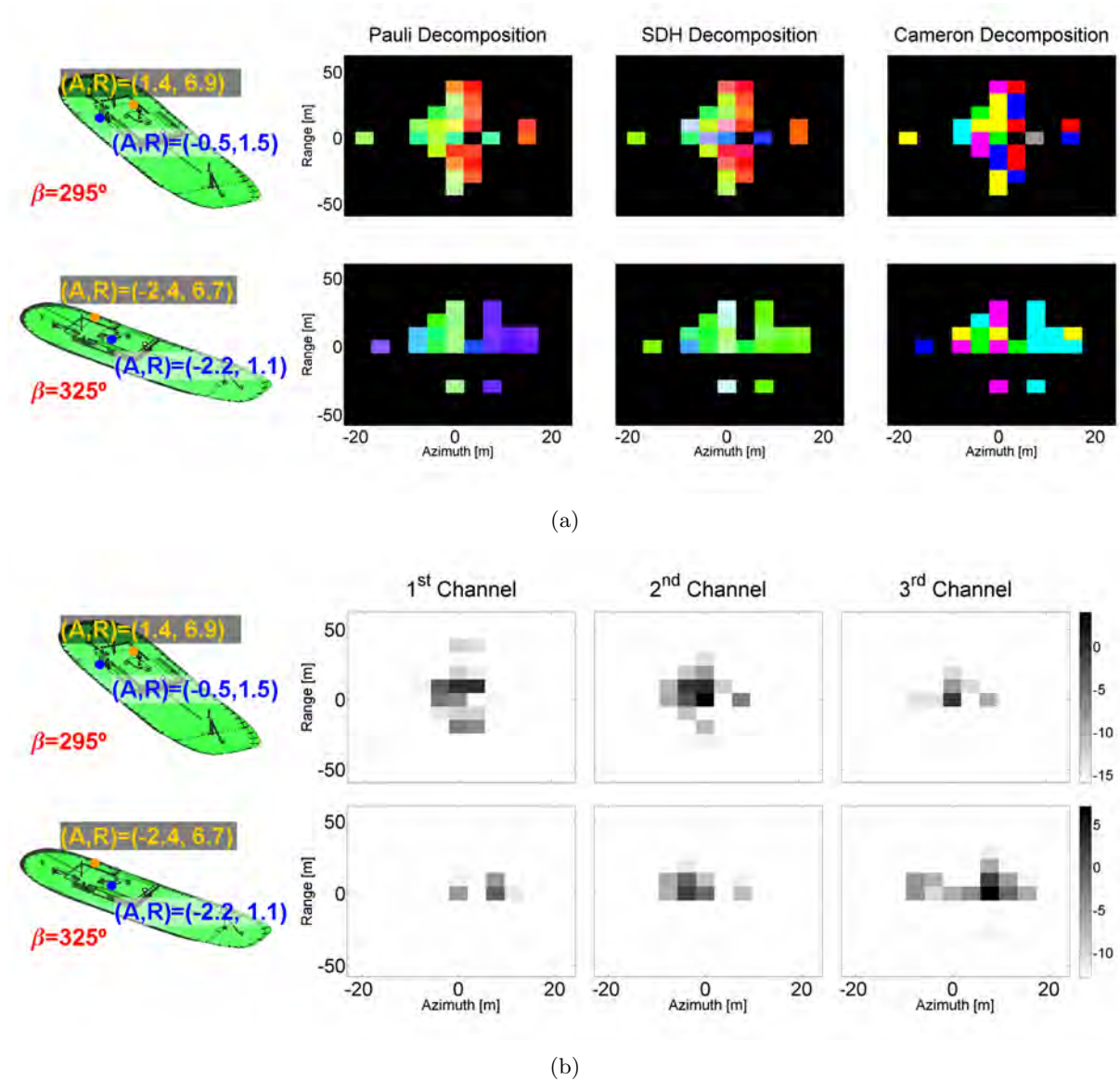


Figure 6.21: Polarmetric SAR dataset obtained for the SPA model at C band and  $\phi = 20^\circ$ . The bearing angles are  $\beta + \phi = 295, 325^\circ$ . The data have been analyzed with the Pauli, SDH and Cameron theorems for a dynamic range of 25 dB. Two sets of images are attached, namely: 1) the combined weight of all the simple mechanisms of each decomposition expressed via colored images (a) and 2) the weight of the Pauli mechanisms isolated in gray images (b). In both cases, a snapshot of the point of view of the satellite is included with the azimuth x range ( $A, R$ ) location of two reference points.

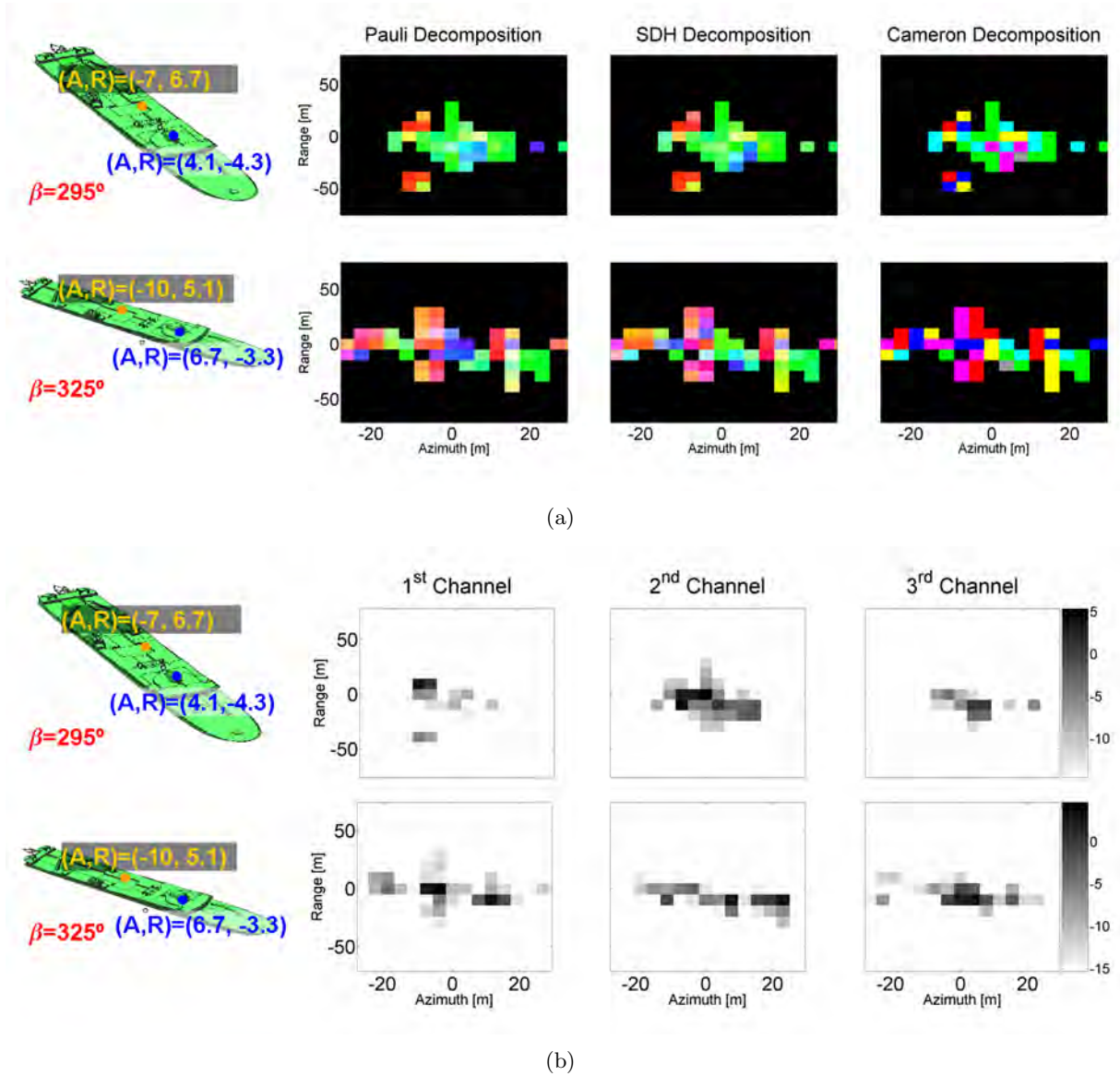


Figure 6.22: Polarimetric SAR dataset obtained for the ICE model at C band and  $\phi = 20^\circ$ . The bearing angles are  $\beta + \phi = 295, 325^\circ$ . The data have been analyzed with the Pauli, SDH and Cameron theorems for a dynamic range of 25 dB. Two sets of images are attached, namely: 1) the combined weight of all the simple mechanisms of each decomposition expressed via colored images (a) and 2) the weight of the Pauli mechanisms isolated in gray images (b). In both cases, a snapshot of the point of view of the satellite is included with the azimuth x range  $(A, R)$  location of two reference points.

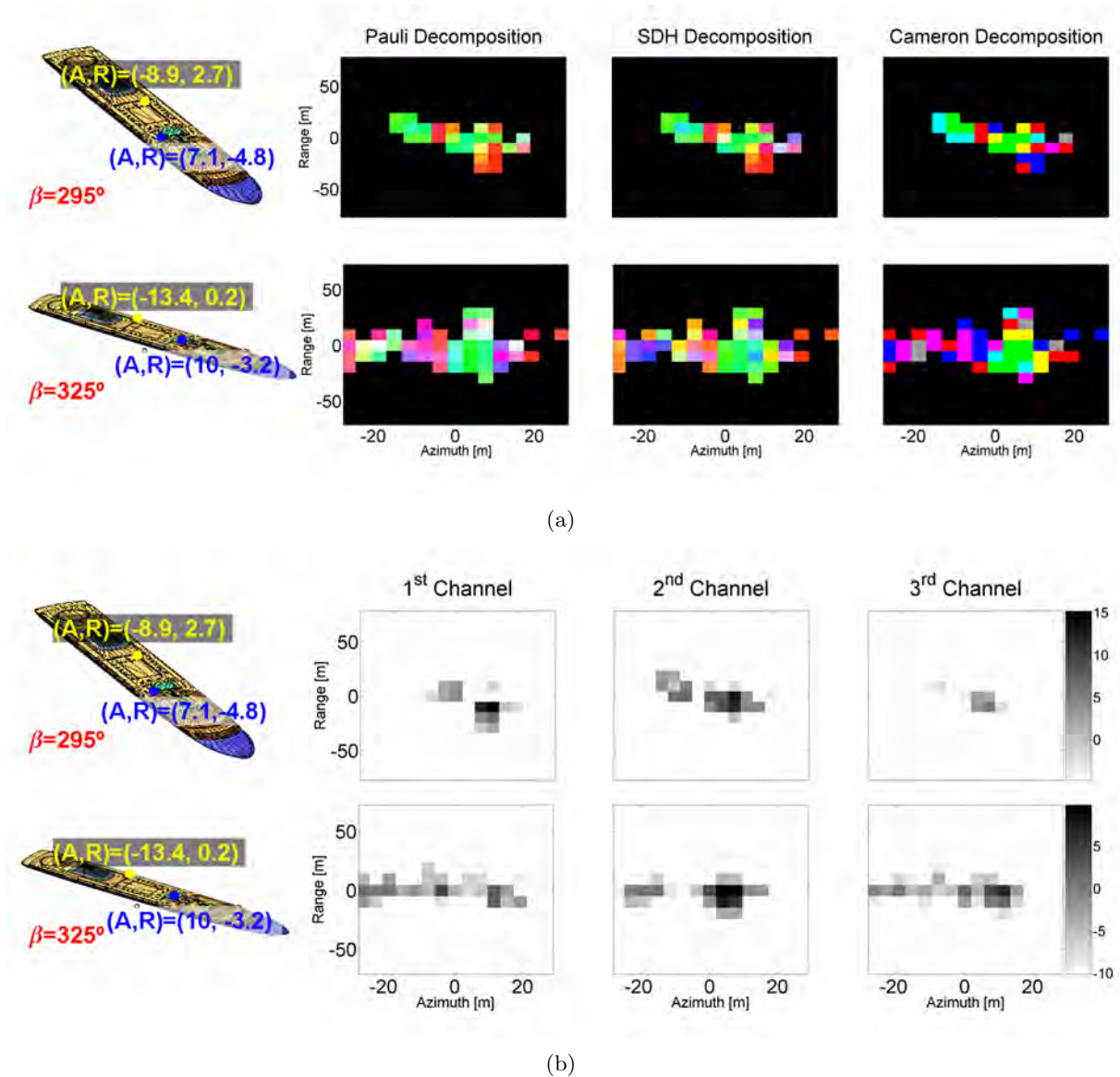


Figure 6.23: Polarimetric SAR dataset obtained for the FER model at C band and  $\phi = 20^\circ$ . The bearing angles are  $\beta + \phi = 295, 325^\circ$ . The data have been analyzed with the Pauli, SDH and Cameron theorems for a dynamic range of 25 dB. Two sets of images are attached, namely: 1) the combined weight of all the simple mechanisms of each decomposition expressed via colored images (a) and 2) the weight of the Pauli mechanisms isolated in gray images (b). In both cases, a snapshot of the point of view of the satellite is included with the azimuth x range  $(A, R)$  location of two reference points.



### 6.2.2 X band

This section analyzes the results obtained by processing the previous simulations with the X band sensor. The final images related to the Pauli, SDH and Cameron CTD are gathered in Fig. E.7 (SPA), E.9 (ICE), E.11 (FER) (colored images) and Fig. E.8 (SPA), E.10 (ICE), E.12 (FER) (Pauli gray images) of Appendix E. Two samples for  $\beta + \varphi = 295, 325^\circ$  are summarized in Fig. 6.24 - 6.26.

The analysis of these images show that:

1. The behavior of vessels can be described in almost all the situations by the trihedral and dihedral simple mechanisms. Now, all CTD provide almost the same polarimetric interpretation.
2. The analysis of the Pauli polarimetric channels (see Fig. 6.24(b) - 6.26(b)) allows, for each vessel, the isolation of a set of main scattering centers which spatial distribution and polarimetric behavior is preserved for almost all views. Such distribution is similar to the reference scattering maps derived from the analysis of ISAR data performed in Section 6.1.4.
3. Note the presence of anti-symmetric mechanisms despite none of them is adopted in the reference scattering maps. As observed in the analysis of the ISAR data, they are only important in some specific bearings.
4. In general, it appears that with the proper resolution it is possible to retrieve the scattering maps defined with ISAR imagery. These maps provide a reasonable characterization of the geometry of each vessel that may be useful for its identification. However, the obtained information is projected in two dimensions and this format does not seem to be the most suitable one for developing a reliable algorithm. In this sense, the possibility to retrieve the third dimension of the space via single-pass interferometry may be, if available, an important improvement. Chapter 7 exploits this approach and it shows that this additional channel allows the development of a new method that may be quite robust within real scenarios.

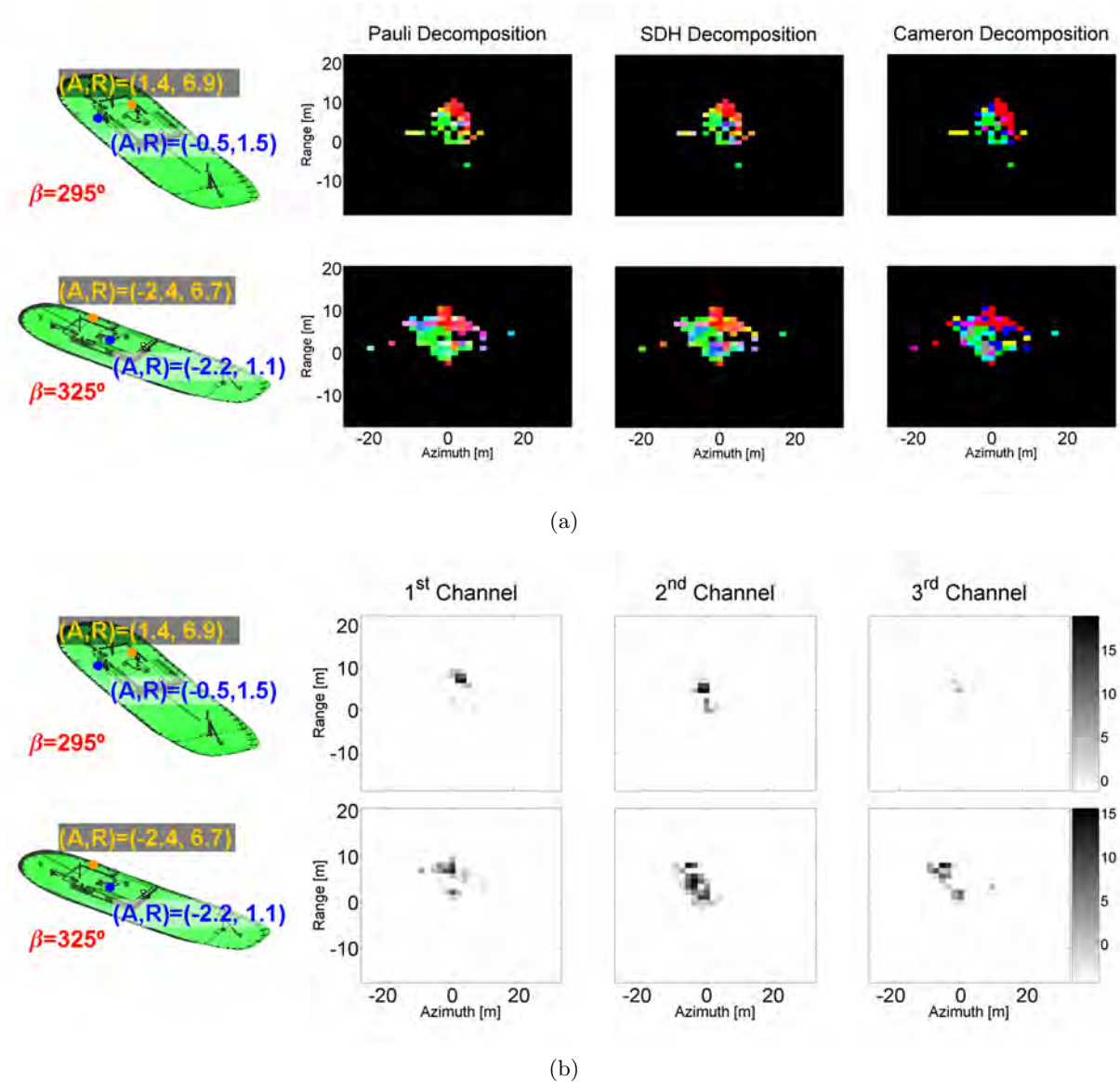


Figure 6.24: Polarmetric SAR dataset obtained for the SPA model at X band and  $\phi = 20^\circ$ . The bearing angles are  $\beta + \phi = 295, 325^\circ$ . The data have been analyzed with the Pauli, SDH and Cameron theorems for a dynamic range of 25 dB. Two sets of images are attached, namely: 1) the combined weight of all the simple mechanisms of each decomposition expressed via colored images (a) and 2) the weight of the Pauli mechanisms isolated in gray images (b). In both cases, a snapshot of the point of view of the satellite is included with the azimuth x range  $(A, R)$  location of two reference points.

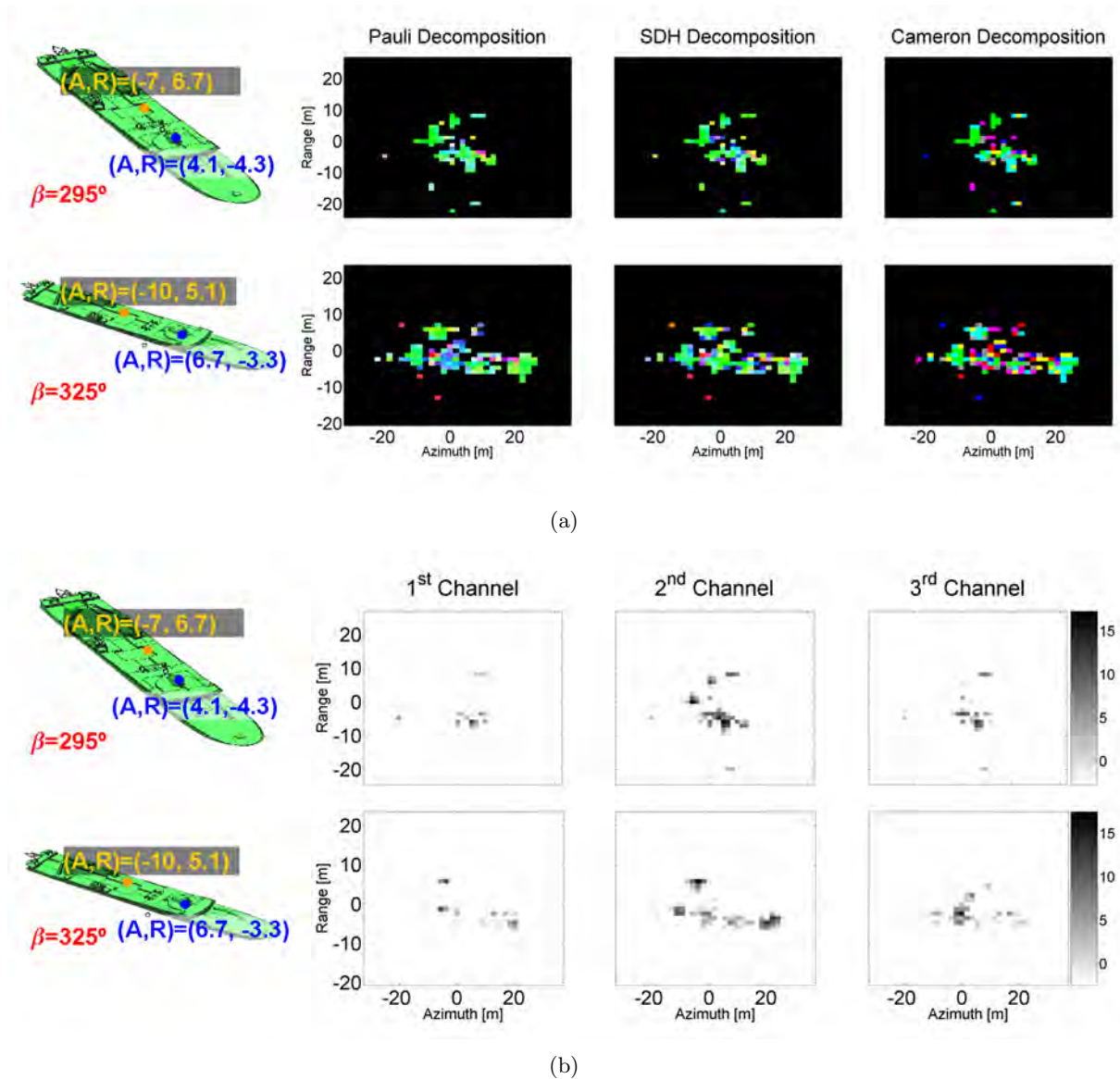


Figure 6.25: Polarimetric SAR dataset obtained for the ICE model at X band and  $\phi = 20^\circ$ . The bearing angles are  $\beta + \phi = 295, 325^\circ$ . The data have been analyzed with the Pauli, SDH and Cameron theorems for a dynamic range of 25 dB. Two sets of images are attached, namely: 1) the combined weight of all the simple mechanisms of each decomposition expressed via colored images (a) and 2) the weight of the Pauli mechanisms isolated in gray images (b). In both cases, a snapshot of the point of view of the satellite is included with the azimuth x range  $(A, R)$  location of two reference points.

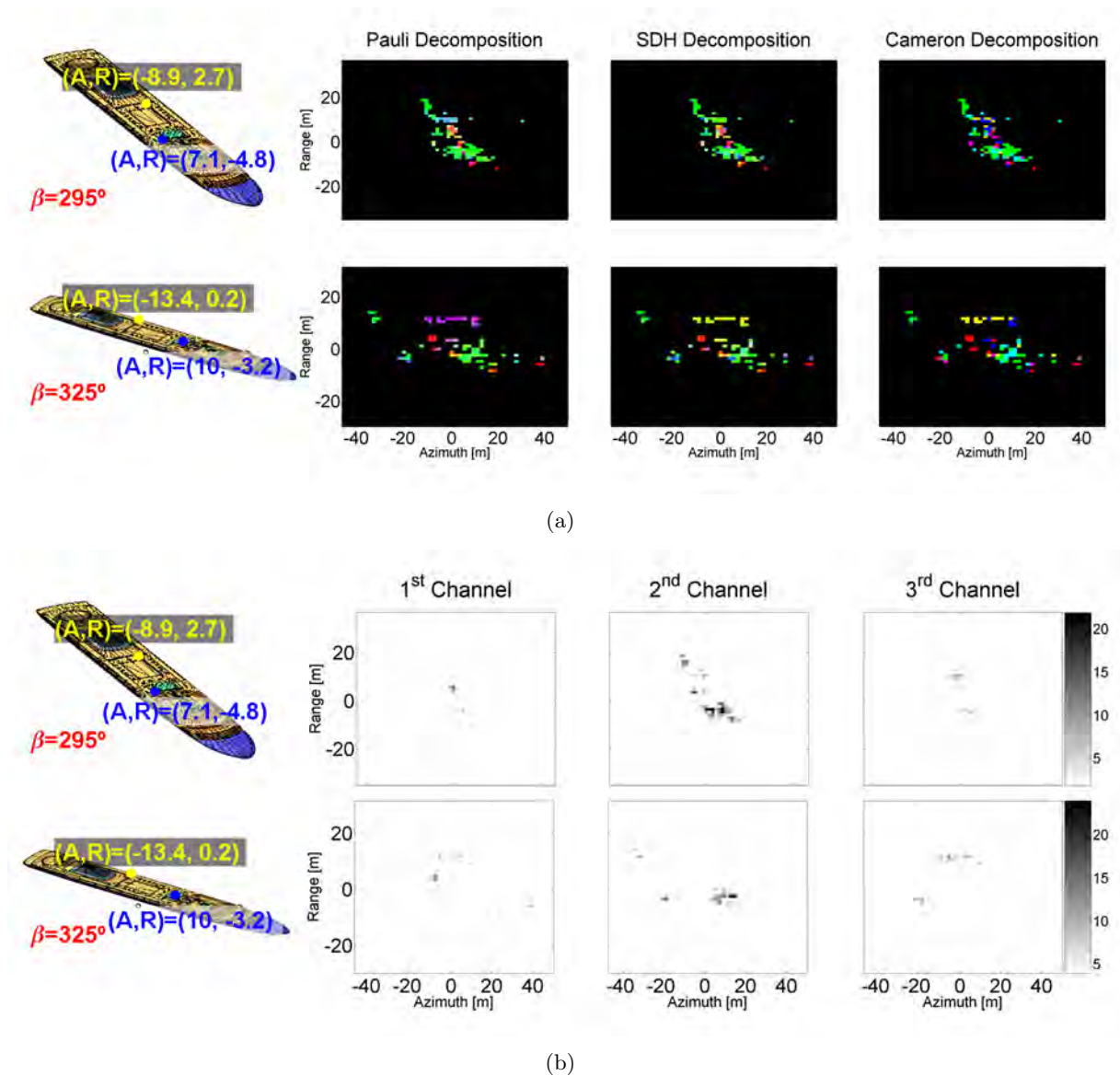


Figure 6.26: Polarimetric SAR dataset obtained for the FER model at X band and  $\phi = 20^\circ$ . The bearing angles are  $\beta + \phi = 295, 325^\circ$ . The data have been analyzed with the Pauli, SDH and Cameron theorems for a dynamic range of 25 dB. Two sets of images are attached, namely: 1) the combined weight of all the simple mechanisms of each decomposition expressed via colored images (a) and 2) the weight of the Pauli mechanisms isolated in gray images (b). In both cases, a snapshot of the point of view of the satellite is included with the azimuth x range  $(A, R)$  location of two reference points.

Table 6.7: Vessel motions adopted for the images presented in Fig. 6.27 - 6.29.

$\beta$	$\dot{\delta}_{roll}$ [rad/s]	$\dot{\delta}_{pitch}$ [rad/s]	$\beta$	$\dot{\delta}_{roll}$ [rad/s]	$\dot{\delta}_{pitch}$ [rad/s]
295	-1.56	-0.26	335	-0.98	-1.16
305	-1.43	-0.52	345	-0.76	-1.32
315	-1.32	-0.76	355	-0.52	-1.43
325	-1.16	-0.98	-	-	-

### 6.2.3 Influence of the Sea Surface

This section addresses the effect of vessel motions and sea surface. The main goal is to know if the distribution of scattering centers useful for vessel identification can be isolated in adverse environmental conditions [163]. For such purpose, two data sets of PolSAR images have been generated for  $\beta + \varphi = [295..10..355]^\circ$  and different environmental conditions, namely: 1) the set of vessel motions summarized in Table 6.7 and 2) the sea surface model of *GRECOSAR*. The results related to the Pauli, SDH and Cameron CTD are gathered in Appendix E (Fig. E.13 - E.18 for vessel motions and Fig. E.19 - E.24 for the sea surface). Two samples for  $\beta + \varphi = 295, 325^\circ$  are attached in Fig. 6.27 - 6.29 (vessel motions) and Fig. 6.30 - 6.32 (sea surface)<sup>10</sup>.

Regarding vessel motions, the polarimetric traces of vessels do not appear notably distorted and, thus, the reference scattering centers demanded for a proper identification can be differentiated from the other ones (in some cases, even better than in the free motion situation). The only main difference is the spatial distribution of such scatterers that is affected by the azimuth distortions due to vessel motions (see Fig. 6.27(b), 6.28(b), 6.29(b) and extensively Fig. E.14, E.16, E.18 in Appendix E). Note that for lower resolutions these shifts can induce more important modifications in the polarimetric information of vessels as the responses of some key scatterers can be complexly mixed within a particular resolution cell.

Regarding the sea surface, the simulated data confirm that outlined with ISAR simulations: the influence of the sea at high incidence appears to be not so important. Two reasons may explain this behavior, namely: 1) the absence of sea clutter that in some situations can affect the isolation of the main scattering centers and 2) the point of view of the satellite that at high incidence makes difficult to observe the dihedral-like mechanisms that can be performed at the lateral side of the hull. In real scenarios, it is expected that the presence of the sea clutter can take more significance in vessel classification. For such purpose, further research is required in this field in order to obtain more reliable conclusions.

<sup>10</sup>In all the cases, the different data sets are supported by the gray scale images providing the weight of the Pauli mechanisms.

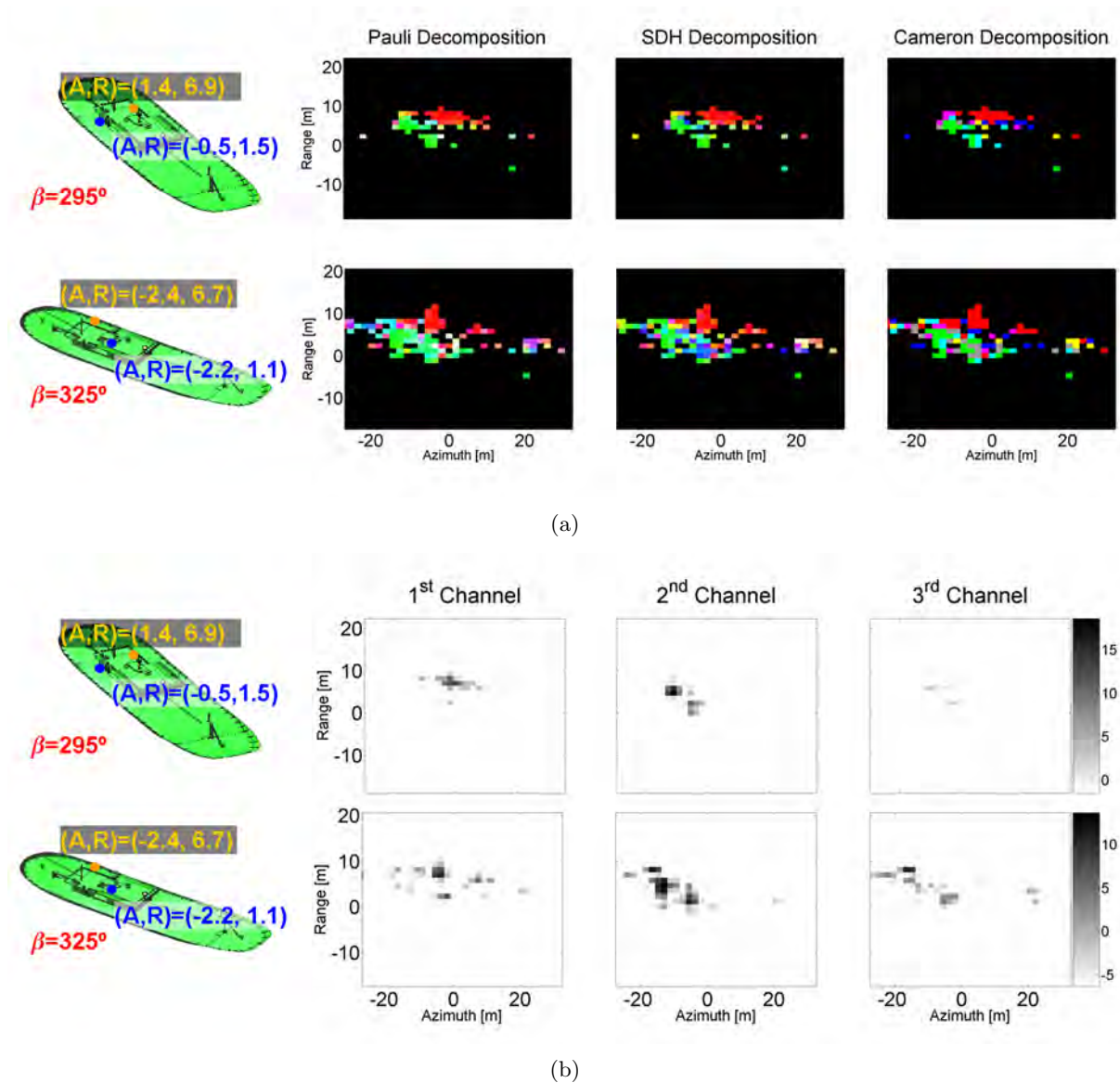


Figure 6.27: Polarimetric SAR dataset obtained for the SPA model at X band and  $\phi = 20^\circ$ . The bearing angles are  $\beta + \phi = 295, 325^\circ$  and the vessel experiments the rotational motions summarized in Table 6.7. The data have been analyzed with the Pauli, SDH and Cameron theorems for a dynamic range of 25 dB. Two sets of images are attached, namely: 1) the combined weight of all the simple mechanisms of each decomposition expressed via colored images (a) and 2) the weight of the Pauli mechanisms isolated in gray images (b). In both cases, a snapshot of the point of view of the satellite is included with the azimuth x range  $(A, R)$  location of two reference points.

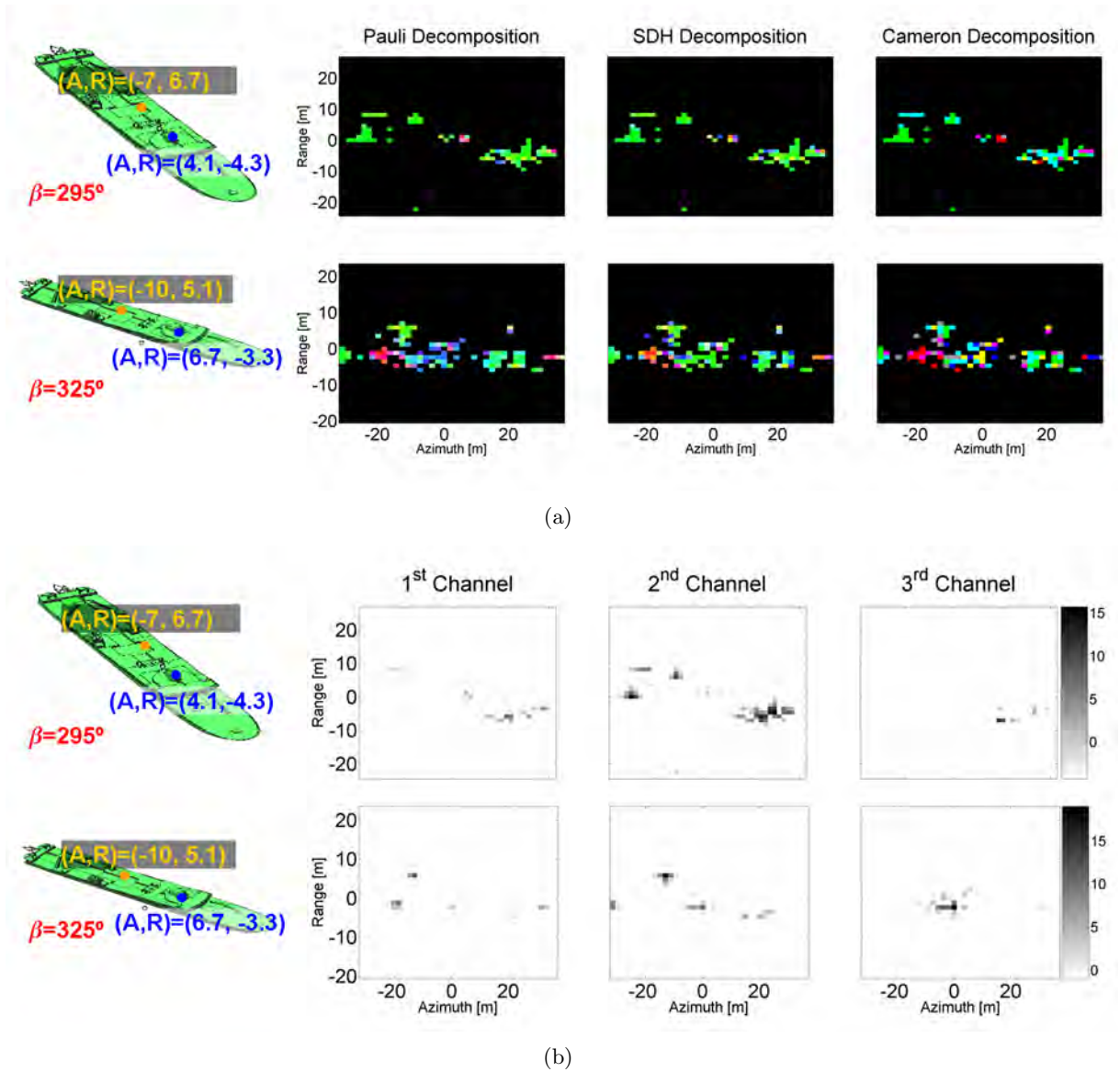


Figure 6.28: Polarimetric SAR dataset obtained for the ICE model at X band and  $\phi = 20^\circ$ . The bearing angles are  $\beta + \phi = 295, 325^\circ$  and the vessel experiments the rotational motions summarized in Table 6.7. The data have been analyzed with the Pauli, SDH and Cameron theorems for a dynamic range of 25 dB. Two sets of images are attached, namely: 1) the combined weight of all the simple mechanisms of each decomposition expressed via colored images (a) and 2) the weight of the Pauli mechanisms isolated in gray images (b). In both cases, a snapshot of the point of view of the satellite is included with the azimuth x range  $(A, R)$  location of two reference points.

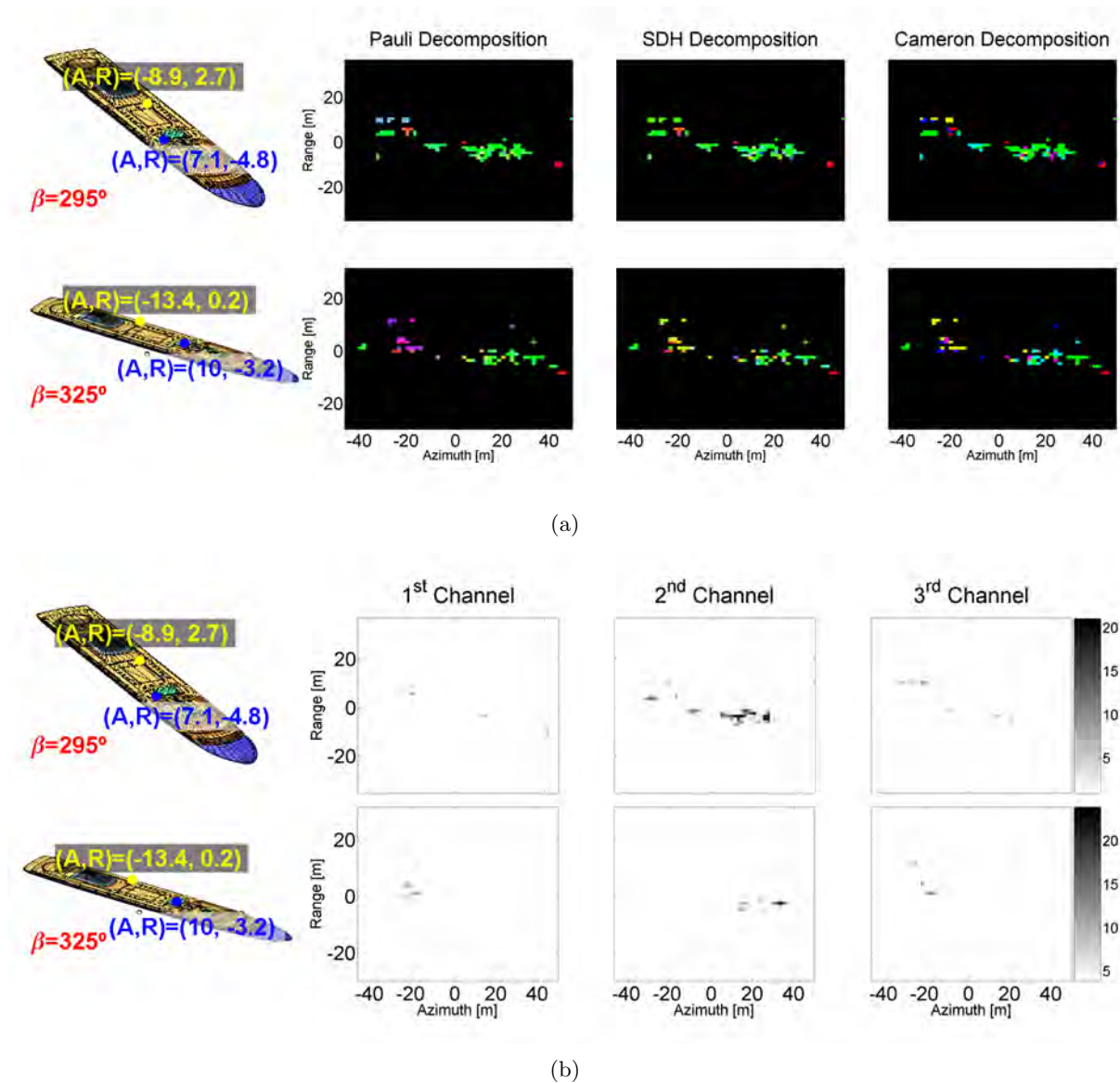


Figure 6.29: Polarimetric SAR dataset obtained for the FER model at X band and  $\phi = 20^\circ$ . The bearing angles are  $\beta + \phi = 295, 325^\circ$  and the vessel experiments the rotational motions summarized in Table 6.7. The data have been analyzed with the Pauli, SDH and Cameron theorems for a dynamic range of 25 dB. Two sets of images are attached, namely: 1) the combined weight of all the simple mechanisms of each decomposition expressed via colored images (a) and 2) the weight of the Pauli mechanisms isolated in gray images (b). In both cases, a snapshot of the point of view of the satellite is included with the azimuth x range  $(A, R)$  location of two reference points.



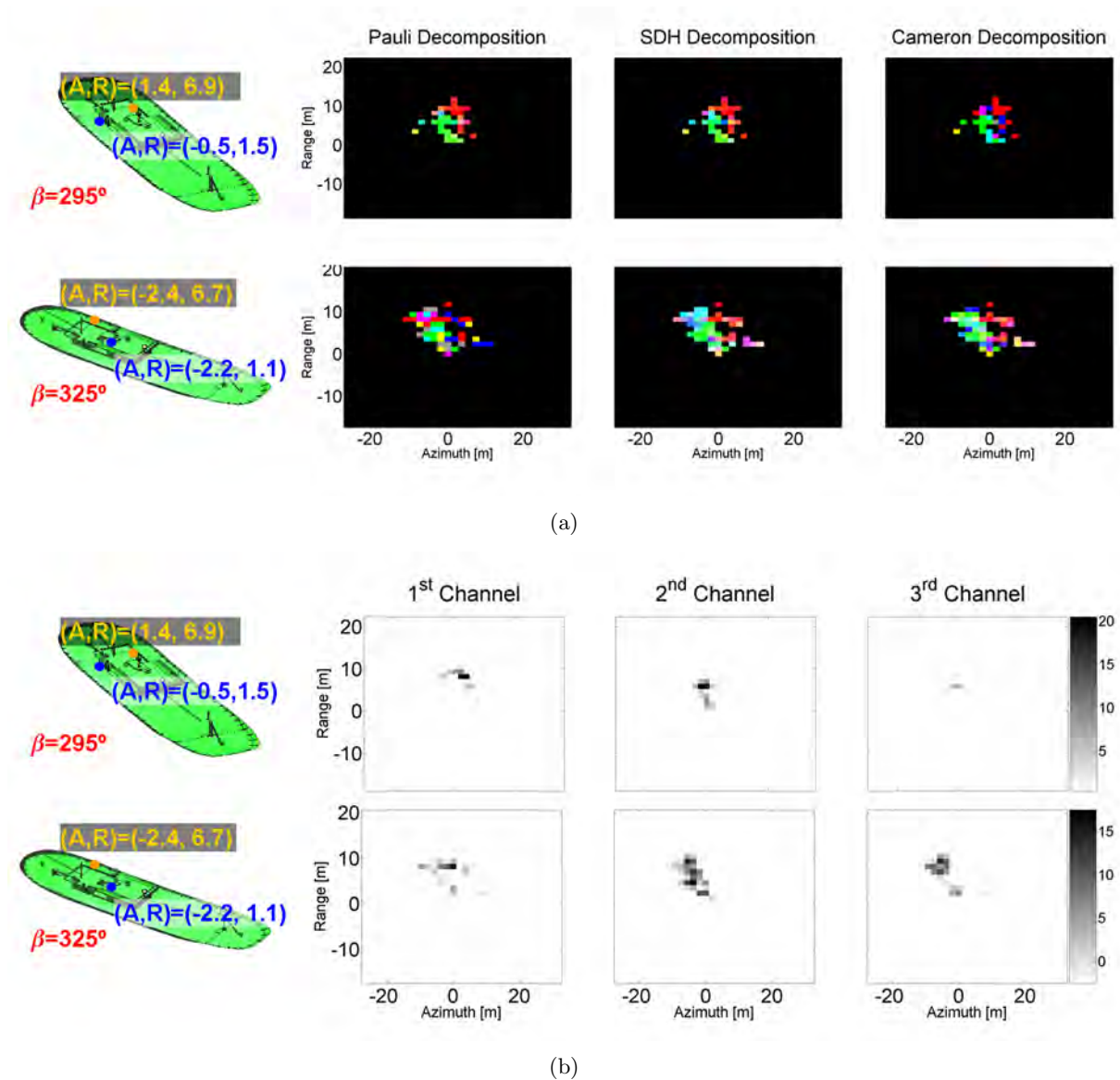
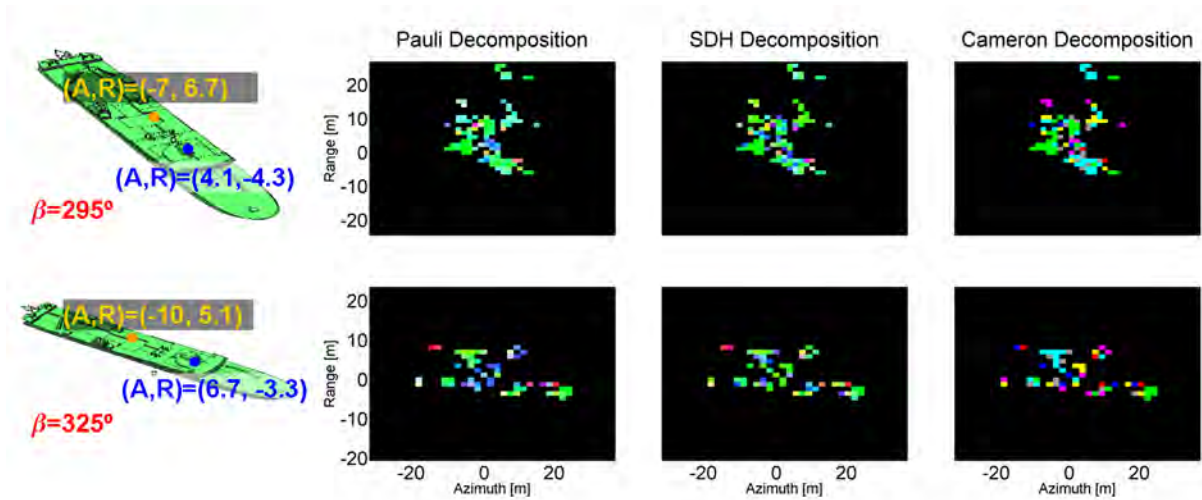
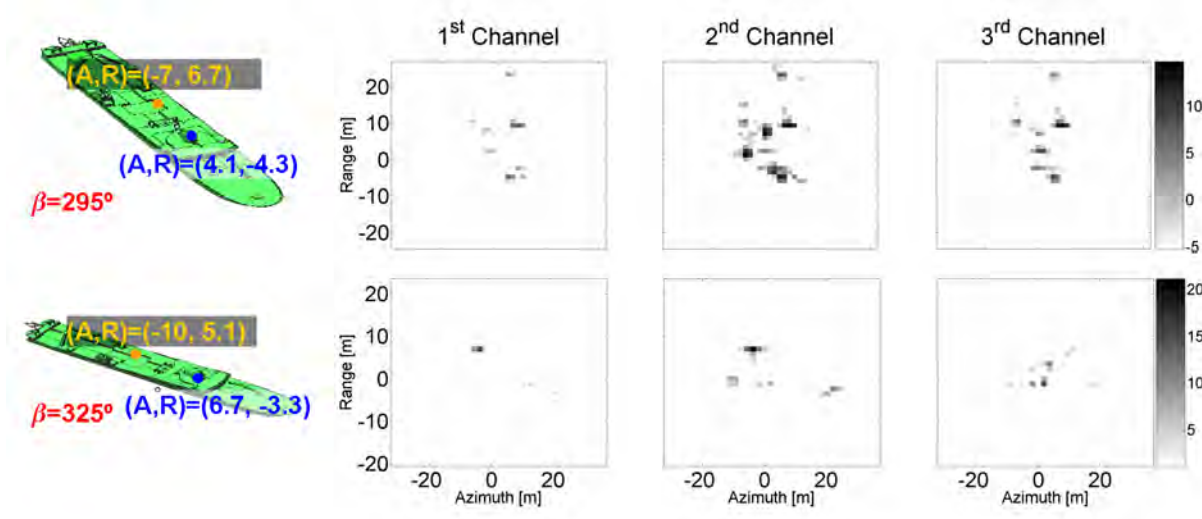


Figure 6.30: Polarimetric SAR dataset obtained for the SPA model at X band and  $\phi = 20^\circ$ . The bearing angles are  $\beta + \phi = 295, 325^\circ$  and the sea surface model of *GRECOSAR* is taken into account. The data have been analyzed with the Pauli, SDH and Cameron theorems for a dynamic range of 25 dB. Two sets of images are attached, namely: 1) the combined weight of all the simple mechanisms of each decomposition expressed via colored images (a) and 2) the weight of the Pauli mechanisms isolated in gray images (b). In both cases, a snapshot of the point of view of the satellite is included with the azimuth x range  $(A, R)$  location of two reference points.



(a)



(b)

Figure 6.31: Polarimetric SAR dataset obtained for the ICE model at X band and  $\phi = 20^\circ$ . The bearing angles are  $\beta + \phi = 295, 325^\circ$  and the sea surface model of *GRECOSAR* is taken into account. The data have been analyzed with the Pauli, SDH and Cameron theorems for a dynamic range of 25 dB. Two sets of images are attached, namely: 1) the combined weight of all the simple mechanisms of each decomposition expressed via colored images (a) and 2) the weight of the Pauli mechanisms isolated in gray images (b). In both cases, a snapshot of the point of view of the satellite is included with the azimuth x range ( $A, R$ ) location of two reference points.

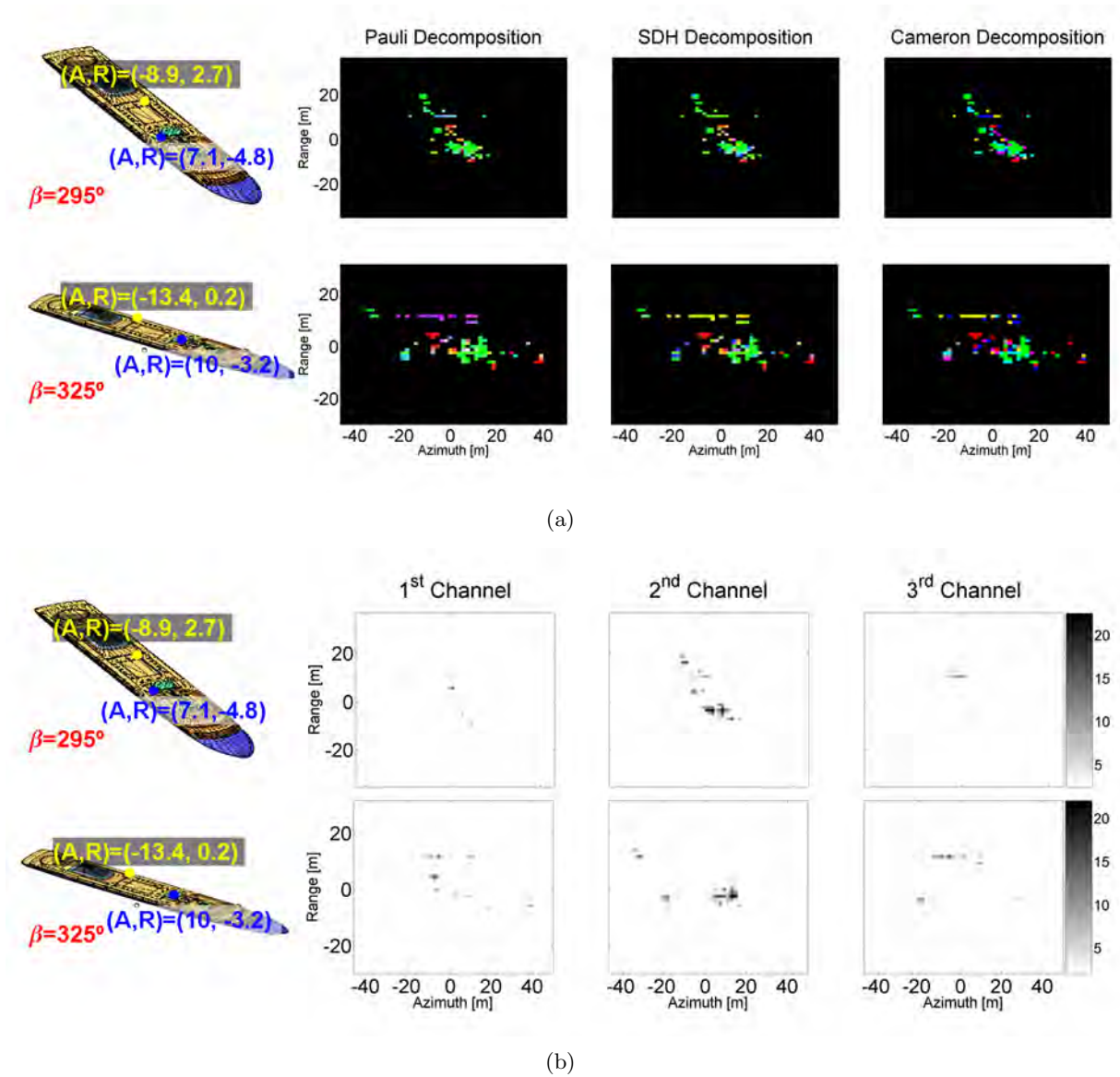


Figure 6.32: Polarimetric SAR dataset obtained for the FER model at X band and  $\phi = 20^\circ$ . The bearing angles are  $\beta + \phi = 295, 325^\circ$  and the sea surface model of *GRECOSAR* is taken into account. The data have been analyzed with the Pauli, SDH and Cameron theorems for a dynamic range of 25 dB. Two sets of images are attached, namely: 1) the combined weight of all the simple mechanisms of each decomposition expressed via colored images (a) and 2) the weight of the Pauli mechanisms isolated in gray images (b). In both cases, a snapshot of the point of view of the satellite is included with the azimuth x range ( $A, R$ ) location of two reference points.

### 6.3 Real Data Analysis

Once some useful ideas about vessel scattering have been derived from simulated data, it is interesting to know if they are valid for real scenarios and if they really match the actual vessel scattering observed in real images. This will help to establish the reliability of *GRECOSAR*'s data in vessel scattering studies and of the results presented in this Chapter for developing a new approach suitable for vessel classification. It is worth noting that the validation with real data is not easy because the number of airborne/orbital fully-polarimetric SAR data sets related to marine scenarios is nowadays insufficient. In addition, most of them suffer from a lack of accurate ground-truth that limits the interpretation that can be performed.

A first analysis has been carried out for the scenario presented in Fig. 6.33. It corresponds to the Storebaelt bridge in Denmark that links the Zealand and Funen Islands by means of two sections joined at the small island of Sprogø. A first section is a 6,611 meters long combined rail and road bridge (South) whereas the second one is a 6,790 meters long suspension bridge with two 254 meters high pylons. A 8 km long rail tunnel links the island of Sprogø and Zealand. The image has been acquired by the Danish EMISAR airborne sensor in fully-polarimetry mode at C band with a resolution around 1 x 1 meter [36]. The imaged area is 25 x 3 km<sup>2</sup>. Unfortunately, no ground-truth is available for this dataset and, hence, definitive conclusions about the polarimetric properties of vessels can not be derived.

The inspection of this marine scenario reveals different spots on the sea that can be interpreted as vessels. For this study, four have been selected (see the red rectangles) which signatures have been processed with the Pauli theorem <sup>11</sup>. The results are gathered in Fig. 6.34. First of all, note that the signatures are spread in azimuth due to the distortions induced by vessel motions. In this sense, it can be observed that the lengths estimated for such ships are around 50 m (vessel 1 and 3) and 30 m (vessel 2 and 4) whereas their breadth are not larger than 7 m (vessel 1 and 3) and 3 m (vessel 2 and 4). These values are unproportionate according to common design values and, thus, it does not seem that they correspond to real structures. This phenomenon can be observed in the whole image. Specially amazing is the case of the large and brilliant vessel signature highlighted by the green rectangle. The retrieved signature has an azimuth length 700-800 % larger than the expected one <sup>12</sup>, which is quite distorting for classification applications. Regarding the polarimetric behavior, most of the traces are dominated by dihedral- and, in less significance, trihedral-like mechanisms. This result is in concordance with what retrieved in simulated scenarios. However, note that vessels seem to be oriented almost parallel to the track of the sensor and this can induce strong dihedral mechanisms at the lateral sides of the cabin and/or hull that can mask the actual scattering behavior.

<sup>11</sup>The color codification is the same than in previous sections.

<sup>12</sup>The azimuth length is assumed as the azimuth extension of the most brilliant section of the signature.

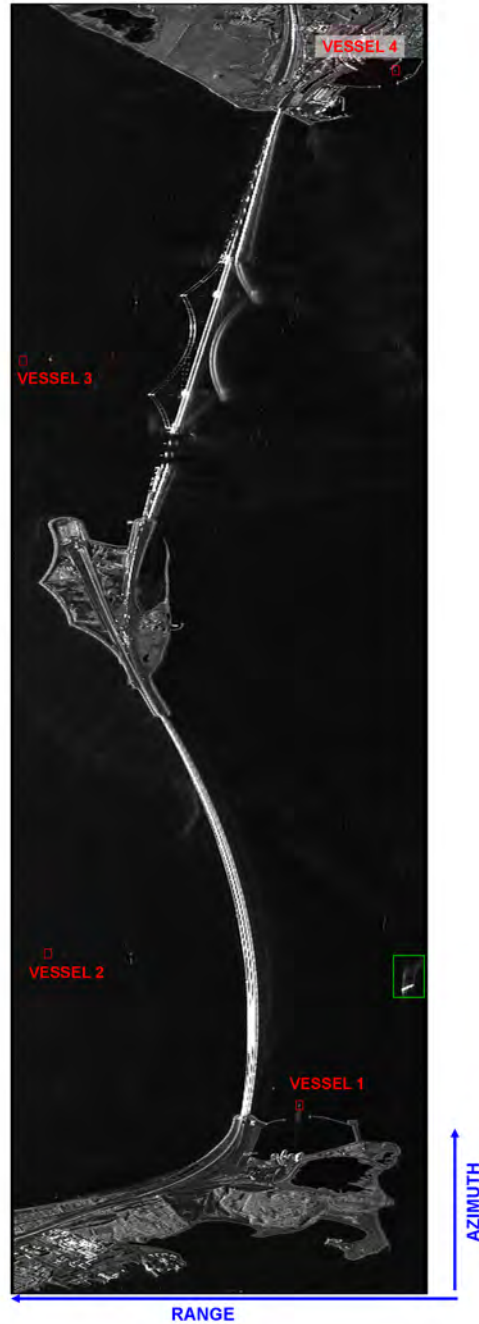


Figure 6.33: Magnitude of the HH channel of a PolSAR dataset acquired by the Danish airborne sensor EMISAR at C band with a resolution around 1 x 1 meters. The marine scenario corresponds to the Danish Storebaelt bridge between the islands of Funen (low) and Zealand (up). Red rectangles highlight the vessel signatures used in the analysis. Image dimensions are not proportional in order to make image interpretation easier.

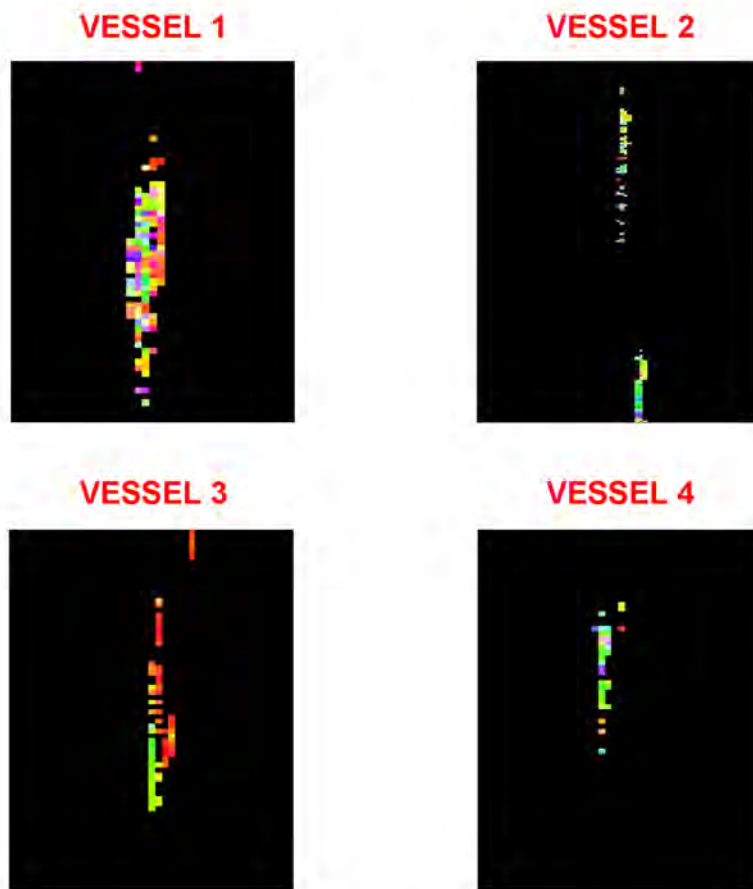


Figure 6.34: RGB images derived by processing the signatures of the four vessels highlighted in Fig. 6.33 with the Pauli theorem.

Another example is provided in Fig. 6.35. It corresponds to the marine area of Plaatgat that has a tidal inlet between the islands of Ameland and Schiermonnikoog in the Dutch side of the Wadden Sea. This image has been acquired by the DLR's airborne sensor ESAR [37] in fully-polarimetric mode at L band with a resolution of 1 m in azimuth and 2 m in range. The imaged area is approximately  $8 \times 2 \text{ Km}^2$  and, as before, no ground truth is available. In this dataset, the signatures of four (supposed) vessels have been analyzed with the Pauli theorem (see the colored rectangles of Fig. 6.35). The results for each vessel are gathered in Fig. 6.36 - 6.39 by means of three different images, namely: 1) a Pauli RGB image related to high Dynamic Range (DR), 2) a Pauli RGB image related to low DR and 3) a Pauli RGB image related to low DR with each pixel weighted by its span value. The analysis of these images show that the signatures of the four vessels are dominated by dihedral-like behaviors (see Fig. 6.36(c) - 6.39(c))<sup>13</sup>. However, important contributions of dipole and, even, trihedral are also appreciable. In this sense, note that vessel signatures are notably spread in azimuth and, hence, the polarimetric information of vessels and the sea can become complexly mixed (in addition, there are severe focusing problems due to the large aperture time at L Band, more than 3 s). As happens for distributed targets such as open fields, the sea behave as a sphere (see Fig. 6.36(a) - 6.39(a)) and this can lead to a misinterpretation of vessel mechanisms. Therefore, with the available information, it is not possible to extract definitive conclusions about the scattering behavior of such vessels. However, it seems that they point towards the behavior retrieved from simulated data.

Besides the previous data, there are other datasets related to vessels imaged at sea. Example is the PolSAR data acquired by the Canadian airborne CCRS C/X sensor [50] within the framework of the Crusade'00 trial project [164]. In this case, it is found that the signatures of vessels are dominated by a set of main scattering centers that behave as a dipole (trihedral + dihedral) [26]. As happens in the simulation environment, they preserve their scattering properties for a specific range of views.

---

<sup>13</sup>Similar results are obtained for the other CTD

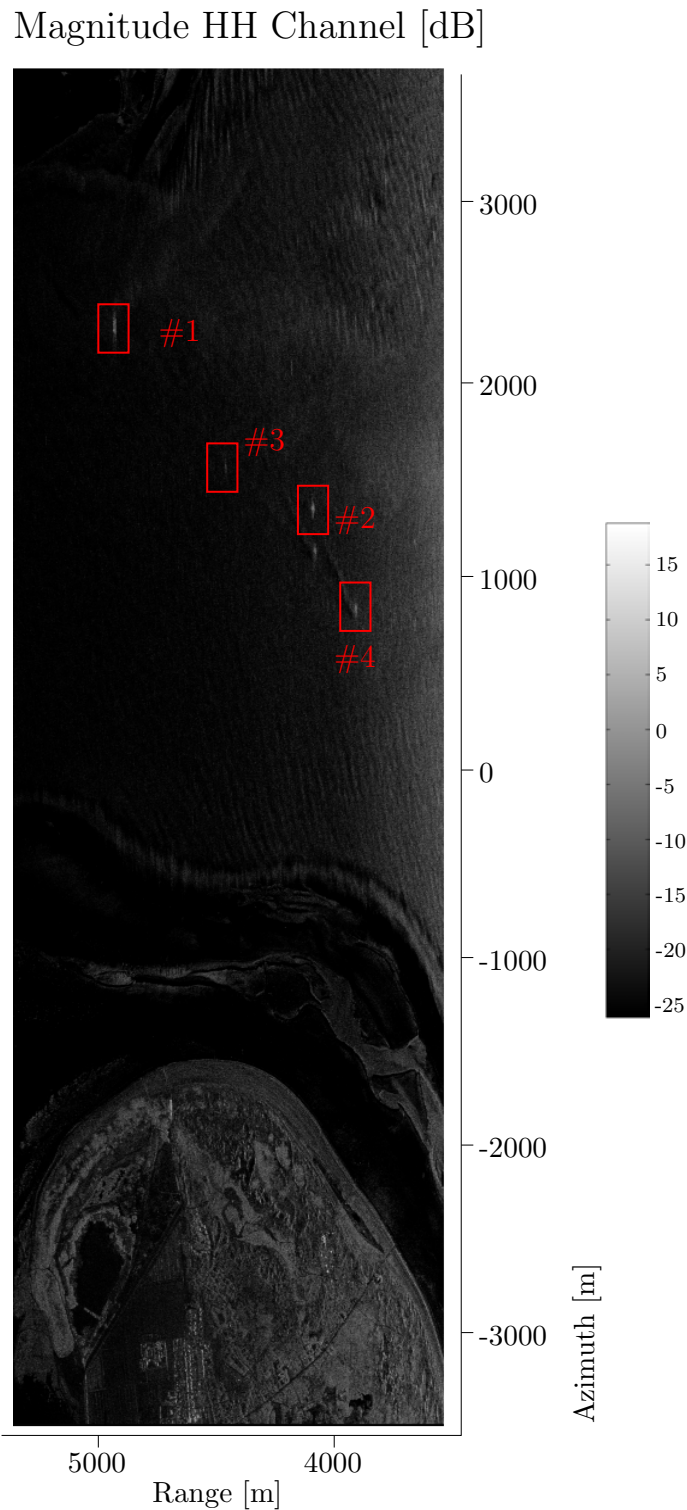


Figure 6.35: Magnitude of the HH channel of a PolSAR dataset acquired by the DLR's airborne sensor ESAR at L band with a resolution around 1 m in azimuth and 2 m in range. The marine scenario corresponds to the Plaatgat area in the Dutch side of the Wadden Sea. Red rectangles highlight the vessel signatures used in the analysis of Fig. 6.36 - 6.39. The range axis is expressed in terms of the mid-slant range whereas the azimuth axis is referenced to the center of the scene.



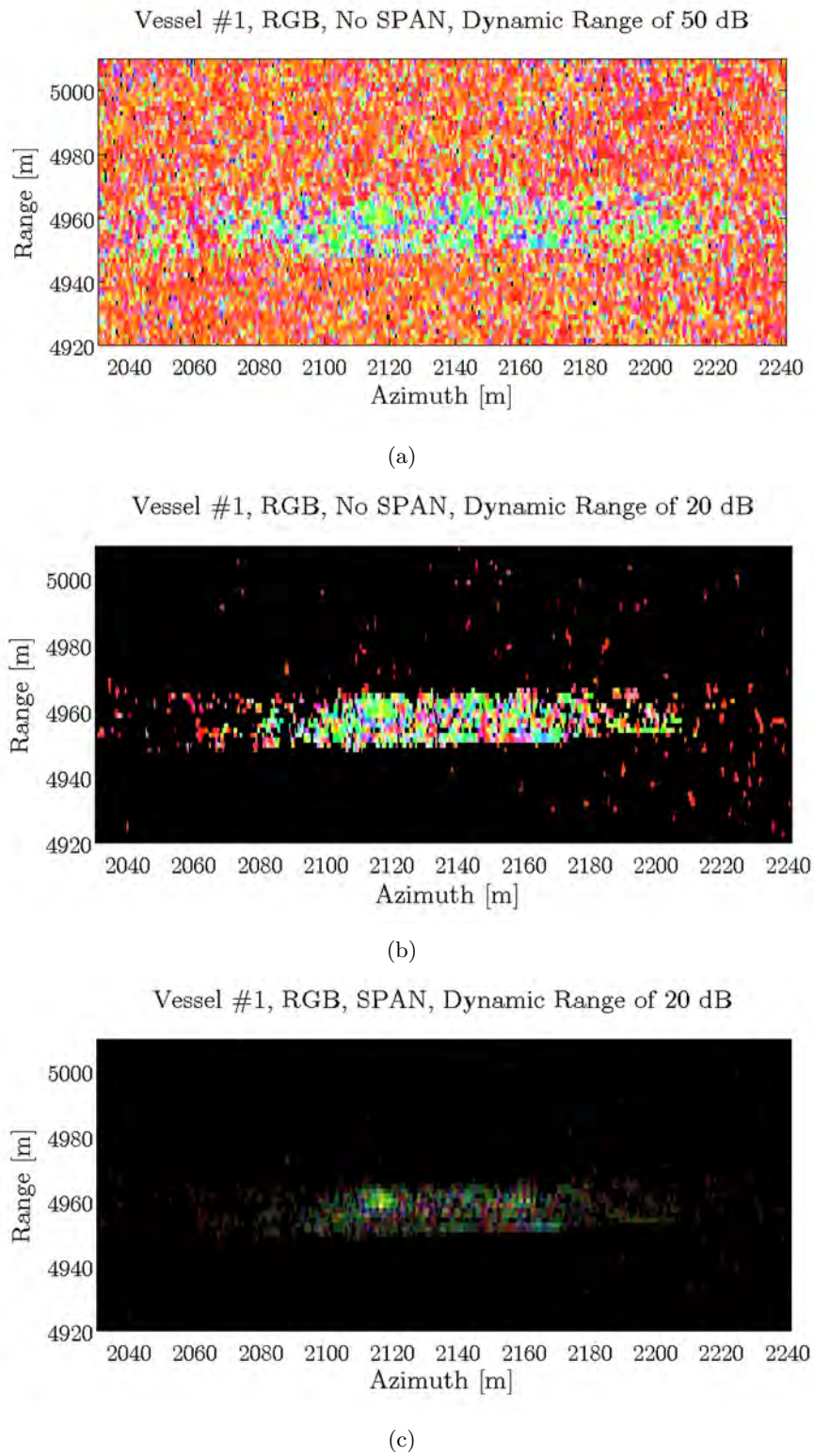


Figure 6.36: Results of analyzing the signature of vessel 1 in Fig. 6.35 with the Pauli theorem. Three images are provided, namely: 1) RGB image for a DR of 50 dB (a), 2) RGB image for a DR of 20 dB (b) and 3) RGB image for a DR of 20 dB with each pixel weighted by the span value.

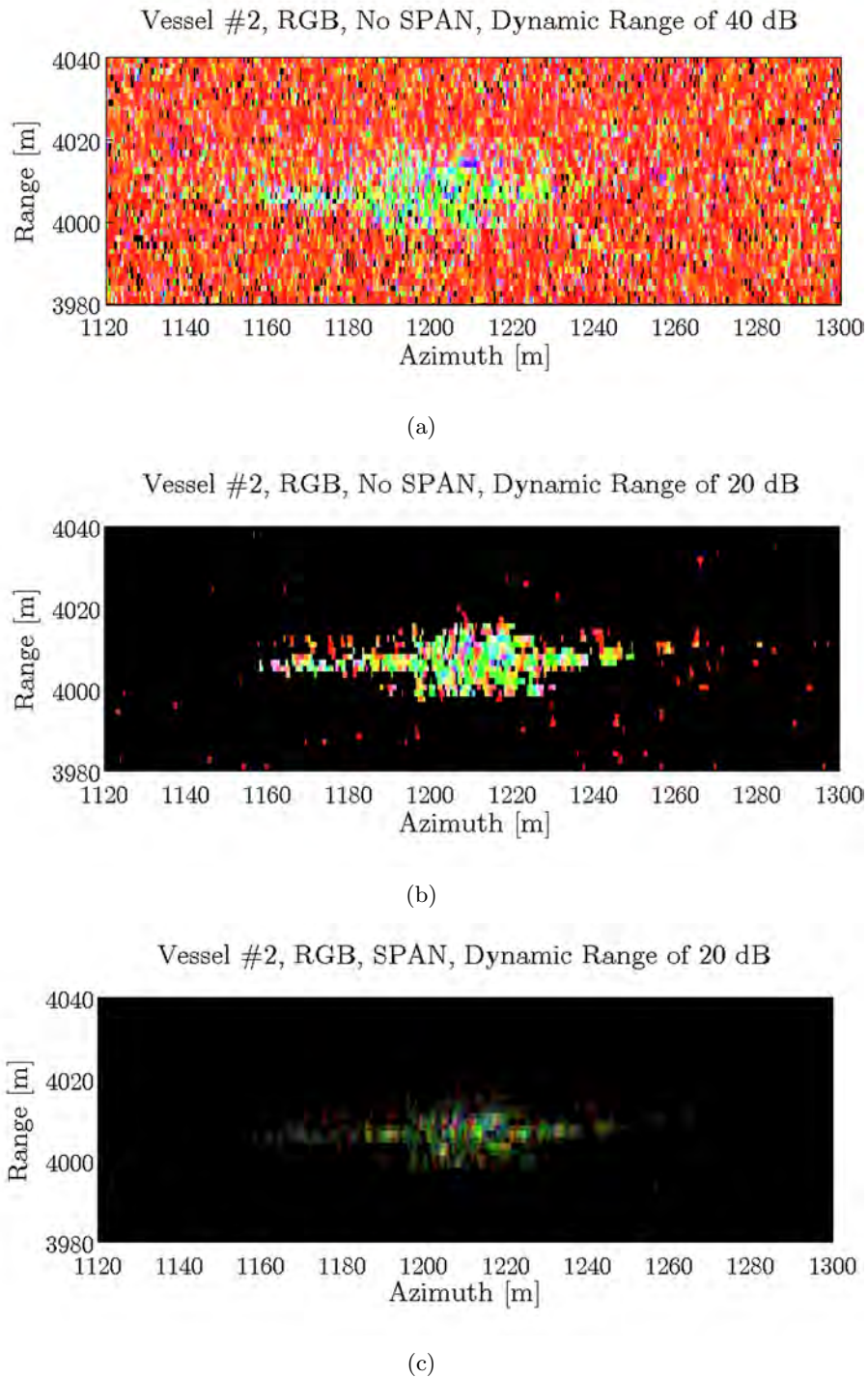


Figure 6.37: Results of analyzing the signature of vessel 2 in Fig. 6.35 with the Pauli theorem. Three images are provided, namely: 1) RGB image for a DR of 40 dB (a), 2) RGB image for a DR of 20 dB (b) and 3) RGB image for a DR of 20 dB with each pixel weighted by the span value.

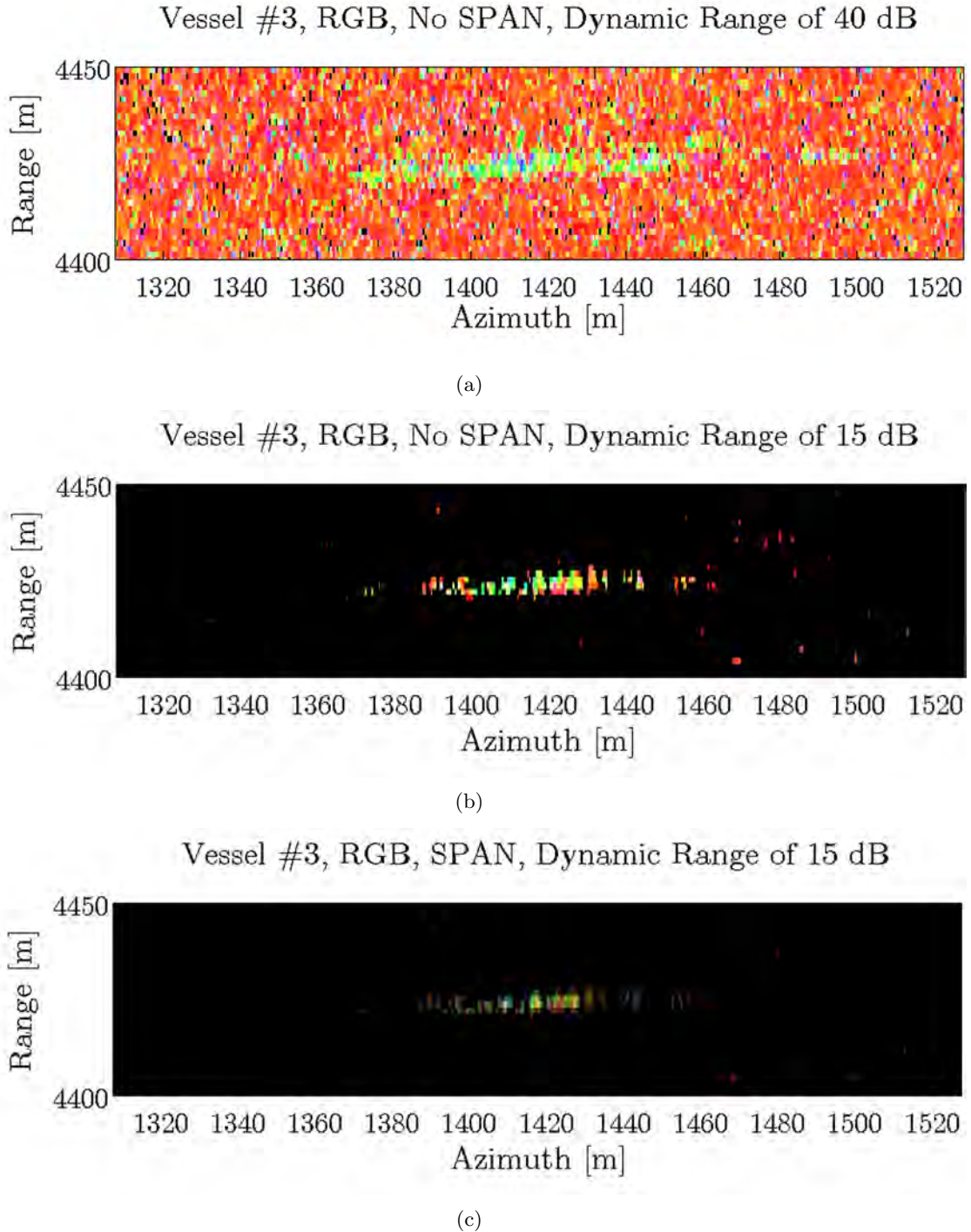


Figure 6.38: Results of analyzing the signature of vessel 3 in Fig. 6.35 with the Pauli theorem. Three images are provided, namely: 1) RGB image for a DR of 40 dB (a), 2) RGB image for a DR of 15 dB (b) and 3) RGB image for a DR of 15 dB with each pixel weighted by the span value.

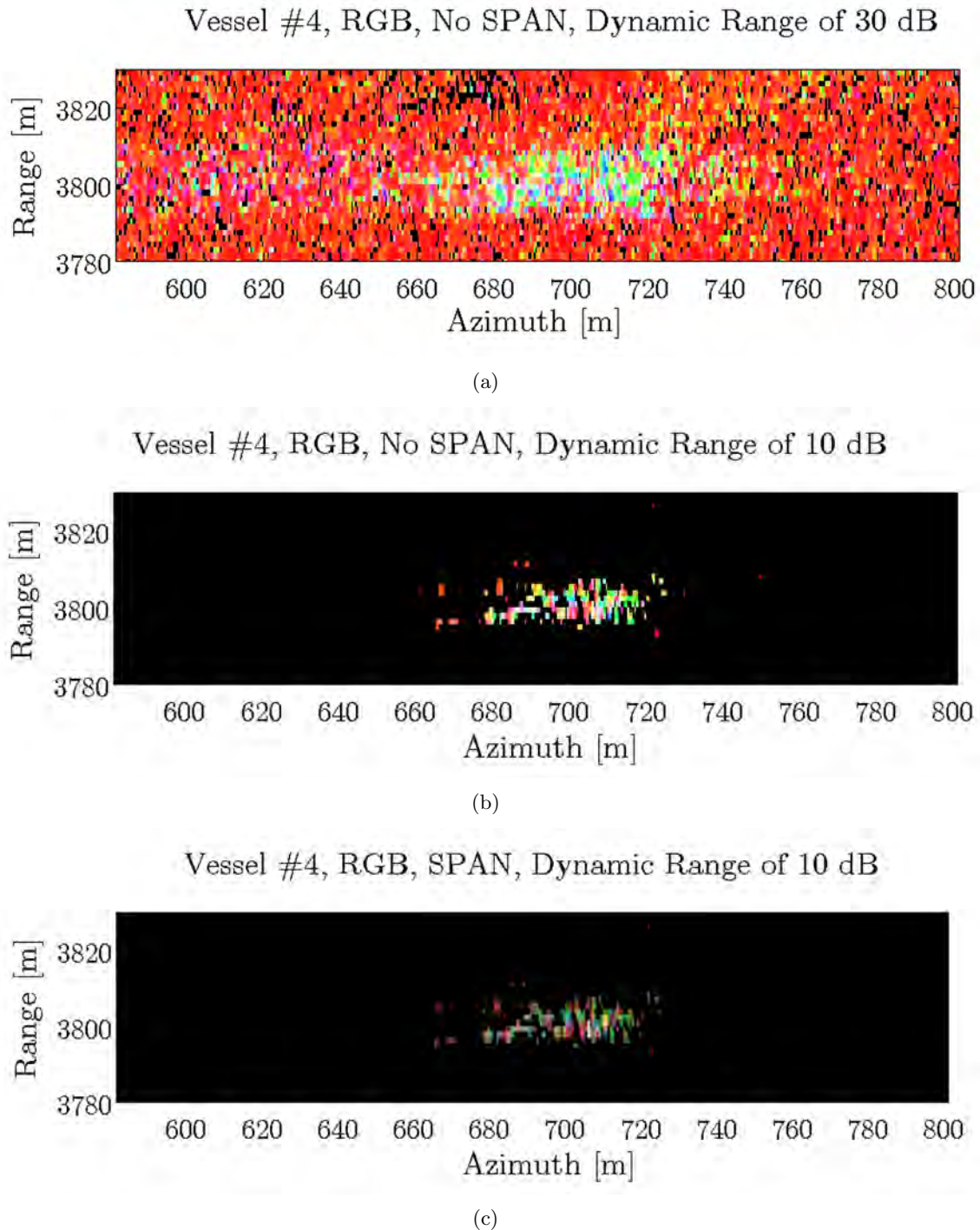


Figure 6.39: Results of analyzing the signature of vessel 4 in Fig. 6.35 with the Pauli theorem. Three images are provided, namely: 1) RGB image for a DR of 30 dB (a), 2) RGB image for a DR of 10 dB (b) and 3) RGB image for a DR of 10 dB with each pixel weighted by the span value.

## 6.4 Summary

This Chapter has shown that vessel scattering may provide key information for a proper vessel identification. The analysis of simulated data has revealed that each vessel can be characterized by a particular polarimetric trace dominated by a set of *permanent polarimetric* scattering centers. These scatterers have associated strongly polarized mechanisms similar to the Pauli ones that can be related to specific parts of the vessel structure for different views<sup>14</sup>. The analysis with different bands has shown that the scattering behavior of vessels appears to be independent of their electrical length. So, the overall size of vessels (understood as the 3D distribution of the main scattering centers) is also independent of the electrical length and, hence, it may be retrieved with SAR imagery. With these results, the scattering information of vessels makes possible to build a set of reference scattering maps that may be useful for their identification.

In SAR imagery, the retrieval of these maps needs from a minimum of resolution according to the imaged vessels in order to isolate the guide scatterers. Otherwise, the coherent assumption of CTD theorems makes the polarimetric scattering data to be mixed in a complex way. For the particular case of the current study, resolutions around 2.5 m in azimuth and 1.5 m in range appear to be enough. These values are close to the nominal resolution that the incoming TanDEM-X sensor may reach. With the guide scatterers isolated, the scattering response of vessels can be linked with the related reference map retrieved from the scattering studies. This allows to make an estimation of the observed geometry and, hence, to provide an identification decision. First tests performed for adverse environmental conditions have shown that the presence of vessels motions and sea-ship interaction do not induce at high incidence important modifications<sup>15</sup>.

But in PolSAR data the reflectivity information is projected in two dimensions and this does not allow to accurately retrieve the scattering maps. Some distortions related to the range dependent projection into the slant-range plane make data interpretation quite difficult. In this framework, an additional information channel that makes possible to retrieve the third dimension of the space will be very useful. This can be obtained via single-pass SAR interferometry as it provides the relative height among scatterers. For vessel classification, this parameter becomes an important improvement because it gives a direct measurement of a quantitative physical feature not available before with PolSAR images. In this sense, polarimetry only allows to establish qualitative relations between the geometry of vessels and their reflectivity behavior that, under certain conditions, can lead to erroneous interpretations.

---

<sup>14</sup>Permanent polarimetric scatterers refer to that hot spots that present a RCS 10 dB higher than the values of the surrounding scatterers and keep their scattering properties for a range of bearing angles larger than 30°.

<sup>15</sup>For poor resolutions, the distortions of vessel motions in polarimetric scattering are more noticeable.

Therefore, the scattering study performed in this Chapter shows that the usage of PolSAR images supported with single-pass interferometry may allow reliable vessel classification. Next Chapter will explore this approach. Although the current work has been performed with a limited set of images obtained mainly from a SAR simulator, the concepts outlined here appear to be quite reliable. However, further tests dealing with more observation conditions and complex scenarios are demanded in order to confirm them. In such a work, the analysis of both simulated and real data is necessary.

## Chapter 7

# The Unsupervised PaulInSAR Ship Identification Method

This Chapter presents a novel method for vessel classification working on single-pass polarimetric SAR interferometry. It has been developed according to the conclusions drawn in the previous Chapter that show most of vessels have a particular polarimetric response that can be characterized in terms of the simple Pauli mechanisms. The Chapter starts by describing exhaustively the algorithm placing the focus in the correlation process between the measured signature and the reference scattering maps. The advantages and limitations of the method are then analyzed in relation to other approaches. Simple tests performed with canonical targets are used to show that the relative height among scatterers is an important aid for geometry discrimination. The performances of the proposed method have been tested with *GRECOSAR*. Different vessel models within complex scenarios have been tested for a sensor configuration similar to the incoming TanDEM-X. The analysis of diverse vessel bearing, vessel speed and sea state values show that a correct identification is possible, even for adverse environmental conditions.

### 7.1 Method Description

The unsupervised *PaulInSAR* ship identification method [49] [165] [166] [167] [168] is based on the scattering study performed in the previous Chapter. There, it has been shown that each vessel can have associated a particular polarimetric trace that can be described in terms of the Pauli mechanisms [19], [34]. This means that the main scattering centers in SAR signatures behave as the elements of the Pauli basis and, hence, their phase contributions can be isolated with the Pauli theorem. If this property is combined with single-pass interferometry, an accurate three-dimensional scatter discrimination can be obtained.

### 7.1.1 The Algorithm

The scheme of the proposed technique is illustrated in Fig. 7.1. In the first step, the polarimetric analysis of the master and slave images ( $M_i$  and  $S_i$  for  $i \in \{HH, HV, VV\}$ ) is performed via CTD. For such process, any theorem can be adopted as the mechanisms expected for the main scattering centers are like trihedrals and/or dihedrals, common in all the decomposition basis. In the current approach, the Pauli theorem is used as the orthogonality of its basis makes phase isolation easier. The result is a set of images  $M_i$  and  $S_i$  for  $i \in \{0, 1, 2\}$  that contain the information related to each Pauli mechanism. For the  $i$ -th pixel with the mono-static scattering matrix

$$S_i^m = \begin{bmatrix} (S_{hh})_i^m & (S_{hv})_i^m \\ (S_{hv})_i^m & (S_{vv})_i^m \end{bmatrix} \quad (7.1)$$

the Pauli theorem leads to

$$f_i^m = \frac{1}{\sqrt{2}} \begin{bmatrix} f_{0i}^m & f_{1i}^m & f_{2i}^m \end{bmatrix} = \frac{1}{\sqrt{2}} \begin{bmatrix} (S_{hh} + S_{vv})_i^m & (S_{hh} - S_{vv})_i^m & (2S_{hv})_i^m \end{bmatrix}^T \quad (7.2)$$

where  $m$  stands for master ( $m=M$ ) or slave ( $m=S$ ) image and  $[\dots]^T$  denotes transpose operation.  $f_i^m$  is the Pauli vector for the pixel  $i$  in the image  $m$ . The first component  $f_{1i}^m$  refers to *odd number of reflections* -trihedrals-, the second one  $f_{2i}^m$  to *even number of reflections* -dihedrals  $0^\circ$ - and finally the third one  $f_{3i}^m$  to *anti-symmetric* components -dihedrals  $45^\circ$ .

After the polarimetric data analysis, the co-registration techniques are properly applied and the interferograms for each Pauli channel derived. As the algorithm works directly with the scattering matrix, which is a first order polarimetric descriptor, the co-registration is based on the cross-correlation of the squared amplitudes of the two images in all channels. This process gives to the  $i$ -th pixel three interferometric values

$$\begin{aligned} I_i^0 &= f_{0i}^M \cdot (f_{0i}^S)^* \\ I_i^1 &= f_{1i}^M \cdot (f_{1i}^S)^* \\ I_i^2 &= f_{2i}^M \cdot (f_{2i}^S)^* \end{aligned} \quad (7.3)$$

where  $(\dots)^*$  denotes complex conjugate. In this step, the same scattering matrix is assumed for both master and slave images (except phase terms) as in the orbital case the look angle difference is for moderate baselines low. In practice, this means that the scattering properties of targets are almost identical in both views.

For each Pauli interferogram ( $I_i$  for  $i \in \{0, 1, 2\}$ ), three height images are derived ( $H_i$  for  $i \in \{0, 1, 2\}$ ). In them, the local maxima related to a fixed dynamic range provide the



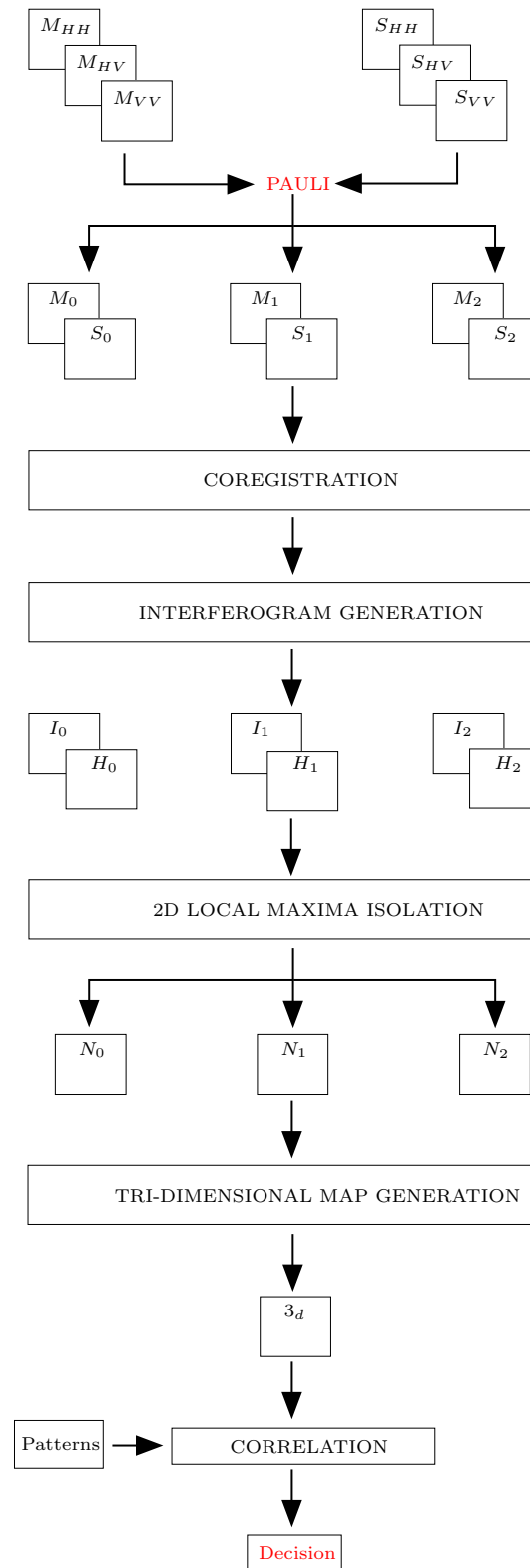


Figure 7.1: Scheme of the PaulInSAR classification algorithm.

relative height of the most important scattering centers, i.e. those scatterers that can lead to a proper identification. This information, which is stored in a set of vectors of length  $N_i$  (for  $i \in \{0, 1, 2\}$ ), allows to build, jointly with the azimuth x range position, a three-dimensional map of scatterers quite similar to the scattering maps analyzed in the last Chapter. This map provides a reasonable representation of the structure of vessels and, hence, it is used to base the decision rule of the classification algorithm. The rule is implemented in last step of the algorithm and it correlates the measured map with the different reference scattering maps or *patterns* tackled by the algorithm. In this way, the observed ship is identified with that vessel which pattern has the highest similarity with respect to the measured geometry.

### 7.1.2 Classification Patterns

The classification patterns provide the height, ground location and Pauli mechanism of a set of reference points within the structure of vessels that have, for a fixed solid angle, the highest significance in the SAR response <sup>1</sup>. This information is quite similar to that included in the reference scattering maps isolated in the previous Chapter. There, the guide scatterers can be considered *Permanent Polarimetric Scatters* (PePS) as they allow to predict the height map that the PaulInSAR method can provide under a specific set of observation conditions.

Note that a proper distribution of PePS is essential for making vessel classification more reliable. Certainly, if PePS are located in such a way that their identification is clear, resolutions requirements can be relaxed and, even more important, the sensitivity with respect to the distortions induced by the sea reduces. In this sense, three main considerations are taken into account, namely: 1) the relative distance and height among PePS should be the maximum possible, 2) they should have associated a good Signal-to-Clutter Ratio (SCR) considering clutter the surrounding scatterers <sup>2</sup> and 3) they should not be located in areas where strong mechanisms can interfere them in some punctual views, for instance near the base of cabin where dihedral-like behaviors are observed when the vessel is parallel/perpendicular to the sensor track. With these additional restrictions, the definite patterns can be different to the original reference scattering maps, thus demanding some tests before finding the optimal configuration.

Up to now, three patterns are available corresponding to the three models analyzed in Chapter 6. They are illustrated in Fig. 7.2. There, full white circles highlight PePS locations whereas red labels the corresponding height and Pauli mechanism. For the particular imaging geometry used in this study, these patterns are valid for a range of vessel bearing angles of 90 degrees ( $275^\circ \leq \delta \leq 355^\circ$ ) and for a range of incidence angles of 20 degrees ( $15^\circ \leq \phi \leq 35^\circ$ ).

<sup>1</sup>The positions are provided according to the reference system used by the SAR sensor.

<sup>2</sup>According to Chapter 6, a minimum value should be 10 dB.

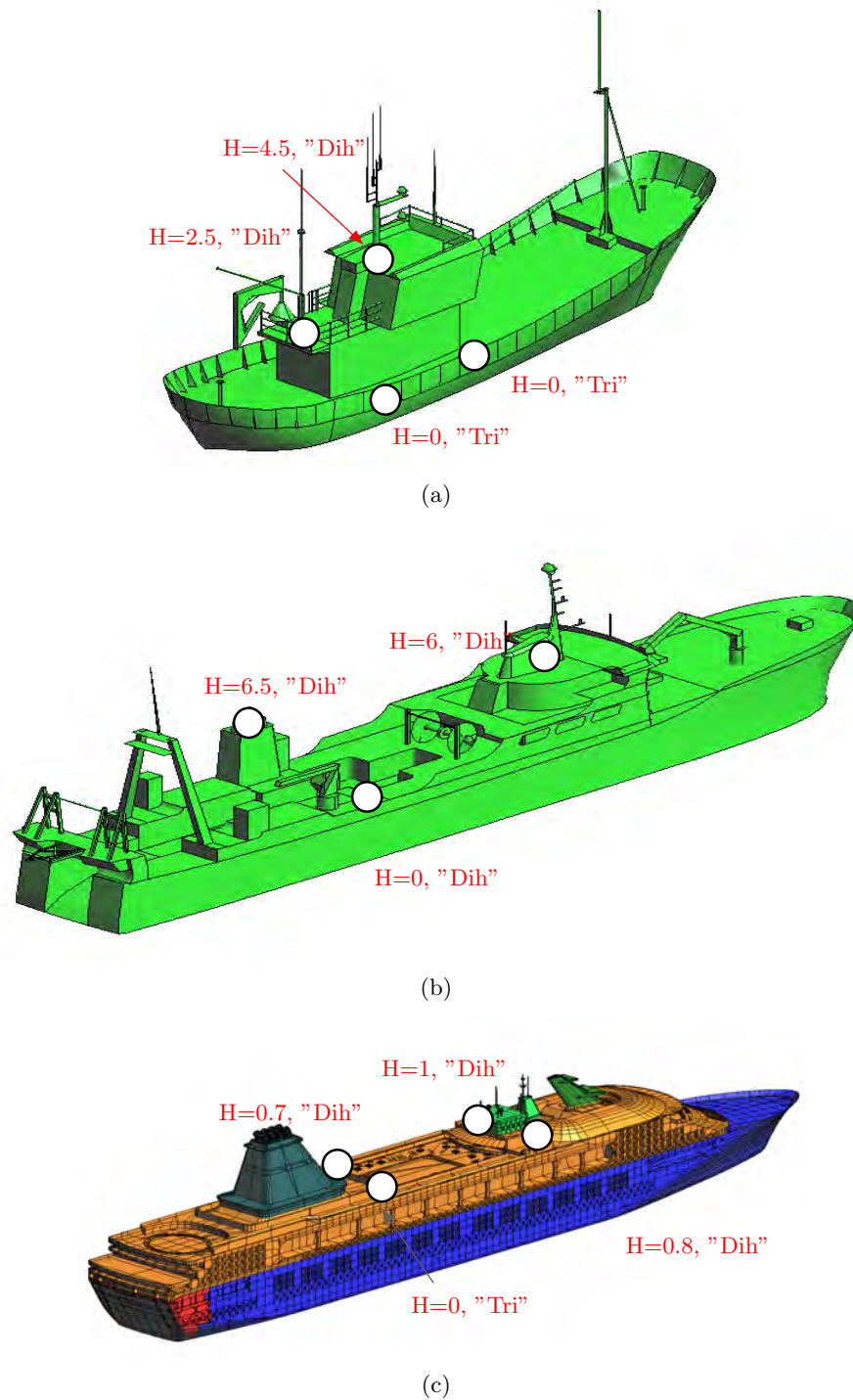


Figure 7.2: Classification patterns for the SPA, ICE and FER models. Full white circles provide PePS location whereas red labels the corresponding height and pauli mechanisms ( $f_0 \rightarrow "Tri"$ ,  $f_1 \rightarrow "Dih"$ ).

### 7.1.3 The Similarity Value

The correlation process between the measured signature and the different patterns is based on the similarity parameter  $S$ . This parameter can be understood as the Euclidean distance between the three-dimensional locations of the main scatterers isolated in the SAR image and the PePS of the processed pattern. It is defined as

$$S \doteq \frac{r}{R} \cdot \left(1 - \sum_{j=1}^4 e_j \cdot W_j\right) \quad (7.4)$$

where  $0 \leq S \leq 1$  and  $0 \geq e_j \geq 1$  are four different errors fixed by

$$e_j = \frac{1}{r} \sum_{n=1}^r e_{j,n} \quad (7.5)$$

with  $j \in \{\text{"azi"}, \text{"ran"}, \text{"hei"}, \text{"pol"}\}$  indicating the so-called *azimuth* ( $e_{azi}$ ), *range* ( $e_{ran}$ ), *height* ( $e_{hei}$ ) and *polarimetric* ( $e_{pol}$ ) errors. These errors point out the mean error made when the value of these parameters is retrieved for all the main scatterers of the measured map. In these expressions,  $r$  indicates the number of PePS with a corresponding reference scatter in the measured map and  $R$  the total number of PePS in the processed pattern. As observed later, the ratio  $r/R$  plays an important role for discriminating those patterns that have no relation with the measured structure, specially when they do not have the same number of guide scatterers in the different Pauli mechanisms. The factors ( $0 \geq W_j \geq 1$  for  $j \in \{1 \dots 4\}$ ) are weights that give different "significance" to each error in the identification process. Empirical analysis have shown that the following values may provide the best overall results ( $W_{hei} = 0.35, W_{pol} = 0.35, W_{azi} = 0.15, W_{ran} = 0.15$ ). They reduce the influence of azimuth and range errors that can cause severe mismatching when the image distortions due to sea surface are evident [18] [19]. In this context, the higher the number of analyzed vessels, the better these factors become tuned.

As a matter of fact, one important item when managing the parameter  $S$  in the decision step of the algorithm is the limited measurement accuracy of SAR systems in each of the three dimensions. This means that for each correlation run a set of unavoidable errors depending on the system performance will be always present. For the azimuth and range dimension, these inherent errors are fixed by the image resolution<sup>3</sup> whereas for the vertical dimension (the height) by the phase accuracy of the system (see Equation 3.46 in Chapter 3). Therefore, all the subsequent errors are normalized by these parameters in order to clearly distinguish the inaccuracies due to the geometry of the ships from the system related ones.

<sup>3</sup>They indicate the maximum error that can be made due to the system performance.

According to the previous comments, the expression of the azimuth error is

$$\begin{aligned} e_{azi,n} &= 1 & \text{if } \frac{|P_{azi,n}^{mea} - P_{azi,n}^{PePS}|}{\Delta x} &\geq 1 \\ e_{azi,n} &= 0 & \text{if } \frac{|P_{azi,n}^{mea} - P_{azi,n}^{PePS}|}{\Delta x} &< 1 \end{aligned} \quad (7.6)$$

where  $P_{azi,n}^{PePS}$  is the azimuth location expected for the  $n$ -th PePS of the pattern and  $P_{azi,n}^{mea}$  the azimuth position of that scattering center associated to it. Their difference is normalized to the azimuth cell dimension  $\Delta x$ . Similarly, for the range dimension

$$\begin{aligned} e_{ran,n} &= 1 & \text{if } \frac{|P_{ran,n}^{mea} - P_{ran,n}^{PePS}|}{\Delta r} &\geq 1 \\ e_{ran,n} &= 0 & \text{if } \frac{|P_{ran,n}^{mea} - P_{ran,n}^{PePS}|}{\Delta r} &< 1 \end{aligned} \quad (7.7)$$

where as before  $P_{ran,n}^{PePS}$  is the range location expected for the  $n$ -th PePS of the pattern,  $P_{ran,n}^{mea}$  the range position of that scattering center associated to it and  $\Delta r$  the range cell dimension. For the height error, the expression is

$$\begin{aligned} e_{hei,n} &= 1 & \text{if } \frac{|P_{hei,n}^{mea} - P_{hei,n}^{PePS}|}{\sigma_h} &\geq 1 \\ e_{hei,n} &= \frac{|P_{hei,n}^{mea} - P_{hei,n}^{PePS}|}{\sigma_h} & \text{if } \frac{|P_{hei,n}^{mea} - P_{hei,n}^{PePS}|}{\sigma_h} &< 1 \end{aligned} \quad (7.8)$$

where  $P_{hei,n}^{PePS}$  is the height expected for the  $n$ -th PePS of the pattern and  $P_{hei,n}^{mea}$  the height measured for that scattering center associated to it. In this case,  $\sigma_h$  is the height bias experimented by the system according to the inherent phase error  $\sigma_\phi$

$$\sigma_h = \frac{\lambda \sin \phi r}{4\pi B_\perp} \sigma_\phi \quad (7.9)$$

In the polarimetric error,  $e_{pol,n}$  is equal to 0 if the  $n$ -th PePS of the pattern is within the same Pauli polarimetric channel than the scattering center associated to it. Otherwise, it is equal to 1.

Based on the parameter  $S$ , the three-stage correlation procedure used to provide the final classification decision is summarized following:

1. For each pattern and fixed dynamic range, the distribution of scattering mechanisms that better fits the PePS distribution is found. The selection of the optimal configuration does not only take into account the relative positions of such mechanisms, but also their different Pauli behaviors (see Fig. 7.3). This means that, according to the

number of PePS and local maxima within each Pauli channel, all the possible combinations are tested. As an example, let to consider a possible pattern with two trihedral<sup>4</sup> ( $PePS_1^t, PePS_2^t$ ) and two dihedral PePS ( $PePS_1^{d0}, PePS_2^{d0}$ ) (see Fig. 7.3). In addition, consider also an input dataset with three local maxima: one behaving as a trihedral ( $LM_1^t$ ) and the other two as a dihedral ( $LM_1^{d0}, LM_2^{d0}$ )<sup>5</sup>. In this context, the algorithm evaluates Equation 7.4 for all permutations with  $r = 3$  and  $R = 4$ . Examples of such permutations are ( $PePS_1^t \leftrightarrow LM_1^t, PePS_2^t \leftrightarrow LM_1^{d0}, PePS_1^{d0} \leftrightarrow LM_2^{d0}$ ), ( $PePS_1^t \leftrightarrow LM_1^t, PePS_2^t \leftrightarrow LM_1^{d0}, PePS_2^{d0} \leftrightarrow LM_2^{d0}$ ) or ( $PePS_2^t \leftrightarrow LM_1^t, PePS_1^{d0} \leftrightarrow LM_1^{d0}, PePS_2^{d0} \leftrightarrow LM_2^{d0}$ ). Among all these permutations, the one providing the highest similarity value  $S$  is selected. In this process, possible offsets in each error are canceled. In addition, there is a "suitability scatter" step that discards, for a fixed permutation, those measured scattering centers providing a height error higher than  $\sigma_h$  or an azimuth and range error equal to 1. This modifies the value of  $r$  with respect to  $R$  giving sense to the ratio  $r/R$  of Equation 7.4.

2. Once each pattern has associated a particular distribution of local maxima in the measured signature with a specific value of  $S$ , the algorithm identifies the observed ship with that model having the highest similarity. In this process, the labels "PePS" and "mea" of Equations 7.6 - 7.8 are respectively associated to the PePS scatterers of the pattern and to the measured scattering centers related to them.
3. Steps 1-2 are iterated for different dynamic ranges in order to isolate different combinations of local maxima. The idea is to reach the maximum similarity and/or the best discrimination among the different models. The model which pattern is selected the highest number of times becomes the final decision of the algorithm. The final similarity value is that value providing the best discrimination among models. In the current version of the algorithm, vessel bearing is assumed to be known according to some of the methods available in the literature [9] [169]. In a near future, it is expected to develop a vessel bearing estimator that estimates vessel bearing according to that value providing the best overall correlation between the azimuth x range position of the measured scattering centers with respect to the position of the PePS of the patterns.

It is worth noting that the previous rule is empirical and it has been motivated by the information that the algorithm has to deal with. It has been adopted because they allow to evaluate the performances of the proposed method in an easy and quick way. Obviously, better and more sophisticated decision rules may be developed in a future.

<sup>4</sup>Each scatter has associated an azimuth position, range position and height value.

<sup>5</sup>The selection of the local maxima is performed for those scatterers which RCS is within the margin defined by the dynamic range.

$PePS_j^i \rightarrow$  Vector providing the azimuth x range position and height for the reference scatter  $j$  of the pattern  $i$   
 $Mea_n \rightarrow$  Vector providing the azimuth x range position and height for the scattering center  $n$  of the interferogram  
 $S_{p_i} \rightarrow$  Similarity value obtained for the permutation  $p_i$

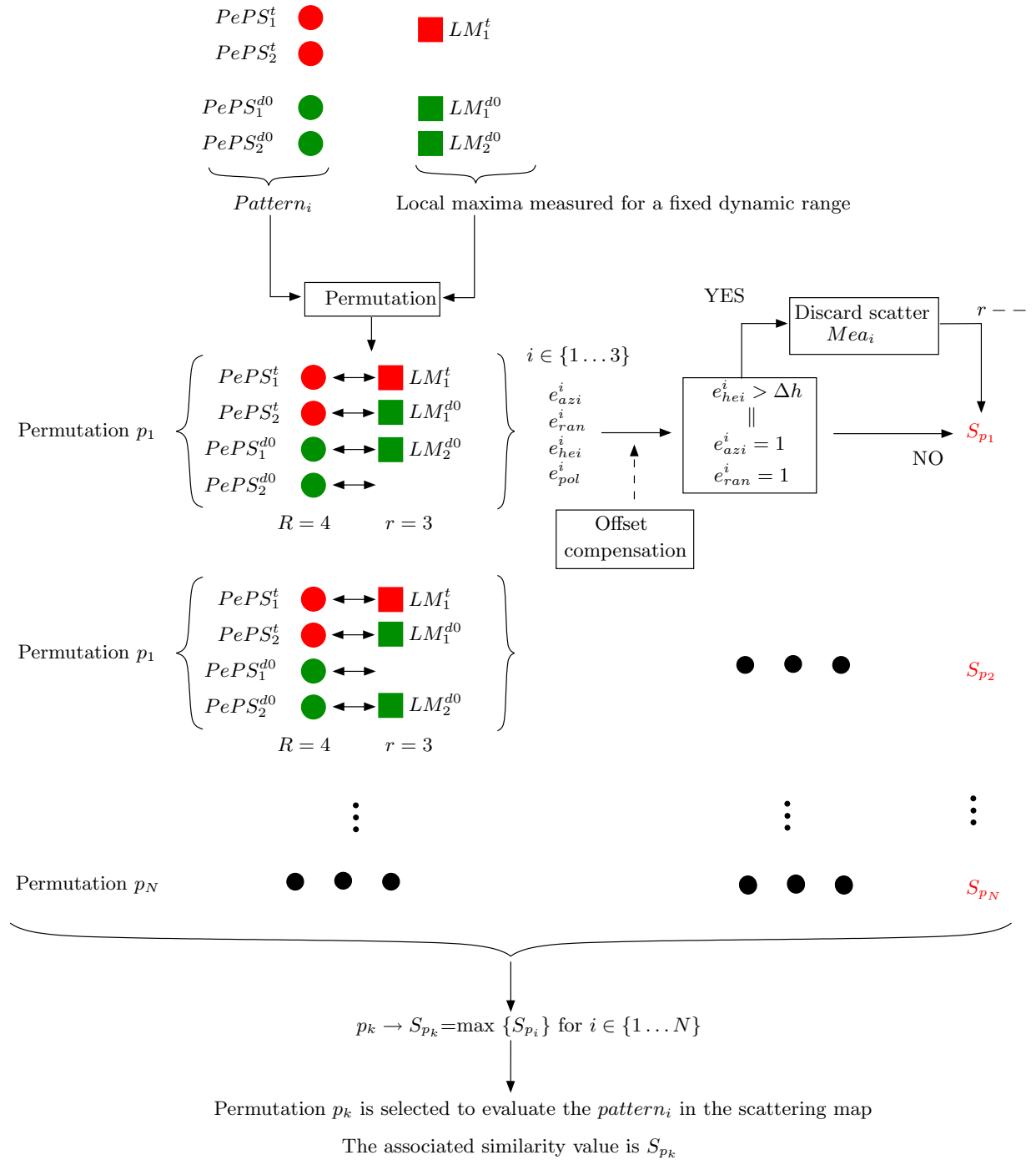


Figure 7.3: Detail of the first step of the correlation procedure. Red entities (circles or squares) indicate trihedral-like mechanisms whereas the green ones dihedral-like mechanisms.

## 7.2 Advantages and Limitations of the PaulInSAR Method

The main advantage of the current method is the retrieval of the third dimension of vessel structure that allows, jointly with a proper polarimetric processing, an identification based on quantitative measurements. To appreciate the powerfulness of such statement, a simulation for the array of canonical targets presented in Fig. 7.4 has been carried out. There, two dihedrals and two trihedrals with a 1 m long edge are grouped in two different resolution cells. The target has been processed in the scenario illustrated in Fig. 7.5 for the X band sensor summarized in Table 7.1. Two sets of images have been derived (see Fig. 7.6), namely: 1) two images providing the weight of the first and second Pauli channels expressed in terms of RCS (Fig. 7.6(a)) and 2) the three-dimensional scattering map provided by the PaulInSAR method (Fig. 7.6(b)). These images show that, although the four scatterers can be properly isolated in both cases, interferometry provides a better discrimination thanks to the height of scatterers. This allows a more accurate representation of the observed geometry<sup>6</sup> that makes easier the isolation of those key structures that can lead to a reliable identification.

The previous data show another important feature. It refers to the capability to provide, under certain conditions, up to three height values within the same resolution cell [151]. This property is possible if and only if the scatterers within a cell behave each one with a particular and different Pauli mechanism, as shown in Fig. 7.6(b). In the case that these mechanisms did not perfectly behave as the Pauli ones, their relative height would not be perfectly retrieved and, then, the accuracy would depend on their degree of similarity and radar wavelength. The extreme situation appears when the scatterers share the same polarimetric behavior. In such a case, the only retrieved height corresponds to the center of phase that, as observed in Chapter 3, is extremely dependent on the observation conditions. For such reason, it is very important to assure that the resolution of the adopted SAR system allows the discrimination of the different guide scatterers of the managed vessels (at least, those sharing the same Pauli mechanism). Otherwise, they will not be eligible to be monitored with that system. This situation points out the importance of selecting PePS as separated possible in order to avoid that system resolution restricts in excess the application of the algorithm.

It is worth noting that the current algorithm is a particular case of the general theory developed for the characterization of urban areas [170] [171]. In that case, the idea is to find which combination of scattering mechanisms (not necessarily orthogonal) allow to reach for each pixel the maximum of coherence and, hence, the best quality in the retrieved interferometric phase. As in the current case, it is possible to retrieve up to three different heights in a resolution cell.

---

<sup>6</sup>The averaged mean height error is lower than 1 cm. This error is related with the simulation accuracy of the simulator, not with the height bias that a system can experiment due to the standard deviation of the phase.



Table 7.1: Main parameters of the Sen\_X sensor.  $D_r$  and  $D_a$  expresses the pixel extend in both range and azimuth dimensions.

$h$ [Km]	514	$r_o$ [km]	544	$V_{plat}$ [m/s]	7686
$\phi$ [°]	20	$\varphi$ [°]	11.8	$\vartheta$ [°]	18.447
$f$ [GHz]	9.65	PRF [Hz]	3736	$L_a, L_r$ [m]	4.6, 0.9
BW [MHz]	125	FS [MHz]	137.5	$\tau$ [ $\mu$ s]	28
$\delta_r$ [m]	1.2	$\delta_a$ [m]	2.3	$D_r, D_a$ [m]	1.2, 2

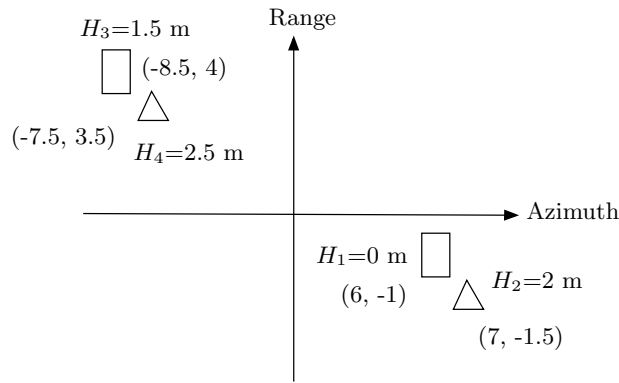


Figure 7.4: Array of two trihedrals and two dihedrals grouped in two different resolution cells. Azimuth and range positions are provided between parenthesis whereas the height by means of the label "H".

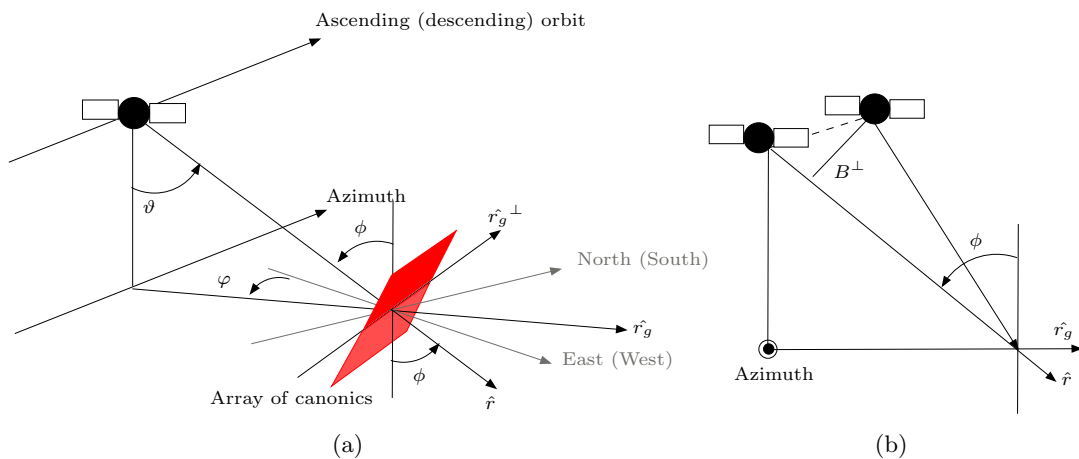


Figure 7.5: SAR (a) and InSAR (b) imaging geometry for the simulations presented in Section 7.2. In both cases, the array of canonic scatterers faces the radar.

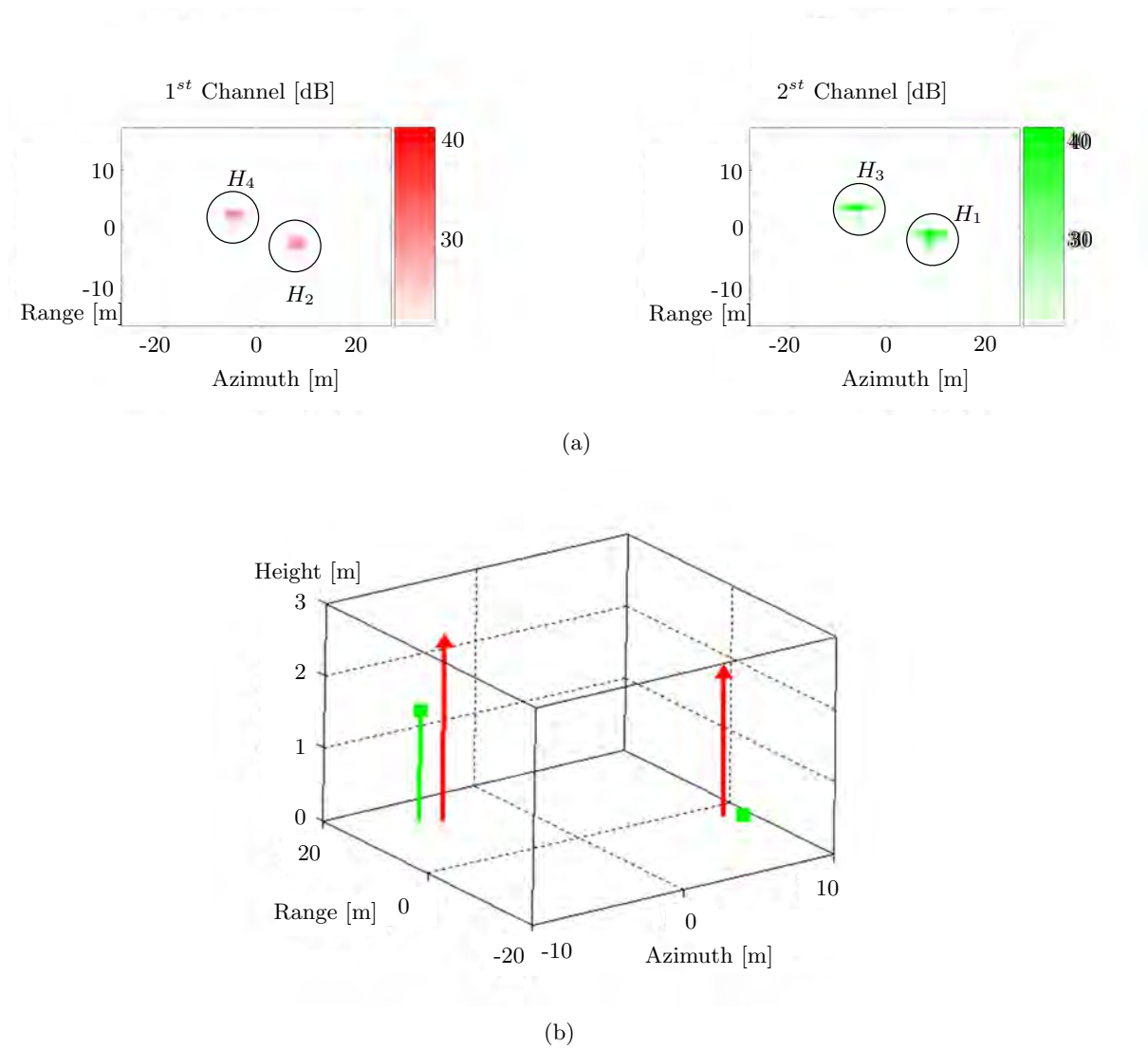


Figure 7.6: The weight of the first and second Pauli channels (a), and the three-dimensional PaulInSAR scattering map (b) derived for the target illustrated in Fig. 7.4 when processed for the X band sensor summarized in Table 7.1. The color codification is the same than in other images, namely: red  $\rightarrow f_0$ , green  $\rightarrow f_1$  and blue  $\rightarrow f_2$ .

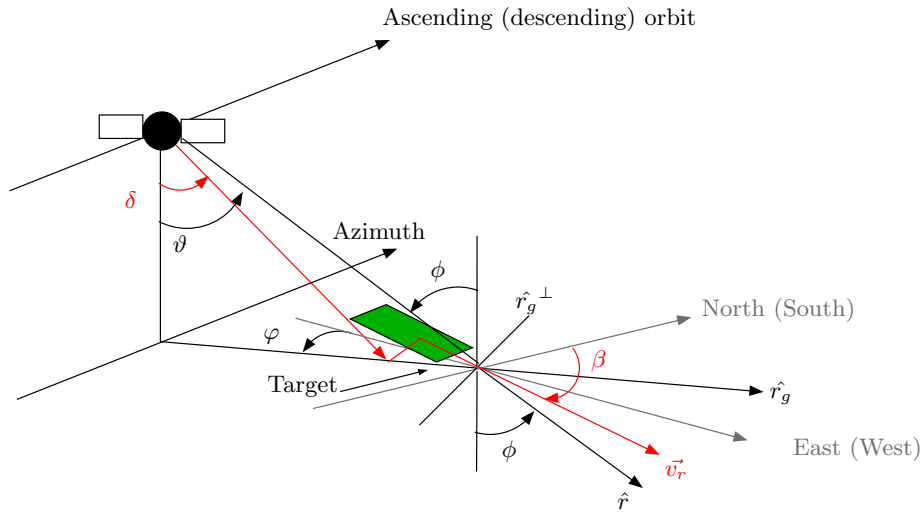


Figure 7.7: SAR imaging geometry for the simulations of Section 7.3 with the green rectangle simplifying a generic target. The interferometric configuration of the sensor is the same as that presented in Fig. 7.5.

Table 7.2: Main parameters of the Sen\_X\_5 sensor.  $D_r$  and  $D_a$  express the pixel extend in the range and azimuth dimensions.

$h$ [Km]	514	$r_o$ [km]	544	$V_{plat}$ [m/s]	7686
$\phi$ [°]	20	$\varphi$ [°]	11.8	$\vartheta$ [°]	18.447
$f$ [GHz]	9.65	PRF [Hz]	1735	$L_a, L_r$ [m]	10, 1
BW [MHz]	30	FS [MHz]	36	$\tau$ [ $\mu s$ ]	20
$\delta_r$ [m]	5	$\delta_a$ [m]	5	$D_r, D_a$ [m]	4.25, 4.4

### 7.3 Analysis with Simulated Data

The performances of the PaulInSAR method have been tested with *GRECOSAR* for the scenario environment depicted in Fig. 7.7. There, the near-far angle  $\delta$  fixes the ground-range position of the target,  $\beta$  its bearing and  $v_r = |\vec{v}_r|$  the cruising velocity. Three different X band sensors have been considered in the simulations, namely: 1) the Sen\_X sensor summarized in Table 7.1 with an azimuth x range resolution of 2.3 x 1.3 m, 2) the Sen\_X.5 sensor summarized in Table 7.2 with an azimuth x range resolution of 5 x 5 m and 3) the Sen\_X.10 sensor summarized in Table 7.3 with an azimuth x range resolution of 10 x 10 m.

Table 7.3: Main parameters of the Sen\_X\_10 sensor.  $D_r$  and  $D_a$  expresses the pixel extend in the range and azimuth dimensions.

$h$ [Km]	514	$r_o$ [km]	544	$V_{plat}$ [m/s]	7686
$\phi$ [°]	20	$\varphi$ [°]	11.8	$\vartheta$ [°]	18.447
f [GHz]	9.65	PRF [Hz]	1050	$L_a, L_r$ [m]	20, 1
BW [MHz]	15	FS [MHz]	18	$\tau$ [ $\mu$ s]	20
$\delta_r$ [m]	10	$\delta_a$ [m]	10	$D_r, D_a$ [m]	8.3, 7.32

### 7.3.1 First Example

A first simulation has been performed for the Sen\_X sensor and SPA model with  $\beta = 295^\circ$ ,  $\delta = \vartheta$ ,  $v_r = 0$  and no sea surface. The obtained results are shown in Fig. 7.8 with a set of intermediate results that clarify the procedure used by the PaulInSAR method. The process starts with the log-magnitudes of the input master and slave polarimetric datasets. They allow the algorithm to isolate the contributions of the three Pauli channels and, hence, to build the three Pauli interferograms. The height values related to their local maxima, which correspond to the main scattering centers, are gathered to generate the three-dimensional scattering map. As observed, this image is quite similar to the ISAR images managed in the previous Chapter and it schematizes the observed geometry. According to this map, the similarity values retrieved for the SPA, ICE and FER models are 0.82, 0.11 and 0.26, which allows a proper discrimination of the processed vessel.

### 7.3.2 Performance Evaluation as a Function of System Resolution

This section analyzes the resolution requirements of the PaulInSAR method. For such purpose, a set of simulations have been performed for each one of the three X band sensors. In them, the SPA, ICE and FER vessels have been processed for the environments detailed in Table 7.4. In environments A and B no sea surface is considered whereas in environments C and D the simple sea model of *GRECOSAR* is adopted. Environments B and D consider additionally pitching and rolling according to the linear terms provided in Table 7.4. Each environment tackles seven bearings ranging from  $295^\circ$  to  $355^\circ$  in steps of  $10^\circ$ . This results in 28 simulations for each sensor-model combination.

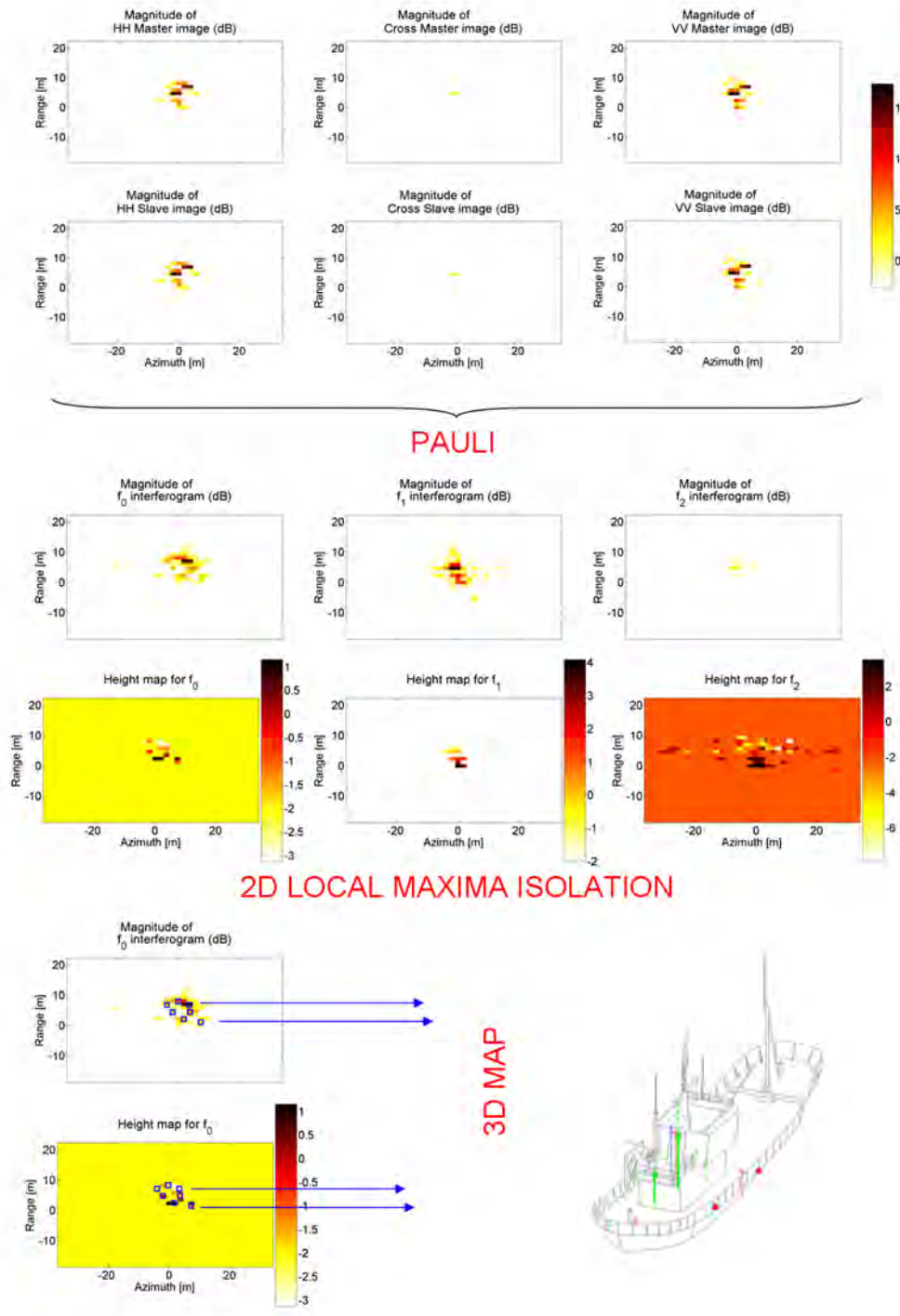


Figure 7.8: PaulInSAR results for a simulation performed for the X band sensor and SPA model. The environmental conditions are  $\beta = 295^\circ$ ,  $\delta = \vartheta$ ,  $v_r = 0$  and no sea surface.

Table 7.4: Environmental conditions for the simulations presented in Section 7.3

Environment A				
Simulation label	$\beta$ [°]	$\dot{\delta}_{pitch}$ [rad/s]	$\dot{\delta}_{roll}$ [rad/s]	sea surface
Sim. 1	295	0	0	NO
Sim. 2	305	0	0	NO
Sim. 3	315	0	0	NO
Sim. 4	325	0	0	NO
Sim. 5	335	0	0	NO
Sim. 6	345	0	0	NO
Sim. 7	355	0	0	NO
Environment B				
Sim. 8	295	-1.52	-0.26	NO
Sim. 9	305	-1.43	-0.52	NO
Sim. 10	315	-1.32	-0.76	NO
Sim. 11	325	-1.16	-0.98	NO
Sim. 12	335	-0.98	-1.16	NO
Sim. 13	345	-0.76	-1.32	NO
Sim. 14	355	-0.52	-1.43	NO
Environment C				
Sim. 15	295	0	0	YES
Sim. 16	305	0	0	YES
Sim. 17	315	0	0	YES
Sim. 18	325	0	0	YES
Sim. 19	335	0	0	YES
Sim. 20	345	0	0	YES
Sim. 21	355	0	0	YES
Environment D				
Sim. 22	295	-1.52	-0.26	YES
Sim. 23	305	-1.43	-0.52	YES
Sim. 24	315	-1.32	-0.76	YES
Sim. 25	325	-1.16	-0.98	YES
Sim. 26	335	-0.98	-1.16	YES
Sim. 27	345	-0.76	-1.32	YES
Sim. 28	355	-0.52	-1.43	YES

Table 7.5: Ratio of positive matches  $p$  for the different dataset presented in Fig. 7.9(a)-7.11(c)

p %	Sen_X_10	Sen_X_5	Sen_X
SPA	21.42	32.14	96.42
ICE	42.85	75	85.71
FER	50	21.42	89.28

The classification results provided by the method for the Sen\_X\_10, Sen\_X\_5 and Sen\_X sensors are respectively presented in Fig. 7.9, Fig. 7.10 and Fig. 7.11. In each set, the three figures show the similarity history plots retrieved by the algorithm when each model is processed in the 28 scenarios. For each plot, three graphs can be distinguished according to the three available patterns. All the plots have four sections identifying the four environments of Table 7.4 and a straight line showing the medium similarity value  $S_m$ .

According to the values presented in these figures, Table 7.5 summarizes the ratio of positive matches  $p$  for each sensor-model combination, i.e. the number of times that the processed vessel is properly identified in relation to the number of analyzed situations <sup>7</sup>.

In the light of the obtained results, some comments are in order:

1. For the Sen\_X\_10 and Sen\_X\_5 sensors, the reduced resolution avoids the PaulInSAR method to properly identify the processed vessels and, thus, a low ratio of positive matches is retrieved. The exception is the ICE model that reaches for the Sen\_X\_5 sensor a value of  $p$  close to 75 %. The best overall results are for the Sen\_X sensor as the available resolution is enough for isolating the key scattering centers.
2. For the Sen\_X sensor, the PaulInSAR method presents a notable robustness against the image distortions induced by the sea. In this field, neither vessel motions nor the influence of the sea surface worsens in excess the classification results. To confirm this point, Table 7.6 summarizes the ratio of positive matches  $p_D$  retrieved for the simulations related to ENVIRONMENT D where both vessel motions and sea surface are taken into account. In this case, the ratios are higher than 70 %.
3. For those bearings where the vessels are almost parallel to the satellite track, classification capabilities drop appreciably. This is due to the strong dihedral-like mechanisms originated at the lateral sides of the cabin and/or hull (see Chapter 6) that mask the polarimetric trace inherent to the different vessel models.
4. In summary, it appears that for the proper resolution the PaulInSAR method may be useful for vessel classification. Certainly, it provides reliable identification based on

<sup>7</sup>It is assumed that a vessel is properly identified if the related pattern has the highest similarity value.

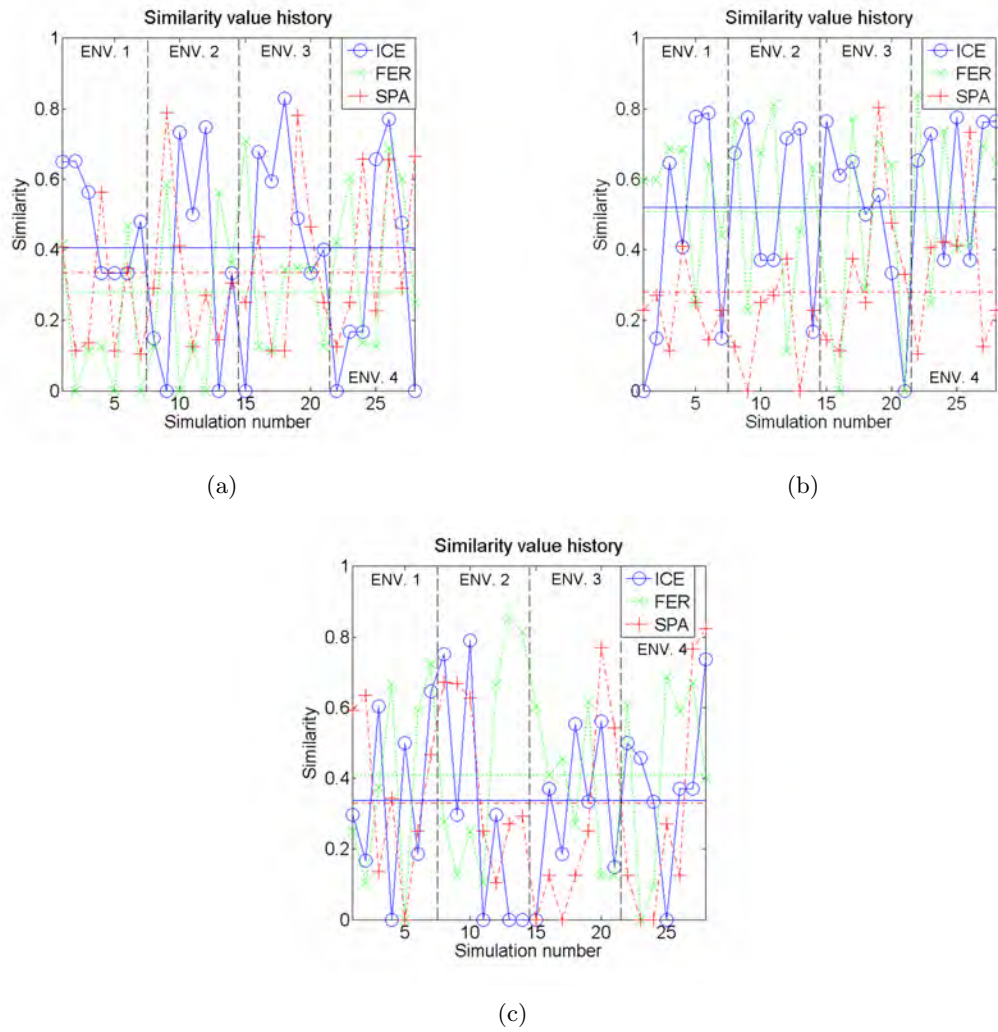


Figure 7.9: Similarity values retrieved for all the patterns (SPA  $\rightarrow$  Red/+, ICE  $\rightarrow$  blue/ $\bigcirc$ , SPA  $\rightarrow$  green/ $\times$ ) when the SPA (a), ICE (b) and FER (c) model are processed for the Sen\_X\_10 sensor under the environmental conditions summarized in Table 7.4.



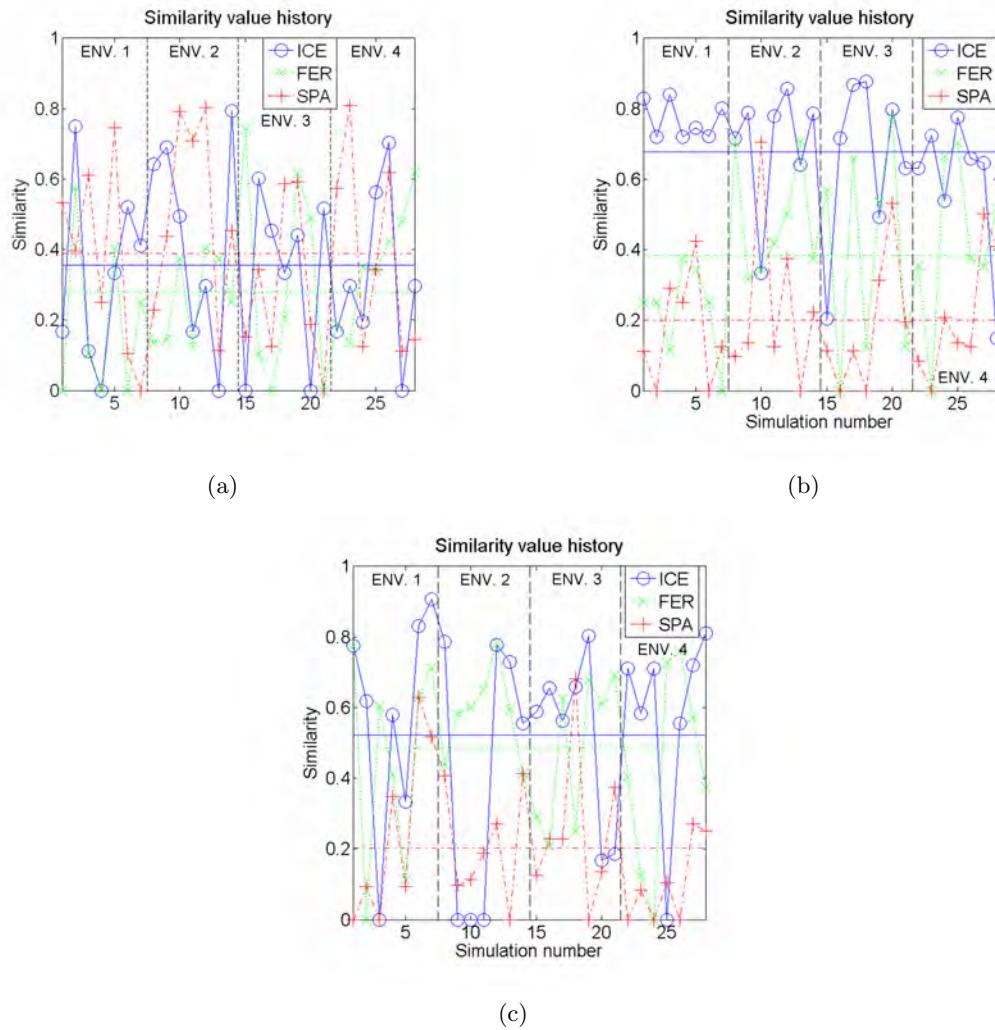


Figure 7.10: Similarity values retrieved for all the patterns (SPA  $\rightarrow$  Red/+, ICE  $\rightarrow$  blue/O, SPA  $\rightarrow$  green/x) when the SPA (a), ICE (b) and FER (c) model are processed for the Sen\_X\_5 sensor under the environmental conditions summarized in Table 7.4.

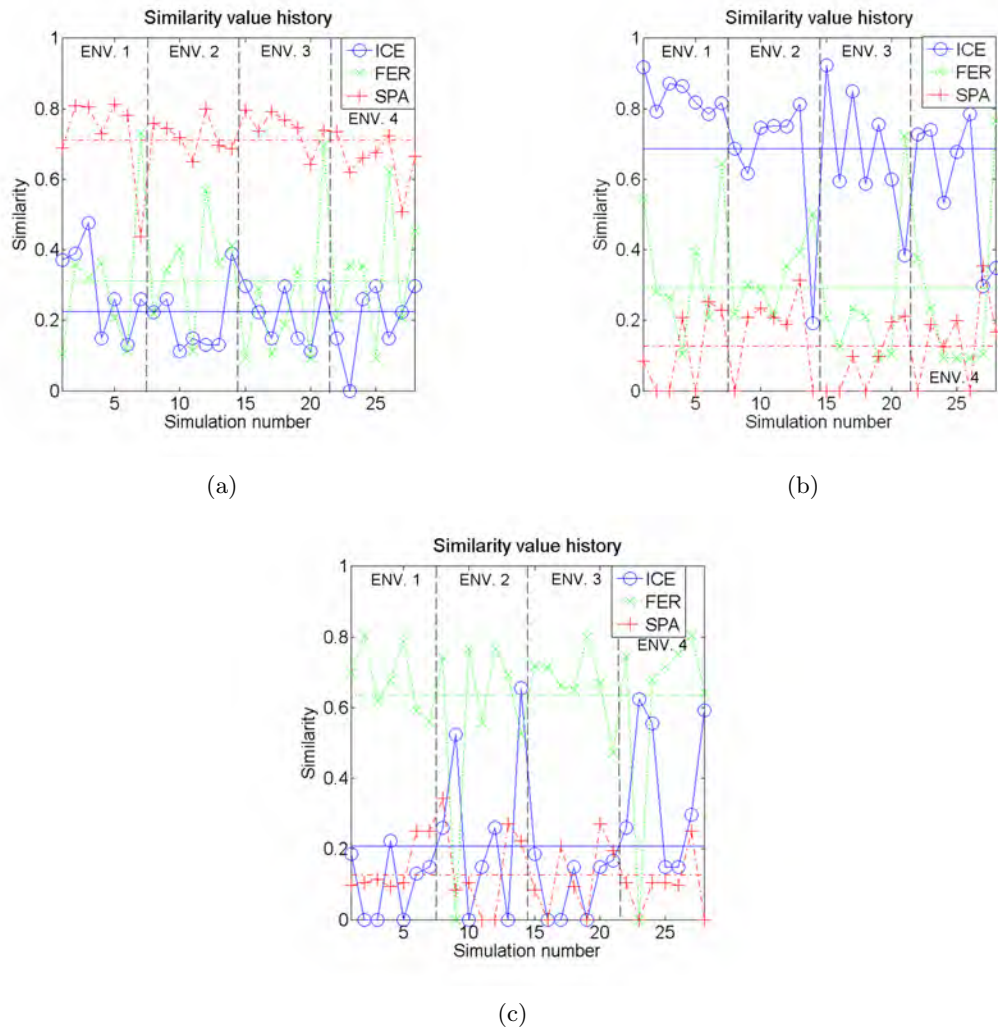


Figure 7.11: Similarity values retrieved for all the patterns (SPA  $\rightarrow$  Red/+, ICE  $\rightarrow$  blue/O, SPA  $\rightarrow$  green/x) when the SPA (a), ICE (b) and FER (c) model are processed for the Sen<sub>X</sub> sensor under the environmental conditions summarized in Table 7.4.

Table 7.6: Ratio of positive matches  $p_D$  related to ENVIRONMENT D for the different dataset presented in Fig. 7.9(a)-7.11(c)

$p_D$ %	Sen_X_10	Sen_X_5	Sen_X
SPA	28.57	28.57	100
ICE	57.14	71.42	71.42
FER	42.85	28.57	85.71

Table 7.7: Ratio of positive matches  $p$  for the different dataset presented in Fig. 7.12(a)-7.12(c)

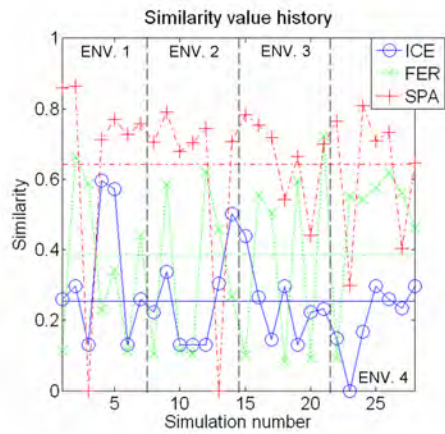
p	Sen_X	Sen_X_B20
SPA	92.85	82.14
ICE	85.71	82.14
FER	82.14	78.57

quantitative measurements of the observed geometry with a reduced sensitivity with respect to the sea environment. This is an important advantage in relation to currently available methods, mainly oriented to establish qualitative relations between the measured scattering and the observed geometry. However, it is important to note that the proposed method needs from a minimum of resolution that may be fulfilled by some airborne sensors and by the new generation of spaceborne SAR, such as Tandem TerraSAR-X [58]. In addition, the presence of intense sea clutter may affect the method performance, specially when retrieving the height. So, future versions of *GRECOSAR* should improve the sea model so that the effects of sea clutter can be further studied.

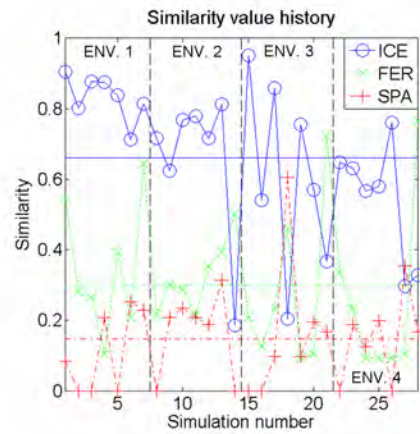
### 7.3.3 Performance Evaluation as a Function of System Baseline

This section provides the results obtained when the previous simulations (Sen\_X sensor) are run for a perpendicular baseline of 20 meters (Sen\_X\_B20 sensor). The idea is to evaluate the sensibility of the identification performance as a function of the system baseline. Fig. 7.12 shows the new similarity values retrieved for all the patterns when the three vessel models are processed.

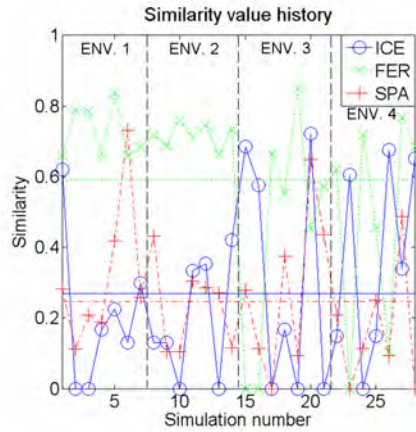
As observed, the results are quite similar, despite an appreciable confidence have been lost. This can be noted in the ratios of positive matches summarized in Table 7.7 that now are lower than the ones retrieved for the baseline of 30 meters.



(a)



(b)



(c)

Figure 7.12: Similarity values retrieved for all the patterns (SPA  $\rightarrow$  Red/+, ICE  $\rightarrow$  blue/ $\circ$ , SPA  $\rightarrow$  green/ $\times$ ) when the SPA (a), ICE (b) and FER (c) model are processed for the Sen\_X\_20 sensor under the environmental conditions summarized in Table 7.4.

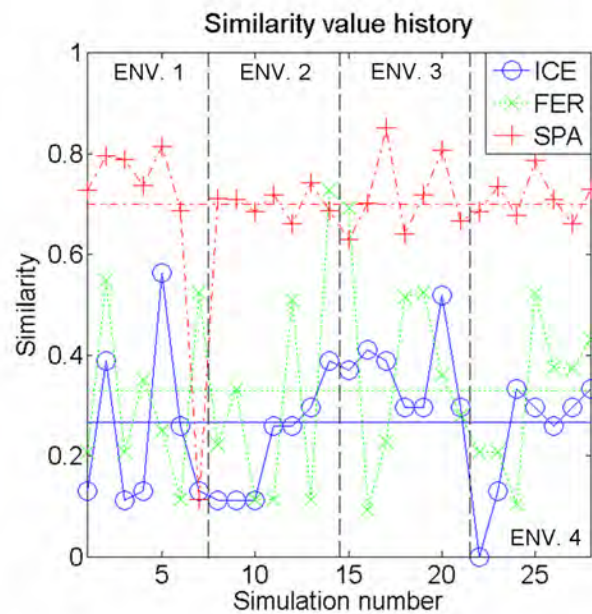


Figure 7.13: Similarity values retrieved for all the patterns (SPA  $\rightarrow$  Red/+, ICE  $\rightarrow$  blue/ $\circ$ , SPA  $\rightarrow$  green/ $\times$ ) when the SPAv2 model is processed for the Sen\_X sensor under the environmental conditions summarized in Table 7.4.

### 7.3.4 Performance Evaluation as a Function of the Geometry of Ships

This section evaluates the Sen\_X dataset (see Section 7.3.2) for the SPAv2 vessel model. The idea is to test the classification performance as a function of the geometrical complexity of the processed models and the discrimination capability of the method for two quite similar targets. The related similarity history plot is presented in Fig. 7.13<sup>8</sup>.

As observed, the ratio of positive matches is almost the same for both models (92.85 %  $\rightarrow$  SPA model and 89.28 %  $\rightarrow$  SPAv2 model)<sup>9</sup>. However, the overall response of the SPAv2 model is more stable than the response of the original version of the ship. This allows to achieve a better discrimination, specially for the most realistic environment. Therefore, it seems that in a simulation environment classification performances are better evaluated with models having the highest accuracy in their geometries possible. The opposite idea must be rejected as the excessive simplification of complex models becomes in SAR simulation an important source of error.

<sup>8</sup>This dataset has to be compared with the similarity history plot within Fig. 7.11(a).

<sup>9</sup>It is assumed that both are related to the same pattern.

Table 7.8: Environmental conditions for the simulations presented in Section 7.3.5

Simulation label	$\beta$ [°]	$\dot{\delta}_{pitch}$ [rad/s]	$\dot{\delta}_{roll}$ [rad/s]	sea surface
Sim. 1B	35	0.76	-1.32	YES
Sim. 2B	65	1.32	-0.76	YES
Sim. 3B	95	1.52	0	YES
Sim. 4B	125	1.32	0.76	YES
Sim. 5B	155	0.76	1.32	YES
Sim. 6B	185	0	1.52	YES
Sim. 7B	215	0.76	1.32	YES

### 7.3.5 Performance Evaluation as a Function of Bearing

In this section, the possible usage of the patterns (see Fig. 7.2) for bearing values out of the range specified in Section 7.1.2 is considered. For such purpose, the three vessel models have been processed with the Sen\_X sensor under the environmental conditions summarized in Table 7.8. The resulting similarity plots are gathered in Fig. 7.14. As observed, classification performances are notably worsened as a proper identification is only achieved for very specific bearings (most of them close to the former bearing range). In this way, the solid angle associated to the patterns (bearing  $\rightarrow (275^\circ \leq \delta \leq 355^\circ)$ , incidence  $\rightarrow (15^\circ \leq \phi \leq 35^\circ)$ ) can not be extended and, thus, other patterns are required for covering the remaining views.

### 7.3.6 Performance Evaluation with Single Channel Interferometry

This section will show the role of polarimetry in the classification method. For such purpose, the set of simulations run for the Sen\_X sensor in Section 7.3.2 are analyzed with a version of PaulInSAR where polarimetry is not taken into account. This version deals with a new similarity parameter

$$S^{np} \doteq \frac{r}{R} \cdot \left(1 - \sum_{j=1}^3 e_j^{np} \cdot W_j\right) \quad (7.10)$$

where  $0 \geq e_j^{np} \geq 1$  are the *azimuth* ( $e_{azi}^{np}$ ), *range* ( $e_{ran}^{np}$ ) and *height* ( $e_{hei}^{np}$ ) errors defined in Equation 7.6, 7.7 and 7.8. In these formulas, the information related to the "mea" label correspond to the main scattering centers isolated in the HH channel. This means that the correlation between the pattern database and the input image does not consider the Pauli mechanisms.

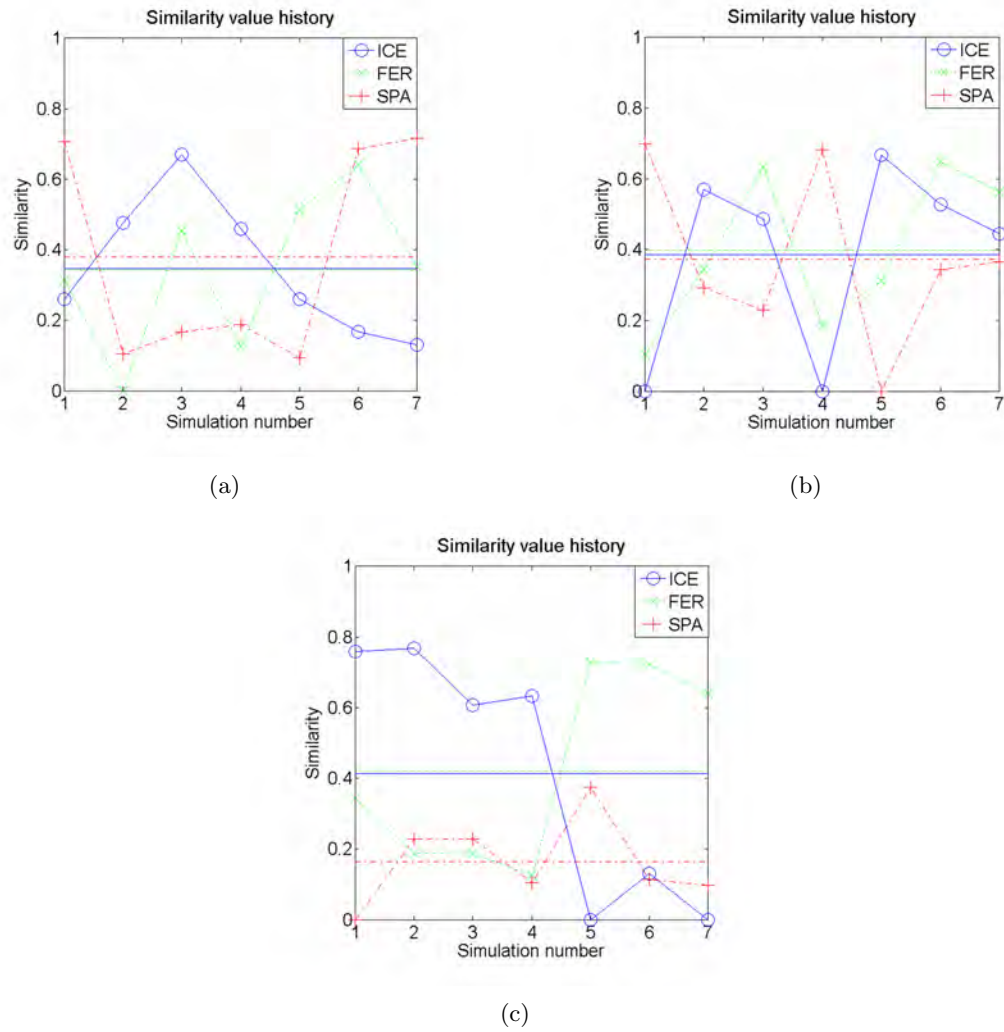


Figure 7.14: Similarity values retrieved for all the patterns (SPA  $\rightarrow$  Red/+, ICE  $\rightarrow$  blue/O, SPA  $\rightarrow$  green/x) when the SPA (a), ICE (b) and FER (c) model are processed for the Sen\_X sensor under the environmental conditions summarized in Table 7.8.

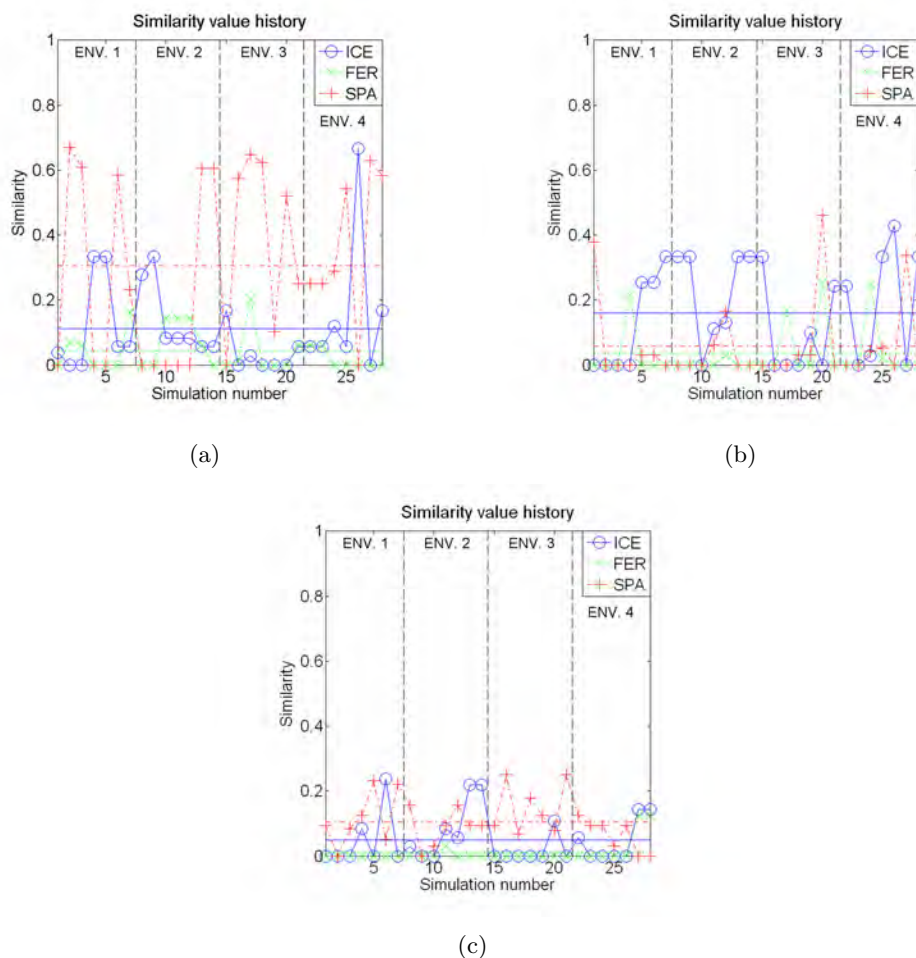


Figure 7.15: Similarity values retrieved for all the patterns (SPA  $\rightarrow$  Red/+, ICE  $\rightarrow$  blue/O, SPA  $\rightarrow$  green/x) when the SPA (a), ICE (b) and FER (c) model are processed for the Sen\_X sensor under the environmental conditions summarized in Table 7.4. Polarimetric information is not considered in the correlation process.

The classification results provided by this no-polarimetry (np) version of PaulInSAR are gathered in Fig. 7.15. They correspond to the three vessel models processed for the environmental conditions of Table 7.4. As observed, the overall confidence of the method drops notably and, thus, the proper identification of vessels becomes very difficult. In this way, polarimetry appears to be important in vessel classification as more additional information channels related with the structure of vessels are available for the discrimination of the different geometries.



## 7.4 Summary

This Chapter has presented (for the first time to author's knowledge) a new vessel identification method based on polarimetric SAR interferometry (PaulInSAR). The basic rationale lies on the combined usage of polarimetry and interferometry for distinguishing different types of geometries according to the scattering and height information included in the images. The result is a three-dimensional map of scatterers that describe with good agreement the geometrical structure of vessels. With this map, reliable vessel identification may be possible. The only requirement is the generation of patterns that summarize, for a specific range of views, the three-dimensional scattering maps expected for the different vessels under monitoring. In the current work, the patterns have been defined via simulated images as they represent the simplest and cheapest way to do it. However, studies in real scenarios are more recommendable as they provide more accuracy.

In order to evaluate the performance of this new method, an Euclidean-based decision rule has been developed. It basically consists on comparing the three-dimensional locations of the hot spots measured in the images with the reference scatter distribution of each vessel to monitor. This rule has appeared to be efficient when the number of patterns is relatively low, as in the current work. It has the advantage to simplify image processing and to optimize processing time when large amounts of simulated images is the main goal. In the case that large pattern databases have to be managed, more sophisticated methodologies based on neural networks or genetic algorithms become advisable.

The test of PaulInSAR for different scenarios, sensors and vessels have shown a high ratio of positive matches even for adverse environmental conditions. Two main items have been analyzed, namely: 1) vessel motions and 2) sea-ship interaction. Other items such as sea clutter has been discarded although they are very important for the application in mind. The complexity on embedding them into the current version of *GRECOSAR* has been the main reason.

The technical constraints of PaulInSAR have been checked in terms of image resolutions, system baseline and polarimetric operating mode. The results have shown that the algorithm provides optimum results for a recommended resolution range of 1 - 3 m, an effective baseline of 30 m and fully-polarimetric modes. Such requirements are quite changing for orbital sensors, despite they are more reliable for the airborne ones. Next Chapter will further analyze such issue.

Therefore, this Chapter, in combination with the previous one, has shown that vessel identification in SAR imagery is reliable with the exploitation of PolInSAR systems. Otherwise, the available information appears to be not enough for achieving a reasonable confidence.



## Chapter 8

# SAR Sensor Configurations in Vessel Monitoring

This Chapter is devoted to study which SAR sensor configurations are useful in vessel monitoring. Although the work is based on the recommendations outlined in the previous Chapter, it is conceived to provide a general framework where the technological requirements that this application may impose can be analyzed, evaluated and solved. In the first part of the Chapter, a general overview of the basic theory regarding SAR sensor design is provided. The discussion is supported by a set of graphs that illustrate the main relations among the most important parameters. In the second part of the Chapter, these graphs are used to base the methodology that should be followed in order to find the optimum configuration. This will allow to test different proposals and provide guidelines for future designs.

### 8.1 Main Design Parameters

This section reviews the main parameters that have to be considered when tackling SAR design in vessel monitoring<sup>1</sup>. Jointly with the basic formulae, a set of plots that graphically illustrate the relations among these parameters are also included. They help to fix the range of feasible values as well as the main restrictions that may appear along the design process.

---

<sup>1</sup>The provided list of parameters is tentative and it has been developed under the basis to consider SAR design a general problem rather than a task for a particular sensor.

### 8.1.1 Basic Formulae

#### Operating Mode

According to the recommendations of the previous Chapter, single-pass Polarimetric Interferometric SAR (PolInSAR) systems are demanded as they provide multidimensional SAR data, essential in vessel identification. The inclusion of these new information channels adds some specific characteristics to SAR sensors that are going to be review following. The most important one lies on the necessity to emit more than one pulse within the time slot assigned to each orbital position. This modifies PRF requirements affecting, thus, the design of the antenna aperture (extensively of the azimuth resolution) as well as of swath coverage.

Mechanical and hardware aspects are also important. In fully-polarimetric systems, duplicates of the receiving chain are required in order to receive the information referred to horizontal and vertical polarization. The option to consider an unique receiving chain with two receiving antennas and a circulator has been discarded because in interferometric systems it will make quite difficult to deal with those PRF values required for the demanded resolutions. Note that two chains are useless in the transmitter because the two pulses related to horizontal and vertical polarizations can not be emitted at the same time.

Regarding single-pass interferometric systems, the necessity to have two receivers separated a specific physical distance is the main difficulty to solve. Two options are available, namely: 1) to share the same platform or 2) to use a twin sensor in *tandem* configuration. In the first situation, the slave receiver is integrated in the system platform by means of a mast which longitude is fixed by the geometrical baseline. This option is the cheapest one as it can share most of the electronic sub-systems for both antennas. However, it has an important disadvantage: the mast can experiment unexpected motions that can modify the nominal value of the synthesized baseline<sup>2</sup>. This avoids to accurately know the real baseline for latter InSAR processing. In order to compensate the phase errors due to baseline inaccuracies, mast motion has to be tracked [173]. This implies the usage of complex optic-based systems that increase design complexity and power requirements among others. In practical terms, mast motion limits the reliable baseline values that can be used. For instance, the SRTM mission carried out in 2000 over a Shuttle platform has shown the problems on managing real baselines of 60 meters [173].

The other option in InSAR systems is to completely reproduce the master sensor in a twin slave sensor flying almost parallel. This option is more expensive but has the advantage to allow a better confidence in the synthesized baseline avoiding the mechanical problems related with the mast. For such purpose, accurate attitude control is mandatory for keeping

---

<sup>2</sup>Phase problems related to the cable length and caused by the temperature gradients experimented by orbital sensors are also appreciable [172].

the positions of both sensors where expected. Note that twin systems do not increase in excess manufacturing costs as some processes can be shared for both. Hereinafter, twin sensors are considered as it is the option adopted for the incoming German TanDEM-X sensor [174]. This sensor is used as a basis in the later discussion.

### Timing schemes

The *timing schemes* are the timing schedule defined for transmitting and receiving the pulses. For PolInSAR systems, there are basically two main options, namely <sup>3</sup>: *Standard* and *Ping-Pong* configurations. In the former, the master antenna emits a signal and both master and slave receive the echoes. In the latter, each sensor emits and receives their own echoes sequentially. The timing schemes for both modes are respectively illustrated in Fig. 8.1 and 8.2. There, it can be observed that a master PRF ( $PRF_m$ ) higher than the effective one ( $PRF$ ) <sup>4</sup> is required in order to allow the polarimetric measurements within the time slot assigned to each azimuth position <sup>5</sup>. In this context, the following relation applies

$$PRF_m = nPRF \leq \frac{1}{\tau + \frac{2r_{far}}{c}} \quad (8.1)$$

where  $n$  is a factor due to polarimetric measurements ( $n = 2 \rightarrow$  Standard and  $n = 4 \rightarrow$  Ping-Pong) and  $r_{far}$  the far-range defined as the range between the sensor and farthest point illuminated by the antenna. In addition to PRF, both operating modes stand for different relations between the effective ( $B^\perp$ ) and real baseline ( $B_{real}^\perp$ ). In standard mode, the fact that both receivers share the reception of the signal makes the center of phase to be between both sensors and, hence,  $B^\perp = B_{real}^\perp/2$ . This does not happen for ping-pong operating modes where an efficient use of the geometrical baseline is achieved  $B^\perp = B_{real}^\perp$ .

For both standard and ping-pong operating schemes, it is possible to use efficient configurations in which the echo of a specific pulse is received  $k$  pulses after its emission. This allows to deal with higher PRF values that are essential for achieving high azimuth resolutions. In such a case, the timing schemes for  $k = 1$  are modified as observed in Fig. 8.3 and 8.4. The new upper bound for PRF is

$$PRF_m = nPRF \leq \frac{1}{2\tau + \frac{2(r_{far} - r_{near})}{c}} \quad (8.2)$$

<sup>3</sup>Stripmap mode is assumed.

<sup>4</sup>The effective PRF can be understood as the PRF related to the time slot between two successive orbital positions, i.e. the PRF value used in the SAR processing stage.

<sup>5</sup>Two receiving chains are assumed for horizontally- and vertically-polarized signals.

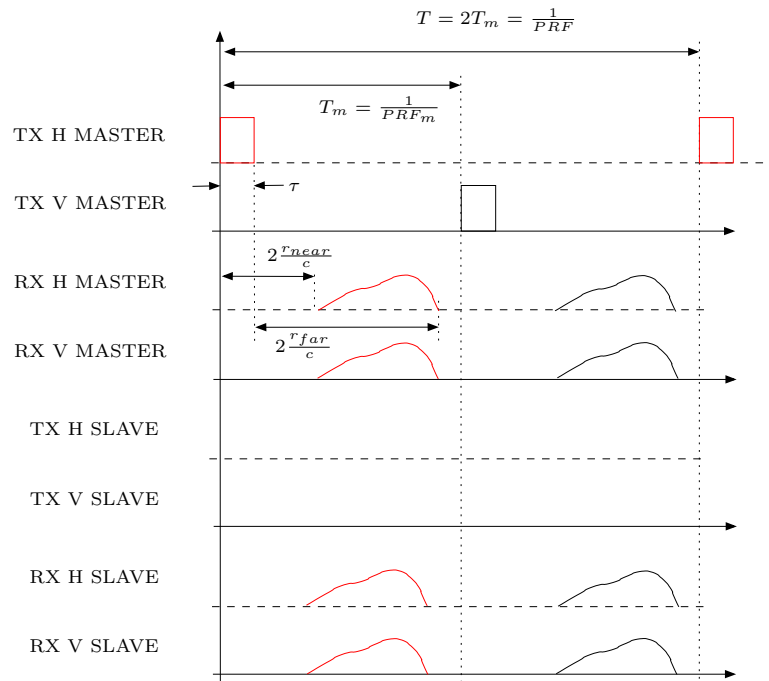


Figure 8.1: Timing scheme for standard PolInSAR imagery. Echo reception is just after the emission of the pulse.

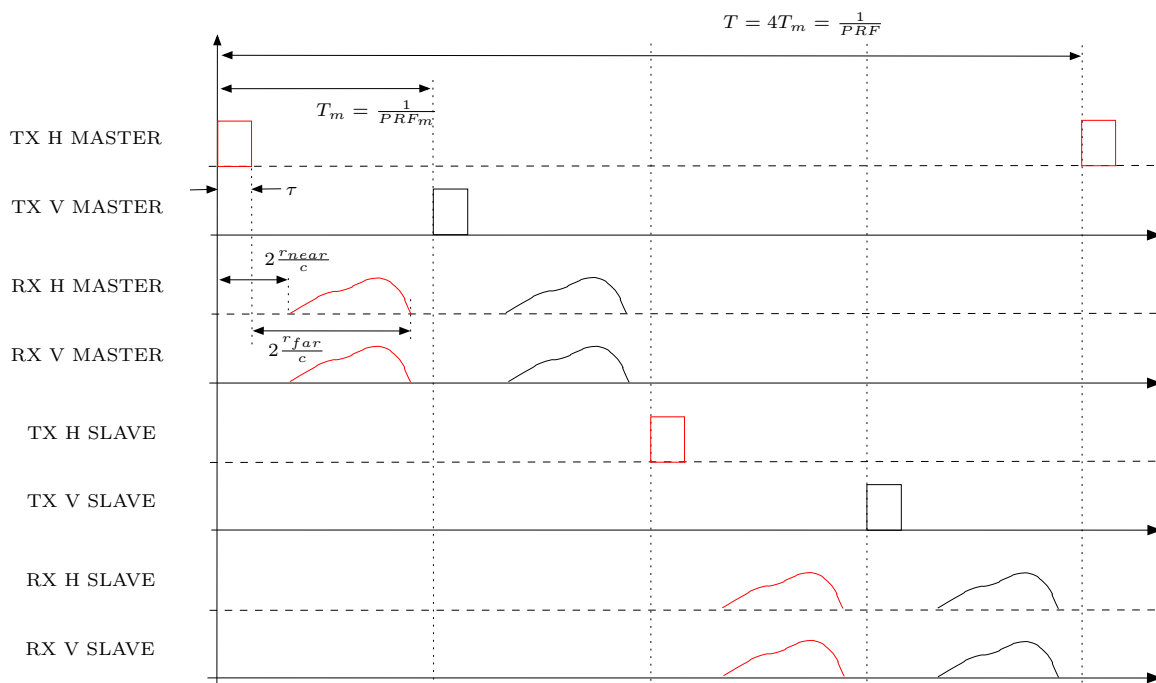


Figure 8.2: Timing scheme for ping-pong PolInSAR imagery. Echo reception is just after the emission of the pulse.

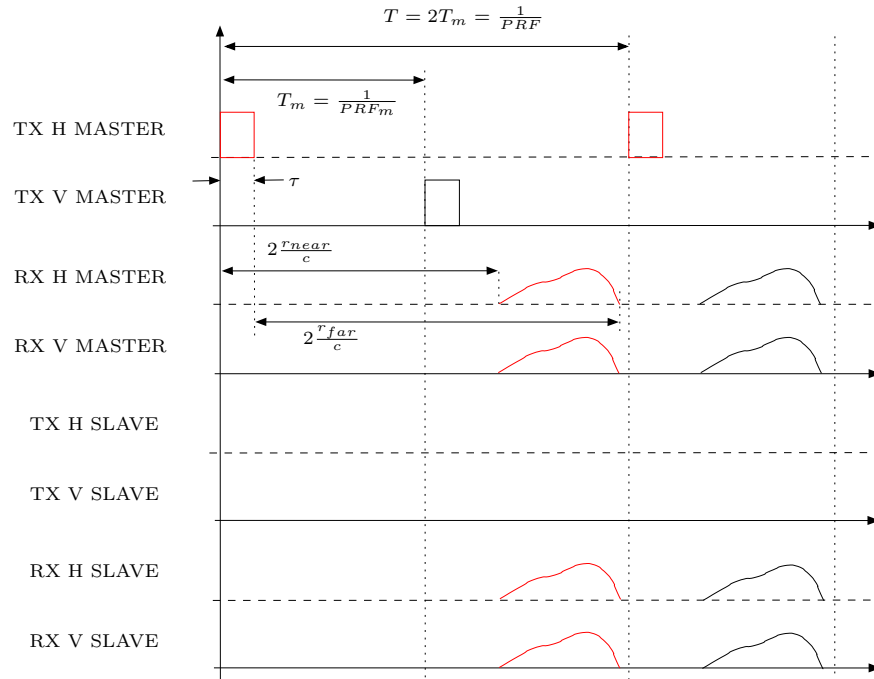


Figure 8.3: Timing scheme for standard PolInSAR imagery. Echo reception is  $k=1$  pulses after the emission of the pulse.

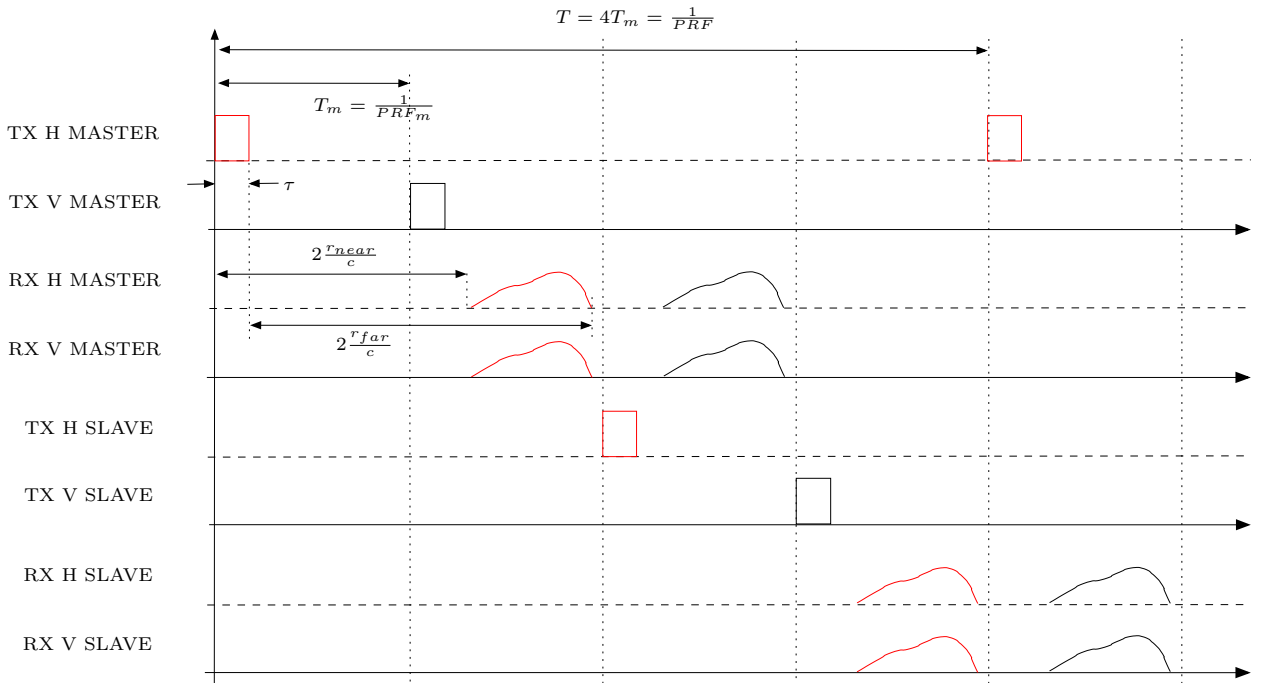


Figure 8.4: Timing scheme for ping-pong PolInSAR imagery. Echo reception is  $k=1$  pulses after the emission of the pulse.

where  $r_{near}$  is the near-range defined as the range between the sensor and nearest point illuminated by the antenna. Note that the factor  $2\tau + \frac{2(r_{far}-r_{near})}{c}$  is lower than the factor  $\tau + \frac{2r_{far}}{c}$  of Equation 8.2 and, hence, the upper bound is increased giving a wider margin for the design. This last configuration is the one adopted here.

### Swath Coverage

The range extension of the antenna footprint is

$$\Delta w_g = \frac{r_{near}\lambda}{L_r \cos \phi} \approx \frac{r_o\lambda}{L_r \cos \phi} \quad (8.3)$$

where  $L_r$  is the antenna length orthogonal to the azimuth and antenna pointing direction. If projected in the slant-range plane, this parameter results on

$$\Delta w = r_{far} - r_{near} \approx \frac{r_o\lambda \tan \phi}{L_r} \quad (8.4)$$

where  $r_{near}$  is normally evaluated with the mid-slant range  $r_o$ .

### PRF

As commented in Chapter 3 (Section 3.1.3), PRF has to be within a specific range of values in order to properly sample the azimuth spectra according to the Nyquist criteria. This range is defined by

$$PRF^{min} = k_{PRF} \frac{2V_{plat}}{L_a} \leq PRF \leq k_{PRF} \frac{1}{2n \cdot \left(\tau + \frac{\Delta w}{c}\right)} = PRF^{max} \quad (8.5)$$

where  $\tau$  is the pulse time extend,  $V_{plat}$  the platform velocity,  $L_a$  the real antenna aperture and  $k_{PRF} = 1.1$  a non-dimensional factor that provides a guard band oriented to avoid problems with aliasing. Due to the fact that  $PRF^{max} > PRF^{min}$ , the previous formula allows to fix an upper bound for the effective area of the antenna

$$L_r L_a \geq \frac{4nV_{plat}r_o\lambda}{c} \tan \phi \quad (8.6)$$

where it is assumed that  $\tau \ll \frac{\Delta w}{c}$ .



### Image resolutions

In real scenarios, image resolutions may be degraded when post-processing operations are used to improve the quality of SAR images. A typical operation is the windowing operation applied to the range spectrum that helps to reduce the weight of the sidelobes of the Point Spread Function (PSF) and, thus, improve the capability to detect weak targets close to the bright ones. According to the adopted criteria, different factors and windows can be used. In this work, the Hamming window with a reduction factor of  $k_r = 1.2$  has been used as a similar criteria has been adopted by TerraSAR-X [175]. This modify the actual resolution value by

$$\delta'_r = k_r \frac{c}{2\Delta f} \quad (8.7)$$

For the azimuth resolution, it is very usual to deliberately limit the available bandwidth in order to reduce the ambiguities caused by the finite sampling of the doppler spectrum and, hence, improve the shape of PSF. In this case, a degradation factor of  $k_a = 1.2$  is used according to TerraSAR-X's recommendations [175]. This modifies the expression of the azimuth resolution by

$$\delta'_{azi} = k_a k_v \frac{L_a}{2} \quad (8.8)$$

where  $k_v = 0.9$  is the orbital factor due to the orbital imaging geometry (see Equation 3.19 in Chapter 3).

### Duty cycle

For polarimetric systems, the duty cycle  $D_c$  is equal to

$$D_c = 100 \cdot \tau \cdot PRF_m = 100 \cdot \tau \cdot n \cdot PRF \quad [\%] \quad (8.9)$$

where  $D_c$  is defined within  $15 \leq D_c \leq 20$ . This range of values is selected according to the design values of some incoming orbital sensors, such as TerraSAR-X [176] and RADARSAT-2 [35]. Note that for extreme situations duty cycle problems can be partially solved by adopting different chirp signals with different chirp rates.

## Revisit Time

The revisit time is defined as the time a specific area of Earth surface can be imaged with the same imaging geometry. This time is initially fixed for TerraSAR-X in 11 days [177]. However, thanks to the electronically steerable antenna this area can be observed more frequently with different incidence angles. This will allow to take, once the TanDEM mission becomes operative, 12 different interferometric pairs in a slot time of 12 days<sup>6</sup>. But Chapter 6 has revealed that the scattering response of vessels may notably vary with respect to vessel bearing for incidence angles higher than 40°. So, those acquisition geometries with an incidence angle higher than such threshold are not suitable for vessel identification. This restricts the number of feasible interferometric pairs in six with an acquisition scheme of 1-3-2-1-1 days (slot time of 9 days). From these six pairs, three are acquired for antenna direction looking to the right whereas the other three for antenna direction looking to the left. According to TerraSAR-X specifications, left look direction has some operational deficiencies [177] and, hence, the related pairs have to be discarded.

As a result, a specific area can be monitored with TanDEM-X three times in 7 days with a acquisition scheme of 5-1 days. This fixes the revisit time in 5 days. For tracking individual vessels, such value are not suitable (in such a case, airborne sensors may provide better operational solutions), but for monitoring an specific area, they are not useless at all.

### 8.1.2 Comparative Graphs

The previous section has shown that the important parameters in SAR sensors are interconnected among them and, thus, it is not normally possible to modify a parameter without affecting the value of the other ones. In this context, the starting point has to be fixed by a set of *key parameters* which values are determined by the requirements imposed by the pursued application. In vessel identification, these key parameters are image resolutions and swath coverage. For the former, the recommended range of values should be lower than 3 m (see Chapter 7) whereas for the latter should be higher than 10 km.

Before tackling SAR sensor design, it is very instructive to analyze a set of plots where the relations among the key parameters are illustrated. They give an idea about the range of feasible values that should be used and the strategies that should be followed in order to properly tune the different parameters according to the imposed requirements. One simple way to do this lies on plotting 3D surface plots of  $PRF^{min}$  and  $PRF^{max}$  in terms of  $\delta'_{azi}$ ,  $\delta'_r$  and  $\Delta w_g$ . Certainly, these plots allow to easily recognize those values where sensor design is reliable according to the areas where  $PRF^{max} \geq PRF^{min}$ . In addition, they help to observe

---

<sup>6</sup>These numbers correspond to a simulation carried out by DLR for the test site of Oberpfaffenhofen (Germany) at 49° latitude within one orbital cycle.

the weight of each key parameter in the design process, and which can easily take values close to the ideal ones and which not. Some examples of these graphs are presented in Fig. 8.5 - 8.8. They are related to Standard (Fig. 8.5 - 8.6) and Ping-Pong (Fig. 8.7 - 8.8) operating modes for different swath coverage values.

In these figures, the  $PRF^{max}$  surface graph is colored whereas the  $PRF^{min}$  one not. In red, there are the areas of feasible resolution values that meet the two following conditions, namely: 1)  $PRF^{max} > PRF^{min}$  and 2)  $\delta_r, \delta_{azi} < 3$ . For those image resolutions where the first condition is not met, the values of  $PRF^{max}$  are highlighted in gray. If the second condition is not met, the blue color is used. The analysis of these images shows the following items, namely:

1. In all the cases, the larger the coverage the lower the area of feasible values. Certainly, for larger coverage the slope of  $PRF^{max}$  decreases making both graphs to keep closer.
2. Good range resolution values ( $1 < \delta_r < 1.5$ ) can be achieved with reasonable azimuth values ( $\delta_{azi} < 3$ ). This does not apply for the azimuth dimension as the asymptotic behavior of  $PRF^{min}$  forces to use large range resolutions ( $\delta_r > 3$ ) in order to achieve accurate azimuth resolutions ( $1 < \delta_{azi} < 1.5$ ). This sets the azimuth resolution one of the most restrictive parameters in the SAR design.
3. In Ping-Pong operating modes, large swath coverage ( $\Delta w_g$ ) is not reliable because the number of measurements required within the slot time of each position are so high than the PRF margin is reduced in excess. This is the compensation for maximizing the geometrical baseline.

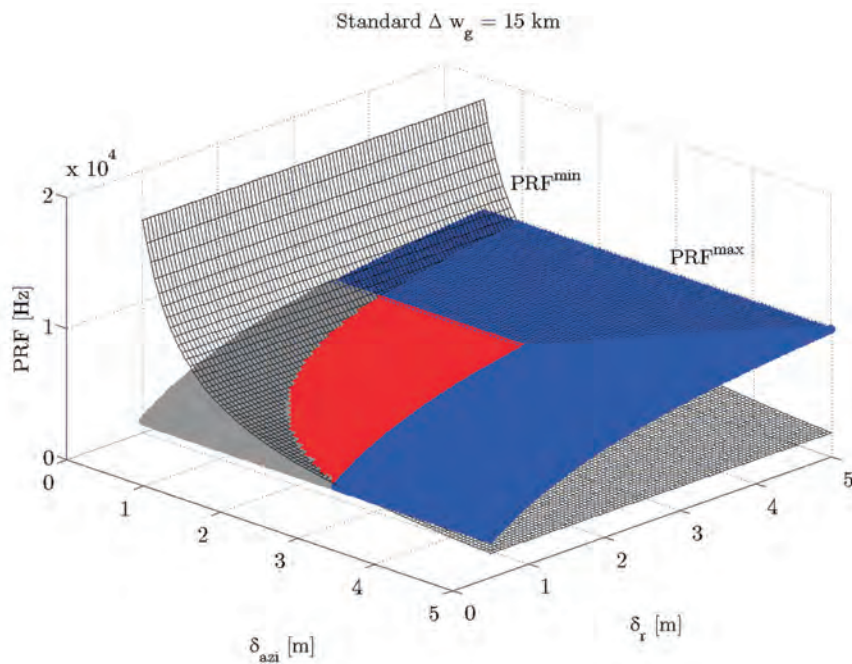
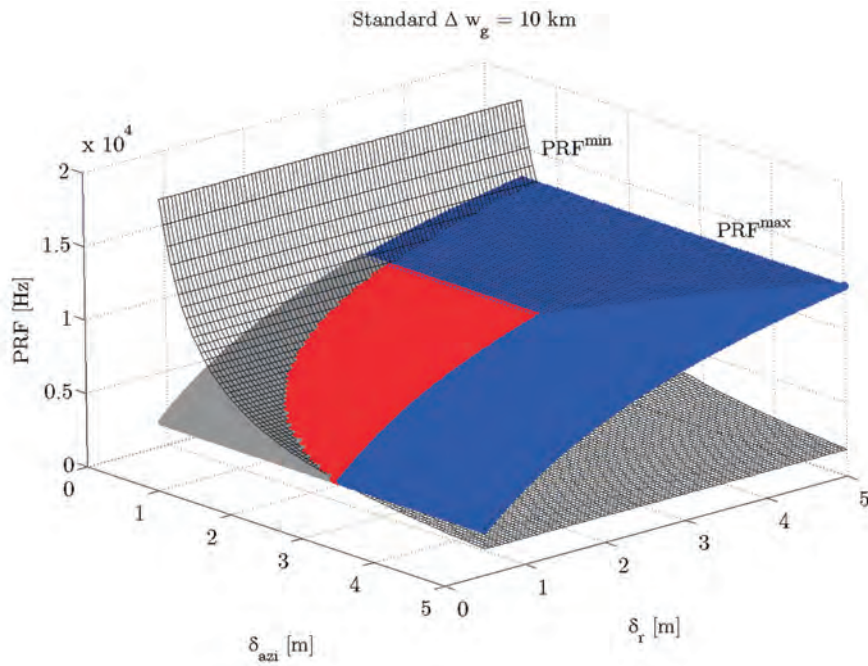


Figure 8.5: Comparative graphs showing the values of  $PRF^{max}$  and  $PRF^{min}$  as a function of range and azimuth resolutions for a swath coverage of 10 km (a) and 15 km (b). Standard operating mode is assumed with  $K = 6 \cdot 10^{12}$  and  $V_{plat} = 7686$  m/s.

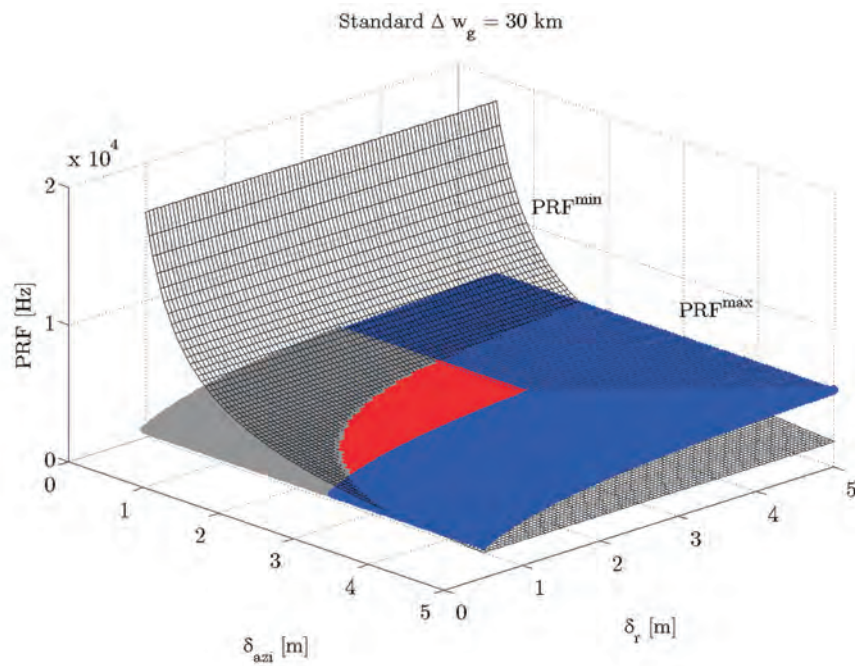
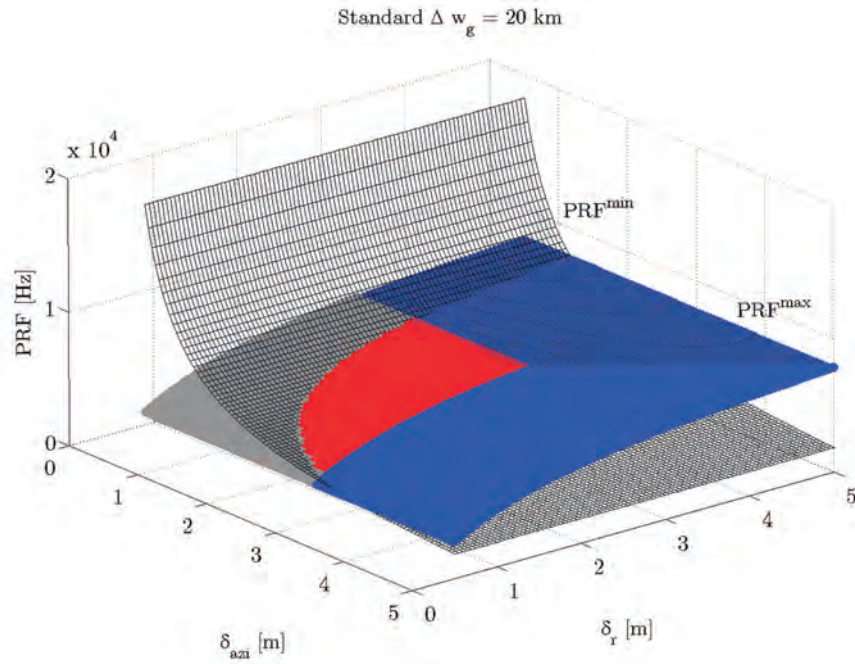


Figure 8.6: Comparative graphs showing the values of  $PRF^{max}$  and  $PRF^{min}$  as a function of range and azimuth resolutions for a swath coverage of 20 km (a) and 30 km (b). Standard operating mode is assumed with  $K = 6 \cdot 10^{12}$  and  $V_{plat} = 7686$  m/s.

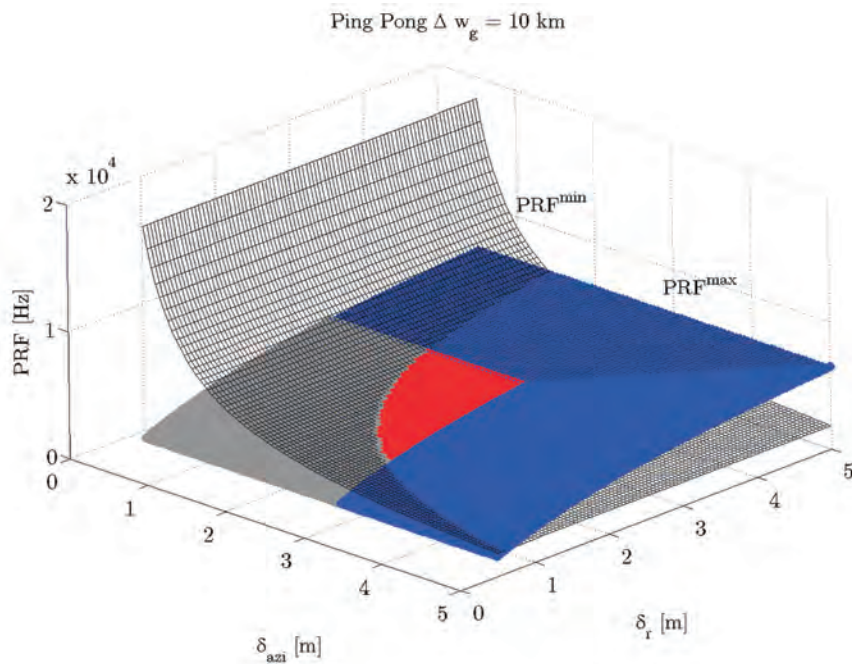
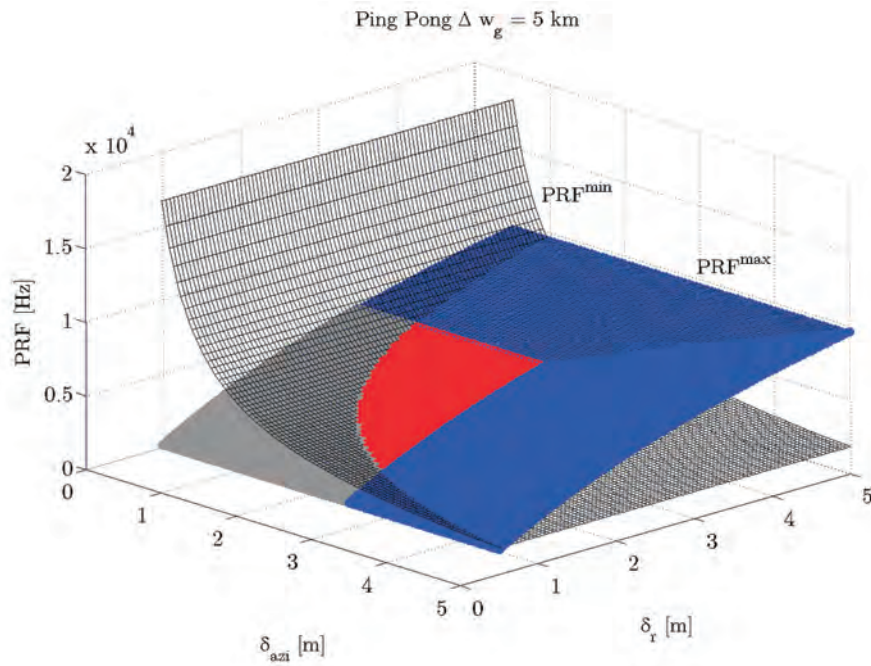
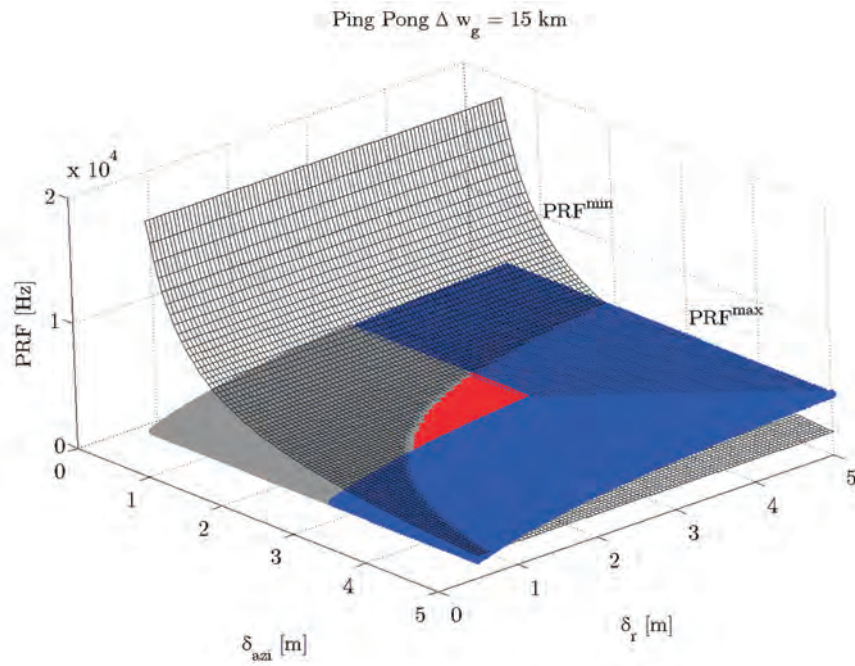
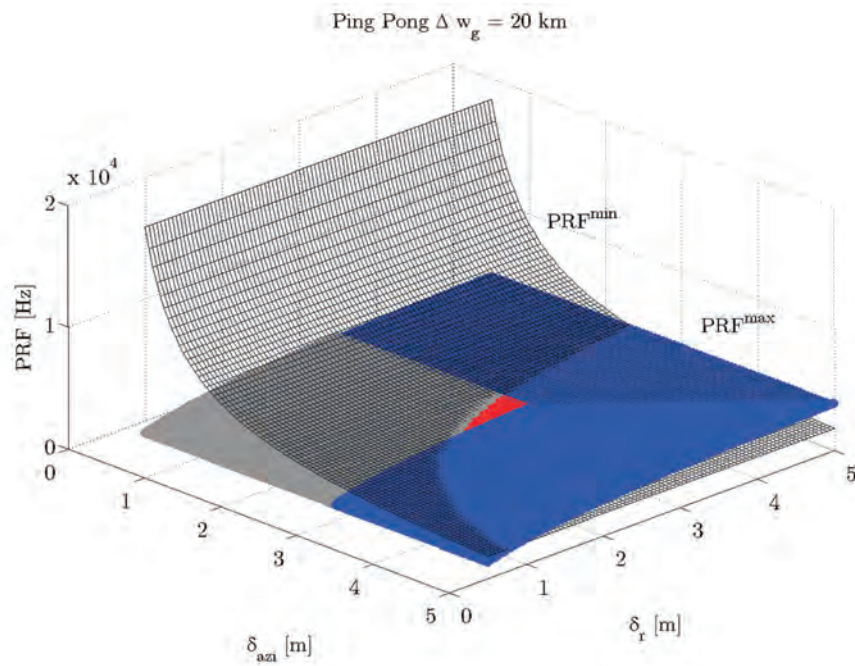


Figure 8.7: Comparative graphs showing the values of  $PRF^{max}$  and  $PRF^{min}$  as a function of range and azimuth resolutions for a swath coverage of 5 km (a) and 10 km (b). Ping-pong operating mode is assumed with  $K = 6 \cdot 10^{12}$  and  $V_{plat} = 7686$  m/s.



(a)



(b)

Figure 8.8: Comparative graphs showing the values of  $PRF^{max}$  and  $PRF^{min}$  as a function of range and azimuth resolutions for a swath coverage of 15 km (a) and 20 km (b). Ping-pong operating mode is assumed with  $K = 6 \cdot 10^{12}$  and  $V_{plat} = 7686$  m/s.

## 8.2 SAR Design

The concepts reviewed in the previous section are used to test different designs. In all the cases, the incidence angle ( $\phi = 20^\circ$ ) and the perpendicular baseline ( $B^\perp = 20, 30$ ) are updated according to the parameters used in Chapter 7. The current work should be understood as a preliminary discussion about the possibilities to find a particular configuration that can be exploited for vessel classification. In any case, the provided parameters has to be considered definitive, but tentative for guiding the design of future sensors.

### 8.2.1 Standard Mode

This section analyzes the possible PolInSAR designs working in standard mode. Three different configurations are proposed, namely: 1) the  $Sen\_ST_{v1.0}$  sensor summarized in Table 8.1 and providing an azimuth x range resolution of 2.4 x 1.2 m, close to the ideal sensor adopted in Chapter 7 (see Table 7.1); 2) the  $Sen\_ST_{v2.0}$  sensor summarized in Table 8.2 and providing an azimuth x range resolution of 2.7 x 1.4 m and 3) the  $Sen\_ST_{v3.0}$  sensor summarized in Table 8.3 and providing an azimuth x range resolution of 3.2 x 1.8 m. In all the cases, the orbit of TanDEM-X has been adopted [175]<sup>7</sup> and  $PRF = PRF^{min} + (PRF^{max} - PRF^{min})/4$ .  $\Delta_{f_D}$  stands for the processed doppler bandwidth.

In the light of these designs some comments are in order

1. The three designs provide enough image resolution for vessel identification.
2. In the  $Sen\_ST_{v1.0}$  sensor, PRF is the most restrictive parameter as the adopted value is not quite usual. However, it is not unrealistic at all because there are some examples in other application areas where such value is used in real devices [178].
3. In the  $Sen\_ST_{v2.0}$  and  $Sen\_ST_{v3.0}$  sensors, the design parameters are more usual (in some cases close to the nominal values of TanDEM-X) allowing to reach a swath coverage between 20 and 30 km.
4. In summary, it appears that in standard mode it is possible to reach a sensor configuration close to the ideal one defined in Chapter 7. The only disadvantage is that the real baseline should be equal at least to 40 m, but preferably to 60 m. SRTM-like missions can support such a value, but tandem solutions appears to be more efficient in the long term.

---

<sup>7</sup>The height is measured at the equator, the ascending node provides in local time the equatorial crossing time ( $18:00 \pm 0.25 h$ ), the number of Orbits/days is  $15 \frac{2}{11}$  and the azimuth extension of the image is limited to 1650 Km as this is the area that the TerraSAR-X sensor can cover in the unique non-stop acquisition available per orbit.



Table 8.1: Design proposal  $Sen\_ST_{v1.0}$  for standard operating mode ( $n = 2$ ) according to the ideal configuration.

Orbit					
Nominal height	514 Km	Inclination	97.44 [°]	Revisit time	5 days
Platform					
$L_a$	4.5 m	$L_r$	0.34 m	$B_{real}^\perp$	60 m
$V_{plat}$	7686 m	$\phi$	20 [°]	$r_o$	544 Km
Chirp signal					
$f_o$	9.65 Ghz	$\Delta_f$	150 MHz	$f_{FS}$	165 MHz
$\tau$	25 $\mu$ s	$K$	$6 \cdot 10^{12}$	Peak power	2 kW
$PRF$	4000 Hz	$PRF^{max}$	4700 Hz	$PRF^{min}$	3750 Hz
$PRF_m$	8000 Hz	Duty cycle	$\sim 19\%$	$\Delta_{fD}$	2850 Hz
Image					
$k_r$	1.2	$k_a$	1.2	$k_v$	0.9
$\delta'_r$	1.2 m	$\delta'_{azi}$	2.4 m	$\Delta\omega_g$	20 Km

Table 8.2: Design proposal  $Sen\_ST_{v2.0}$  for standard operating mode and based on the  $Sen\_ST_{v1.0}$  sensor defined in Table 8.1. The modified parameters are highlighted in blue.

Orbit					
Nominal height	514 Km	Inclination	97.44 [°]	Revisit time	5 days
Platform					
$L_a$	5 m	$L_r$	0.27 m	$B_{real}^\perp$	60 m
$V_{plat}$	7686 m	$\phi$	20 [°]	$r_o$	544 Km
Chirp signal					
$f_o$	9.65 Ghz	$\Delta_f$	125 MHz	$f_{FS}$	137.5 MHz
$\tau$	25 $\mu$ s	$K$	$5 \cdot 10^{12}$	Peak power	2 kW
$PRF$	3800 Hz	$PRF^{max}$	4200 Hz	$PRF^{min}$	3380 Hz
$PRF_m$	7600 Hz	Duty cycle	$\sim 16\%$	$\Delta_{fD}$	2560 Hz
Image					
$k_r$	1.2	$k_a$	1.2	$k_v$	0.9
$\delta'_r$	1.4 m	$\delta'_{azi}$	2.7 m	$\Delta\omega_g$	25 Km

Table 8.3: Design proposal  $Sen\_ST_{v3.0}$  for standard operating mode and based on the  $Sen\_ST_{v1.0}$  sensor defined in Table 8.1. The parameters modified with respect to the  $Sen\_ST_{v1.0}$  version are highlighted in green.

Orbit					
Nominal height	514 Km	Inclination	97.44 [°]	Revisit time	5 days
Platform					
$L_a$	6 m	$L_r$	0.23 m	$B_{real}^\perp$	60 m
$V_{plat}$	7686 m	$\phi$	20 [°]	$r_o$	544 Km
Chirp signal					
$f_o$	9.65 Ghz	$\Delta_f$	100 MHz	$f_{FS}$	111 MHz
$\tau$	25 $\mu$ s	$K$	$4 \cdot 10^{12}$	Peak power	2 kW
$PRF$	3300 Hz	$PRF^{max}$	4000 Hz	$PRF^{min}$	2800 Hz
$PRF_m$	6600 Hz	Duty cycle	~ 14%	$\Delta_{fD}$	2135 Hz
Image					
$k_r$	1.2	$k_a$	1.2	$k_v$	0.9
$\delta'_r$	1.8 m	$\delta'_{azi}$	3.2 m	$\Delta\omega_g$	30 Km

## 8.2.2 Ping-Pong Mode

This section explores the possibility to perform reliable designs with the Ping-Pong operating mode. As before, three designs are proposed, namely: 1) the  $Sen\_PP_{v1.0}$  sensor summarized in Table 8.4 and providing an azimuth x range resolution of 2.6 x 1.4, 2) the  $Sen\_PP_{v2.0}$  sensor summarized in Table 8.5 and providing an azimuth x range resolution of 3.2 x 1.8 m and 3) the  $Sen\_PP_{v3.0}$  sensor summarized in Table 8.6 and providing an azimuth x range resolution of 4.3 x 1.8 m. Again, the orbit of TanDEM-X has been adopted [175]<sup>8</sup> for  $PRF$  being defined as  $PRF = PRF^{min} + (PRF^{max} - PRF^{min})/4$ .  $\Delta_{fD}$  stands for the processed doppler bandwidth.

In the light of the results, some comments are in order.

1. In general, system performance is worse than for standard mode designs due to the high number of measurements within the slot time of each orbital position.
2.  $Sen\_PP_{v2.0}$  sensor appears to be the most efficient design with a swath coverage limited to 10 km. Certainly,  $Sen\_PP_{v1.0}$  deals with an extremely low swath width and high duty cycle whereas  $Sen\_PP_{v3.0}$  provides a poor azimuth resolution.

<sup>8</sup>The height is measured at the equator, the ascending node provides in local time the equatorial crossing time ( $18:00 \pm 0.25 h$ ), the number of Orbits/days is  $15 \frac{2}{11}$  and the azimuth extension of the image is limited to 1650 Km as this is the area that the TerraSAR-X sensor can cover in the unique non-stop acquisition available per orbit.

Table 8.4: Design proposal  $Sen\_PP_{v1.0}$  for ping-pong operating mode ( $n = 4$ ) according to the ideal configuration.

Orbit					
Nominal height	514 Km	Inclination	97.44 [°]	Revisit time	5 days
Platform					
$L_a$	4.6 m	$L_r$	1.4 m	$B_{real}^\perp$	30 m
$V_{plat}$	7686 m	$\phi$	20 [°]	$r_o$	544 Km
Chirp signal					
$f_o$	9.65 Ghz	$\Delta_f$	126 MHz	$f_{FS}$	138.2 MHz
$\tau$	18 $\mu$ s	$K$	$7 \cdot 10^{12}$	Peak power	2 kW
$PRF^9$	3950 Hz	$PRF^{max}$	4750 Hz	$PRF^{min}$	3700 Hz
$PRF_m$	15800 Hz	Duty cycle	26%	$\Delta_{f_D}$	2780 Hz
Image					
$k_r$	1.2	$k_a$	1.2	$k_v$	0.9
$\delta'_r$	1.4 m	$\delta'_{azi}$	2.5 m	$\Delta\omega_g$	5 Km

Table 8.5: Design proposal  $Sen\_PP_{v2.0}$  for ping-pong operating mode and based on the  $Sen\_PP_{v1.0}$  sensor defined in Table 8.4. The parameters modified with respect to the  $Sen\_PP_{v1.0}$  version are highlighted in blue.

Orbit					
Nominal height	514 Km	Inclination	97.44 [°]	Revisit time	5 days
Platform					
$L_a$	6.5 m	$L_r$	0.88 m	$B_{real}^\perp$	30 m
$V_{plat}$	7686 m	$\phi$	20 [°]	$r_o$	544 Km
Chirp signal					
$f_o$	9.65 Ghz	$\Delta_f$	100 MHz	$f_{FS}$	111 MHz
$\tau$	20 $\mu$ s	$K$	$5 \cdot 10^{12}$	Peak power	2 kW
$PRF$	2850 Hz	$PRF^{max}$	3600 Hz	$PRF^{min}$	2400 Hz
$PRF_m$	11600 Hz	Duty cycle	21%	$\Delta_{f_D}$	1970 Hz
Image					
$k_r$	1.2	$k_a$	1.2	$k_v$	0.9
$\delta'_r$	1.8 m	$\delta'_{azi}$	3.5 m	$\Delta\omega_g$	10 Km

Table 8.6: Design proposal  $Sen\_PP_{v3.0}$  for ping-pong operating mode and based on the  $Sen\_PP_{v1.0}$  sensor defined in Table 8.4. The parameters modified with respect to the  $Sen\_PP_{v1.0}$  version are highlighted in green.

Orbit					
Nominal height	514 Km	Inclination	97.44 [°]	Revisit time	5 days
Platform					
$L_a$	8.5 m	$L_r$	0.45 m	$B_{real}^\perp$	30 m
$V_{plat}$	7686 m	$\phi$	20 [°]	$r_o$	544 Km
Chirp signal					
$f_o$	9.65 Ghz	$\Delta_f$	100 MHz	$f_{FS}$	111 MHz
$\tau$	25 $\mu$ s	$K$	$4 \cdot 10^{12}$	Peak power	2 kW
$PRF$	2150 Hz	$PRF^{max}$	2670 Hz	$PRF_{eff}^{min}$	2000 Hz
$PRF_m$	8600 Hz	Duty cycle	20%	$\Delta_{fD}$	1500 Hz
Image					
$k_r$	1.2	$k_a$	1.2	$k_v$	0.9
$\delta'_r$	1.8 m	$\delta'_{azi}$	4.6 m	$\Delta\omega_g$	15 Km

### 8.3 Summary

This Chapter has shown that in InSAR systems two main configurations can be managed: standard and ping-pong. If the pursued application demands the maximum resolution and swath coverage possible, then sensors operating in standard mode have to be selected. In the opposite, if the geometrical baseline is the critical parameter ping-pong configurations become more suited. In vessel identification, the most important parameter is image resolution as identification performance varies notably for resolution values higher than 4 meters. So, sensors in standard mode seems advisable.

In this Chapter, different designs has been analyzed and they show that realistic configurations for reliable vessel identification may be possible. In fact, they are close to the configuration of the incoming TanDEM-X sensor. According to the obtained results, a preliminary design has been established. Their key features are, namely: operating frequency in X band, high incidence, single-pass interferometry in tandem configuration, fully-polarimetric capabilities, strimap imagery mode, image resolutions lower than 3 m, signal bandwidth up to 150 Mhz and swath coverage around 20 km. Note that this configuration is tentative and it has to be accurately tune with further research in this field. Other solutions based on spotlight imagery mode can also valid. In this case, the azimuth resolution increases whereas the azimuth extend of the image reduces.

## Chapter 9

# Conclusions

The work carried out in this thesis has shown that the combination of SAR polarimetry and SAR interferometry appears to be an efficient RS-based approach for complementing vessel monitoring. This proposal has been conceived in order to overcome the limitations of classical methods that are not able to *exclusively* and *completely* base a reliable classification algorithm. In the current methodology, the possibility to infer vessel geometrical features via robust and quantitative measurements that are almost insensitive to atmospheric conditions, day/night cycle and external devices is an advantageous help for the application in mind.

One of the main problems in vessel classification studies is related with the *quality* and *quantity* of real SAR data. On the one hand, current sensors present a set of technological limitations that avoid to take all the information demanded for achieving a proper identification performance. On the other hand, the lack of measurement flexibility in marine scenarios and the difficulties on retrieving accurate ground-truth limit the number of images currently available. In this framework, one of the main objectives of this thesis has been oriented to develop a SAR simulator of complex targets able to provide SAR images similar to those obtained in real scenarios. This goal has been fulfilled with the development of *GRECOSAR*. *GRECOSAR* is a numerical tool based on the UPC's EM solver *GRECO*<sup>®</sup> that estimates in the frequency domain the RCS of three-dimensional complex targets via high frequency methods. It simulates the SAR signal with two main operations, namely: 1) the simulation of the imaging geometry and 2) the synthesization of the SAR signal from EM estimates. The former implies the simulation of the orbit and environment in order to fix the point of view of the satellite. The latter simulates the different SAR signal terms according to the chirp signal and range history.

The tests carried out with *GRECOSAR* and *GRECO*<sup>®</sup> have shown that the derived SAR images are useful for vessel classification studies and, hence, the outlined conclusions can be in principle extrapolated to real scenarios. Three items are important in *GRECOSAR*, namely:

1) the computational efficiency that makes possible to process large vessels in a simple PC, 2) the sensor flexibility that allows to deal with diverse orbital sensors operating at different bands and with improved capabilities not available yet in actual systems and 3) the scenario flexibility that allows to evaluate vessel scattering in terms of some environmental conditions, for instance vessel bearing, vessel speed, vessel rotational and translational motions and sea surface. In contrast, the main limitation of *GRECOSAR* is the absence of sea dynamics along the observation time. This item has not been included because it is out of the scope of the current thesis more focused to the practical application of SAR imagery in vessel classification, rather than to the development and/or improvement of SAR simulation tools. Note that an accurate simulation of sea dynamics in a vessel SAR simulation framework is not an easy task and it needs from intensive research efforts that may lead to the development of a new thesis. The work may start by considering the sea a facet-based model with dielectric properties where the height information of the scene is updated at each orbital position according to the wave descriptive parameters.

In this thesis, *GRECOSAR* has been used to develop an exhaustive scattering study oriented to know which mechanisms are the responsible of the scattering behavior observed in SAR images. In a first step, polarimetric ISAR data with centimetric resolutions have been generated for different vessels, sensors and environmental conditions. Their analysis with CTD has allowed to identify which objects and geometries are behind the scattering mechanisms observed by radars. Four important points have been observed, namely: 1) the polarimetric scattering behavior of vessels is dominated by geometries with strongly polarized trihedral- and dihedral-like mechanisms; 2) each vessel has a particular scattering response that identifies its geometry and allows its discrimination with respect to other vessels; 3) the scattering maps of vessels are dominated by the response of few scatterers (*guide scatterers*) that present a high RCS and keep their scattering properties for a range of bearing values around  $30^\circ$  and of incidence angles around  $20^\circ$ ; and 4) the guide scatterers are mainly illustrated by the dihedral interaction performed at the base of cylindrical structures such as masts and by trihedral corner reflections as those generated in the buttresses.

The analysis of different operating frequencies has revealed that vessels preserve their scattering properties with frequency and, hence, they can provide a similar polarimetric response in different bands. As a result, the scattering behavior of vessels becomes independent from the electrical length and this can be used to estimate their overall dimension with SAR imagery (understood as the 3D distribution of scattering centers). In *GRECOSAR*, this property has allowed to scale down very large vessels in order to drop the number of analyzed samples and, hence, meet the memory requirements of the available PC. The suitability of this operation has been tested by comparing in different bands the data related to the original version of some models with the corresponding scaled ones. The results have shown that with this operation the scattering behavior of vessels is not modified in excess.

In a second step, the previous simulations have been repeated with SAR imagery taking both vessel motions and sea surface into account. The idea was to observe how the basic mechanisms of vessel scattering are combined in SAR images and if it is possible to base an identification procedure. In this case, two sensors have been considered, namely: 1) one emulating the ESA's ERS-1 satellite (C band) and 2) the other inspired in the incoming TerraSAR-X sensor (X band). The analysis of the obtained data with CTD have shown that with the proper resolution it is possible to observe the same scattering behavior than the one retrieved with the scattering maps. In this way, the following items apply, namely: 1) vessel scattering is similarly interpreted with any decomposition theorem as the main scattering centers present an almost pure trihedral- and dihedral-like behaviors; 2) the guide scatterers useful for vessel discrimination can be isolated with the same polarimetric behavior; 3) extreme bearings, for instance parallel or perpendicular to the sensor track, make the key scattering centers to be masked by strong mechanisms generated at the lateral side of the hull and/or cabin; and 4) the sea surface does not almost modify the results at high incidence. The most noticeable effect comes from vessel motions that distort the spatial distribution of the guide scatterers without affecting their polarimetric behavior. At low incidence, the sea generates dihedral-like mechanisms at the base of the hull that, under certain conditions, can mask and/or modify some of the key mechanisms.

According to the previous conclusions, it appears that polarimetry may provide useful information for vessel identification. In this context, it is mandatory to check these results with real data in order to know if the proposed ideas are valid. Such data should be acquired, if possible, for different environmental conditions and vessels, and they have to be associated accurate ground-truth. Some preliminary works are currently available in this field. They have shown the usefulness of polarimetry in vessel monitoring giving sense to some of the concepts outlined here. But although different works support the idea that polarimetry helps on vessel identification, it is important to realize that it does not provide enough information for basing a reliable decision rule. The main limitations are, namely: 1) the lack of quantitative measurements related to the geometrical features of vessels; 2) the mixing of the key mechanisms that can appear when image resolutions are not high enough according to vessel dimensions; and 3) the 2D SAR projection of the scene into the slant-range plane that generates a set of geometrical distortions that make the inversion of vessel geometry difficult. In addition, the presence of vessel motions can significantly alter the distribution of the mechanisms and, in extreme situations, the associated polarimetric behavior;

All the previous limitations may be solved up to certain extend if the third dimension of the scene is retrieved via single-pass interferometry. This makes possible the retrieval of three-dimensional maps of scatterers that can reproduce the scattering maps derived with ISAR imagery. In that way, vessel identification becomes more accurate and the development of the decision rule easier. This basis has been used to propose a novel vessel classification approach (PaulInSAR) working with single-pass PolInSAR imagery. It takes profit of the fact

that the main scattering centers of vessel SAR images behave as the Pauli mechanisms and, hence, their phase information can be isolated with the Pauli theorem. For such reason, this method combines polarimetric data analysis with height retrieval techniques. The adopted methodology is quite simple. The input data is analyzed with the Pauli theorem to derive an interferogram for each Pauli channel. Then, the height of the main scattering centers is used to build a three-dimensional map of scatterers that is correlated with a set of reference scattering maps. These maps identifies particular ships and according to the correlation result they permit the classification decision.

The reference scattering maps or patterns are derived from the analysis of ISAR data. They are built according to some PERmanent Polarimetric Scatters (PePS) (similar to the guide scatterers of ISAR images) that summarize the scattering behavior of vessels for a set of views. The role of PePS in vessel classification is quite important because they fix the resolution requirements and the degree of sensibility of the method with respect to the image distortions induced by vessel motions. In this sense, their selection accounts for two important considerations, namely: 1) the relative distance and height among PePS should be the maximum possible; and 2) they should be placed in areas where no other scatterers can interfere them. According to the different patterns, the method identifies the observed ship with that vessel model which pattern provides the highest similarity. This parameter is computed in terms of a 3D Euclidean norm between the location of the main scatterers isolated in SAR images and the location of PePS in the different patterns.

The performance of this new classification method has been tested at X band for different sensors managing diverse resolutions. The results have shown that PaulInSAR provide a good identification capability for image resolutions lower than 3 m. In addition, it presents a notable robustness against the image distortions caused by vessel motions and against the polarimetric interference induced by the sea-ship interaction. The analysis of different baselines shows that the method can deal with effective baselines of 20 m despite better confidence is achieved with 30 m. The necessity of polarimetry has become manifested in some additional tests carried out in one polarimetric channel. In that case, polarimetric information has not been taken into account in the decision rule and the three-dimensional location of the main scatterers has been the only available information for vessel discrimination. The results have given a low identification confidence as, in extreme situations, it is not possible to properly discriminate the vessels as happened when polarimetry was taken into account. So, PolSAR images are required for vessel identification, but in combination with the InSAR ones.

Therefore, it seems feasible that with single-pass PolInSAR imagery reliable vessel classification would be possible. For such goal, the forthcoming sensors have to fulfill some requirements. The most important ones are, namely: 1) they should operate at high incidence in order to drop the influence of the sea surface; 2) reliable designs are only possible for



tandem configurations operating in standard mode. In that case, the nominal swath coverage is not expected to be larger than 20-30 km despite lower values are recommended in order to avoid a restrictive PRF; and 3) image resolutions should be lower, if possible, than 3 m in order to deal with typical fishing vessels. Note that these requirements are only tentative and, in any case, they are not binding the design of future sensors. However, it has been shown that if they are not taken into account the performance of the method will be strongly related to the dimensions of the observed vessels.

In future works, it is essential to work in real scenarios in order to observe the vessel signatures retrieved by actual sensors. This will help to evaluate the polarimetric scattering of vessels and, extensively, if the proposed identification method has sense. In this field, ISAR measurements in anechoic chambers may be helpful for interpreting vessel scattering. However, there are currently few facilities where C and X band measurements can take place.

Before real data become available, some interesting points with simulated images have to be addressed. First of all, the extension of the pattern database is mandatory as with the current three vessel models an overestimation of the results may be observed. Once available, the improved database has to be evaluated for different scenarios and vessels in order to explore the limitations of the proposed method and the possible solutions that can overcome them. This process will demand improved versions of the simulation environment that allow to deal with more realistic scenarios. The extension of the current sea model with sea dynamics and sea clutter is the most important item. In parallel, the inclusion of neural networks and/or genetic codes in the decision rule is also advisable as these codes are more suited for managing the high number of patterns that the algorithm will have to deal with.

As a conclusion, the work developed in the current thesis has shown that only with PolInSAR systems a reliable classification algorithm could be possible (neither PolSAR nor InSAR appears to provide the demanded confidence). Such systems are not only useful in vessel monitoring, but also in other applications that are essential for better understanding the Earth and monitoring its natural activity. So, their promotion is important for the scientific community. The incoming German Tandem X mission scheduled at 2009 may be the seed for the development of new missions.



# Appendix A

## Coordinate Systems

This Appendix describes the coordinate systems used by GRECOSAR. Besides their definition in the space, the matrices allowing coordinate transformation are also presented.

### A.1 Definition

#### A.1.1 POCS

The POCS coordinate system provides the cartesian position of the satellite within the orbital plane. This system is strongly related with the so-called *Keplerian* parameters that fix the position of the orbital plane within the space.

1.  $a$ : Fixes the magnitude of the *semi-major* axis of the orbit. This parameter can be expressed in terms of the *mean motion* or the time of one revolution.
2.  $e$ : Fixes the *eccentricity* of the ellipse of the orbit.
3.  $T_o$ : Provides the time at which the Keplerian elements are defined (*epoch* of the orbit).
4.  $m_o$ : Fixes the *mean anomaly* or the position of the satellite inside the orbit at the epoch time. It is simply an angle that marches *uniformly* in time from 0 to 360 degrees during one revolution. For circular orbits with constant speeds, the mean anomaly points always to the satellite, but for elliptical orbits with non-constant velocities does not. There are only two points where this relation always holds with independence of the eccentricity, namely: 1) the *perigee* ( $m_o = 0$ ) and 2) the *apogee* ( $m_o = 180$ ). These points are respectively defined as the closest and farthest locations of the satellite with respect to the focus of the ellipse, normally located at the center of the Earth.

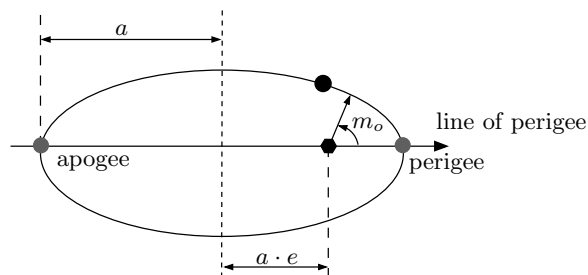


Figure A.1: Kepler parameters defining the shape of the orbit within the orbital plane.

5.  $\Omega$ : It is the *right ascension of the ascending node* that provides the angle, measured at the center of the Earth, between the *vernal equinox* ( $\Upsilon$ ) and the *ascending node*. On the one hand, the ascending node is the crossing point between the equatorial plane and orbit when the satellite goes from South to North. On the other hand, the vernal point is a reference point in the sky ( $\Omega = 0$ ) that defines the ascending node of the orbit of the sun.
6.  $\omega$  or the *argument of perigee* is the angle between the line of nodes and the line of perigee. The line of nodes links the ascending and descending nodes (the descending node is the complementary point of the ascending one) whereas the line of perigee links the perigee and the apogee.
7.  $i$  is the inclination of the orbit measured from the equatorial to the orbital plane. By convention, inclination is a number between 0 and 180 degrees.

The first four parameters describe the shape of the orbit within the orbital plane (see Fig. A.1) whereas the other three fix the position of this plane in the space (see Fig. A.2). The POCS system is defined as shown in Fig. A.2. There, the origin is at the center of the Earth (the focus of the ellipse), the x-axis points to perigee parallel to  $a$ , the y-axis points parallel to  $b$  (the semi-minor axis) and the z-axis is perpendicular to both.

### A.1.2 ECI

The ECI coordinate system is a static reference system with the origin at the center of the Earth. The x-axis points to  $\Upsilon$ , the z-axis points to the heavenly North Pole and the y-axis is perpendicular to both. It is illustrated in Fig. A.2.

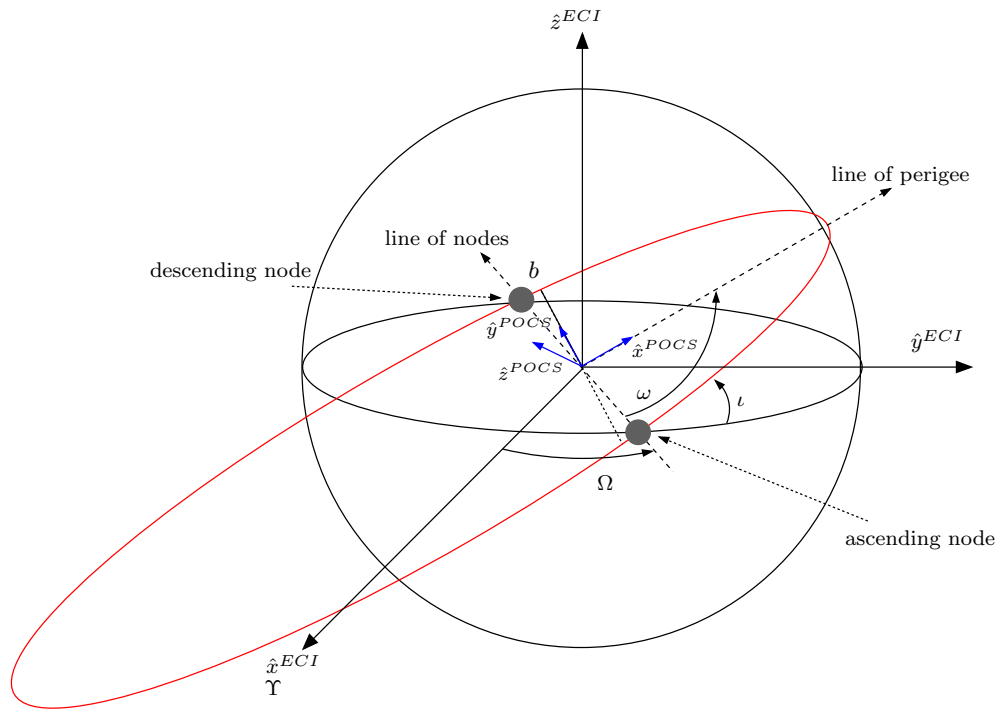


Figure A.2: Kepler parameters fixing the position of the orbital plane in the space. The blue axis generates the POCS coordinate system whereas the black ones the ECI coordinate system.

### A.1.3 ECEF

The ECEF system is in motion with the Earth having an angular motion of  $\omega_T \sim \frac{2\pi}{24 \cdot 3600}$ . The x-axis points to the intersection between the equator and the Greenwich meridian, the z-axis points to the heavenly North Pole and the y-axis is perpendicular to both. It is illustrated in Fig. A.3. Normally, the coordinates of a point are expressed in polar format with the triplet  $\{R, \Psi, \Phi\}$ .  $R = \sqrt{x^2 + y^2 + z^2}$  is the range,  $\Psi = \arctan \left[ \frac{y_{ecef}}{x_{ecef}} \right]$  the longitude angle and  $\Phi = \arctan \left[ \frac{z_{ecef}}{\sqrt{x_{ecef}^2 + y_{ecef}^2}} \right]$  the latitude angle. This angle is defined from 0 to  $90^\circ$  in the North hemisphere and from 0 to  $-90^\circ$  in the South one (see Fig. A.4).

### A.1.4 GRECO<sup>®</sup> system

For ascending/descending mode, GRECO<sup>®</sup> has the convention to define the x-axis pointing to the South/North, the z-axis pointing to the West/East and the y-axis pointing to the perpendicular of both. It is illustrated in Fig. A.4.

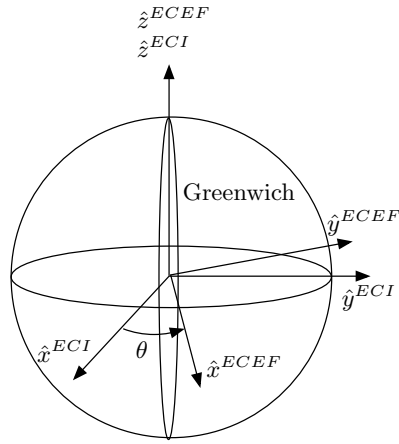


Figure A.3: The ECEF coordinate system

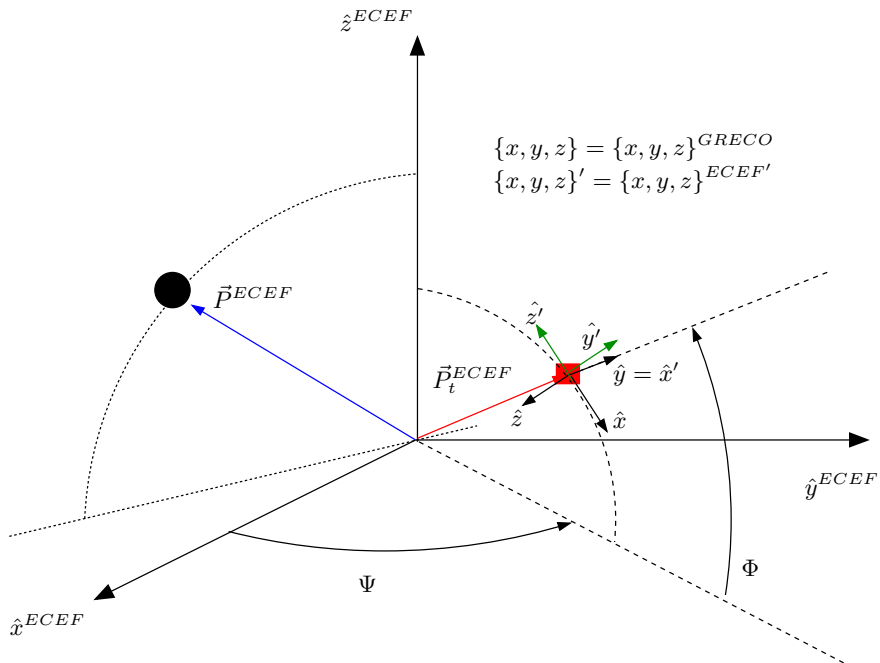


Figure A.4: The GRECO coordinate system. The green axes show the triplet  $\{x, y, z\}_{ecf'}$  useful for computing the  $ECEF \rightarrow GRECO$  transformation matrix.

## A.2 Transformation Matrices

### A.2.1 POCS $\rightarrow$ ECI

The POCS  $\rightarrow$  ECI transformation is achieved after applying the following Euler rotations <sup>1</sup> (see Fig. A.2):

1. Yaw rotation of  $-\omega$ ,  $[T_{-\omega}^{yaw}]$ .
2. Roll rotation of  $-\iota$ ,  $[T_{-\iota}^{roll}]$ .
3. Yaw rotation of  $-\Omega$ ,  $[T_{-\Omega}^{yaw}]$ .

Then, the transformation matrix is defined as

$$\begin{bmatrix} x \\ y \\ z \end{bmatrix}^{ECI} = [T_{-\Omega}^{yaw}][T_{-\iota}^{roll}][T_{-\omega}^{yaw}] \begin{bmatrix} x \\ y \\ z \end{bmatrix}^{POCS} = [T^{POCS \rightarrow ECI}] \begin{bmatrix} x \\ y \\ z \end{bmatrix}^{POCS} \quad (\text{A.1})$$

where

$$[T^{POCS \rightarrow ECI}] = \begin{bmatrix} \cos \Omega \cos \omega - \sin \Omega \cos \iota \sin \omega & \cos \Omega \sin \omega - \sin \Omega \cos \iota \cos \omega & \sin \Omega \sin \iota \\ \sin \Omega \cos \omega + \cos \Omega \cos \iota \sin \omega & -\sin \Omega \sin \omega - \sin \Omega \cos \iota \cos \omega & -\cos \Omega \sin \iota \\ \sin \omega \sin \iota & \cos \omega \sin \iota & \cos \iota \end{bmatrix} \quad (\text{A.2})$$

and

$$[T_{-\omega}^{yaw}] = \begin{bmatrix} \cos \omega & -\sin \omega & 0 \\ \sin \omega & \cos \omega & 0 \\ 0 & 0 & 1 \end{bmatrix} \quad (\text{A.3})$$

$$[T_{-\iota}^{roll}] = \begin{bmatrix} 1 & 0 & 0 \\ 0 & \cos \iota & -\sin \iota \\ 0 & \sin \iota & \cos \iota \end{bmatrix} \quad (\text{A.4})$$

$$[T_{-\Omega}^{yaw}] = \begin{bmatrix} \cos \Omega & -\sin \Omega & 0 \\ \sin \Omega & \cos \Omega & 0 \\ 0 & 0 & 1 \end{bmatrix} \quad (\text{A.5})$$

<sup>1</sup>Here, the so-called *x-convention* of Euler rotations is used. *Roll*, *pitch* and *yaw* terms are used to indicate rotations around x-, y- and z- axis respectively.

### A.2.2 ECI $\rightarrow$ ECEF

The ECI  $\rightarrow$  ECEF transformation is achieved after applying the following time-dependent yaw rotation

$$\begin{bmatrix} x \\ y \\ z \end{bmatrix}^{ECEF} = [T^{ECI \rightarrow ECEF}] \begin{bmatrix} x \\ y \\ z \end{bmatrix}^{ECI} \quad (\text{A.6})$$

where

$$[T^{ECI \rightarrow ECEF}] = \begin{bmatrix} \cos \theta & \sin \theta & 0 \\ -\sin \theta & \cos \theta & 0 \\ 0 & 0 & 1 \end{bmatrix} \quad (\text{A.7})$$

and  $\theta = \omega_T t$  for  $-\frac{t_{obs}}{2} \leq t \leq \frac{t_{obs}}{2}$ . This time-dependence makes the transformation rule for the velocity vector to be

$$\frac{d}{dt} \begin{bmatrix} x \\ y \\ z \end{bmatrix}^{ECEF} = \frac{d}{dt} [T^{ECI \rightarrow ECEF}] \begin{bmatrix} x \\ y \\ z \end{bmatrix}^{ECI} + [T^{ECI \rightarrow ECEF}] \frac{d}{dt} \begin{bmatrix} x \\ y \\ z \end{bmatrix}^{ECI} \quad (\text{A.8})$$

with

$$\frac{d}{dt} [T^{ECI \rightarrow ECEF}] = \begin{bmatrix} -\sin \theta & \cos \theta & 0 \\ -\cos \theta & -\sin \theta & 0 \\ 0 & 0 & 1 \end{bmatrix} \omega_T \quad (\text{A.9})$$

### A.2.3 ECEF $\rightarrow$ GRECO

The ECEF  $\rightarrow$  GRECO transformation needs the following procedure, namely:

1. Yaw rotation of angle  $\Psi$ .
2. Pitch rotation of angle  $\Phi$ .
3. Apply the following axis modifications,  $\hat{x}_{GRECO} = -\hat{z}_{ecef'}$ ,  $\hat{y}_{GRECO} = \hat{x}_{ecef'}$  and  $\hat{z}_{GRECO} = -\hat{y}_{ecef'}$  where  $\{x, y, z\}_{ecef'}$  is the coordinate system resulting after the yaw and pitch rotations.



So,

$$\begin{bmatrix} x \\ y \\ z \end{bmatrix}^{ECEF'} = [T_{\Phi}^{pitch}][T_{\Psi}^{yaw}] = [T^{ECEF \rightarrow ECEF'}] \begin{bmatrix} x \\ y \\ z \end{bmatrix}^{ECEF} \quad (\text{A.10})$$

where

$$[T^{ECEF \rightarrow ECEF'}] = \begin{bmatrix} \cos \Phi \cos \Psi & \cos \Phi \sin \Psi & \sin \Phi \\ -\sin \Psi & \cos \Psi & 0 \\ -\sin \Phi \cos \Psi & -\sin \Phi \sin \Psi & \cos \Phi \end{bmatrix} \quad (\text{A.11})$$

and

$$[T_{\Psi}^{yaw}] = \begin{bmatrix} \cos \Psi & \sin \Psi & 0 \\ -\sin \Psi & \cos \Psi & 0 \\ 0 & 0 & 1 \end{bmatrix} \quad (\text{A.12})$$

$$[T_{\Phi}^{pitch}] = \begin{bmatrix} \cos \Phi & 0 & -\sin \Phi \\ 0 & 1 & 0 \\ \sin \Phi & 0 & \cos \Phi \end{bmatrix} \quad (\text{A.13})$$

Finally, it follows that

$$\begin{bmatrix} x \\ y \\ z \end{bmatrix}^{GRECO} = [T^{ECEF' \rightarrow GRECO}] \begin{bmatrix} x \\ y \\ z \end{bmatrix}^{ECEF'} \quad (\text{A.14})$$

with

$$[T^{ECEF' \rightarrow GRECO}] = \begin{bmatrix} \sin \Phi \cos \Psi & \sin \Phi \sin \Psi & -\cos \Phi \\ \cos \Phi \cos \Psi & \cos \Phi \sin \Psi & \sin \Phi \\ \sin \Psi & -\cos \Psi & 0 \end{bmatrix} \quad (\text{A.15})$$



## Appendix B

# Yaw steering in *GRECOSAR*

This Appendix describes the two main blocks required to simulate the yaw steering process in *GRECOSAR*, namely: 1) Compute Position and 2) Compute Doppler Centroid ( $f_d$ ).

### B.1 Compute position

According to the location of the satellite at the middle of the aperture ( $\vec{P}^{ECI}|_{m'_o=m_o}$ )<sup>1</sup> and the antenna pointing fixed by  $(\varphi, \vartheta)$ , the position of the target over the Earth surface ( $\vec{P}_t^{ECI} = P_{earth}$ ) can be obtained by

$$\vec{P}_t^{ECI} = \vec{P}^{ECI}|_{m'_o=m_o} + r\hat{P}_{s \rightarrow t}^{ECI} \quad (\text{B.1})$$

where  $\hat{P}_{s \rightarrow t}^{ECI}$  is the sensor-to-target unitary vector and  $r$  the sensor-to-target range, as shown in Fig. B.1. The vector  $\hat{P}_{s \rightarrow t}^{ECI}$  is calculated in four main steps, namely:

1. Define the local coordinate system  $\{\hat{x}^s, \hat{y}^s, \hat{z}^s\}$  where  $\hat{x}^s = \vec{P}^{ECI}/|\vec{P}^{ECI}|$ ,  $\hat{y}^s = \vec{P}^{ECI} \times \vec{P}^{ECI}/|\vec{P}^{ECI} \times \vec{P}^{ECI}|$ ,  $\hat{z}^s = \vec{P}^{ECI}/|\vec{P}^{ECI}|$ . As shown in Fig. B.1,  $\vec{P}^{ECI}$  and  $\vec{P}^{ECI}$  are the position and velocity unitary vectors of the satellite.
2. Define the transformation matrix from this local coordinate system to ECI via the

---

<sup>1</sup> $\vec{P}^{ECI}|_{m'_o=m_o}$  is obtained by evaluating Equations 5.26 - 5.38 with the medium anomaly parameter  $m_o$  provided by the user.

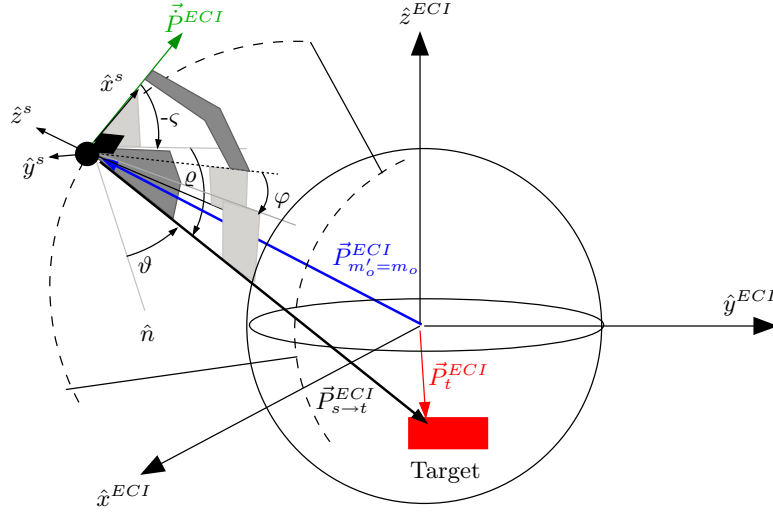


Figure B.1: Local coordinate system demanded for computing  $\hat{P}_{s \rightarrow t}^{ECI}$

direction cosine. The result is

$$[T^{local \rightarrow ECI}] = \begin{bmatrix} \hat{x}^{ECI} \cdot \hat{x}^s & \hat{x}^{ECI} \cdot \hat{y}^s & \hat{x}^{ECI} \cdot \hat{z}^s \\ \hat{y}^{ECI} \cdot \hat{x}^s & \hat{y}^{ECI} \cdot \hat{y}^s & \hat{y}^{ECI} \cdot \hat{z}^s \\ \hat{z}^{ECI} \cdot \hat{x}^s & \hat{z}^{ECI} \cdot \hat{y}^s & \hat{z}^{ECI} \cdot \hat{z}^s \end{bmatrix} \quad (B.2)$$

3. Select the  $\hat{x}^s$  axis and apply the rotations demanded to simulate the squint  $\varphi$  and look  $\vartheta$  angle. According to the geometry of Fig. B.1, the first angle needs a yaw rotation whereas the second one a pitch rotation. The matrices of such rotations are

$$[T_{\vartheta}^{yaw}] = \begin{bmatrix} \cos \varrho & \sin \varrho & 0 \\ -\sin \varrho & \cos \varrho & 0 \\ 0 & 0 & 1 \end{bmatrix} \quad (B.3)$$

$$[T_{\varsigma}^{pitch}] = \begin{bmatrix} \cos \varsigma & 0 & -\sin \varsigma \\ 0 & 1 & 0 \\ \sin \varsigma & 0 & \cos \varsigma \end{bmatrix} \quad (B.4)$$

where  $\varrho = \pm 90 + \varphi$  and  $\varsigma = -(90 - \vartheta)$ . In this expression, the sign indeterminacy illustrates the pointing criteria of the satellite, rightwards (sign +) or leftwards (sign -).  $\vartheta$  is defined counterclockwise from the nadir direction  $\hat{n}$

$$\hat{n} = \begin{bmatrix} \cos -90 & 0 & -\sin -90 \\ 0 & 1 & 0 \\ \sin -90 & 0 & \cos -90 \end{bmatrix} \hat{x}^s \quad (B.5)$$

4. Find  $\hat{P}_{s \rightarrow t}^{ECI}$  as

$$\hat{P}_{s \rightarrow t}^{ECI} = [T^{local \rightarrow ECI}] [T_{\varrho}^{yaw}] [T_{\zeta}^{pitch}] \begin{bmatrix} 1 \\ 0 \\ 0 \end{bmatrix} \quad (\text{B.6})$$

Once  $\hat{P}_{s \rightarrow t}^{ECI}$  is found,  $r$  is fixed by minimizing the following cost function

$$F(r) = \left| \vec{P}^{ECI} |_{m'_o=m_o} + r \hat{P}_{s \rightarrow t}^{ECI} - R_T \right| \quad (\text{B.7})$$

where  $R_T$  indicates a height equal to 0, as happens on the sea. Finally,  $\vec{P}_t^{ECI}$  becomes

$$\vec{P}_t^{ECI} = \vec{P}^{ECI} |_{m'_o=m_o} + r_o \hat{P}_{s \rightarrow t}^{ECI} \quad (\text{B.8})$$

where  $F(r_o) \cong 0$ . The position vector of the target in ECEF is the same as in ECI because  $\vec{P}_t^{ECI}$  has been computed for the satellite position at the middle of the aperture. In such a case, the time variable  $t$  in Equation A.7 becomes 0 and, hence,  $[T^{ECI \rightarrow ECEF}]$  in Equation A.7 is equal to the unitary matrix. In polar format, the coordinates of the target position expressed in the ECEF reference ellipsoid WGS-84 are

$$\Psi = \arctan \left\{ \frac{y_{ecef}}{x_{ecef}} \right\} \quad (\text{B.9})$$

$$\Phi = \arctan \left\{ \frac{z_{ecef} + \frac{a^2 - b^2}{a} \sin^3 \zeta}{\sqrt{x_{ecef}^2 + y_{ecef}^2 - \frac{a^2 - b^2}{a} \cos^3 \zeta}} \right\} \quad (\text{B.10})$$

$$h = \frac{\sqrt{x_{ecef}^2 + y_{ecef}^2}}{\cos \Phi} - \frac{a}{\sqrt{1 - (1 - (1 - f)^2) \sin^2 \Phi}} \quad (\text{B.11})$$

where

$$\zeta = \arctan \left\{ \frac{z_{ecef} a}{\sqrt{x_{ecef}^2 + y_{ecef}^2} b} \right\} \quad (\text{B.12})$$

and  $b = a(1 - f)$  being  $f = 3.35281066475 \cdot 10^{-3}$  the flattening factor. In the previous formulae,  $\vec{P}_t^{ECEF} = [x_{ecef} \ y_{ecef} \ z_{ecef}] = \vec{P}_t^{ECI}$ .

## B.2 Compute fd

The block **Compute Doppler Centroid** computes the Doppler Centroid  $f_d$  and Doppler Rate  $f_r$  terms according to a particular target position over Earth surface ( $\vec{P}_t^{ECI} = P_{earth}$ , Equation B.8) and the satellite location at the middle of the aperture ( $\vec{P}^{ECI}|_{m'_o=m_o}$ , Equation B.1). This function is based on the development presented in [11].

The definition of Doppler Centroid and Doppler Rate terms is

$$f_d = -\frac{2\dot{R}(t_c)}{\lambda} \quad (\text{B.13})$$

$$f_r = -\frac{2\ddot{R}(t_c)}{\lambda} \quad (\text{B.14})$$

where  $\dot{R}(t_c)$  and  $\ddot{R}(t_c)$  are the first and second derivative of the target-to-sensor range along time evaluated at the middle of the aperture  $t = t_c$ . According to Fig. B.1,

$$R(t) = \left| \vec{P}_{t \rightarrow s}^{ECI}(t) \right| = \left| -\vec{P}_{s \rightarrow t}^{ECI}(t) \right| = \left| \vec{P}^{ECI}(t) - \vec{P}_t^{ECI}(t) \right| \quad (\text{B.15})$$

that results on

$$R^2(t) = \left( \vec{P}^{ECI}(t) - \vec{P}_t^{ECI}(t) \right) \cdot \left( \vec{P}^{ECI}(t) - \vec{P}_t^{ECI}(t) \right) \quad (\text{B.16})$$

The derivative of this expression along time is

$$2R(t)\dot{R}(t) = 2 \left( \vec{P}^{ECI}(t) - \vec{P}_t^{ECI}(t) \right) \cdot \left( \vec{\dot{P}}^{ECI}(t) - \vec{\dot{P}}_t^{ECI}(t) \right) \quad (\text{B.17})$$

that can be arranged as

$$R(t)\dot{R}(t) = \vec{\dot{P}}^{ECI}(t) \left( \vec{P}^{ECI}(t) - \vec{P}_t^{ECI}(t) \right) - \vec{\dot{P}}_t^{ECI}(t) \left( \vec{P}^{ECI}(t) - \vec{P}_t^{ECI}(t) \right) \quad (\text{B.18})$$

with  $\vec{\dot{P}}^{ECI}(t)$  (Equation 5.36) and  $\vec{\dot{P}}_t^{ECI}(t)$  expressing respectively the velocity vectors of the satellite and the target. If the target is assumed to be static, then

$$\vec{\dot{P}}_t^{ECI}(t) = \vec{\Omega}_o \times \vec{P}_t^{ECI}(t) \quad (\text{B.19})$$

where  $\vec{\Omega}_o = \omega_T \cdot \hat{z}^{ECI}$  is the velocity vector due to Earth rotation. In this way, Equation B.18 becomes

$$R(t)\dot{R}(t) = \vec{P}^{ECI}(t) \left( \vec{P}^{ECI}(t) - \vec{P}_t^{ECI}(t) \right) - \vec{\Omega}_o \left( \vec{P}^{ECI}(t) \times \vec{P}_t^{ECI}(t) \right) \quad (\text{B.20})$$

The final expression of the Doppler Centroid is obtained by evaluating the previous formula with  $t = t_c$ . Thus,

$$f_d = -\frac{2}{\lambda} \frac{\vec{P}^{ECI}(t_c) \left( \vec{P}^{ECI}|_{m'_o=m_o} - \vec{P}_t^{ECI}(t_c) \right) - \vec{\Omega}_o \left( \vec{P}^{ECI}|_{m'_o=m_o} \times \vec{P}_t^{ECI}(t_c) \right)}{\left| \vec{P}^{ECI}|_{m'_o=m_o} - \vec{P}_t^{ECI}(t_c) \right|} \quad (\text{B.21})$$

where all the terms refer to the middle of the aperture. Similarly, the Doppler Rate term can be calculated by deriving Equation B.20 along time. The new expression is

$$\begin{aligned} R(t)\ddot{R}(t) + \dot{R}^2(t) &= f_r^1(t) - f_r^2(t) = \\ &= \vec{P}^{ECI}(t) \left( \vec{P}^{ECI}(t) - \vec{P}_t^{ECI}(t) \right) + \vec{P}^{ECI}(t) \left( \vec{P}^{ECI}(t) - \vec{P}_t^{ECI}(t) \right) - \\ &= \vec{\Omega}_o \left( \vec{P}^{ECI}(t) \times \vec{P}_t^{ECI}(t) + \vec{P}^{ECI}(t) \times \vec{P}_t^{ECI}(t) \right) \end{aligned} \quad (\text{B.22})$$

where  $\vec{P}^{ECI}(t)$  is the acceleration vector of the satellite. As before, the evaluation of  $t$  with  $t_c$  leads to

$$f_r = -\frac{2}{\lambda} \frac{f_r^1(t_c) - f_r^2(t_c) - \left( -\frac{f_d \lambda}{2} \right)^2}{\left| \vec{P}^{ECI}|_{m'_o=m_o} - \vec{P}_t^{ECI}(t_c) \right|} \quad (\text{B.23})$$

where all the terms refer to the middle of the aperture.





## Appendix C

# Wave model of *GRECOSAR*

This Appendix describes the wave model of *GRECOSAR* that provides the values of  $\alpha_{roll}(t_j^m)$  and  $\alpha_{pitch}(t_j^m)$  according to target dimensions (length  $t_l$  and breadth  $t_b$ ) and wave parameters (length  $w_l$ , height  $w_h$ , period  $w_p$ , course  $w_b$  and phase  $w_{ph}$ ). This model is quite simple and it considers waves as sinusoids without taking the hydrodynamic forces into account. The basic formulation is

$$\alpha_{roll}(t_j^m) = A_{roll} \sin \left\{ \frac{\text{mod}(t_j^m + w_{ph}, w_p) \pi}{w_p/4} \frac{\pi}{2} \right\} \quad (\text{C.1})$$

$$\alpha_{pitch}(t_j^m) = A_{pitch} \sin \left\{ \frac{\text{mod}(t_j^m + w_{ph}, w_p) \pi}{w_p/4} \frac{\pi}{2} \right\} \quad (\text{C.2})$$

where  $t_j^m$  is defined in Equation 5.48,  $w_{ph}$  provides the starting time of the simulation within one wave period (see Fig. C.1(a)) and

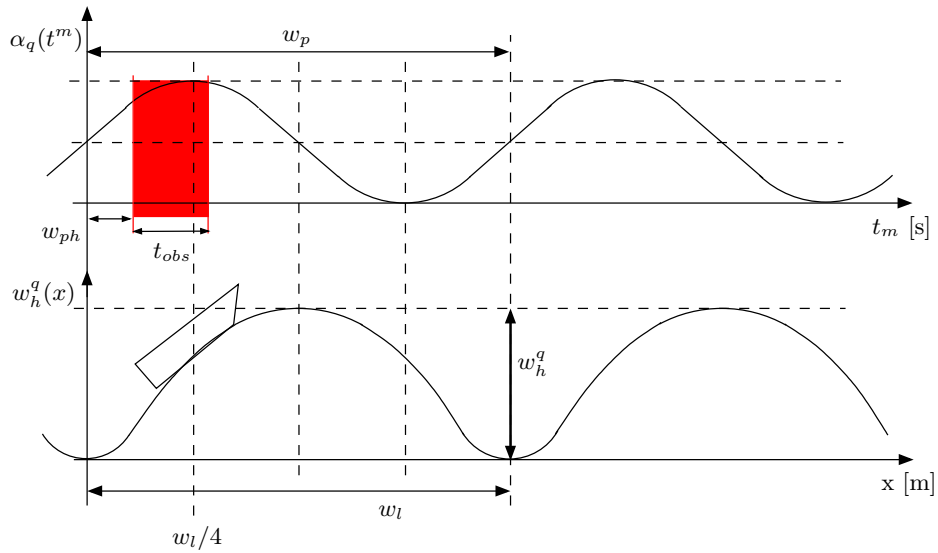
$$A_{roll} = \arctan \left\{ \frac{3w_h^{roll}(\sqrt{3} - 1)}{w_l} \right\} \quad (\text{C.3})$$

$$A_{pitch} = \arctan \left\{ \frac{3w_h^{pitch}(\sqrt{3} - 1)}{w_l} \right\} \quad (\text{C.4})$$

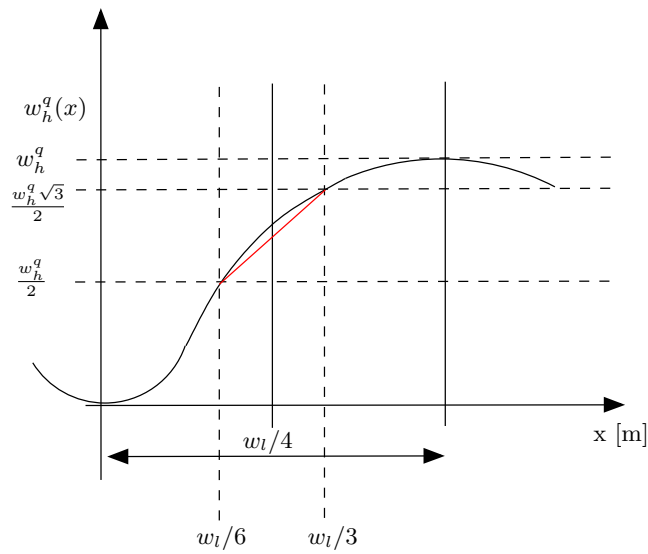
with

$$w_h^{roll} = w_h \sin(|w_b - \beta|) \quad (\text{C.5})$$

$$w_h^{pitch} = w_h \cos(|w_b - \beta|) \quad (\text{C.6})$$



(a)



(b)

Figure C.1: Detail of the wave model of *GRECOSAR* (a). The peak of angular velocity is computed as the slope at  $w_l/4$  (b).

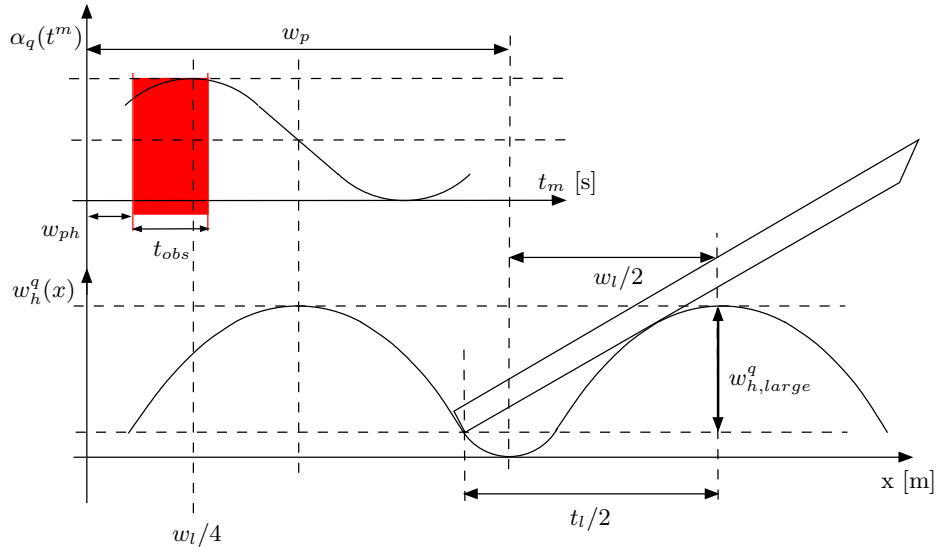


Figure C.2: Detail of the amplitude of the angular velocity for vessels as large as  $t_l > w_l$ .

According to Equations C.1 - C.2, the peak of angular velocity is reached at  $w_l/4$ , i.e. when the vessel has the maximum inclination (see Fig. C.1(a)). In this sense, the amplitude factors  $A_q$  for  $q \in \{\text{roll}, \text{pitch}\}$  are calculated as the slope of the wave at  $w_l/4$  (see Fig. C.1(b)). So,

$$A_q = \arctan \left\{ \frac{w_h^q (\sin\{w_l/3\} - \sin\{w_l/6\})}{\frac{w_l}{3} - \frac{w_l}{6}} \right\} \quad (\text{C.7})$$

that results on

$$A_q = \arctan \left\{ \frac{\frac{w_h^q}{2} (\sqrt{3} - 1)}{\frac{w_l}{6}} \right\} = \arctan \left\{ \frac{3w_h^q (\sqrt{3} - 1)}{w_l} \right\} \quad (\text{C.8})$$

The previous values are valid if  $t_l/2 \leq w_l/2$ . In the contrary, they are replaced by (see Fig. C.2)

$$A_q^{large} = \arctan \left\{ \frac{w_h^q \left(1 - \left| \sin \left\{ \frac{t_l/2 - w_l/2}{w_l/2} \frac{\pi}{2} \right\} \right| \right)}{\frac{t_l}{2}} \right\} = \arctan \left\{ \frac{2w_h^q}{t_l} \right\} \quad (\text{C.9})$$



# Appendix D

## Vessel Scattering Study with Polarimetric ISAR images

This Appendix gathers the results of analyzing the scattering maps used in the vessel scattering study presented in Chapter 6 with the Pauli, SDH and Cameron CTD. The images are organized according to the selected center frequency. Each figure contains the information related to one of the three CTD for the bearing range defined by  $\beta + \phi = 295 + 10 * i$  for  $i \in \{0..6\}$ .

### D.1 L Band

In this section, the L band data are presented. Their main characteristics and the list of figures where the images are included are summarized in Table D.1.

Table D.1: Main Characteristics of the PolISAR images included in Section D.1

Model	Scaled	$\beta + \phi$ [°]	$\phi$ [°]	vessel motions	sea surface	Fig.
SPA	NO	295-355	20	NO	NO	D.1 (Pauli) D.2 (SDH) - D.3 (Cameron)
ICE	NO	295-355	20	NO	NO	D.4 (Pauli) D.5 (SDH) - D.6 (Cameron)
FER	NO	295-355	20	NO	NO	D.7 (Pauli) D.8 (SDH) - D.9 (Cameron)

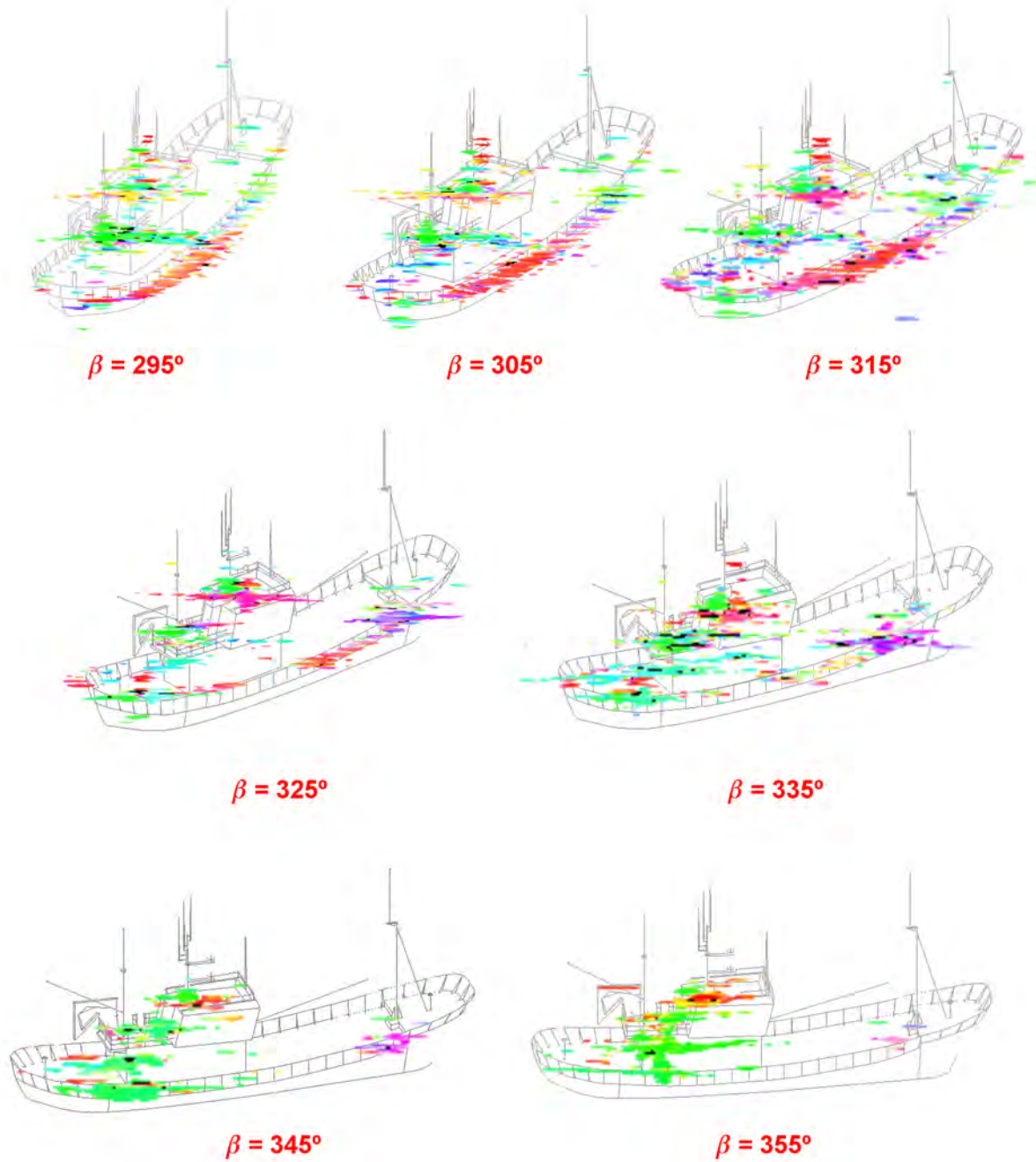


Figure D.1: Polarimetric ISAR dataset obtained for the SPA model at L band and  $\phi = 20^\circ$ . The bearing range is  $\beta \in \{295 + 10 * i\}$  for  $i \in \{0..6\}$ . The images have been analyzed with the Pauli theorem for a dynamic range of 25 dB.

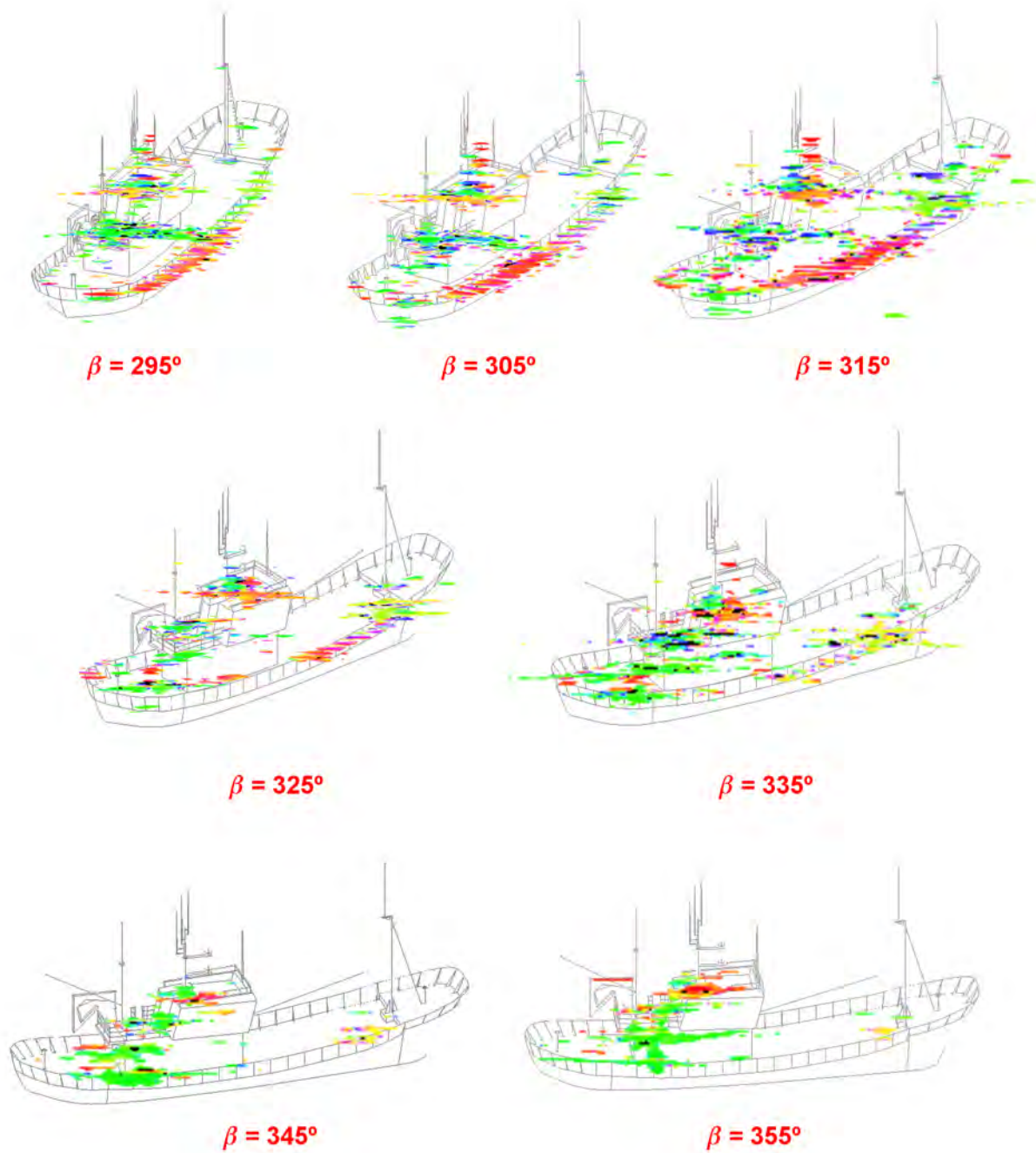


Figure D.2: Polarimetric ISAR dataset obtained for the SPA model at L band and  $\phi = 20^\circ$ . The bearing range is  $\beta \in \{295 + 10 * i\}$  for  $i \in \{0..6\}$ . The images have been analyzed with the SDH theorem for a dynamic range of 25 dB.

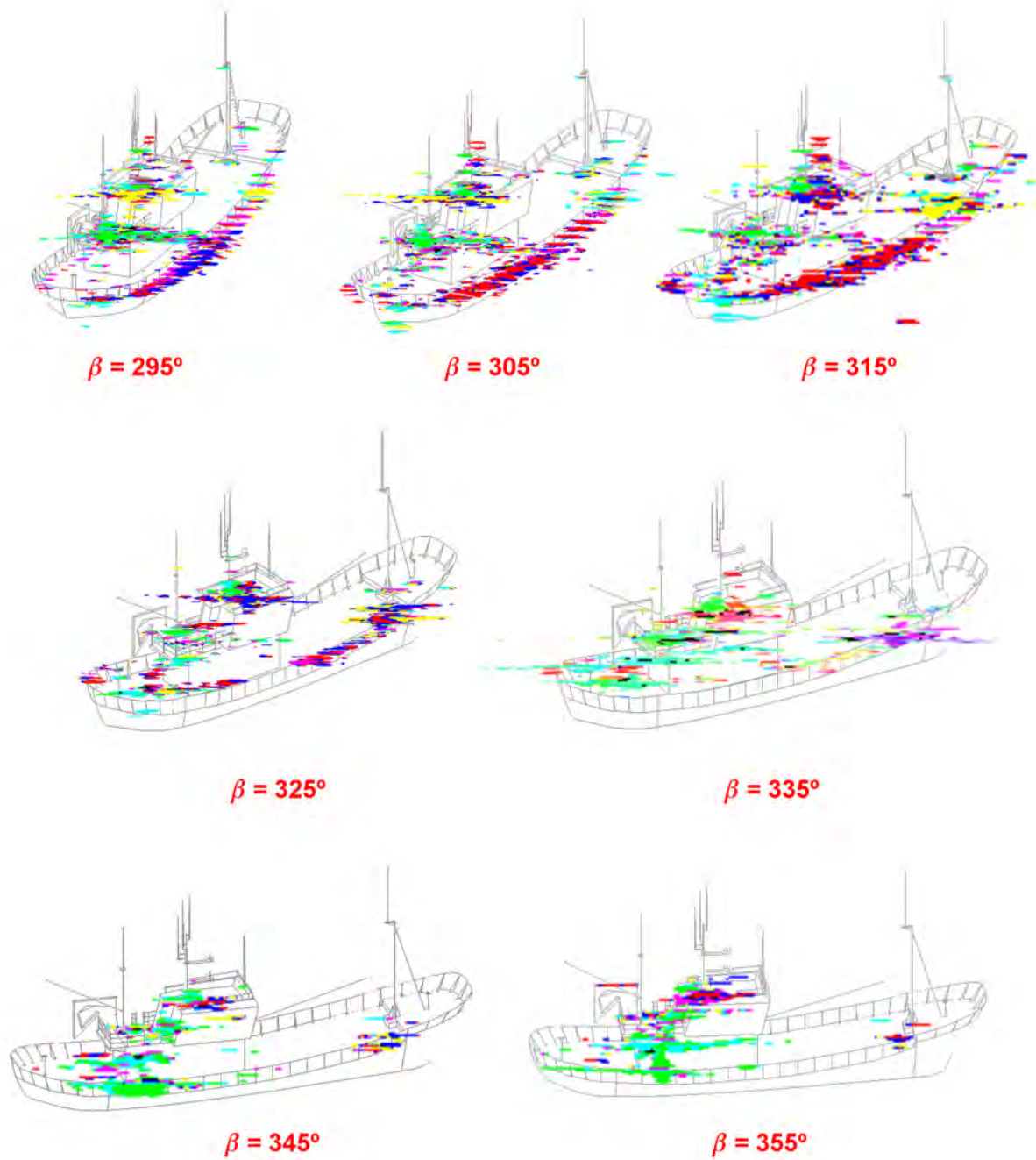


Figure D.3: Polarimetric ISAR dataset obtained for the SPA model at L band and  $\phi = 20^\circ$ . The bearing range is  $\beta \in \{295 + 10 * i\}$  for  $i \in \{0..6\}$ . The images have been analyzed with the Cameron theorem for a dynamic range of 25 dB.



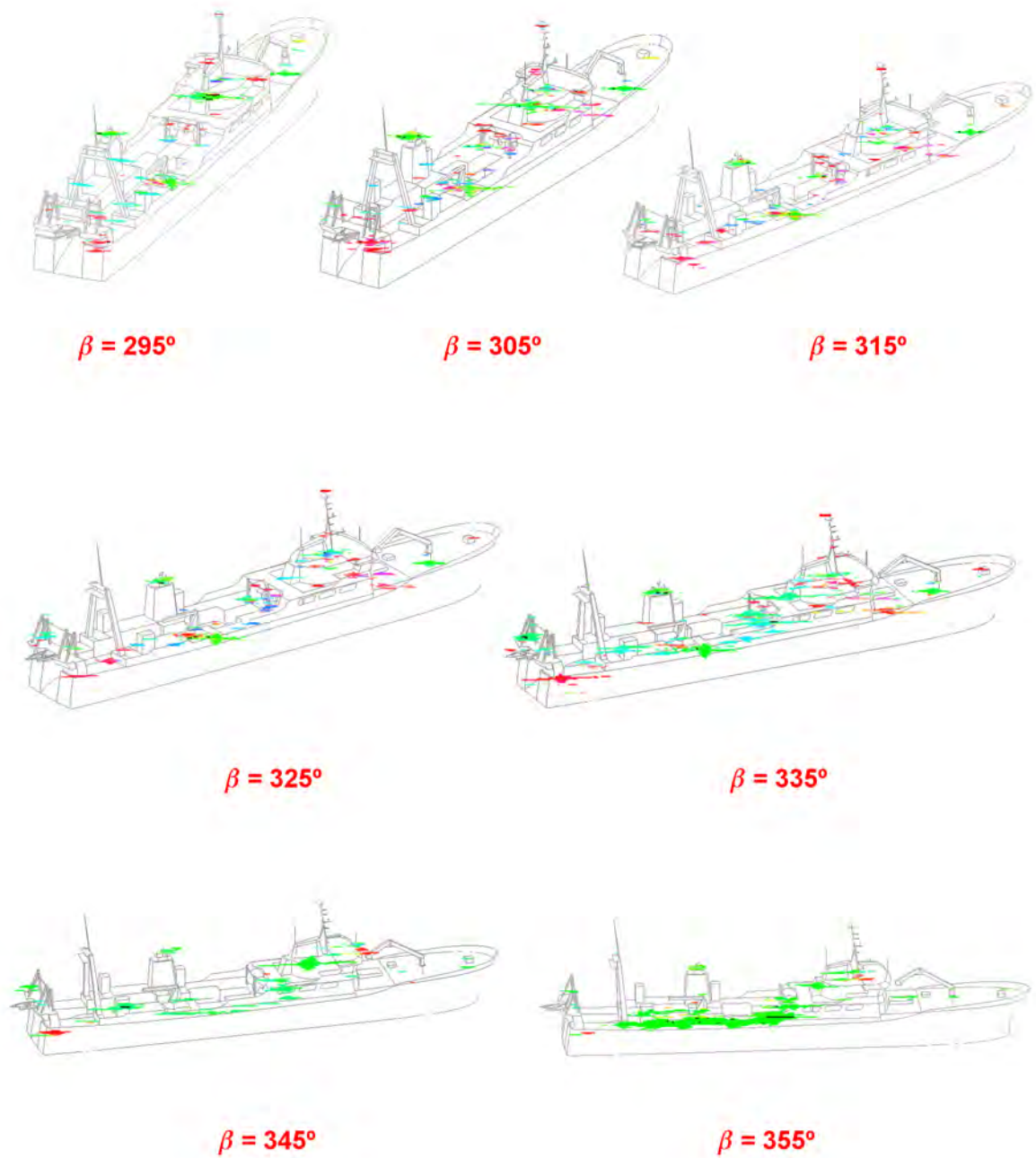


Figure D.4: Polarimetric ISAR dataset obtained for the ICE model at L band and  $\phi = 20^\circ$ . The bearing range is  $\beta \in \{295 + 10 * i\}$  for  $i \in \{0..6\}$ . The images have been analyzed with the Pauli theorem for a dynamic range of 25 dB.

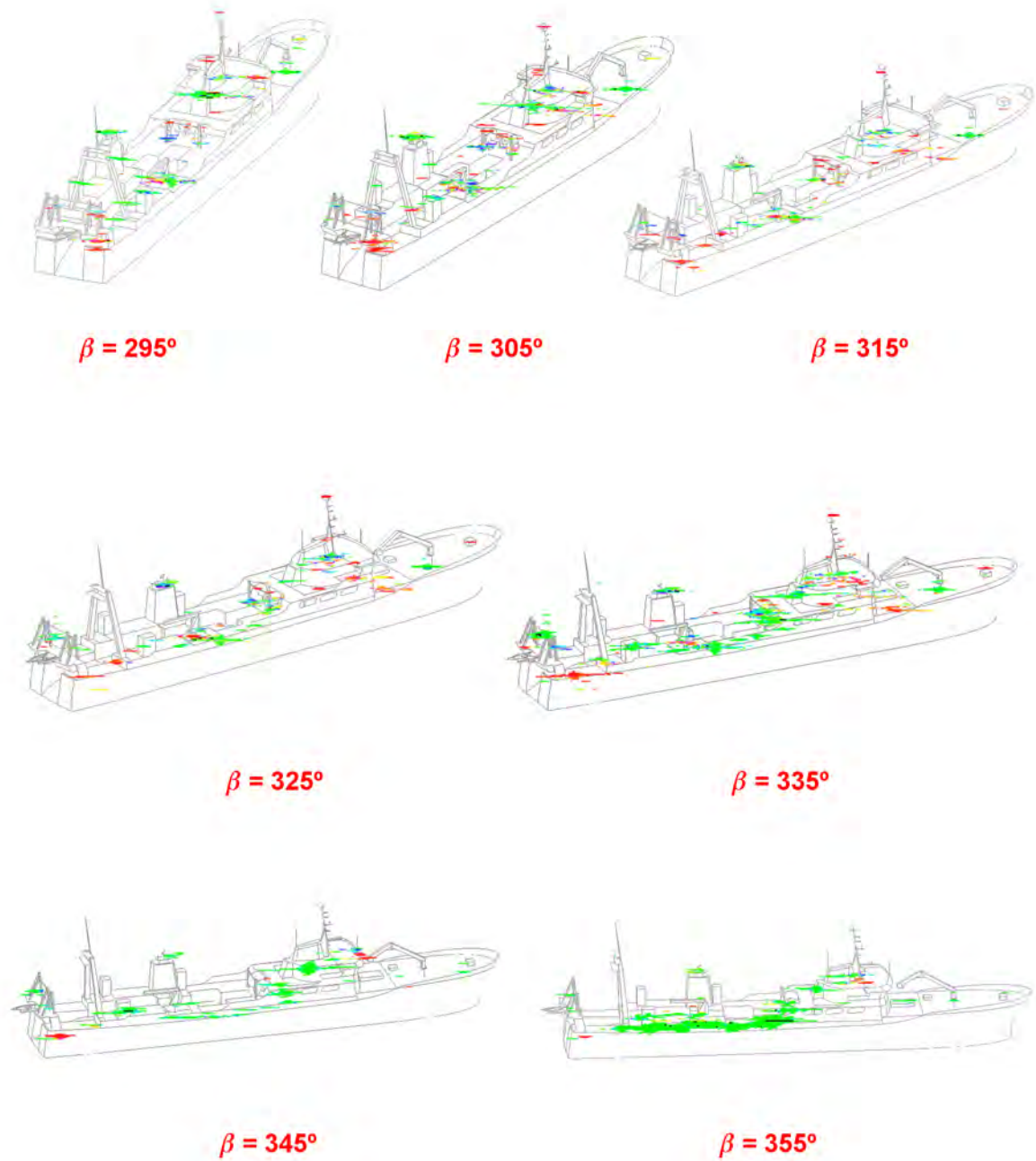


Figure D.5: Polarimetric ISAR dataset obtained for the ICE model at L band and  $\phi = 20^\circ$ . The bearing range is  $\beta \in \{295 + 10 * i\}$  for  $i \in \{0..6\}$ . The images have been analyzed with the SDH theorem for a dynamic range of 25 dB.

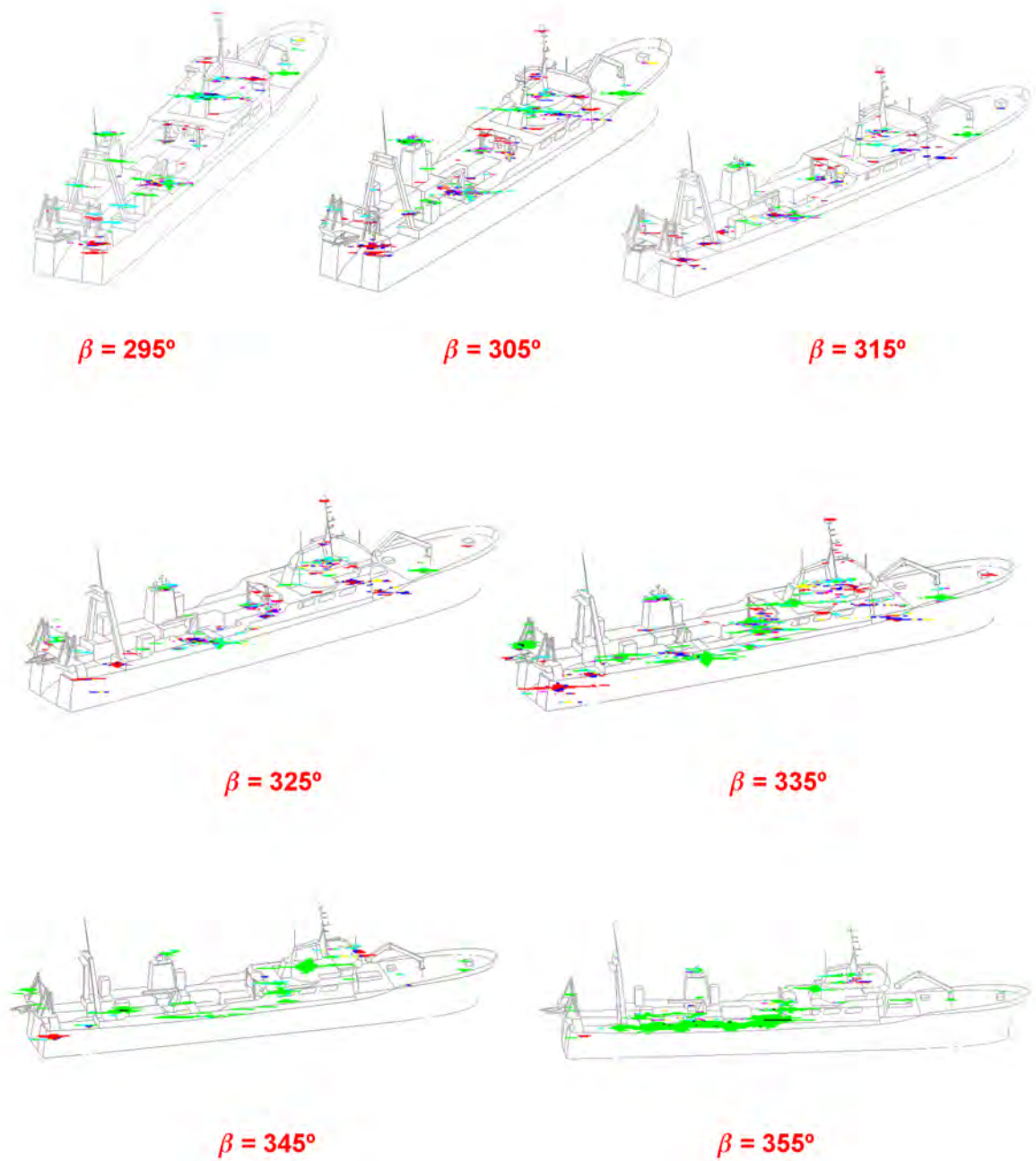


Figure D.6: Polarimetric ISAR dataset obtained for the ICE model at L band and  $\phi = 20^\circ$ . The bearing range is  $\beta \in \{295 + 10 * i\}$  for  $i \in \{0..6\}$ . The images have been analyzed with the Cameron theorem for a dynamic range of 25 dB.

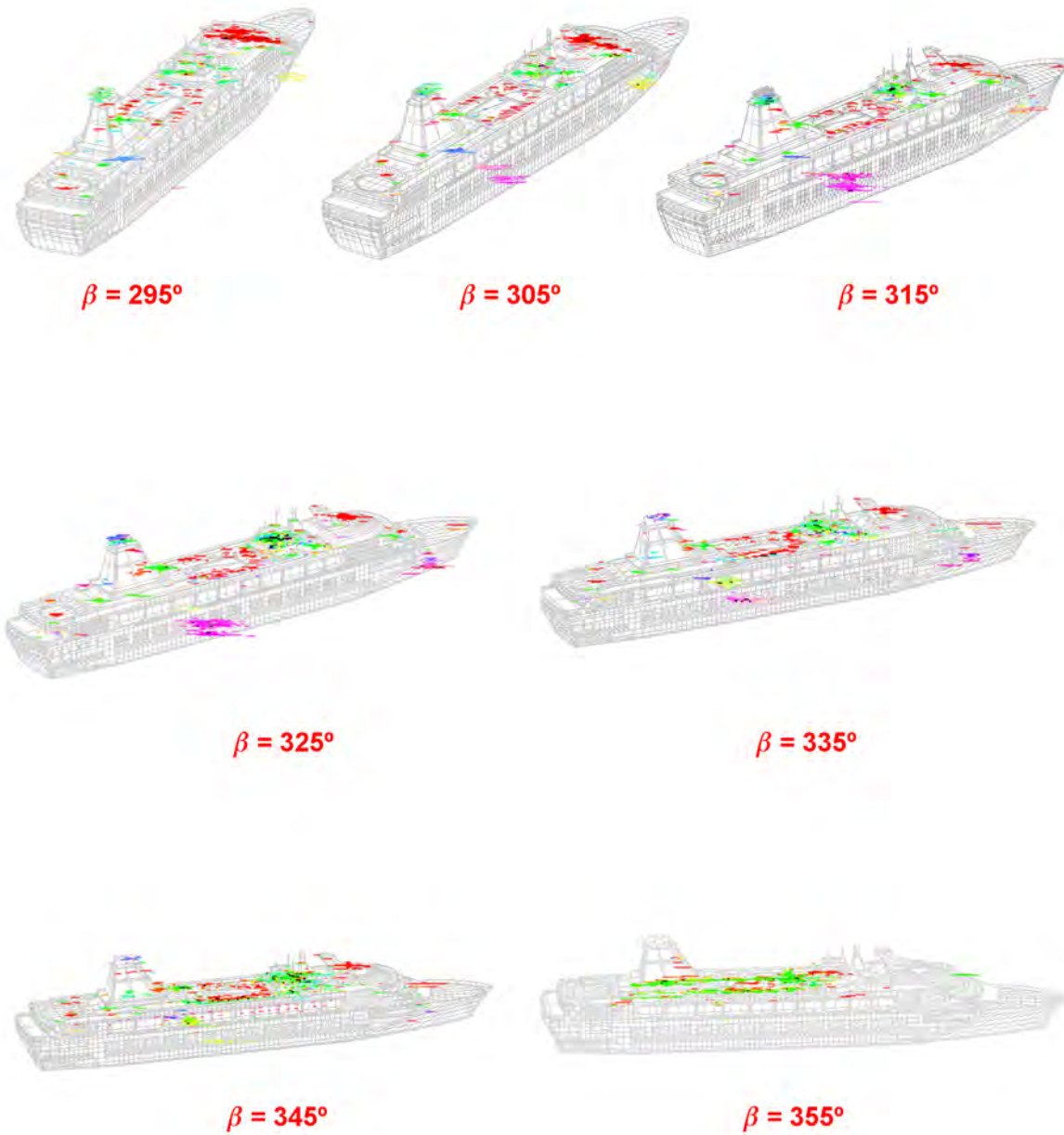


Figure D.7: Polarimetric ISAR dataset obtained for the FER model at L band and  $\phi = 20^\circ$ . The bearing range is  $\beta \in \{295 + 10 * i\}$  for  $i \in \{0..6\}$ . The images have been analyzed with the Pauli theorem for a dynamic range of 25 dB.

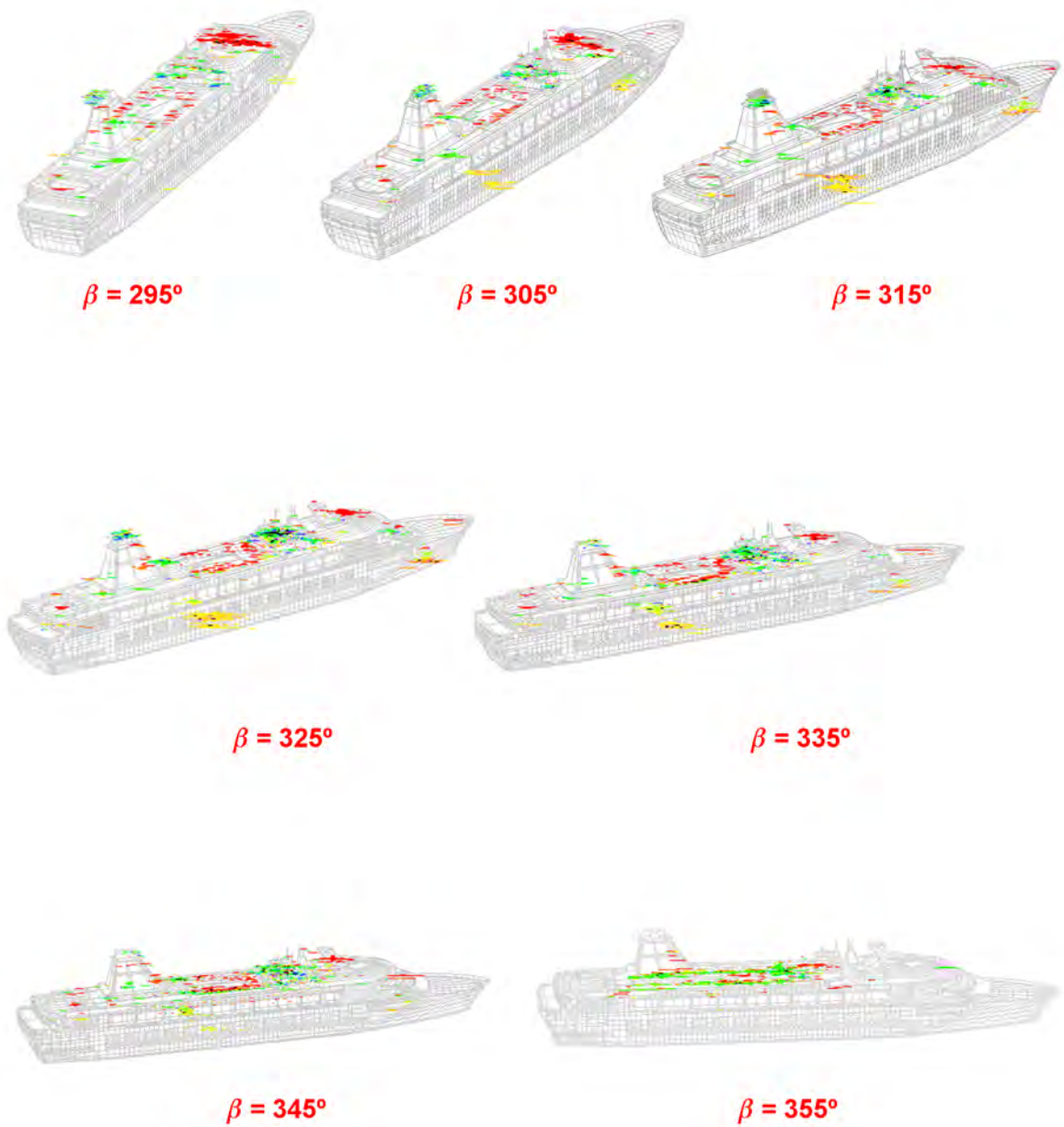


Figure D.8: Polarimetric ISAR dataset obtained for the FER model at L band and  $\phi = 20^\circ$ . The bearing range is  $\beta \in \{295 + 10 * i\}$  for  $i \in \{0..6\}$ . The images have been analyzed with the SDH theorem for a dynamic range of 25 dB.

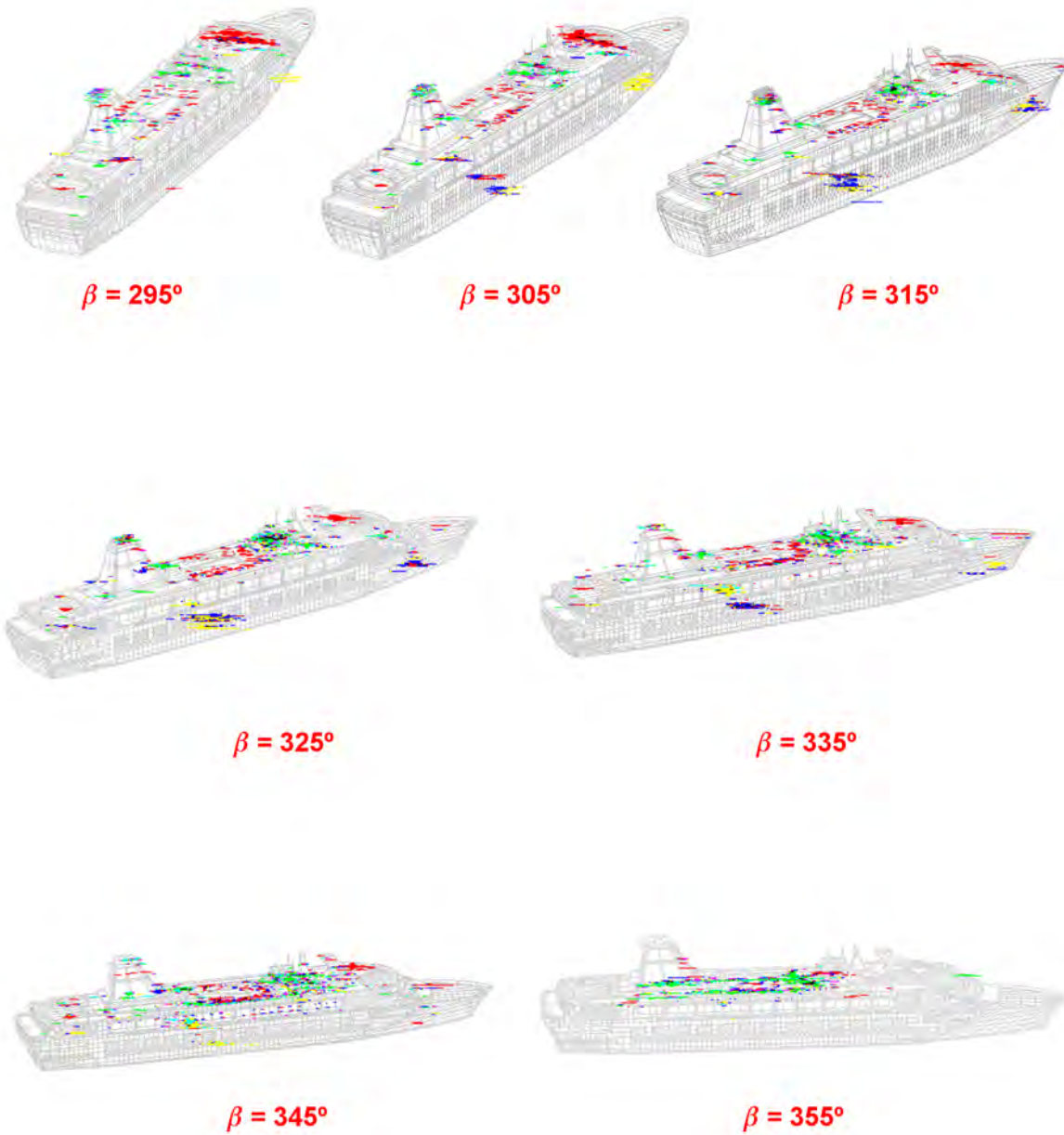


Figure D.9: Polarimetric ISAR dataset obtained for the FER model at L band and  $\phi = 20^\circ$ . The bearing range is  $\beta \in \{295 + 10 * i\}$  for  $i \in \{0..6\}$ . The images have been analyzed with the Cameron theorem for a dynamic range of 25 dB.

Table D.2: Main Characteristics of the PolSAR images included in Section D.2

Model	Scaled	$\beta + \phi$ [°]	$\phi$ [°]	vessel motions	sea surface	Fig.
SPA	NO	295-355	20	NO	NO	D.10 (Pauli) D.11 (SDH) - D.12 (Cameron)
ICE	NO	295-355	20	NO	NO	D.13 (Pauli) D.14 (SDH) - D.15 (Cameron)
FER	NO	295-355	20	NO	NO	D.16 (Pauli) D.17 (SDH) - D.18 (Cameron)
ICE	YES	295-355	20	NO	NO	D.19 (Pauli) D.20 (SDH) - D.21 (Cameron)
FER	YES	295-355	20	NO	NO	D.22 (Pauli) D.23 (SDH) - D.24 (Cameron)

## D.2 S Band

In this section, the S band data are presented. Their main characteristics and the list of figures where the images are included are summarized in Table D.2.

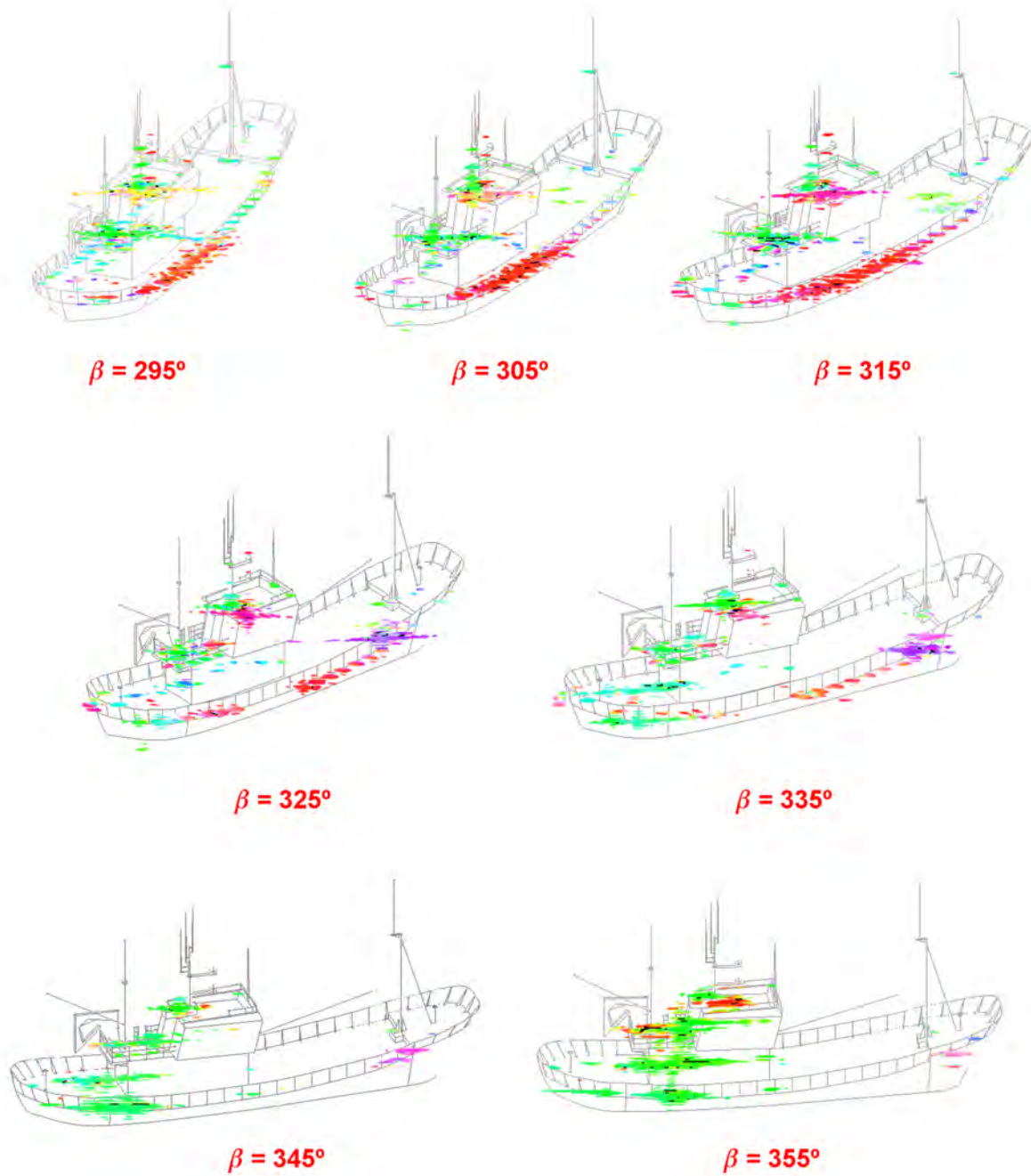


Figure D.10: Polarimetric ISAR dataset obtained for the SPA model at S band and  $\phi = 20^\circ$ . The bearing range is  $\beta \in \{295 + 10 * i\}$  for  $i \in \{0..6\}$ . The images have been analyzed with the Pauli theorem for a dynamic range of 25 dB.



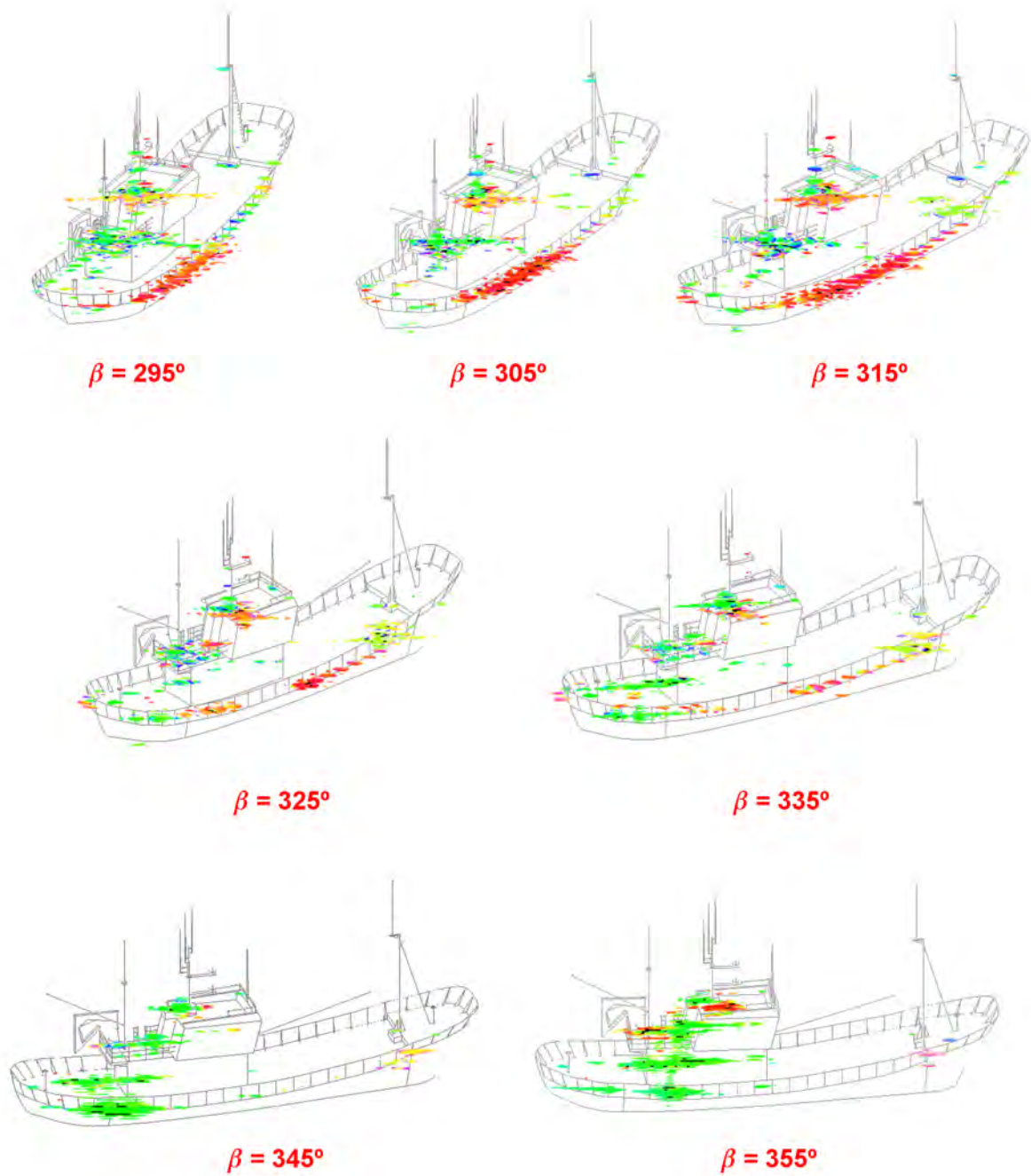


Figure D.11: Polarimetric ISAR dataset obtained for the SPA model at S band and  $\phi = 20^\circ$ . The bearing range is  $\beta \in \{295 + 10 * i\}$  for  $i \in \{0..6\}$ . The images have been analyzed with the SDH theorem for a dynamic range of 25 dB.

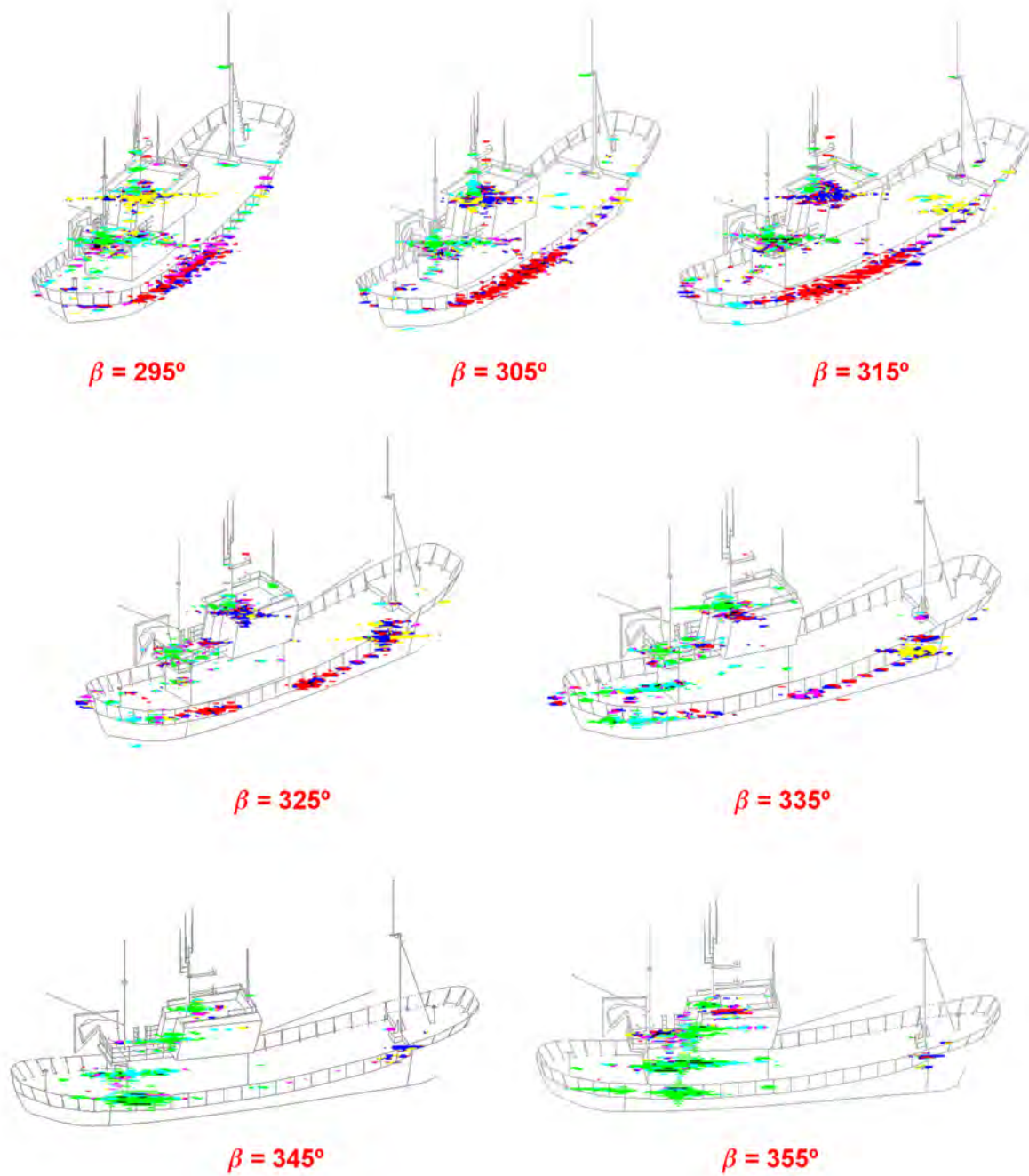


Figure D.12: Polarimetric ISAR dataset obtained for the SPA model at S band and  $\phi = 20^\circ$ . The bearing range is  $\beta \in \{295 + 10 * i\}$  for  $i \in \{0..6\}$ . The images have been analyzed with the Cameron theorem for a dynamic range of 25 dB.

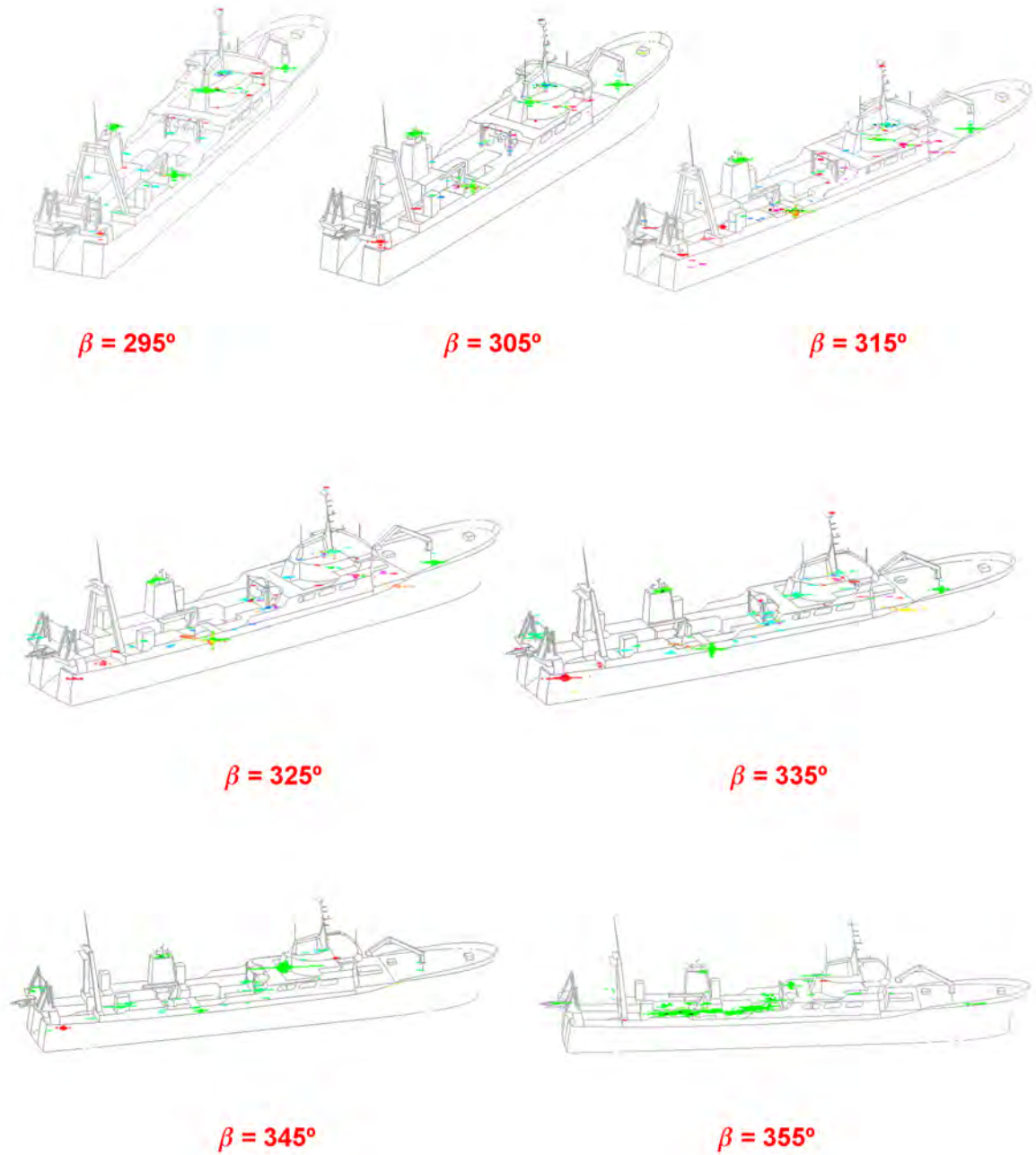


Figure D.13: Polarimetric ISAR dataset obtained for the ICE model at S band and  $\phi = 20^\circ$ . The bearing range is  $\beta \in \{295 + 10 * i\}$  for  $i \in \{0..6\}$ . The images have been analyzed with the Pauli theorem for a dynamic range of 25 dB.

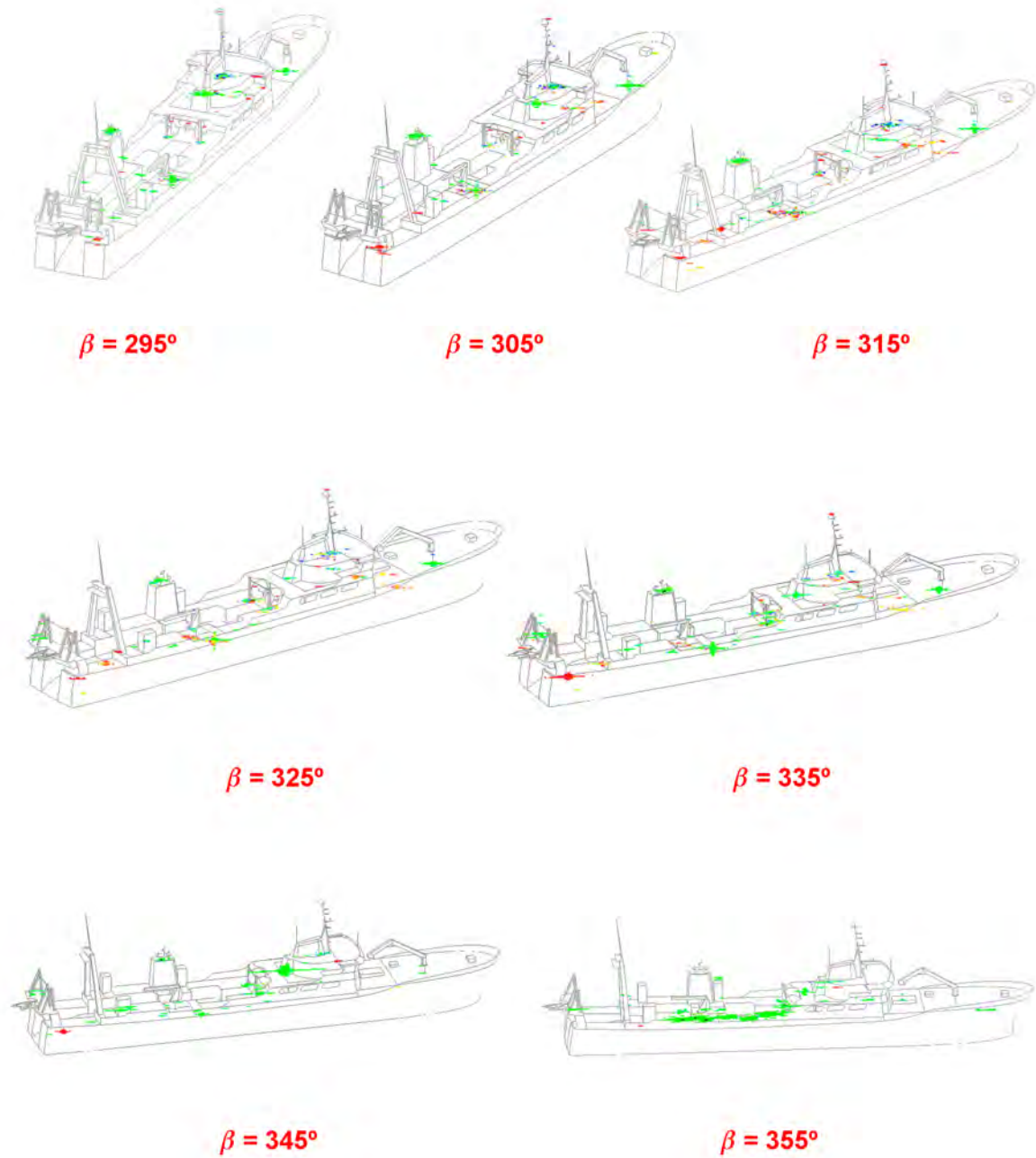


Figure D.14: Polarimetric ISAR dataset obtained for the ICE model at S band and  $\phi = 20^\circ$ . The bearing range is  $\beta \in \{295 + 10 * i\}$  for  $i \in \{0..6\}$ . The images have been analyzed with the SDH theorem for a dynamic range of 25 dB.

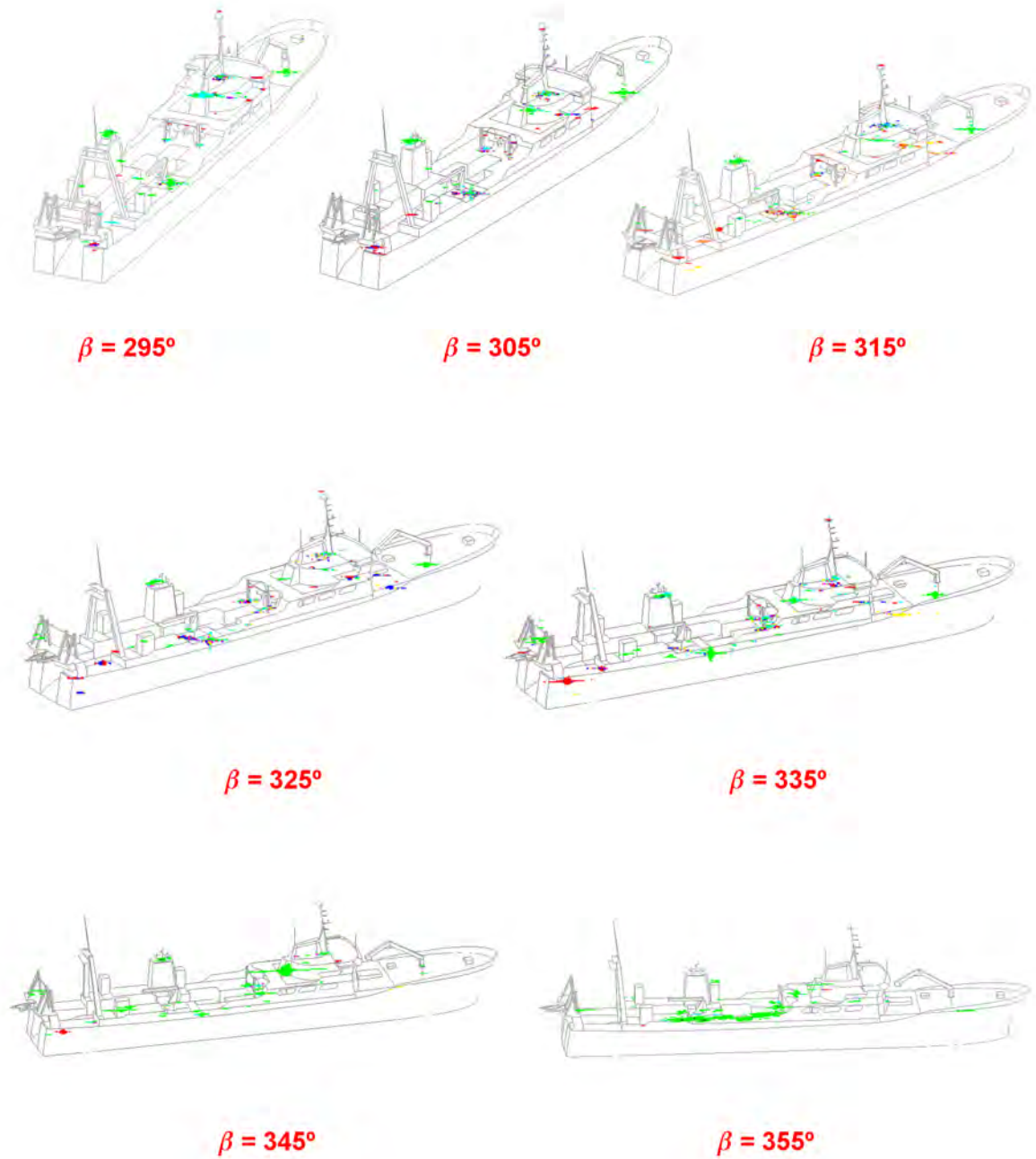


Figure D.15: Polarimetric ISAR dataset obtained for the ICE model at S band and  $\phi = 20^\circ$ . The bearing range is  $\beta \in \{295 + 10 * i\}$  for  $i \in \{0..6\}$ . The images have been analyzed with the Cameron theorem for a dynamic range of 25 dB.

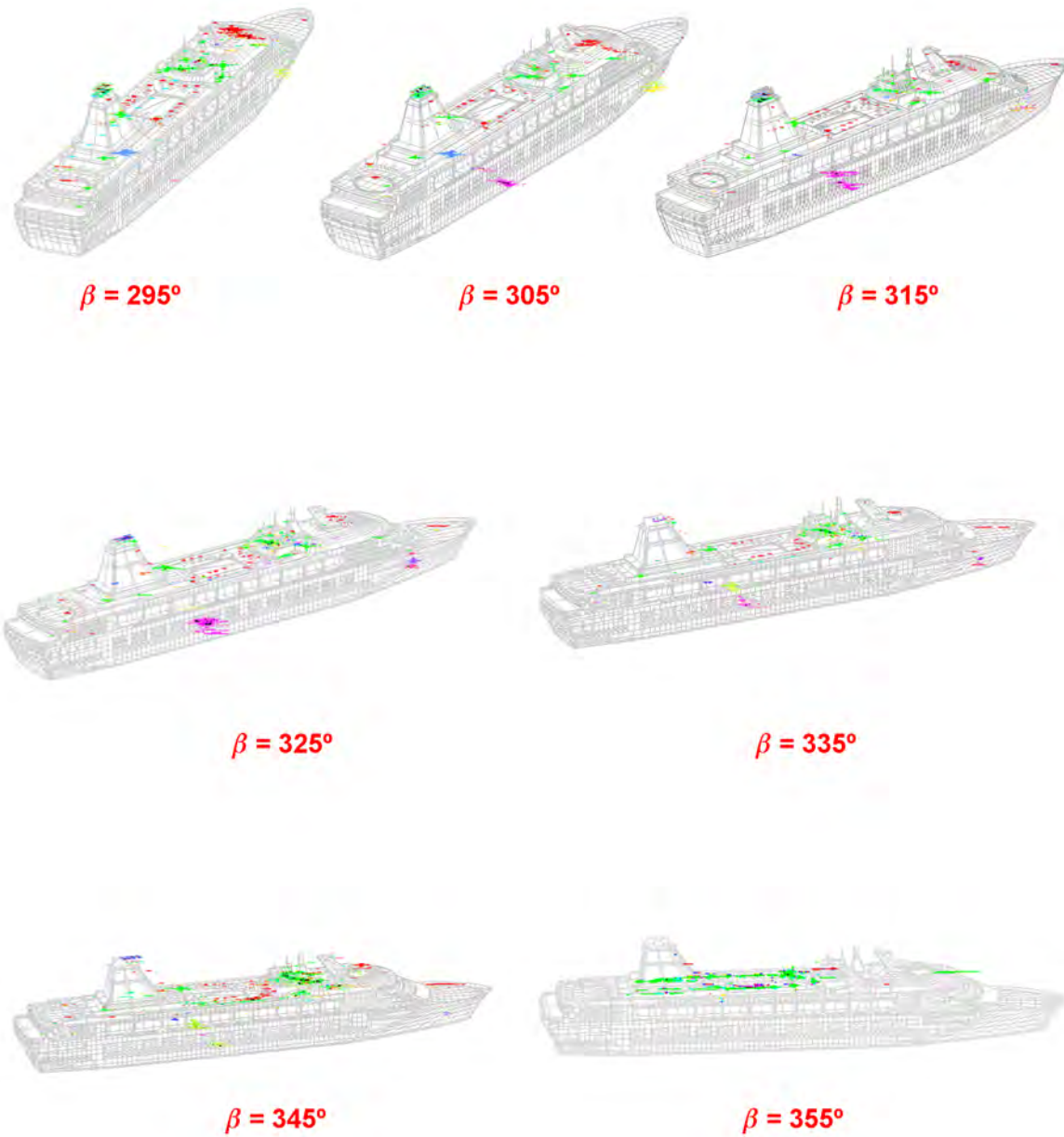


Figure D.16: Polarimetric ISAR dataset obtained for the FER model at S band and  $\phi = 20^\circ$ . The bearing range is  $\beta \in \{295 + 10 * i\}$  for  $i \in \{0..6\}$ . The images have been analyzed with the Pauli theorem for a dynamic range of 25 dB.

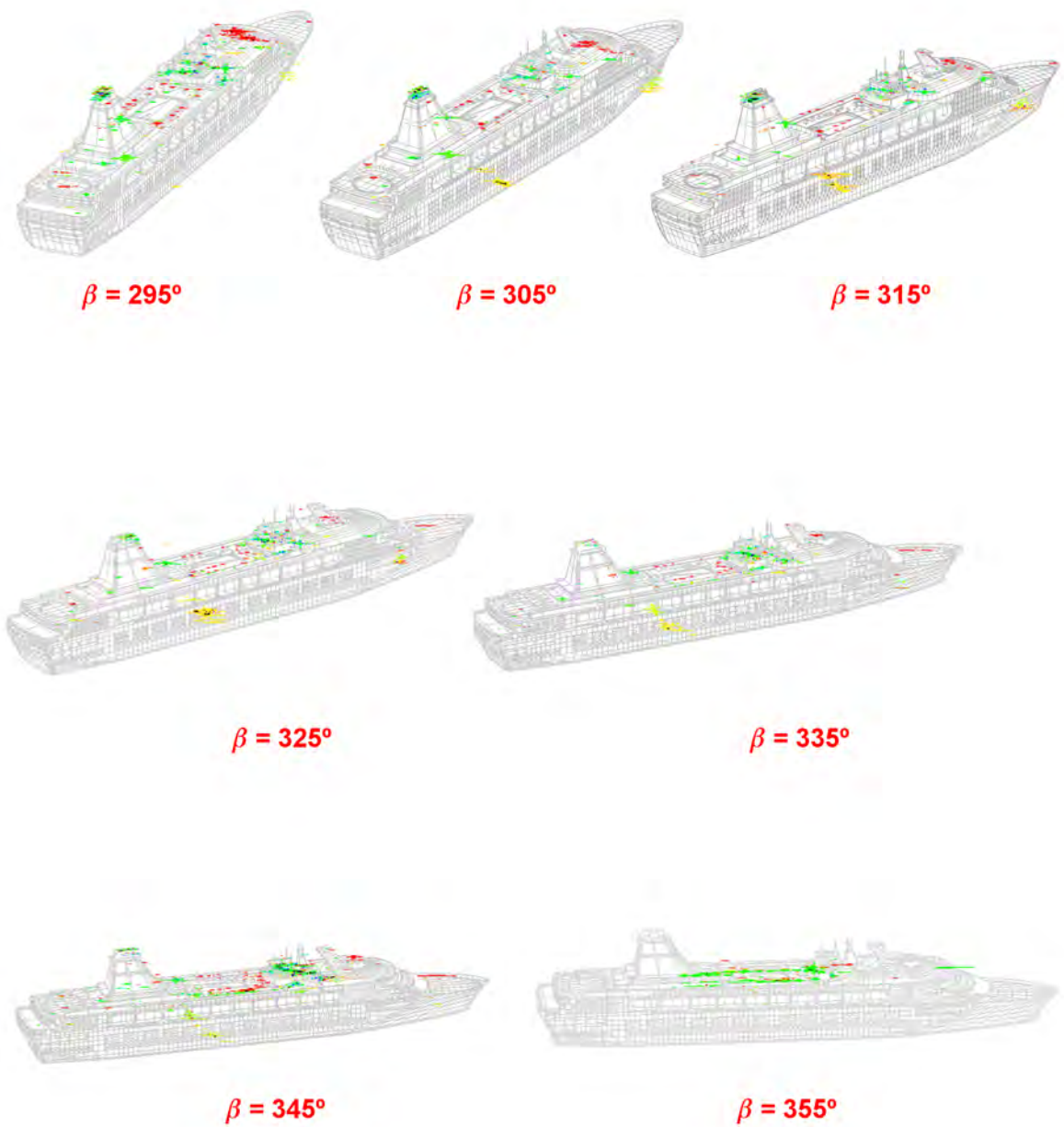


Figure D.17: Polarimetric ISAR dataset obtained for the FER model at S band and  $\phi = 20^\circ$ . The bearing range is  $\beta \in \{295 + 10 * i\}$  for  $i \in \{0..6\}$ . The images have been analyzed with the SDH theorem for a dynamic range of 25 dB.

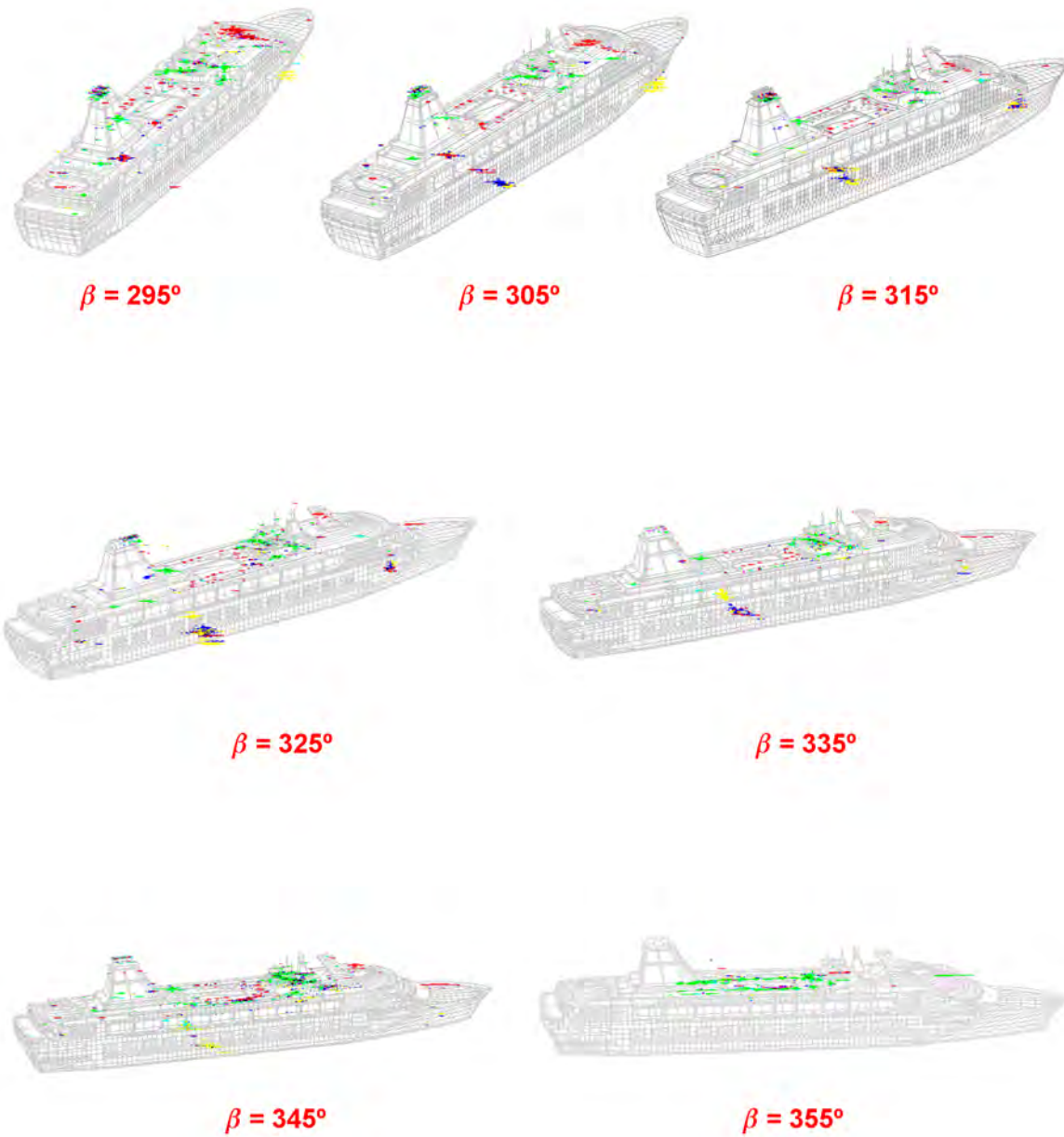


Figure D.18: Polarimetric ISAR dataset obtained for the FER model at S band and  $\phi = 20^\circ$ . The bearing range is  $\beta \in \{295 + 10 * i\}$  for  $i \in \{0..6\}$ . The images have been analyzed with the Cameron theorem for a dynamic range of 25 dB.



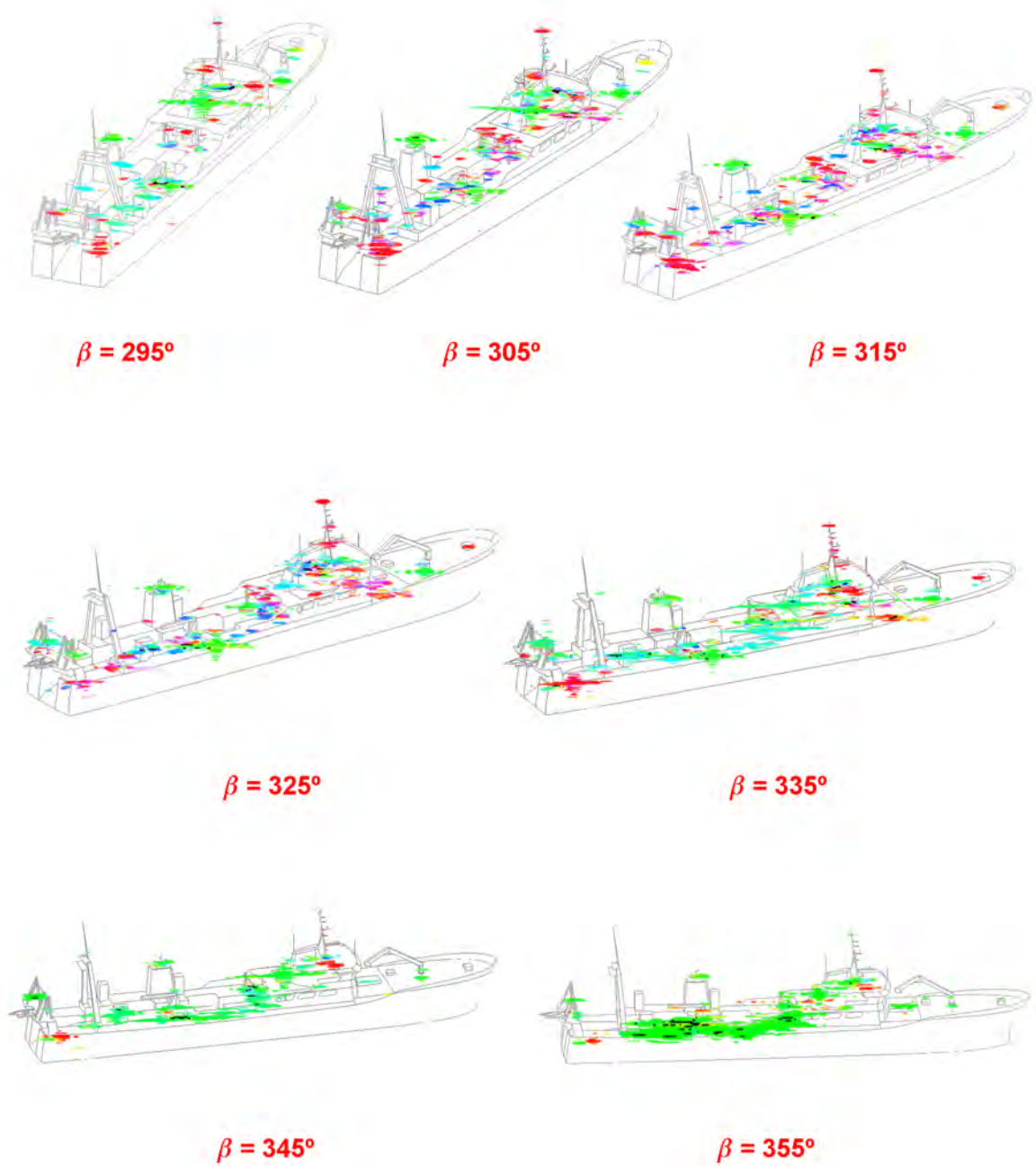


Figure D.19: Polarimetric ISAR dataset obtained for the scaled version of the ICE model at S band and  $\phi = 20^\circ$ . The bearing range is  $\beta \in \{295 + 10 * i\}$  for  $i \in \{0..6\}$ . The images have been analyzed with the Pauli theorem for a dynamic range of 25 dB.

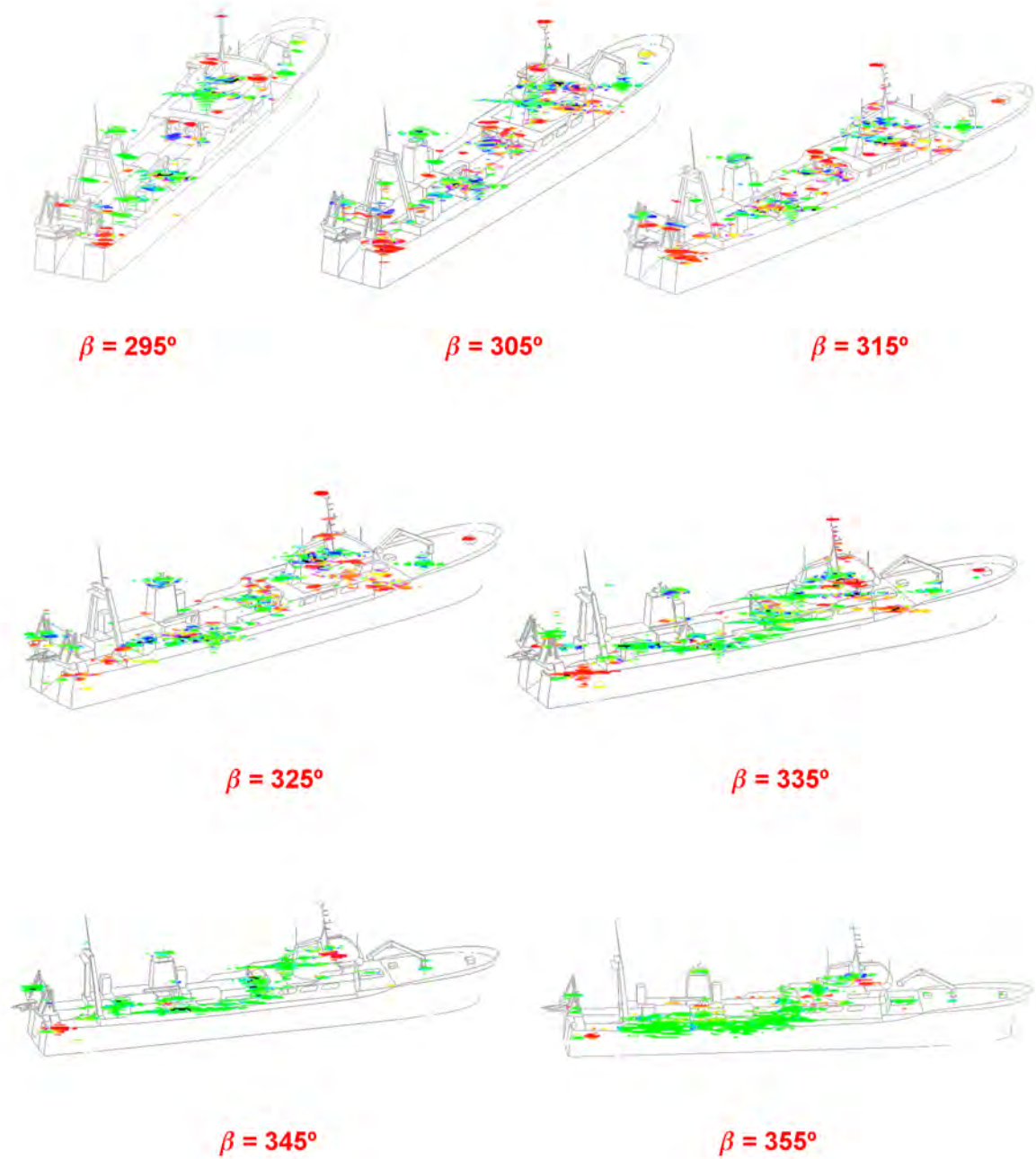


Figure D.20: Polarimetric ISAR dataset obtained for the scaled version of the ICE model at S band and  $\phi = 20^\circ$ . The bearing range is  $\beta \in \{295 + 10 * i\}$  for  $i \in \{0..6\}$ . The images have been analyzed with the SDH theorem for a dynamic range of 25 dB.

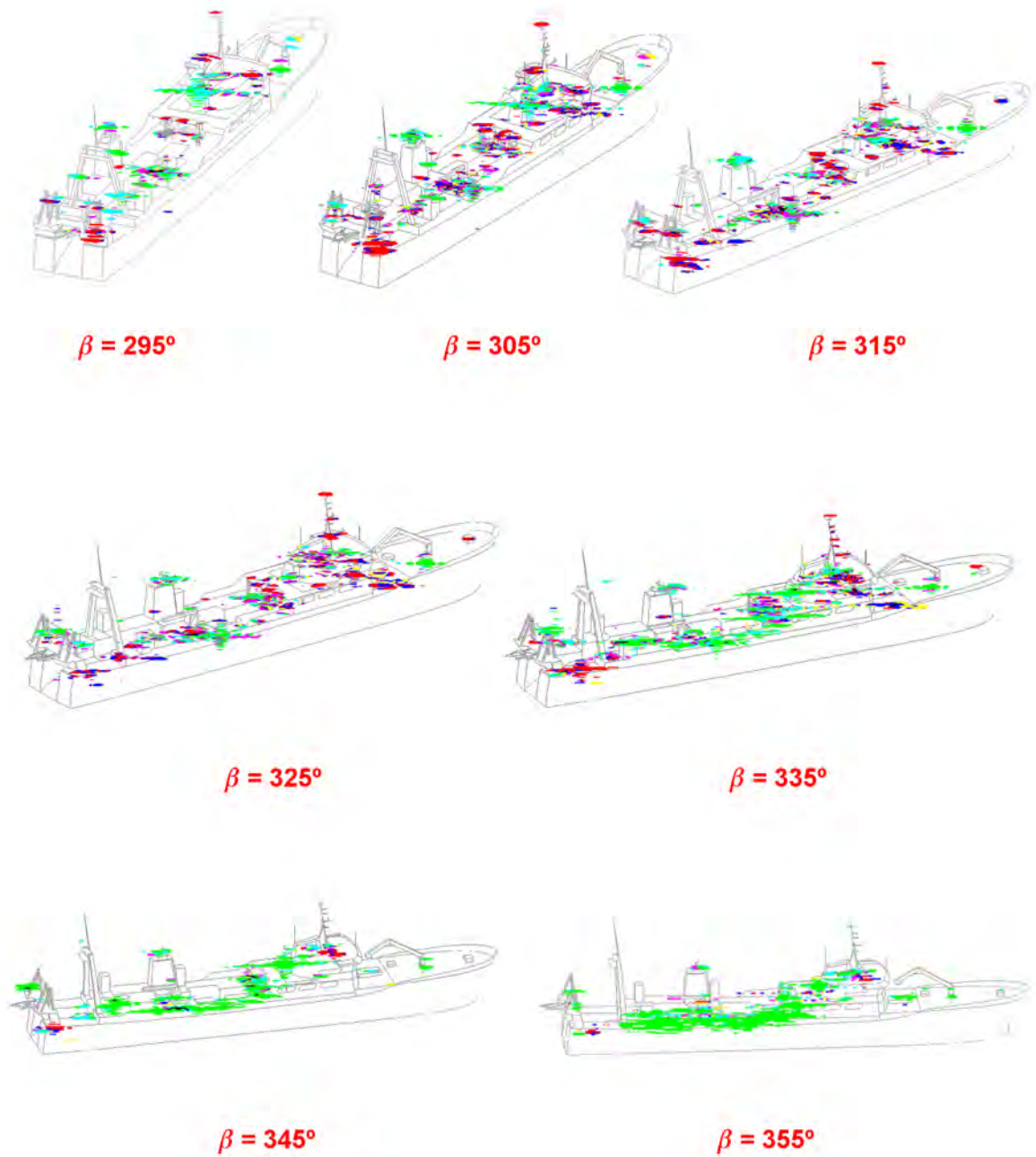


Figure D.21: Polarimetric ISAR dataset obtained for the scaled version of the ICE model at S band and  $\phi = 20^\circ$ . The bearing range is  $\beta \in \{295 + 10 * i\}$  for  $i \in \{0..6\}$ . The images have been analyzed with the Cameron theorem for a dynamic range of 25 dB.

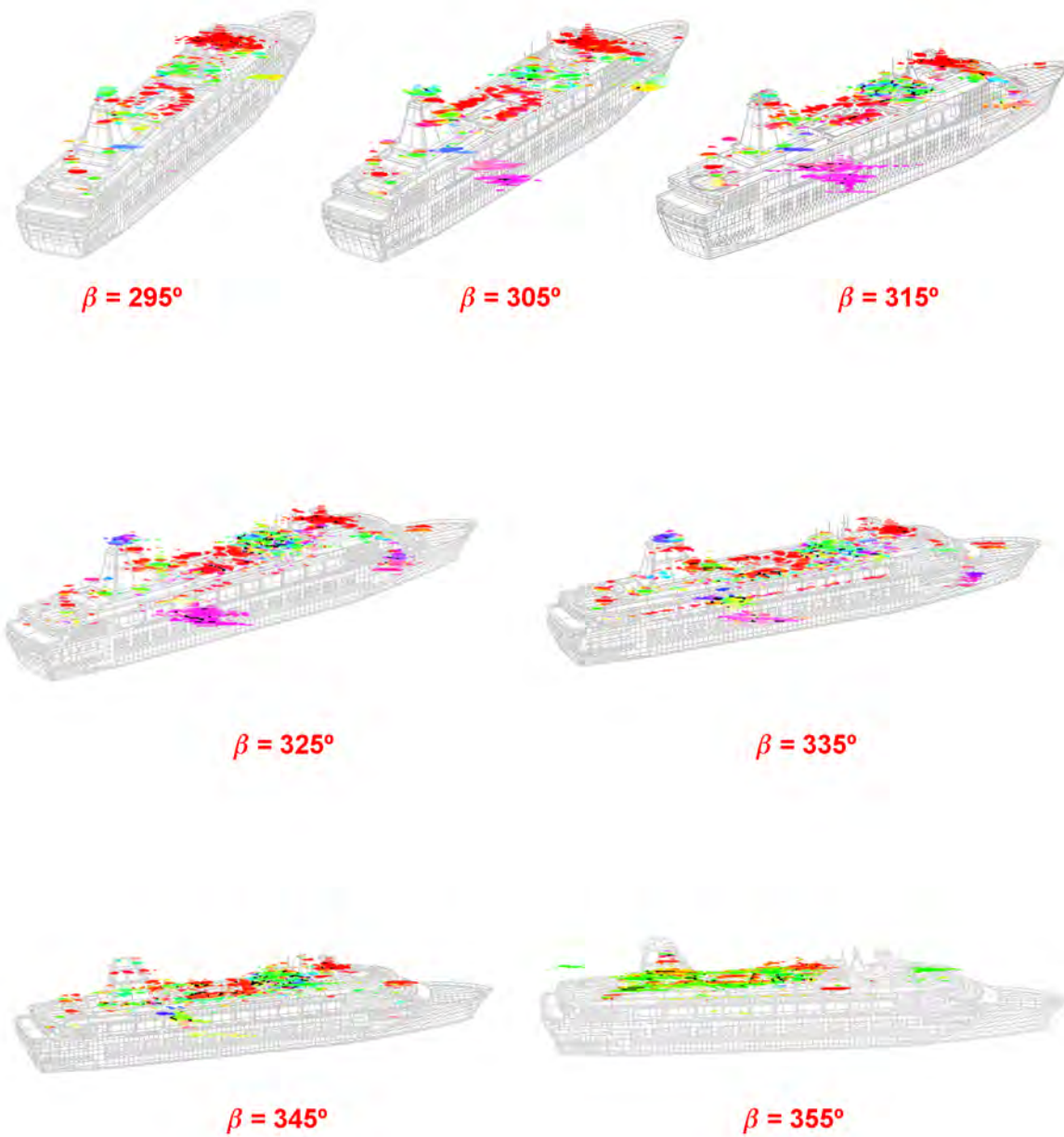


Figure D.22: Polarimetric ISAR dataset obtained for the scaled version of the FER model at S band and  $\phi = 20^\circ$ . The bearing range is  $\beta \in \{295 + 10 * i\}$  for  $i \in \{0..6\}$ . The images have been analyzed with the Pauli theorem for a dynamic range of 25 dB.

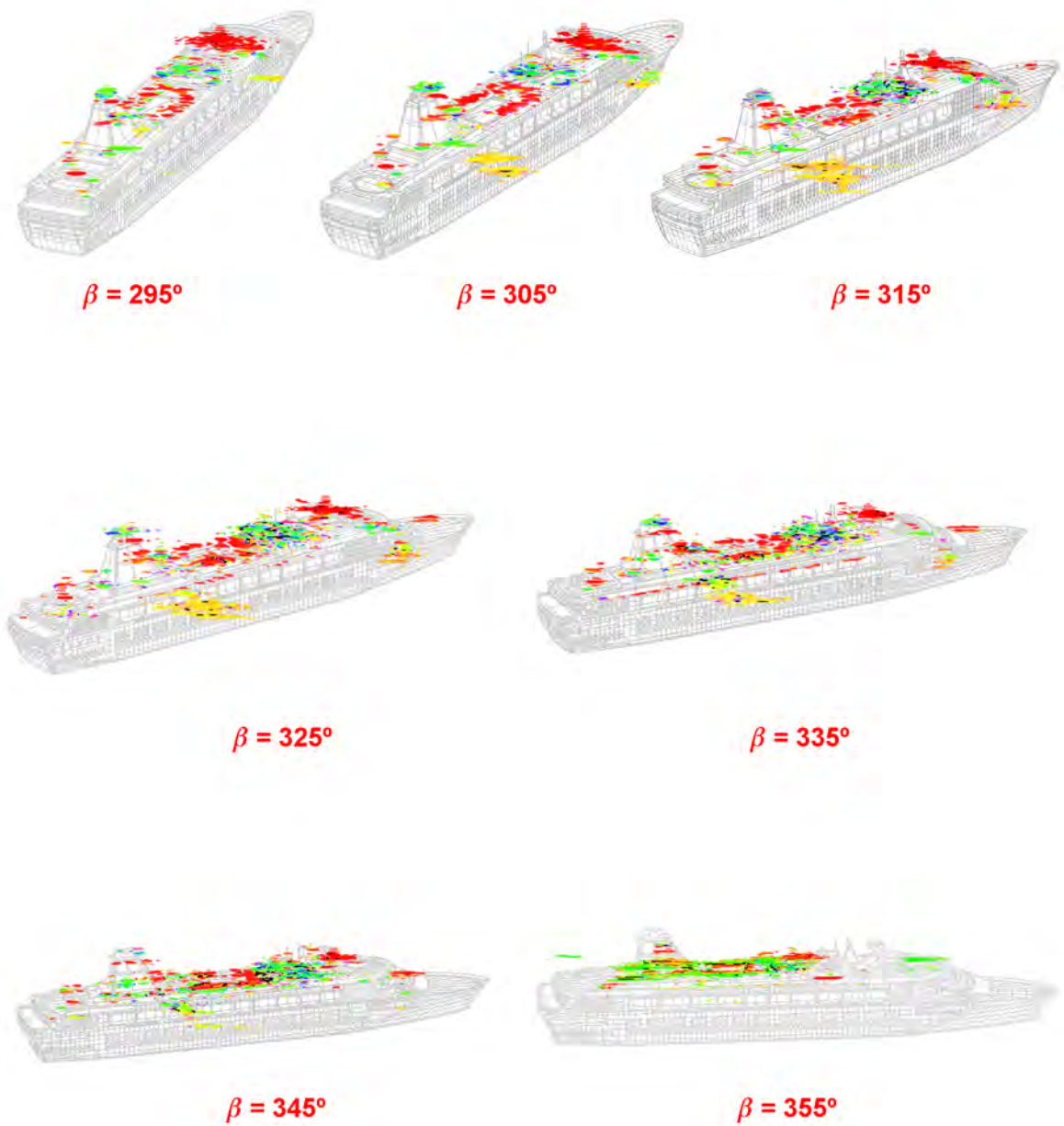


Figure D.23: Polarimetric ISAR dataset obtained for the scaled version of the FER model at S band and  $\phi = 20^\circ$ . The bearing range is  $\beta \in \{295 + 10 * i\}$  for  $i \in \{0..6\}$ . The images have been analyzed with the SDH theorem for a dynamic range of 25 dB.

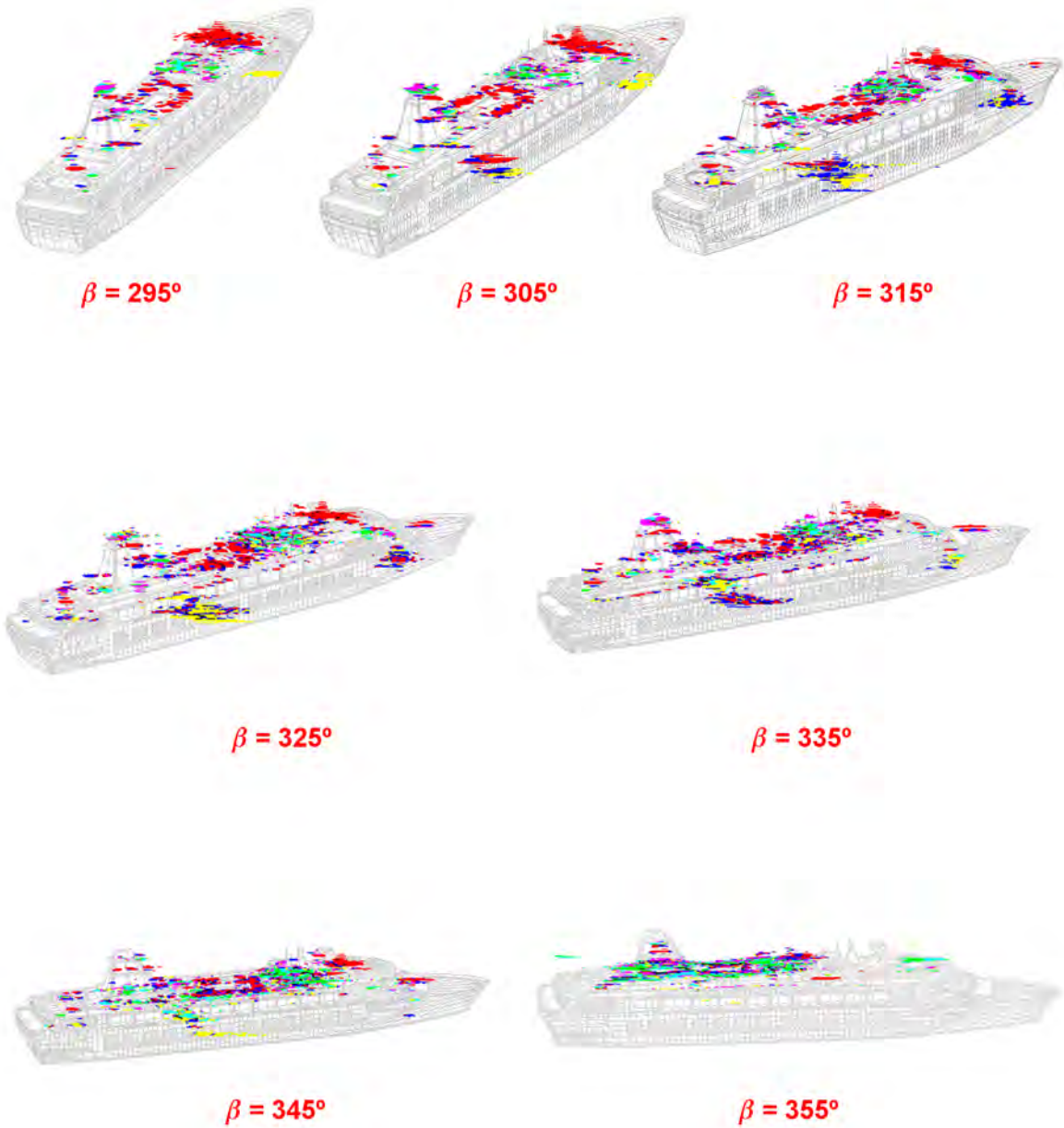


Figure D.24: Polarimetric ISAR dataset obtained for the scaled version of the FER model at S band and  $\phi = 20^\circ$ . The bearing range is  $\beta \in \{295 + 10 * i\}$  for  $i \in \{0..6\}$ . The images have been analyzed with the Cameron theorem for a dynamic range of 25 dB.

Table D.3: Main Characteristics of the PolSAR images included in Section D.3

Model	Scaled	$\beta + \phi$ [°]	$\phi$ [°]	vessel motions	sea surface	Fig.
SPA	NO	295-355	20	NO	NO	D.25 (Pauli) D.26 (SDH) - D.27 (Cameron)
ICE	NO	295-355	20	NO	NO	D.28 (Pauli) D.29 (SDH) - D.30 (Cameron)
FER	NO	295-355	20	NO	NO	D.31 (Pauli) D.32 (SDH) - D.33 (Cameron)
ICE	YES	295-355	20	NO	NO	D.34 (Pauli) D.35 (SDH) - D.36 (Cameron)

## D.3 C Band

In this section, the C band data are presented. Their main characteristics and the list of figures where the images are included are summarized in Table D.3.

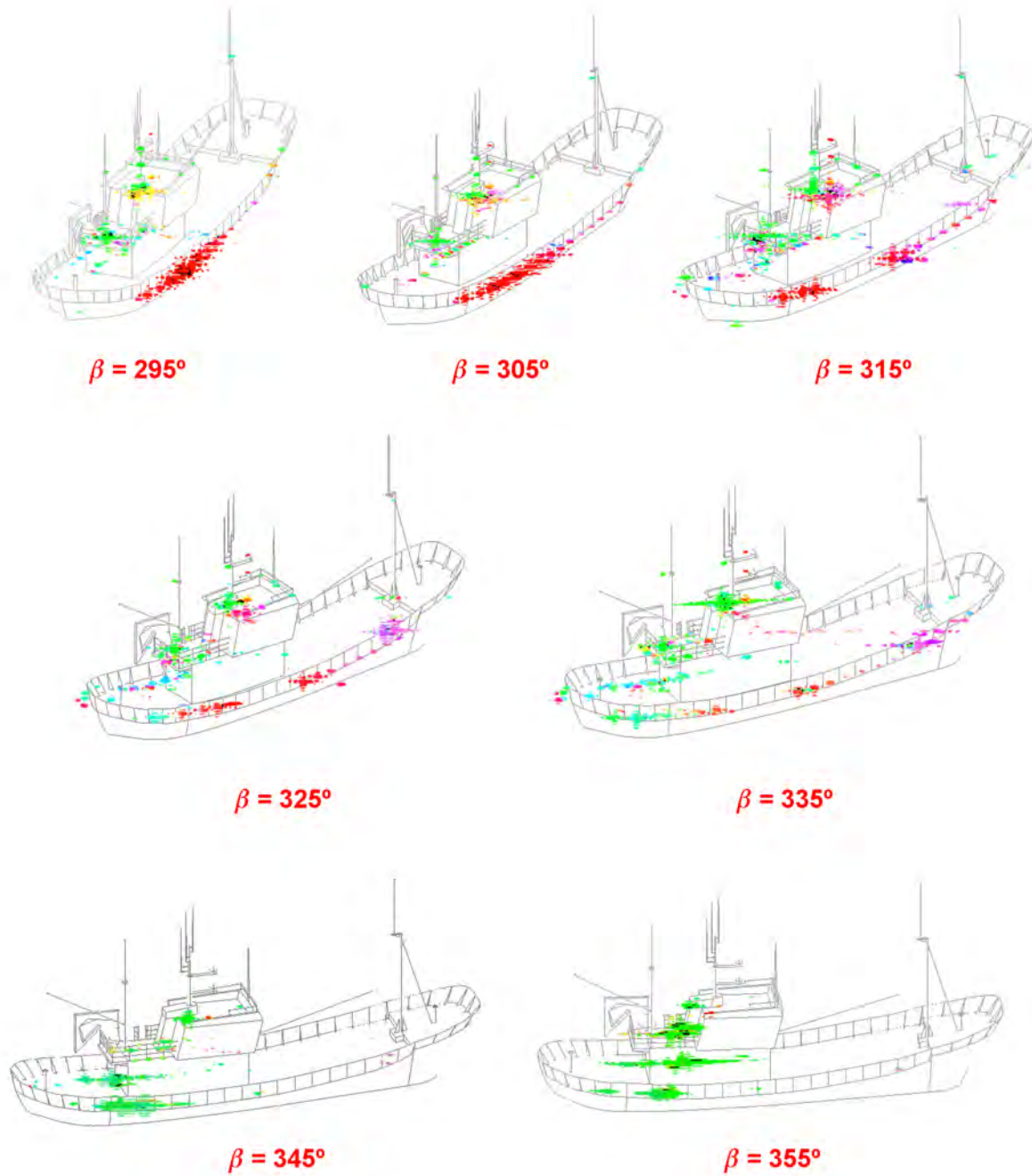


Figure D.25: Polarimetric ISAR dataset obtained for the SPA model at C band and  $\phi = 20^\circ$ . The bearing range is  $\beta \in \{295 + 10 * i\}$  for  $i \in \{0..6\}$ . The images have been analyzed with the Pauli theorem for a dynamic range of 25 dB.



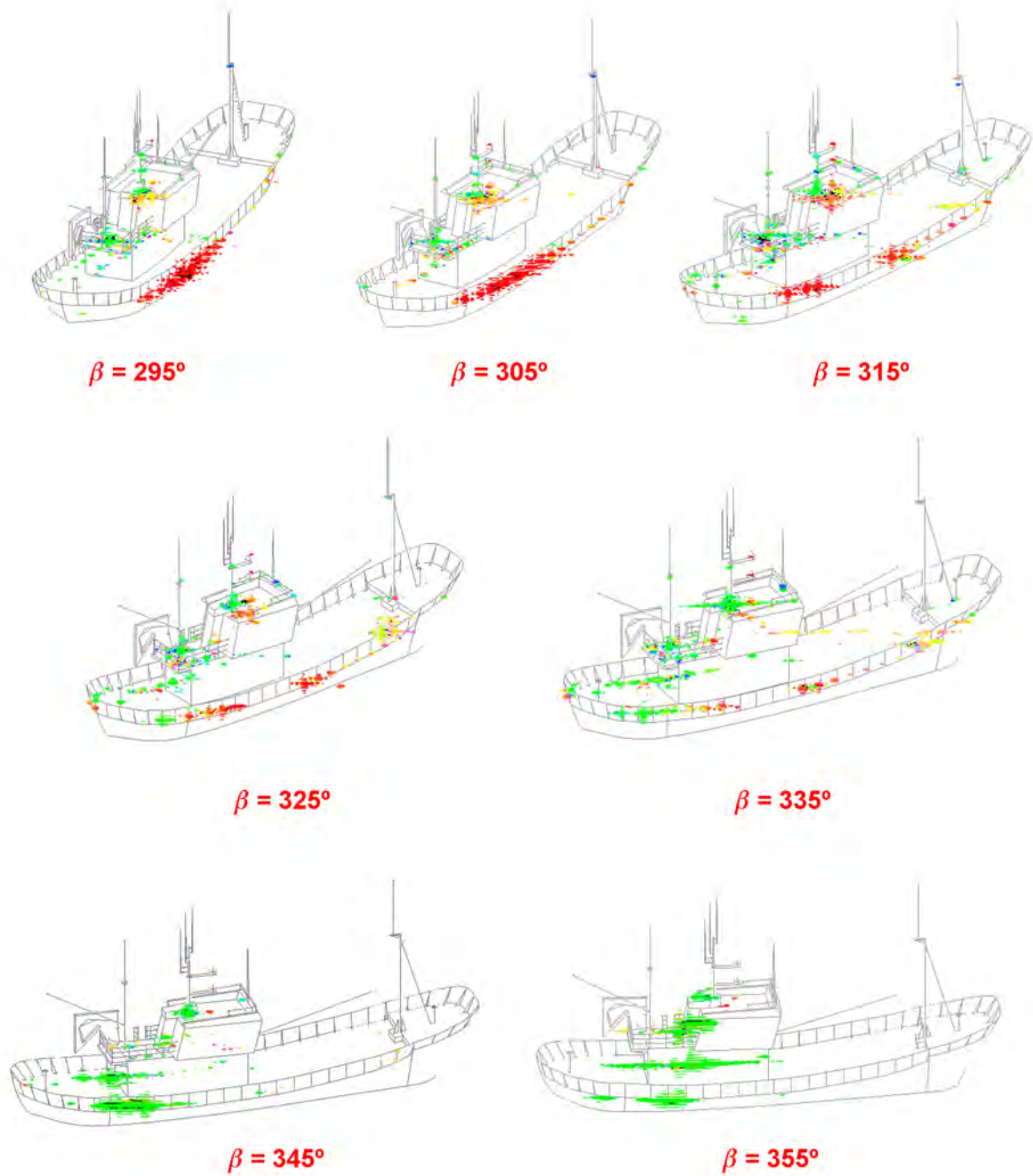


Figure D.26: Polarimetric ISAR dataset obtained for the SPA model at C band and  $\phi = 20^\circ$ . The bearing range is  $\beta \in \{295 + 10 * i\}$  for  $i \in \{0..6\}$ . The images have been analyzed with the SDH theorem for a dynamic range of 25 dB.

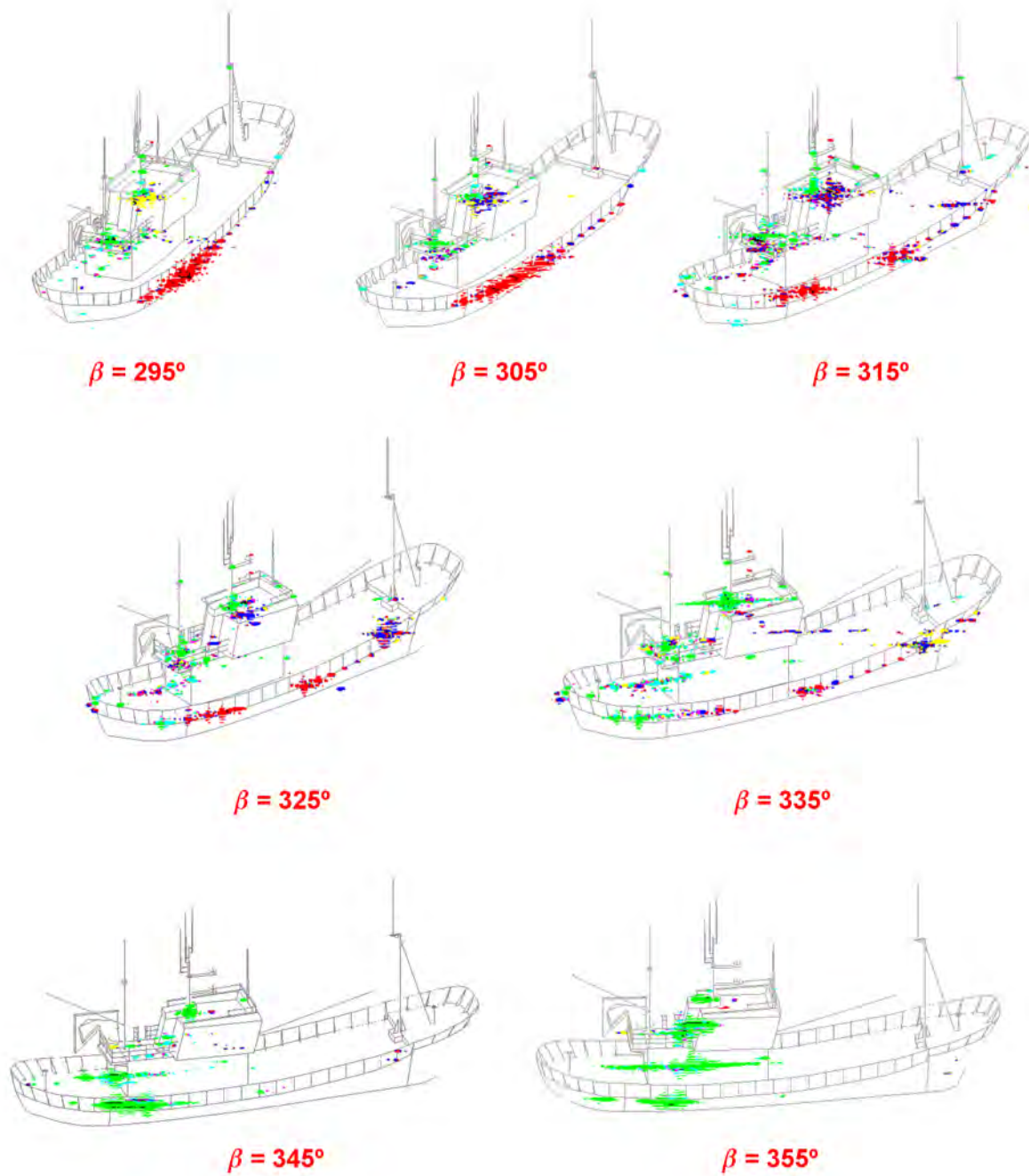


Figure D.27: Polarimetric ISAR dataset obtained for the SPA model at C band and  $\phi = 20^\circ$ . The bearing range is  $\beta \in \{295 + 10 * i\}$  for  $i \in \{0..6\}$ . The images have been analyzed with the Cameron theorem for a dynamic range of 25 dB.

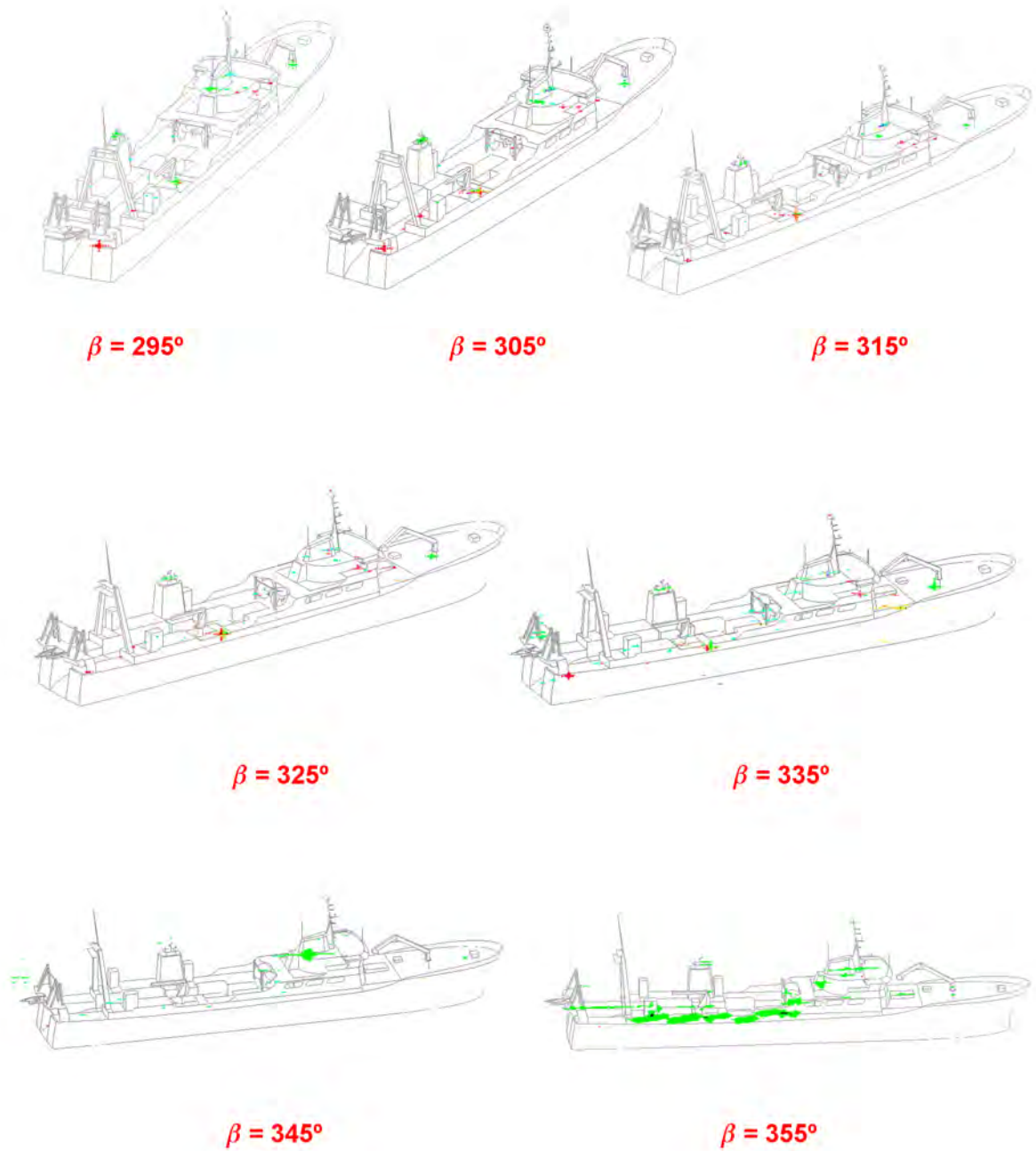


Figure D.28: Polarimetric ISAR dataset obtained for the ICE model at C band and  $\phi = 20^\circ$ . The bearing range is  $\beta \in \{295 + 10 * i\}$  for  $i \in \{0..6\}$ . The images have been analyzed with the Pauli theorem for a dynamic range of 25 dB.

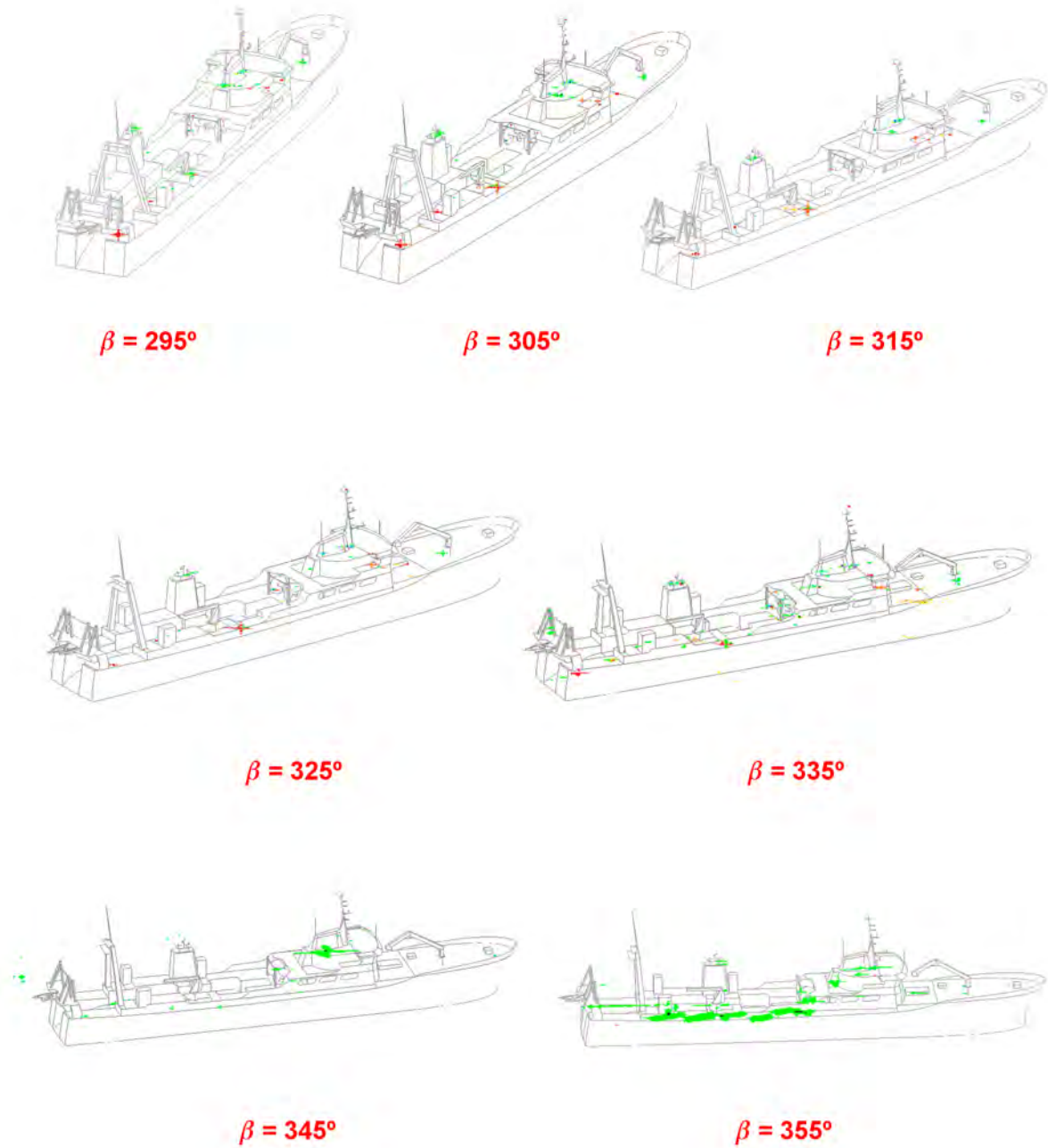


Figure D.29: Polarimetric ISAR dataset obtained for the ICE model at C band and  $\phi = 20^\circ$ . The bearing range is  $\beta \in \{295 + 10 * i\}$  for  $i \in \{0..6\}$ . The images have been analyzed with the SDH theorem for a dynamic range of 25 dB.

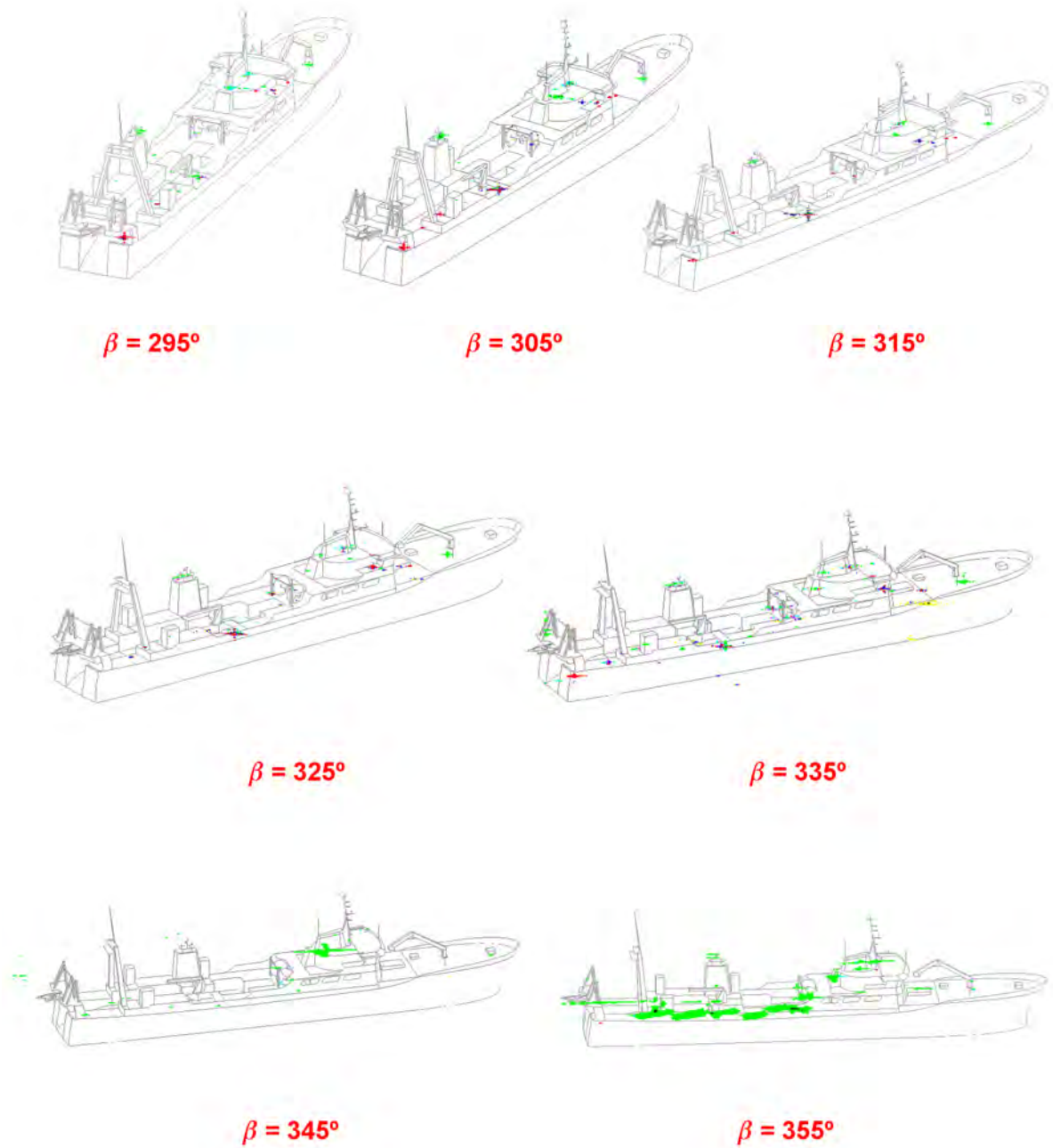


Figure D.30: Polarimetric ISAR dataset obtained for the ICE model at C band and  $\phi = 20^\circ$ . The bearing range is  $\beta \in \{295 + 10 * i\}$  for  $i \in \{0..6\}$ . The images have been analyzed with the Cameron theorem for a dynamic range of 25 dB.

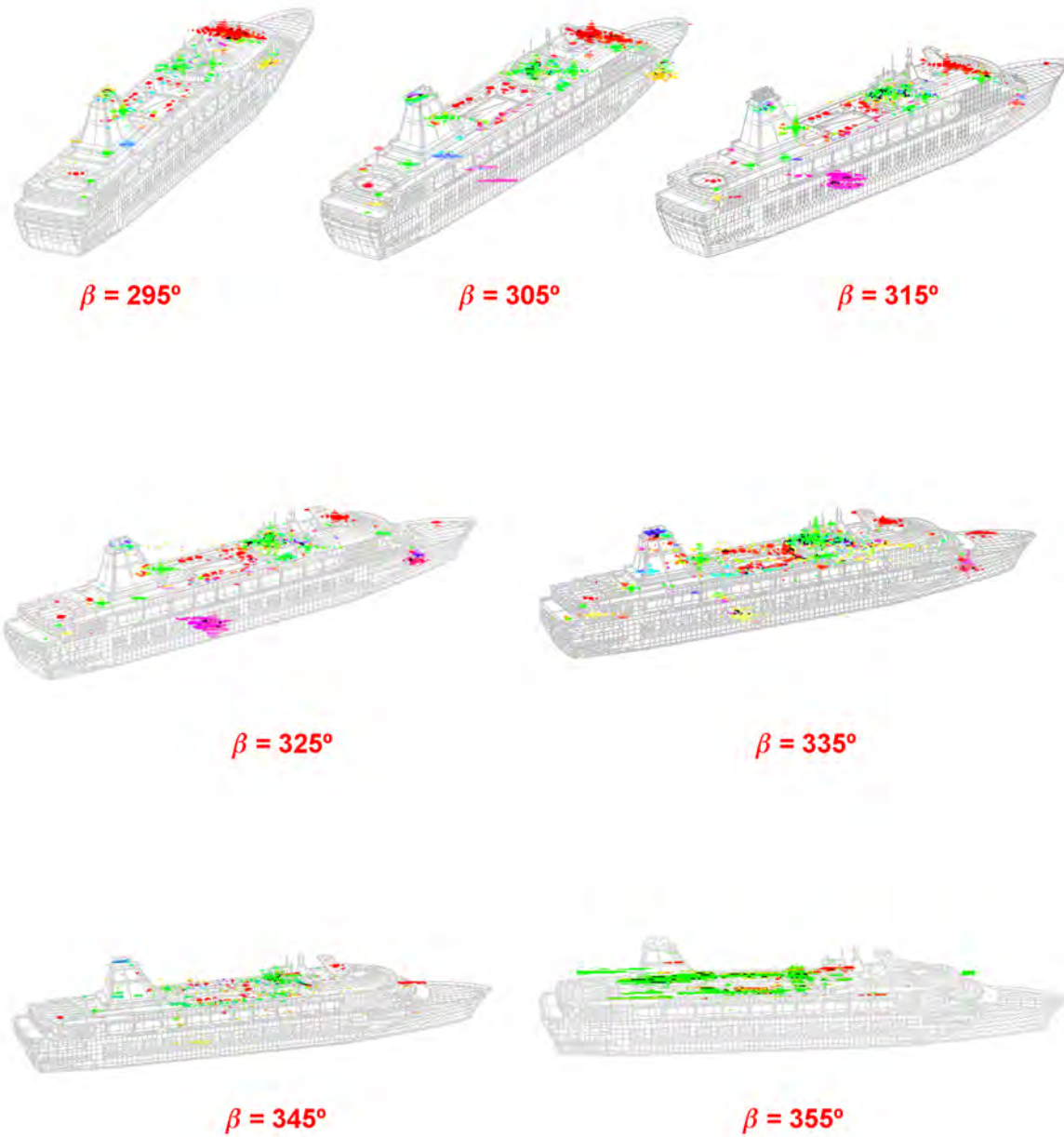


Figure D.31: Polarimetric ISAR dataset obtained for the scaled version of the FER model at C band and  $\phi = 20^\circ$ . The bearing range is  $\beta \in \{295 + 10 * i\}$  for  $i \in \{0..6\}$ . The images have been analyzed with the Pauli theorem for a dynamic range of 25 dB.

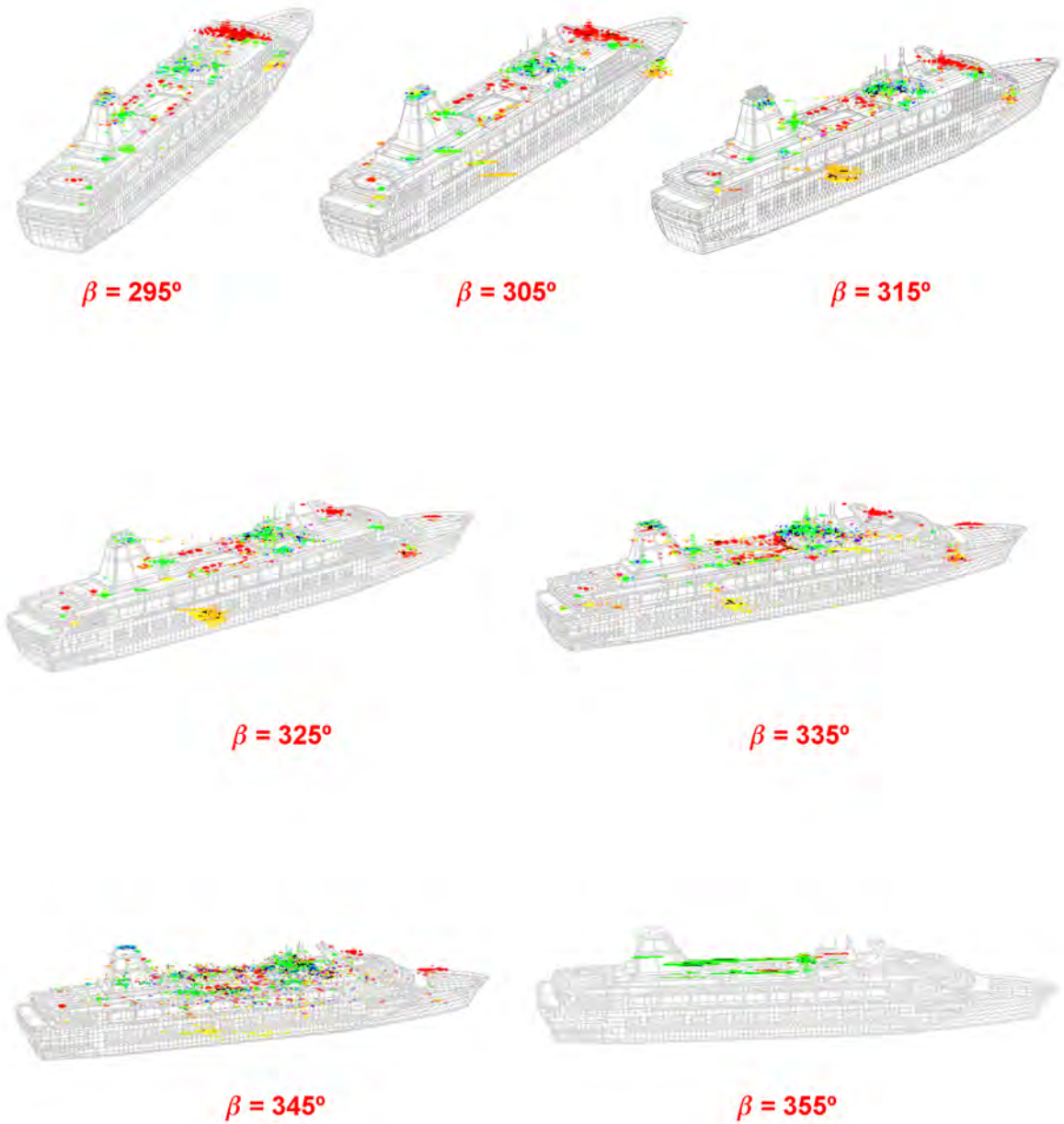


Figure D.32: Polarimetric ISAR dataset obtained for the scaled version of the FER model at C band and  $\phi = 20^\circ$ . The bearing range is  $\beta \in \{295 + 10 * i\}$  for  $i \in \{0..6\}$ . The images have been analyzed with the SDH theorem for a dynamic range of 25 dB.

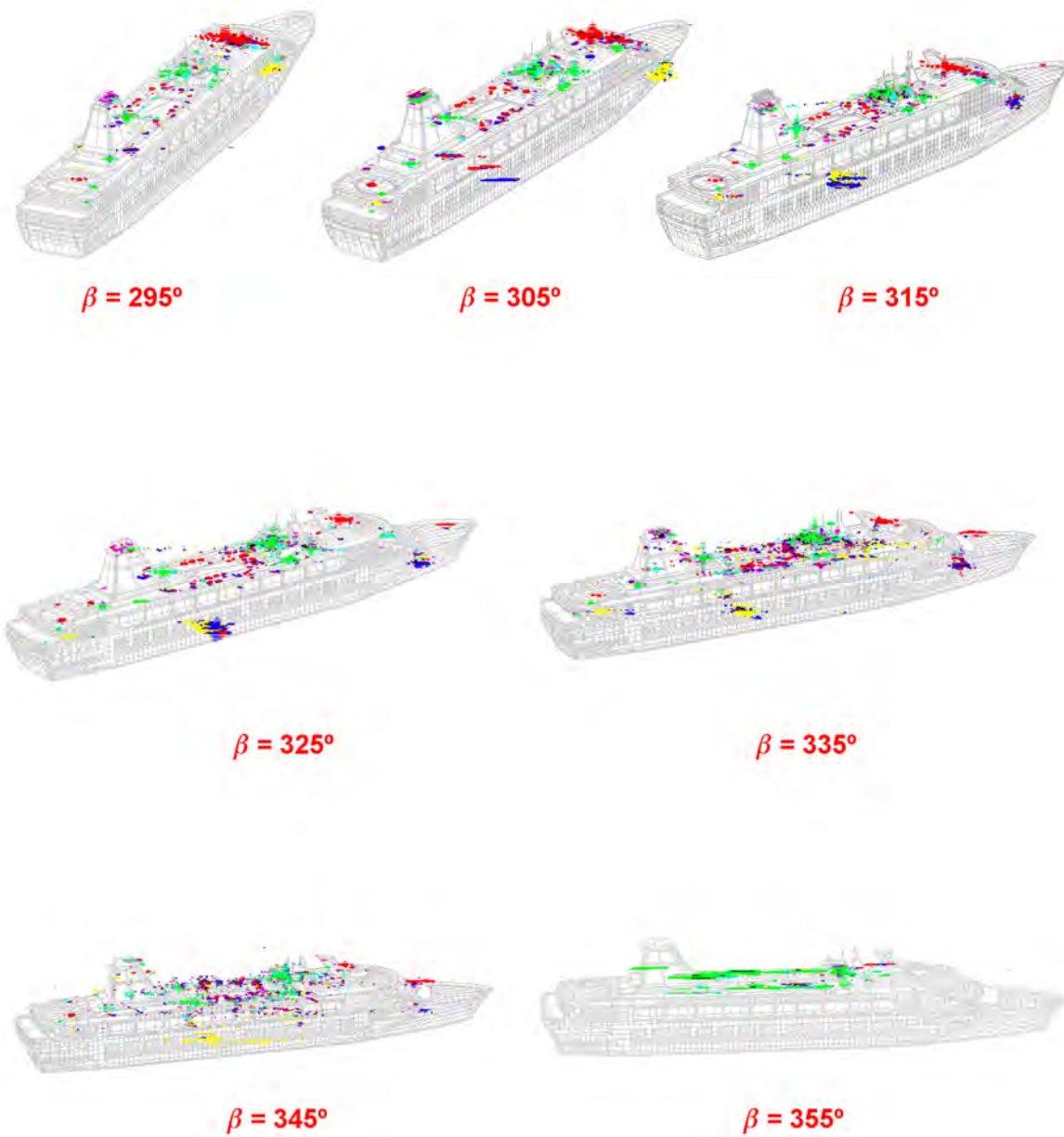


Figure D.33: Polarimetric ISAR dataset obtained for the scaled version of the FER model at C band and  $\phi = 20^\circ$ . The bearing range is  $\beta \in \{295 + 10 * i\}$  for  $i \in \{0..6\}$ . The images have been analyzed with the Cameron theorem for a dynamic range of 25 dB.



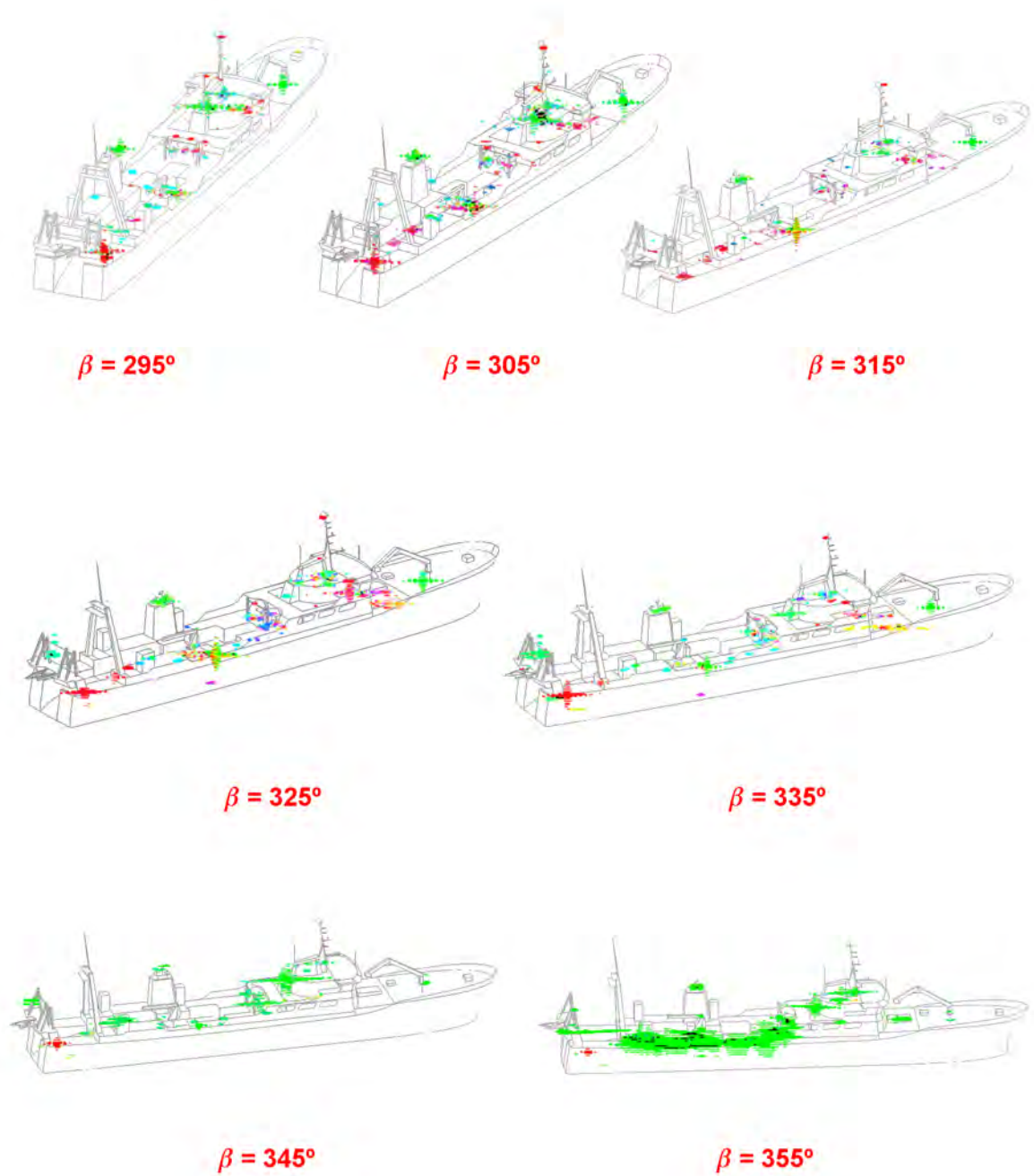


Figure D.34: Polarimetric ISAR dataset obtained for the scaled version of the ICE model at C band and  $\phi = 20^\circ$ . The bearing range is  $\beta \in \{295 + 10 * i\}$  for  $i \in \{0..6\}$ . The images have been analyzed with the Pauli theorem for a dynamic range of 25 dB.

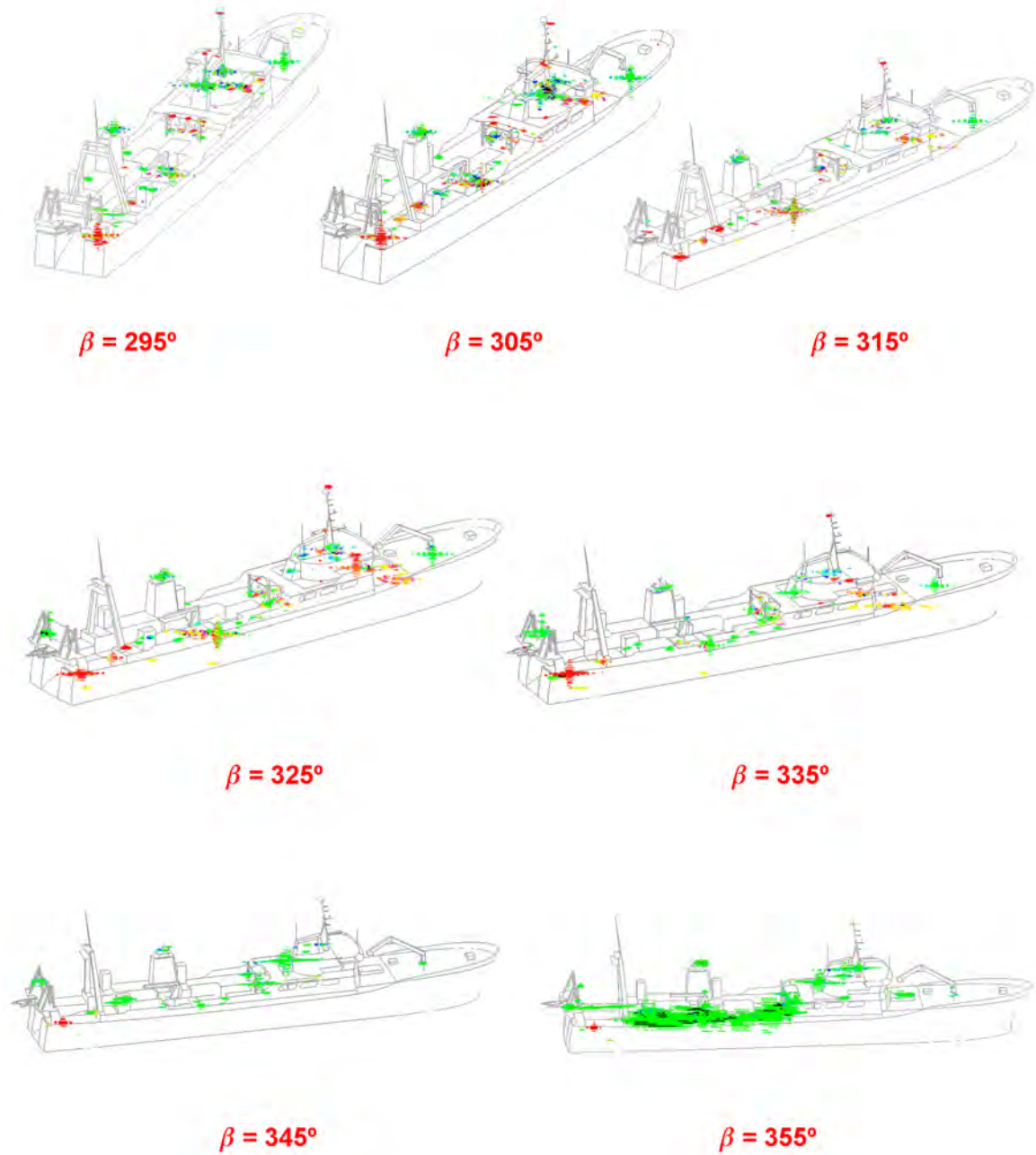


Figure D.35: Polarimetric ISAR dataset obtained for the scaled version of the ICE model at C band and  $\phi = 20^\circ$ . The bearing range is  $\beta \in \{295 + 10 * i\}$  for  $i \in \{0..6\}$ . The images have been analyzed with the SDH theorem for a dynamic range of 25 dB.

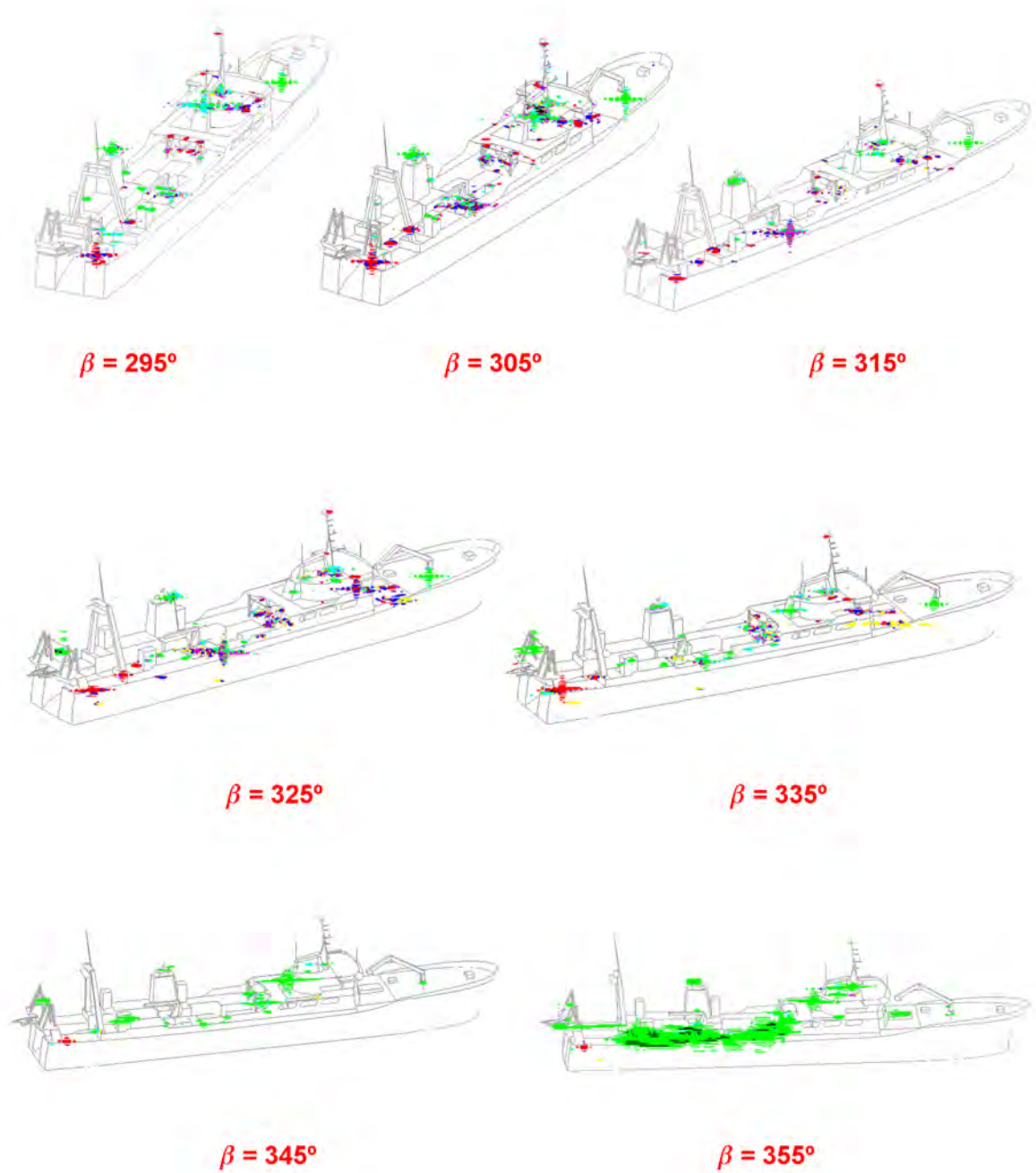


Figure D.36: Polarimetric ISAR dataset obtained for the scaled version of the ICE model at C band and  $\phi = 20^\circ$ . The bearing range is  $\beta \in \{295 + 10 * i\}$  for  $i \in \{0..6\}$ . The images have been analyzed with the Cameron theorem for a dynamic range of 25 dB.

Table D.4: Main Characteristics of the PolISAR images included in Section D.4

Model	Scaled	$\beta + \phi$ [°]	$\phi$ [°]	vessel motions	sea surface	Fig.
SPA	NO	<i>295-355</i>	<i>20</i>	NO	NO	<b>D.37</b> (Pauli)
ICE	NO	<i>295-355</i>	<i>20</i>	NO	NO	<b>D.38</b> (Pauli)
FER	NO	<i>295-355</i>	<i>20</i>	NO	NO	<b>D.39</b> (Pauli)
SPAv2	NO	<i>295-355</i>	<i>20</i>	NO	NO	<b>D.40</b> (Pauli)

## D.4 X Band

In this section, the X band data are presented. Their main characteristics and the list of figures where the images are included are summarized in Table D.4. In this case, only the information for the Pauli theorem is presented as the polarimetric interpretation retrieved for the other CTD is almost identical.

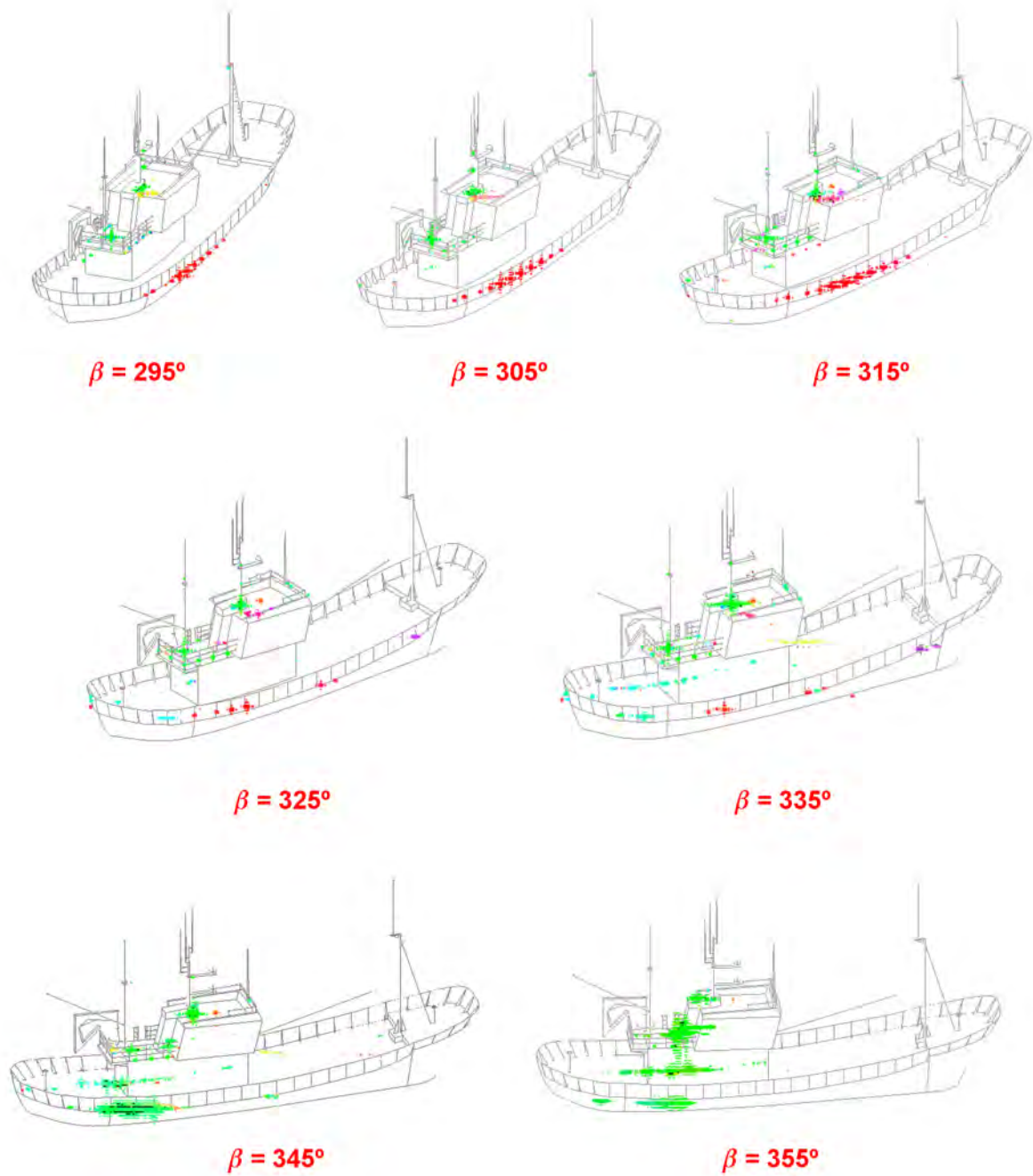


Figure D.37: Polarimetric ISAR dataset obtained for the SPA model at X band and  $\phi = 20^\circ$ . The bearing range is  $\beta \in \{295 + 10 * i\}$  for  $i \in \{0..6\}$ . The images have been analyzed with the Pauli theorem for a dynamic range of 25 dB.

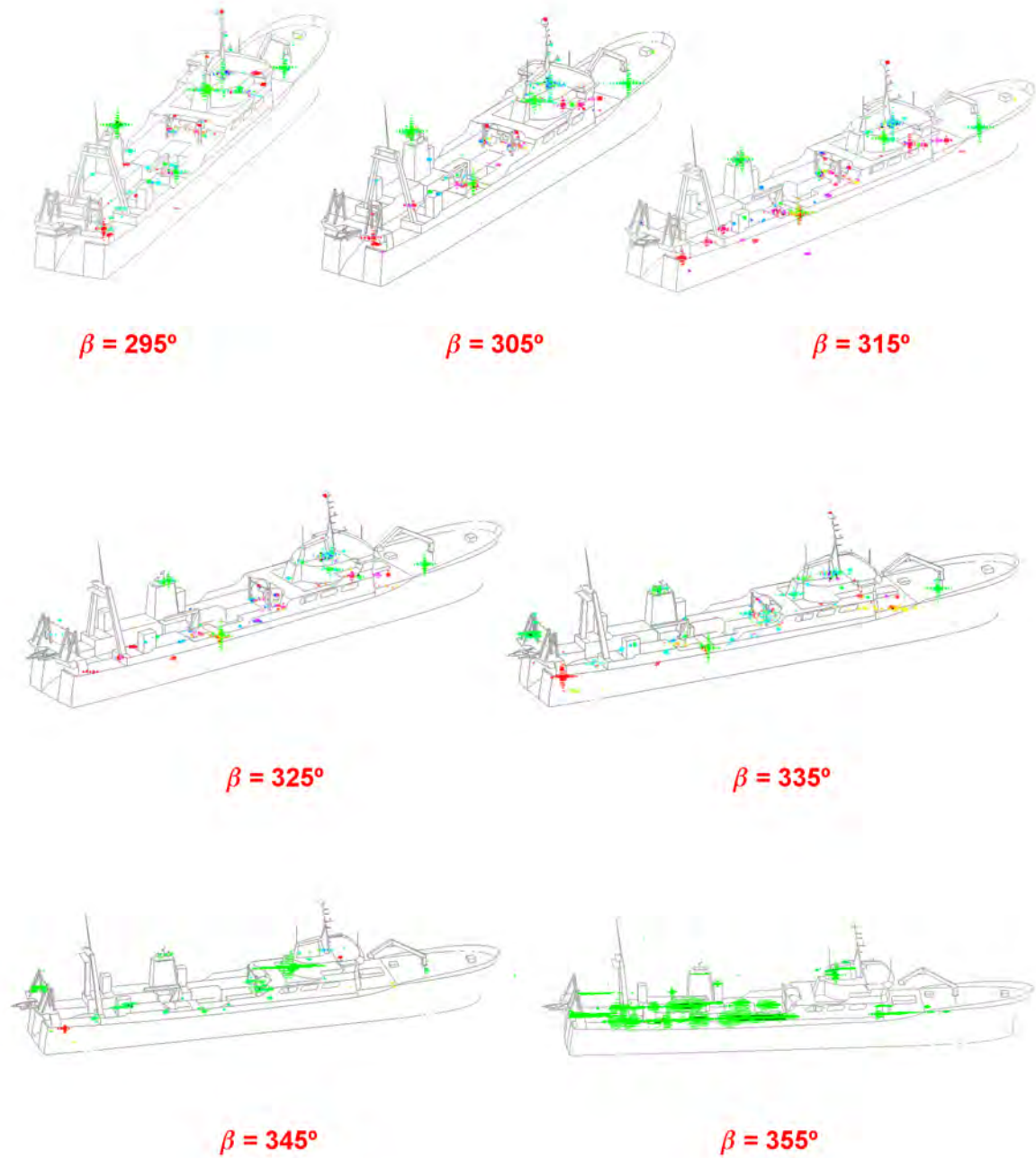


Figure D.38: Polarimetric ISAR dataset obtained for the scaled version of the ICE model at X band and  $\phi = 20^\circ$ . The bearing range is  $\beta \in \{295 + 10 * i\}$  for  $i \in \{0..6\}$ . The images have been analyzed with the Pauli theorem for a dynamic range of 25 dB.

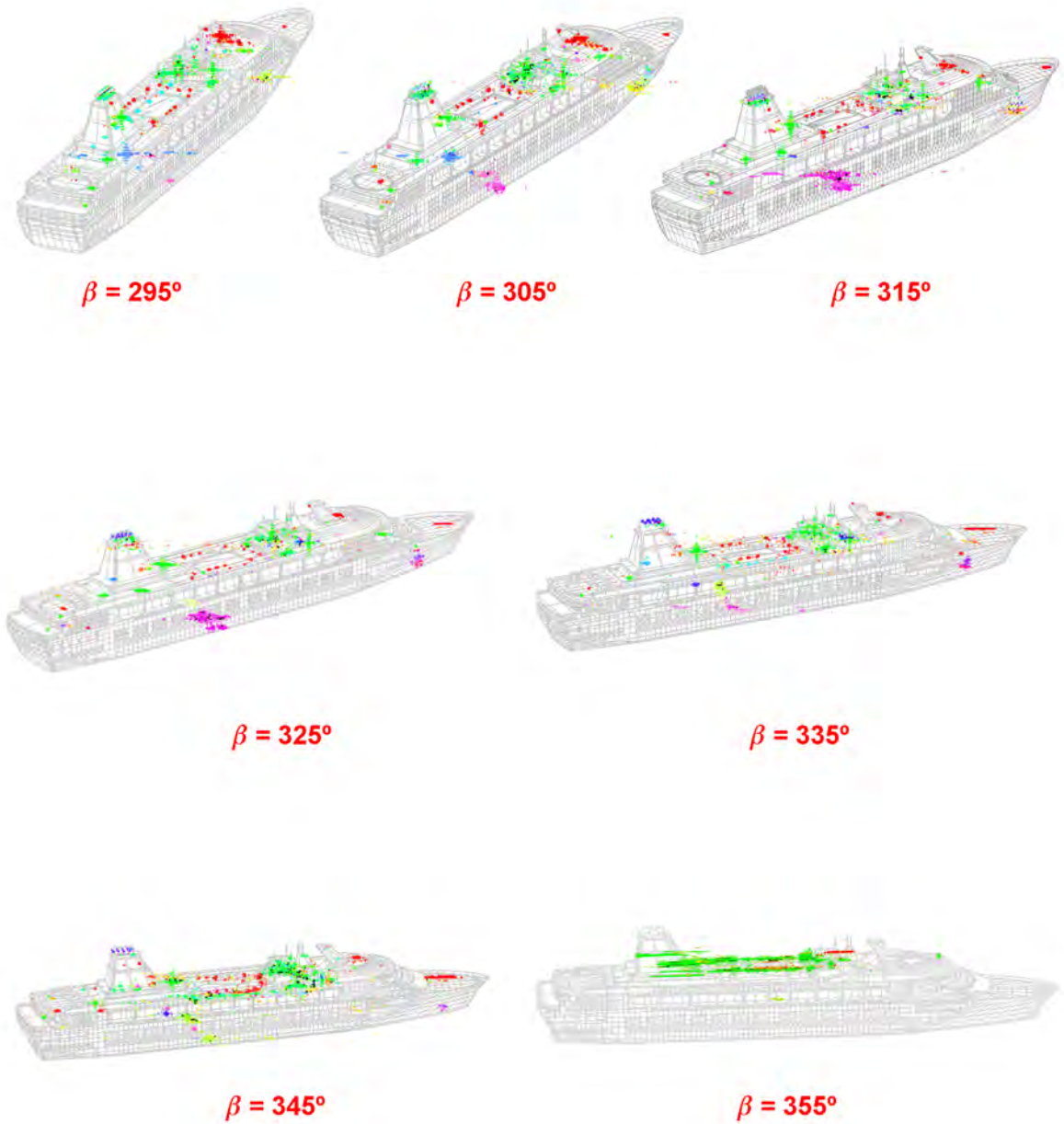


Figure D.39: Polarimetric ISAR dataset obtained for the scaled version of the FER model at X band and  $\phi = 20^\circ$ . The bearing range is  $\beta \in \{295 + 10 * i\}$  for  $i \in \{0..6\}$ . The images have been analyzed with the Pauli theorem for a dynamic range of 25 dB.

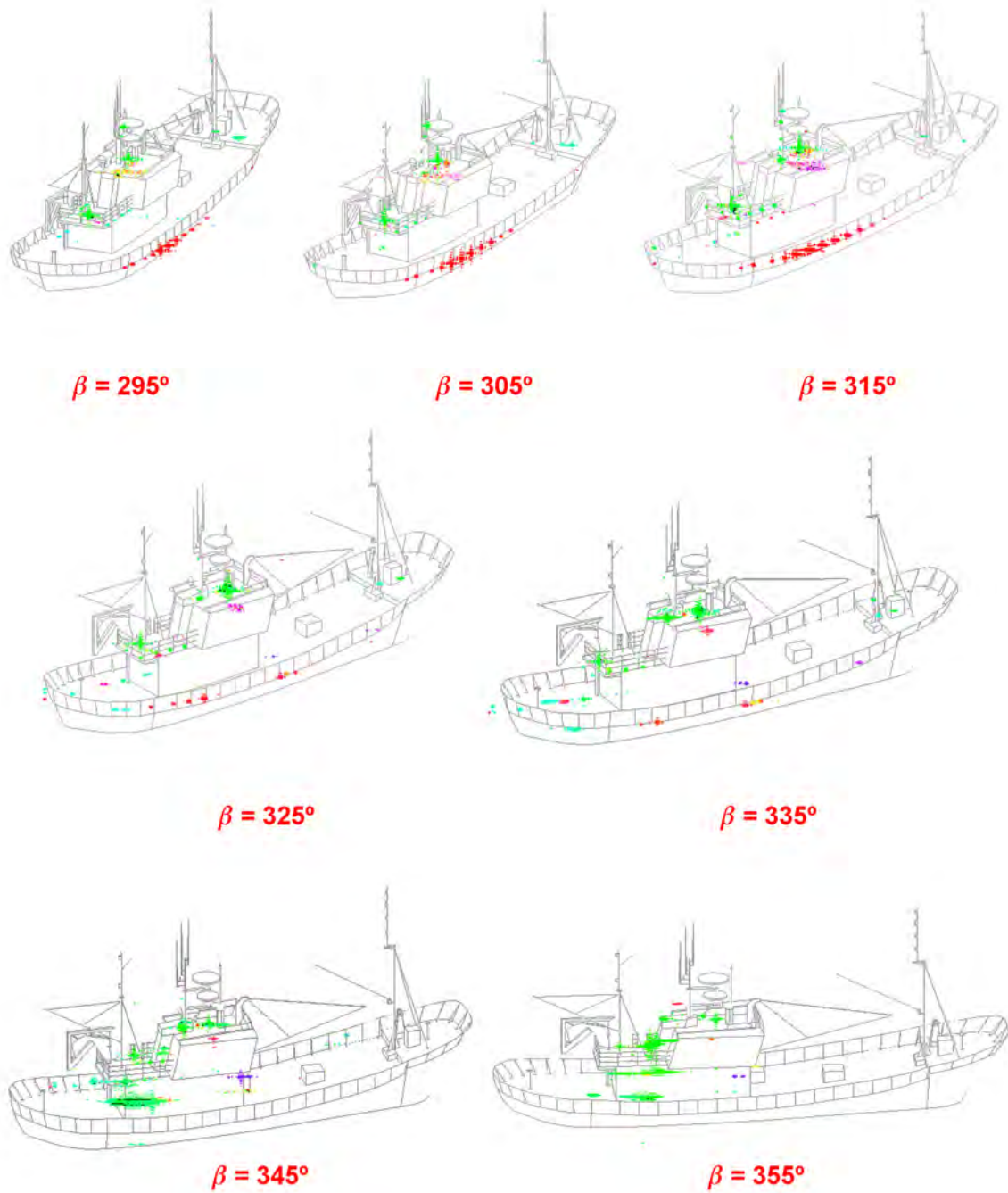


Figure D.40: Polarimetric ISAR dataset obtained for the SPAv2 model at X band and  $\phi = 20^\circ$ . The bearing range is  $\beta \in \{295 + 10 * i\}$  for  $i \in \{0..6\}$ . The images have been analyzed with the Pauli theorem for a dynamic range of 25 dB.



## Appendix E

# Vessel Scattering Study with Polarimetric SAR images

This Appendix gathers the results of analyzing the PolSAR images used in the vessel scattering study presented in Chapter 6 with the Pauli, SDH and Cameron CTD. The images are organized according to the selected center frequency. Each figure contains the information related to the three CTD for the bearing range defined by  $\beta + \phi = 295 + 10 * i$  for  $i \in \{0..6\}$ . Two sets of images are attached, namely: 1) the combined weight of all the simple mechanisms of each decomposition expressed via colored images and 2) the weight of the Pauli mechanisms isolated in gray images. In both cases, a snapshot of the point of view of the satellite is included with the azimuth x range ( $A, R$ ) location of two reference points.

### E.1 C Band

In this section, the C band data are presented. Their main characteristics and the list of figures where the images are included are summarized in Table E.1.

Table E.1: Main Characteristics of the PolSAR images included in Section E.1

Model	Scaled	$\beta + \phi$ [°]	$\phi$ [°]	vessel motions	sea surface	Fig.
SPA	NO	295-355	20	NO	NO	E.1 (colored) E.2 (gray)
ICE	NO	295-355	20	NO	NO	E.3 (colored) E.4 (gray)
FER	NO	295-355	20	NO	NO	E.5 (colored) E.6 (gray)

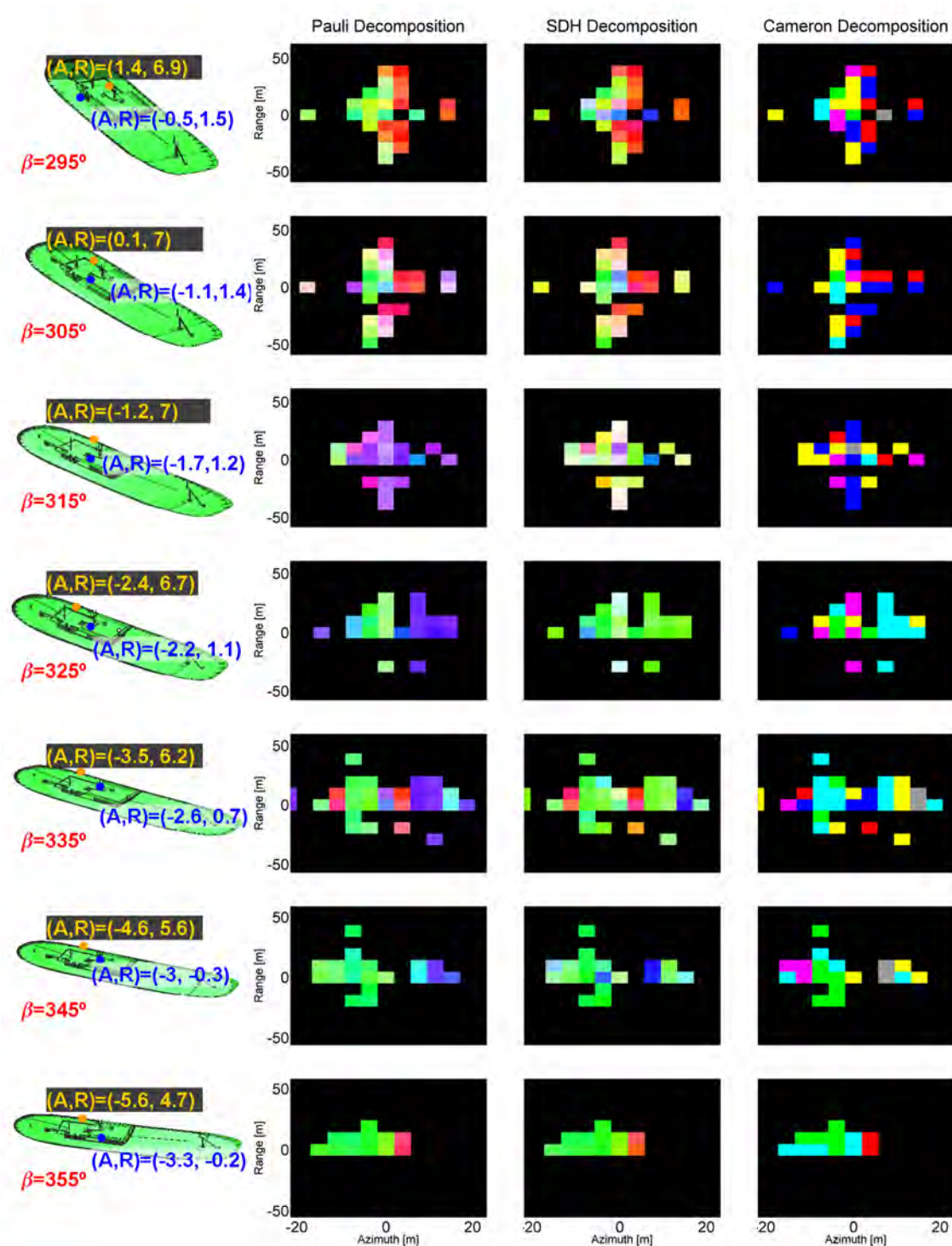


Figure E.1: Polarimetric SAR dataset obtained for the SPA model at C band and  $\phi = 20^\circ$ . The bearing angles are  $\beta \in \{295 + 10 * i\}$  for  $i \in \{0..6\}$ . The images have been analyzed with the Pauli, SDH and Cameron theorems for a dynamic range of 25 dB.

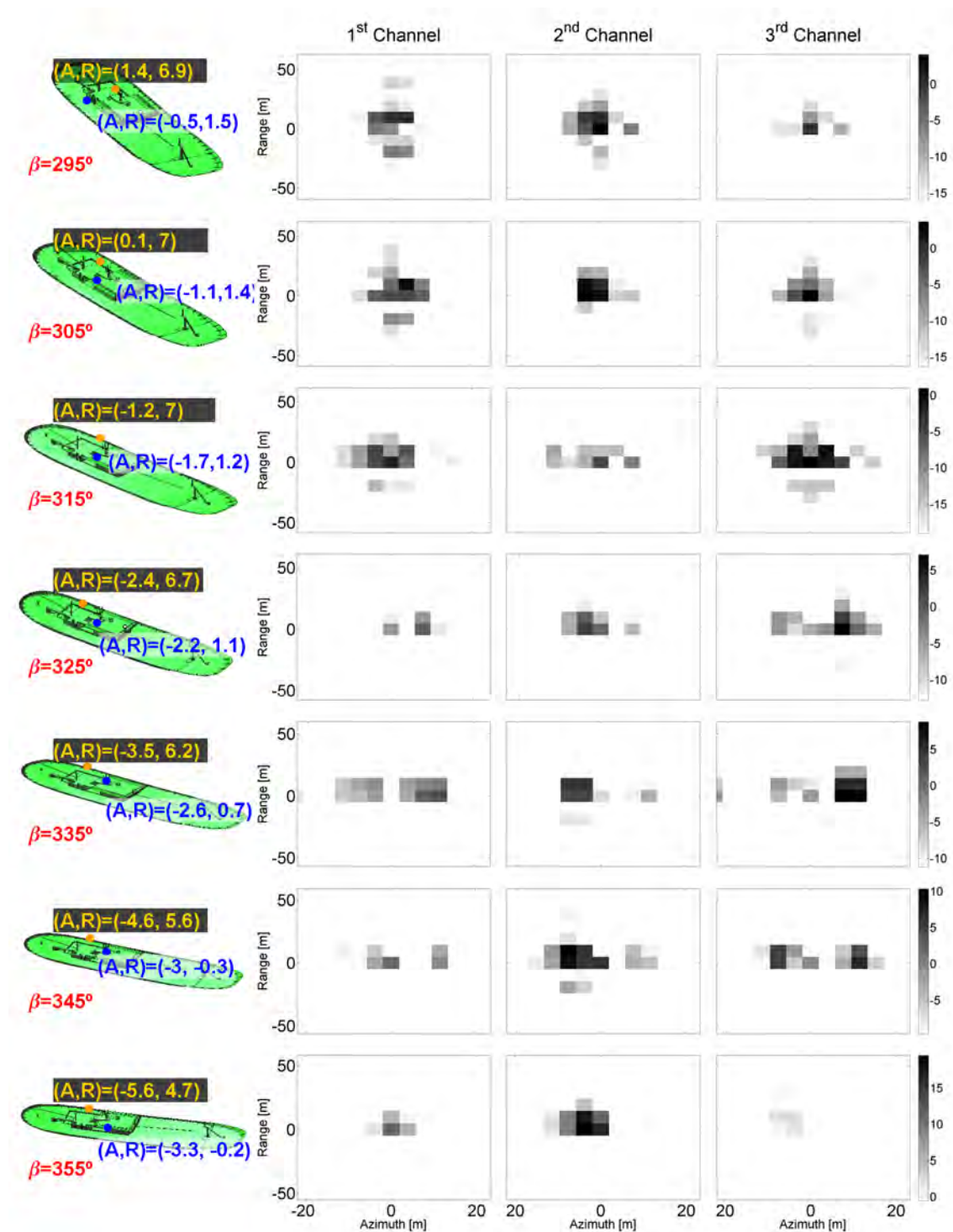


Figure E.2: Weight of the Pauli polarimetric channels related to the polarimetric SAR dataset depicted in Fig. E.1. The values are expressed with respect to the inter-channel maximum value.

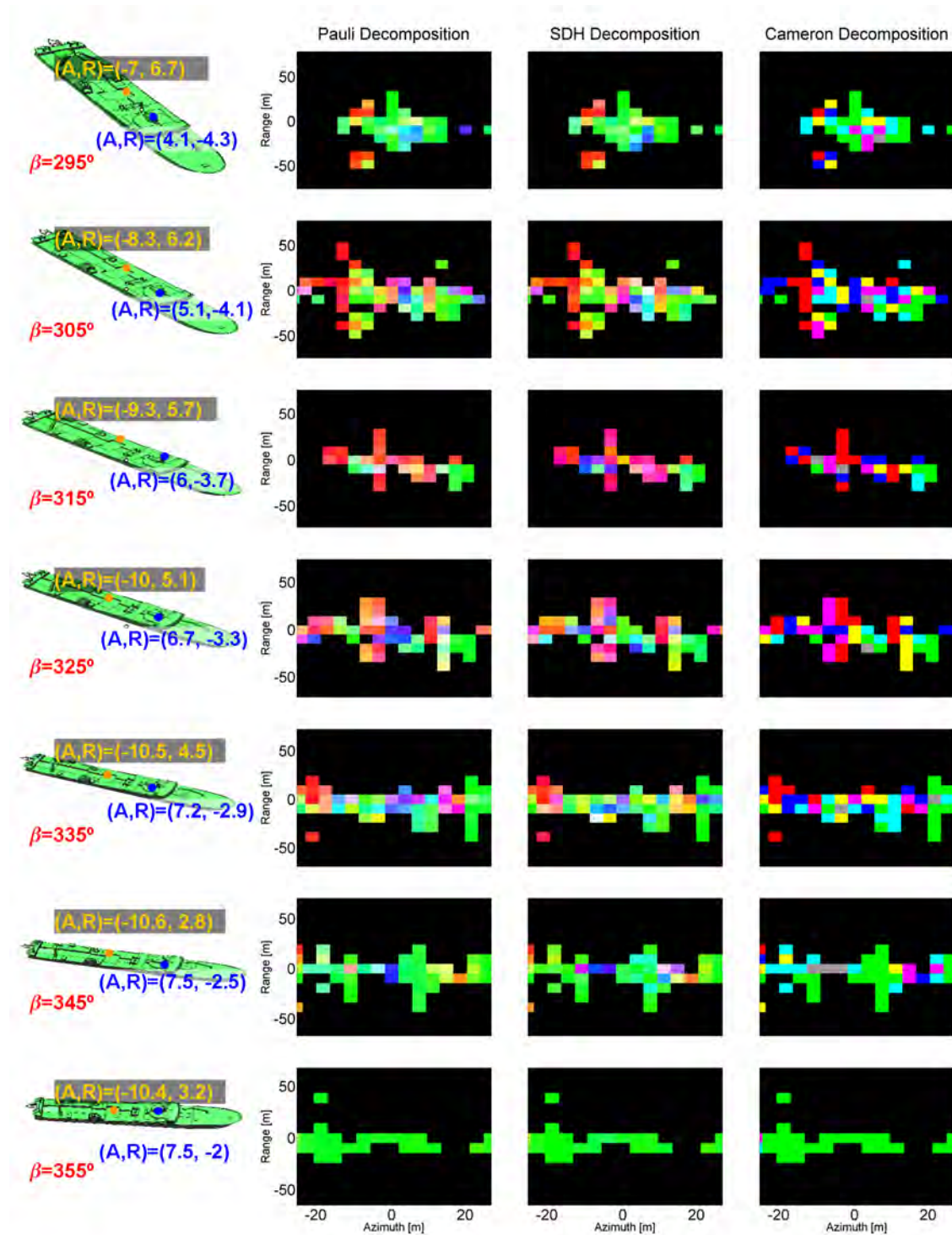


Figure E.3: Polarimetric SAR dataset obtained for the ICE model at C band and  $\phi = 20^\circ$ . The bearing angles are  $\beta \in \{295 + 10 * i\}$  for  $i \in \{0..6\}$ . The images have been analyzed with the Pauli, SDH and Cameron theorems for a dynamic range of 25 dB.

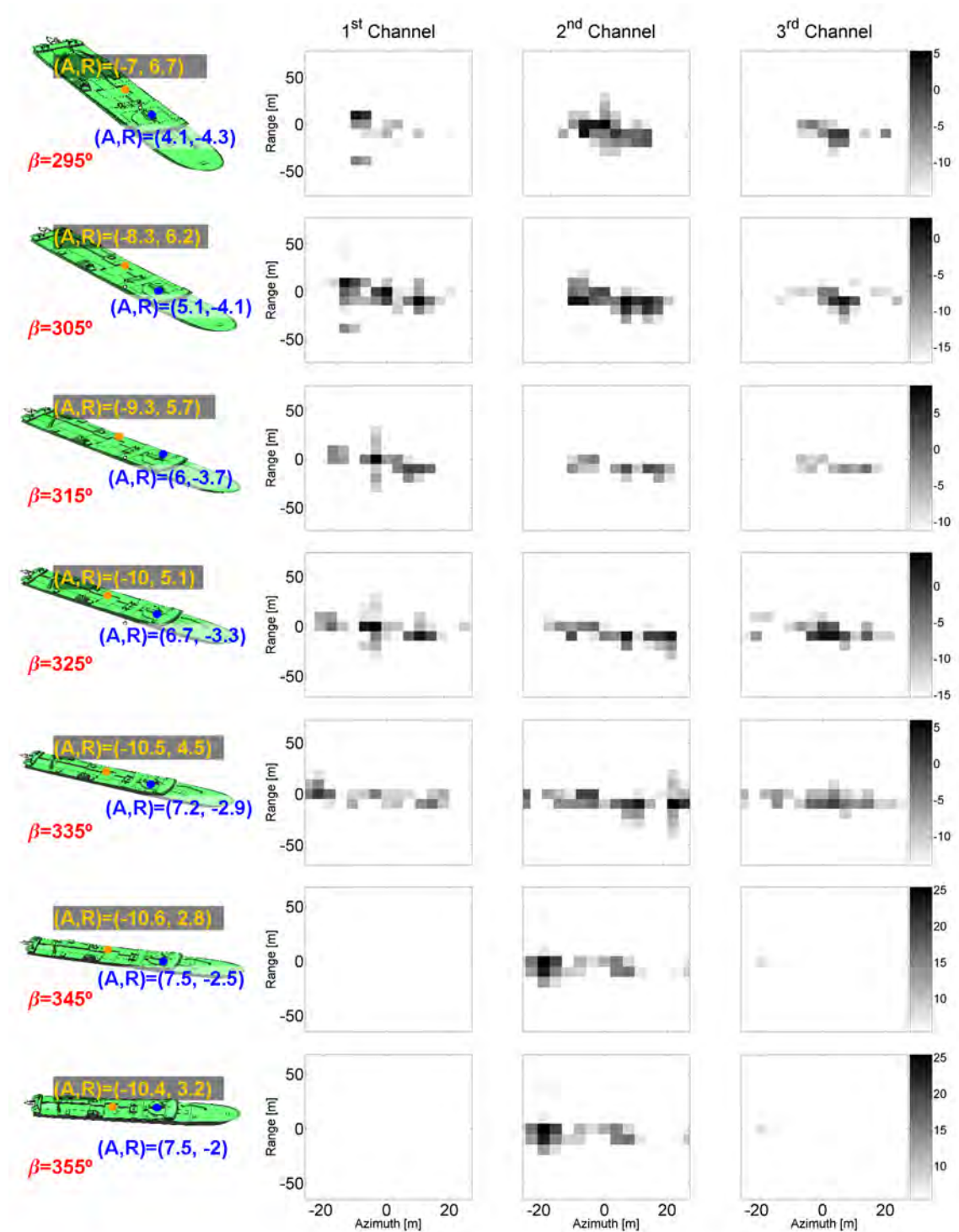


Figure E.4: Weight of the Pauli polarimetric channels related to the polarimetric SAR dataset depicted in Fig. E.3. The values are expressed with respect to the inter-channel maximum value.

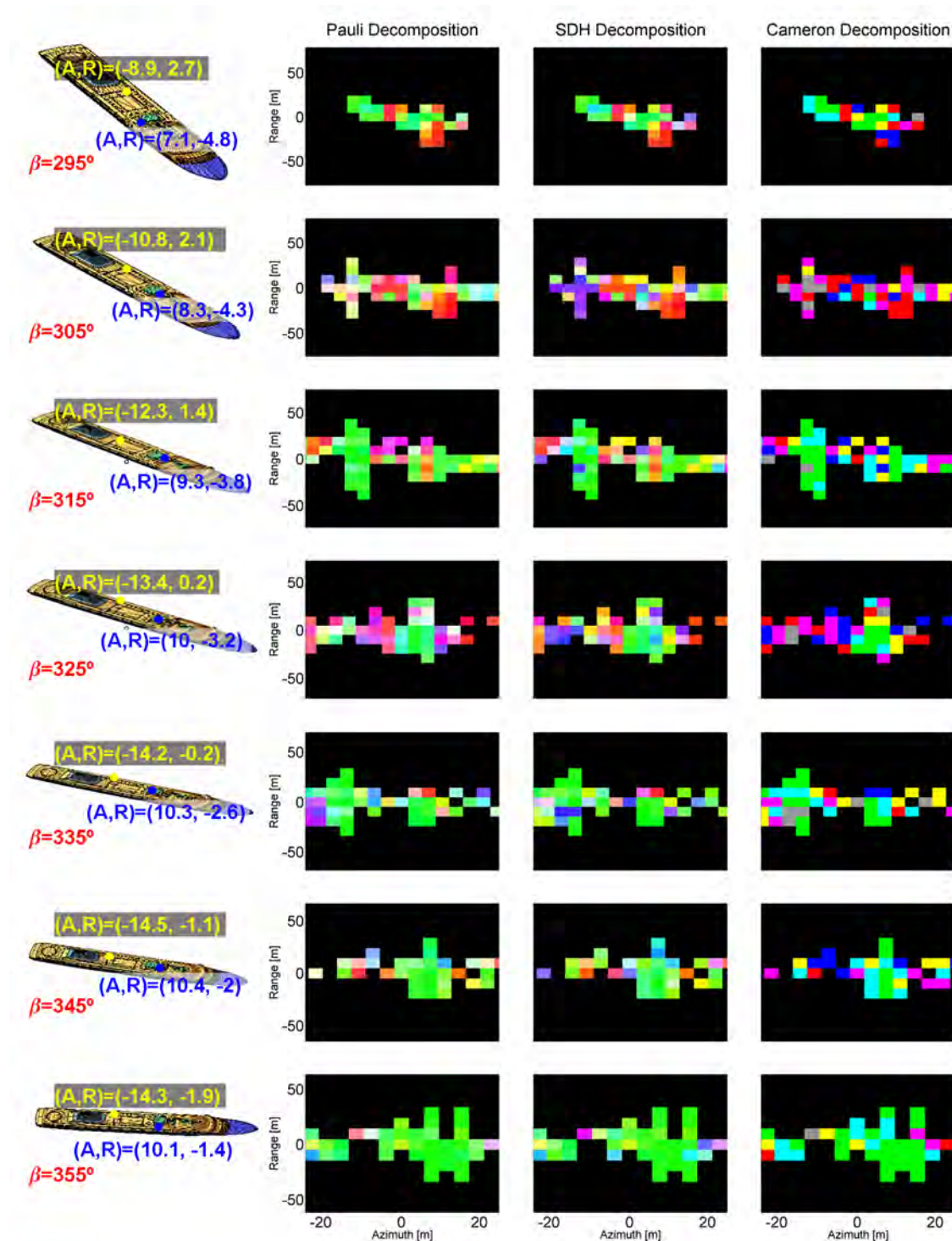


Figure E.5: Polarimetric SAR dataset obtained for the FER model at C band and  $\phi = 20^\circ$ . The bearing angles are  $\beta \in \{295 + 10 * i\}$  for  $i \in \{0..6\}$ . The images have been analyzed with the Pauli, SDH and Cameron theorems for a dynamic range of 25 dB.

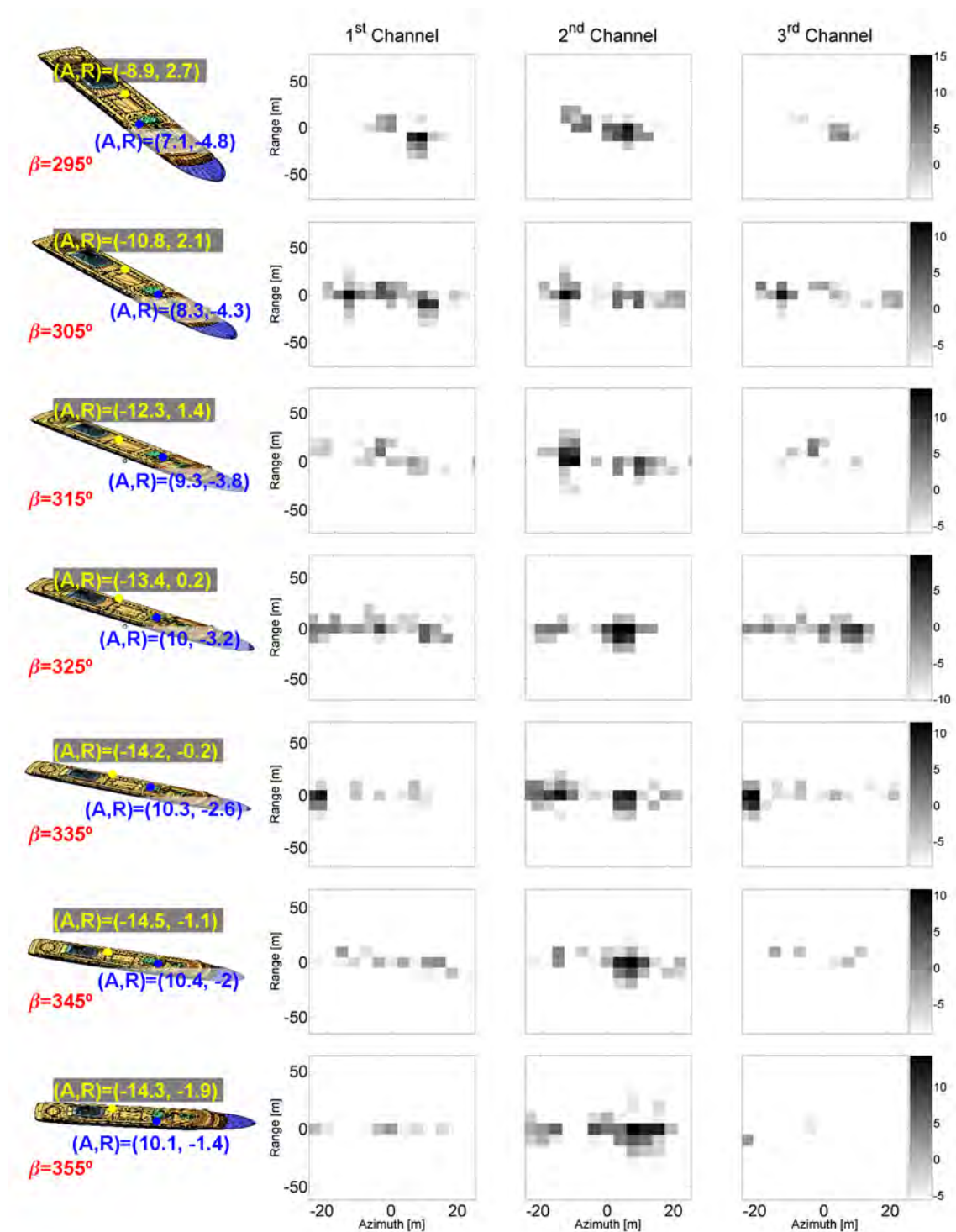


Figure E.6: Weight of the Pauli polarimetric channels related to the polarimetric SAR dataset depicted in Fig. E.5. The values are expressed with respect to the inter-channel maximum value.

Table E.2: Main Characteristics of the PolISAR images included in Section E.2

Model	Scaled	$\beta + \phi$ [°]	$\phi$ [°]	vessel motions	sea surface	Fig.
SPA	NO	295-355	20	NO	NO	E.7 (colored) E.8 (gray)
ICE	NO	295-355	20	NO	NO	E.9 (colored) E.10 (gray)
FER	NO	295-355	20	NO	NO	E.11 (colored) E.12 (gray)

## E.2 X Band

In this section, the X band data are presented. Their main characteristics and the list of figures where the images are included are summarized in Table E.2.



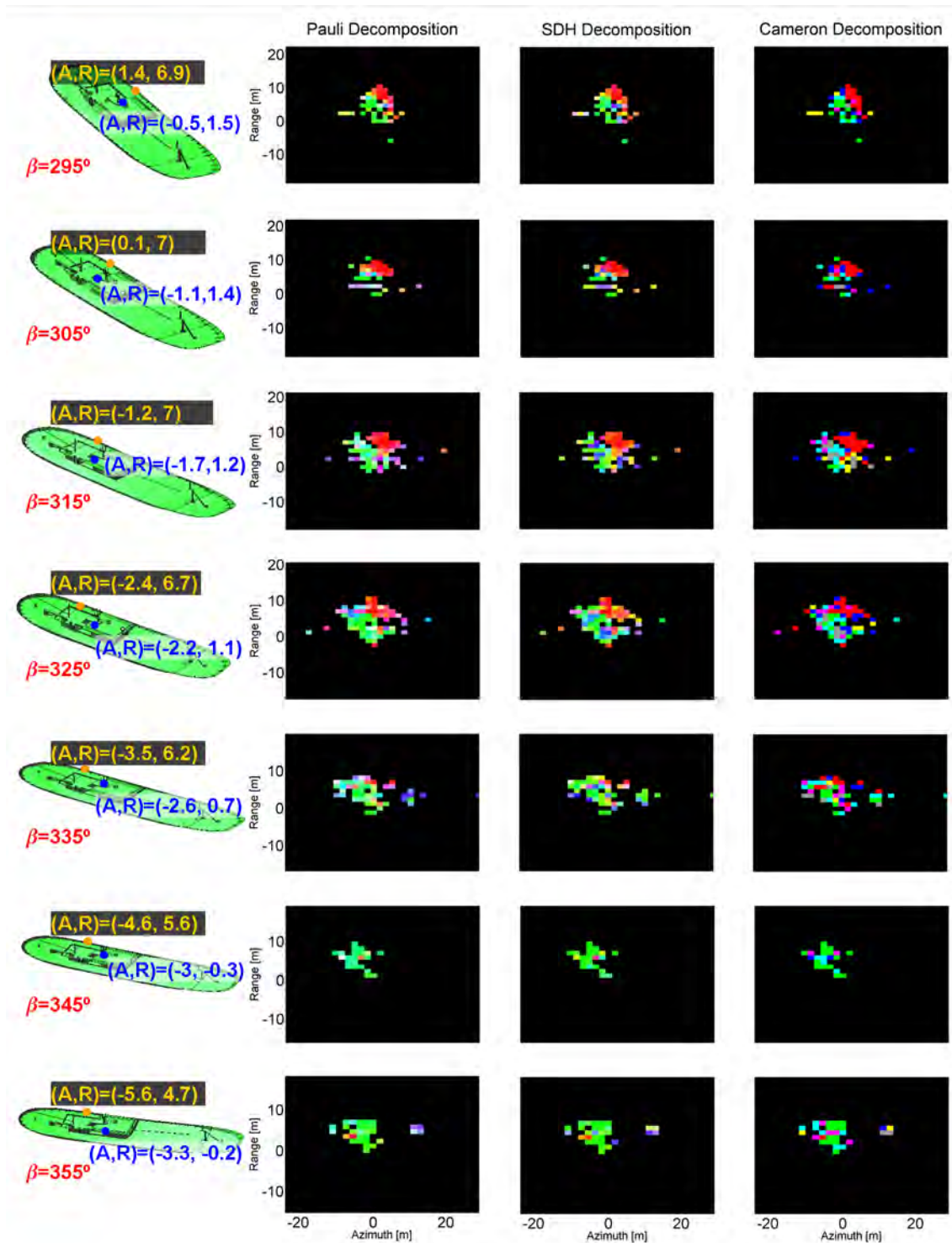


Figure E.7: Polarimetric SAR dataset obtained for the SPA model at X band and  $\phi = 20^\circ$ . The bearing angles are  $\beta \in \{295 + 10 * i\}$  for  $i \in \{0..6\}$ . The images have been analyzed with the Pauli, SDH and Cameron theorems for a dynamic range of 25 dB.



Figure E.8: Weight of the Pauli polarimetric channels related to the polarimetric SAR dataset depicted in Fig. E.7. The values are expressed with respect to the inter-channel maximum value.

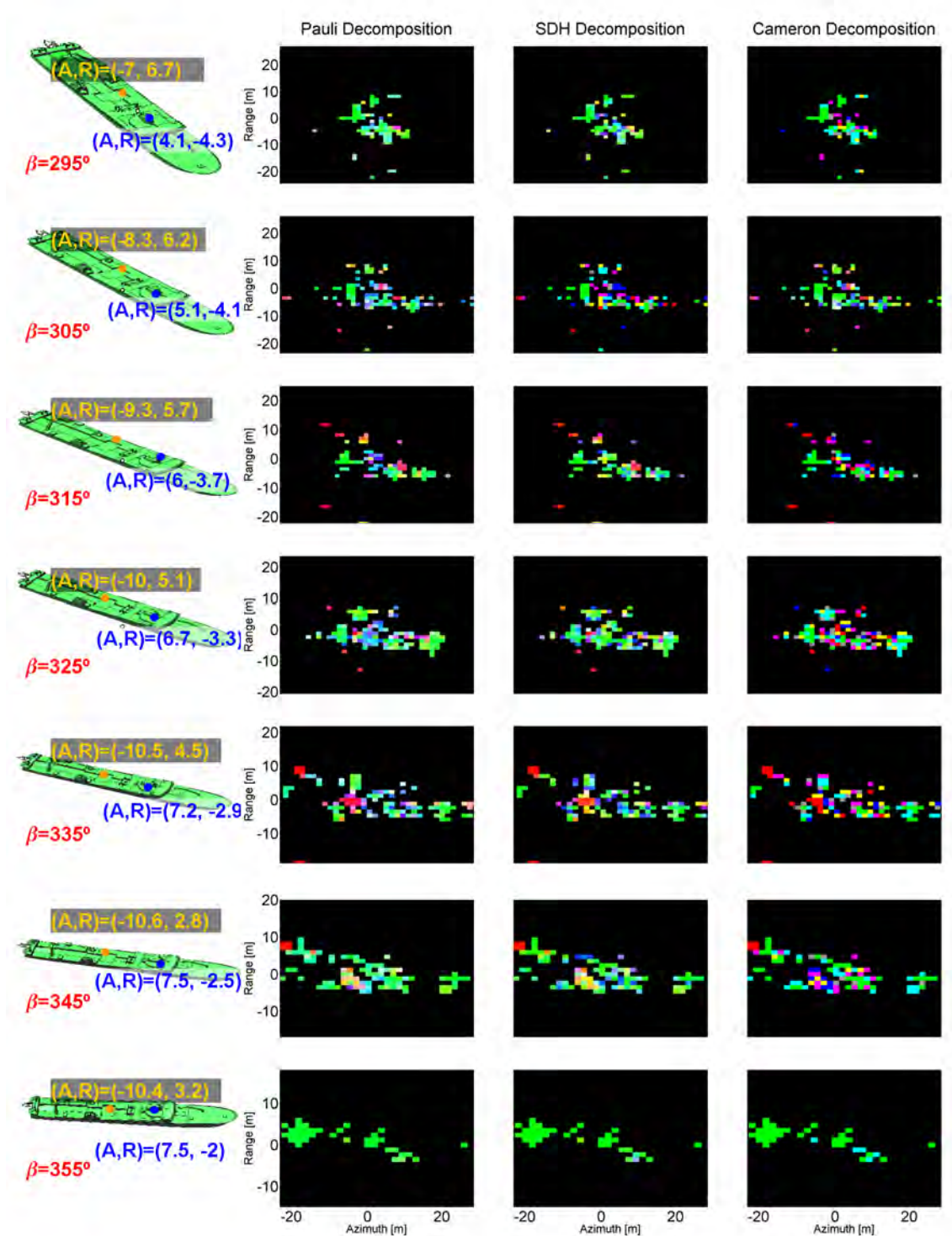


Figure E.9: Polarimetric SAR dataset obtained for the ICE model at X band and  $\phi = 20^\circ$ . The bearing angles are  $\beta \in \{295 + 10 * i\}$  for  $i \in \{0..6\}$ . The images have been analyzed with the Pauli, SDH and Cameron theorems for a dynamic range of 25 dB.

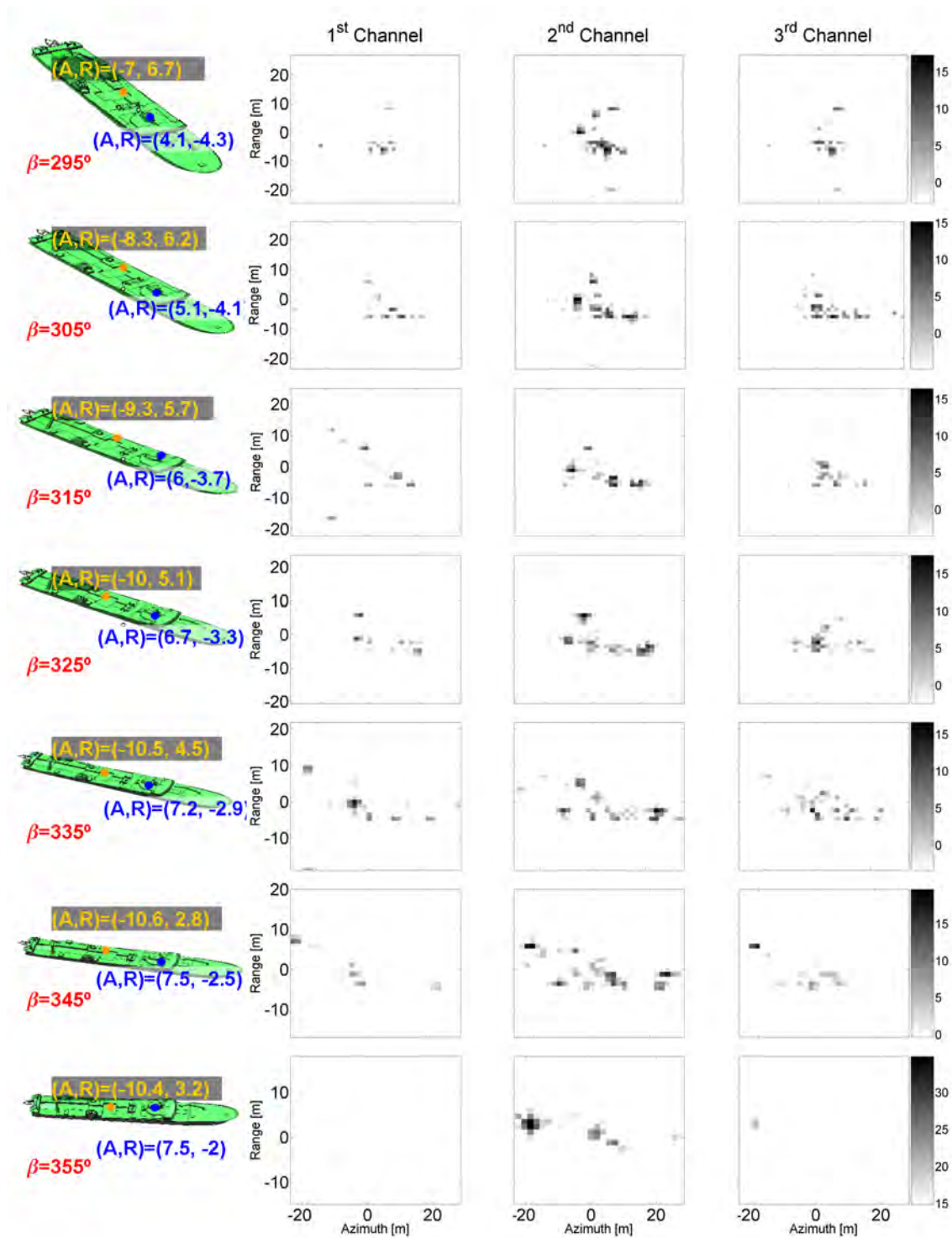


Figure E.10: Weight of the Pauli polarimetric channels related to the polarimetric SAR dataset depicted in Fig. E.9. The values are expressed with respect to the inter-channel maximum value.

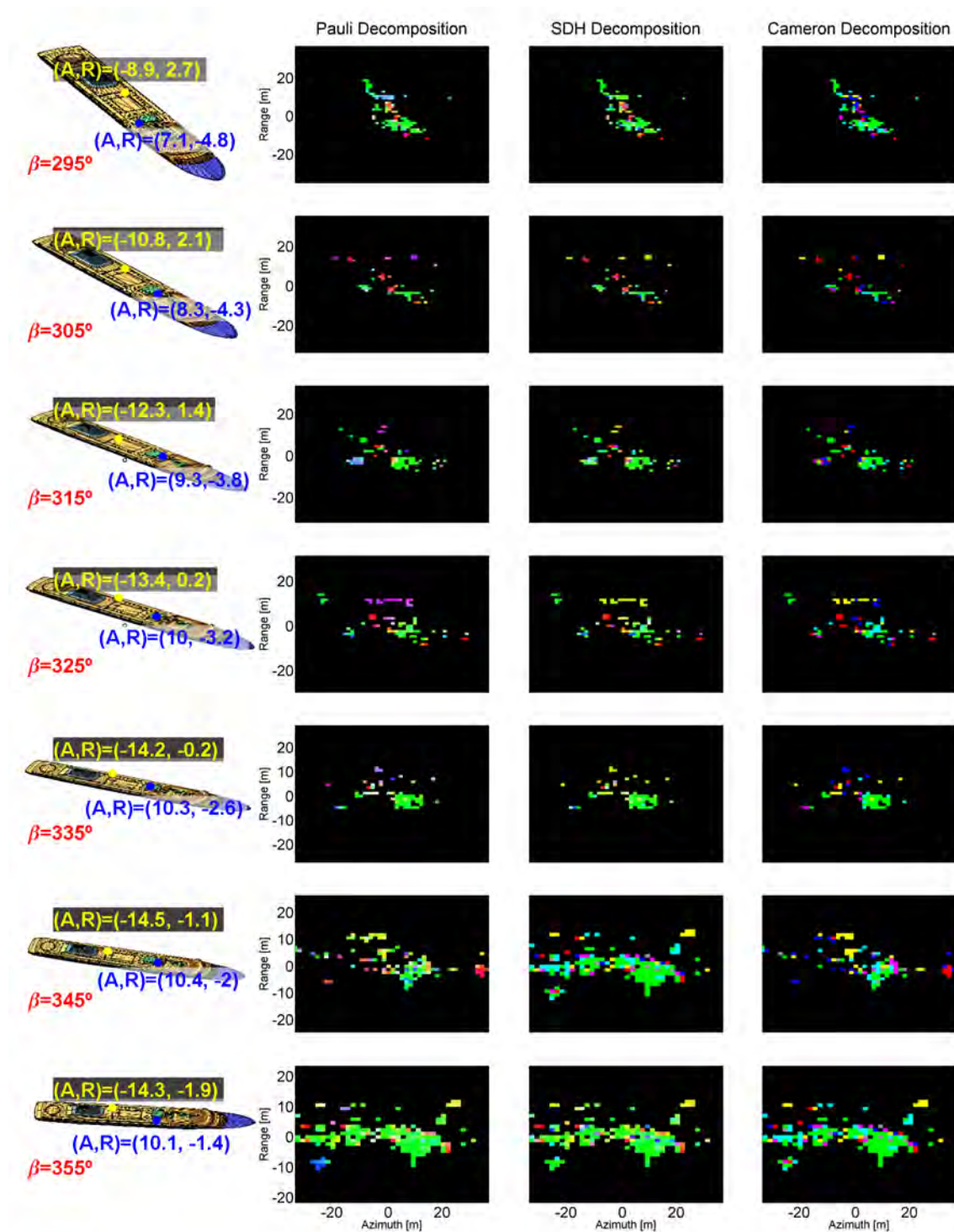


Figure E.11: Polarimetric SAR dataset obtained for the FER model at X band and  $\phi = 20^\circ$ . The bearing angles are  $\beta \in \{295 + 10 * i\}$  for  $i \in \{0..6\}$ . The images have been analyzed with the Pauli, SDH and Cameron theorems for a dynamic range of 25 dB.

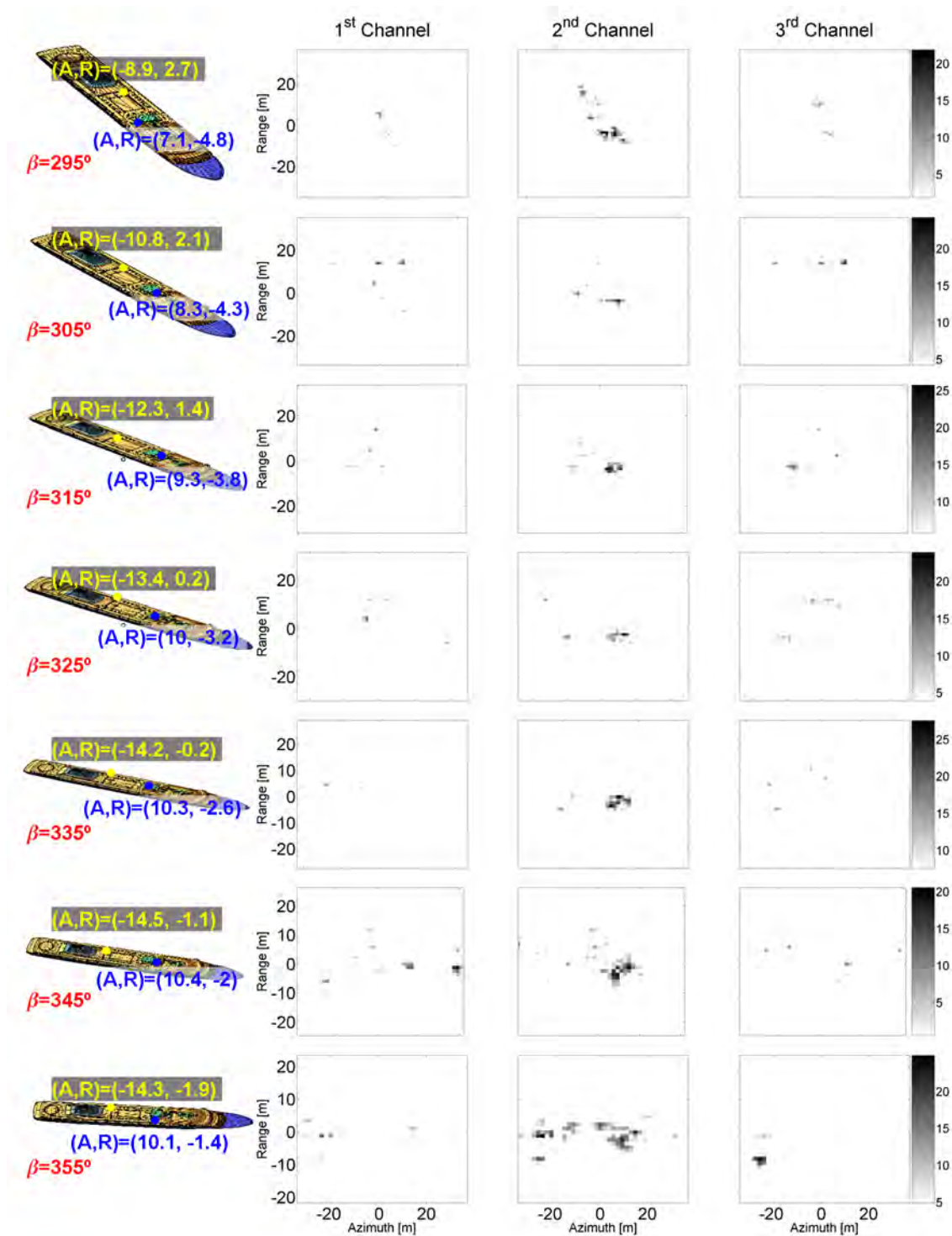


Figure E.12: Weight of the Pauli polarimetric channels related to the polarimetric SAR dataset depicted in Fig. E.11. The values are expressed with respect to the inter-channel maximum value.

Table E.3: Main Characteristics of the PolSAR images included in Section E.2.1

Model	Scaled	$\beta + \phi$ [°]	$\phi$ [°]	vessel motions	sea surface	Fig.
SPA	NO	295-355	20	YES	NO	E.13 (colored) E.14 (gray)
ICE	NO	295-355	20	YES	NO	E.15 (colored) E.16 (gray)
FER	NO	295-355	20	YES	NO	E.17 (colored) E.18 (gray)

### E.2.1 X Band with Motions

In this section, the X band data processed with the vessels in motion are presented. Their main characteristics and the list of figures where the images are included are summarized in Table E.4. Vessel motions are defined according to the rotational motions summarized in Table 6.7 of Chapter 6.

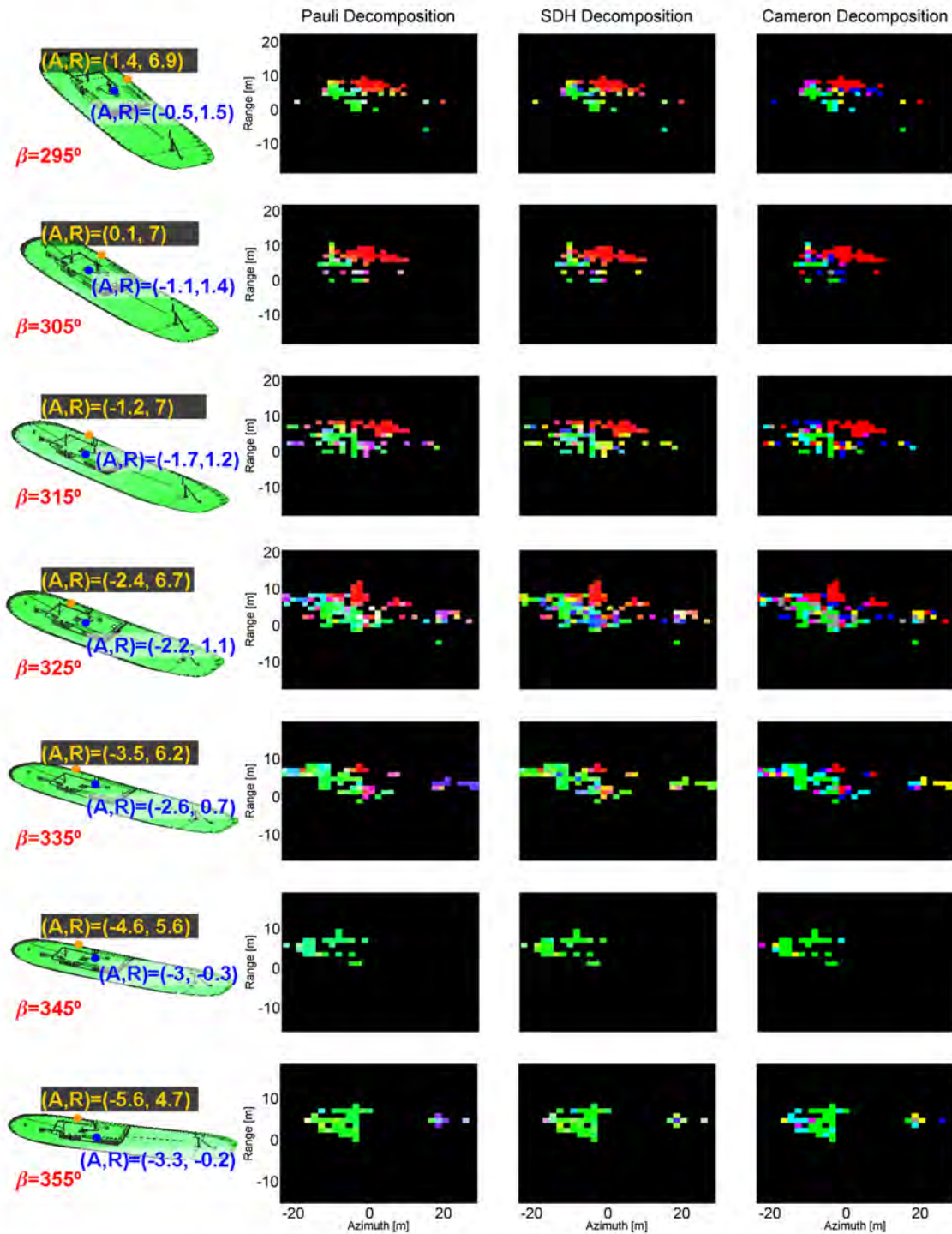


Figure E.13: Polarimetric SAR dataset obtained for the SPA model at X band and  $\phi = 20^\circ$ . The vessel experiments rotational motions and it adopts the bearing angles  $\beta \in \{295 + 10 * i\}$  for  $i \in \{0..6\}$ . The images have been analyzed with the Pauli, SDH and Cameron theorems for a dynamic range of 25 dB.



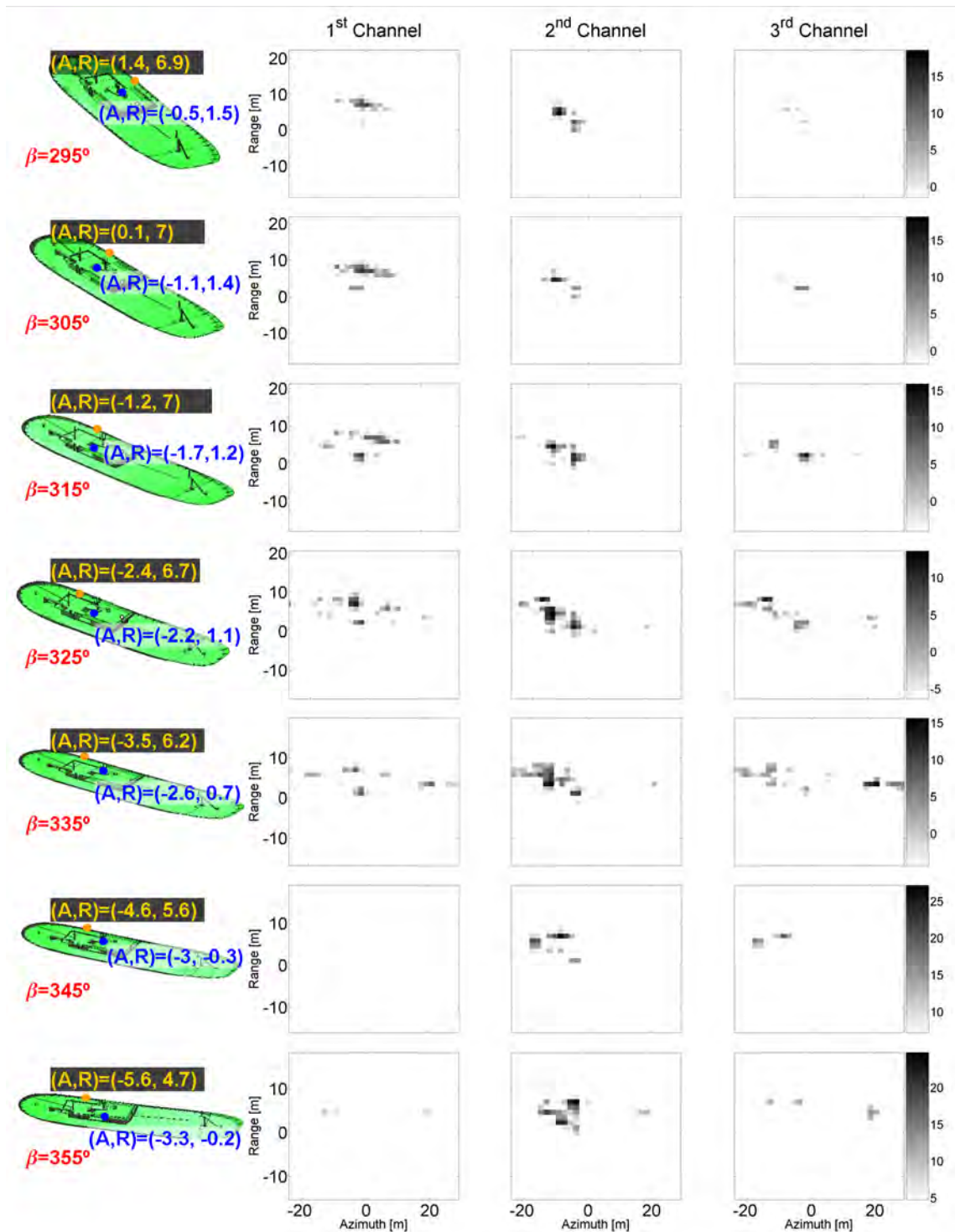


Figure E.14: Weight of the Pauli polarimetric channels related to the polarimetric SAR dataset depicted in Fig. E.13. The values are expressed with respect to the inter-channel maximum value.

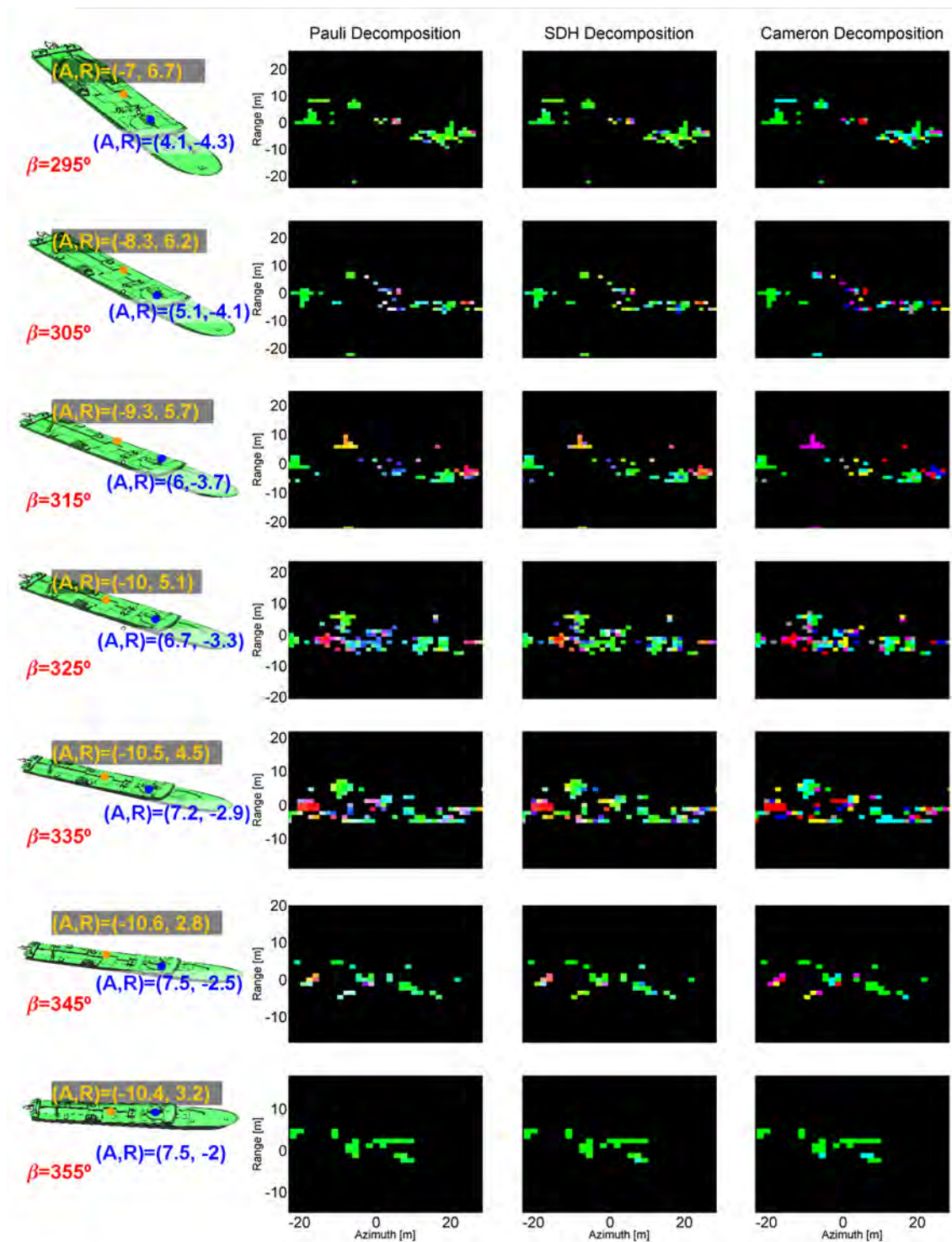


Figure E.15: Polarimetric SAR dataset obtained for the ICE model at X band and  $\phi = 20^\circ$ . The vessel experiments the motions summarized in Table ?? and it adopts the bearing angles  $\beta \in \{295 + 10 * i\}$  for  $i \in \{0, 6\}$ . The images have been analyzed with the Pauli, SDH and Cameron theorems for a dynamic range of 25 dB.

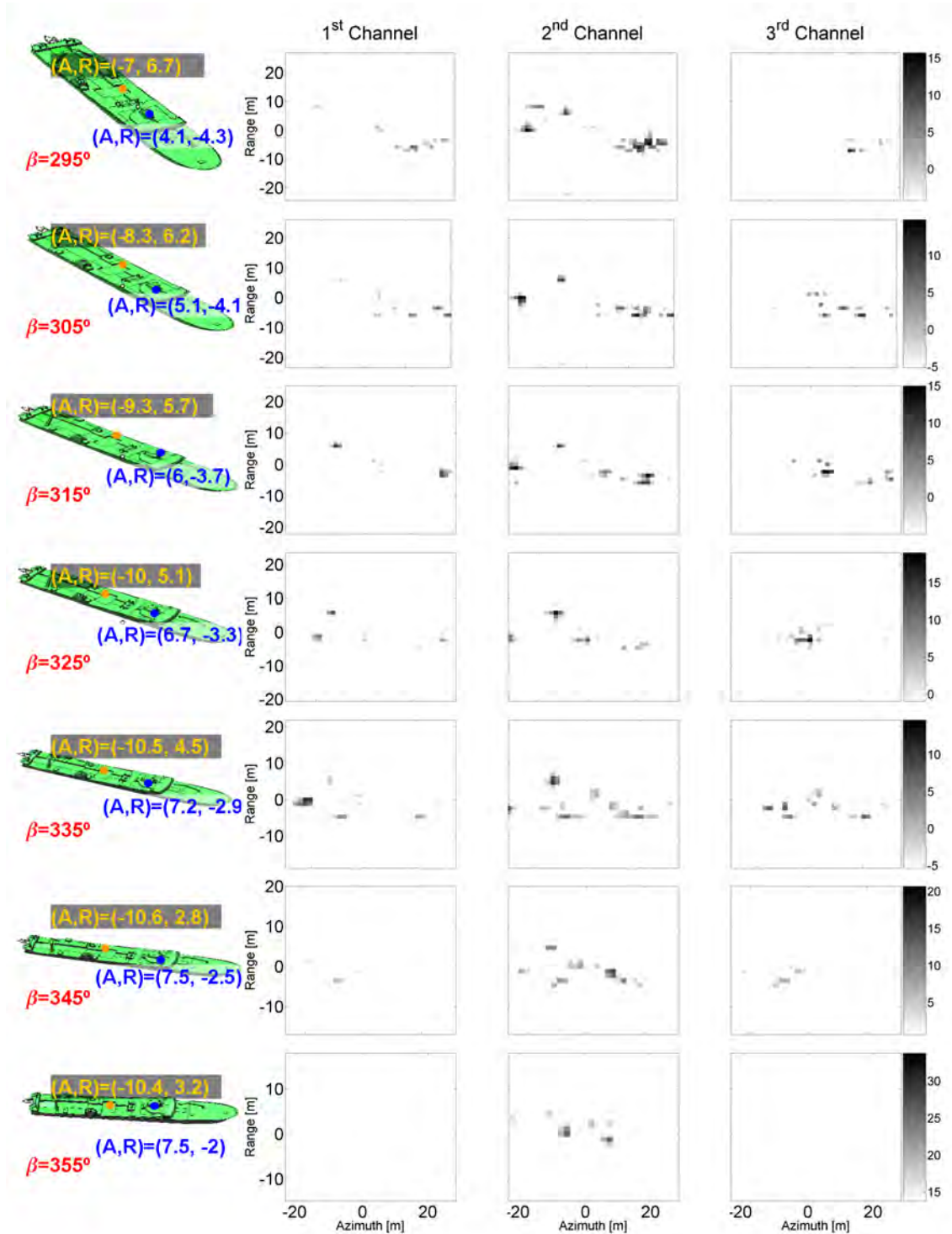


Figure E.16: Weight of the Pauli polarimetric channels related to the polarimetric SAR dataset depicted in Fig. E.15. The values are expressed with respect to the inter-channel maximum value.

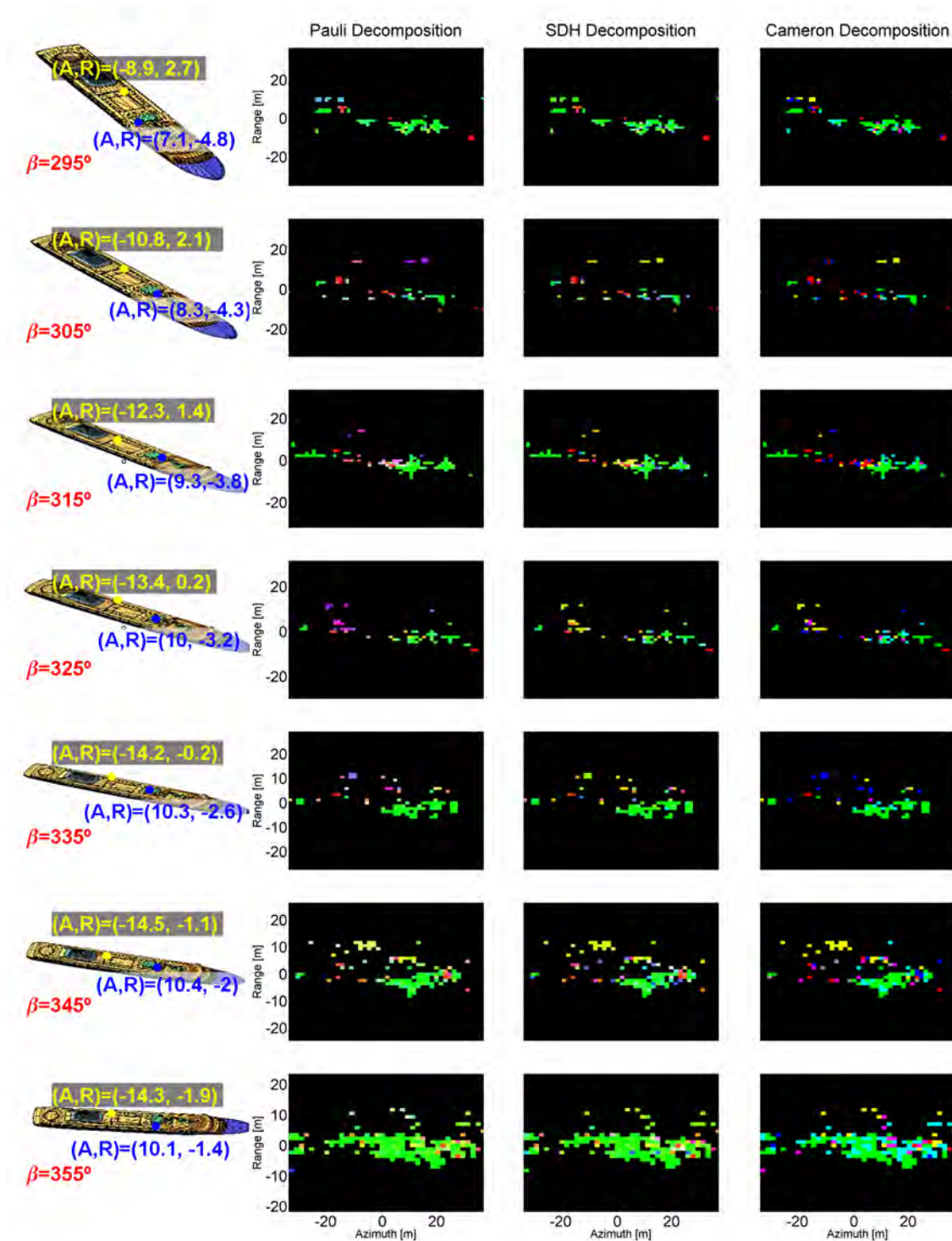


Figure E.17: Polarimetric SAR dataset obtained for the FER model at X band and  $\phi = 20^\circ$ . The vessel experiments the motions summarized in Table ?? and it adopts the bearing angles  $\beta \in \{295 + 10 * i\}$  for  $i \in \{0, 6\}$ . The images have been analyzed with the Pauli, SDH and Cameron theorems for a dynamic range of 25 dB.

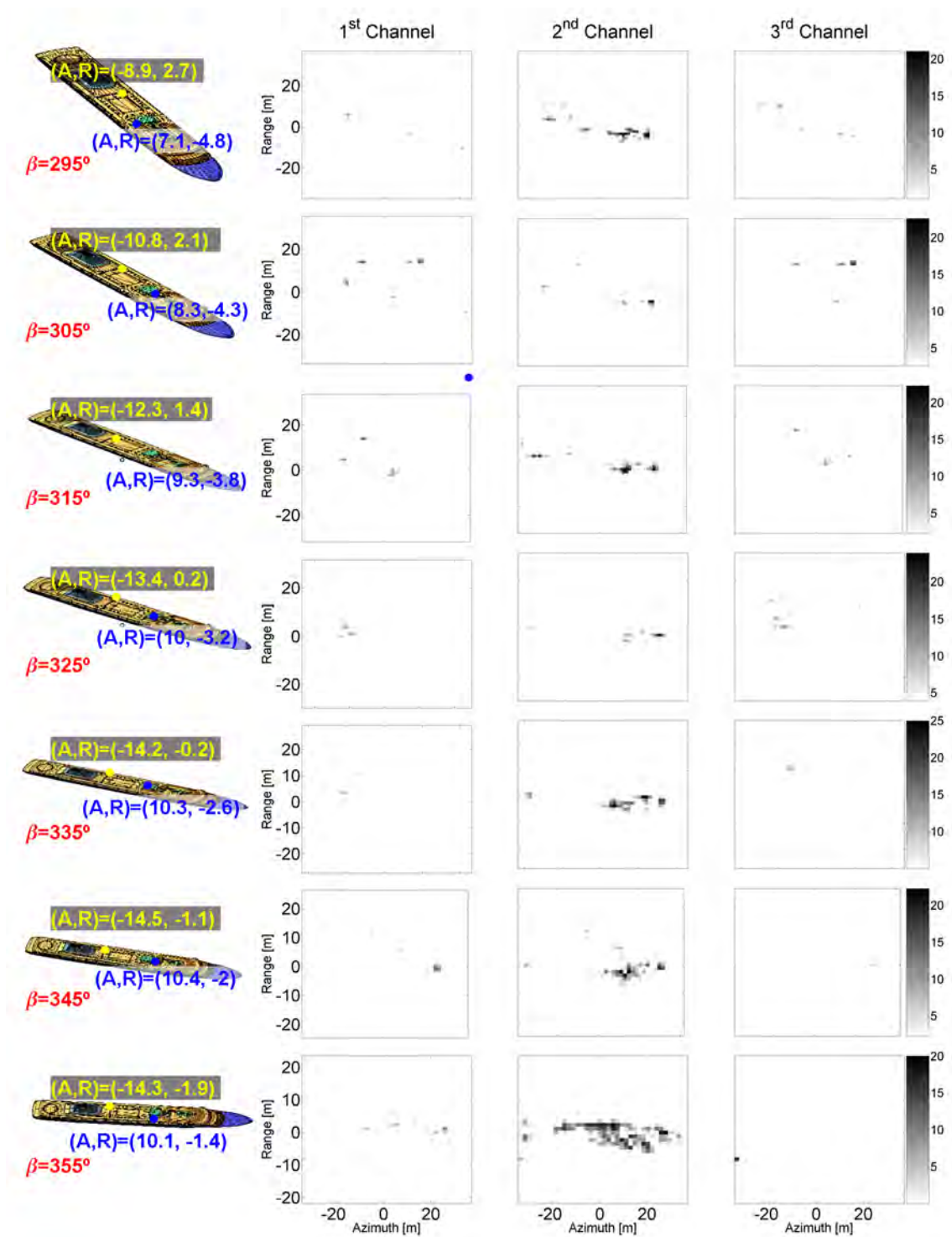


Figure E.18: Weight of the Pauli polarimetric channels related to the polarimetric SAR dataset depicted in Fig. E.17. The values are expressed with respect to the inter-channel maximum value.

Table E.4: Main Characteristics of the PolISAR images included in Section E.2.1

Model	Scaled	$\beta + \phi$ [°]	$\phi$ [°]	vessel motions	sea surface	Fig.
SPA	NO	295-355	20	NO	YES	E.19 (colored) E.20 (gray)
ICE	NO	295-355	20	NO	YES	E.21 (colored) E.22 (gray)
FER	NO	295-355	20	NO	YES	E.23 (colored) E.24 (gray)

## E.2.2 X Band with Sea Surface

In this section, the X band data processed with the sea surface model of *GRECOSAR* are presented. Their main characteristics and the list of figures where the images are included are summarized in Table E.4.

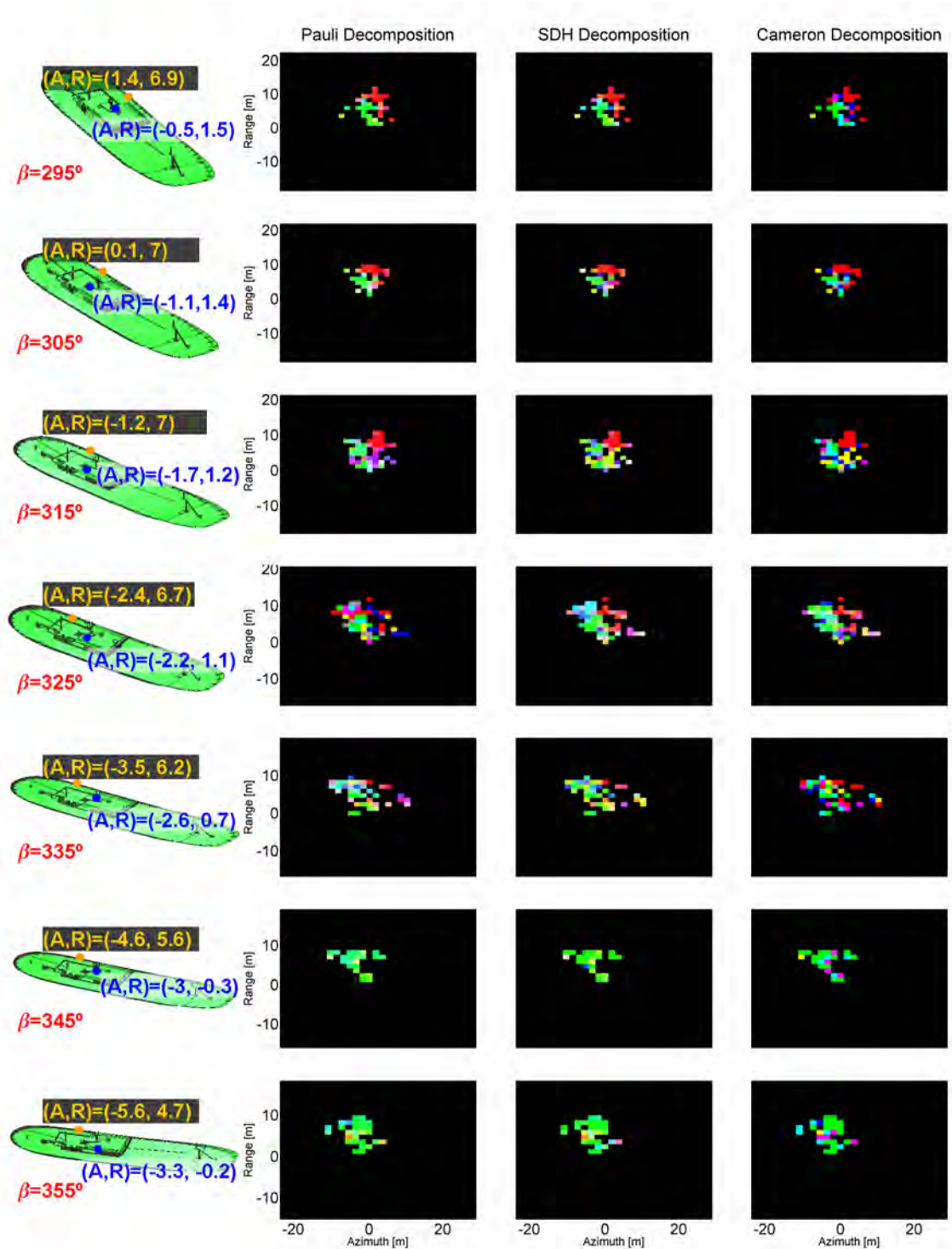


Figure E.19: Polarimetric SAR dataset obtained for the SPA model at X band and  $\phi = 20^\circ$ . The sea surface model of *GRECOSAR* has been considered for the range of bearing angles defined by  $\beta \in \{295 + 10 * i\}$ ,  $i \in \{0..6\}$ . The images have been analyzed with the Pauli, SDH and Cameron theorems for a dynamic range of 25 dB.



Figure E.20: Weight of the Pauli polarimetric channels related to the polarimetric SAR dataset depicted in Fig. E.19. The values are expressed with respect to the inter-channel maximum value.



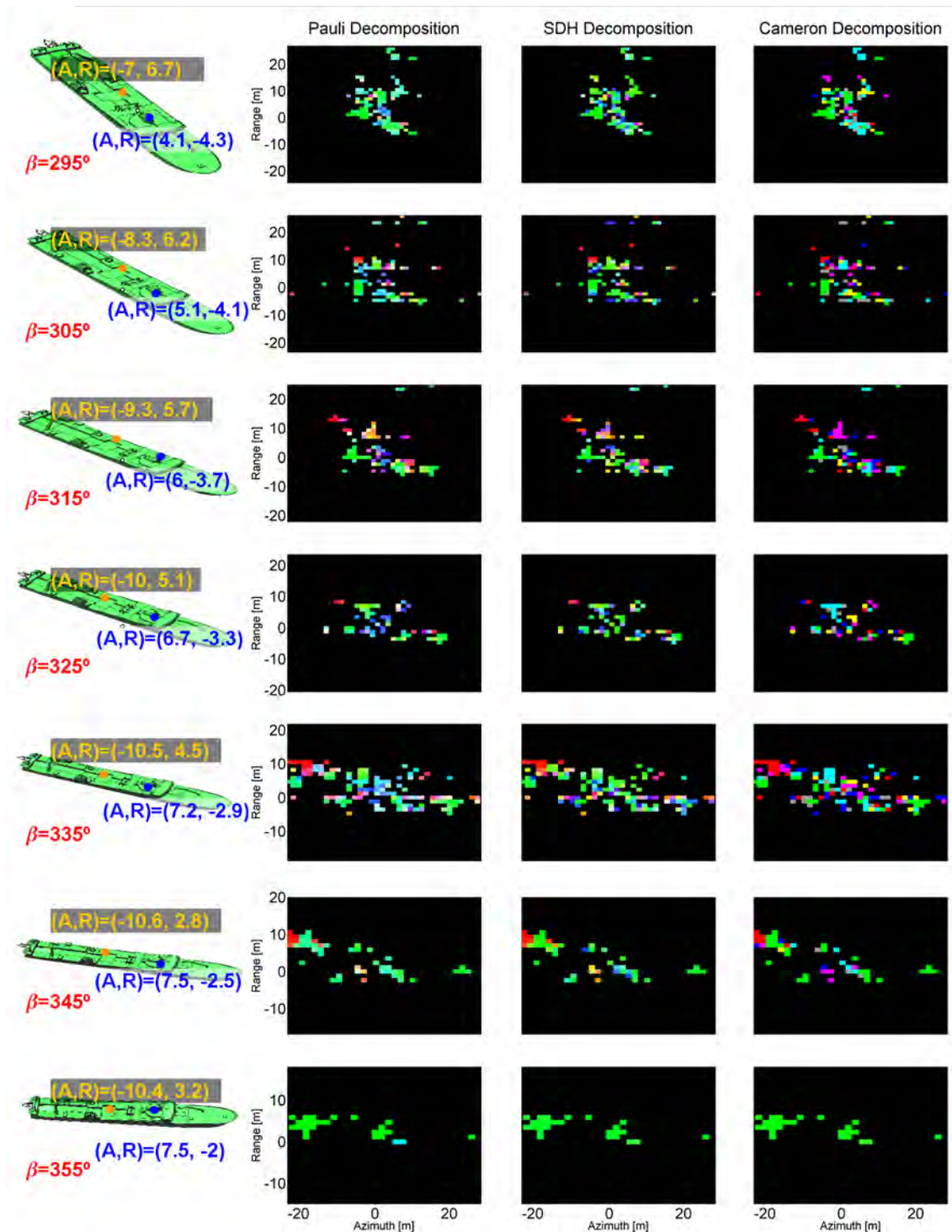


Figure E.21: Polarimetric SAR dataset obtained for the ICE model at X band and  $\phi = 20^\circ$ . The sea surface model of *GRECOSAR* has been considered for the range of bearing angles defined by  $\beta \in \{295 + 10 * i\}$ ,  $i \in \{0..6\}$ . The images have been analyzed with the Pauli, SDH and Cameron theorems for a dynamic range of 25 dB.

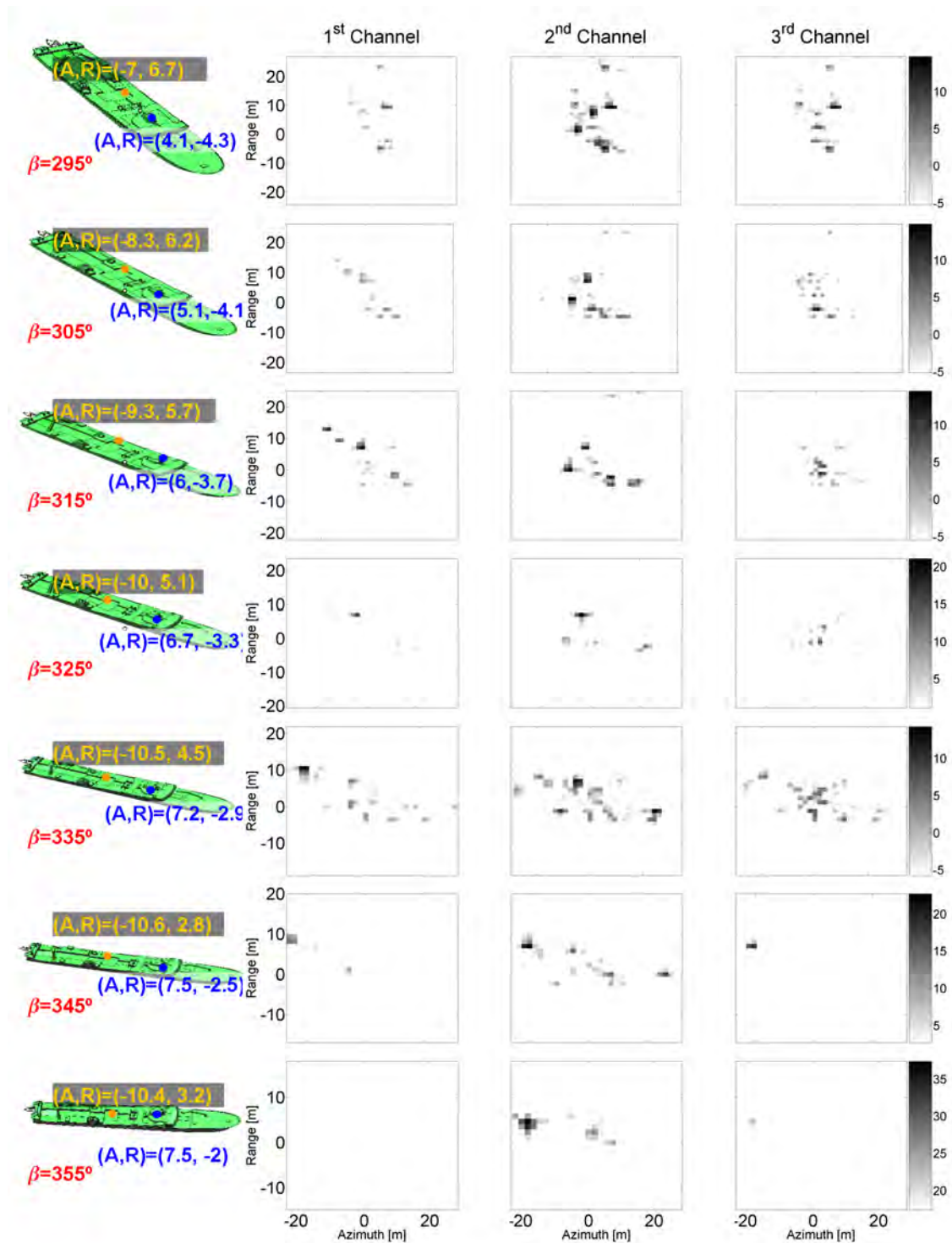


Figure E.22: Weight of the Pauli polarimetric channels related to the polarimetric SAR dataset depicted in Fig. E.21. The values are expressed with respect to the inter-channel maximum value.

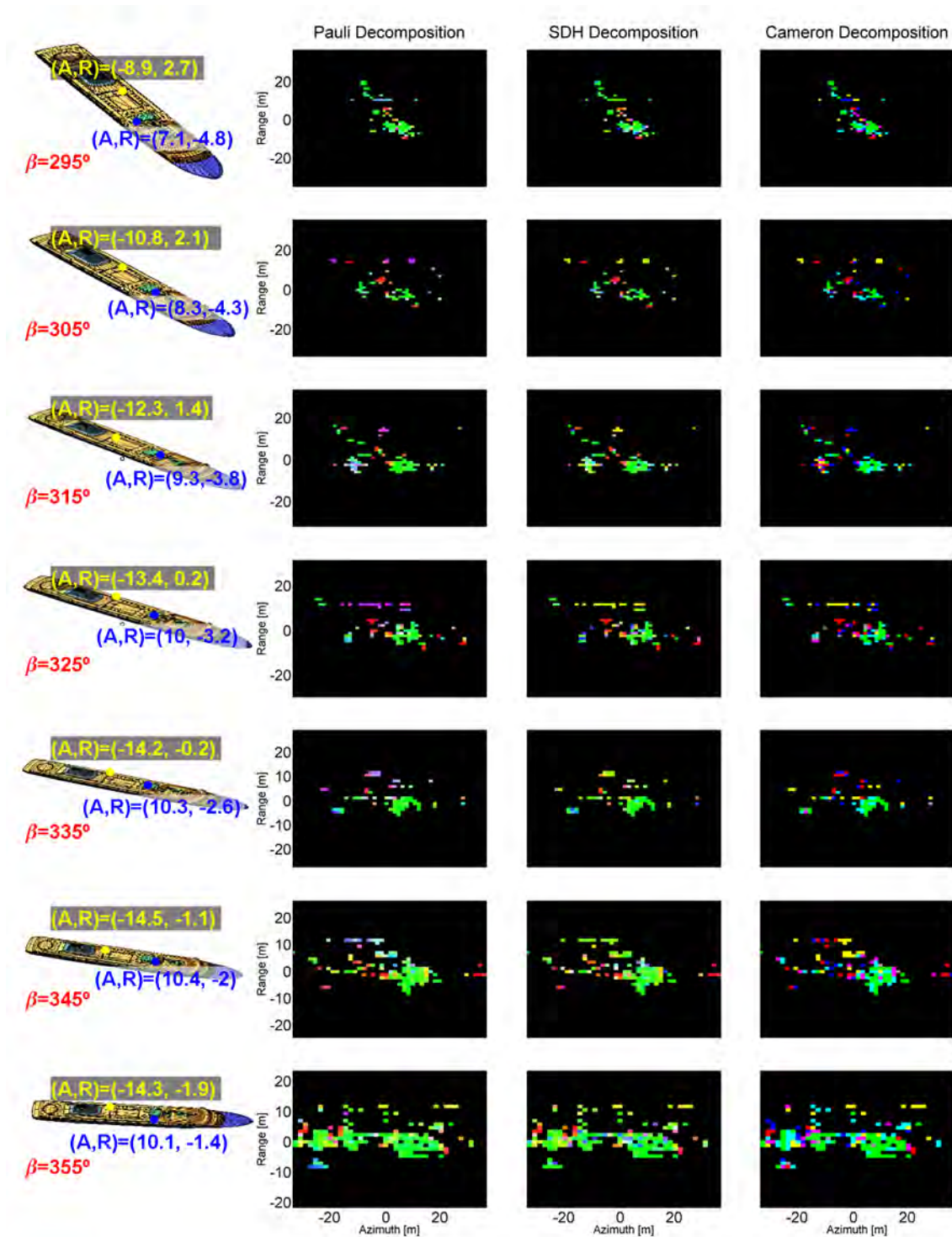


Figure E.23: Polarimetric SAR dataset obtained for the FER model at X band and  $\phi = 20^\circ$ . The sea surface model of *GRECOSAR* has been considered for the range of bearing angles defined by  $\beta \in \{295 + 10 * i\}$ ,  $i \in \{0..6\}$ . The images have been analyzed with the Pauli, SDH and Cameron theorems for a dynamic range of 25 dB.

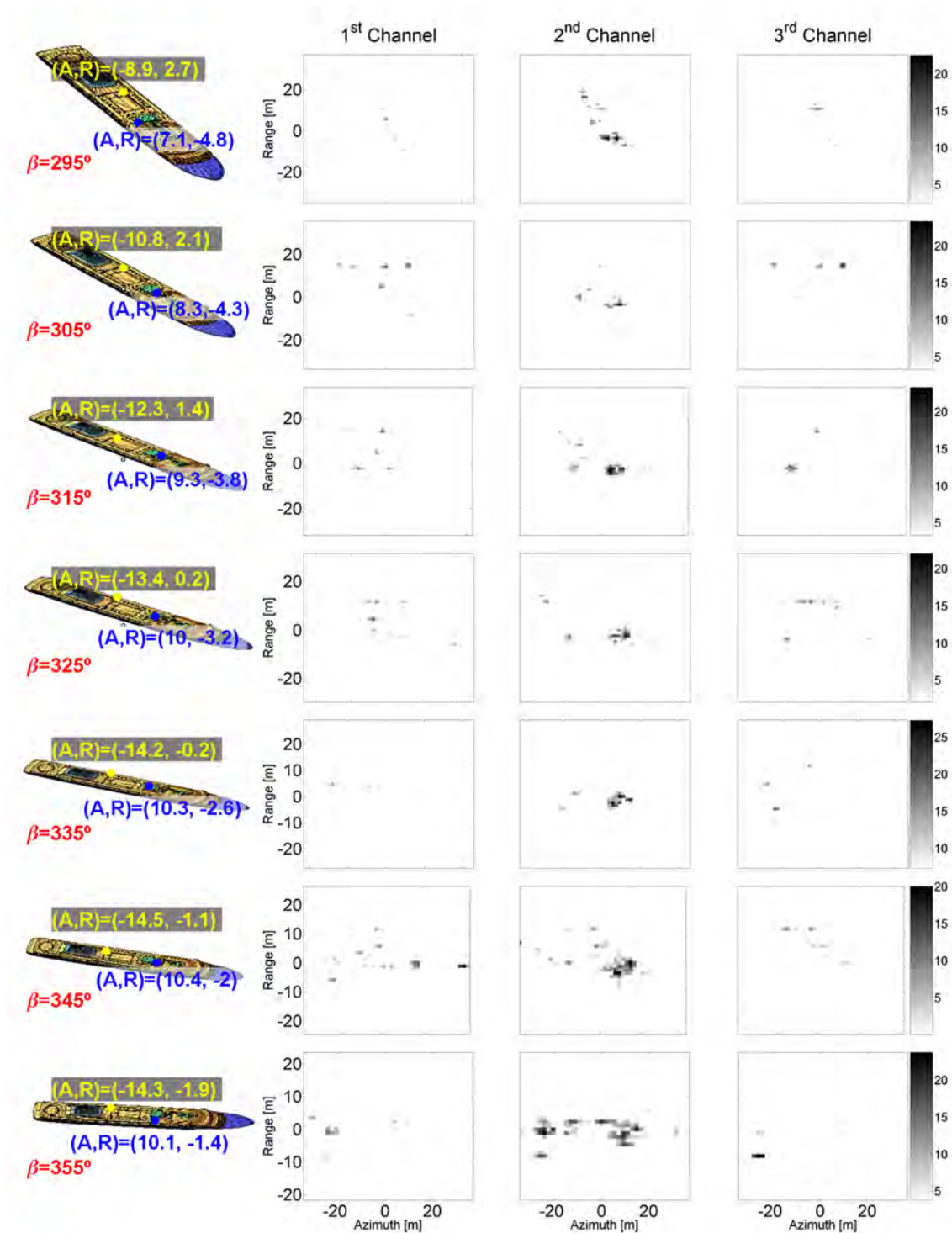


Figure E.24: Weight of the Pauli polarimetric channels related to the polarimetric SAR dataset depicted in Fig. E.23. The values are expressed with respect to the inter-channel maximum value.

# References

- [1] *-Energy and Transport in Figures 2005, Part 3: Transport-*, [Online]. Available at: [EC DGS database](#), Directorate General Energy and Transport (DGS), European Commission (EC).
- [2] *-Review of the State of world marine fisheries resources-*, *FAO fisheries technical paper 457*, [Online]. Available at: [FAO database](#), Food and Agriculture organization (FAO) of United Nations (UN), Rome, 2005.
- [3] *-Food Balance Sheet-*, [Online]. Available at: [FAOSTAT database](#), Food and Agriculture organization (FAO) of United Nations (UN), Rome, 2003.
- [4] J. Verborgh, “The european VMS: An illustration of the successful introduction of advanced technologies for MCS,” in *Proceedings of the International Conference on Fisheries Monitoring, Control and Surveillance*. [Online] Available at: [EC fisheries web page](#), 2000, pp. 1–16.
- [5] *VMS*: [Online] Available at: [VMS web page](#), Manual of; European Commission.
- [6] *Automatic Identification System (AIS)*, [Online] Available at: [IMO web page](#), Manual of; International Maritime Organization (IMO) of United Nations (UN).
- [7] *Orbital Sensor, SPOT*: [Online] Available at: [SPOT web page](#), Manual of; Partnership with CNES, Spot image and Astrium.
- [8] *IMPAST project final report with reference (IMPAST/D 1.4/2.0) and under contract nr: Q5RS-2001-02266*. [Online] Available at: [IMPAST web page](#), IMPAST consortium, DG-FISH.
- [9] S. Musman, D. Kerr, and C. Bachmann, “Automatic recognition of ISAR ship images,” *IEEE Trans. Aerosp. Electron. Syst.*, vol. 32, no. 4, pp. 1392–1404, Oct. 1996.
- [10] G. Franceschetti and R. Lanari, *Synthetic Aperture Radar Processing*. Boca Raton, Florida: CRC Press, 1999.

- 
- [11] J. C. Curlander and R. N. McDonough, *Synthetic Aperture Radar: Systems and Signal Processing*. New York, USA: John Wiley & Sons, 1991.
- [12] I. G. Cumming and F. H. Hong, *Digital processing of Synthetic Aperture Radar*. Norwood, MA, USA: Artech House, INC., 2005.
- [13] P. Lombardo and M. Sciotti, "Segmentation-based technique for ship detection in SAR images," in *Proc. of IEEE on Radar, Sonar and Navigation*, vol. 148, no. 3, June 2001, pp. 147–159.
- [14] K. Eldhuset, "An automatic ship and ship wake detection system for spaceborne SAR images in coastal regions," *IEEE Trans. Geosci. Remote Sensing*, vol. 34, no. 4, pp. 1010–1019, July 1996.
- [15] M. Tello, C. Lopez-Martinez, and J. Mallorqui, "A novel algorithm for ship detection in SAR imagery based on the wavelet transform," *IEEE Trans. Geosci. Remote Sensing*, vol. 2, no. 2, pp. 201–205, Apr. 2005.
- [16] F. T. Ulaby, R. K. Moore, and A. K. Fung, *Microwave Remote Sensing: Active and Passive*. Norwood, MA: Artech House, 1982, vol. II.
- [17] C. Lopez-Martinez, "Multidimensional speckle noise. Modelling and filtering related to SAR data," Ph.D. dissertation, Remote Sensing Laboratory (RSLab), Universitat Politècnica de Catalunya, Barcelona, Spain, Apr. 2003.
- [18] K. Ouchi, M. Iehara, K. Morimura, S. Kumano, and I. Takami, "Nonuniform azimuth image shift observed in the radarsat images of ships in motion," *IEEE Trans. Geosci. Remote Sensing*, vol. 40, no. 10, pp. 2188–2195, Oct. 2002.
- [19] G. Margarit, J. J. Mallorqui, J. M. Rius, and J. Sanz-Marcos, "On the usage of GRE-COSAR, an orbital polarimetric SAR simulator of complex targets, for vessel classification studies," *IEEE Trans. Geosci. Remote Sensing*, vol. 44, no. 12, pp. 3517–3526, Dec. 2006.
- [20] W. M. Boerner and et al., "Direct and inverse methods in radar polarimetry," in *NATO ASI Series C, Math. and Phys. Science*, Kluwer Academic Publishers, Netherlands, 1985.
- [21] ———, *Polarimetry in radar remote sensing. Basic and applied concepts*. in *Manual of Remote Sensing: Principles and Applications of Imaging Radar* (F. M. Henderson and A. J. Lewis, eds.), vol. 8, ch. 5, 3 ed., 1998.
- [22] S. R. Cloude and E. Pottier, "A review of target decomposition theorems in radar polarimetry," *IEEE Trans. Geosci. Remote Sensing*, vol. 34, no. 2, pp. 498–518, Mar. 1996.

- [23] W. L. Cameron, N. N. Youssef, and L. L. Leung, "Simulated polarimetric signatures of primitive geometrical shapes," *IEEE Trans. Geosci. Remote Sensing*, vol. 34, no. 3, pp. 793–803, May 1996.
- [24] P. A. Rosen, S. Hensley, I. R. Joughin, F. K. Li, S. N. Madsen, E. Rodriguez, and R. M. Goldstein, "Synthetic aperture radar interferometry," in *Proc. of IEEE*, vol. 88, no. 3, 2000, pp. 333–382.
- [25] R. Touzi and F. Charbonneau, "Characterization of target symmetric scattering using polarimetric SARs," *IEEE Trans. Geosci. Remote Sensing*, vol. 40, no. 11, pp. 2507–2516, Nov. 2002.
- [26] R. Touzi, R. K. Raney, and F. Charbonneau, "On the use of permanent symmetric scatterers for ship characterization," *IEEE Trans. Geosci. Remote Sensing*, vol. 42, no. 10, pp. 2039–2045, Oct. 2004.
- [27] *Orbital Communication Satellite, INMARSAT: [Online] Available at: [INMARSAT web page](#)*, Manual of; International Maritime Satellite Organization (INMARSAT).
- [28] J. G. Lourens, "Classification of ships using underwater radiated noise," in *Proc. Communications and Signal Processing Symposium*, 1988, pp. 130–134.
- [29] S. Yang, "Classification of ship-radiated signals via chaotic features," *Electronic Letters*, vol. 39, no. 4, pp. 395–397, Feb. 2003.
- [30] Y. Zhang, J. Zheng, H. Liu, and L. Jiao, "An efficient method of radar target classification," in *Proc. of IEEE International Conference on Radar*, Oct. 2001, pp. 502–505.
- [31] J. A. A. Arantes do Amaral, P. L. Botelho, N. F. F. Ebecken, and L. P. Caloba, "Ship's classification by its magnetic signature," in *Proceedings of International Joint Conference on Neural Networks and Computational Intelligence*, vol. 3, May 1998, pp. 1889–1892.
- [32] L. Gagnon and R. Klepko, "Hierarchical classifier design for airborne ISAR images of ships\*," in *Proc. of SPIE in Automatic Target Recognition*, vol. 8, Sept. 1998, pp. 38–49.
- [33] A. Poelman and J. R. F. Guy, "SAR image processing using probabilistic winner-take-all learning and artificial neural networks," in *Paper reference: 0-7803-3258-X/96*, 1996, pp. 613–616.
- [34] G. Margarit, X. Fabregas, and J. J. Mallorqui, "Study of the polarimetric mechanisms on simulated vessels with SAR and ISAR imaging," in *Proc. IEEE of European SAR Symposium (EUSAR'04)*, vol. 1, May 2004, pp. 447–450.

- [35] *Orbital Sensor, [RADARSAT]: [Online] Available at: [RADARSAT web page](#)*, Manual of; Natural Resources CANada (NRCAN), Canada Centre for Remote Sensing (CCRS).
- [36] *Airborne Sensor, EMISAR: [Online] Available at: [EMISAR web page](#)*, Manual of; Danish Center for Remote Sensing (DCRS) at the Technical University of Denmark (DTU).
- [37] *Airborne sensor, ESAR: [Online] Available at: [DLR web page](#)*, Manual of; Deutsches Zentrum für Luft- und Raumfahrt (DLR).
- [38] *Airborne Sensor, RAMSES: [Online] Available at: [ONERA web page](#)*, Manual of; Office National d'Études et de Recherches Aérospatiales (ONERA).
- [39] Y. Huang, G. Séguin, and N. Sultan, "Multi-frequency and multipolarization SAR systems analysis with simulation software developed at CSA," in *Proc. IEEE of Geoscience and Remote sensing Symposium, (IGARSS'97)*, vol. 1, July 1997, pp. 536–538.
- [40] G. Franceschetti, M. Migliaccio, D. Riccio, and G. Schrinzi, "SARAS: A synthetic aperture radar SAR raw signal simulator," *IEEE Trans. Geosci. Remote Sensing*, vol. 30, no. 1, pp. 110–123, Jan. 1992.
- [41] G. Franceschetti, M. Migliaccio, and D. Riccio, "On ocean raw data simulator," *IEEE Trans. Geosci. Remote Sensing*, vol. 36, no. 1, pp. 84–100, Jan. 1998.
- [42] S. H. W. Simpson, P. Galloway, and M. Harman, "Applications of epsilon a radar signature prediction and analysis tool," in *Proceedings of the International Radar Symposium (IRS'98)*, vol. Available at [Online]: [Library database of Roke Manor](#), Roke Manor Research Ltd. Romsey, Hants, England S051 0ZN, no. 2, 1990, pp. 148–151.
- [43] *RadBase: [Online] Available at: [RADBASE technical site](#)*, Manual of; Surface Optics Corporation, San Diego.
- [44] J. J. Mallorqui, J. M. Rius, and M. Bara, "Simulation of polarimetric SAR vessel signatures for satellite fisheries monitoring," in *Proc. IEEE of Geoscience and Remote sensing Symposium (IGARSS'02)*, vol. 5, July 2002, pp. 2711–2713.
- [45] J. M. Rius and et al., "GRECO: Graphical electromagnetic computing for RCS prediction in real time," *IEEE Antennas Propagat. Mag.*, vol. 35, no. 2, pp. 7–17, Apr. 1993.
- [46] —, "High frequency RCS of complex radar targets in real time," *IEEE Trans. Antennas Propagat.*, vol. 41, no. 9, pp. 1308–1319, Sept. 1993.
- [47] —, "GRECO: Graphical processing methods for high frequency RCS prediction," *Annals of Telecommunications, Special Issue on Radar Cross Section of Complex Objects*, vol. 50, no. 5-6, pp. 551–556, June 1995.



- [48] G. Margarit, X. Fabregas, and J. J. Mallorqui, "Study of the vessel speed and sea swell effects on simulated polarimetric high resolution SAR images," in *Proc. IEEE of European SAR Symposium (EUSAR'04)*, vol. 2, May 2004, pp. 603–606.
- [49] G. Margarit, J. J. Mallorqui, J. M. Rius, J. Sanz-Marcos, and X. Fabregas, "Orbital single-pass interferometry for vessel detection and classification," in *Proc. ESA of FRINGE workshop*, Dec. 2005.
- [50] *Airborne Sensor, CCRS C/X: [Online] Available at: [CCRS web page](#)*, Manual of; Natural Resources CANada (NRCAN), Canada Centre for Remote Sensing (CCRS).
- [51] Q. Zhang, T. S. Yeo, G. Du, and S. Zhang, "Estimation of three-dimensional motion parameters in interferometric ISAR imaging," *IEEE Trans. Geosci. Remote Sensing*, vol. 42, no. 2, pp. 292–300, Feb. 2004.
- [52] Q. Zhang and T. S. Yeo, "Three-dimensional SAR imaging of a ground moving target using the InSAR technique," *IEEE Trans. Geosci. Remote Sensing*, vol. 42, no. 9, pp. 1818–1828, Sept. 2004.
- [53] C. Oliver and S. Quegan, *Understanding Synthetic Aperture Radar Images*. Boston, USA: Artech House, 1998.
- [54] C. A. Wiley, *Pulsed Doppler Radar Methods and Apparatus*. Goodyear Aircraft Corporation, US: U.S. Patent 3,196,436, 1954.
- [55] *Orbital Sensor, ENVISAT: [Online] Available at: [ENVISAT web page](#)*, Manual of; European Space Agency (ESA).
- [56] *Orbital Sensor, ERS: [Online] Available at: [ERS web page](#)*, Manual of; European Space Agency (ESA).
- [57] *Orbital Sensor, ALOS-PALSAR: [Online] Available at: [ALOS web page](#)*, Manual of; Earth Observation Research Center (EORC), Japan Aerospace Exploration Agency (JAXA).
- [58] *Orbital Sensor, TerraSAR: [Online] Available at: [TerraSAR web page](#)*, Manual of; Partnership of Deutsche Forschungsanstalt für Luft- und Raumfahrt (DLR) with Astrium GmbH.
- [59] R. Bamler and M. Eineder, "ScanSAR processing using standard high precision SAR algorithms," *IEEE Trans. Geosci. Remote Sensing*, vol. 34, no. 1, pp. 212–218, Jan. 1996.
- [60] A. Moreira, "Improved multilook techniques applied to SAR and ScanSAR imagery," *IEEE Trans. Geosci. Remote Sensing*, vol. 29, no. 4, pp. 529–534, July 1991.

- [61] A. Moreira, J. Mittermayer, and R. Scheiber, "Extended chirp scaling algorithm for air- and spaceborne SAR data processing in stripmap and scanSAR imaging modes," *IEEE Trans. Geosci. Remote Sensing*, vol. 34, no. 5, pp. 1123–1136, Sept. 1996.
- [62] J. Mittermayer, A. Moreira, and O. Loffeld, "Spotlight SAR data processing using the frequency scaling algorithm," *IEEE Trans. Geosci. Remote Sensing*, vol. 37, no. 5, pp. 2198–2214, Sept. 1999.
- [63] J. Mittermayer, R. Lord, and E. Borner, "Sliding spotlight SAR processing for TerraSAR-X using a new formulation of the extended chirp scaling algorithm," in *Proc. IEEE International Geoscience and Remote Sensing Symposium (IGARSS'03)*, vol. 3, 2003, pp. 1462–1464.
- [64] D. Mensa, *High Resolution Radar Imaging*. Norwood, USA: Artech House, 1981.
- [65] A. Mudukutore, V. Chandrasekar, and R. Keeler, "Pulse compression for weather radars," *IEEE Trans. Geosci. Remote Sensing*, vol. 36, no. 1, pp. 125–142, Jan. 1998.
- [66] F. Li and W. Johnson, "Ambiguities in spaceborne synthetic aperture radar data," *IEEE Trans. Aerosp. Electron. Syst.*, vol. 19, pp. 389–397, 1983.
- [67] A. Moreira, "Suppressing the azimuth ambiguities in synthetic aperture radar images," *IEEE Trans. Geosci. Remote Sensing*, vol. 31, no. 4, pp. 885–895, July 1993.
- [68] G. W. Davidson and I. G. Cumming, "Signal properties of spaceborne squint-mode SAR," *IEEE Trans. Geosci. Remote Sensing*, vol. 35, no. 5, pp. 611–617, May 1997.
- [69] G. Franceschetti and G. Schrinzi, "A SAR processor based on two-dimensional FFT codes," *IEEE Trans. Aerosp. Electron. Syst.*, vol. 26, no. 2, pp. 356–366, Mar. 1990.
- [70] P. Prats, "Airborne differential SAR interferometry," Ph.D. dissertation, Remote Sensing Laboratory (RSLab), Universitat Politècnica de Catalunya, Barcelona, Spain, Feb. 2006.
- [71] J. S. Lee, K. P. Papathanassiou, T. L. Ainsworth, M. R. Grunes, and A. Reigber, "A new technique for noise filtering of SAR interferometric phase images," *IEEE Trans. Geosci. Remote Sensing*, vol. 36, no. 4, pp. 1456–1465, Sept. 1998.
- [72] J. S. Lee, M. Grunes, D. Schuler, E. Pottier, and L. Ferro-Famil, "Scattering-model-based speckle filtering of polarimetric SAR data," *IEEE Trans. Geosci. Remote Sensing*, vol. 44, no. 1, pp. 176–187, Jan. 2006.
- [73] C. Lopez-Martinez, E. Pottier, and S. R. Cloude, "Statistical assessment of eigenvector-based target decomposition theorems in radar polarimetry," *IEEE Trans. Geosci. Remote Sensing*, vol. 43, no. 09, pp. 2058–2074, Sept. 2005.

- [74] J. J. Entzminger, C. Fowler, and W. Kenneally, "JointSTARS and GMTI: past, present and future," *IEEE Trans. Aerosp. Electron. Syst.*, vol. 35, no. 2, pp. 748–761, Apr. 1999.
- [75] J. J. Sharma, C. H. Gierull, and M. J. Collins, "The influence of target acceleration on velocity estimation in dual-channel SAR-GMTI," *IEEE Trans. Geosci. Remote Sensing*, vol. 44, no. 1, pp. 134–147, Jan. 2006.
- [76] A. Thompson, J. M. Moran, and G. W. Swenson, *Interferometry and Synthesis in Radio Astronomy*. New York, USA: Wiley Interscience, 1986.
- [77] L. C. Graham, "Synthetic interferometric radar for topographic mapping," in *Proc. of IEEE*, vol. 62, June 1974, pp. 763–768.
- [78] H. A. Zebker, T. G. Farr, R. P. Salazar, and T. H. Dixon, "Mapping the world's topography using radar interferometry: The TOPSAT mission," in *Proc. of IEEE*, vol. 82, Dec. 1994, pp. 1774–1786.
- [79] G. Rufino, A. Moccia, and S. Esposito, "DEM generation by means of ERS tandem," *IEEE Trans. Geosci. Remote Sensing*, vol. 36, no. 6, pp. 1905–1912, Nov. 1998.
- [80] N. Marechal, "Tomographic formulation of interferometric SAR for terrain elevation mapping," *IEEE Trans. Geosci. Remote Sensing*, vol. 33, pp. 726–739, 1995.
- [81] S. N. Madsen, H. A. Zebker, and J. Martin, "Topographic mapping using radar interferometry: Processing techniques," *IEEE Trans. Geosci. Remote Sensing*, vol. 31, no. 1, pp. 246–256, Jan. 1993.
- [82] R. Lanari, G. Fornaro, D. Riccio, M. Migliaccio, K. P. Papathanassiou, and et al., "Generation of digital elevation models by using SIR-C/X-SAR multifrequency two-pass interferometry: The etna case study," *IEEE Trans. Geosci. Remote Sensing*, vol. 34, no. 5, pp. 1097–1114, Sept. 1996.
- [83] R. Abdelfattah and J. M. Nicolas, "Topographic SAR interferometry formulation for high-precision dem generation," *IEEE Trans. Geosci. Remote Sensing*, vol. 40, no. 11, pp. 2415–2426, Nov. 2002.
- [84] A. M. Guarnieri and F. Rocca, "Combination of low- and high-resolution SAR images for differential interferometry," *IEEE Trans. Geosci. Remote Sensing*, vol. 37, no. 4, pp. 2035–2049, July 1989.
- [85] A. Reigber and R. Scheiber, "Airborne differential SAR interferometry: First results at L-band," *IEEE Trans. Geosci. Remote Sensing*, vol. 41, no. 6, pp. 1516–1520, June 2003.

- [86] P. A. Rosen, C. Werner, E. Fielding, S. Hensley, S. Buckley, and P. Vincent, "Aseismic creep along the san andreas fault northwest of parkfield, california, measured by radar interferometry," *J. Geophys. Res.*, vol. 25, no. 6, pp. 825–828, Sept. 1998.
- [87] D. Massonet and K. L. Feigl, "Radar interferometry and its application to changes in the earth's surface," *Rev. Geophys.*, vol. 36, no. 4, pp. 441–500.
- [88] J. Dall, K. P. Papathanassiou, and H. Skriver, "SAR interferometry applied to land ice: first results," in *Proc. IEEE International Geoscience and Remote Sensing Symposium (IGARSS'03)*, vol. 3, July 2003, pp. 1432–1434.
- [89] I. R. Joughin, "Estimation of ice sheet topography and motion using interferometric synthetic aperture radar," Ph.D. dissertation, University of Washington, Washington, USA, 1995.
- [90] K. P. Papathanassiou and S. Cloude, "Single-baseline polarimetric SAR interferometry," *IEEE Trans. Geosci. Remote Sensing*, vol. 39, no. 11, pp. 2352–2363, Nov. 2001.
- [91] S. N. Madsen, *Synthetic Aperture Radar Interferometry: Principles and Applications*. Boston, MA: Artech House, 1999.
- [92] D. Carrasco, "SAR interferometry for digital elevation model generation and differential applications," Ph.D. dissertation, Remote Sensing Laboratory (RSLab), Universitat Politècnica de Catalunya, Barcelona, Spain, Mar. 1998.
- [93] O. Mora, "Advanced differential interferometric SAR techniques for detection of terrain and building displacements," Ph.D. dissertation, Remote Sensing Laboratory (RSLab), Universitat Politècnica de Catalunya, Barcelona, Spain, Apr. 2004.
- [94] B. Fruneau, J. Achache, and C. Delacourt, "Observation and modeling of the saint-etienne de tinee landslide using SAR interferometry," *Tectonophysics*, vol. 265, no. 3-4, pp. 181–190, 1996.
- [95] D. Massonet, T. Holzer, and H. Vadon, "Land subsidence caused by the east mesa geothermal field, california, observed using SAR interferometry," *Geophys. Res. Lett.*, vol. 24, no. 8, pp. 901–904, 1997.
- [96] E. J. Price and D. T. Sandwell, "Small-scale deformations associated with the 1992, lands, california, earthquake mapped by synthetic aperture radar interferometry phase gradients," *J. Geophys. Res.*, vol. 103, pp. 27 001–27 016, 1998.
- [97] R. Lanari, P. Lundgren, and E. Sansosti, "Dynamic deformation of etna volcano observed by satellite radar interferometry," *J. Geophys. Res.*, vol. 25, no. 10, pp. 1541–1543, 1998.

- [98] R. M. Goldstein and H. A. Zebker, "Interferometric radar measurement of ocean surface currents," *Nature*, vol. 328, pp. 707–709, 1987.
- [99] R. M. Goldstein, H. Engelhardt, B. Kamb, and R. M. Frolich, "Satellite radar interferometry for monitoring ice sheet motion: Application to an antarctic ice stream," *Science*, vol. 262, pp. 1525–1530, 1993.
- [100] E. Rodriguez and J. M. Martin, "Theory and design of interferometric synthetic aperture radars," in *Radar and Signal Processing, Proc. of IEEE*, vol. 139, no. 2, 1992, pp. 147–159.
- [101] C. Prati and F. Rocca, "Improving slant-range resolution with multiple SAR surveys," *IEEE Trans. Aerosp. Electron. Syst.*, vol. 29, no. 1, Jan. 1993.
- [102] F. Gatelli, A. Guarnieri, F. Parizzi, P. Pasquali, C. Prati, and F. Rocca, "The wavenumber shift in SAR interferometry," *IEEE Trans. Geosci. Remote Sensing*, vol. 32, no. 4, pp. 855–864, July 1994.
- [103] L. Sagues, "Surface and volumetric scattering analysis of terrains for polarimetric and interferometric SAR applications," Ph.D. dissertation, Remote Sensing Laboratory (RSLab), Universitat Politècnica de Catalunya, Barcelona, Spain, 2000.
- [104] R. Scheiber and A. Moreira, "Coregistration of interferometric SAR images using spectral diversity," *IEEE Trans. Geosci. Remote Sensing*, vol. 38, no. 5, pp. 2179–2191, July 2000.
- [105] S. Madsen, "On absolute phase determination techniques in SAR interferometry," in *Proc. IEEE SPIE on Radar Sensor Technology*, 1995, pp. 19–21.
- [106] A. Moreira and R. Scheiber, "A new method for accurate co-registration of interferometric SAR images," in *Proc. IEEE International Geoscience and Remote Sensing Symposium (IGARSS'98)*, vol. 2, 1998, pp. 1091–1093.
- [107] W. Xu and I. Cumming, "A region growing algorithm for InSAR phase unwrapping," *IEEE Trans. Geosci. Remote Sensing*, vol. 37, no. 1, pp. 124–134, Jan. 1999.
- [108] R. M. Goldstein, H. A. Zebker, and C. L. Werner, "Satellite radar interferometry: Two-dimensional phase unwrapping," *Radio Science*, vol. 23, no. 4, pp. 713–720, July 1988.
- [109] G. Fornaro, G. Franceschetti, and R. Lanari, "Interferometric SAR phase unwrapping using green's formulation," *IEEE Trans. Geosci. Remote Sensing*, vol. 34, no. 3, pp. 720–727, May 1996.
- [110] M. Bara, R. Scheiber, A. Broquetas, and A. Moreira, "Interferometric SAR signal analysis in the presence of squint," *IEEE Trans. Geosci. Remote Sensing*, vol. 38, no. 5, pp. 2164–2178, Sept. 2000.

- [111] M. Bara, "Airborne SAR interferometric techniques for mapping applications," Ph.D. dissertation, Remote Sensing Laboratory (RSLab), Universitat Politècnica de Catalunya, Barcelona, Spain, Sept. 2000.
- [112] J. A. Given and W. R. Schmidt, "Generalized ISAR-part I: An optimal method for imaging large naval vessels," *IEEE Trans. Image Processing*, vol. 14, no. 11, pp. 1783–1791, Nov. 2005.
- [113] D. R. Wehner, *High Resolution Radar*. Boston: Artech House, 1995.
- [114] V. C. Chen and S. Qian, "Joint time-frequency transform for radar range-doppler imaging," *IEEE Trans. Aerosp. Electron. Syst.*, vol. 34, no. 2, pp. 486–499, Apr. 1998.
- [115] F. Berizzi, E. D. Mese, M. Diani, and M. Martorella, "High-resolution ISAR imaging of maneuvering targets by means of the range instantaneous doppler technique: Modeling and performance analysis," *IEEE Trans. Image Processing*, vol. 10, no. 12, pp. 1880–1890, Dec. 2001.
- [116] L. Cohen, "Time-frequency distributions-a review," in *Proc. of IEEE*, vol. 77, July 1989, pp. 941–980.
- [117] W. Krattenthaler and F. Hlawatsch, "Time frequency design and processing of signals via smoothed wigner distributions," *IEEE Trans. Signal Processing*, vol. 41, pp. 288–295, Jan. 1993.
- [118] V. C. Chen, "Reconstruction of inverse synthetic aperture radar image using adaptive time-frequency wavelet transform," in *SPIE Proceedings on Wavelet Applications, 2491*, 1995, pp. 373–386.
- [119] J. A. Given and W. R. Schmidt, "Generalized ISAR-part II: Interferometric techniques for three-dimensional location of scatterers," *IEEE Trans. Image Processing*, vol. 14, no. 11, pp. 1792–1797, Nov. 2005.
- [120] G. Wang, X. Xia, and V. C. Chen, "Radar imaging of moving targets in foliage using multifrequency multiaperture polarimetric SAR," *IEEE Trans. Geosci. Remote Sensing*, vol. 41, no. 8, pp. 1755–1764, Aug. 2003.
- [121] K. Ouchi, "On the multilook images of moving targets by synthetic aperture radars," *IEEE Trans. Antennas Propagat.*, vol. 33, no. 8, pp. 823–827, Aug. 1985.
- [122] K. Tomiyasu, "Tutorial review of synthetic-aperture radar (SAR) with applications to imaging of the ocean surface," in *Proc. of IEEE*, vol. 66, no. 5, May 1978, pp. 563–587.
- [123] G. Sinclair, "The transmission and reception of elliptically polarized waves," in *Proceedings of IRE*, vol. 38, no. 2, 1950, pp. 148–151.

- [124] E. M. Kennaugh, "Polarization properties of radar reflections," Ph.D. dissertation, Ohio State University, Columbus, USA, Mar. 1952.
- [125] G. A. Deschamps, "Geometrical representation of the polarization of a plane electromagnetic wave," in *Proceedings of IRE*, vol. 39, no. 4, 1951, pp. 540–544.
- [126] G. A. Deschamps and P. E. Mast, "Poincaré sphere representation of partially polarized fields," *IEEE Trans. Antennas Propagat.*, vol. 21, pp. 474–478, July 1973.
- [127] M. L. Kales, "Elliptically polarized waves and antennas," in *Proceedings of IRE*, vol. 39, no. 4, 1951, pp. 544–549.
- [128] C. D. Graves, "Radar polarization power scattering matrix," in *Proceedings of IRE*, vol. 44, 1956, pp. 248–252.
- [129] S. H. Bickel, "Some invariant properties of the polarization scattering matrix," in *Proceedings of IRE*, vol. 53, 1965, pp. 1070–1072.
- [130] J. R. Huynen, "Phenomenological theory of radar targets," Ph.D. dissertation, Technical University, Delft, The Netherlands, 1970.
- [131] J. R. Copeland, "Radar target classification by polarization properties," in *Proceedings of IRE*, vol. 48, 1960, pp. 1290–1296.
- [132] S. Chandrasekhar, *Radiative Transfer*, Dover, UK, 1960.
- [133] W. M. Boerner, M. B. El-Arini, C.-Y. Chan, and P. M. Mastoris, "Polarization dependence in electromagnetic inverse problems," *IEEE Trans. Antennas Propagat.*, vol. 29, pp. 262–271, Mar. 1981.
- [134] J. J. van Zyl, H. A. Zebker, and C. Elachi, "Imaging radar polarization signatures," *Radio Science*, vol. 22, pp. 529–543, July 1987.
- [135] W. M. Boerner and et al., "Inverse methods in electromagnetic imaging," in *NATO ASI Series C, Math. and Phys. Science*, Kluwer Academic Publishers, Netherlands, 1992.
- [136] E. Lüneburg, "Aspects of radar polarimetry," *Turk Journal of Electric Engineering*, vol. 10, no. 02, pp. 219–243, 2002.
- [137] W. M. Boerner and et al., "Radar polarimetry and interferometry," in *NATO RTO Lecture Series SET-081 (RTO-EN-SET-081)*, 2004.
- [138] F. T. Ulaby and C. Elachi, *Radar Polarimetry for Geoscience Applications*. Norwood, MA: Artech House, 1990.
- [139] C.-Y. Chan, "Studies on the power scattering matrix of radar targets," Ph.D. dissertation, University of Illinois, Chicago, USA, 1981.

- [140] A.-Q. Xi and W.-M. Boerner, "Determination of characteristic polarization states of the target scattering matrix for the coherent monostatic and reciprocal propagation space using the polarization transformation ratio formulation," in *JOSA-A/2*, 9(3), 1992, pp. 437–455.
- [141] J. Yang, Y.-M. Peng, and S.-M. Lin, "Similarity between two scattering matrices," *Electronic Letters*, vol. 37, no. 3, pp. 193–194, Feb. 2001.
- [142] J. R. Huynen, "Measurements of the target scattering matrix," Aug. 1965, pp. 936–946.
- [143] E. Krogager, "Decomposition of the radar target scattering matrix with application to high resolution target imaging," 1991, pp. 77–82.
- [144] X. Fabregas, "Localization and classification of polarimetric scattering centers within complex targets by means of radar imagery," Ph.D. dissertation, Remote Sensing Laboratory (RSLab), Universitat Politècnica de Catalunya, Barcelona, Spain, 1995.
- [145] W. L. Cameron and L. K. Leung, "Feature motivated polarization scattering matrix decomposition," in *Proc. IEEE International Radar Conference*, vol. 2, 1990, pp. 549–557.
- [146] J. J. van Zyl and F. T. Ulaby, *Scattering matrix representation for simple targets*. Norwood, MA: in -Radar Polarimetry for Geoscience Applications- (F. T. Ulaby and C. Elachi, Eds), ch. 2, pp: 17-50, Artech House, 1991.
- [147] J. W. Goodman, *Laser Speckle and Related Phenomena*. New York, USA: J. C. Dainty, Ed., 1975.
- [148] R. Touzi and K. Raney, "Effect of doppler centroid mis-tracking on the parameter estimation of point target complex signals," in *Proc. IEEE International Geoscience and Remote Sensing Symposium (IGARSS'94)*, Pasadena, CA, USA, 1994.
- [149] G. Margarit, P. Blanco, J. Sanz, and J. J. Mallorqui, "Orbital SAR simulator of fishing vessel polarimetric signatures based on high frequency electromagnetic calculations," in *Proc. IEEE of Geoscience and Remote sensing Symposium, (IGARSS'03)*, vol. 7, July 2003, pp. 4459–4461.
- [150] G. Margarit, P. Blanco, J. Sanz, J. J. Mallorqui, and J. M. Rius, "Simulation of fishing vessel polarimetric signatures as first step to vessel classification," in *Proc. SPIE of International Symposium Remote Sensing Europe (SPIE'03)*, vol. 8, Sept. 2003, pp. –.
- [151] G. Margarit, X. Fabregas, J. J. Mallorqui, L. Pipia, and T. Broquetas, "Polarimetric SAR interferometry simulator of complex targets," in *Proc. IEEE of Geoscience and Remote sensing Symposium (IGARSS'05)*, Aug. 2005.



- [152] J. Sanz, P. Prats, and J. Mallorqui, "Platform and mode independent sar data processor based on the extended chirp scaling algorithm," in *Proc. IEEE International Geoscience and Remote Sensing Symposium (IGARSS'03)*, vol. 6, July 2003, pp. 4086–4088.
- [153] A. L. Maffet, *Topics for a Statistical Description of Radar Cross Section*. New York: Wiley, 1989.
- [154] E. F. Knott, J. F. Shaeffer, and M. T. Tuley, *Radar Cross Section*. New York: Artech House, 1985.
- [155] J. M. Rius, "Sección recta de blancos radar complejos en tiempo real," Ph.D. dissertation, Remote Sensing Laboratory (RSLab), Universitat Politècnica de Catalunya, Barcelona, Spain, July 1991.
- [156] J. M. Rius and et al., "Discretization errors in the graphical computation of physical optics surface integral," *Applied Computational Electromagnetics Society (ACES) Journal*, vol. 13, no. 3, pp. 255–263, Nov. 1998.
- [157] *Standardized Wave and Wind Environments and Shipboard Reporting of Sea Conditions, NATO STANAG 4194, ED 1 AMD 5*, Manual of; North Atlantic Treaty Organization (NATO).
- [158] *GRECO*. Available at: [UPC's RSLab web page](#), Manual of; Remote Sensing Laboratory (RSLab) of UPC.
- [159] *GID: [Online]* Available at: [GID web page](#), Manual of; International Center for Numerical Methods in Engineering (CIMNE).
- [160] J. E. Prussing and B. A. Conway, *Orbital Mechanics*. New York, USA: Oxford University Press, 1993.
- [161] H. Laur, P. Meadows, J. I. Sanchez, and E. Dwyer, "ERS-1 SAR radiometric calibration," in *Proceedings of the CEOS SAR Calibration Workshop (ESA WPP-048)*. [Online] Available at: [ESA web page](#), Sept. 1993.
- [162] G. Margarit, X. Fabregas, J. J. Mallorqui, and T. Broquetas, "Analysis of the limitations of coherent polarimetric decompositions on vessel classification using simulated images," in *Proc. IEEE of Geoscience and Remote sensing Symposium (IGARSS'04)*, vol. 4, Sept. 2004, pp. 2483–2486.
- [163] G. Margarit, X. Fabregas, and J. J. Mallorqui, "Study of the influence of vessel motions and sea-ship interaction on classification algorithms based on single-pass polarimetric sar interferometry," in *Proc. IEEE of Geoscience and Remote sensing Symposium (IGARSS'06)*, Aug. 2006.

- [164] R. K. Hawkins, K. P. Murnaghan, M. Jeremy, and M. Rey, "Ship detection using airborne polarimetric SAR," in *Proc. CEOS SAR Workshop*, 2001.
- [165] G. Margarit, J. J. Mallorqui, and X. Fabregas, "Tri-dimensional vessel classification patterns inferred via single-pass polarimetric SAR interferometry," in *Proc. ESA of SEASAR workshop*, Jan. 2006.
- [166] G. Margarit, X. Fabregas, and J. J. Mallorqui, "On the usage of polarimetric SAR across-track interferometry for vessel classification," in *Proc. IEEE of European SAR Symposium (EUSAR'06)*, May 2006.
- [167] G. Margarit, J. J. Mallorqui, and X. Fabregas, "Single-pass polarimetric SAR interferometry for vessel classification," *IEEE Trans. Geosci. Remote Sensing*, Accepted to the EUSAR Special Issue.
- [168] G. Margarit, X. Fabregas, and J. J. Mallorqui, "Ship classification performance in single-pass polarimetric SAR interferometry: Evaluation of the sea interaction," in *Proc. ESA of POLINSAR workshop*, Jan. 2007.
- [169] G. Zilman, A. Zapolski, and M. Marom, "The speed and beam of a ship from its wake's SAR images," *IEEE Trans. Geosci. Remote Sensing*, vol. 42, no. 10, pp. 2335–2343, Oct. 2004.
- [170] R. Zandoná, K. P. Papathanassiou, I. Hajnsek, and A. Moreira, "Polarimetric and interferometric characterization of coherent scatters in urban areas," *IEEE Trans. Geosci. Remote Sensing*, vol. 44, no. 4, pp. 971–984, Apr. 2006.
- [171] E. Colin, C. Titin-Schnaider, and W. Tabbara, "An interferometric coherence optimization method in radar polarimetry for high-resolution imagery," *IEEE Trans. Geosci. Remote Sensing*, vol. 44, no. 1, pp. 167–175, Jan. 2006.
- [172] M. Werner, "Shuttle radar topography mission (srtm): experience with the X-band SAR interferometer," in *Proc. of the CIE International Conference on Radar*, Oct. 2001, pp. 634–638.
- [173] S. Hensley, P. Rosen, and E. Gurrola, "The SRTM topographic mapping processor," in *Proc. IEEE of Geoscience and Remote sensing Symposium (IGARSS'00)*, vol. 3, July 2000, pp. 1168–1170.
- [174] M. Zink, H. Fiedler, I. Hajnsek, G. Krieger, A. Moreira, and M. Werner, "The TanDEM-X mission concept," in *Proc. IEEE International Geoscience and Remote Sensing Symposium (IGARSS'06)*, 2006.
- [175] *TerraSAR-X Ground Segment. Basic Product Specification Document. CAF, Cluster Applied Remote Sensing. Ref. TX-GS-DD-3302*, DLR.

- 
- [176] *TerraSAR-X Ground Segment: [Online] Available at: [DLR's Documentation web page](#), Manual of;* Deutsche Forschungsanstalt für Luft- und Raumfahrt (DLR).
- [177] M. Eineder, H. Runge, E. Boerner, R. Bamler, N. Adam, B. Schättler, H. Breit, and S. Suchandt, "SAR interferometry with TerraSAR-X," in *Proc. ESA of FRINGE workshop*, Dec. 2003.
- [178] *Effects of RF Interference on Radar Receivers, NTIA Report TR-06-444 [Online]. Available at: [ITS publication service](#), Institute for Telecommunication Sciences, National Telecommunication and Information Administration (NTIA) (of the U.S. Department of Commerce), Boulder, Colorado.*